


2016

Sulfur-induced structural motifs on copper and gold surfaces

Holly Walen
Iowa State University

Follow this and additional works at: <https://lib.dr.iastate.edu/etd>

 Part of the [Analytical Chemistry Commons](#), [Condensed Matter Physics Commons](#), and the [Physical Chemistry Commons](#)

Recommended Citation

Walen, Holly, "Sulfur-induced structural motifs on copper and gold surfaces" (2016). *Graduate Theses and Dissertations*. 15212.
<https://lib.dr.iastate.edu/etd/15212>

This Dissertation is brought to you for free and open access by the Iowa State University Capstones, Theses and Dissertations at Iowa State University Digital Repository. It has been accepted for inclusion in Graduate Theses and Dissertations by an authorized administrator of Iowa State University Digital Repository. For more information, please contact digirep@iastate.edu.

Sulfur-induced structural motifs on copper and gold surfaces

Holly Walen

A dissertation submitted to the graduate faculty
in partial fulfillment of the requirements for the degree of
DOCTOR OF PHILOSOPHY

Major: Analytical Chemistry

Program of Study Committee:

Patricia A. Thiel, Major Professor
James W. Evans
R. S. Houk
Emily A. Smith
Wenyu Huang

Iowa State University
Ames, Iowa
2016

Copyright © Holly Walen, 2016. All rights reserved.

Dedicated to my mother.

TABLE OF CONTENTS

	Page
ABSTRACT.....	xi
CHAPTER I. GENERAL INTRODUCTION	1
1. Motivation.....	1
1.1 Metal transport	1
1.2 SAMs on Au surfaces	2
2. Methods and Materials.....	3
2.1 Experimental methods	3
2.2 Materials	4
2.3 Data analysis	6
3. Dissertation Organization	7
Figures.....	8
References	14
CHAPTER II. Cu_2S_3 ON $\text{Cu}(111)$ AS A CANDIDATE FOR MASS TRANSPORT ENHANCEMENT	19
Abstract	19
1. Introduction.....	20
2. Experimental and computational details.....	21
3. Identification of a Cu_2S_3 complex from STM and DFT	22
4. Factors that stabilize Cu-S complexes	26

5. Role of Cu_2S_3 complexes in Cu mass transport	29
6. Conclusions.....	31
Acknowledgements.....	32
Figures	33
Appendix 1. STM imaging conditions	39
Appendix 2. Additional experimental data	39
References	46

CHAPTER III. SULFUR-INDUCED STRUCTURES AT STEPS

ON THE $\text{Cu}(111)$ SURFACE.....	50
Abstract	50
1. Introduction.....	51
2. Experimental and computational details.....	52
2.1 Experimental description	52
2.2 Computational Description	55
3. Experimental Results	55
3.1 Overview of Features on Terraces and Steps.....	55
3.2 STM Examination of Features at and near Step Edges.....	57
4. DFT Analysis of Features at and near Step Edges	59
4.1 Benchmark: Sulfur Adsorbed on Terraces.....	59
4.2 Extended Structures at Step Edges	60
4.3 Triangular Features on B-steps	64
5. Discussion	66

6. Conclusions.....	69
Acknowledgements	69
Figures	71
Appendix 1. Additional Structures Studied with DFT	83
Appendix 2. Additional STM Information	90
Appendix 3. Additional Analysis of Terrace Features.	91
References	98
CHAPTER IV. CHEMISORPTION OF S ATOMS ON	
CU(100) AT LOW COVERAGE.....	
CU(100) AT LOW COVERAGE.....	102
Abstract	102
1. Introduction.....	102
2. Experimental Description	103
3. Results	104
3.1 Chemisorption on Terraces.....	104
3.2 Step Edges.....	106
4. Discussion.....	107
4.1 Bias Dependence of S Appearance in STM.....	107
4.2 Comparison to S/Ag(100)	108
4.3 Comparison to Cu(111) Under Identical Experimental Conditions	110
5. Conclusions.....	110
Acknowledgements.....	111
Figures	112
Appendix 1. Tunneling Conditions.....	119

References	120
CHAPTER V. SELF-ORGANIZATION OF S ADATOMS ON AU(111):	
$\sqrt{3}R30^\circ$ ROWS AT LOW COVERAGE.....	127
Abstract	127
1. Introduction.....	128
2. Experimental and Computational Details	129
2.1 Experimental Description	129
2.2 Computational Description	131
3. Experimental Results	132
4. Theoretical and Computational Results	134
4.1 Overview: Purpose and Approach	134
4.2 DFT Results	135
4.3 Lattice-gas Models.....	139
4.4 Monte Carlo Simulations based on the Lattice-Gas Hamiltonians.....	143
5. Discussion.....	144
6. Conclusions.....	148
Acknowledgements.....	148
Figures	150
Appendix 1. STM Data.....	156
Appendix 2. Additional DFT information	164
Appendix 3. Sample bias effect on appearance	172
References	173

CHAPTER VI. LARGE-SCALE DISPLACIVE RECONSTRUCTION OF AU(110)

TRIGGERED BY LOW COVERAGE OF SULFUR	180
Abstract	180
1. Introduction.....	181
2. Experimental and Computational details	185
2.1 Experimental Description	185
2.2 Computational Description	186
3. Experimental and Computational Results.....	187
3.1 Overview.....	187
3.2 Chemisorbed Phase: Sulfur on the (1x2) Au Reconstructed Surface	188
3.3 c(4x2) Phase.....	194
4. Discussion	198
5. Conclusions	202
Acknowledgements	203
Figures	204
Appendix 1. Tunneling conditions for images in the main text.....	215
Appendix 2. Details about definition and implementation of chemical potential, μ , and formation energy, E_f	216
Appendix 3. Summary of μ_S^u values for additional S-Au structures studied with DFT	217
Appendix 4. Bias effect on S_{ad} height and area	223
References	224
CHAPTER VII. IDENTIFICATION OF AU-S COMPLEXES ON AU(100)	229
Abstract	229

1. Introduction.....	230
2. Experimental and computational details.....	232
2.1 Experimental Description	232
2.2 Computational Description.....	233
3. Results	235
3.1 Clean Surface	235
3.2 Features associated with chemisorbed sulfur.....	235
3.3 Au-S Complexes	238
3.4 Mass balance on terraces	242
4. Discussion.....	243
5. Conclusions.....	248
Acknowledgements.....	248
Figures	250
Appendix 1. Tunneling conditions for STM images in the main text	263
Appendix 2. Details of determining Au mass balance.....	264
Appendix 3. Additional DFT analysis	264
References	271
CHAPTER VIII. EVIDENCE OF CU-SE STRUCTURES ON CU(111)	
AT LOW COVERAGE	278
Abstract	278
1. Introduction.....	279
2. Experimental and computational details.....	280

2.1 Experimental Conditions	280
2.2 Computational Description	282
3. Results	282
3.1 Experimental Results	282
3.2 Computational Results	284
4. Discussion	292
5. Conclusions	295
Acknowledgements	295
Figures	297
Appendix 1.	306
References	334
APPENDIX I. SEARCH FOR THE STRUCTURE OF A SULFUR-INDUCED RECONSTRUCTION ON CU(111).....	338
APPENDIX II. PRELIMINARY DATA FOR S ADSORPTION ON PD(111) AND PT(111)	360
APPENDIX III. DETERMINATION OF S COVERAGE ON SILVER SURFACES	380
APPENDIX IV. MODIFICATION OF THE <i>IN SITU</i> EVAPORATOR FOR SE DEPOSITION.....	386
APPENDIX V. OBSERVED S AND S-M SPECIES HEIGHT AND WIDTH IN STM	394
APPENDIX VI. EXPERIMENTAL DATABASE.....	395

ACKNOWLEDGEMENTS 402

ABSTRACT

The interaction of sulfur with copper and gold surfaces plays a fundamental role in important phenomena that include coarsening of surface nanostructures, and self-assembly of alkanethiols. Here, we identify and analyze unique sulfur-induced structural motifs observed on the low-index surfaces of these two metals. We seek out these structures in an effort to better understand the fundamental interactions between these metals and sulfur that leads to the stability and favorability of metal-sulfur complexes vs. chemisorbed atomic sulfur.

We choose very specific conditions: very low temperature (5 K), and very low sulfur coverage (≤ 0.1 monolayer). In this region of temperature-coverage space, which has not been examined previously for these adsorbate-metal systems, the effects of individual interactions between metals and sulfur are most apparent and can be assessed extensively with the aid of theory and modeling. Furthermore, at this temperature diffusion is minimal and relatively-mobile species can be isolated, and at low coverage the structures observed are not consumed by an extended reconstruction. The primary experimental technique is scanning tunneling microscopy (STM).

The experimental observations presented here—made under identical conditions— together with extensive DFT analyses, allow comparisons and insights into factors that favor the existence of metal-sulfur complexes, vs. chemisorbed atomic sulfur, on metal terraces. We believe this data will be instrumental in better understanding the complex phenomena occurring between the surfaces of coinage metals and sulfur.

CHAPTER I

GENERAL INTRODUCTION

1. Motivation

We are interested in studying the coinage metals copper, silver, and gold, due to their interesting plasmonic¹ and catalytic²⁻⁴ properties especially in the form of nanoparticles. In addition, alkanethiol self-assembled monolayers (SAMs) on gold surfaces and nanoparticles have interesting biological,⁵ electronic,⁶ and tribological applications.⁷ In the context of these properties, sulfur is an important adsorbate: sulfur is known to enhance metal transport, and sulfur-gold bonding guides the formation of SAMs on gold surfaces.

1.1 Metal transport

Adsorbates on metal surfaces may induce several different changes in the metal structure, including faceting of step edges, coarsening of metal structures, pitting, and reconstruction. All of these effects are due to the movement of metal atoms along the surface. Metal mass transport is especially important in the field of heterogeneous catalysis, where dynamic restructuring of the metal influences the effectiveness of a catalyst.⁸ Adsorbate effects are coverage and temperature dependent.

For example, on both Ag(111) and Cu(111), small amounts of sulfur (< 0.1 ML, monolayer, where 1 ML is defined as a 1:1 ratio of S:M atoms on the surface) increase the movement of metal atoms by several orders of magnitude at or near room temperature.⁹⁻¹¹ Metal transport on these surfaces, in the absence of adsorbates, occurs via adatom diffusion by hopping between binding sites, or by exchange with the substrate atoms.¹² Enhanced

transport in the presence of sulfur has been interpreted to mean that a sulfur-metal molecule on the surface (hereafter referred to as a “S-M complex”) is mediating metal movement rather than a metal adatom.¹³ Such complexes are predicted to have higher stability, and therefore population, though the diffusion barrier is moderately higher compared to a metal adatom.¹³ The structure of these complexes, however, is difficult to study due to their small size (generally a few atoms) and their high mobility at typical experimental conditions.

1.2 SAMs on Au surfaces

Molecular self-assembly can be found in supramolecular systems (micelles, liquid crystal phases), biological systems (DNA, lipid bilayers or membranes) as well as nanotechnology.¹⁴ Self-assembly is an important aspect of the bottom-up approach for fabrication of nanomaterials.¹⁵

SAMs form by the long-range spontaneous ordering of organic molecules attached to a surface by a functional group. The most extensively studied SAMs are those of alkanethiols on Au(111) and Au(100), where the S-Au bond creates a metal-organic interface.

While this system has been studied in depth, the structure of the S-Au interface is still under debate. Briefly, there are two major schools of thought.¹⁶⁻¹⁸ Upon adsorption of alkanethiols, the reconstructed Au(111) surface ejects Au adatoms which are mobile at ambient temperatures. One model proposes that these Au adatoms are incorporated into the SAM, forming a linear S-Au-S “staple” motif at the surface.¹⁹ The other proposes that ejected Au atoms are not incorporated by the SAM, and that the binding geometry is strictly mediated by chemisorption of S to the surface.²⁰ At low coverage, there is strong microscopic evidence of the staple structure for several alkanethiols deposited in UHV.²¹⁻²² However,

microscopic studies of the S-M interface at high coverage are complicated by the upright orientation of the SAM molecules, so it is unclear which of these models best represents the structure at a full monolayer.²³

The primary goal of this dissertation is to investigate and describe the fundamental favorable S-M bonding motifs and complexes under conditions of low sulfur coverage and low temperature (5 K). We utilize such experimental conditions to isolate small S-M complexes and immobilize these potentially mobile species. Dr. Da-Jiang Liu of the Ames Laboratory has collaborated with us on all of our work, performing calculations with the targeted goal of explaining the experimental results. This experimental and theoretical combination has led to fascinating new insight into S-M bonding.

2. Methods and Materials

2.1 Experimental methods

The primary tool for experimental analysis is low-temperature scanning tunneling microscopy (LT-STM). In STM, an atomically sharp metal tip is brought within a fraction of a nanometer of an electrically conducting sample, overlapping the electron wavefunctions of the tip apex and sample.²⁴ A net current of electrons tunnels in one direction between the tip apex and sample when a potential difference is applied. An electronic feedback loop maintains constant current as the tip scans laterally, moving the tip vertically as it encounters different surface features. The resulting data is a three-dimensional map of the contour of electron density at the surface, integrated over a narrow window of energies. This contour map allows us to visualize features on the surface down to the sub-atomic level.

In our experiments, sulfur is deposited via an *in situ* electrochemical Ag|AgI|Ag₂S|Pt cell.²⁵ The cell is made up of a Ag plate, two chemical pellets, and a Pt wire. Cell components are held in a quartz tube with several W springs to maintain contact and promote current flow during cell operation. The cell vapor has been characterized in the literature,²⁶⁻²⁷ and thus we choose operating conditions such that the primary product is S₂(g). The vapor composition is checked prior to experiments using a mass spectrometer mounted on the chamber opposite the evaporator. More detail about the evaporator hardware can be found in Ref. ²⁸, and details of operation can be found in Ref. ²⁹.

The experiments are executed at the RIKEN Institute in Wako, Saitama, Japan in ultrahigh vacuum (UHV, pressure < 10⁻⁹ Torr). Preparing and performing experiments in UHV conditions allows us to limit the amount of contamination on a surface, as well as carefully control the identity and quantity of a desired adsorbate. The UHV chamber has two primary components, the preparation chamber and the STM chamber, separated by a gate valve (Figure 1). Metal samples are cleaned in the preparation chamber (P < 10⁻⁹ Torr) by Ar⁺ sputtering and annealing cycles, and the cleanliness of the surface is determined in the LT-STM (P ~ 10⁻¹¹ Torr). Transferring the sample between chambers takes about 5 minutes. Sulfur deposition is performed in the preparation chamber with the sample held at room temperature, followed by quenching to 5K for imaging. Temperature equilibration in the LT-STM stage takes ~50 minutes from room temperature.

2.2 Materials

Our experiments are conducted with single-crystal samples, mounted on a single Ta plate that fits in the STM stage.

Most face centered cubic metals, like Cu, present low-index (111), (100), and (110) surfaces (Fig. 2), when cut down the primary crystallographic planes. Cu(111) has hexagonal symmetry. The terraces present two different three-fold hollow (3fh) sites, the “fcc” and the “hcp”, designated by their stacking relative to the 1st layer beneath the surface. In addition, the (111) surface presents two types of close-packed step edge geometries. One is a (100)-microfacet made up of pseudo-4fh sites, and the other is a (111)-microfacet made up of pseudo-3fh sites. Clean binding sites on terraces and step edges are indistinguishable in STM. Cu(100) has square symmetry, and terraces present 4fh adsorption sites. The close-packed step edges present a (111)-microfacet.

Cut along the same planes, Au surfaces reconstruct in UHV. The low-index Au reconstructions are shown in Fig. 3. Au(111) presents the $(22 \times \sqrt{3})$ herringbone reconstruction; the Au(100) presents the “hex” reconstruction. Both of these reconstructions are a pseudo-hexagonal arrangement, increasing the packing density in the surface layer. This results in excess Au atoms in the surface relative to the bulk layers, with 1.04 ML of Au in the Au(111) herringbone,³⁰ and ~1.25 ML of Au in the Au(100)-hex.³¹ Adsorbates have been shown to lift the herringbone and hex reconstructions, restoring the bulk-terminated 3fh and 4fh terrace sites, respectively.³²⁻³³ This process releases the excess gold, which may migrate to the step edges,³⁴ or form Au islands.³² Au(110) forms a (1×2) missing row reconstruction, where the inner faces of the rows resemble a (111)-microfacet.³⁵

2.3 Data analysis

STM images were collected using Omicron Scala software, and processed and analyzed using WSxM software, which is open-access.³⁶ Numerical analyses were performed in Microsoft Excel.

In WSxM, I typically use local or global planing and the derivative functions to prepare images for presentation. The plane function fits a portion (local) or all (global) of an image to a plane, which is then subtracted. This filtering method preserves relative height information of features. The derivative function calculates the derivative of the vertical displacement (z , perpendicular to the surface) along the x -axis. This function enhances the edges of a feature, making it easier to discern the shape of something particularly short or near a step edge. Two-dimensional Fast Fourier Transform (FFT) filtering was occasionally used to subtract periodic noise.

A brief description of how the STM piezo calibration was determined is given in Fig. 4, and examples of some other measurements are shown in Fig. 5.

Sulfur coverage was usually determined by counting the S atoms in all images and dividing by the calculated number of metal surface atoms in the corresponding total area. In cases where S-M reconstructions formed, the areal coverage was used. Areal coverage was determined using the flooding function in WSxM for S-M species, and then dividing by the image area (Fig. 5). This was done for S/Cu(111), where we observed the $\sqrt{43}$ reconstruction.³⁷ For that system, absolute coverage relative to areal coverage could be approximated using the work of Wahlström *et al.*³⁸⁻³⁹ as a reference.

3. Dissertation Organization

This dissertation includes six published papers: Chapters II, III, V, VI, VII, and Appendix I. We are currently preparing to submit Chapters IV and VIII for review.

Chapters II – IV and Appendix I describe the results of sulfur adsorption on Cu(111) and Cu(100). Chapters V – VII describe sulfur adsorption on Au(111), Au(110), and Au(100).

The results of Se deposition on Cu(111) are described in Chapter VIII. The sulfur evaporator used at RIKEN was developed by Selena M. Russell.²⁸ The sulfur evaporator was modified to deposit Se₂(gas) with minor changes to the evaporator set-up, and by altering my settings for operation per Keller *et al.*⁴⁰ Details of converting the evaporator can be found in Appendix IV.

Preliminary data for sulfur adsorption on Pd(111) and Pt(111) are summarized in Appendix II.

A summary of the dimensions for all identified S-species on all substrates described within this thesis can be found in Appendix V.

Appendix VI contains the experimental database, describing each experiment performed at RIKEN, including settings for S deposition and experimental data file names.

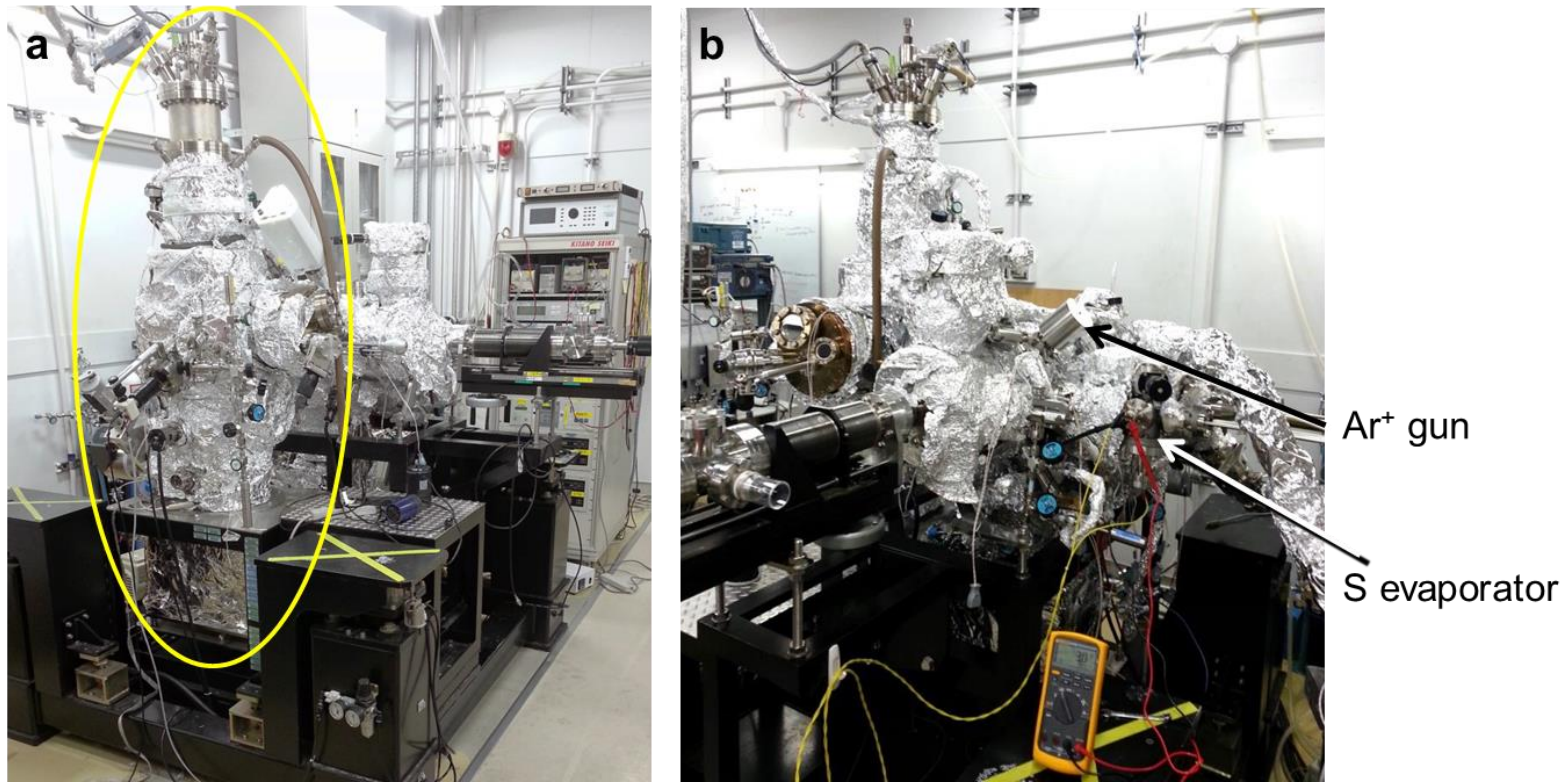


Figure 1. Pictures of the chamber at RIKEN. a) Low temperature STM chamber (highlighted in yellow). B) Preparation chamber with the Ar⁺ gun and S evaporator highlighted.

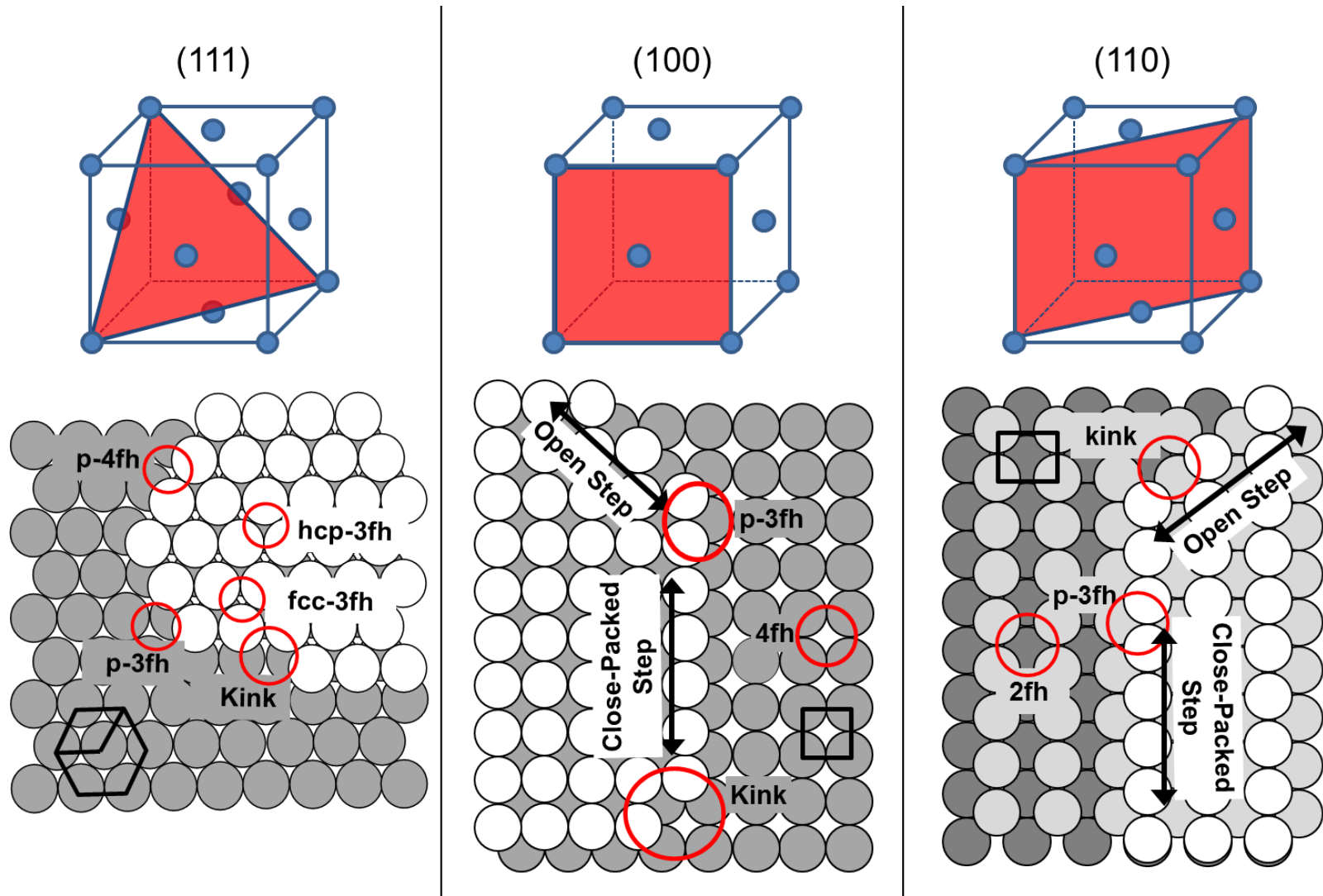


Figure 2. Top row: Low-index planes of a face centered cubic crystal, indicated in red. Bottom row: Corresponding schemes of the low-index surfaces, with the labelled binding sites.

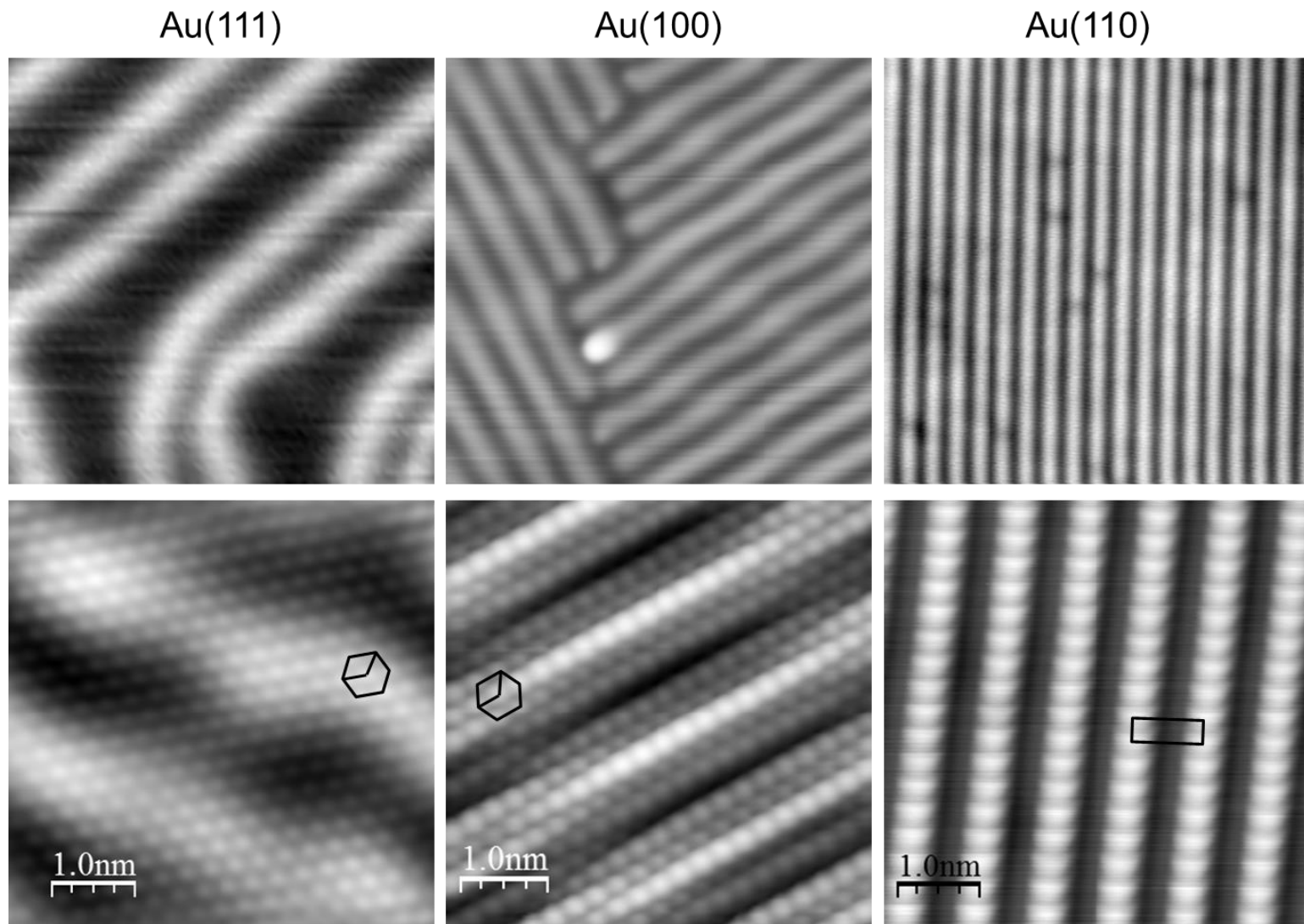


Figure 3. STM images of the low-index Au reconstructions. *Top row:* All 15 x 15 nm². *Bottom row:* Atomic resolution images with the unit cell outlined; all 5 x 5 nm².

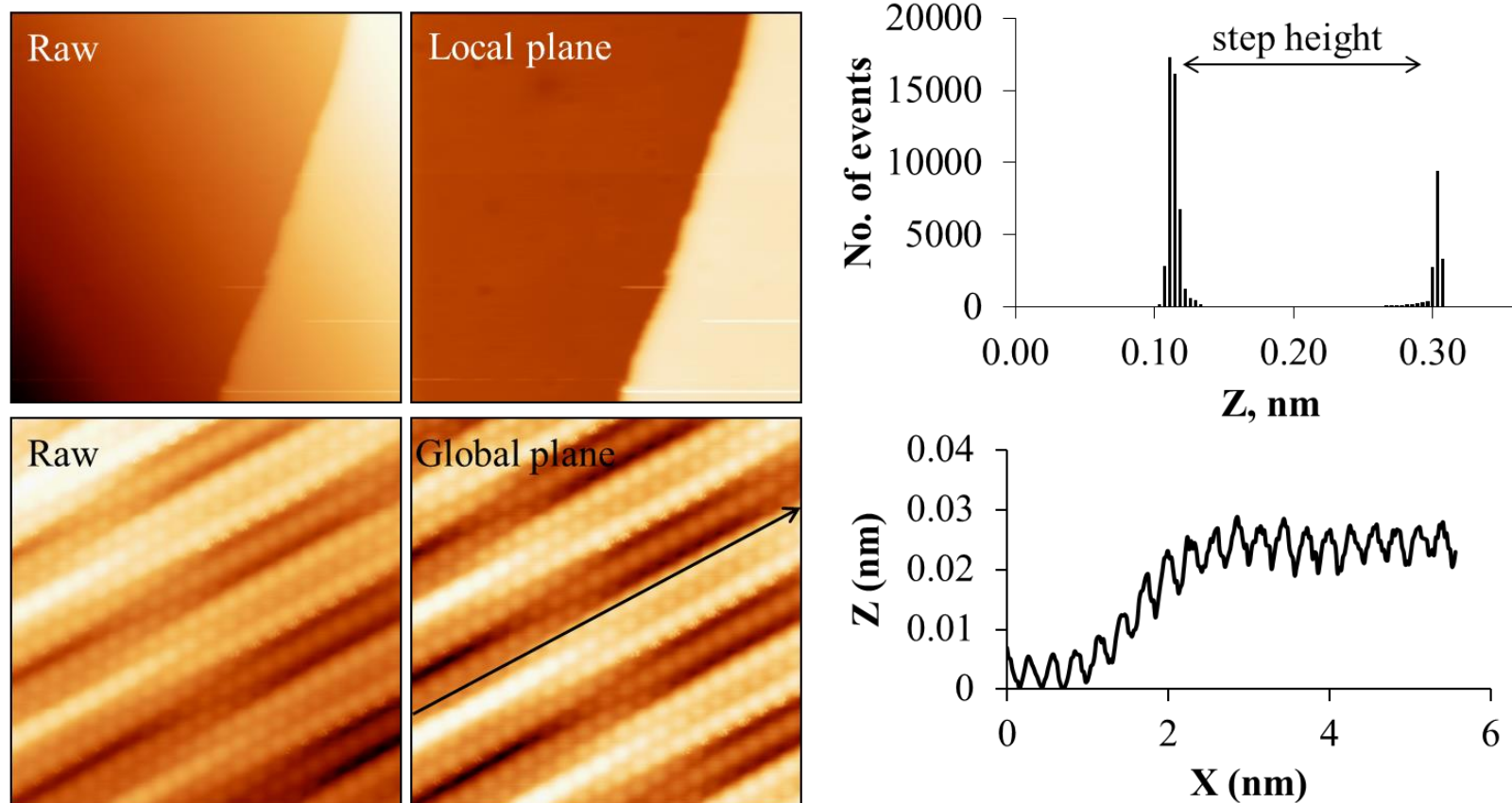


Figure 4. Determining STM piezo calibration using images. *Top row:* Step height analysis on Cu(111). The raw image is first filtered using the local plane function (both $50 \times 50 \text{ nm}^2$). The roughness analysis function is used to find the average step height for the entire image, which is taken as the separation between peaks. *Bottom row:* Atomic lattice spacing on Au(100). Raw and planed images are $5 \times 5 \text{ nm}^2$. After using the global plane function, we use line profiles along all close-packed directions (one is shown on the far right) to determine the average periodicity, which is interpreted as the measured lattice spacing.

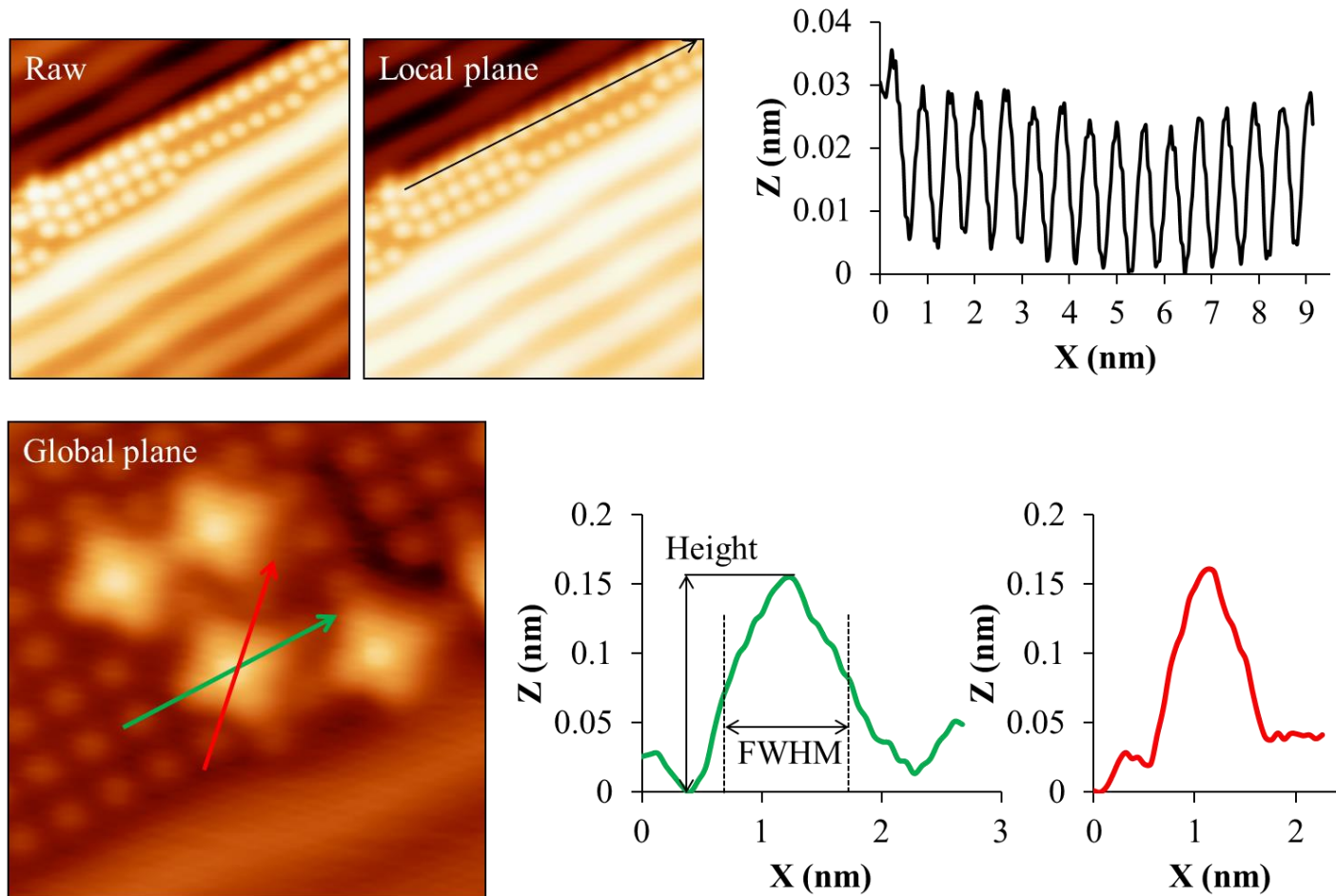


Figure 5. Typical measurements of S-induced features. *Top row:* Ordered structures, or decoration along step edges. The separation between sulfur atoms in an ordered structure is determined much like the atomic separation. The separation distance is taken as the average periodicity of the line profile. *Bottom row:* Height and width measurements are also taken using line profiles, shown in green and red. Height is measured from the lowest point adjacent to the feature, to the tallest point at the center. Width is measured as the full width at half the maximum (FWHM). (continued on next page)

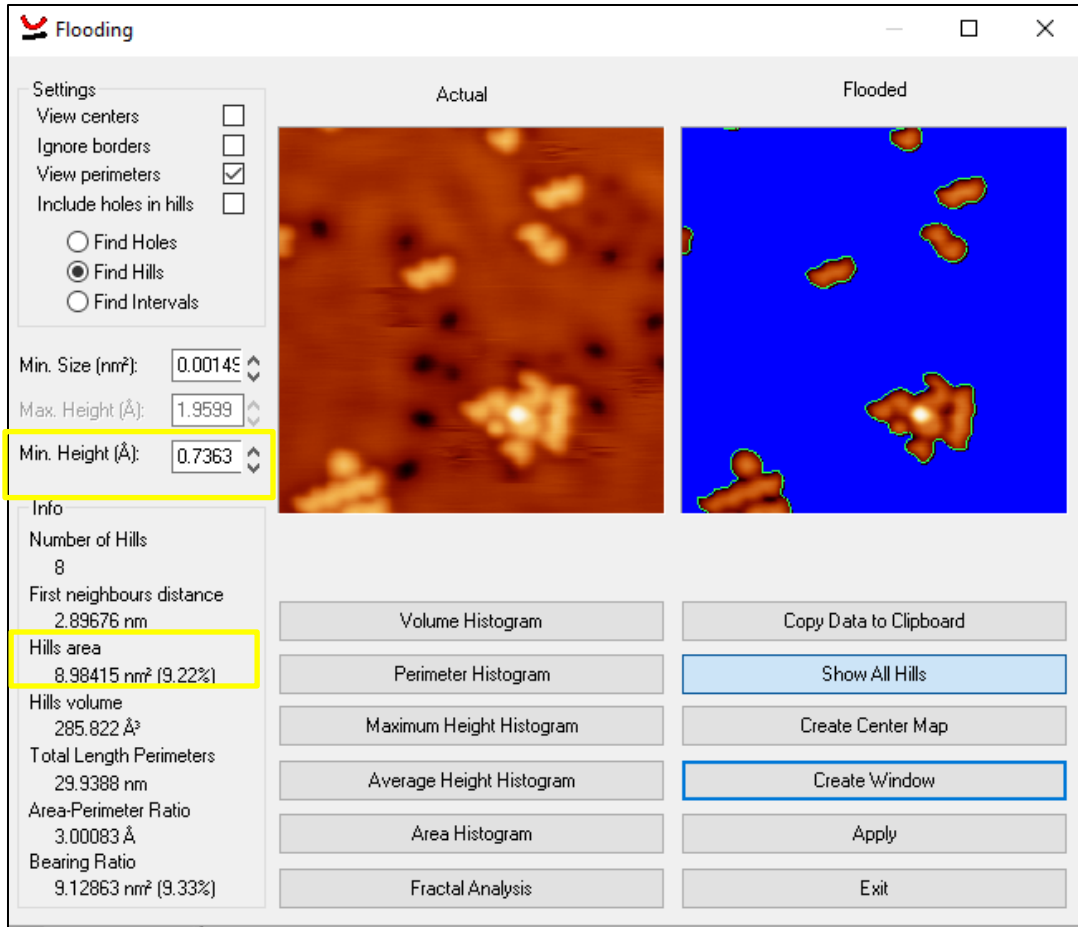


Figure 5(continued). Area is measured using the flooding function, after the image is planed. This function is useful for taking the area of individual features, or determining areal coverage on single terraces (shown above). “Find Hills” tells the function to look for features taller than the terrace, and the minimum height is selected to be at or near half the maximum height. The “Hills area” value is recorded, and the sum of the Hills area for all images divided by the total area for all images is the areal coverage.

References

1. Jain, P. K.; Huang, X.; El-Sayed, I. H.; El-Sayed, M. A., "Review of Some Interesting Surface Plasmon Resonance-Enhanced Properties of Noble Metal Nanoparticles and Their Applications to Biosystems". *Plasmonics* **2007**, *2*, 107-118.
2. Verykios, X. E.; Stein, F. P.; Coughlin, R. W., "Oxidation of Ethylene over Silver: Adsorption, Kinetics, Catalyst". *Catal. Rev.* **1980**, *22*, 197-234.
3. Verykios, X. E.; Stein, F. P.; Coughlin, R. W., "Metal-Support Interaction Effects of Silver Catalysts During Ethylene Oxidation". *J. Catal.* **1980**, *66*, 147-154.
4. Park, P. W.; Ledford, J. S., "The Influence of Surface Structure on the Catalytic Activity of Alumina Supported Copper Oxide Catalysts. Oxidation of Carbon Monoxide and Methane". *Appl. Catal. B* **1998**, *15*, 221-231.
5. Wink, T.; van Zuilen, S. J.; Bult, A.; van Bennekom, W. P., "Self-Assembled Monolayers for Biosensors". *Analyst* **1997**, *122*, 43R-50R.
6. DiBenedetto, S. A.; Facchetti, A.; Ratner, M. A.; Marks, T. J., "Molecular Self-Assembled Monolayers and Multilayers for Organic and Unconventional Inorganic Thin-Film Transistor Applications". *Adv.Mater.* **2009**, *21*, 1407-1433.
7. Schonherr, H.; Vancso, G. J., "Lattice Imaging of Self-Assembled Monolayers of Partially Fluorinated Disulfides and Thiols on Sputtered Gold by Atomic Force Microscopy". *Langmuir* **1997**, *13*, 3769-3774.
8. Serafin, J. G.; Liu, A. C.; Seyedmonir, S. R., "Surface Science and the Silver-Catalyzed Epoxidation of Ethylene". *J. Mol. Cat. A* **1998**, *131*, 157-168.
9. Shen, M.; Russell, S. M.; Liu, D.-J.; Thiel, P. A., "Destabilization of Ag Nanoislands on Ag(100) by Adsorbed Sulfur". *J. Chem. Phys.* **2011**, *135*, 154701.

10. Shen, M.; Liu, D.-J.; Jenks, C. J.; Thiel, P. A.; Evans, J. W., "Accelerated Coarsening of Ag Adatom Islands on Ag(111) Exposed to S: Mass-Transport Mediated by Ag-S Complexes". *J. Chem. Phys.* **2009**, *130*, 094701.
11. Ling, W. L.; Bartelt, N. C.; Pohl, K.; de la Figuera, J.; Hwang, R. Q.; McCarty, K. F., "Enhanced Self-Diffusion on Cu(111) by Trace Amounts of S: Chemical-Reaction-Limited Kinetics". *Phys. Rev. Lett.* **2004**, *93*, 166101.
12. Thiel, P. A.; Shen, M.; Liu, D.-J.; Evans, J. W., "Coarsening of Two-Dimensional Nanoclusters on Metal Surfaces". *J. Phys. Chem. C* **2009**, *113*, 5047-5067.
13. Feibelman, P. J., "Formation and Diffusion of S-Decorated Cu Clusters on Cu(111)". *Phys. Rev. Lett.* **2000**, *85*, 606-609.
14. Whitesides, G. M.; Boncheva, M., "Beyond Molecules: Self-Assembly of Mesoscopic and Macroscopic Components". *Proc. Natl. Acad. Sci. USA* **2002**, *99*, 4769-4774.
15. Iqbal, P.; Preece, J. A.; Mendes, P. M., Nanotechnology: The "Top-Down" and "Bottom-up" Approaches. In *Supramolecular Chemistry*, John Wiley & Sons, Ltd: 2012.
16. Woodruff, D. P., "The Interface Structure of N-Alkylthiolate Self-Assembled Monolayers on Coinage Metal Surfaces". *Phys. Chem. Chem. Phys.* **2008**, *10*, 7211-7221.
17. Love, J. C.; Estroff, L. A.; Kriebel, J. K.; Nuzzo, R. G.; Whitesides, G. M., "Self-Assembled Monolayers of Thiolates on Metals as a Form of Nanotechnology". *Chem. Rev.* **2005**, *105*, 1103-1169.
18. Pensa, E.; Cortes, E.; Corthey, G.; Carro, P.; Vericat, C.; Fonticelli, M. H.; Benitez, G.; Rubert, A. A.; Salvarezza, R. C., "The Chemistry of the Sulfur-Gold Interface: In Search of a Unified Model". *Acc. Chem. Res.* **2012**, *45*, 1183-1192.

19. Häkkinen, H., "The Gold-Sulfur Interface at the Nanoscale". *Nat. Chem.* **2012**, *4*, 443-455.
20. Dubois, L. H.; Nuzzo, R. G., "Synthesis, Structure, and Properties of Model Organic Surfaces". *Ann. Rev. Phys. Chem.* **1992**, *43*, 437-463.
21. Maksymovych, P.; Yates Jr., J. T., "Au Adatoms in Self-Assembly of Benzenethiol on the Au(111) Surface". *J. Am. Chem. Soc.* **2008**, *130*, 7518-7519.
22. Maksymovych, P.; Sorescu, D. C.; Yates Jr., J. T., "Gold-Adatom-Mediated Bonding in Self-Assembled Short-Chain Alkanethiolate Species on the Au(111) Surface". *Phys. Rev. Lett.* **2006**, *97*, 146103.
23. Burgi, T., "Properties of the Gold-Sulphur Interface: From Self-Assembled Monolayers to Clusters". *Nanoscale* **2015**, *7*, 15553-15567.
24. Chen, C. J., *Introduction to Scanning Tunneling Microscopy*; Oxford University Press: New York/Oxford, 1993.
25. Wagner, C., "Investigation on Silver Sulfide". *J. Chem. Phys.* **1953**, *21*, 1819-1827.
26. Heegemann, W.; Meister, K. H.; Bechtold, E.; Hayek, K., "The Adsorption of Sulfur on the (100) and (111) Faces of Platinum; a LEED and AES Study". *Surf. Sci.* **1975**, *49*, 161-180.
27. Detry, D.; Drowart, J.; Goldfinger, P.; Keller, H.; Rickert, H., "Zur Thermodynamik Von Schwefeldampf". *Z. Phys. Chem.* **1967**, *55*, 314-319.
28. Russell, S. M. Mass Transport and Chalcogen-Silver Interactions on Silver Surfaces. Ph.D., Iowa State University, Ames, Iowa, 2012.
29. Shen, M. Sulfur Adsorption, Structure, and Effects on Coarsening on Ag(111) and Ag(100). Iowa State University, Ames, IA, 2009.

30. Barth, J. V.; Brune, H.; Ertl, G.; Behm, R. J., "Scanning Tunneling Microscopy Observations on the Reconstructed Au(111) Surface: Atomic Structure, Long-Range Superstructure, Rotational Domains, and Surface Defects". *Phys. Rev B* **1990**, *42*, 9307-9318.
31. Ocko, B. M.; Wang, J.; Davenport, A.; Isaacs, H., "In Situ X-Ray Reflectivity and Diffraction Studies of the Au(001) Reconstruction in an Electrochemical Cell". *Phys. Rev. Lett.* **1990**, *65*, 1466-1469.
32. Jiang, Y.; Liang, X.; Ren, S.; Chen, C.-L.; Fan, L.-J.; Yang, Y.-W.; Tang, J.-M.; Luh, D.-A., "The Growth of Sulfur Adlayers on Au(100)". *J. Chem. Phys.* **2015**, *142*, 064708.
33. Min, B. K.; Alemozafar, A. R.; Biener, M. M.; Biener, J.; Friend, C. M., "Reaction of Au(111) with Sulfur and Oxygen: Scanning Tunneling Microscopic Study". *Top. Catal.* **2005**, *36*, 77-90.
34. Biener, M. M.; Biener, J.; Friend, C. M., "Sulfur-Induced Mobilization of Au Surface Atoms on Au(111) Studied by Real-Time STM". *Surf. Sci* **2007**, *601*, 1659-1667.
35. Moritz, W.; Wolf, D., "Structure Determination of the Reconstructed Au(110) Surface". *Surf. Sci.* **1979**, *88*, L29-L34.
36. Horcas, I.; Fernandez, R.; Gomez-Rodriguez, J. M.; Colchero, J.; Gomez-Herrero, J.; Baro, A. M., "WSXM: A Software for Scanning Probe Microscopy and a Tool for Nanotechnology". *Rev. Sci. Instrum.* **2007**, *78*, 013705.
37. Liu, D.-J.; Walen, H.; Oh, J.; Lim, H.; Evans, J. W.; Kim, Y.; Thiel, P. A., "Search for the Structure of a Sulfur-Induced Reconstruction on Cu(111)". *J. Phys. Chem. C* **2014**, *118*, 29218-29223.
38. Wahlström, E.; Ekvall, I.; Kihlgren, T.; Olin, H.; Lindgren, S. A.; Wallden, L., "Low-Temperature Structure of S/Cu(111)". *Phys. Rev. B* **2001**, *64*, 155406.

39. Wahlström, E.; Ekvall, I.; Olin, H.; Lindgren, S. A.; Wallden, L., "Observation of Ordered Structures for S/Cu(111) at Low Temperature and Coverage". *Phys. Rev. B* **1999**, *60*, 10699.
40. Keller, H.; Rickert, H.; Detry, D.; Droward, J.; Goldfinger, P., "Zur Thermodynamik Von Selendampf Massenspektrometrische Untersuchungen Mit Der Elektrochemischen Knudsen-Zelle". *Z. Phys. Chem.* **1971**, *75*, 273-286.

CHAPTER II

CU₂S₃ COMPLEX ON CU(111) AS A CANDIDATE FOR MASS TRANSPORT ENHANCEMENT

Holly Walen,^a Da-Jiang Liu,^b Junepyo Oh,^c Hyunseob Lim,^c J. W. Evans,^{b,d} Christine Aikens,^e Yousoo Kim,^c and P. A. Thiel^{a,b,f}

A paper published in Physical Review B[†]

Abstract

Sulfur-metal complexes, containing only a few atoms, can open new, highly efficient pathways for transport of metal atoms on surfaces. For example, they can accelerate changes in the shape and size of morphological features, such as nanoparticles, over time. In this study, we perform STM under conditions that are designed to specifically isolate such complexes. We find a new, unexpected S-Cu complex on the Cu(111) surface, which we identify as Cu₂S₃. We propose that Cu₂S₃ enhances mass transport in this system, which contradicts a previous proposal based on Cu₃S₃. We analyze bonding within these Cu-S complexes, identifying a new principle for stabilization of sulfur complexes on coinage metal surfaces.

Departments of ^aChemistry, ^dPhysics & Astronomy, and ^fMaterials Science & Engineering, Iowa State University, Ames, Iowa 50011 USA

^b Ames Laboratory of the USDOE, Ames, Iowa 50011 USA

^c RIKEN Surface and Interface Science Laboratory, Wako, Saitama 351-0198, Japan

^e Kansas State University, Department of Chemistry, Manhattan, Kansas 66506 USA

[†] *Phys. Rev. B* **91** 045426 (2015)

1. Introduction

It has been proposed that metal-adsorbate complexes can greatly accelerate rearrangements of metal nanostructures and surfaces. This issue is of importance for stability of catalysts or nanostructures, and has been the subject of prolonged speculation given that the complexity of such systems typically precludes definitive analysis.¹⁻² Nonetheless, evidence continues to accumulate supporting the presence of mobile complexes on surfaces and, by implication, their role in metal transport. Recently, for instance, Parkinson et al. have shown that CO interacts with Pd atoms adsorbed on a Fe_3O_4 surface, forming a highly-mobile Pd-CO complex.³ Other adsorbates that form mobile surface complexes with metals include hydrogen,⁴⁻⁵ oxygen,⁶⁻⁷ alkylsulfides,⁸ and—the subject of this study—sulfur.⁹⁻¹⁴ The soft metals Cu, Ag, and Au, which are of great interest because of their catalytic and plasmonic properties, are expected to be particularly susceptible to this effect.

The challenge in identifying such complexes is their high mobility, plus their potential condensation into extended ordered structures at moderate to high coverage. Together, these considerations mean that conditions of low temperature and low coverage offer the best chance for isolating and observing such species. The present work is a search for S-Cu complexes under these conditions.

Previously, Feibelman⁹ proposed that a Cu_3S_3 complex can enhance metal transport on Cu(111), not because of high mobility (relative to metal adatoms), but rather because of high population (reflecting high stability), combined with moderate mobility (cf. Ref. ¹). The stability of the cluster was attributed to the fact that S atoms could adsorb at pseudo-4-fold-hollow (p4fh) sites created at the edges of the metal trimer, in accord with a long-standing principle that S binds more strongly to higher-coordination sites.^{9, 15-16} This conjecture

seemed compatible with later experimental work,¹⁰ where coarsening kinetics of Cu islands above room temperature, in the presence of adsorbed S, were interpreted in terms of Feibelman's model. However, the Cu_3S_3 clusters were not observed directly.

In this paper, we present direct evidence for an abundant small cluster that is not Cu_3S_3 , but rather Cu_2S_3 , on Cu(111). This cluster is immobile and stable at 5 K, where our observations are made. It forms when the Cu(111) surface is exposed to sulfur at room temperature and then quenched. Thus, it is likely to exist and participate in dynamic processes that occur at higher temperature.

2. Experimental and computational details

All STM imaging was done at 5 K in vacuum, at a pressure lower than 2.5×10^{-11} Torr¹⁷. Assessment of the sulfur coverage, θ_s , [the ratio of S atoms to Cu atoms in the (111) plane] was guided by the prior observation that a honeycomb-like reconstruction first appears at $\theta_s \sim 0.05$ ¹⁸⁻¹⁹. We report S coverage on the terraces, rather than the total S coverage (which includes step decoration).

DFT calculations for surfaces used the VASP²⁰ code with the projector-augmented wave (PAW) method²¹. The surface was modeled by a periodic slab of L layers, separated by 1.2 nm of vacuum. Additional Cu and S atoms were added to one side of the slab. Most of the results reported used the Perdew-Burke-Ernzerhof (PBE) approximation²² for the exchange-correlation functional. The energy cutoff for the plane-wave basis set was 280 eV. Simulated STM images are created from DFT calculations using the Tersoff-Hamman method²³⁻²⁴. Due to the existence of surface states on the Cu(111) surface, k-points convergence is slow. Averaging results for slabs of different thickness can significantly

reduce the errors due to insufficient k-points. Energetics reported in this paper are obtained from k-point grids that approximately correspond to $(24 \times 24 \times 1)$ for the primitive cell, averaging results from $L = 4$ to 7. Some key results were reproduced using DFT codes with dispersion interactions, e.g., DFT-D2 and optB88-vdW. Compared with PBE, absolute values were shifted by as much as 0.20 eV, but trends were preserved.

DFT calculations on gas phase on gas phase CuS_2 and Cu_2S_3 molecules with varying charge states were performed with the Amsterdam Density Functional (ADF) code²⁵. In the ADF program, the PBE functional²² and a triple-zeta polarized (TZP) basis set with the frozen core approximation were used for geometry optimizations and Kohn-Sham orbital calculations. Relativistic effects were considered using the zeroth order regular approximation (ZORA)²⁶⁻²⁷.

3. Identification of a Cu_2S_3 complex from STM and DFT

The inset in Fig. 1(a) shows an image of the clean $\text{Cu}(111)$ surface with atomic resolution. This allows us to define crystallographic directions as shown, with arrows indicating two of the six close-packed directions.

Fig. 1(a) shows a representative image of $\text{S}/\text{Cu}(111)$ terraces at relatively low magnification, and at $\theta_{\text{S}} = 0.004$. At this low coverage, the main features are small, uniform bright spots. Closer inspection reveals that these are actually heart-shaped clusters, as shown in Fig. 1(c-e). They adopt three different orientations, rotated by 120° , in equal abundance. These orientations are such that the lobes of the heart align with three of the six close-packed directions of the $\text{Cu}(111)$ surface.

We can identify the orientations of the hearts more exactly by using step edges as reference. There are two types of close-packed step edges in an fcc system. These are commonly denoted A and B, where A is a (100) microfacet exposing p4fh sites, and B is a (111) microfacet exposing p3fh sites. In experiment, both types of steps exist on the clean surface and they are not easily distinguishable. Sulfur adsorbs preferentially at steps and fully decorates the steps, even at lowest θ_S , in our experiments. After adsorption of sulfur, one type of step is long and straight, as exemplified in Fig. 2(a), while the other has a faceted sawtooth structure, as shown in Fig. 2(b).¹⁸⁻¹⁹ Notably, the inner edges of the sawtooth have the same orientation as the more extended, straight steps. We identify the straight steps as A-steps because these naturally present p4fh adsorption sites where S is more stable. Using this as reference, our STM images show that the heart-shaped clusters are oriented *exclusively* with their lobes toward downgoing B-steps.

We attribute the hearts to Cu_2S_3 clusters of the type shown in Fig. 3(a). There is one S atom on the upper side of the Cu dimer in the figure, in a p4fh site formed by the Cu dimer plus two Cu atoms in the terrace. There are two S atoms on the lower side of the Cu dimer, each near a 3fh site on the terrace and adjoining one of the Cu atoms in the dimer. These would shape the lobes of the heart.

We have used density functional theory (DFT) to check whether this assignment is reasonable in terms of stability, shape, orientation, and density. A variety of possible adsorbed clusters, with optimized configurations, are represented in Fig. 3. The chemical potential of S (μ_S) and the cluster diffusion barrier (E_d) appear at the top of each panel. μ_S is defined as:

$$\mu_S = [E(\text{Cu}_m\text{S}_n + \text{slab}) - E(\text{slab}) - m\mu_{\text{Cu}}]/n - E(\text{S}_{2,\text{g}})/2 \quad (1)$$

where E is energy, μ_{Cu} is the cohesive energy of a bulk Cu atom, and m and n are the number of Cu and S atoms in the complex, respectively. By this definition, μ_S measures the decrease in energy per S when a limited supply of atomic S on terraces is incorporated into clusters (given an unlimited supply of metal atoms available from steps). This equation also defines the energy of gaseous S_2 as the reference point for μ_S .

A related quantity, the formation energy, E_{form} , is defined by:

$$E_{\text{form}}(\text{Cu}_m\text{S}_n) = n[\mu_S(\text{Cu}_m\text{S}_n) - \mu_S(\text{S})] \quad (2)$$

E_{form} gives the energy cost to create a Cu_mS_n complex by extracting m Cu atoms from the step edge and combining them with n S atoms already on the terrace. However, Eq. (2) includes $\mu_S(\text{S})$, which varies with θ_S . Since we are dealing with low θ_S , we choose the value of $\mu_S(\text{S})$ that is calculated from DFT for a “large” 4×4 supercell, corresponding to $\theta_S = 0.0625$ ML, which is $\mu_S(\text{S}) = -1.91$ eV. The sulfur atoms are in fcc sites. This results in the values of E_{form} shown in Table 1 for the optimized configurations of several Cu-S complexes. To facilitate comparisons, the values of μ_S and E_d are also shown.

TABLE I. Energetic values calculated from VASP for optimized configurations of several Cu-S complexes, and an isolated Cu atom, on Cu(111).

Complex	μ_S , eV	E_d , eV	E_{form} , eV
Cu atom at an fcc terrace site	n/a	0.05	+0.78
CuS	-1.24	0.33	+0.67
CuS ₂	-1.82	0.34	+0.15
CuS ₃	-1.83	0.36	+0.24
Cu ₂ S ₃	-1.87	0.35	+0.11
Cu ₃ S ₃	-1.82	0.36	+0.24

The Cu₂S₃ complex in Fig. 3(a) has lower μ_S than any others we have found. The 3 next-best complexes are shown Fig. 3(c-e). However, the ordering of μ_S for various complexes can be sensitive to the dimension and orientation of the supercell, meaning that lateral interactions between complexes can affect the relative energies significantly. These are best taken into account by comparing μ_S , not at fixed supercell size as in Fig. 3, but rather at fixed θ_S , as in Fig. 4. At all θ_S , μ_S of Cu₂S₃ is lower than μ_S of Cu₃S₃, and at most coverages, it is below μ_S of atomic adsorbed S.

Second, we have simulated the shape of the complexes using the Tersoff-Hamman method.²³⁻²⁴ Results are shown in Fig. 5, where panels (a) and (b) correspond to the configurations shown in Fig. 3(a) and 3(c), respectively. The heart shape is evident for Cu₂S₃, whereas Cu₃S₃ is three-fold symmetric and incompatible with the data. Furthermore, the area of the simulated Cu₂S₃ complex is 0.40-0.42 nm², in good agreement with the experimental result (0.39 ± 0.04 nm²).

Third, to assess orientation, we contemplate the two Cu_2S_3 complexes shown in Fig. 3(a-b). The one in Fig. 3(a) can have 3 energetically-equivalent orientations. In each orientation, there is one S atom in a p4fh site and two S atoms in asymmetrical sites. Considering the pair of Cu atoms as a one-dimensional step edge, one S atom lies along an A-step, and the others (comprising the lobes) are along a B-step. This is exactly the experimental observation. On the other hand, the complex in Fig. 3(b) has one S atom along a B-step, and the lobes along an A-step, inconsistent with the data. The stability of complex (a) can be rationalized by the presence of one S atom in a p4fh site, whereas (b) has none.

Finally, we considered whether the observed density of complexes is consistent with our analysis of the above energetics. A simple Boltzmann factor analysis given the positive formation energy implies that the density predicted under preparation conditions at 300 K should exceed the static density observed at the lower observation temperature (5 K). (The density observed at 5 K should reflect the equilibrium density for the temperature at which the complexes are frozen in place during cooling. This freeze-in temperature lies between 300 K and 5 K, but is otherwise unknown.) The formation energy for Cu_2S_3 is +0.11 eV, so the equilibrium population predicted at 300 K is $0.25/\text{nm}^2$. This is well above the observed value of $0.02/\text{nm}^2$. Hence the two values are consistent.

4. Factors that stabilize Cu-S complexes

The existence of Cu_2S_3 complexes is surprising, given that analogous clusters have not been observed (to our knowledge) in other surface systems. To understand why they exist, we first recall the well-known principle governing S adsorption on metal surfaces is that S bonds preferentially at 4fh sites, and in some cases metal surfaces rearrange to provide

such sites.¹⁶ The stability of the (hypothetical) Cu_3S_3 complex, for instance, was attributed to S atoms occupying three p4fh sites at the edges of the metal trimer⁹ [Fig. 3(c)]. However, in the Cu_2S_3 cluster, two of the p4fh sites are sacrificed by virtue of the missing Cu atom. Thus, a factor must exist that competes with, or complements, the influence of the 4fh site. We suggest that this is the formation of linear S-Cu-S units. The Cu_2S_3 complex consists of two such linear units, sharing a S atom at the apex. Adding a Cu atom to form Cu_3S_3 breaks the linearity of the individual S-Cu-S units, as can be discerned in Fig. 3(c).

Insight into this configuration can be developed by starting with the isolated CuS_2 molecule, where we define the z-axis as the internuclear axis. In a linear ligand field, the Cu d orbitals split into two doubly-degenerate orbitals, $(d_{x^2-y^2}, d_{xy})$ and (d_{xz}, d_{yz}) , and a nondegenerate d_{z^2} orbital. Of these, the d_{z^2} orbital is positioned for the best overlap with ligand s or p orbitals, followed by the (d_{xz}, d_{yz}) set and finally the essentially nonbonding $(d_{x^2-y^2}, d_{xy})$ set.

The calculated Kohn-Sham molecular orbitals for CuS_2^- at the PBE/TZP level of theory agree with this picture. Kohn-Sham orbitals for CuS_2 are shown in Fig. 11 (the -3 charge state is shown here; different charge states vary in their occupation of the HOMO). The lowest energy orbital shown here (HOMO-6) is a bonding interaction between the Cu d_{z^2} orbital and the S $2p_z$ orbitals. π -like orbitals between Cu d_{xz} and d_{yz} and the corresponding S $2p_x$ and $2p_y$ atomic orbitals also aid in the strong bonding interaction. In Cu_2S_3 , the Kohn-Sham orbitals are more delocalized, but still fit with the CuS_2 picture.

Hence, linearity of the S-Cu-S unit is favored in isolated molecules because it maximizes overlap between Cu d_{z^2} and S $2p_z$ orbitals. Analysis of VASP-based isodensity plots of adsorbed Cu-S complexes reveals that this trend is preserved on the surface. The

isodensity plots for CuS_2 generated from VASP (Fig. 7) show similar results for the lowest energy orbitals. Isodensity plots for states 3 and 4 for one Cu layer ($L=1$) display the bonding and antibonding configurations of the CuS_2 HOMO-6 orbital with the Cu substrate. A small energy splitting indicates that there is a weak interaction between this orbital and the Cu substrate. Isodensity plots for states 5 and 6 for $L=1$ show bonding interactions between S 2p orbitals that are perpendicular to the plane of the Cu surface and the underlying Cu layer. This indicates that the stability of the CuS_2 units on the surface can be understood both in terms of the S-Cu-S interactions and the S-surface interactions. Isodensity plots for Cu_2S_3 in vacuum and on one layer of Cu substrate are shown in Fig. 8. The 2p orbitals of the S atom in the middle have a different symmetry than the rest of the atoms in the chain. One component is perpendicular to the chain, the lower lobe of which interacts with the two $\text{Cu } d_{z^2} \text{ S } p_z$ orbitals, shown as vacuum state 4 in Fig. 8. The other component is along the chain, and each lobe interacts separately with the $\text{Cu } d_{z^2} \text{ S } p_z$ orbitals, shown as vacuum state 5 in Fig. 8. These bonding interactions are also present for the cluster on one Cu layer. The states 4 and 5 in vacuum become states 5 and 6 with $L=1$. In addition, low energy states exhibit isodensity plots with significant S 2p character perpendicular to the surface (e.g., the $L=1$ state 4 in Fig. 8). Again, the stability of the Cu_2S_3 cluster is represented by the S-Cu-S interactions and the S-surface interactions.

In fact, linear S-M-S units are known in some related systems. Thiolates adsorbed on $\text{Au}(111)$,^{8, 28} and thiolates at the periphery of Au nanoclusters, form species that include linear S-M-S units.²⁸⁻²⁹ Linear S-M-S complexes (without alkyl ligands) have also been postulated—but not observed directly—on the basis of DFT and experimental data for $\text{S}/\text{Ag}(100)$,¹⁴ and on the basis of DFT alone for $\text{S}/\text{Ag}(111)$.² These results suggest that the

linear S-M-S unit has generic stability across coinage metals. This is thus a new, complementary principle for understanding and predicting stability of S-induced structures on metal surfaces.

5. Role of Cu_2S_3 complexes in Cu mass transport

The remaining issue to be addressed is the role of the Cu_2S_3 complex in mass transport, relative to other complexes. For a realistic analysis, one must consider a coupled set of non-linear steady-state reaction-diffusion equations (RDEs) describing the formation, dissociation, and diffusion of various possible complexes.^{10, 12} Given that CuS_3 is reasonably stable and is a natural precursor to Cu_2S_3 , we focus on the reaction $\text{Cu} + \text{CuS}_3 \leftrightarrow \text{Cu}_2\text{S}_3$, and let $F(R)$ denote the rate for the forward (reverse) process. Then, one obtains

$$\begin{aligned} D_{\text{Cu}} \nabla^2 \theta_{\text{Cu}} - F(\text{Cu} + \text{CuS}_3) + R(\text{Cu} + \text{CuS}_3) - \dots &\approx 0, \\ D_{\text{Cu}_2\text{S}_3} \nabla^2 \theta_{\text{Cu}_2\text{S}_3} + F(\text{Cu} + \text{CuS}_3) - R(\text{Cu} + \text{CuS}_3) + \dots &\approx 0, \quad \dots \end{aligned} \quad (3)$$

where D is the diffusion coefficient, and implicit terms account for contributions from other reactions. A typical feature of surface mass transport is that it is driven by weak spatial variations (and accompanying gradients) in coverages relative to their uniform quasi-equilibrium values. Thus, it is natural to write $\theta_{\text{Cu}} = \theta_{\text{Cu}}^{\text{eq}} + \delta\theta_{\text{Cu}}$, etc., and to linearize the above RDE, which results in equations of the form

$$\begin{aligned} \nabla^2 \delta\theta_{\text{Cu}} - \delta\theta_{\text{Cu}} / L_{\text{Cu}}(\text{CuS}_3)^2 + \dots &\approx 0 \\ \text{with } L_{\text{Cu}}(\text{CuS}_3) = [D_{\text{Cu}} / k_{\text{Cu}}(\text{CuS}_3)]^{1/2} \text{ and } k_{\text{Cu}}(\text{CuS}_3) = (D_{\text{Cu}} + D_{\text{CuS}_3}) \theta_{\text{CuS}_3}^{\text{eq}}, \text{ etc.} & \quad (4) \end{aligned}$$

DFT indicates that $D_{\text{Cu}} \gg D_{\text{CuS}_3}$, so one has

$$L_{\text{Cu}}(\text{CuS}_3) \approx [\theta_{\text{CuS}_3}^{\text{eq}}]^{-1/2} \text{ with } \theta_{\text{CuS}_3}^{\text{eq}} = \exp[-\beta E_{\text{form}}(\text{CuS}_3)](\theta_{\text{S}})^3 \quad (5)$$

where $L_{\text{Cu}}(\text{CuS}_3)$ is the reaction length describing how far Cu diffuses before reacting with CuS_3 to form Cu_2S_3 at rate k_{Cu} .

Further analysis of behavior requires specification of the conditions under which complexes form. In one scenario, complexes are formed by Cu and S *on terraces*; only Cu adatoms detach/attach at step edges, without any barrier except the terrace diffusion barrier. However, in order for complexes to contribute to mass transport, there must be sufficient probability that they form on the terraces within a length scale much shorter than the average mass transport distance, L_{av} . In other words, any gradient in θ_{Cu} must couple sufficiently to that of $\theta_{\text{Cu}_2\text{S}_3}$. From (4), this requires that the reaction length be significantly smaller than the average mass transport distance. Then there is an enhanced flux $J_{\text{Cu}_2\text{S}_3} \sim D_{\text{Cu}}\theta_{\text{Cu}}^{\text{eq}}/L_{\text{Cu}}$ in the presence of S, vs. $J_{\text{Cu}} \sim D_{\text{Cu}}\theta_{\text{Cu}}^{\text{eq}}/L_{\text{av}}$ without S.

To give a concrete example, consider the model case of sulfur-enhanced Cu island coarsening on Cu(111), where the transport distance becomes the island separation. Under the experimental conditions used by Ling *et al.*,¹⁰ $L_{\text{av}} \approx 1 \mu\text{m}$. This is a factor of 10 smaller than the reaction length $L_{\text{Cu}}(\text{CuS}_3) \approx 10 \mu\text{m}$, calculated from Eq. (5) using $T = 490 \text{ K}$,¹⁰ $\theta_{\text{S}} \approx 6 \times 10^{-3} \text{ ML}$,¹⁰ and $E_{\text{form}}(\text{CuS}_3) = +0.24 \text{ eV}$ as given in Table 1. Hence, a diffusing Cu atom is far more likely to be captured by a Cu island than it is to form a complex on the terrace.

Thus, this picture does not allow enhanced mass transport by Cu_2S_3 *formed on terraces*. If the carrier is Cu_3S_3 formed from the reaction $\text{Cu} + \text{Cu}_2\text{S}_3 \leftrightarrow \text{Cu}_3\text{S}_3$ on terraces, a

similar analysis shows that $L_{\text{Cu}}(\text{Cu}_2\text{S}_3)$ far exceeds L_{isl} , so mass transport cannot be dominated by Cu_3S_3 formed on terraces, either. Again, even if $L_{\text{Cu}}(\text{Cu}_2\text{S}_3)$ was below L_{isl} , the corresponding enhanced flux $J_{\text{Cu}_2\text{S}_3}$ would scale like $(\theta_S)^{3/2}$, contrasting experiment.¹⁰

We propose an alternative picture where complexes attach and detach directly from step edges and their coverage at step edges is determined by their local chemical potential, which depends on step edge curvature. Then they directly contribute to mass transport, and the associated mass current of a complex C can be estimated from $J_C \sim D_C \theta_C^{\text{eq}} \sim \exp[-E_{\text{OR}}(\text{C})/(k_B T)]$ where $E_{\text{OR}}(\text{C}) = E_d(\text{C}) + E_{\text{form}}(\text{C})$. Thus, the species with the lowest E_{OR} should dominate mass transport. Values of E_d and E_{form} for the clusters can be taken from Fig. 8 and Eq. (2), and for Cu atoms from Ref.³⁰. This leads to values of $E_{\text{OR}} = 0.91$ eV, 0.49 eV, 0.46 eV, and 0.60 eV for Cu, CuS_2 , Cu_2S_3 , and Cu_3S_3 , respectively. Therefore Cu_2S_3 should be the dominant mass carrier, with CuS_2 also playing a possible role. The above expression for the mass current due to Cu_2S_3 is consistent with the observed third-order kinetics in the S-coverage using that $\theta_{\text{Cu}_2\text{S}_3}^{\text{eq}} = \exp[-\beta E_{\text{form}}(\text{Cu}_2\text{S}_3)](\theta_S)^3$. We also note the likelihood that there is an extra attachment barrier inhibiting the decomposition of Cu_2S_3 at S-decorated step edges and incorporation of the Cu. This would explain the attachment-limited kinetics observed in experiment.¹⁰

6. Conclusions

In summary, the predominant S-induced features on the Cu(111) terraces, at very low S coverages, are heart-shaped protrusions. DFT supports their assignment as Cu_2S_3 clusters. These clusters are always oriented such that the lobes of the heart point toward downgoing B-steps, because this allows one S atom in the cluster to bond at a p4fh site. This is different

than any type of metal-sulfur surface complex observed previously, to our knowledge. It may reflect the stability of linear S-metal-S geometries. Kinetic analysis shows that Cu_2S_3 is more important than Cu_3S_3 in mass transport.

Acknowledgements

The experimental component of this work was supported by several sources. From the U.S., it was NSF Grants CHE-1111500 and CHE-1507223. From Japan, support was provided by a Grant-in-Aid for Scientific Research on Priority Areas “Electron Transport Through a Linked Molecule in Nano-scale”; and a Grant-in-Aid for Scientific Research(S) “Single Molecule Spectroscopy using Probe Microscope” from the Ministry of Education, Culture, Sports, Science, and Technology (MEXT). The theoretical analysis of kinetics was also supported by NSF Grants CHE-1111500 and CHE-1507223. The DFT analysis of the energetics of chemisorbed complexes and of simulated STM images was supported by the Division of Chemical Sciences, Basic Energy Sciences, US Department of Energy (DOE). This part of the research was performed at Ames Laboratory, which is operated for the U.S. DOE by Iowa State University under contract No. DE-AC02-07CH11358. This part also utilized resources of the National Energy Research Scientific Computing Center, which is supported by the Office of Science of the U.S. DOE under Contract No. DE-AC02-05CH11231. The theoretical molecular orbital analysis for gas phase species was supported by the National Science Foundation under Grant No. CHE-1213771. C.M.A. also thanks the Camille and Henry Dreyfus Foundation for a Camille Dreyfus Teacher-Scholar Award (2011–2016). We thank Kan Ueji and Hiroshi Imada for assistance with the experiments, and Gordon J. Miller for useful discussions.

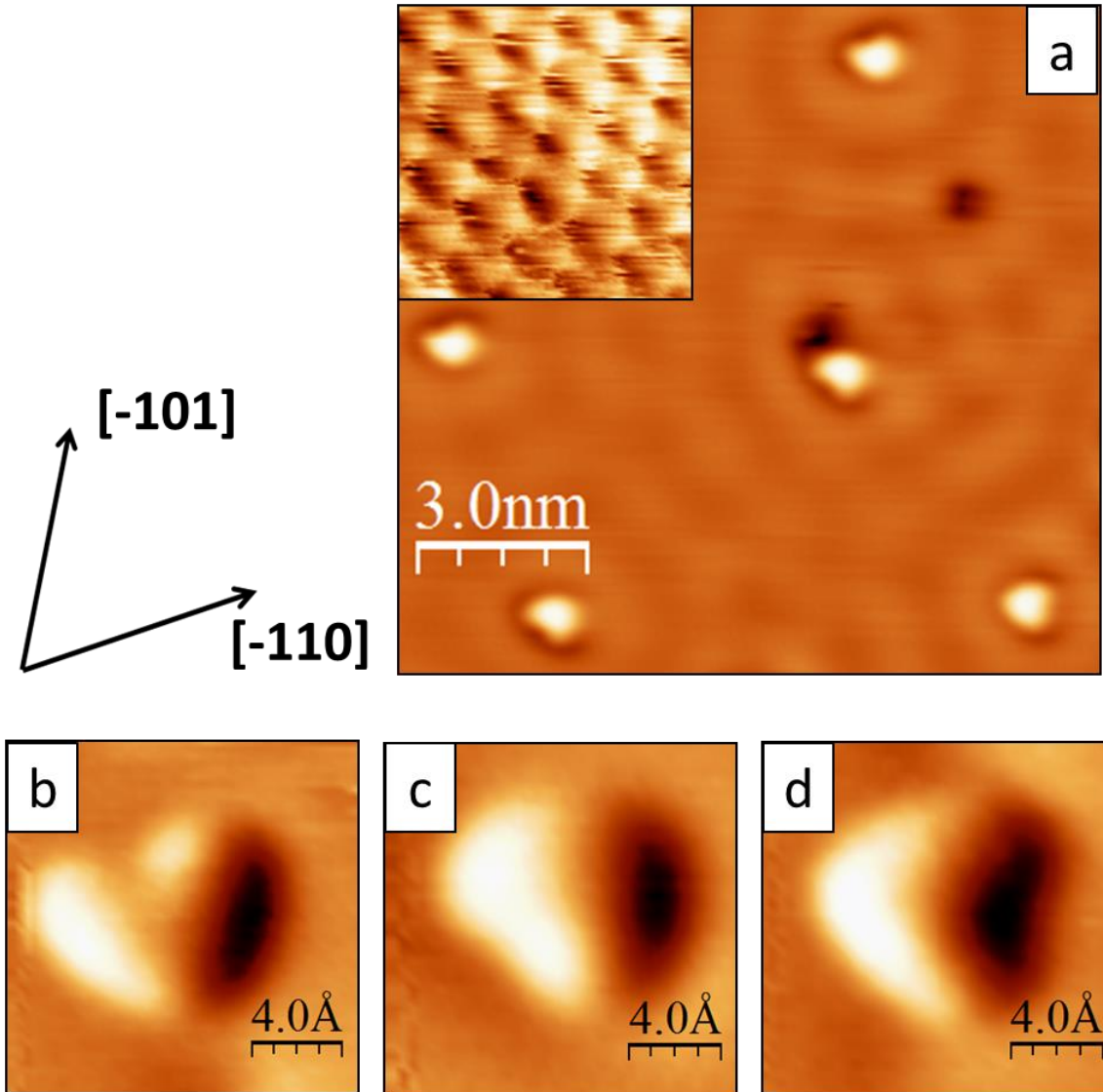


Figure 1. STM images of Cu_2S_3 on $\text{Cu}(111)$. a) Several Cu_2S_3 hearts on the terrace at low sulfur coverage, $12 \times 11.5 \text{ nm}^2$. Inset: atomic resolution of clean $\text{Cu}(111)$; $1.2 \times 1.2 \text{ nm}^2$. b)-d) Derivative images of the three orientations of the hearts, $1.5 \times 1.5 \text{ nm}^2$.

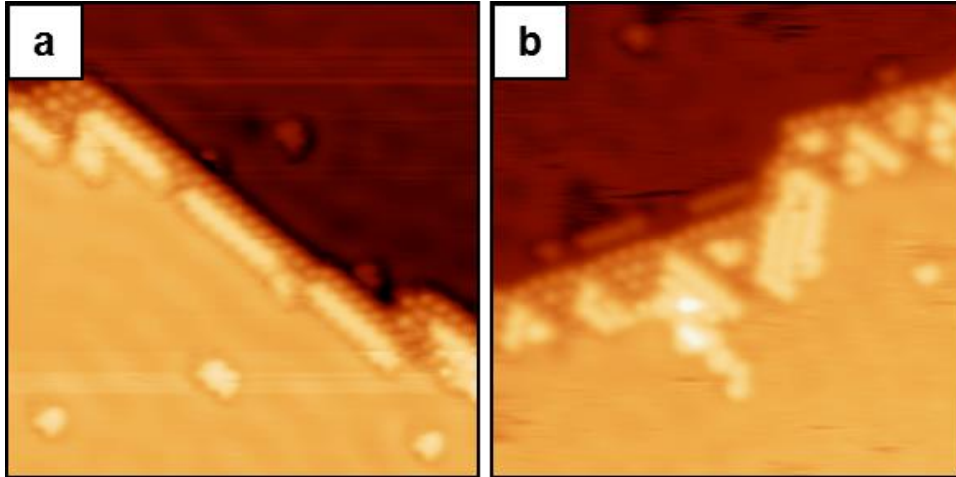


Figure 2. Topographic STM images of the two step edge types with S adsorption. a) A-type (100-microfacet) edge; 20 x 20 nm². b) B-type (111-microfacet) edge; 15 x 15 nm².

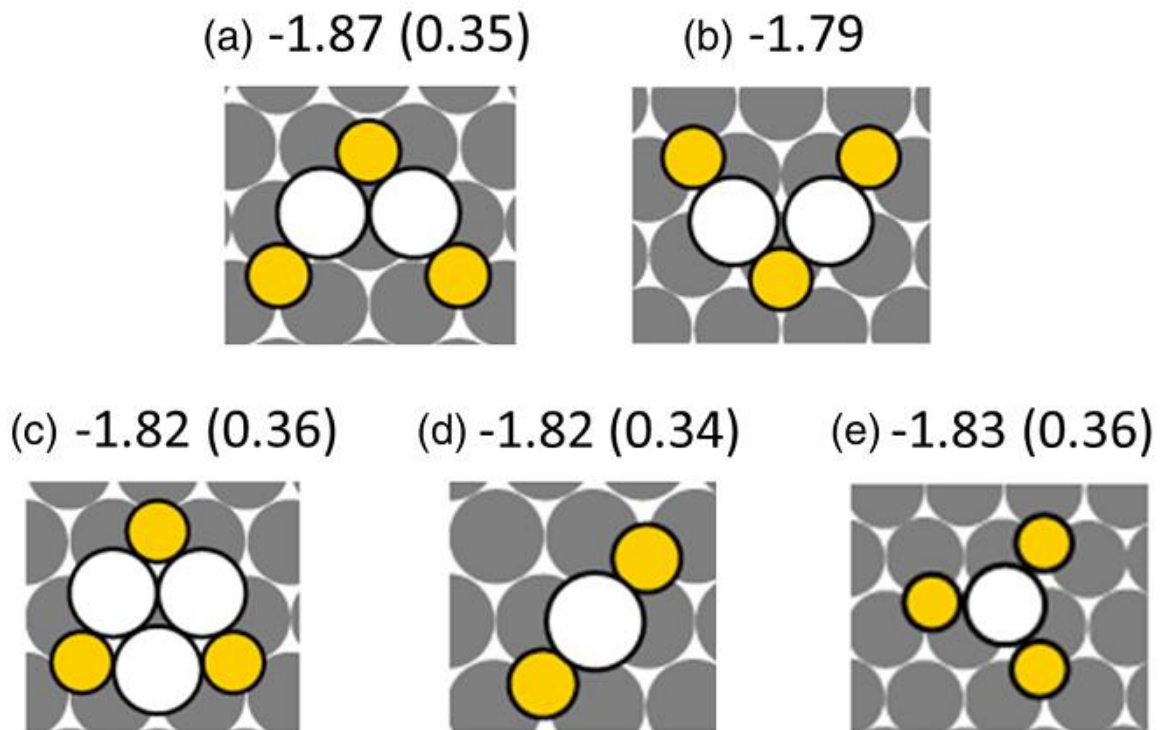


Figure 3. Cu-S clusters on Cu(111) with lowest chemical potentials. Values of μ_S are given in eV. Diffusion barriers, E_d , are given in parentheses, also in eV. White circles represent Cu adatoms, small yellow (on-line) are S adatoms, and gray are Cu atoms in the Cu(111) surface. Panels (a) and (b) are different configurations of Cu₂S₃, (c) is Cu₃S₃, (d) CuS₂, and (e) CuS₃.

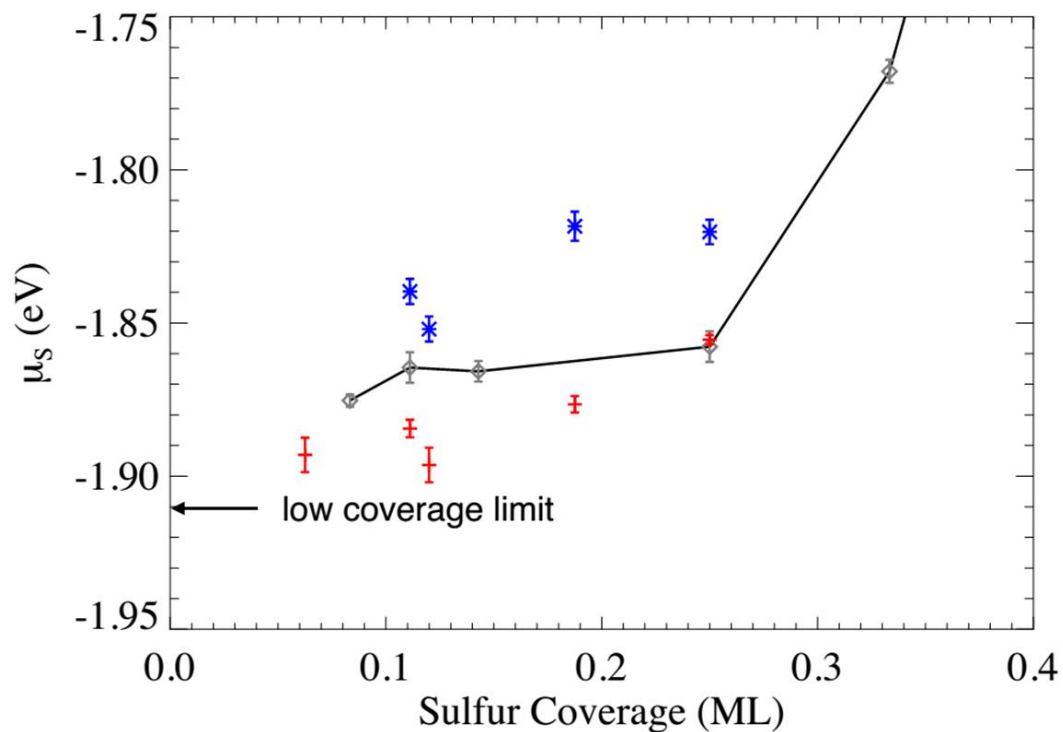


Figure 4. Comparison between μ_S for Cu_2S_3 (red pluses) and Cu_3S_3 (blue asterisks) with that of S adatom (gray line and gray circles) on fcc sites of the Cu(111) surface. Results for various supercell sizes and azimuthal orientations are plotted as a function of S coverage.

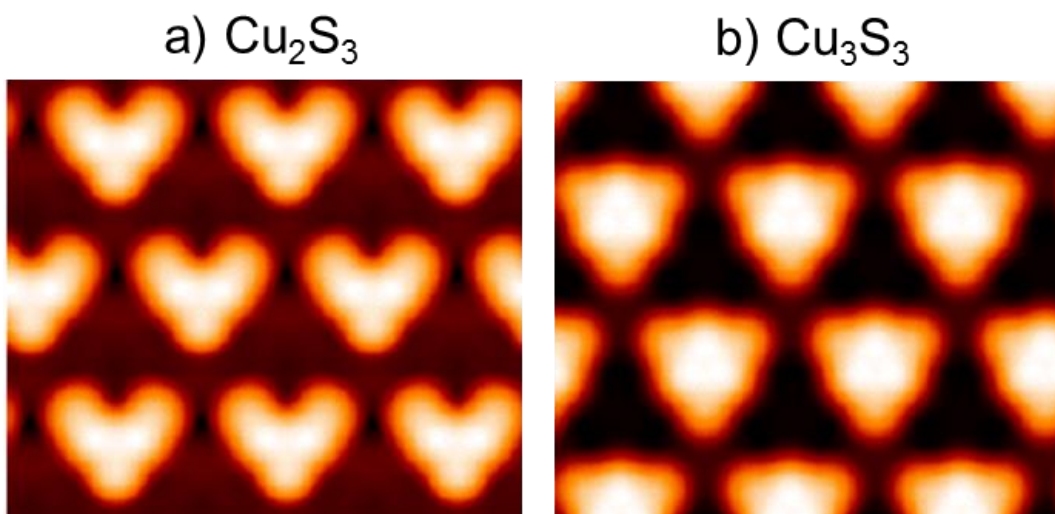


Figure 5. Shapes of two complexes, Cu_2S_3 and Cu_3S_3 on Cu(111), simulated from DFT.

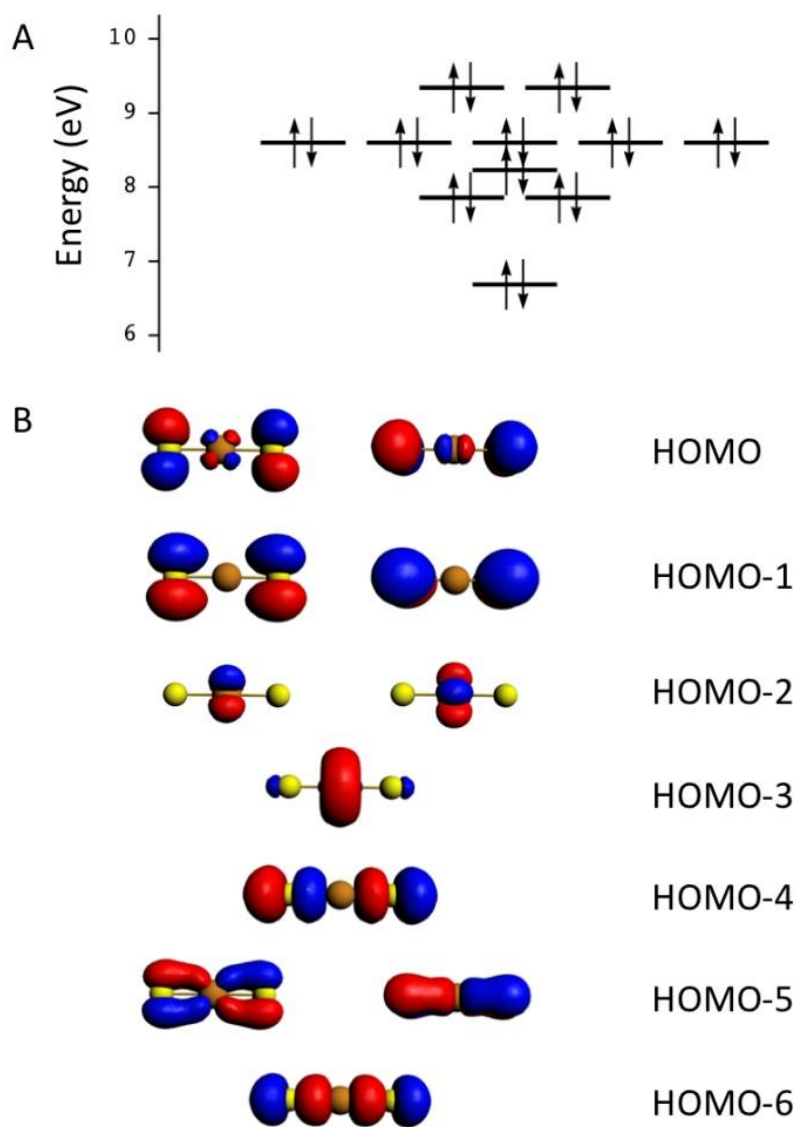


Figure 6. A) PBE/TZP orbital energy diagram and B) Kohn-Sham orbitals for CuS_2^{3-} .

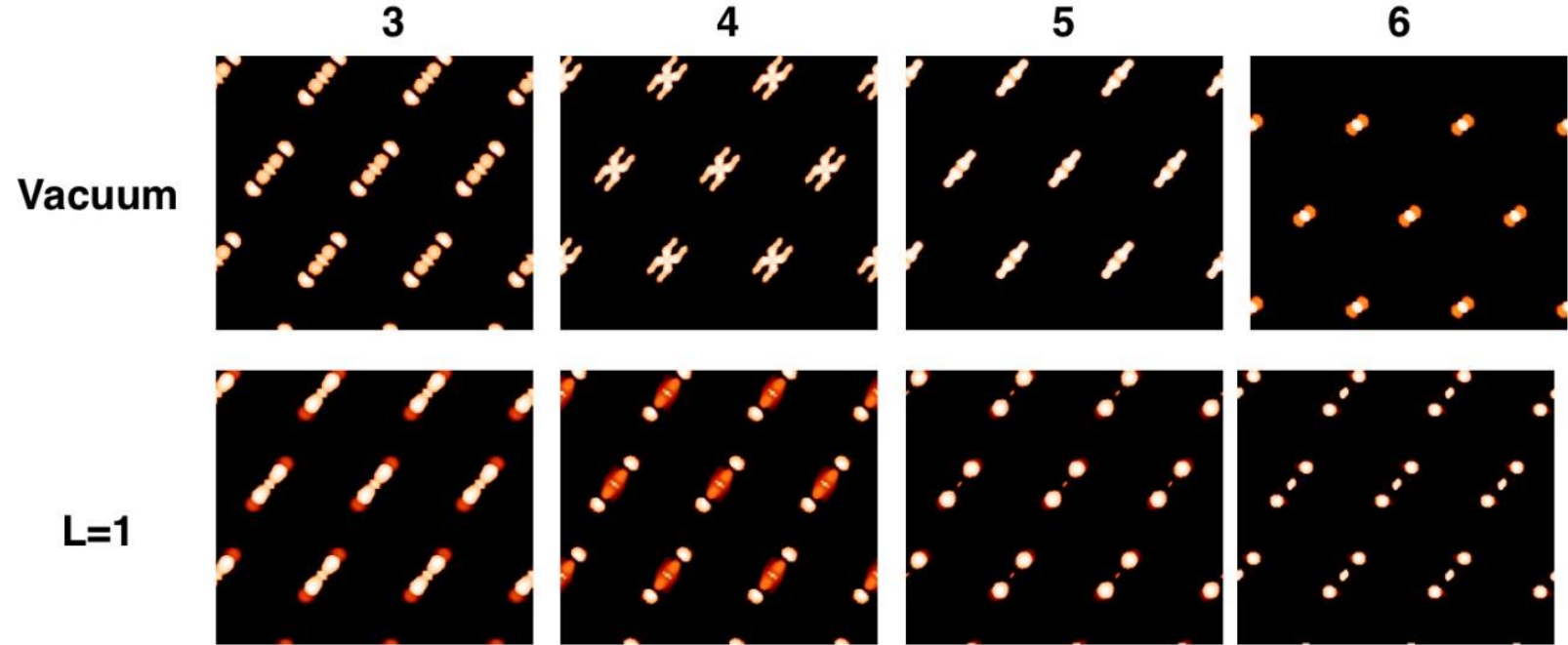


Figure 7. VASP isodensity plots for low energy bonding states of CuS_2 in vacuum and on one layer ($L=1$) of Cu substrate.

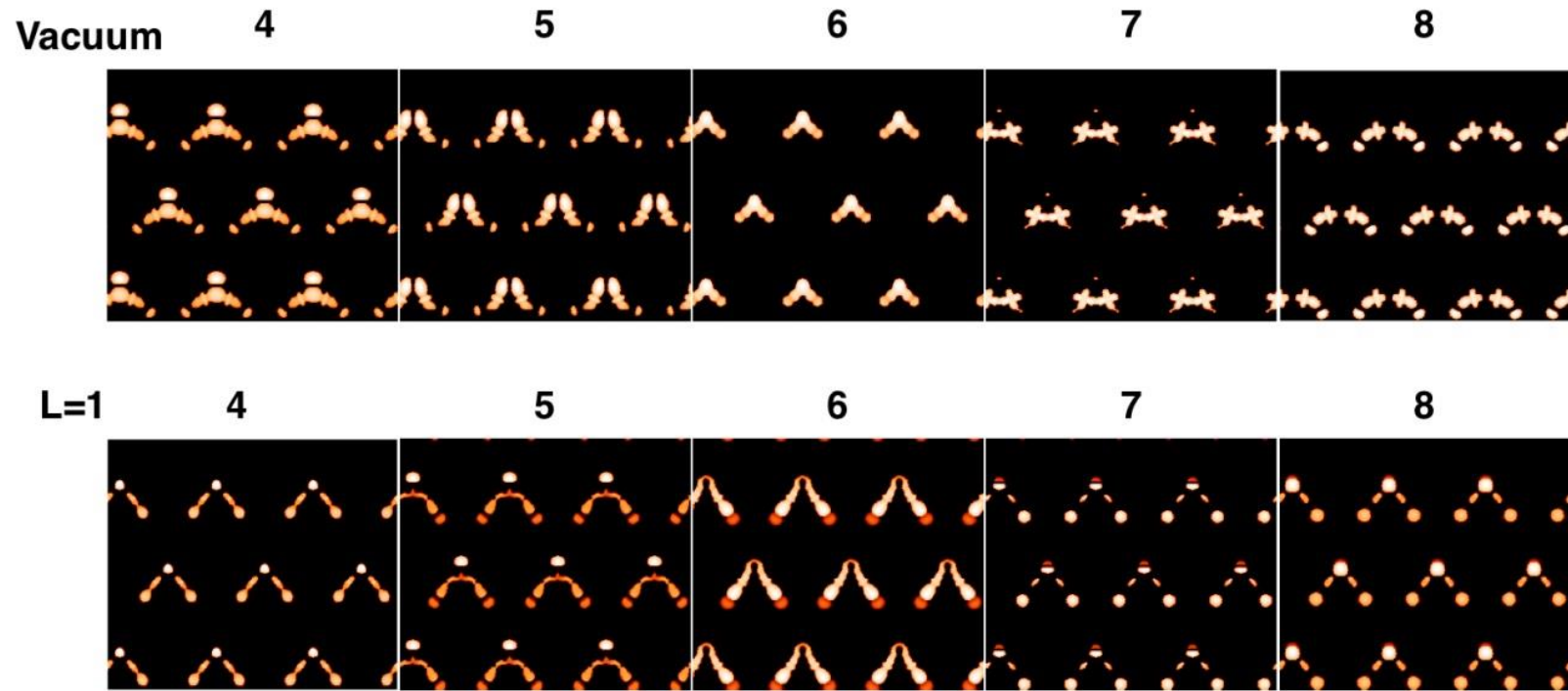


Figure 8. VASP isodensity plots for low energy bonding states of Cu_2S_3 in vacuum and on one layer ($L=1$) of Cu substrate.

Appendix 1. STM imaging conditions.

Tunneling conditions for the STM images presented in the main text figures are listed in Table II.

TABLE II. Tunneling conditions for main text figures.

Figure name	Image dimensions (nm ²)	Tunneling Current (nA)	Sample bias (V)
1a	12 x 11.5	1.24	-0.002
1a inset	1.2 x 1.2	1.72	-0.004
1b	1.5 x 1.5	1.17	-0.004
1c	1.5 x 1.5	1.29	-0.020
1d	1.5 x 1.5	1.06	-0.050
2a	20 x 20	1.24	-0.002
2b	15 x 15	0.65	-0.050

Appendix 2. Additional experimental data

The Cu(111) sample was cleaned with several cycles of annealing the sample at ~820 K while sputtering (Ar⁺, 12 μ A, 2.0 kV, 10 min) and then flashing the sample to ~800 K. The clean sample was then transferred into an adjacent chamber that houses the LT-STM. Typical tunneling conditions utilized here were -1.0 – 1.0 V sample bias, and 0.3 – 1.5 nA tunneling current. By scanning over the same region several times, we determined that the structures were immobile under the experimental conditions. In all the experiments, the sample was re-heated to room temperature and then cooled down again for imaging. This treatment had no effect on the distribution of the observed structures.

The STM piezoelectric calibration was checked by measuring a , the atomic separations along close-packed directions (Fig. A1(a-d)), and by measuring step heights (Fig. A1(f-h)). The average spacing along the close packed directions are provided in Fig. A1(e), and the average step height was 0.19 ± 0.02 nm [as visualized in the line profile in Fig. A1(g) and from the separation between peaks in Fig. A1(h)]. Within the stated uncertainties, these

equal the bulk parameters of 0.255 nm and 0.208 nm, respectively.³¹ Thus, the calibration was validated.

Additional Cu_2S_3 data are provided in Figures A2 –A4. The width and height of the complexes were measured by taking the line profile from the tip of a lobe to the flat opposite side [indicated in Fig. A4(a-b)]. The complexes had an average height of 0.04 ± 0.01 nm (Fig. A4(i)), average width of 0.67 ± 0.05 nm (Fig. A4(h)), and average area of 0.39 ± 0.04 nm². The width was measured at half maximum (FWHM); height was measured from minimum to maximum in the line profile. Area was measured by first isolating individual complexes and using the flooding function in WSxM.

The complexes adopted three different orientations, rotated by 120° [Fig. A4(d-f)] and the orientations existed in equal abundance.

Figure A4(g) shows an image of the clean Cu(111) surface with atomic resolution. This allowed us to define crystallographic directions as shown beneath Fig. A4(g). The complexes had orientation such that the lobes of the heart aligned with three of the six close-packed directions of the Cu(111) surface.

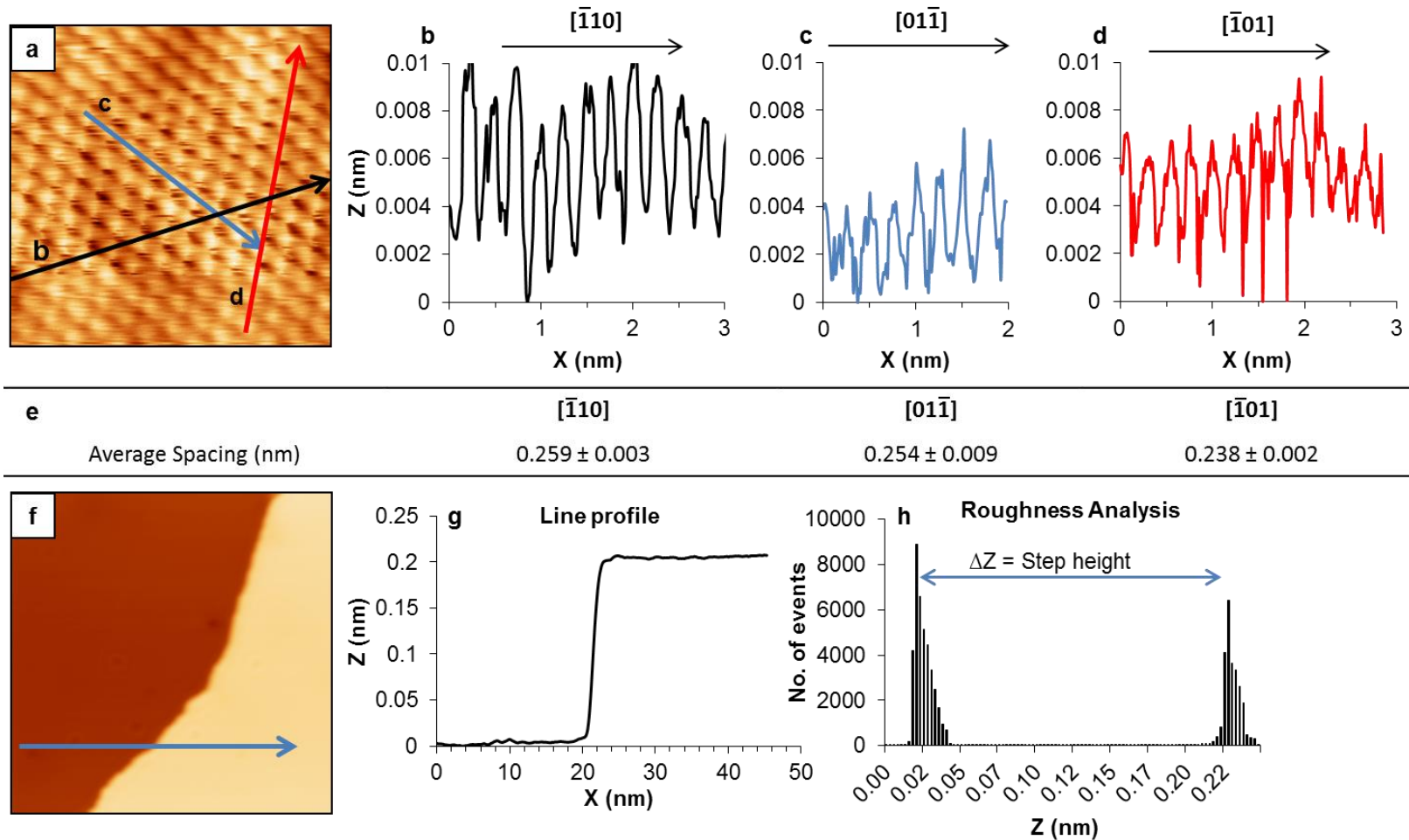


Figure A1. Evaluation of clean Cu(111). a) Atomically-resolved clean surface. Arrows match the line profiles shown in (b-d); $3 \times 3 \text{ nm}^2$. e) Average separation distance between maxima in line profiles. f) Clean step edge; $50 \times 50 \text{ nm}^2$. g) Line profile from (f). h) Roughness analysis of (f). Separation between peaks yields step height.

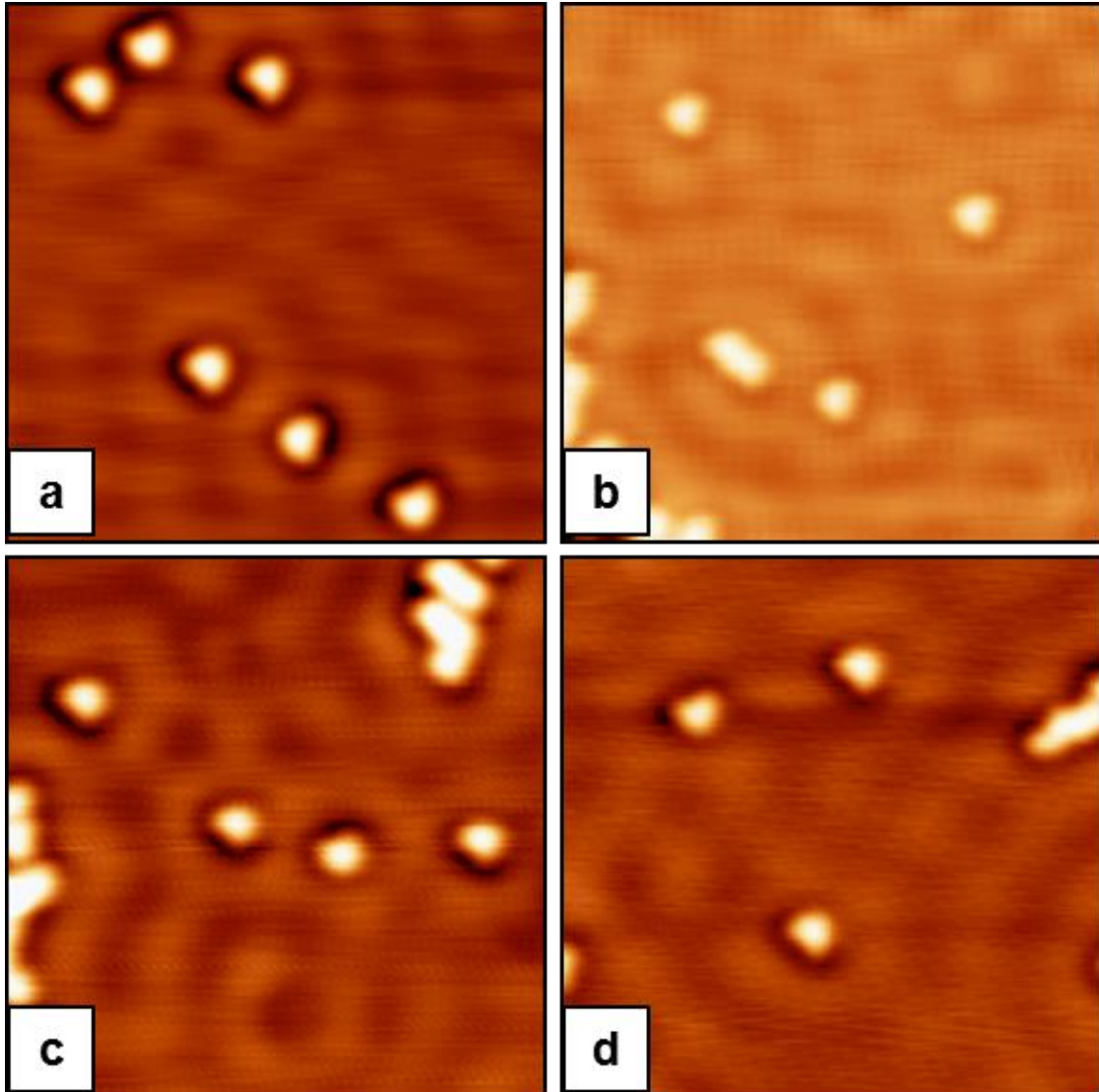


Figure A4. STM images of hearts. All images ($10 \times 10 \text{ nm}^2$). a) $\theta_S = 0.004$. b) $\theta_S = 0.016$. c) $\theta_S = 0.023$. d) $\theta_S = 0.050$.

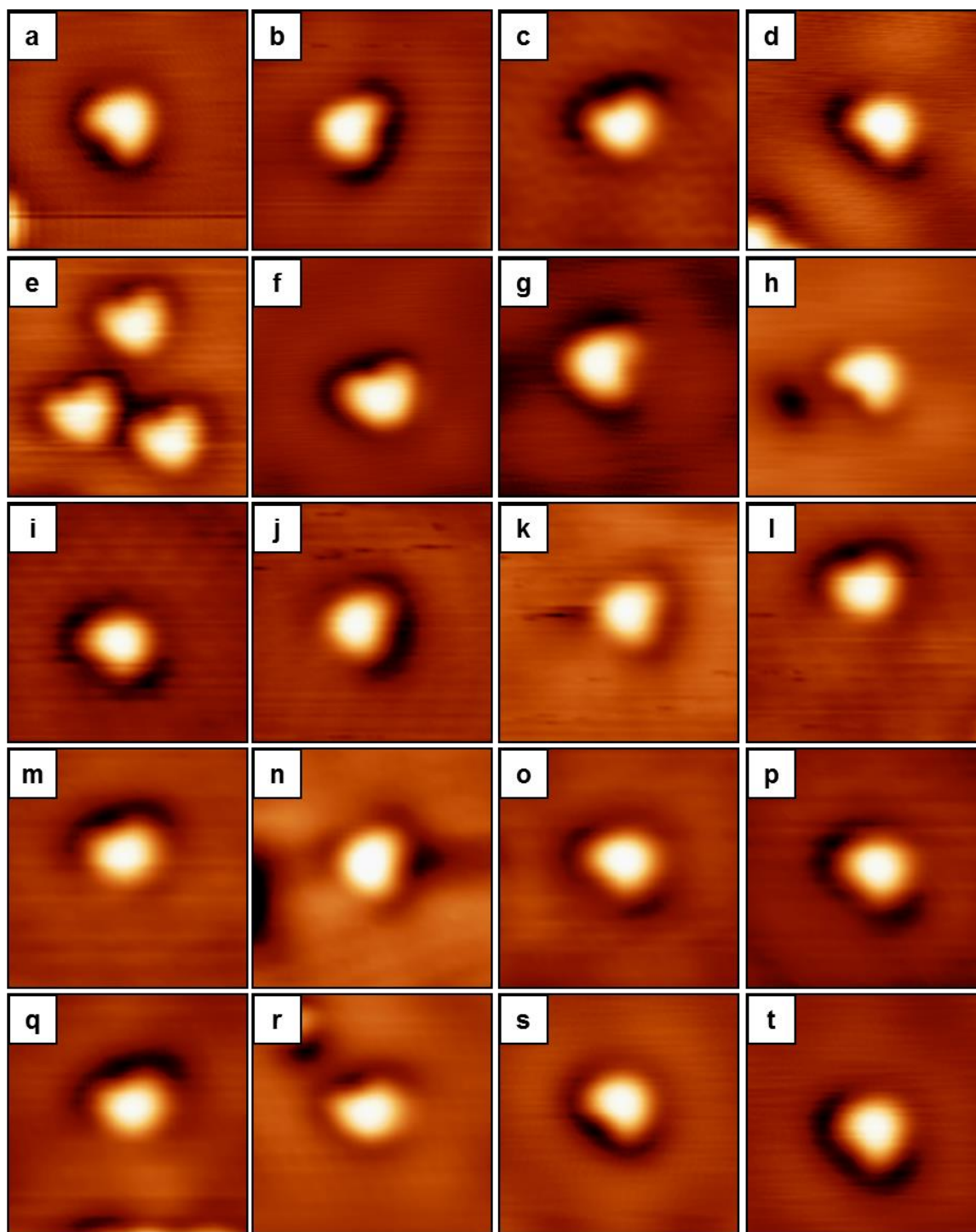


Figure A3. Topographic STM images of Cu_2S_3 hearts. All images are $3 \times 3 \text{ nm}^2$.

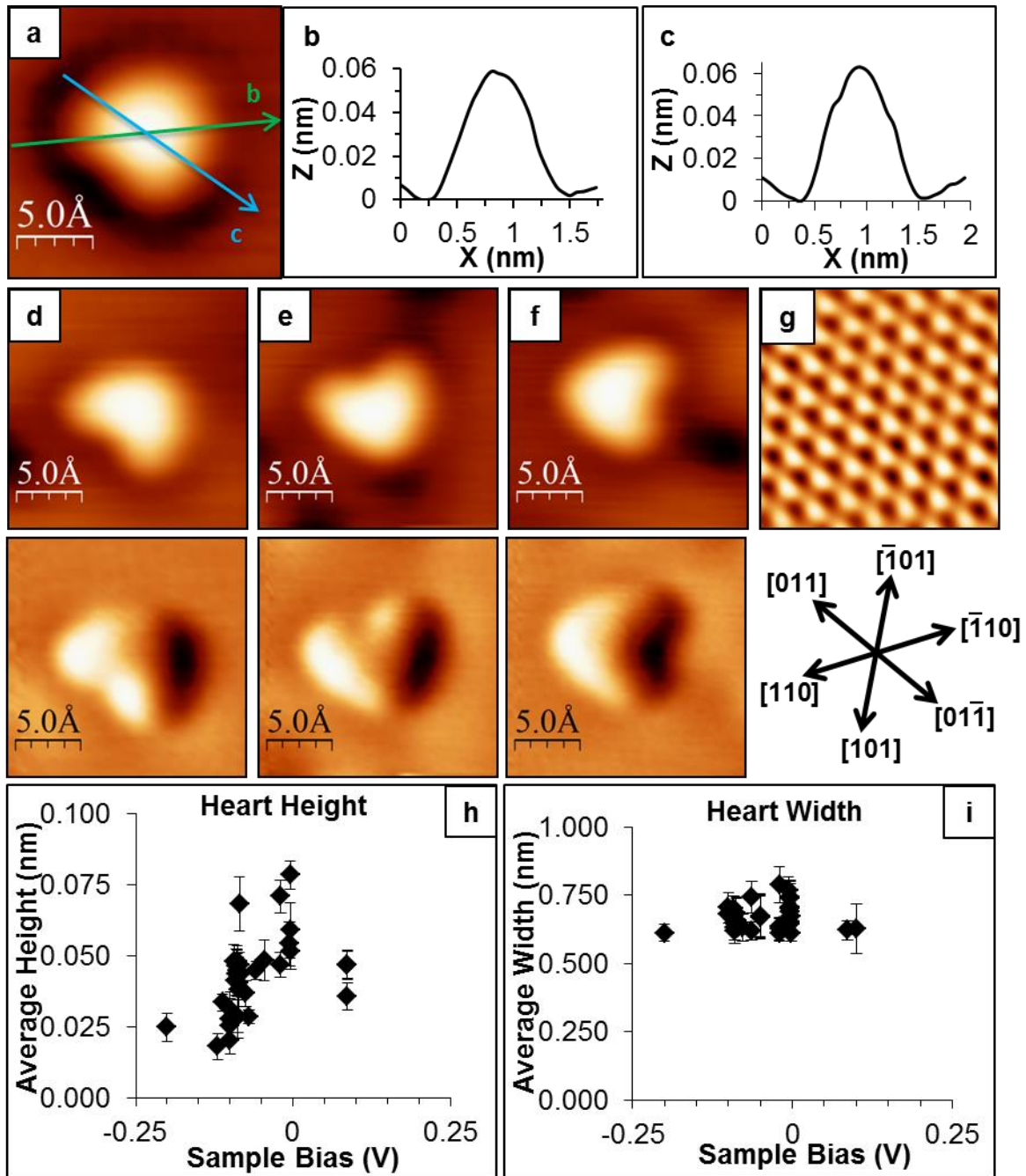


Figure A4. Physical description of the Cu_2S_3 hearts. a) Topographic STM image ($1.8 \times 1.8 \text{ nm}^2$). b) Line profile from lobe-side, as indicated in (a). c) Line profile from side to side, as indicated in (a). d)-f) Three orientations of Cu_2S_3 . Top images are topographic, bottom images are derivative (and the same from Fig. 1(b-d)). All are $1.8 \times 1.8 \text{ nm}^2$. g) FFT-filtered topographic image of atomically-resolved $\text{Cu}(111)$; $1.8 \times 1.8 \text{ nm}^2$. Arrows below indicate close-packed directions. h) Bias dependence of Cu_2S_3 height. i) Bias dependence of Cu_2S_3 width.

TABLE III. Tunneling conditions for Figures A1-A4.

Figure name	Image dimensions (nm ²)	Tunneling Current (nA)	Sample bias (V)	File name
A1a	3 x 3	2.63	-0.004	2131114 m82
A1f	50 x 50	0.31	-0.169	2131108 m50
A2a	10 x 10	1.27	-0.096	2131119 m44
A2b	10 x 10	0.382	+0.100	2131113 m66
A2c	10 x 10	0.382	-0.086	2131114 m10
A2d	10 x 10	0.374	-0.090	2131112 m14
A3a	3 x 3	0.39	-0.078	2131110 m32
A3b	3 x 3	0.29	-0.086	2131110 m58
A3c	3 x 3	0.37	-0.090	2131112 m14
A3d	3 x 3	0.37	-0.090	2131112 m21
A3e	3 x 3	0.24	-0.088	2131112 m44
A3f	3 x 3	0.21	-0.085	2131113 m66
A3g	3 x 3	0.21	-0.085	2131113 m68
A3h	3 x 3	1.06	-0.004	2131114 m45
A3i	3 x 3	0.46	-0.090	2131110 m77
A3j	3 x 3	0.46	-0.090	2131110 m76
A3k	3 x 3	0.46	-0.090	2131110 m77
A3l	3 x 3	0.46	-0.090	2131110 m77
A3m	3 x 3	0.46	-0.090	2131110 m80
A3n	3 x 3	0.46	-0.090	2131110 m80
A3o	3 x 3	0.46	-0.090	2131110 m80
A3p	3 x 3	0.46	-0.090	2131110 m79
A3q	3 x 3	0.46	-0.090	2131110 m79
A3r	3 x 3	1.24	-0.002	2131119 m17
A3s	3 x 3	1.29	-0.020	2131119 m31
A3t	3 x 3	1.29	-0.020	2131119 m35
A4a	1.8 x 1.8	1.27	-0.096	2131114 m47
A4d	1.8 x 1.8	1.06	-0.004	2131114 m45
A4e	1.8 x 1.8	1.17	-0.005	2131114 m69
A4f	1.8 x 1.8	1.17	-0.005	2131114 m69
A4g	1.8 x 1.8	1.72	-0.004	2131114 m82

References

1. Harris, P. J. F., "Growth and Structure of Supported Metal Catalyst Particles". *Int. Mat. Rev.* **1995**, *40*, 97.
2. Thiel, P. A.; Shen, M.; Liu, D.-J.; Evans, J. W., "Critical Review: Adsorbate-Enhanced Transport of Metals on Metal Surfaces: Oxygen and Sulfur on Coinage Metals". *J. Vac. Sci. Technol. A* **2010**, *28*, 1285.
3. Parkinson, G. S.; Novotny, Z.; Argentero, G.; Schmid, M.; Pavelec, J.; Kosak, R.; Blaha, P.; Diebold, U., "Carbon Monoxide-Induced Adatom Sintering in a Pd-Fe₃O₄ Model Catalyst". *Nat. Mater.s* **2013**, *12*, 724-728.
4. Kellogg, G. L., "Hydrogen Promotion of Surface Self-Diffusion on Rh(100) and Rh(311)". *Phys. Rev. B* **1997**, *55*, 7206-7212.
5. Horch, S.; Lorensen, H. T.; Helveg, S.; Laegsgaard, E.; Stensgaard, I.; Jacobsen, K. W.; Norskov, J. K.; Besenbacher, F., "Enhancement of Surface Self-Diffusion of Platinum Atoms by Adsorbed Hydrogen". *Nature* **1999**, *398*, 134-136.
6. Layson, A. R.; Thiel, P. A., "Testing Realistic Environments for Metal Film Growth and Aging: Chemical Insights into the Effect of Oxygen on Ag/Ag(100)". *Surf. Sci.* **2001**, *472*, L151-L156.
7. Layson, A. R.; Evans, J. W.; P.A.Thiel, "Additive-Enhanced Coarsening and Smoothing of Metal Films: Complex Mass-Flow Dynamics Underlying Nanostructure Evolution". *Phys. Rev. B* **2002**, *65*, 193409.
8. Maksymovych, P.; Voznyy, O.; Dougherty, D. B.; Sorescu, D. C.; Yates Jr., J. T., "Gold Adatom as a Key Structural Component in Self-Assembled Monolayers of Organosulfur Molecules on Au(111)". *Prog. Surf. Sci.* **2010**, *85*, 206-240.

9. Feibelman, P. J., "Formation and Diffusion of S-Decorated Cu Clusters on Cu(111)". *Phys. Rev. Lett.* **2000**, *85*, 606-609.
10. Ling, W. L.; Bartelt, N. C.; Pohl, K.; de la Figuera, J.; Hwang, R. Q.; McCarty, K. F., "Enhanced Self-Diffusion on Cu(111) by Trace Amounts of S: Chemical-Reaction-Limited Kinetics". *Phys. Rev. Lett.* **2004**, *93*, 166101.
11. Morgenstern, K.; Laegsgaard, E.; Besenbacher, F., "Sintering of Cobalt Nanoclusters on Ag(111) by Sulfur: Formation of One-, Two-, and Three-Dimensional Cobalt Sulfide". *Surf. Sci.* **2008**, *602*, 661-670.
12. Shen, M.; Liu, D.-J.; Jenks, C. J.; Thiel, P. A.; Evans, J. W., "Accelerated Coarsening of Ag Adatom Islands on Ag(111) Exposed to S: Mass-Transport Mediated by Ag-S Complexes". *J. Chem. Phys.* **2009**, *130*, 094701.
13. Shen, M.; Liu, D.-J.; Jenks, C. J.; Thiel, P. A., "The Effect of Chalcogens (O, S) on Coarsening of Nanoislands on Metal Surfaces". *Surf. Sci.* **2009**, *603*, 1486-1491.
14. Shen, M.; Russell, S. M.; Liu, D.-J.; Thiel, P. A., "Desabilization of Ag Nanoislands on Ag(100) by Adsorbed Sulfur". *J. Chem. Phys.* **2011**, *135*, 154701.
15. Foss, M.; Feidenhans'l, R.; Nielsen, M.; Findeisen, E.; Buslaps, T.; Johnson, R. I.; Besenbacher, F.; Stensgaard, I., "Sulfur Chemisorption on Ni(111): The Clock Structure of the $(5\sqrt{3}\times 2)S$ Phase". *Phys. Rev. B* **1994**, *50*, 8950-8953.
16. Foss, M.; Feidenhans'l, R.; Nielsen, M.; Findeisen, E.; Buslaps, T.; Johnson, R. L.; Besenbacher, F., "Sulfur Induced Cu_4 Tetramers on Cu (111)". *Surf. Sci.* **1997**, *388*, 5-14.
17. Russell, S. M.; Kim, Y.; Liu, D.-J.; Evans, J. W.; Thiel, P. A., "Structure, Formation, and Equilibration of Ensembles of Ag-S Complexes on an Ag Surface". *J. Chem. Phys.* **2013**, *138*, 071101.

18. Wahlström, E.; Ekvall, I.; Olin, H.; Lindgren, S. A.; Wallden, L., "Observation of Ordered Structures for S/Cu(111) at Low Temperature and Coverage". *Phys. Rev. B* **1999**, *60*, 10699.
19. Wahlström, E.; Ekvall, I.; Kihlgren, T.; Olin, H.; Lindgren, S. A.; Wallden, L., "Low-Temperature Structure of S/Cu(111)". *Phys. Rev. B* **2001**, *64*, 155406.
20. Kresse, G.; Furthmüller, J., "Efficiency of Ab-Initio Total Energy Calculations for Metals and Semiconductors Using a Plane-Wave Basis Set". *Comput. Mater. Sci.* **1996**, *6*, 15-50.
21. Blöchl, P. E., "Projector Augmented-Wave Method". *Phys. Rev. B* **1994**, *50*, 17953-17979.
22. Perdew, J. P.; Burke, K.; Ernzerhof, M., "Generalized Gradient Approximation Made Simple". *Phys. Rev. Lett.* **1996**, *77*, 3865-3868.
23. Tersoff, J.; Hamann, D. R., "Theory and Application for the Scanning Tunneling Microscope". *Phys. Rev. Lett.* **1983**, *50*, 1998-2001.
24. Tersoff, J.; Hamann, D. R., "Theory of the Scanning Tunneling Microscope". *Phys. Rev. B* **1985**, *32*, 805-813.
25. te Velde, G.; Bickelhaupt, F. M.; Baerends, E. J.; Fonseca Guerra, C.; van Gisbergen, S. J. A.; Snijders, J. G.; Ziegler, T., "Chemistry with ADF". *J. Comput. Chem.* **2001**, *22*, 931-967.
26. van Lenthe, E.; Baerends, E. J.; Snijders, J. G., "Relativistic Total Energy Using Regular Approximations". *J. Chem. Phys.* **1994**, *101*, 9783-9792.

27. van Lenthe, E.; Ehlers, A.; Baerends, E.-J., "Geometry Optimizations in the Zero Order Regular Approximation for Relativistic Effects". *J. Chem. Phys.* **1999**, *110*, 8943-8953.
28. Häkkinen, H., "The Gold-Sulfur Interface at the Nanoscale". *Nat. Chem.* **2012**, *4*, 443-455.
29. Jadzinsky, P. D.; Calero, G.; Ackerson, C. J.; Bushnell, D. A.; Kornberg, R. D., "Structure of a Thiol Monolayer-Protected Gold Nanoparticle at 1.1 Å Resolution". *Science* **2007**, *318*, 430.
30. Liu, D.-J., "Density Functional Analysis of Key Energetics in Metal Homoepitaxy: Quantum Size Effects in Periodic Slab Calculations". *Phys. Rev. B* **2010**, *81*, 035415.
31. Driver, S. M.; Woodruff, D. P., "A New Pseudo-(100) Sulphur-Induced Reconstruction of Cu(111) Observed by Scanning Tunnelling Microscopy". *Surf. Sci.* **2001**, *479*, 1-10.
32. Wahlstrom, E.; Ekvall, I.; Olin, H.; Wallden, L., "Long-Range Interaction between Adatoms at the Cu(111) Surface Imaged by Scanning Tunneling Microscopy". *Appl. Phys. A* **1998**, *66*, S1107-S1110.
33. Rose, M. K.; Borg, A.; Mitsui, T.; Ogletree, D. F.; Salmeron, M., "Subsurface Impurities in Pd(111) Studied by Scanning Tunneling Microscopy". *J. Chem. Phys.* **2001**, *115*, 10927-10934.

CHAPTER III

RECONSTRUCTION OF STEPS ON THE CU(111) SURFACE
INDUCED BY SULFUR

Holly Walen,^a Da-Jiang Liu,^b Junepyo Oh,^c Hyunseob Lim,^c J. W. Evans,^{b,d} Yousoo Kim,^c
and P. A. Thiel^{a,b,e}

A paper published in Journal of Chemical Physics[†]

Abstract

A rich menagerie of structures is identified at 5 K following adsorption of low coverages (≤ 0.05 ML) of S on Cu(111) at room temperature. This paper emphasizes the reconstructions at the steps. The A-type close-packed step has 1 row of S atoms along its lower edge, where S atoms occupy alternating pseudo-fourfold-hollow (p4fh) sites. Additionally, there are 2 rows of S atoms of equal density on the upper edge, bridging a row of extra Cu atoms, together creating an extended chain. The B-type close-packed step exhibits an even more complex reconstruction, in which triangle-shaped groups of Cu atoms shift out of their original sites and form a base for S adsorption at (mostly) 4fh sites. We propose a mechanism by which these triangles could generate Cu-S complexes and short chains like those observed on the terraces.

Departments of ^aChemistry, ^dPhysics & Astronomy, and ^eMaterials Science & Engineering, Iowa State University, Ames, Iowa 50011 USA

^bAmes Laboratory of the USDOE, Ames, Iowa 50011 USA

^cRIKEN Surface and Interface Science Laboratory, Wako, Saitama 351-0198, Japan

[†]*J. Chem. Phys.* **142** 194711 (2015)

1. Introduction

Because of the low coordination of atoms at surface steps, steps are important active sites in many surface processes, from heterogeneous catalysis,¹ to thin film growth,² to oxidation.³ They often serve as a dynamic reservoir of atoms in cases where the surface itself is a reactant. The signature of such a reaction can be etching, recession, and/or faceting of the steps. For example, Ruan *et al.* showed that sulfur-induced reconstruction on Cu(111) is accompanied by step recession at room temperature, and concluded that Cu is incorporated into the reconstructed phase.⁴

There is mounting evidence that metal atoms react with sulfur or sulfur-containing molecules to form localized complexes on surfaces of the coinage metals.⁵⁻⁷ (Molecules with some other functional groups, such as cyano groups, can also self-metallate on these surfaces.⁸⁻⁹) Sulfur on Cu(111) is one such system. On Cu(111), Feibelman first proposed a Cu_3S_3 complex as an agent of mass transport on the basis of density functional theory (DFT).¹⁰⁻¹¹ It is a triangle of Cu atoms, decorated by nearly-coplanar S atoms at its edges. Its stability was attributed to the fact that S is in pseudo-fourfold-hollow (p4fh) sites, which are more favorable for S adsorption than the three-fold hollow (3fh) sites present on the terraces. This is in accord with a long-standing principle that high-coordination sites, such as 4fh sites, stabilize adsorbed S, and are created in some S-induced reconstructions.^{10, 12-13} Recently, we identified a different complex, heart-shaped Cu_2S_3 , as the dominant terrace species at very low sulfur coverage and very low temperature (5 K), based on scanning tunneling microscopy (STM) and DFT.¹⁴ We proposed that the Cu_2S_3 species owes its stability to the linearity of its S-Cu-S subunits, in addition to the presence of one S atom at a p4fh site.

There have been a number of other studies of S on Cu(111).^{4, 12, 15-21} The work most relevant to the current study is that of Wahlström *et al.*,²⁰⁻²¹ who characterized this system at temperatures down to 50 K, and discovered a number of low-temperature ordered phases. The lowest-coverage phase was a ($\sqrt{43} \times \sqrt{43}$) $R \pm 7.5^\circ$ (hereafter referred to as $\sqrt{43}$) reconstruction with an ideal coverage of 0.27 monolayers (ML) and a disordering temperature of 170 K. We recently re-examined the structure of this phase, and proposed a model that is not related in any straightforward way either to bulk CuS (the original model²¹) or to the Cu₂S₃ (or Cu₃S₃) complex.²² Additionally, Wahlström *et al.* observed pronounced triangular features at some step edges.

In this paper, we find that sulfur induces complex reconstructions of the steps, which we identify on the basis of STM and DFT. The paper is organized as follows. Section 2 provides experimental and computational details, Sec. 3 and 4 present experimental and computational results, respectively, and Sec. 5 is a discussion of the results.

2. Experimental and computational details

2.1 Experimental description

All STM imaging was done at 5 K with a low-temperature STM (LT-STM Omicron GmbH) in a UHV chamber with base pressure below 2.5×10^{-11} Torr. Images were obtained using a W tip. In an adjacent chamber, the Cu(111) sample was cleaned. Each cleaning cycle consisted of several steps: (1) heating the sample at 820 K for 5 minutes; (2) sputtering with Ar⁺ (12 μ A, 2.0 kV) at 820 K for 10 minutes; (3) continuing to sputter for 2 minutes while the sample cooled; and (4) flashing back to 800 K without sputtering. Cleaning between experiments consisted of two to three such cycles. Sample temperatures during cleaning were

measured with an optical pyrometer, for which the uncertainty was estimated as ± 10 K, based on variation of the reading with the emission angle.

The adjacent chamber also contained the sulfur source, a solid-state electrochemical Ag|AgI|Ag₂S|Pt cell.²³ To generate sulfur, the Pt cathode was biased at 0.20 - 0.25 V with respect to the Ag anode and the cell was heated independently. The cell temperature was recorded via a thermocouple located near, but not in direct contact, with the chemical components of the cell. The thermocouple reading corresponded to a temperature of 160°C during cell operation. Work by Detry *et al.* indicates that these conditions of cell operation produce mainly S₂(gas).²⁴ We verified the production of sulfur by measuring a mass spectrum with the evaporator running, and observing peaks at mass-to-charge ratios of 32 and 64.

During sulfur deposition, the sample was held at room temperature to ensure dissociative adsorption.²⁵ The sample was then transferred into the STM stage and cooled to the imaging temperature, 5 K. Typical tunneling conditions were -1.0 V to +1.0 V sample bias (V_s), and 0.3 to 1.5 nA tunneling current (I). We have carefully analyzed the way in which topographic heights and widths of the terrace hearts depend upon tunneling parameters within this range of voltages and currents (see Fig. A4 of Chapter II). There is no statistically significant trend. This, plus our experience in imaging diverse features in other S adsorption systems, leads us to conclude that there is no significant effect of tunneling conditions (within this range) on the step features either. Exact tunneling conditions for each individual image can be found in Appendix 2.

By scanning over the same region several times, we determined that the structures were immobile and stable under these experimental conditions. In all experiments, the

sample was first imaged at 5 K after sulfur deposition, and then it was re-heated to room temperature and re-cooled for imaging. This treatment had no effect on the observed structures or their populations. The sample had the same azimuthal orientation relative to the image frame in all experiments, so orientations of features can be compared directly between all STM images, with the exception of Fig. 13 and 14 where STM images have been rotated to facilitate visual comparison with a model.

The STM piezoelectric calibration was checked by measuring a , the atomic separation along close-packed directions [Fig. 1(a)], and by measuring step heights (not shown). The former value was 0.250 ± 0.005 nm, and the latter was 0.19 ± 0.02 nm. Within the stated uncertainties, these equal the bulk parameters of 0.255 nm and 0.208 nm, respectively. Thus, the calibration was validated. Constant-current STM images are referred to as topographic images. These are presented after minimal correction—planing and flattening—using WSxM software.²⁶

Areal coverage was determined by using the flooding function in WSxM software²⁶ to determine the area of all Cu-S species on the terraces and then dividing by the total image area. Step edges were omitted from this calculation. The areal coverages ranged from 0.010 to 0.125. We determined an approximate absolute coverage by referring to previous work by Wahlström *et al.*, where islands of the Cu-S $\sqrt{43}$ reconstruction were reported to form at $\theta_S \sim 0.05$.²⁰⁻²¹ This occurred at our highest areal coverage of 0.125, so the absolute coverage is roughly 2/5 the areal coverage. Applying this constant to the rest of the areal coverage range, the range of absolute S coverage (θ_S) is approximately 0.004 ML to 0.050 ML, where $\theta_S = 1$ (or a coverage of 1 ML) is defined as a ratio of 1 S atom to 1 Cu atom in the Cu(111) plane.

2.2 Computational Description

The computational approach has been described elsewhere.¹⁴ Energetics are obtained by averaging calculations on 4-7 layer slabs of Cu(111) to minimize the impact of surface states.²⁷ Error bars in graphs, or numerical uncertainties in parentheses, are derived from the range of values for different slab thickness.²⁷ Most of the results shown here used “high” k-point grids corresponding approximately to (24 x 24 x 1) for the primitive cell, and have uncertainties of 5-8 meV. Some results in the Appendix used a “low” k-points grid corresponding to (12 x 12 x 1) for the primitive cell, and have higher uncertainties of 10-20 meV. Images with a periodic arrangement are (2 x 2) or (3 x 2) representations of the original supercells. All models of DFT configurations show the energy-optimized atomic coordinates. In energy optimization, the bottom layer of Cu in the slab is fixed at bulk positions with theoretical bulk lattice constant, and all other atoms are allowed to relax. STM images were simulated from DFT using the Tersoff-Hamann²⁸ method, which essentially generates the electron isodensity contour surface at the Fermi edge.

3. Experimental Results

3.1 Overview of Features on Terraces and Steps

Figure 1(a) is an image of the clean Cu(111) surface with atomic resolution. Consequently, close-packed crystallographic directions are identified in Fig. 1(b). Figure 1(c-d) are examples of step edges on the clean surface. The step in Fig. 1(d) is nearly parallel to a close-packed direction and hence is very smooth, while that in Fig. 1(c) lies between two close-packed directions and is slightly rough, presumably due to kinks.

Figure 2 shows Cu(111) terraces (top panels) and steps (bottom panels), at $\theta_S = 0.004$ to 0.050. At the lowest coverage, the main features on the terraces are small, uniform bright spots that are the heart-shaped Cu_2S_3 complexes discussed elsewhere¹⁴ [Fig. 2(a)]. Close views and schematics of three such complexes are shown in Fig. 3a, b, and e. Even at this low coverage, step edges are heavily decorated.

At $\theta_S = 0.016$, short linear chains appear on the terraces, resembling concatenations of hearts [Fig. 2(b)]. Two high-magnification examples of linear chains, and corresponding models, are shown in Fig. 3(c,d). The arrangements are built from Cu_2S_3 complexes that condense by sharing S atoms. Linear chains observed on the terraces tend to be short, only 2 to 5 units long; linear chains near steps can be much longer, up to 23 units. The spacing between lobes (S atoms) in the middle of the chain should be $2a = 0.51$ nm, according to the models of Fig. 3(c,d). This is exactly the value measured from STM images, 0.51 ± 0.03 nm (for sample size $N = 63$).

By $\theta_S = 0.023$, clump-like features also appear on the terraces. Some consist of hearts or chains, as shown in Fig. 3(e). In others, hearts or chains make only a minor contribution, or are not identifiable at all, as in Fig. 3(f).

At $\theta_S = 0.030$, terraces contain small fragments of the $\sqrt{43}$ reconstruction, such as the individual dark spot encircled by tendrils in Fig. 2(d). At $\theta_S = 0.050$, clear islands of $\sqrt{43}$ appear, as shown in Fig. 2(e). The $\sqrt{43}$ is identified on the basis of its honeycomb pattern of dark spots,²⁰⁻²² together with its unit cell length and orientation.

The observations of the Cu-S complexes and $\sqrt{43}$ reconstruction on the terraces help to define the conditions under which the intricate step structures form.

3.2 STM Examination of Features at and near Step Edges

Identification of A- and B-steps. On an fcc(111) surface there are two types of close-packed step edges, denoted A and B.²⁹ The A-step consists of p4fh sites, and the B-step consists of pseudo-threefold (p3fh) sites. A- and B-steps are difficult to distinguish on the clean surface, but we will show that they can be differentiated on Cu(111) based on their response to S adsorption.

We begin with an experiment in which θ_S is so low that there are no S-induced features on terraces, i.e. lower than the lowest θ_S in Fig. 2. Under these conditions, it is likely that the steps are sub-saturated. In Fig. 4(a), a step is smoothly decorated by a row of protrusions separated by 0.52 ± 0.02 nm, which we assign as S atoms at alternating sites along an A-step. This is very similar to our previous STM observation of S-decorated steps on a different surface, Ag(111)—cf. Fig. 3A of Ref.³⁰. In contrast, the step in Fig. 4(b), at 60° , is slightly irregular but not obviously decorated—and similar to the clean step in Fig. 1(d). We assign this as a nearly-clean B-step.

The difference between A- and B-steps becomes more pronounced at higher θ_S , as shown in Fig. 5 and 6. Steps oriented close to the 3 A-directions are still smooth, while steps at other orientations display the jagged, triangular features first reported by Wahlström *et al.*²¹ We now examine the structures around steps more closely.

Structure around A-steps. The A-steps are characterized by a row of alternating S atoms at the edge, and a bright, linear feature that lies atop the upper terrace, parallel to and near the step. Close inspection reveals that the linear feature resembles a terrace chain. Quantitatively, the full-width at half-maximum (FWHM) of the bright linear feature is the same as the width of the terrace chains, 0.56 ± 0.02 nm. It is significantly wider than single

atoms of S which we have imaged on other surfaces [Au(100), Au(111), Au(110)] under the same conditions. For those cases, the atomic FWHM ranges from 0.29 to 0.38 nm.

Furthermore, the bright feature has a distinctive zig-zag appearance in the differentiated STM images, and this also resembles the chains on the terraces. Examples and a schematic of the structure of the A-steps and the adjacent features are shown in Fig. 5. This model is supported by the DFT calculations presented in Sec. 4.

In addition, other chains are often found in the vicinity of A-steps, both on the upper and the lower terrace. Their lengths are skewed toward longer values than on terraces. Their locations and orientations, relative to the step edge, can vary. In short, the A-steps are rich in chains.

Structure around B-steps. Steps oriented close to the three B directions are lined with triangular features, which were first reported by Wahlström *et al.*²¹ High-magnification images are shown in Fig. 6, together with two schematic interpretations that are consistent with the DFT analysis developed in Sec. 4. Here, we summarize the distinctive features of the triangles, which are illustrated in Fig. 6(c,d).

(i) A slightly-curved row of dots always defines the outer edge of a triangle, which is the edge facing the lower terrace—see green line in Fig. 6(c). These dots are spaced by $2a$, the measured value being 0.51 ± 0.02 nm ($N = 16$).

(ii) The inner edges of a triangle—the edges bordering the upper terrace as outlined in red in Fig. 6(c)—are also decorated by dots, separated by $2a$.

(iii) The features in the middle of the triangle depend on size. The smallest triangles are about 2.0-2.2 nm on each interior edge, and they contain a single dot in the center. Together with the dots mentioned in (i) and (ii), this feature completes a

local (2 x 2)-like pattern. The central dot is often slightly larger and higher than the dots at the edge. For larger triangles, with interior edges 2.9-3.0 nm, the interior region sometimes contains a larger (2 x 2)-like pattern, but more often, it is a diffuse elevated area with about the same apparent height as the upper terrace.

(iv) The inner edges of the triangle are aligned with A-steps.

(v) Immediately adjacent to the inner edges of the triangle, on the upper terrace, there are features with the height and appearance of chains. These are either oriented parallel to, or 60° from, the step edge.

Features ii, iv, and v above show that the orientations and features of the inner edges of the triangle bear a resemblance to the A-steps. Thus it would be easy to conclude that these are facets toward A-steps, as we did at an earlier stage in our analysis of this system.¹⁴ However, the situation is more complex, as will be discussed in Sec. 4.

In addition, B-steps commonly have a high density of miscellaneous extended chains in the near vicinity, both on the upper and lower terraces. This can be seen in Fig. 6(a,b). Again, this is similar to the A-steps. There is no obvious difference between A- and B-steps in the density of these miscellaneous chains.

4. DFT Analysis of Features at and Near Step Edges

4.1 Benchmark: Sulfur Adsorbed on Terraces

In the following analysis, a useful quantity is the chemical potential of S, μ_S , incorporated into a Cu_mS_n complex, $\mu_S(\text{Cu}_m\text{S}_n)$, which is defined as:

$$\mu_S(\text{Cu}_m\text{S}_n) = [E(\text{Cu}_m\text{S}_n + \text{slab}) - E(\text{slab}) - m \mu_{\text{Cu}}]/n - E(\text{S}_{2,\text{g}})/2 \quad (1)$$

The chemical potential of Cu, μ_{Cu} , is the average energy of a Cu atom in the bulk. Note that μ_S reduces to the (average) adsorption energy of S for structures that do not incorporate additional Cu adatoms, i.e. for $m=0$. This quantity, μ_S , allows us to assess the relative stability of various complexes in the presence of excess S beyond that required to saturate step edges.

Figure 7 shows $\mu_S(\text{S})$ as a function of θ_S on the Cu(111) terrace, calculated from DFT. As supercell size decreases, θ_S increases. Three sets of calculations, based on 3 types of supercells, are represented. Green symbols show $(n \times n)$ supercells, blue show $(n\sqrt{3} \times n\sqrt{3})R30^\circ$ supercells, yellow shows a $(\sqrt{7} \times \sqrt{7})R19^\circ$, and purple show honeycomb (hexagonal) supercells in which there are 2 adatoms per unit cell, both occupying fcc sites. At low θ_S , $\mu_S(\text{S})$ depends sensitively on the nature of the supercell. The $(n \times n)$ calculations show high scatter and large error bars at low coverage, so are regarded as least reliable. The points below 0.070 ML cluster around -1.90 to -1.92 eV, which leads to our choice of -1.91 eV as the low-coverage limit for $\mu_S(\text{S})$.

4.2 Extended Structures at Step Edges

For extended structures that run along the step edges, we carry out DFT calculations using $(2 \times 2n)$ supercells, since most of the structures of interest are assumed to have periodicity of $2a$ along the step edge. In practice, we choose the primitive cell for this set of calculations as a rectangular $(1 \times \sqrt{3})$, because k -points grids for asymmetrical supercells are easier to implement with a rectangular lattice than with a triangular lattice. The most

important DFT results for the step edges are shown in this section; other related DFT results are given in the Appendix. For purposes of comparison between STM data and DFT results, we consider that the step edges at $\theta_S \geq 0.004$ are locally saturated, since the features in the immediate vicinity of the steps (e.g. the chain atop the A-step) does not change in this coverage range.

We first consider configurations with a single row of S atoms at a step edge (represented as the edge of a 4 Cu atom wide strip in the first layer). Table I shows the results for supercells of size $(2 \times 2n)$, where we put a $(2 \times n)$ island of Cu adatoms on top of the slab. Figure 8 illustrates the (2×8) supercell configurations.

In Table I, note first that all values of $\mu_S(S)$ are lower than the -1.91 eV for S on fcc sites, so adsorption of S at steps is more favorable than at terraces. Comparing A- and B-steps, $\mu_S(S)$ is always more negative at the A-step than at the B-step, consistent with the interpretation of Fig. 4. Finally, comparing upper and lower step edges, $\mu_S(S)$ is consistently lower when S adsorbs at the lower step edge than at the upper step edge, where the latter is represented by configuration B1.

TABLE I. Chemical potential (adsorption energy, in eV) of a single row of adsorbed S on a A-step and a B-step with different supercells and island widths. B1 is a structure with S on the upper edge of a B-step. Configurations for the (2×8) are shown in Fig. 8.

$\mu_S(S)$ (eV)	2×4	2×6	2×8	2×10
A-step	-2.27(1)	-2.227(6)	-2.240(4)	
B-step	-2.20(1)	-2.15(2)	-2.13(1)	-2.14(1)
B1	-2.16(2)	-2.08(1)	-2.11(1)	-2.11(1)

We next consider 2 rows of S attaching to a step edge (now represented as the edge of a 5 atom wide strip in the first layer). Some configurations are shown in Fig. 9. For the A-step (a-c), we find that the most stable configuration has the Cu atoms in the outermost row of the step shifting and forming a pseudo (100) surface, which can be viewed as an extended step edge reconstruction [see Fig. 9(c)]. For a B-step (d-e), the most stable configuration has the upper row of S atoms adsorbed on the unreconstructed step edge at fcc sites [see Fig. 9(d)].

Can more S aggregate at an A-step? Figure 10(a-c) shows 3 configurations with 3 rows of S close to an A-step. Figure 10(a) does not have any additional Cu atoms beyond the 5 atom wide strip in the first layer also shown in Fig. 9, but the 2 outermost rows of Cu reconstruct forming a pseudo (100) surface. Figure 10(b) and (c) are very similar. Both have 2 extra second-layer Cu atoms in each supercell (in addition to the 10 Cu atoms per unit cell that form the 5-atom wide strip). Together with the 2 S atoms on top of the island, the extra Cu atoms form a one-atom row of Cu with S on either side, i.e. a zigzag S-Cu-S chain. The difference between Fig. 10(b) and 10(c) is the distance between the chain and the step edge, with (c) being closer. With a 5-atom wide island, we find the configuration in Fig 10(c) to be the most stable, involving 3 rows of S around an A-step. (It is interesting to note that Cu atoms in the chain actually are closer to bridge sites than to either of the two 3fh (fcc or hcp) sites.) This structure is entirely consistent with the interpretation of the STM images of the A-step at $\theta_S \geq 0.004$ given in Sec. 3 [Fig. 5], which are based largely on empirical observation. Thus, the configuration in Fig. 10(c) is confirmed experimentally.

Based on DFT, there is a possibility that the A-step in the STM image in Fig. 4(a) is a 2-row decoration of S, rather than the 1-row interpretation given elsewhere in this paper. In

support of this, the circular shape of the dots in the STM data is much better-matched in the simulated image for the double-row model [Fig. 9(c)] than the 1-row model [Fig. 8A].

However, the dot is predicted to be higher (brighter) than the Cu terrace in the double-row model, whereas in experiment the dot is always below the level of the upper terrace [see line profile in Fig. 4(a)]. At present we cannot decide between these two possibilities. In principle, they are not mutually exclusive, since there should be a transition from 1- to 2- to 3-row S structures at the A-steps as θ_S increases. In either case, the A-step is sub-saturated.

Turning now to the B-step, Fig. 10(d-f) shows 3 configurations with 3 rows of S. In Fig. 10(d) the upper terrace S atoms are all on fcc sites. Figure 10(e) has the outmost row of Cu shifted to form a pseudo (100) surface. Figure 10(f) has 2 additional Cu atoms per supercell, forming a zigzag S-Cu-S chain. However, as we show in the next section, the B-step is prone to massive rearrangement at high local θ_S and extended structures such as these are not expected to exist.

Figure 11 summarizes DFT results from this section, showing $\mu_S(S)$ as a function of S coverage at the step edge. Based on the energetics, at an A-step one expects a transition from 1- to 2- to 3-row S structures with increasing θ_S . The same expectation would in principle apply to the B-step, except that the B-step is unstable against massive distortion with increasing θ_S , as will be discussed in the next section. In all cases, $\mu_S(S)$ is lower at a step than on a terrace, for which $\mu_S(S) = -1.91$ eV. This is consistent with the experimental observations of heavy step decoration [Fig. 2, Fig. 5, and Fig. 6] at all except the very lowest θ_S , where the steps are sub-saturated [i.e. in Fig. 4].

TABLE II. Chemical potentials of S, in eV, for most favorable configurations of 1-, 2-, and 3-row S at A- and B-steps of Cu(111).

	1-row S	2-row S	3-row S
A-step	-2.24	-2.14	-2.01 (with chain)
B-step	-2.11	-2.08	n/a

4.3 Triangular Features on B-steps

When θ_S at a B-step increases above a single row, DFT calculations show that distortions of the simple extended structures studied in Sec. 4.2 can lower the energy. Figure 12 provides two examples where the starting point is a partial (a) or complete (b) double extended row of S atoms. Figure 12(a) shows that for a pair of S atoms at the upper step edge separated by $2a$, the energy of the system is reduced if three Cu atoms between the S pair move down from original fcc sites to nearby hcp sites, thus forming two local 4fh sites [denoted by red circles in Fig. 12(a)] where the pair of S atoms can reside. The lower panel shows a similar distortion at higher θ_S , but involving more Cu atoms, and producing local 4fh sites that are further apart. Interestingly, these distortions produce interlocking wedge-shaped regions in the step edge, which can be described as areas where the Cu atoms remain in their original fcc sites, alternating with complementary areas where all Cu atoms are shifted away from original fcc sites.

It is natural to extend the picture to larger distortions so that more 4fh sites are formed. Figure 13(a) shows the structure obtained from DFT using a 3-layer slab with a (9 x 9) supercell (with single k-point). A triangular array of 26 Cu atoms is shifted from fcc sites to hcp sites, forming a domain boundary of 4fh sites. (Not all Cu atoms in the triangle are in

hcp sites; 4 Cu atoms at the bottom are in fcc sites.) Altogether they can accommodate 8 S adatoms on 4fh sites. A 9th S atom is adsorbed on a 3fh site in the center.

The accompanying STM simulation in Fig. 13(b) shows a triangular area with 8 spots at almost the same height as the Cu island. The 9th spot in the center is slightly brighter. [Terms used to describe the STM images are defined in Fig. 13(c).] This simulation is in excellent agreement with the measured STM images of small triangles at B-steps, which can be confirmed by comparing the following aspects of Fig. 13(b and d): (i) A distinctive, slightly-curved row of 4 dots at the outer edge of the triangle (S atoms in 4fh sites); (ii) 4 additional dots along the inner edges of the triangle (S atoms in 4fh sites); (iii) A central dot slightly larger and higher than the dots at the edges (S atom in 3fh site); (iv) Arrangement of the 9 dots together in a (2 x 2)-like pattern; and (v) Interior edges of the triangles parallel to A-steps. We therefore assign small triangles in the B-steps to this structure.

We have extended the calculation to an even larger configuration based on a (12 x 12) supercell, $L=3$, and a single k-point grid. The energy-optimized configuration is shown in Fig. 14(a), and its corresponding STM simulation in Fig. 14(b). This time there are 5 dots along the curved outer edge and 6 dots along the inner edges of the triangle, all corresponding to S atoms in 4fh sites. In addition, the model has 3 central S atoms in 3fh sites. Altogether, in the model, there are 14 S atoms arranged in a (2 x 2)-like array within the triangle. All of these features, including the internal (2 x 2)-like lattice with 3 central dots slightly brighter and larger than the others, are observed experimentally, for instance in the topographic image of Fig. 6(d).

However, the experimental image in Fig. 14(c) shows a heart-shaped feature near the center of the triangle, rather than a (2 x 2)-like array. To mimic this feature, 2 additional Cu

adatoms are inserted [blue circles in Fig. 14(a)] in the space between 3 S atoms, above the layer of displaced Cu atoms. This results in a Cu_2S_3 complex that, in turn, produces a heart shape in the simulated image of Fig. 14(b). This gives a clue as to how and why the interiors of the large triangles are often elevated, or ‘filled in’ in the experimental images: The interiors become populated with second-layer Cu adatoms in addition to S adatoms.

5. Discussion

Our experimental results, interpretation of which is supported and enhanced by DFT analysis, reveal a variety of S-induced structures at step edges, in addition to those on terraces. Two of these are particularly intricate and unanticipated.

The first is the 3-row S structure at the A-steps, shown in Fig. 5(d) and Fig. 10(c). One row of S is at the lower step edge, and two S rows exist as part of a zig-zag S-Cu-S chain which involves an extra row of Cu in the second layer at the upper step edge. Cu adatoms in the chain do not occupy normal fcc sites, but they do provide high-coordination sites for S adatoms on both sides. The result is that S adatoms in all 3 S rows occupy p4fh sites.

The adsorption of Cu adatoms in near-bridge adsorption sites in the upper chain, resulting from global energy optimization in DFT, suggests that the energy penalty for moving Cu away from the natural 3fh fcc adsorption site is offset by the energy gain from Cu-S bonding. This is consistent with the conclusion from our previous study of Cu_2S_3 on terraces.¹⁴ The dominant feature in those complexes is strong Cu-S bonding, both within the complex (which favors linear S-Cu-S units) and between S atoms in the complex and Cu atoms in the substrate (which favors high-coordination adsorption sites for S). Cu-Cu

bonding between the complex and the substrate is of lesser import, so the favored adsorption site of Cu is sacrificed.

The second is the triangle motif at B-steps, shown in Fig. 6(c,d), Fig. 13(a), and Fig. 14(a). The triangles are reconstructions in which a group of Cu atoms moves out of their original fcc sites toward the lower terrace, forming a less-dense network and providing 4fh sites for most of the S adatoms. When a triangle is large enough, its inner area can fill in with additional, upper-level Cu atoms, but the interior edges are always preserved. At the upper level of interior edges, zig-zag S-Cu-S chains can usually be found that are very similar to the A-step upper-level chains. Excellent agreement is obtained between the DFT-based STM images of this complex structure and the experimental STM images. In particular, two distinctive details are reproduced: The slight curvature in the row of dots (S atoms in 4fh sites) at the external edge of the triangle, and the enhanced brightness of the dots (S atoms in 3fh sites) in the center of the triangle relative to those at the edges.

Thus, both structures can be understood as step reconstructions that create (p)4fh sites for S adsorption, at the expense of Cu registry, while also incorporating features (chains) that reflect the importance of the S-Cu-S subunit.

The features in our experiments are completely static at 5 K. Our data do not provide information about thermal stability. However, Wahlström *et al.* observed well-defined triangles, with edge lengths comparable to those in our experiments, at 300 K—cf. Fig. 1 of Ref. ²⁰—along steps aligned with 3 of the close-packed directions, i.e. B-steps. They reported that the triangles changed in both size and position, although this was sensitive to tunneling conditions and hence likely to have been tip-assisted. It is not clear whether chains on upper levels (or elsewhere) were present, but at least one can conclude from their data that the main

bodies of the triangles on B-steps are stable at 300 K. Oriented at 180° , another step was imaged that would necessarily have been an A-step. It was frizzy, and much different than our A-steps at 5 K. The frizziness reflects atomic motion on the time-scale of scanning, and has been well-documented for clean surfaces of Cu(111).³¹ Even though the step structure is dynamic, it is possible that S continues to influence motion along the A-steps, as we demonstrated to be true for sulfur on Ag(111).³² But the main conclusion derived from this comparison is that the static 3-row S structure of the A-step is not retained at 300 K.

We noted in Sec. 3 that ‘miscellaneous’ chains are commonly found around step edges. They are more abundant around steps than on terraces, and also longer on average. This implies that step edges participate in generating the terrace complexes. One possible mechanism involves the triangles at B-steps. The outer edge of the triangle is bounded by Cu atoms [cf. Fig. 13(a) or Fig. 14(a)]. Addition of S atoms at the outer edge could destabilize the structure, whereupon a Cu-S chain parallel to the step edge could peel off and diffuse out onto the terrace, and the triangle would adjust accordingly. This hypothesis is consistent with the fact that a separate chain is sometimes observed adjacent and parallel to the outer edge of a triangle. A clear example is Fig. 6(d). Another possible way of generating chains on terraces could be movement of chains at the upper step edges away from the steps. This finds support in the observation that there are sometimes two or three chains decorating upper A-steps or upper edges of triangles on B-steps, as if chains are generated successively at these upper edges. There may be other mechanisms as well by which chains/hearts on terraces are generated, depending on temperature, θ_s , and step density. The relationship between the steps and the complexes on terraces is a topic of continuing investigation.

Finally, we can compare this study of S/Cu(111) with a prior study of S/Ag(111) under identical conditions.³⁰ At very low θ_S and at 5 K, S-Ag complexes existed on Ag(111) terraces, both in the form of individual units and concatenated chains. The steps were modified by S adsorption. Some evidence suggested that the steps participated in forming the complexes. In these respects, the observations for the two close-packed coinage metal surfaces are analogous. However, the structures proposed for the terrace complexes on Ag(111) were quite different, and triangles were not observed on S/Ag(111) step edges.³⁰

6. Conclusions

We have identified the reconstructions of A- and B-steps on Cu(111) that exist at low θ_S and low T. In both cases, S can adsorb at (p)4fh sites. This is different than the structural motifs of Cu-S moieties on terraces at these coverages, which may be due to the higher local θ_S at the step edges than at the terraces. Based on comparison with other published work, one of these reconstructions is stable to (at least) room temperature.²⁰ A mechanism is postulated by which the reconstructed steps could produce Cu-S chains on terraces.

Acknowledgements

The experimental component of this work was conducted or supervised by HW, JO, HJY, YK, and PAT. It was supported by three sources. From the U.S., it was NSF Grant CHE-1507223. From Japan, support was provided by a Grant-in-Aid for Scientific Research on Priority Areas “Electron Transport Through a Linked Molecule in Nano-scale”; and a Grant-in-Aid for Scientific Research(S) “Single Molecule Spectroscopy using Probe Microscope” from the Ministry of Education, Culture, Sports, Science, and Technology

(MEXT). The theoretical component of this work was carried out by DJL. It was supported by the Division of Chemical Sciences, Basic Energy Sciences, US Department of Energy (DOE). This part of the research was performed at Ames Laboratory, which is operated for the U.S. DOE by Iowa State University under contract No. DE-AC02-07CH11358. This part also utilized resources of the National Energy Research Scientific Computing Center, which is supported by the Office of Science of the U.S. DOE under Contract No. DE-AC02-05CH11231. We thank Kan Ueji and Hiroshi Imada for assistance with the experiments.

Figures

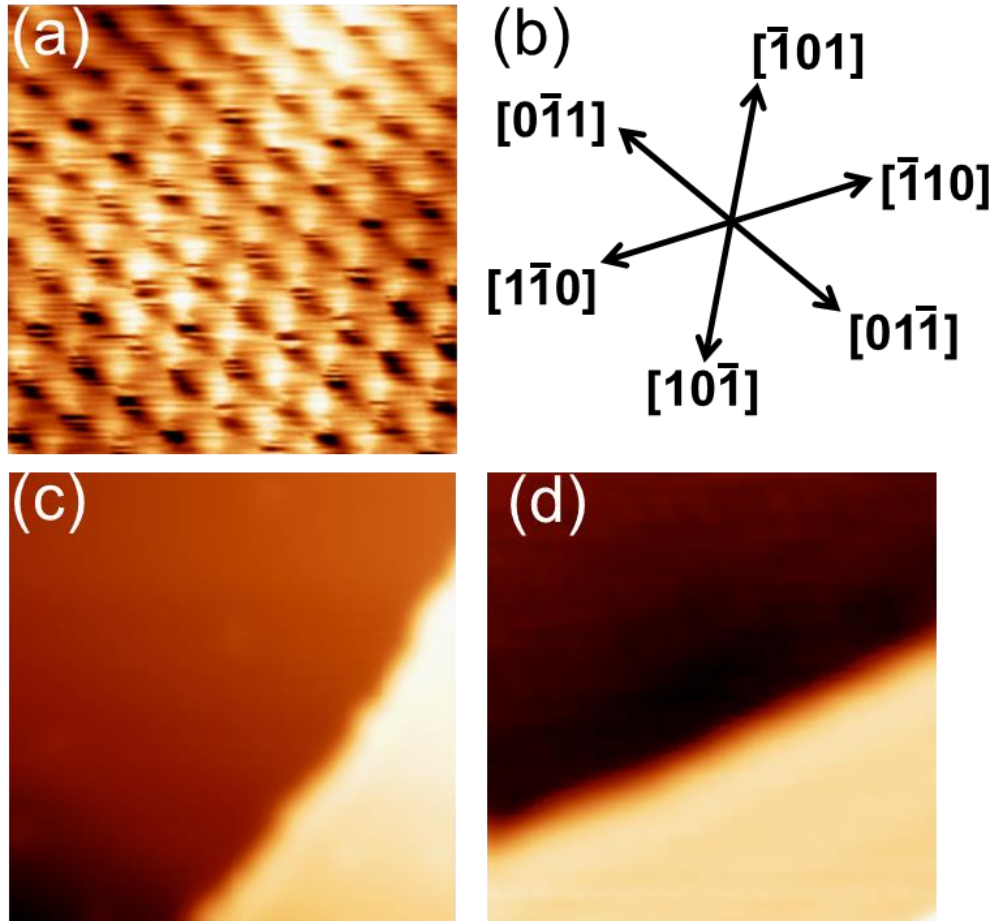


Figure 1. Features of the clean Cu(111) surface. (a) Atomically-resolved STM image, $2.0 \times 2.0 \text{ nm}^2$. (b) Close-packed directions. (c) Clean, $10 \times 10 \text{ nm}^2$. (d) Clean step, $10 \times 10 \text{ nm}^2$.

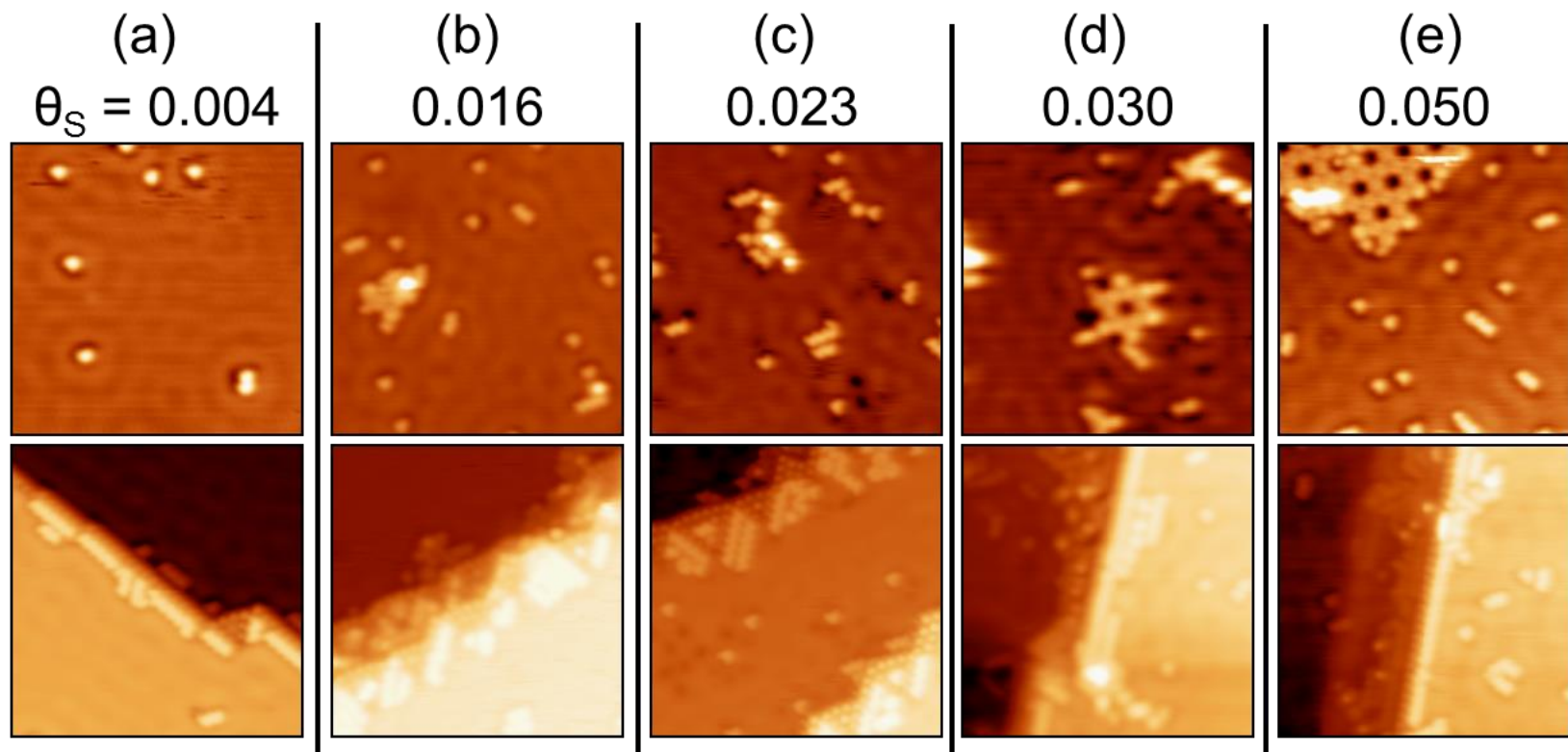


Figure 2. STM topographic images in order of increasing sulfur coverage, θ_s . All images are $15 \times 15 \text{ nm}^2$.

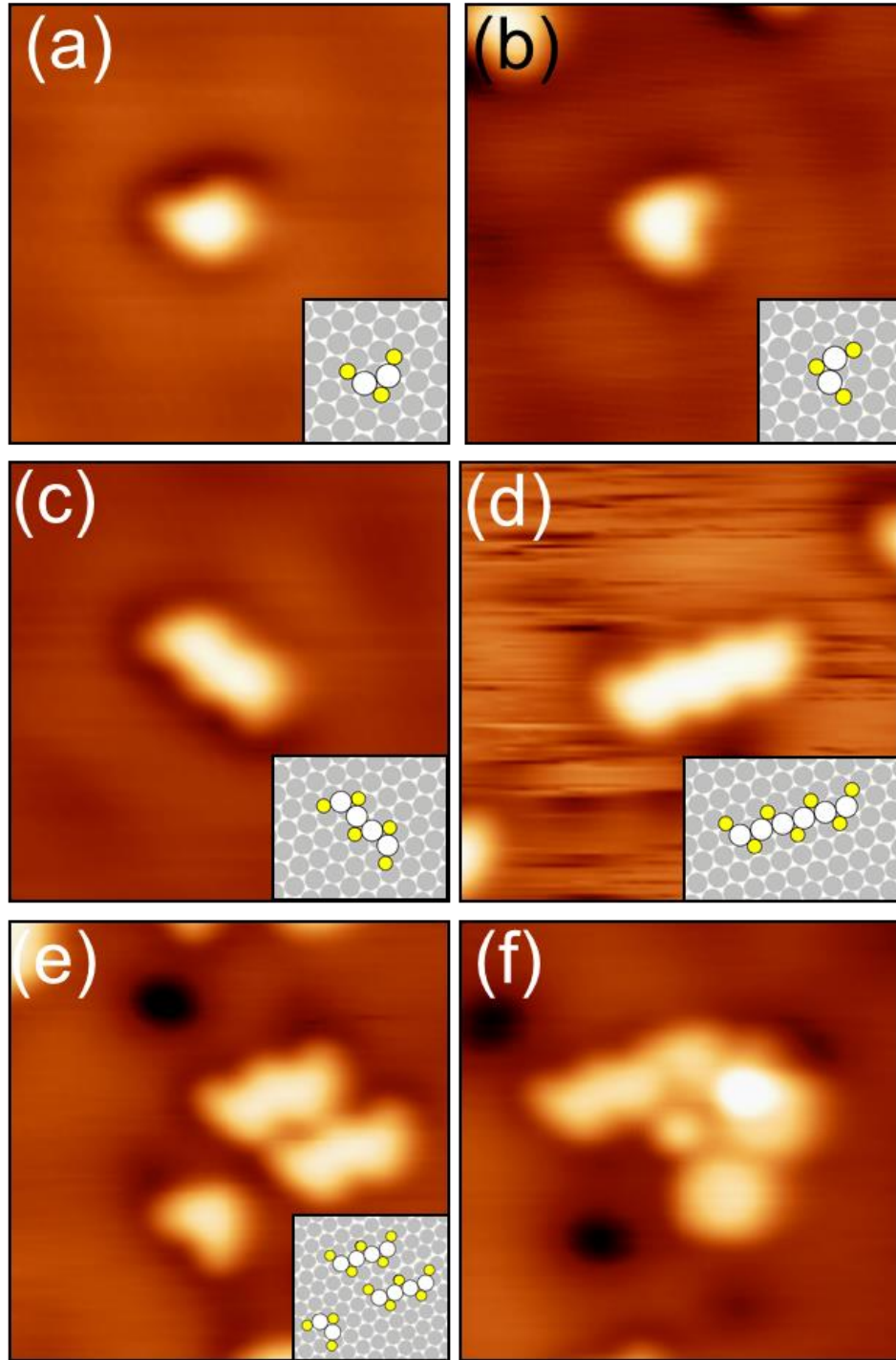


Figure 3. Topographic STM images and proposed structures for Cu-S complexes on Cu(111) terraces. All images are $4.0 \times 4.0 \text{ nm}^2$. Insets show schematics of proposed configurations, with Cu atoms in the complex represented by white circles, S atoms by yellow, and Cu atoms in the substrate by grey (color online). (a) and (b) 1-unit heart. (c) 2-unit linear chain of hearts, plus a heart. (d) 3-unit linear chain of hearts. (e) Two aligned 2-unit chains. (f) Clump.

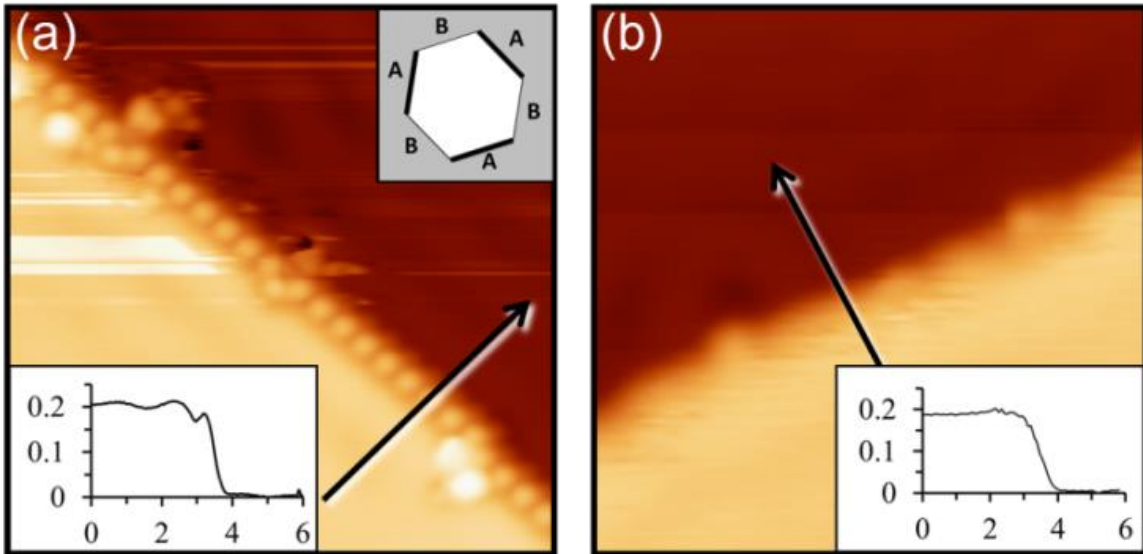


Figure 4. Topographic STM images of A-type and B-type steps at $\theta_s < 0.004$ ML. Both images are $10 \times 10 \text{ nm}^2$. (a) A-type edge. Lower inset: Line profile across the step corresponding to the path indicated by the arrow. The x- and y-axes are in units of nm. Upper inset: Orientation of A- and B-steps in these experiments. The white hexagon represents an upper terrace. (b) B-type step with profile as described in (a).

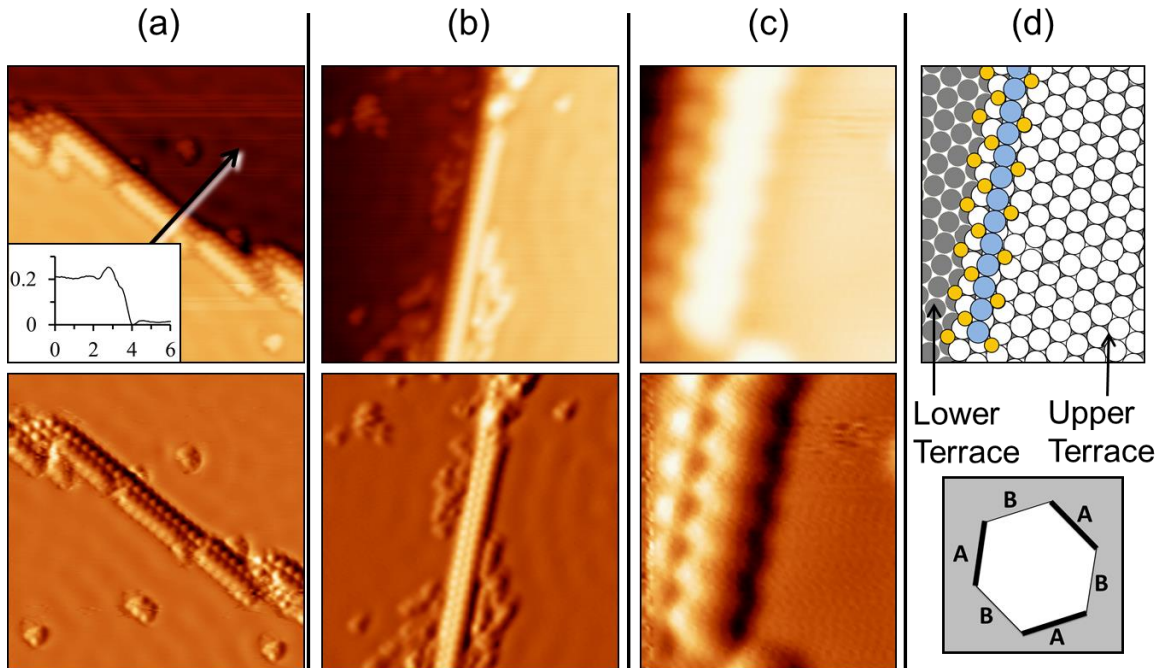


Figure 5. STM images of A-steps with adsorbed sulfur, at high magnification. Each vertical pair shows the same data, but the top panel is topographic and the bottom is differentiated. (a) $\theta_S = 0.004$, $15 \times 15 \text{ nm}^2$. The inset shows the line profile across the step along the path shown by the arrow, with x- and y-axis units of nm. (b) $\theta_S = 0.016$, $15 \times 15 \text{ nm}^2$. (c) $\theta_S = 0.016$, $3.0 \times 3.5 \text{ nm}^2$. (d) Schematic model of (c), at approximately same scale. Grey circles represent Cu atoms at the level of the lower terrace, white circles are Cu atoms at the level of the upper terrace, and blue circles are Cu atoms adsorbed on top of the upper terrace. S atoms are small yellow circles.

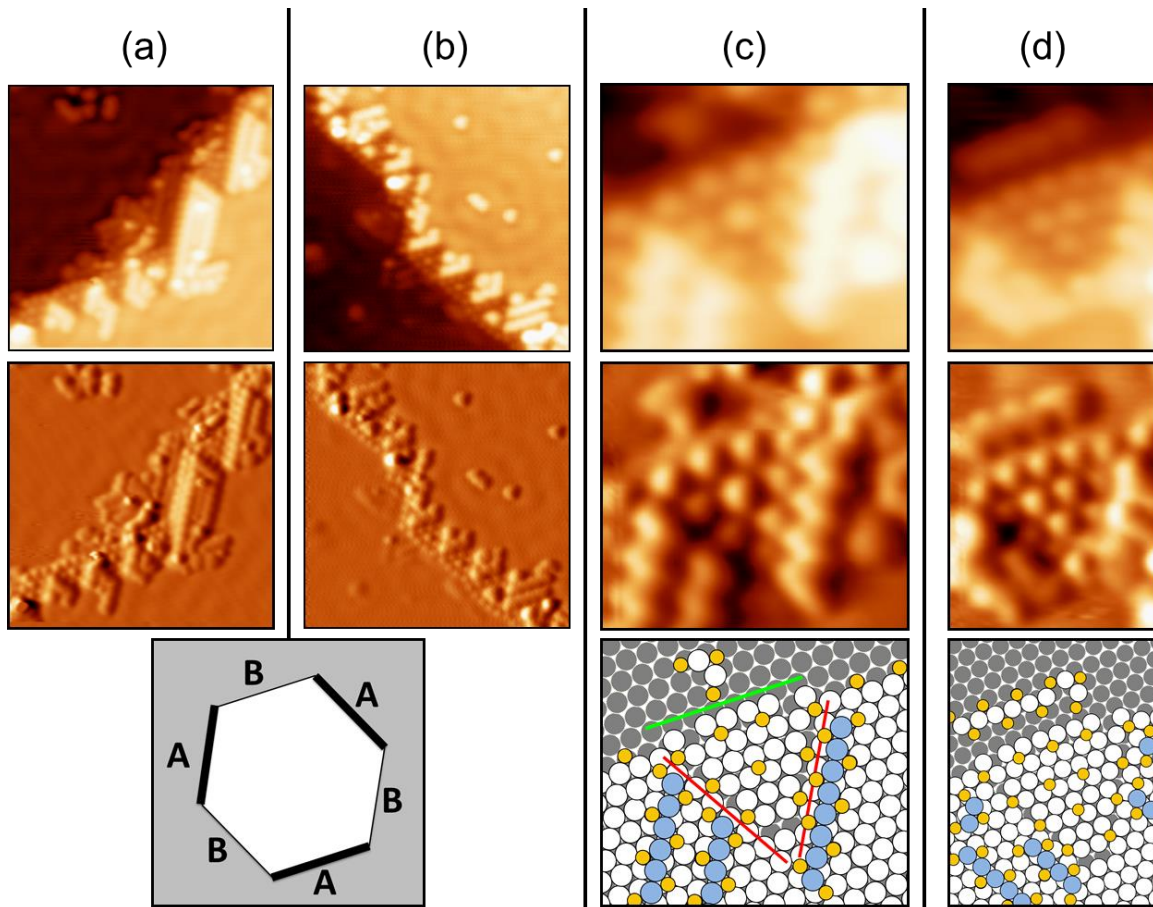


Figure 6. STM images of B-step edges with adsorbed sulfur, at high magnification. Each vertical pair shows the same data, but the top image is topographic and the lower image is differentiated. (a) $\theta_S = 0.016$, $15 \times 15 \text{ nm}^2$. (b) $\theta_S = 0.016$, $15 \times 15 \text{ nm}^2$. (c) Small triangle. $\theta_S = 0.023$, $4.0 \times 3.5 \text{ nm}^2$. (d) Large triangle. $\theta_S = 0.023$, $3.5 \times 4.5 \text{ nm}^2$. In (c) and (d), the lowest panel is a schematic of a possible atomic structure, drawn to approximately the same scale as the STM images. The symbols and colors have the same meaning as in Fig. 5(d). Additionally, in (c), red lines show the triangle's inner edges, and the green line shows its outer edge. (Color online.)

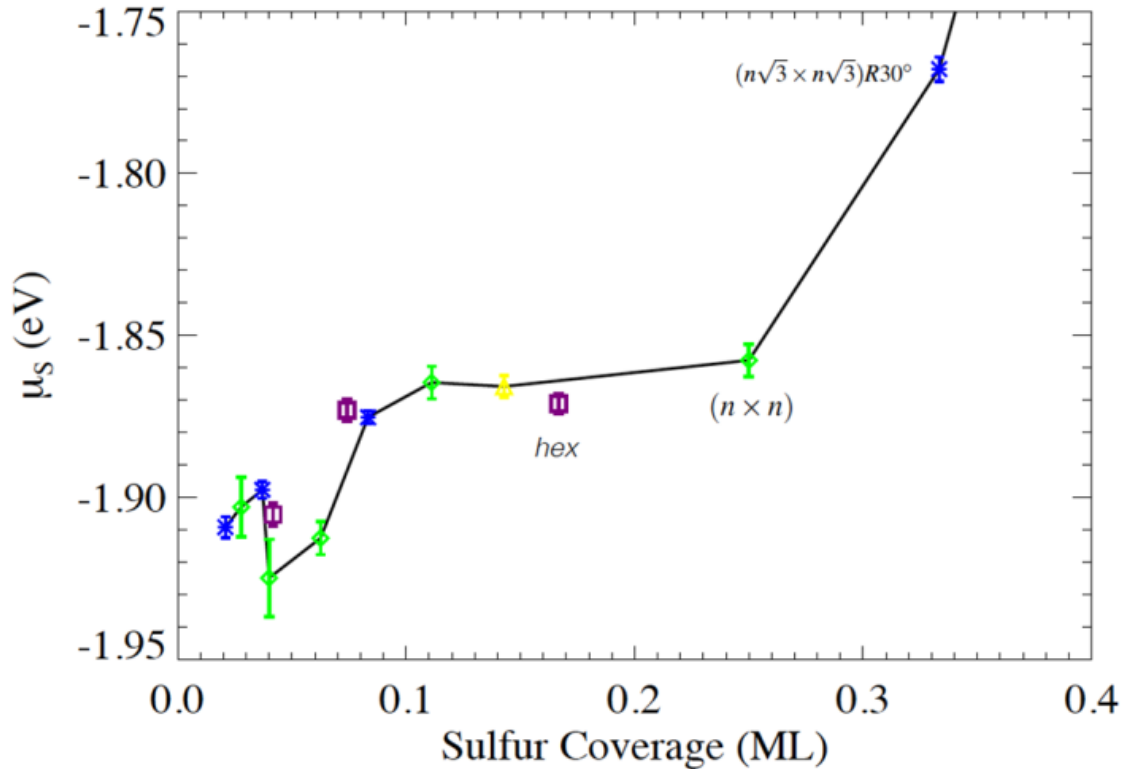


Figure 7. Chemical potential (adsorption energy) of adsorbed S vs. θ_s , calculated from DFT. Green symbols show $(n \times n)$ supercells, blue show $(n\sqrt{3} \times n\sqrt{3})R30^\circ$ supercells, yellow shows a $(\sqrt{7} \times \sqrt{7})R19^\circ$, and purple show honeycomb (hexagonal) supercells in which there are 2 adatoms per unit cell, both occupying fcc sites.

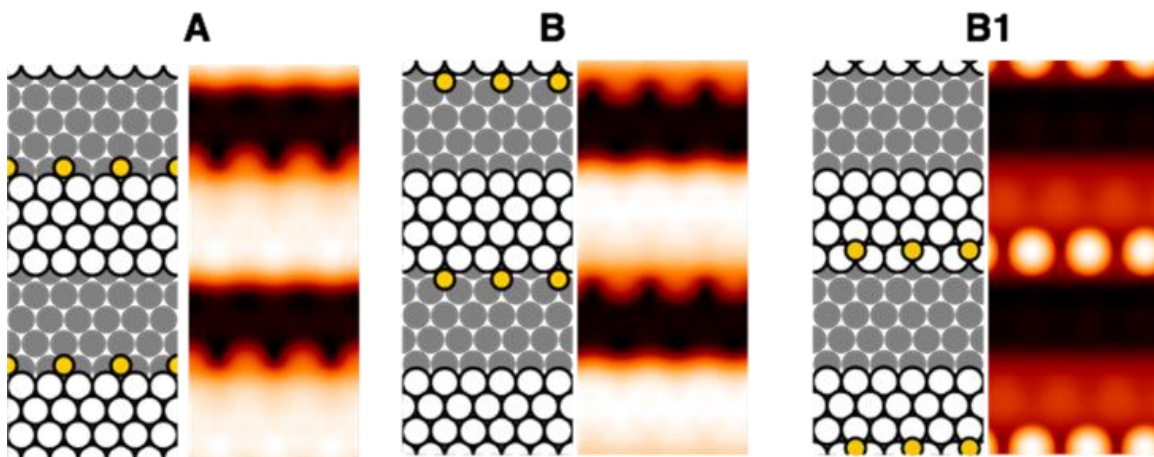


Figure 8. Optimized DFT configurations and simulated STM images of a single-row of S attaching to the A- or B-step, for a (2×8) supercell. Chemical potentials are given in Table I. Symbols and colors in the configurations have the same meaning as in Fig. 5(d).

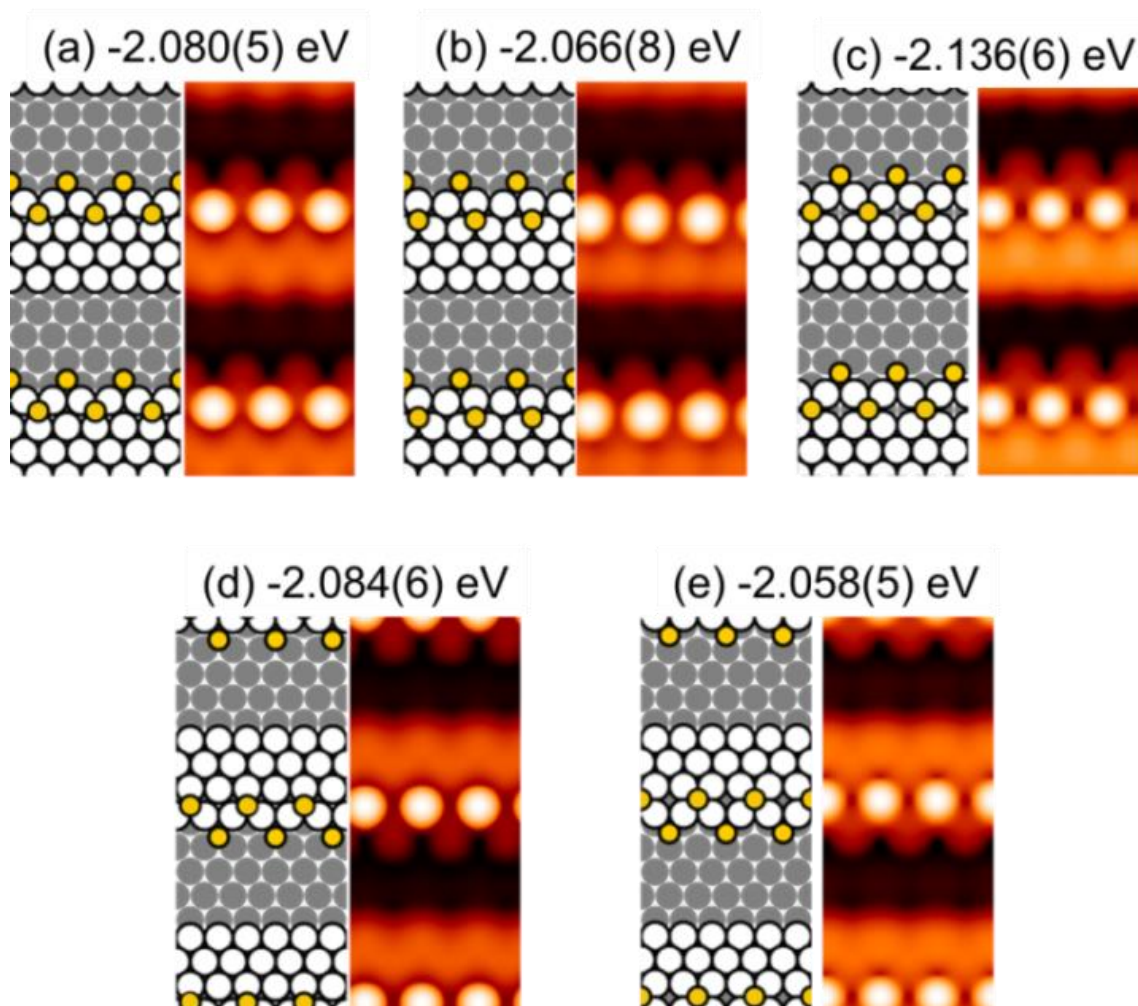


Figure 9. Optimized DFT configurations, simulated STM images, and chemical potentials of S for various 2-row configurations of S at A-steps (a-c) and at B-steps (d-e), for (2x8) supercells. The chemical potential here is the average adsorption energy of S in the two different environments. Symbols and colors in the configurations have the same meaning as in Fig. 5(d).

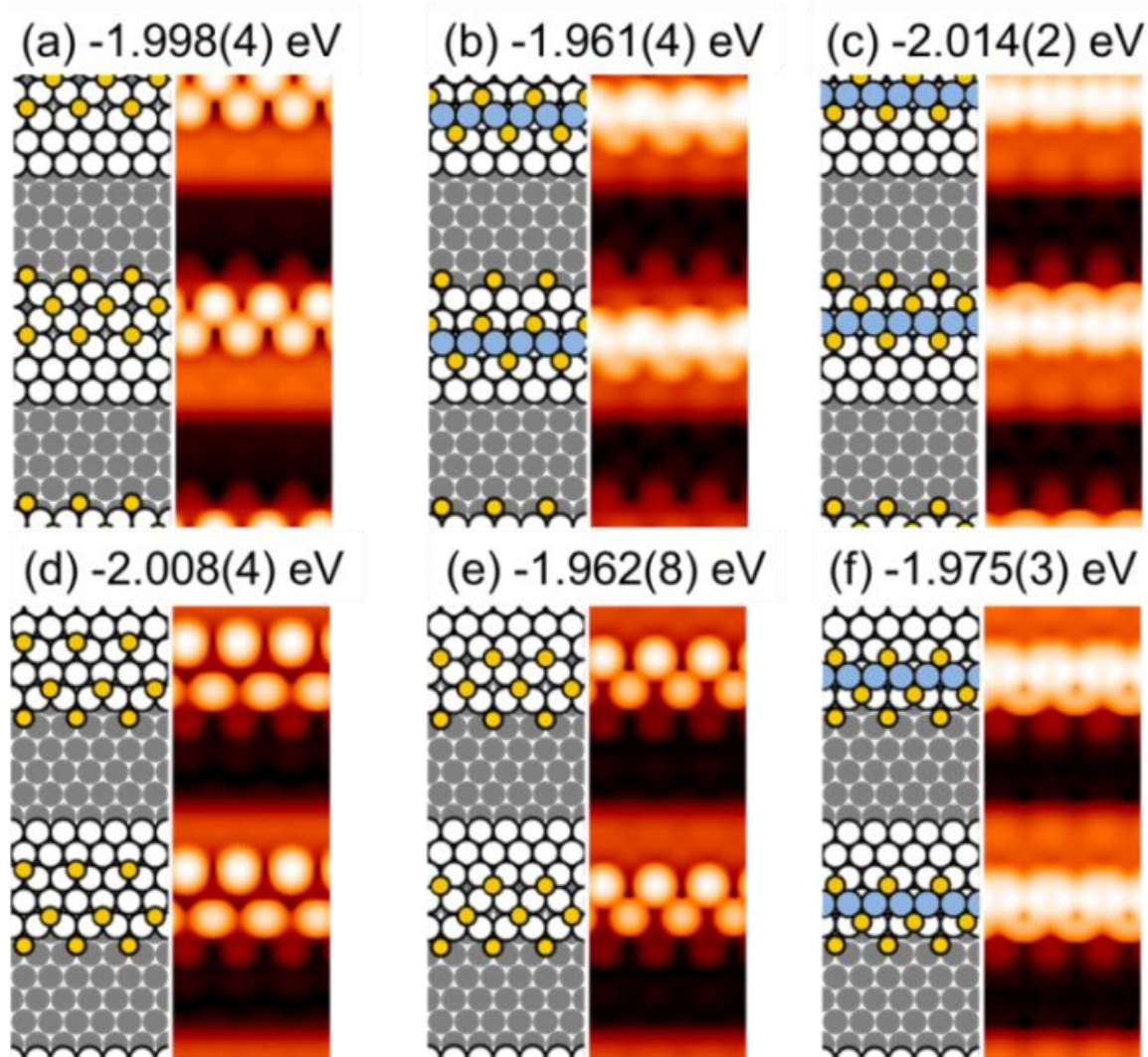


Figure 10. Optimized DFT configurations, simulated STM images, and calculated chemical potentials of S for three rows of S near the A-steps (a-c) and near the B-steps (d-f). In (b), (c), and (f), the blue circles represent an additional row of Cu on the upper terrace. This, combined with two of the three S rows, forms a S-Cu-S chain on the upper terrace. Symbols and colors in the configurations have the same meaning as in Fig. 5(d).

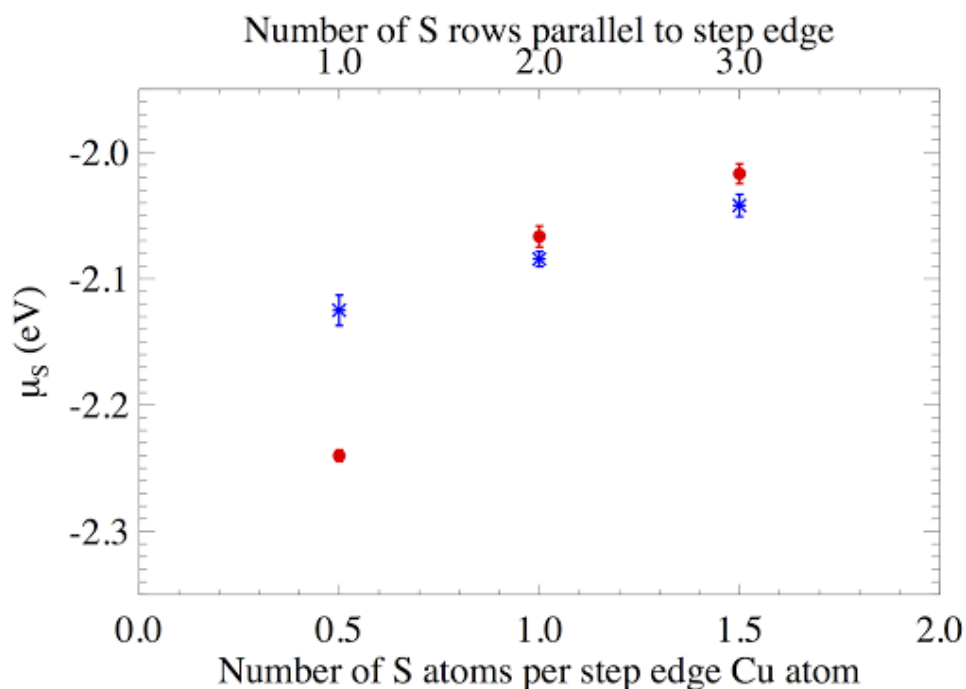


Figure 11. Chemical potential of S decorating A-type (red) and B-type (blue) steps with increasing coverage of sulfur at the step edge, calculated from DFT.

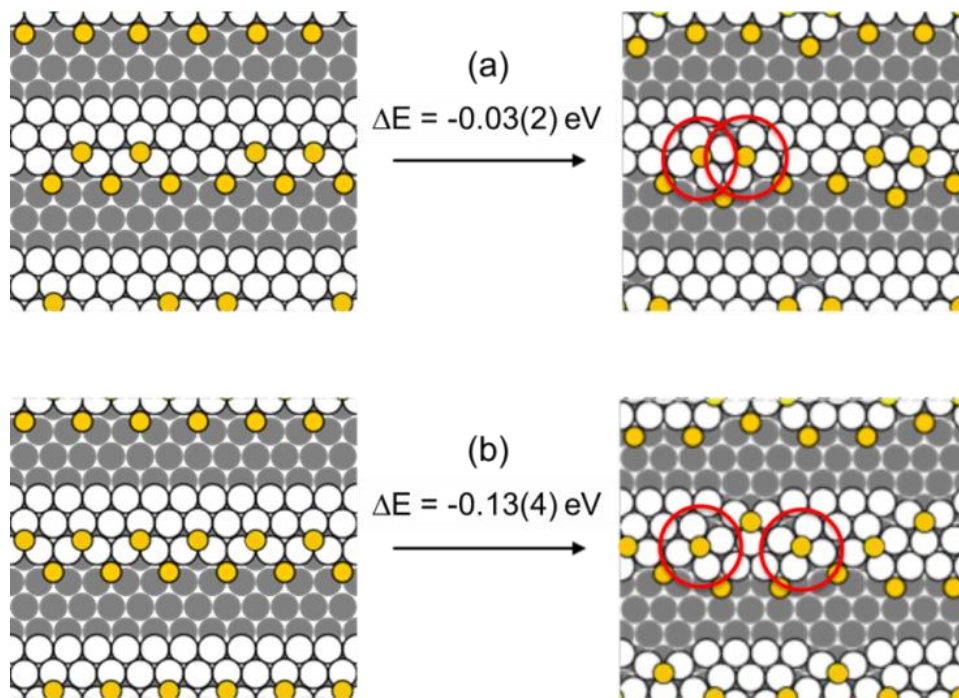


Figure 12. Distortion induced by adsorption of S on B-steps. Symbols and colors in these DFT-optimized configurations have the same meaning as in Fig. 5(d).

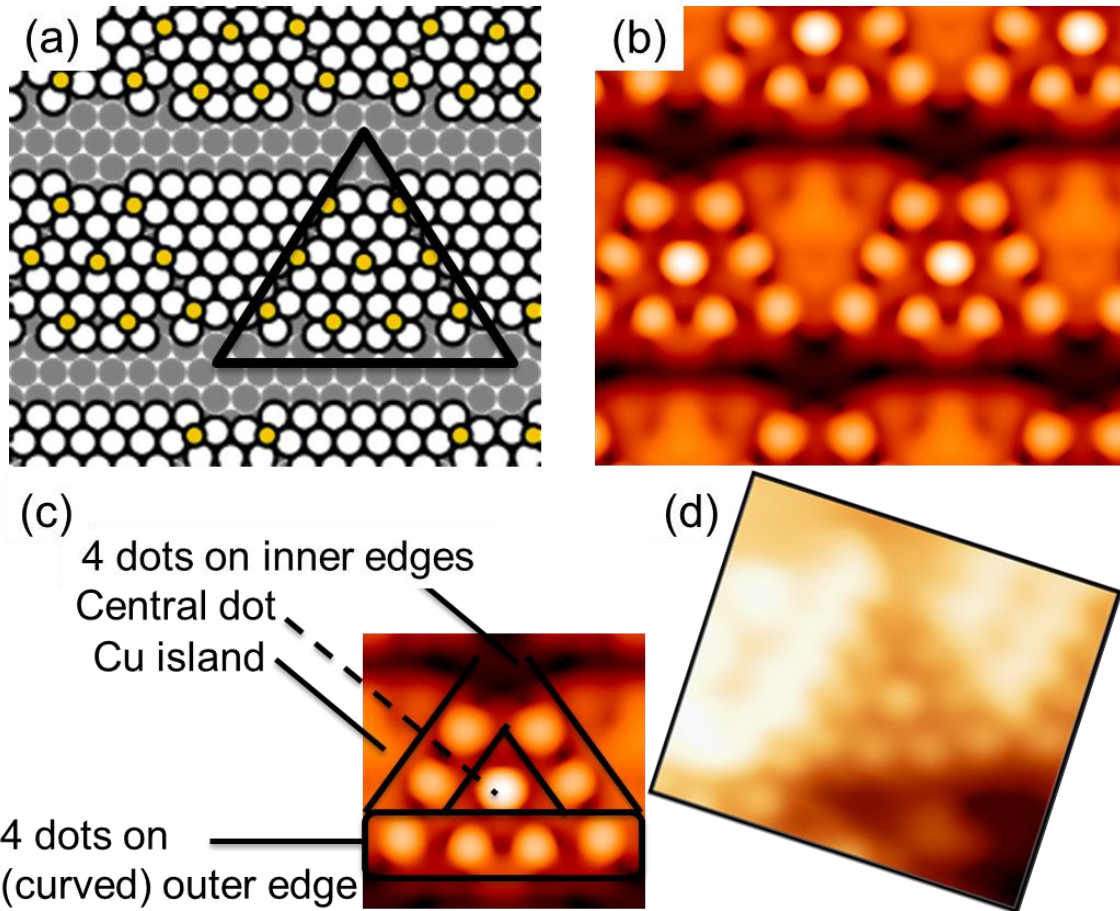


Figure 13. Model for the small triangular features along a B step. (a) Optimized configuration from DFT. The majority of the Cu adatoms inside the outlined triangle are on hcp sites, forming 8 4fh sites, each occupied by a S atom. One extra S atom in the middle of the triangle is on a 3fh site. Symbols and colors have the same meaning as in Fig. 5(d). (b) Simulated STM image. (c) Schematic, clarifying terms used in the discussion of the STM images. (d) Actual topographic STM image of a small triangle [the same as Fig. 6(c)], $4.0 \times 3.5 \text{ nm}^2$. The experimental image is manipulated to be about the same size and orientation as a triangle in the simulated image.

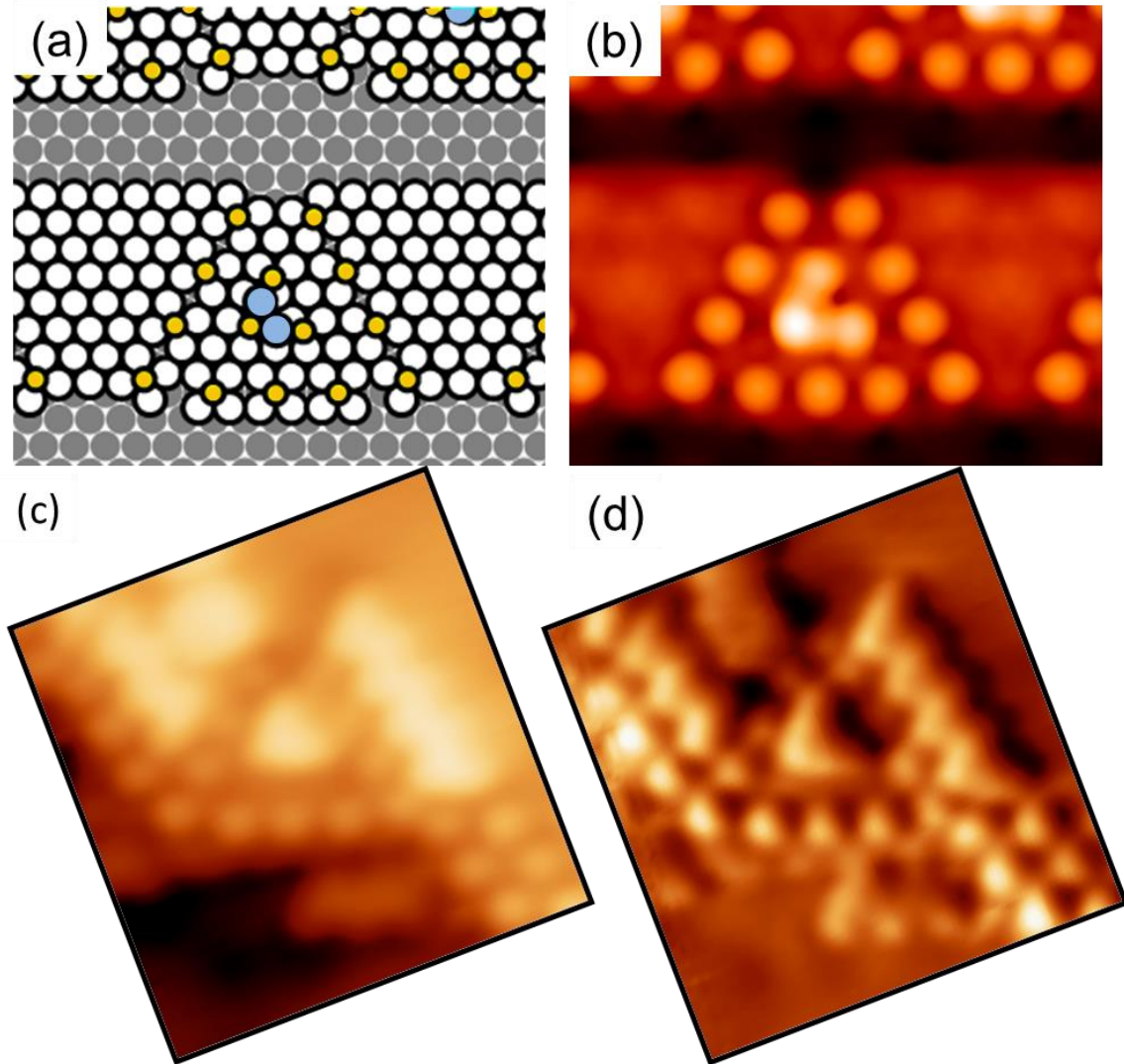


Figure 14. Model for the large triangular features along a B-step. In this particular case, a Cu_2S_3 complex resides in the middle of the triangle. (a) Optimized configuration. Cu atoms in the Cu_2S_3 complex are in blue (on-line). (b) Simulated STM image. (c)-(d) Actual topographic and differentiated STM image of a large triangle (similar to Fig. 6(d), but a different triangle), $4.0 \times 4.5 \text{ nm}^2$. The experimental image is manipulated to be the same size and orientation as a triangle in the simulated image.

Appendix 1: Additional Step Edge Structures Studied with DFT

Other structures of interest that have been studied with DFT, but not discussed in the main text, are included in this appendix.

A. Additional 1-, 2-, and 3-row Configurations

Figure A1 shows some additional examples of 1-row configurations of S at step edges. Figure A1(a) shows the S at a fcc site at the upper A-step edge, in (b) the leading edge Cu atom is shifted outward to an hcp site, forming 4fh sites occupied by S, while (c) is a similar arrangement as (b) but at the B-step.

Figure A2 shows additional 2-row configurations. Figure A2(a) is similar to the 2-row structure shown in the main text at an A-step (Fig. 9), but with the S at the upper step edge at a fcc site, rather than a hcp site, so it is not exactly between the two lower edge S atoms. Figure A2(b) is analogous to (a) but at the B step. Here, the Cu atoms shift slightly away from fcc sites, creating low-symmetry sites for S. Figure A2(c) starts from a reconstructed step edge similar to (b), but with the outermost Cu further away from the step. The optimized structure has the outermost row of Cu moving even further away from the step edge and forming a separated Cu-S zigzag chain.

Figure A3 shows additional 3-row S configurations at step edges. Figure A3(a) has the second row S at hcp sites, and the third row S at fcc sites, at an A-step. Figure A3(b) and (c) involve A-step edge reconstruction, and are subtly different from the reconstructed A-step edge mentioned in the text (Fig. 10). Figure A3(b) shows the second and the fourth row shifted, while in (c) only the first row is shifted. In comparison, the reconstruction mentioned in the main text has the second row shifted. In Fig. A3(d), the third row pushed towards the

second row, thus forming an overly saturated row. Fig A3(e) is similar to (a), but with third row shifted to fcc sites further away from the step edge. Note that it is slightly more stable than (a), indicating there is no driving force for a third row of S to move very close to step edges in these arrangements. Finally (f) is similar to (e) but on a B-step.

B. Step Structures Incorporating Cu Vacancies

Next, we focus on possibilities that a step can be stabilized by the introduction of vacancies. Figure A4 shows some examples with vacancies near the step edge and 2-row S decoration. In all calculations involving step edges, the clean slab has an existing island. The chemical potential thus calculated does not include the energy cost of forming the step edges, but does include the energy cost of forming the vacancies. As shown in these calculations, it is easier to extract a Cu atom not bonded with any S, than to extract a Cu atom bonded with a S, and then let the S fall down into the vacancy. Overall, for the configurations tested, the chemical potentials indicate that vacancies do not stabilize steps.

One can calculate the formation energy of the vacancy using $E_f = n(\mu_S^v - \mu_S^0)$, where $n = 2$ is the number of S atoms, and $\mu_S^{v(0)}$ is the chemical potential of S with (without) the vacancy. For Fig. 18(a) and (c), $E_f = 0.33$ eV and 0.31 eV, respectively. This is much lower than the formation energy of a vacancy on a clean Cu(111) surface, estimated to be 0.78 eV from DFT.²⁷

We also consider some partial 2-row S configurations with vacancies at B steps, and compare them with similar configurations without any vacancy. This is shown in Fig. A5. Based on the chemical potentials, we conclude that vacancies do not stabilize steps in this

range of configurations, either. The configuration with lowest formation energy for a vacancy is in Fig. A5(f), where $E_f = 0.33$ eV.

C. Alternative Formation Mechanism for Cu-S Chains

Figure A6 shows the change in energy by moving two Cu atoms at the B-step away from the step in an attempt to peel off a Cu-S chain from the S decorated B-step. The positive sign of ΔE shows that the configuration on the right is only metastable.

D. Other Configurations for the B-type Triangular Structure

Figure A7 shows samples of other triangular structures that were investigated as part of the effort to interpret the triangular features seen at B-steps in experimental STM images. Most of them are not carried out with sufficient k-points grids or slab thicknesses to have reliable energetics. Based on a combination of approximate energetics and agreement with experimental STM images, we discard these structures in favor of the structure presented in the main text.

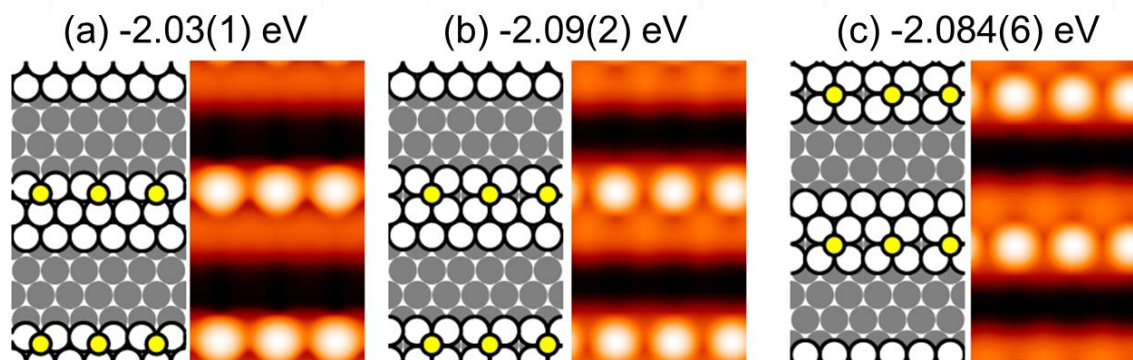


Figure A1. Structures, simulated STM images, and chemical potentials for various 1-row configurations of S at step edges. The A-step is the upper edge of the Cu island, and the B-step is the lower edge.

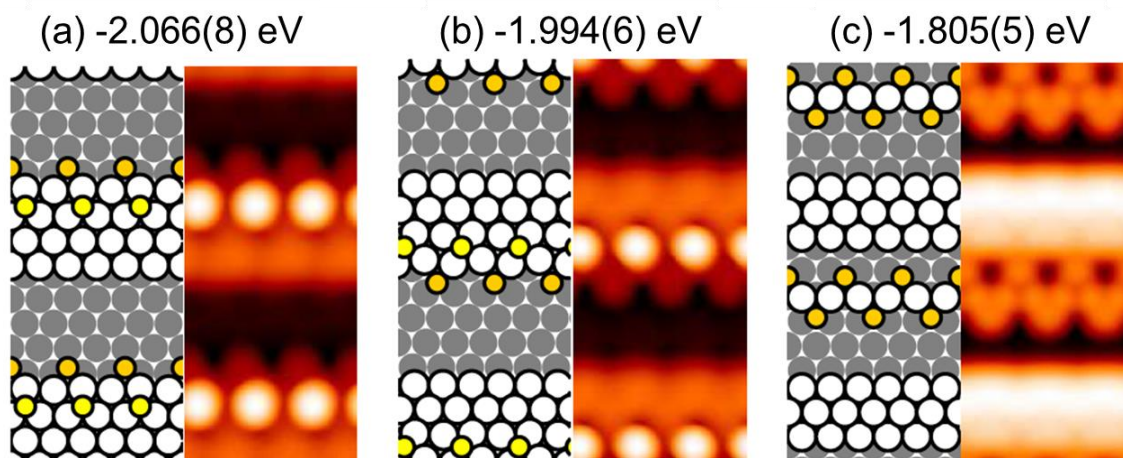


Figure A2. Structures, simulated STM images, and chemical potentials for various 2-row configurations of S at step edges. The A-step is the upper edge of the Cu island, and the B-step is the lower edge.

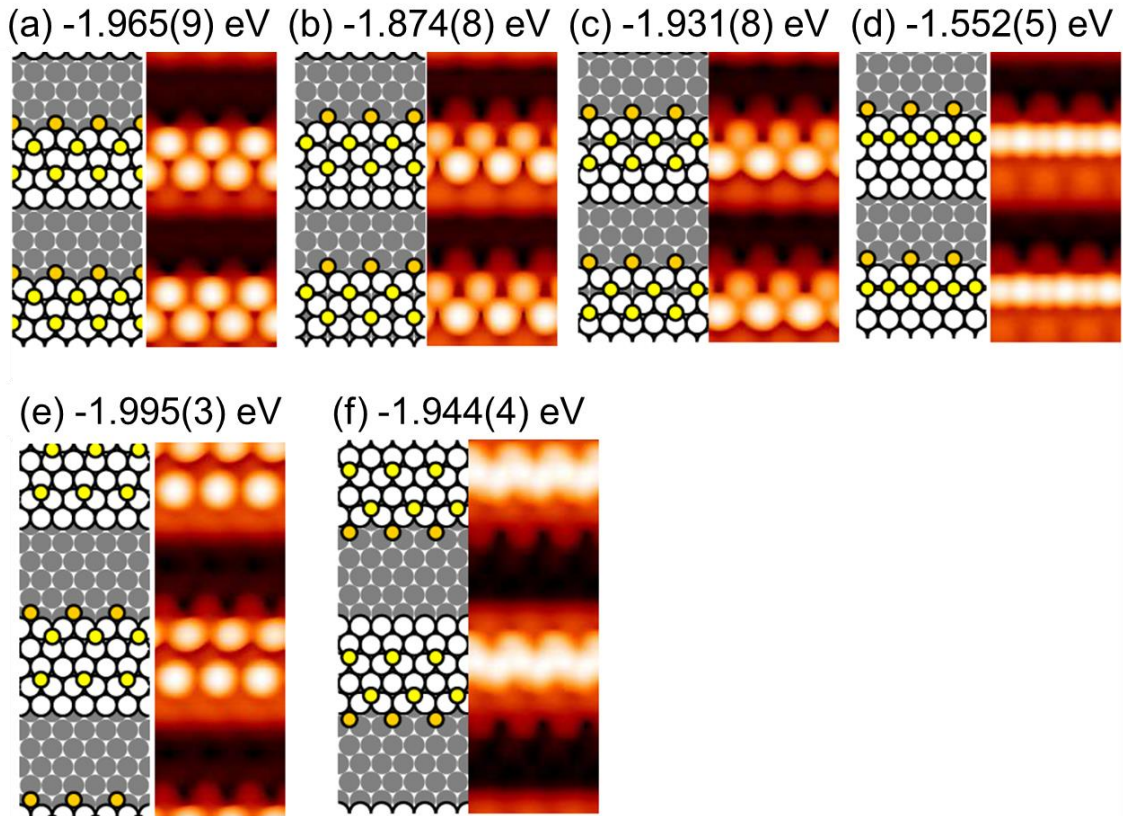


Figure A3. Additional 3-row S configurations. The A-step is the upper edge of the Cu island, and the B-step is the lower edge.

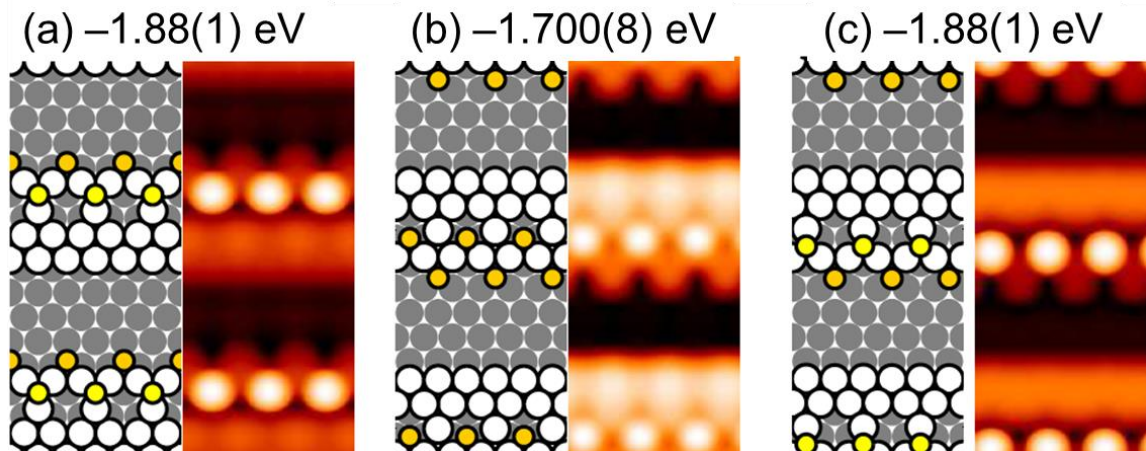


Figure A4. Similar to Fig. 16, but with vacancies introduced near the step edge. The A-step is the upper edge of the Cu island, and the B-step is the lower edge.

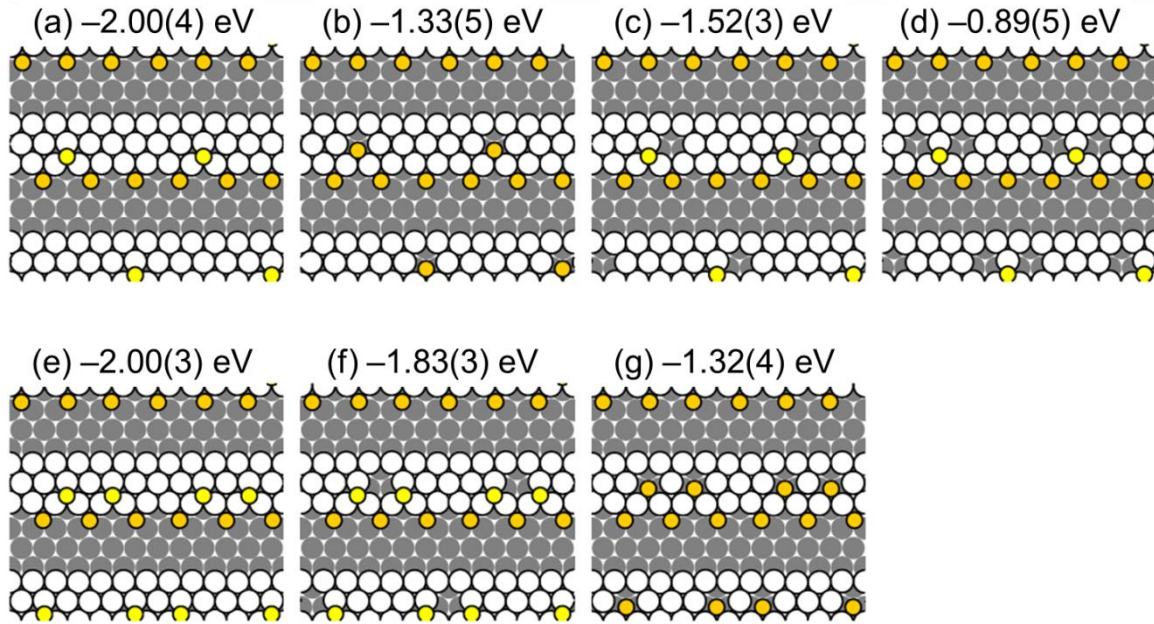


Figure A5. Comparison of chemical potential of 2-row S configurations with and without vacancies. Note that for this figure, μ_S quoted is only for upper edge S.

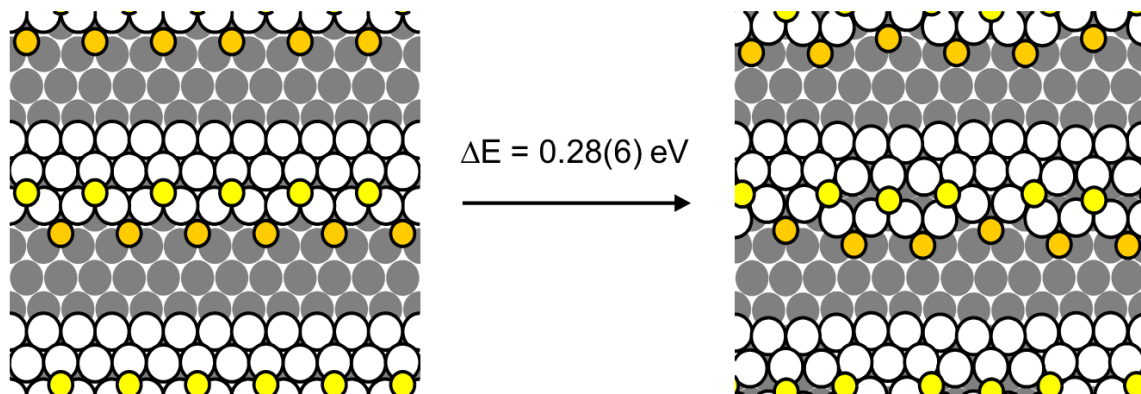


Figure A6. Change in energy by peeling out a row of Cu together with S on a S-decorated B-step.

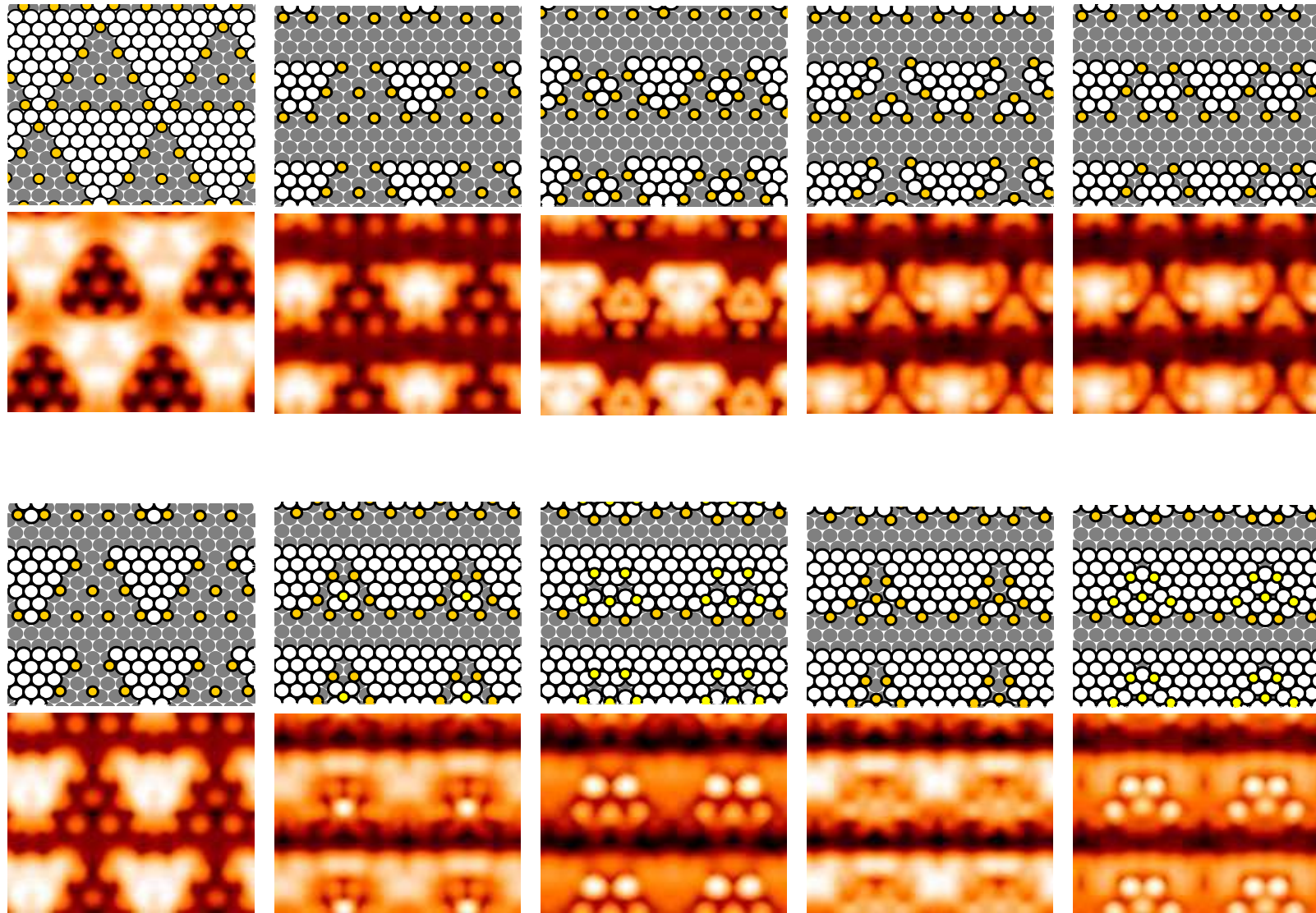


Figure A7. Selected structures and their simulated STM images for triangular features calculated in a (8×8) supercell.

Appendix 2. Additional STM Information

Tunneling conditions for collecting the STM data presented in the manuscript is provided in Table AI. In Appendix 2 of Chapter II, we presented the analysis of topographic heights and widths of the Cu_2S_3 complexes on the terraces as a function of sample bias (V_s) and tunneling current (I). Within the range of voltages and currents used in this study, there is no statistically significant trend. This leads us to conclude that there is no significant difference in step features either.

TABLE AI. Tunneling conditions for the figures within the manuscript. Image sizes can be found in the figure captions of the main text.

Figure Name	Image size (nm^2)	Tunneling Current (nA)	Sample Bias (V)
1a	2.0 x 2.0	2.63	-0.004
1c	10 x 10	1.00	1.000
1d	10 x 10	0.81	-0.094
2a	15 x 15	1.24	-0.070
		1.24	-0.002
2b	15 x 15	0.46	-0.090
		0.40	-0.088
2c	15 x 15	1.06	-0.004
		1.17	-0.005
2d	15 x 15	0.39	-0.088
		0.36	-0.090
2e	15 x 15	0.42	-0.090
		0.43	-0.090
3a	4.0 x 4.0	1.24	-0.002
3b	4.0 x 4.0	0.21	-0.085
3c	4.0 x 4.0	1.06	-0.004
3d	4.0 x 4.0	0.65	-0.050
3e	4.0 x 4.0	1.06	-0.004
3f	4.0 x 4.0	1.17	-0.005
4a	10 x 10	0.56	+0.083
4b	10 x 10	0.41	-0.075
5a	15 x 15	1.29	-0.020
5b	15 x 15	0.45	-0.092
5c	15 x 15	0.65	-0.043
6a	15 x 15	0.44	-0.090

TABLE AI continued.

6b	15 x 15	0.38	+0.100
6c	4.0 x 3.5	1.17	-0.005
6d	3.5 x 4.5	0.65	-0.050
14c, d	4.0 x 4.5	1.167	-0.005

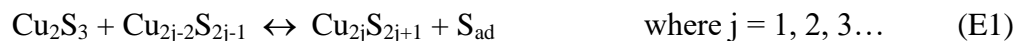
Appendix 3. Additional Analysis of Terrace Features

Figure A8 shows the fractional area covered by each species as a function of sulfur coverage. The order of formation with increasing θ_S is as follows: hearts, chains, clumps, and finally the $\sqrt{43}$. A plateau in the chain and heart populations coincides with the formation of clumps beginning ~ 0.016 ML. The increase of the $\sqrt{43}$ curve coincides with an apparent plateau of the clumps with the other species, ~ 0.03 ML.

A. Cu-S Chains

Figures A9 and A10 show arrangements of chains and hearts in groups and linear singular chains, respectively. As coverage increases, the chains increasingly group together, or form bent configurations, such as in Fig. A9(a) and (e-f).

The Cu_2S_3 complexes (with population P_1) can be considered monomeric precursors of the longer chains $\text{Cu}_{2j}\text{S}_{2j+1}$ of j units (with population P_j), related by the condensation reaction:



Let ΔE_j denote the energy difference between the configuration on the right and the left, thus reflecting the additional stabilization of a chain of length j over one of $j-1$ units. It is

reasonable to write $\Delta E_j = -\varepsilon + (j-1)\delta$ where $\varepsilon > 0$ reflects the strength of the stabilizing interaction between monomer units for short chains and the second term represents destabilization due to strain build up with increasing chain length. If k_F (k_D) represents the rate of the forward association (dissociation) process, so that $k_R = \exp(\beta\Delta E_j)k_F$, where $\beta = 1/(k_B T)$, equilibrium of this chain distribution implies that $k_F P_1 P_{j-1} = k_R P_j \theta_S$ (where θ_S actually denotes the coverage of the excess S not incorporated in step edges). This recurrence relation implies that

$$\ln(P_j/P_1) = (j-1)[\beta\varepsilon + \ln(P_1/\theta_S) - j\beta\delta/2] \approx (j-1)[\beta\varepsilon - \beta E_f + 2 \ln(\theta_S) - j\beta\delta/2], \quad (E2)$$

where the last equality assumes $P_1 \approx \exp(-\beta E_f)(\theta_S)^3$ with $E_f > 0$ as the formation energy of hearts in the presence of excess S. Thus, if $\delta=0$ (no strain build up), one has linear behavior of $\ln(P_j/P_1)$ versus j corresponding to pure exponential decay. Strain effects produce a stronger population decrease for larger j .

Fig. A11 shows the actual distributions of chain lengths at different values of θ_S , each normalized to the density at $j=1$. For each θ_S , one sees that $\ln(P_j/P_1)$ starts to decrease faster than linear for larger j described by the above form with $\delta > 0$ suggesting some strain build-up. The existence of strain is also consistent with the observation that on terraces, the maximum chain length is $j=5$, but for chains close to step edges, j can be as large as 23. Strain may be more readily accommodated near steps as discussed below, hence allowing longer chains. Next considering behavior versus θ_S , the distribution broadens (includes more long chains) as θ_S increases from 0.004 to 0.023, which is a natural consequence of increasing $\mu_S(S_{ad})$ and

consistent with the above form. The distribution narrows again at $\theta_S > 0.023$, perhaps due to competing formation of clumps (resulting in a lower effective value of θ_S).

B. Clumps and reconstruction

As θ_S increases, clumps become increasingly abundant. Some consist of hearts or chains, as shown in Fig. 3(e) and (f) in the main text. In others, hearts or chains are not readily identifiable, or make only a minor contribution to the clump. Examples are given in Fig. A12. We conclude that on terraces, linear chains with $j > 5$ are unstable relative to clumps of either type, again arising from strain in the linear chain.

At $\theta_S \geq 0.030$, the $\sqrt{43}$ appears. As shown in Fig. A8, the populations of chains and clumps level off or decline slightly when the $\sqrt{43}$ emerges suggesting that these features are in direct equilibrium with the $\sqrt{43}$ phase. In other words, the $\sqrt{43}$ phase becomes energetically favorable when the chains and clumps exceed a critical density of 0.01-0.02 nm^{-2} . The structural determination of the $\sqrt{43}$ reconstruction is discussed in Ref. ²² which is reproduced in Appendix I.

C. Atomic sulfur

The absence of S_{ad} on terraces is somewhat surprising, since $\mu_S(S_{\text{ad}}) = -1.91$ eV in the limit $\theta_S \rightarrow 0$.¹⁴ This is lower than μ_S calculated for any cluster. Its absence may be related to the way in which the sample is prepared and observed. At 300 K, S_{ad} and Cu-S complexes co-exist on terraces, and both are mobile. As the sample cools to the observation temperature of 5 K, the Cu_2S_3 complexes freeze first on the terraces because their diffusion barrier is relatively high, about 0.34 eV.¹⁴ Meanwhile, S_{ad} remains mobile, with diffusion barrier 0.17 eV according to our DFT calculations. It continues to respond to the falling temperature by

aggregating more and more strongly at steps. When S_{ad} is finally immobilized, its equilibrium concentration on terraces is very small.

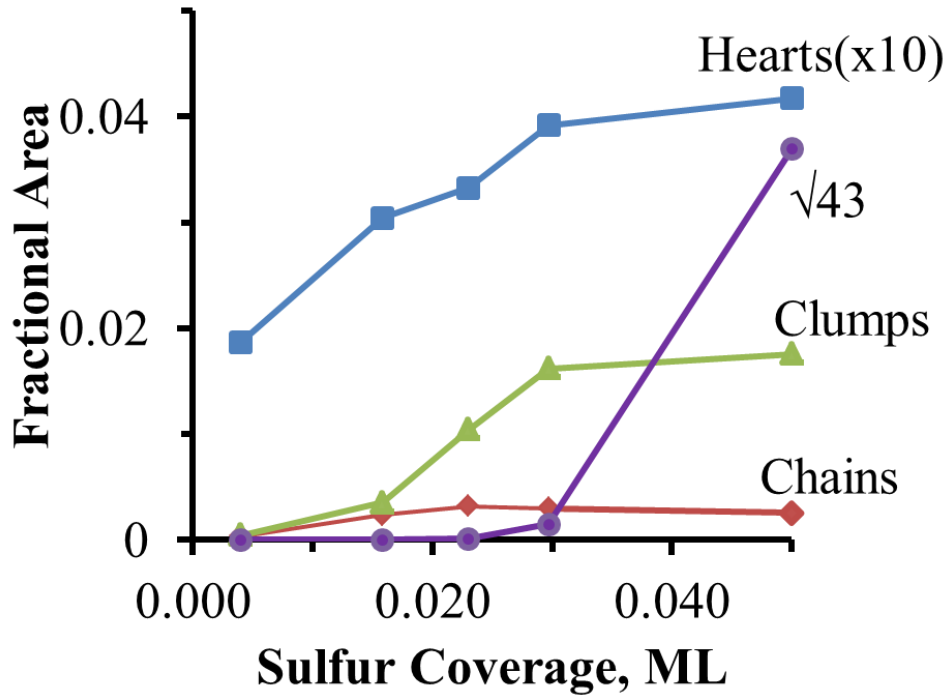


Figure A8. Fractional area of terrace species with increasing coverage.

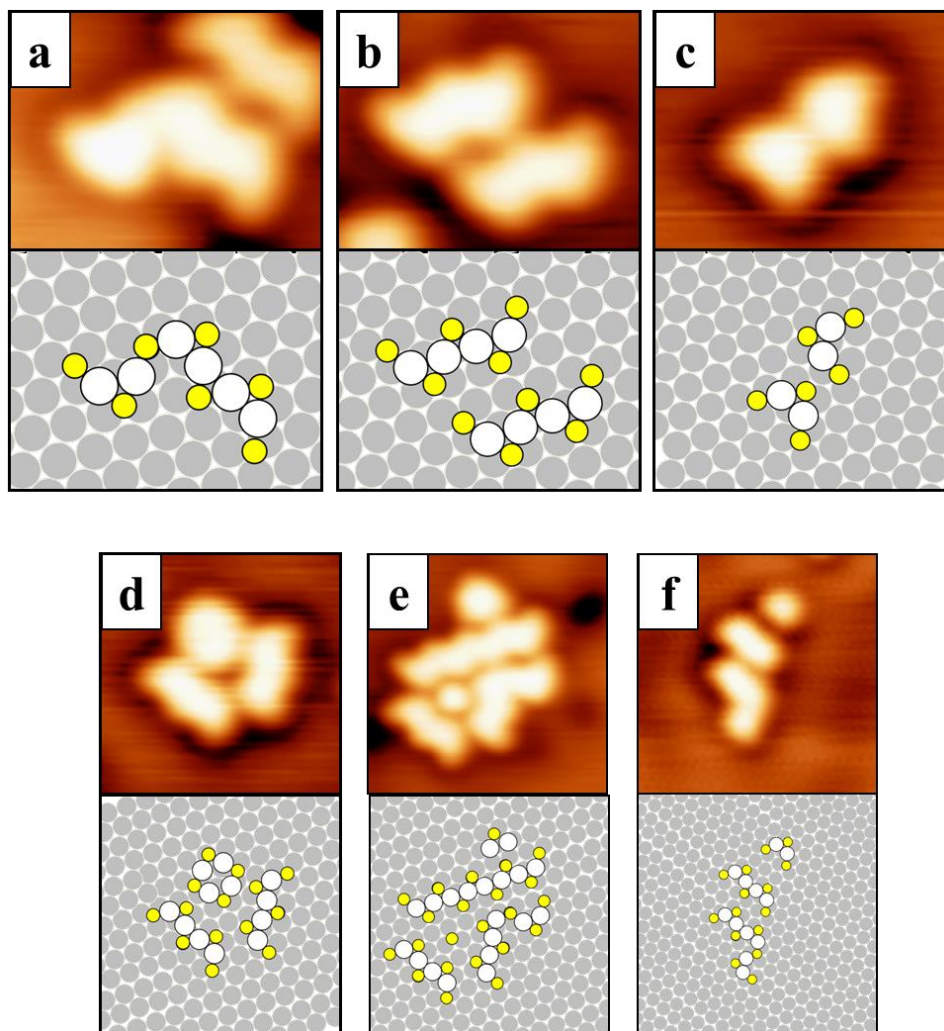


Figure A9. Topographic STM images and proposed structures for multi-unit chain configurations. a) 3-unit bent chain. b) Two aligned 2-unit chains. c) Two hearts point to point. d) Clump of hearts. e) Three chains in a circle. f) 3-unit bent chain aligned with a 2-unit chain. Image details for Figs. A9-12 are in Table AII.

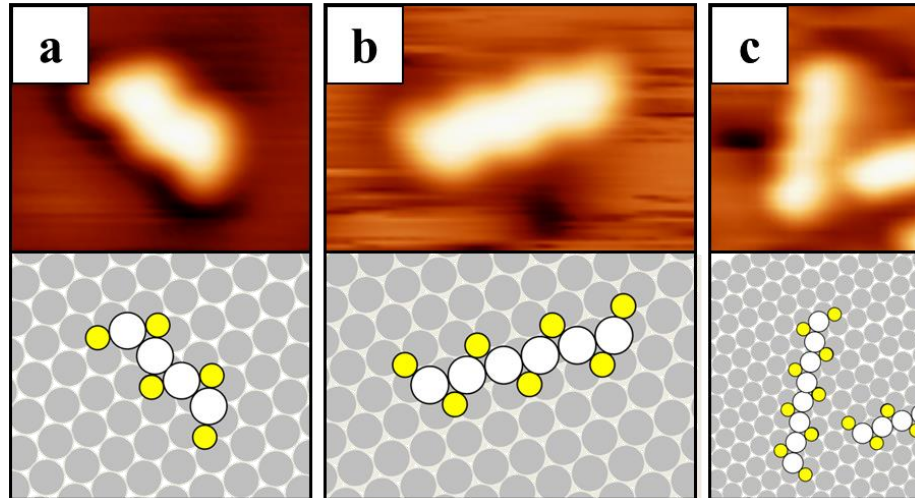


Figure A10. Topographic STM images and proposed structure for multi-unit chains. a) 2-unit chain. b) 3-unit chain. c) 4-unit chain.

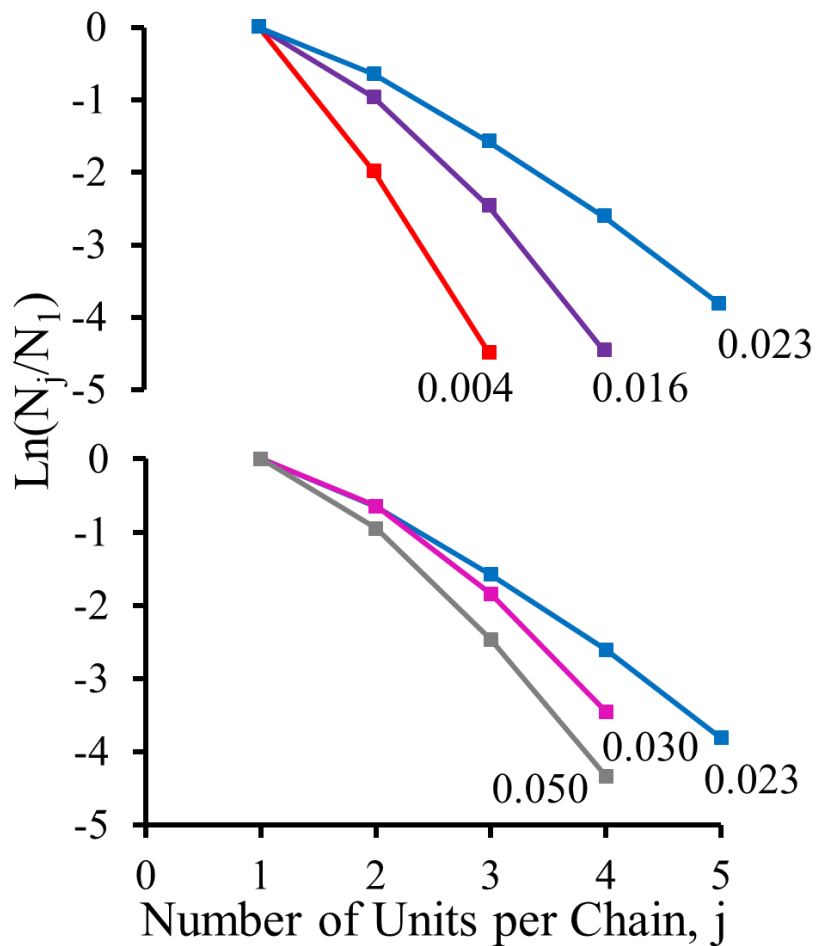


Figure A11. Semi-log plot of the normalized number of chains vs. chain length, j . Each curve is labeled with the corresponding sulfur coverage.

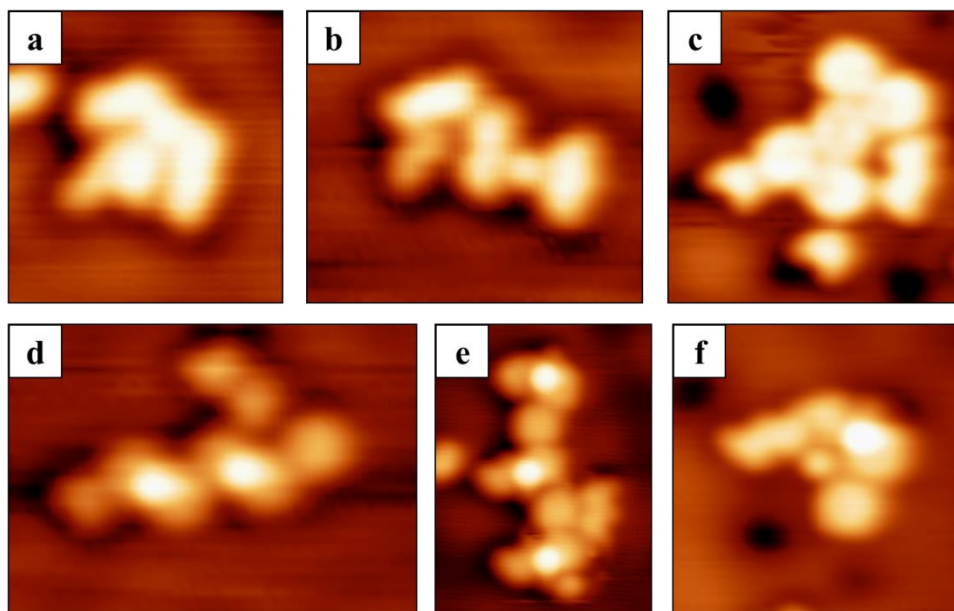


Figure A12. Topographic STM images of Cu-S clump examples.

TABLE AII. STM tunneling conditions for the appendix figures.

Figure Name	Image size (nm ²)	Tunneling Current (nA)	Sample Bias (V)
A9a	2.3 x 1.9	1.17	-0.005
A9b	2.5 x 2.0	1.06	-0.004
A9c	2.5 x 2.0	0.24	-0.088
A9d	3.0 x 3.0	0.24	-0.088
A9e	3.5 x 3.5	1.06	-0.004
A9f	4.5 x 4.5	0.38	-0.085
A10a	2.4 x 2.0	1.06	-0.004
A10b	3.0 x 2.0	0.65	-0.050
A10c	3.0 x 3.5	0.79	-0.050
A12a	3.8 x 4.0	0.39	-0.088
A12b	4.5 x 4.0	0.43	-0.090
A12c	4.0 x 4.0	1.17	-0.005
A12d	5.5 x 4.0	0.43	-0.090
A12e	4.3 x 5.8	0.21	-0.085
A12f	4.0 x 4.0	1.17	-0.005

References

1. Hendriksen, B. L. M.; Ackermann, M. D.; van Rijn, R.; Stoltz, D.; Popa, I.; Balmes, O.; Resta, A.; Wermeille, D.; Felici, R.; Ferrer, S.; Frenken, J. W. M., "The Role of Steps in Surface Catalysis and Reaction Oscillations". *Nat. Chem.* **2010**, *2*, 730-734.
2. Chang, S.-L.; Thiel, P. A., "Atomic-Scale Mechanisms of Metal-on-Metal Film Growth". *CRC Crit. Rev. Surf. Chem.* **1994**, *3*, 239.
3. Li, L.; Luo, L.; Ciston, J.; Saidi, W. A.; Stach, E. A.; Yang, J. C.; Zhou, G., "Surface-Step-Induced Oscillatory Oxide Growth". *Phys. Rev. Lett.* **2014**, *113*, 136104.
4. Ruan, C.-Y.; Stensgaard, I.; Besenbacher, F.; Laegsgaard, E., "A Scanning Tunneling Microscopy Study of the Interaction of S with the Cu(111) Surface". *Ultramicroscopy* **1992**, *42-44*, 498.
5. Thiel, P. A.; Shen, M.; Liu, D.-J.; Evans, J. W., "Critical Review: Adsorbate-Enhanced Transport of Metals on Metal Surfaces: Oxygen and Sulfur on Coinage Metals". *J. Vac. Sci. Technol. A* **2010**, *28*, 1285-1298.
6. Maksymovych, P.; Voznyy, O.; Dougherty, D. B.; Sorescu, D. C.; Yates Jr., J. T., "Gold Adatom as a Key Structural Component in Self-Assembled Monolayers of Organosulfur Molecules on Au(1 1 1)". *Prog. Surf. Sci.* **2010**, *85*, 206-240.
7. Bartels, L., "Tailoring Molecular Layers at Metal Surfaces". *Nat. Chem.* **2010**, *2*, 87-95.
8. Garvey, M.; Kestell, J.; Abuflaha, R.; Bennett, D. W.; Henkelman, G.; Tysoe, W. T., "Understanding and Controlling the 1,4-Phenylene Diisocyanide-Gold Oligomer Formation Pathways". *J. Phys. Chem. C* **2014**, *118*, 20899-20907.

9. Diller, K.; Klappenberger, F.; Allegretti, F.; Papageorgiou, A. C.; Fischer, S.; Wiengarten, A.; Joshi, S.; Seufert, K.; Eciija, D.; Auwarter, W.; Barth, J. V., "Investigating the Molecule-Substrate Interaction of Prototypic Tetrapyrrole Compounds: Adsorption and Self-Metalation of Porphine on Cu(111)". *J. Chem. Phys.* **2013**, *138*.
10. Feibelman, P. J., "Formation and Diffusion of S-Decorated Cu Clusters on Cu(111)". *Phys. Rev. Lett.* **2000**, *85*, 606-609.
11. Ling, W. L.; Bartelt, N. C.; Pohl, K.; de la Figuera, J.; Hwang, R. Q.; McCarty, K. F., "Enhanced Self-Diffusion on Cu(111) by Trace Amounts of S: Chemical-Reaction-Limited Kinetics". *Phys. Rev. Lett.* **2004**, *93*, 166101.
12. Foss, M.; Feidenhans'l, R.; Nielsen, M.; Findeisen, E.; Buslaps, T.; Johnson, R. L.; Besenbacher, F., "Sulfur Induced Cu₄ Tetramers on Cu (111)". *Surf. Sci.* **1997**, *388*, 5-14.
13. Foss, M.; Feidenhans'l, R.; Nielsen, M.; Findeisen, E.; Buslaps, T.; Johnson, R. I.; Besenbacher, F.; Stensgaard, I., "Sulfur Chemisorption on Ni(111): The Clock Structure of the (5√3×2)S Phase". *Phys. Rev. B* **1994**, *50*, 8950-8953.
14. Walen, H.; Liu, D.-J.; Oh, J.; Lim, H.; Evans, J. W.; Aikens, C.; Kim, Y.; Thiel, P. A., "Cu₂S₃ Complex on Cu(111) as a Candidate for Mass Transport Enhancement". *Phys. Rev. B* **2015**, *91*, 045426.
15. Rousset, S.; Gauthier, S.; Siboulet, O.; Sacks, W.; Belin, M.; Klein, J., "Scanning-Tunneling-Microscopy Observation of Adsorbate-Induced Two-Dimensional Step Faceting on the S/Cu(111) Surface". *Phys. Rev. Lett.* **1989**, *63*, 1265-1268.
16. Motai, K.; Hushizume, T.; Lu, H.; Jeon, D.; Sakurai, T., "STM of the Cu(111) 1 × 1 Surface and Its Exposure to Chlorine and Sulfur". *Appl. Surf. Sci.* **1993**, *67*, 246-251.

17. Prince, N.; Seymor, D.; Aswin, M.; McConville, C. F.; Woodruff, D. P., "A SEXAFS and X-Ray Standing Wave Study of the Cu(111) ($\sqrt{7} \times \sqrt{7}$)R 19°-S Surface: Adsorbate-Substrate and Adsorbate-Adsorbate Registry". *Surf. Sci.* **1990**, *230*, 13-26.
18. Campbell, C. T.; Koel, B. E., "H₂S/Cu(111): A Model Study of Sulfur Poisoning of Water-Gas Shift Catalysts". *Surf. Sci.* **1987**, *183*, 100-112.
19. Driver, S. M.; Woodruff, D. P., "A New Pseudo-(100) Sulphur-Induced Reconstruction of Cu(111) Observed by Scanning Tunnelling Microscopy". *Surf. Sci.* **2001**, *479*, 1-10.
20. Wahlström, E.; Ekvall, I.; Olin, H.; Lindgren, S. A.; Wallden, L., "Observation of Ordered Structures for S/Cu(111) at Low Temperature and Coverage". *Phys. Rev. B* **1999**, *60*, 10699.
21. Wahlström, E.; Ekvall, I.; Kihlgren, T.; Olin, H.; Lindgren, S. A.; Wallden, L., "Low-Temperature Structure of S/Cu(111)". *Phys. Rev. B* **2001**, *64*, 155406.
22. Liu, D.-J.; Walen, H.; Oh, J.; Lim, H.; Evans, J. W.; Kim, Y.; Thiel, P. A., "Search for the Structure of a Sulfur-Induced Reconstruction on Cu(111)". *J. Phys. Chem. C* **2014**, *118*, 29218-29223.
23. Wagner, C., "Investigation on Silver Sulfide". *J. Chem. Phys.* **1953**, *21*, 1819-1827.
24. Detry, D.; Drowart, J.; Goldfinger, P.; Keller, H.; Rickert, H., "Zur Thermodynamik Von Schwefeldampf". *Z. Phys. Chem.* **1967**, *55*, 314-319.
25. Shen, M.; Liu, D.-J.; Jenks, C. J.; Thiel, P. A., "Novel Self-Organized Structure of a Ag-S Complex on the Ag(111) Surface Below Room Temperature". *J. Phys. Chem. C* **2008**, *112*, 4281-4290.

26. Horcas, I.; Fernandez, R.; Gomez-Rodriguez, J. M.; Colchero, J.; Gomez-Herrero, J.; Baro, A. M., "WSXM: A Software for Scanning Probe Microscopy and a Tool for Nanotechnology". *Rev. Sci. Instrum.* **2007**, *78*, 013705.
27. Liu, D.-J., "Density Functional Analysis of Key Energetics in Metal Homoepitaxy: Quantum Size Effects in Periodic Slab Calculations". *Phys. Rev. B* **2010**, *81*, 035415.
28. Tersoff, J.; Hamann, D. R., "Theory and Application for the Scanning Tunneling Microscope". *Phys. Rev. Lett.* **1983**, *50*, 1998-2001.
29. Shen, M.; Jenks, C. J.; Evans, J. W.; Thiel, P. A., "Rapid Decay of Vacancy Islands at Step Edges on Ag(111): Step Orientation Dependence". *J. Phys.: Condens. Matter* **2010**, *22*, 215002.
30. Russell, S. M.; Kim, Y.; Liu, D.-J.; Evans, J. W.; Thiel, P. A., "Structure, Formation, and Equilibration of Ensembles of Ag-S Complexes on an Ag Surface". *J. Chem. Phys.* **2013**, *138*, 071101.
31. Giesen, M., "Step and Island Dynamics at Solid/Vacuum and Solid/Liquid Interfaces". *Prog. Surf. Sci.* **2001**, *68*, 1-153.
32. Shen, M.; Liu, D.-J.; Jenks, C. J.; Thiel, P. A.; Evans, J. W., "Accelerated Coarsening of Ag Adatom Islands on Ag(111) Exposed to S: Mass-Transport Mediated by Ag-S Complexes". *J. Chem. Phys.* **2009**, *130*, 094701.

CHAPTER IV

CHEMISORPTION OF S ATOMS ON CU(100) AT LOW COVERAGE

Holly Walen,^a P. M. Spurgeon,^a Junepyo Oh,^b Hyun Jin Yang,^b Yousoo Kim,^b

and P. A. Thiel^{a,c,d}

Abstract

We report short-range ordering of chemisorbed S atoms on Cu(100) at very low coverage (~ 0.02 ML) using low temperature scanning tunneling microscopy. As coverage increases to 0.09 ML, we observe chains of S atoms with spacing of $2a$ (where a is the surface lattice spacing), as well as small areas of $p(2 \times 2)$ arrangement. A comparison to previous work on Cu(100) and Ag(100) is presented.

1. Introduction

Sulfur adsorption studies on the noble metals Cu, Ag, and Au have led to new insights into sulfur-metal and sulfur-sulfur interactions. These studies have shown a propensity of metals to react with sulfur to form small, mobile complexes, or new ordered structures at low sulfur coverage. For example, sulfur adsorbed on Cu(111) at room temperature forms a heart-shaped Cu_2S_3 complex.¹ The energetic motivation for the

Departments of ^aChemistry and ^cMaterials Science & Engineering, Iowa State University, Ames, Iowa 50011 USA

^bRIKEN Surface and Interface Science Laboratory, Wako, Saitama 351-0198, Japan

^dAmes Laboratory of the USDOE, Ames, Iowa 50011 USA

formation of these complexes relies on the linear S-M-S substructure, which is observed also with sulfur on Ag(111),² Au(100),³ and is predicted for sulfur adsorption on Ag(100).⁴

Sulfur adsorption on Cu(100) has been previously studied with Auger electron spectroscopy (AES),⁵⁻⁶ low energy electron diffraction (LEED),⁵⁻¹² scanning tunneling microscopy (STM),¹² radioactive tracer analysis,⁷ x-ray diffraction,¹³ angle-resolved fine structure,¹⁴⁻¹⁷ high-resolution electron energy loss spectroscopy,¹⁸⁻¹⁹ surface-extended x-ray absorption fine structure,²⁰⁻²² and x-ray photoemission.²³⁻²⁴ These studies have been primarily focused on the p(2 x 2) structure that forms around 0.25 ML S at room temperature, where the S atoms occupy the four-fold hollow sites of the surface. A $(\sqrt{17} \times \sqrt{17})R14^\circ$ reconstruction forms at ~0.47 ML (with annealing > 873 K).^{12, 24}

This study is presented in 5 sections. Section 2 contains the experimental details, including the sample preparation and calibration of the STM. Section 3 contains the results of these experiments, and Section 4 discusses these results and puts them in context with the somewhat expansive literature, where appropriate. Section 5 contains the conclusions.

2. Experimental Description

Single-crystal Cu(100) was cleaned under ultrahigh vacuum via Ar⁺ sputtering (12-14 μ A, 2.0 kV, 10 min) and annealing (810 K, 10 min) cycles. The final sputtering was followed by flashing the sample to 770 K. This minimized the number of impurities and defects visible in STM.

Exposure to S₂(gas) was performed with the sample held at room temperature. The sulfur source was an *in situ* electrochemical cell evaporator following the design by Wagner,²⁵ which has been characterized in detail by Detry *et al.*²⁶ and Heegemann *et al.*²⁷

Sulfur coverage (θ_S) is the ratio of adsorbed S atoms to the number of Cu atoms in the surface plane, and was determined by counting individual S atoms and dividing by the total Cu atoms in the area observed.

Low temperature STM was the primary experimental technique, and imaging temperature was 5K. The lateral calibration was checked with atomically-resolved images of the clean Cu(100) surface [Fig. 1(b)]. The Cu(100) lattice constant determined from such images was 0.25 ± 0.01 nm, and the step heights were 0.17 ± 0.01 nm. These values are, within their standard deviations, identical to the accepted values of 0.255 nm and 0.181 nm, respectively.²⁸ Typical tunneling conditions were in the range of 0.93 – 1.22 nA for tunneling current and -1.5 V to +0.149 V sample bias (V_S), unless noted otherwise.

3. Results

3.1 Chemisorption on Terraces

The dominant features after sulfur deposition are small, round protrusions, with dark outer rings. The height and width of the protrusions are sensitive to sample bias during imaging (Fig. 2). Most notably, they are imaged as protrusions with negative V_S , and as depressions with $V > +0.149$ V. This is summarized in Fig. 2. The height of the protrusions as a function of V_S (Fig. 3) is oscillatory from -5 V to +2 V with some exception close to 0 V, and there is a large spike in height from +2 V to +4 V. The height of the protrusions is measured from the lowest part of the surrounding ring to the tallest point in the center (Fig. 2(c-d)), and the depth of the depressions is measured from the lowest point of the depression to the tallest part of the adjacent terrace.

The width (measured at full-width at half-maximum) of the protrusions is constant at negative V_S (0.33 ± 0.04 nm, $N = 2180$), but is not constant at positive V_S (depressions), ranging from 0.23 nm to 1.02 nm (Fig. 3). Thus, the data show that the size and shape of these features depend strongly on tunneling conditions.

We have imaged S adatoms adsorbed on Au(110)²⁹ and Au(111)³⁰ in STM under identical experimental conditions. One example, S atoms on Au(111)³⁰ appear as protrusions using tunneling $V_S = -0.50$ V to $+0.13$ V. The protrusions on Au(111) have width of 0.34 ± 0.04 nm and height of 0.017 ± 0.003 nm. The assignment of the protrusions as S atoms is corroborated by DFT calculations.³⁰ The width of the S/Au(111) is within a standard deviation of the width of the protrusions on Cu(100), 0.33 ± 0.04 nm. Therefore, we assign the protrusions on Cu(100) as single S atoms.

The range of θ_S here extends from 0.002 to 0.091 ML. A summary of STM images in this range is shown in Fig. 4. At $\theta_S < 0.015$ ML, individual S atoms are randomly arranged on the terraces. At 0.015 ML, we begin to observe pairs of S atoms with 0.51 ± 0.01 nm ($2a$) spacing, and as coverage increases further the number of these pairs also increases. Additionally, linear “chains” of $2a$ spacing with more than 2 S atoms are observed, with chains up to 6 S long at 0.091 ML. These chains align along the $[011]$ and $[0\bar{1}1]$ close-packed directions. The chain distribution per unit area is shown in Fig. 5. At 0.085 ML and 0.091 ML there are small areas with local $p(2 \times 2)$ arrangement, as in Fig. 4(g-h).

It is interesting to note that the dark ring observed around the individual S atoms becomes less obvious as θ_S increases (for example, Fig. 4(c) compared to (h)).

The chains and aggregates of S atoms are different from those observed by Colaianni *et al.* (c.f. Fig. 4 of Ref. ¹²), specifically we observe chains with $2a$ spacing aligned along the

close-packed directions and small areas of p(2 x 2)-S arrangement. The chains observed by Colaianni *et al.* are aligned 45° relative to the close-packed directions. Thus, it is unlikely that the S-S spacing within their chains is $2a$, but may be closer to $\sqrt{2}a$. This difference may be because their θ_S is considerably higher, as evidenced by the dramatic amount of terrace roughening concurrently observed.

3.2 Step Edges

The clean step edges of Cu(100) can have 3 geometries: close-packed, kinked close-packed, and open (Fig. 6). S does not preferentially adsorb at any of the edges at $\theta_S \leq 0.015$ ML [Fig. 7(a-b)]. At 0.061 ML there is some decoration of the steps, but the steps remain mostly bare [Fig. 7(c-d)]. At $\theta_S \geq 0.085$ ML, we observe smooth decoration along the close-packed edges, shown in Fig. 7(e-f). The S atoms decorating the close packed edge have spacing of 0.50 ± 0.01 nm, i.e. $2a$. We also observe decoration along short, non-close packed edges, where S-S spacing is 0.58 ± 0.05 nm (two examples are encircled in Fig. 7(e-f)). These edges are oriented $30^\circ \pm 1^\circ$ relative to the close packed edges. This spacing and orientation is consistent with spacing along a kinked-close packed edge, with ideal S-S spacing of $\sqrt{5}a$: 0.57 nm (Fig. 6) and oriented 27° relative to the close-packed directions. The anticipated spacing for S decorating an open edge is 0.36 nm (spacing of $\sqrt{2}a$) or 0.72 nm ($2\sqrt{2}a$) if the sites were alternately occupied. Open edges would be oriented 45° relative to the close packed edges. Finally, at $\theta_S \geq 0.085$ ML, we still observe some bare step edge regions (Fig. 7(g-h)), where the exact edge orientation relative to the close-packed directions is unclear.

4. Discussion

4.1 Bias Dependence of S Appearance in STM

Calculations by Lang³¹⁻³² predict that a sulfur atom adsorbed on a metal surface will appear as a protrusion for V_S of -2.0 V to approximately +1.3 V. Above this voltage, the calculations predict that the tip must move *closer* to the adsorbate as it passes over in order to maintain constant current.³² Therefore, for $V_S > +1.3$ V, S atoms will appear as depressions on the metal surface. Experimentally, we observe the change in appearance predicted by Lang *et al.* at a lower sample bias of +0.15 V (Fig. 3). This change in appearance is reliably reproduced from one experiment to the next—the images in Fig. 2(a) and (b) were recorded on different days, with rigorous tip cleaning on the clean Cu(100) surface between experiments.

As an aside, our previous work studying S atoms on Au surfaces^{3, 29-30} have not demonstrated a bias-dependent contrast for a similar range of V_S .

Oxygen atoms have been found to exhibit a similar bias-dependent contrast on Ag(001), appearing as protrusions for bias between -2.4 V and +0.5 V, and as depressions from +0.66 V - +2 V.³³ Schintke *et al.* analyzed this bias dependence of the local density of states with theoretical methods, and determined that the p_z orbital of the O atom interacts strongly with the s orbital of the Ag atom directly beneath the 4fh site.³³ The orbital interaction leads to a higher tunneling current with the tip is positioned above the O atom.

An *ab initio* study of the p(2 x 2)-S structure by Chiodo *et al.* found that S p_z orbitals hybridize with the s, d_{xz} , and d_{yz} orbitals of the surface Cu, and with the d_{z^2} of the subsurface Cu atoms.³⁴ This interaction may play a role in the bias-dependent contrast observed in Figure 2.

To our knowledge, the literature does not provide other experimental evidence of this bias dependence for S, perhaps due to the propensity for the formation of S-M complexes^{1-3,}
³⁵ and reconstructions,³⁶⁻³⁸ and the lack of studies performed at low coverage (where there are no long-range ordered structures). This makes it difficult to compare the observation of S depressions with other systems, as even S atoms in overlayer structures also generally appear as protrusions rather than depressions.^{3, 12, 39-45}

4.2 Comparison to S/Ag(100)

In a study by Shen *et al.*, STM and DFT are used to investigate the effect of S on the coarsening of Ag islands on Ag(100) at 0.034 to 0.21 ML S.⁴ The proposed coarsening mechanism relies on the formation of AgS₂ complexes, which are not imaged but are predicted by DFT to have a lower diffusion barrier than Ag adatoms on Ag(100). The formation of these complexes is predicted to occur at step edges. Thus, the step structure has been heavily analyzed, and the following picture of the Ag island edges with S can be determined.⁴ First, sulfur does not preferentially bind at step edges on Ag(100) at low coverage due to the high-coordination binding sites available on the terraces. Second, the most stable configuration of S binding at the edges is a double row of S, where the upper terrace resembles a kinked close-packed edge (c.f. Fig. 7(c) of Ref. ⁴) and has a S-S spacing of $\sqrt{5}a$. The second-most stable configuration is a step with deeper kinks, where spacing between S atoms along the upper edge is $2\sqrt{2}a$ (c.f. Fig. 7(d) of Ref. ⁴).

On Cu(100), we also do not observe preferential adsorption to step edges. At 0.091 ML, we observe close-packed step decoration along with kinked close-packed step decoration, in agreement with Ag(100). However, it is unclear from the STM images alone if

a double row of S atoms is present at steps. Finally, we do not observe complexes on Cu(100).

Above 0.21 ML, the S/Ag(100) and S/Cu(100) systems display the same structural phases—the p(2 x 2) and the $\sqrt{17}$ reconstruction.^{12, 38} The p(2 x 2)-S structure was observed on Ag(100) at 300 K and 0.21 ML S by Russell *et al.*³⁸ From combined STM and DFT data, two hypotheses are made to describe this ordering. First, equilibrated S atoms at low θ_S (< 0.21 ML) are disordered due to a high S atom diffusion barrier (0.84 eV),⁴ only progressing to form a p(2 x 2) ordered structure as $\theta_S \rightarrow 0.25$ ML. Second, the diffusion barrier of S atoms on Ag(100) decreases with increasing coverage, promoting the formation of the p(2 x 2). From DFT, the stability of the p(2 x 2) on Ag(100) requires strong 1st and 2nd nearest-neighbor (NN) repulsions, 3rd NN attraction, and 4th NN repulsions.³⁸ Similar interactions have been observed for chalcogens on other metal surfaces: O/Pd(100)⁴⁶⁻⁴⁷ and O/Ni(100)⁴⁸ exhibit 3rd NN attractions, Se/Ni(100)⁴⁹ and O/Rh(100)⁵⁰ exhibit relatively strong 4th NN repulsions.

The hypotheses for Ag(100) do not quite align with our observations on Cu(100), where we observe the formation of 2a chains at 0.061 ML, and some p(2 x 2) arrangement at 0.085 ML. Both of these coverages are substantially lower than 0.21 ML, indicating different S-M or S-S interactions on Cu(100) from those on Ag(100). It is possible that the S diffusion barrier is smaller on Cu(100) than on Ag(100), and thus the S atoms are more mobile at lower coverage. Based on the observations on Ag(100) and those for the other metals and chalcogens presented above, it is not unreasonable to predict that similar NN interactions (specifically the 3rd or 4th NN interactions) play a role in the ordering on Cu(100).

4.3 Comparison to Cu(111) Under Identical Experimental Conditions

Under identical conditions of coverage and temperature, we have previously found that sulfur induces many interesting and striking features on Cu(111), the most prominent being a small, heart-shaped Cu_2S_3 complex.¹ From $0.004 < \theta_s < 0.05$ ML, the hearts progressively coexist on terraces with complexes resembling concatenated hearts, clumps, and finally the $\sqrt{43}$ reconstruction.^{37, 51-52} In addition, the preference for binding at step edges of Cu(111) is very high, and steps are extensively decorated and faceted along the close-packed directions in this small sulfur coverage range.

The observation of complexes on Cu(111) but not on Cu(100) could be due to several factors. Possibly the most important is the available binding sites on the respective surfaces. Cu(100) presents higher-coordination fourfold-hollow (4fh) terrace sites for S adsorption, while Cu(111) terraces present 3fh sites. The higher-coordination sites have been demonstrated to be very stable for S adatom binding on Cu(111) and Ni(111) surfaces.^{51, 53-54} Preliminary DFT calculations in our group have found that S adsorption is 0.547 eV stronger on the 4fh site of Cu(100) than on the 3fh fcc site of Cu(111), based on the chemical potential of the chemisorbed S at low coverage.^{51, 55}

5. Conclusion

Using low-temperature STM, we find chemisorbed S atoms on Cu(100) in the limit of low sulfur coverage. Sulfur appears as protrusions using $V_s < +0.149$ V, and as depressions at $V_s > +0.149$ V. At 0.015 ML we begin to observe pairwise ordering, with spacing of $2a$, and as the sulfur coverage increases we find chains with length of up to 6 S coexisting with small areas of $p(2 \times 2)$ arrangement.

Acknowledgements

The experimental component of this work was conducted or supervised by HW, PM, JO, HJY, YK, and PAT. It was supported by three sources. From the U.S., it was NSF Grant CHE-1507223. From Japan, support was provided by a Grant-in-Aid for Scientific Research on Priority Areas “Electron Transport Through a Linked Molecule in Nano-scale”; and a Grant-in-Aid for Scientific Research(S) “Single Molecule Spectroscopy using Probe Microscope” from the Ministry of Education, Culture, Sports, Science, and Technology (MEXT).

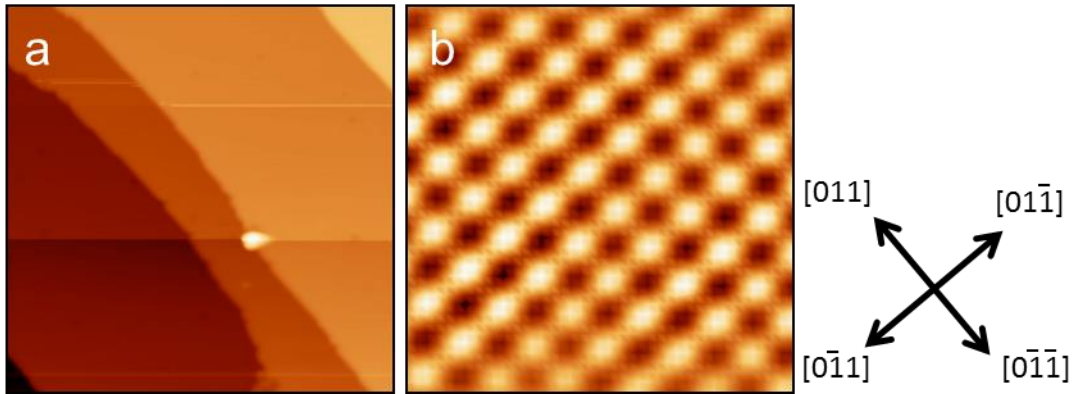
Figures

Figure 1. STM images of the clean Cu(100) surface. a) Large-scale image of step edges with one bright contaminant, $50 \times 50 \text{ nm}^2$. b) Atomically resolved image, $2 \times 2 \text{ nm}^2$.

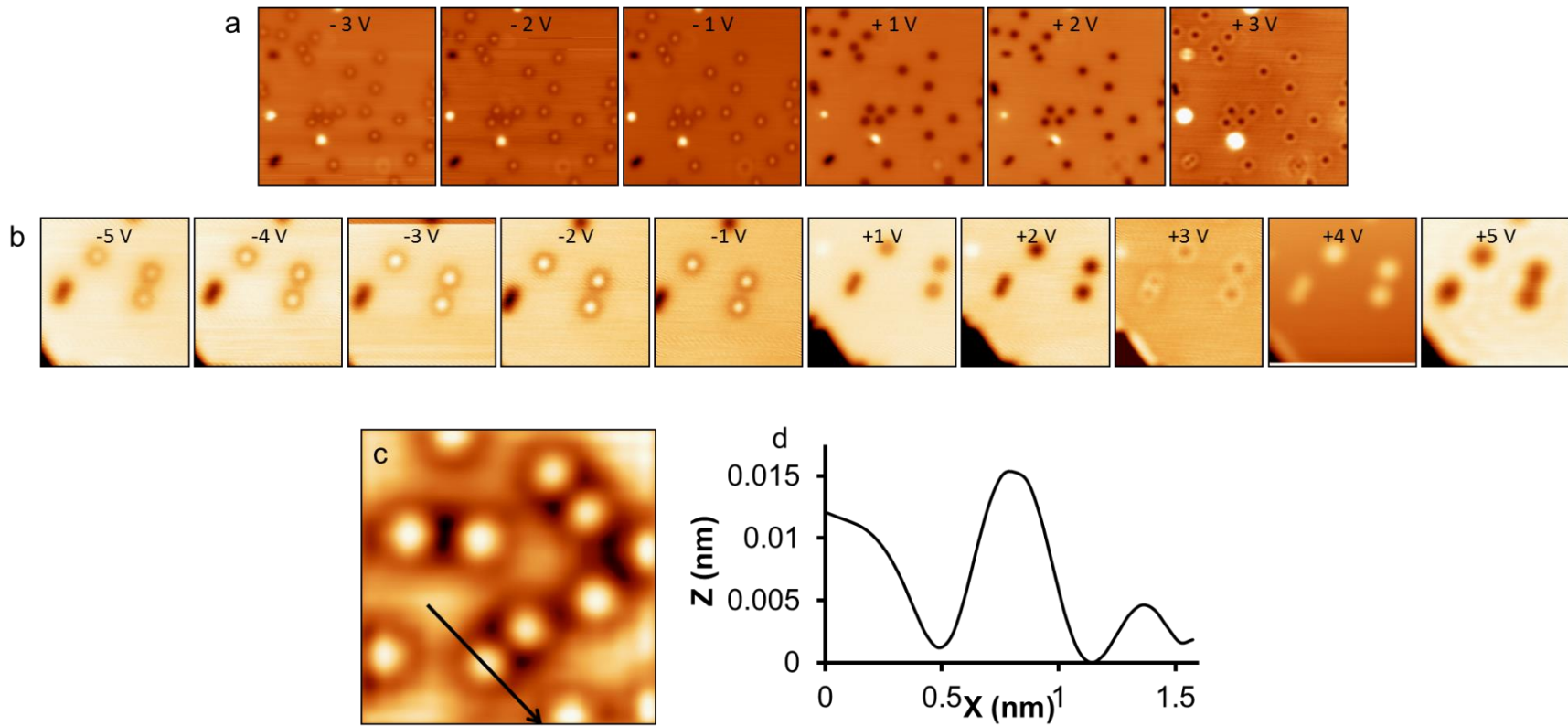


Figure 2. Sample bias effect on S atom imaging. At negative bias, the S atoms appear as short, round protrusions with a dark outer ring. At positive bias, the S atoms appear primarily as round depressions. Some images (for example in (a)) contain very bright contaminants or dark spots that stay consistently bright or dark across the bias range. a) Sequential images of S atoms from $V_S = -3$ to $+3$ V, $\theta_S = 0.006$ ML, 15×15 nm². b) Sequential images of S atoms from a second experiment. $V_S = -5$ to $+5$ V, $\theta_S = 0.002$ ML, 7×7 nm². c) Image with $\theta_S = 0.061$ ML, -0.084 V, and d) line profile over one S atom.

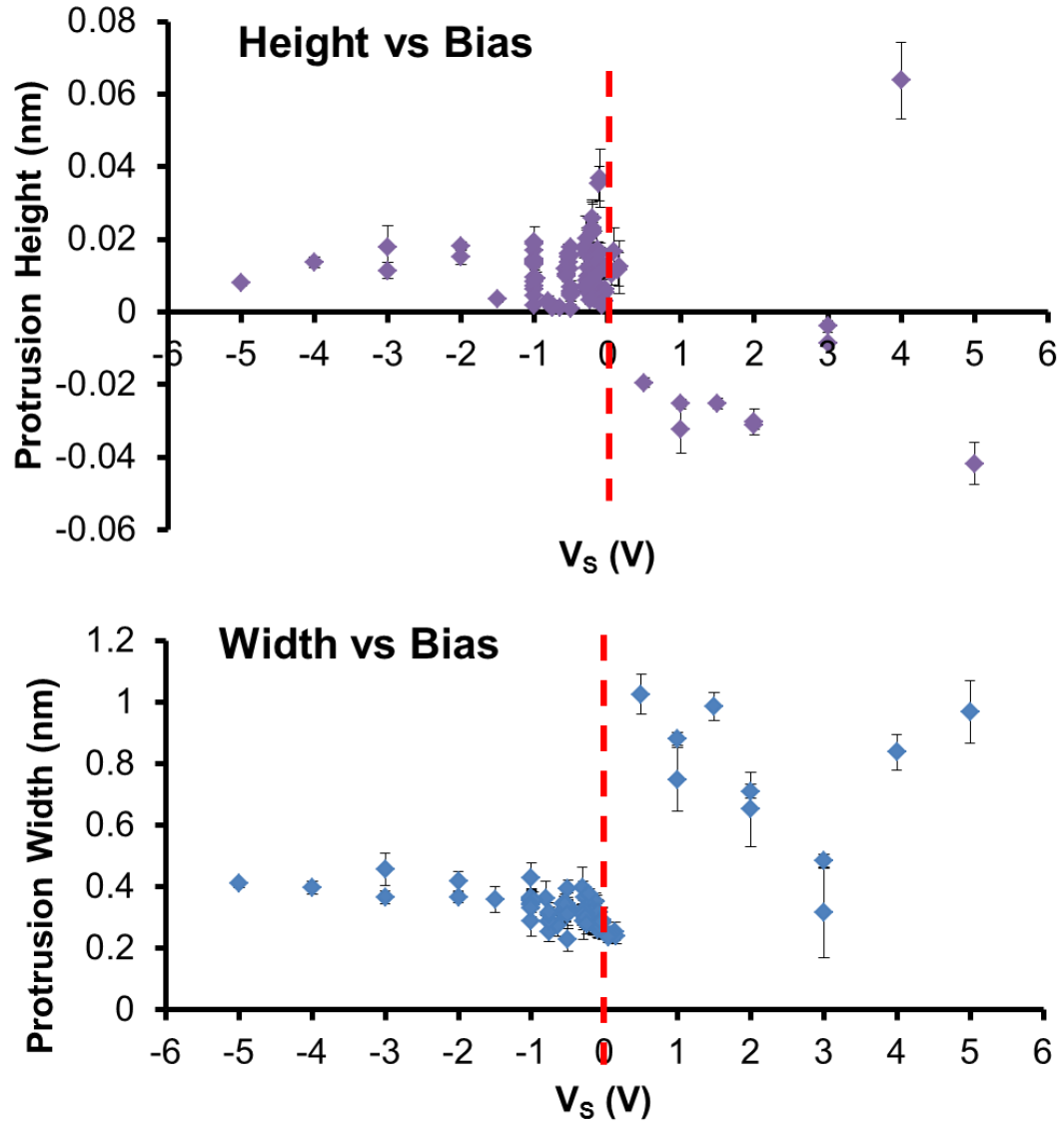


Figure 3. Sample bias effect on protrusion width and height. Each point represents the average of 1 image, error bars indicate the standard deviation.

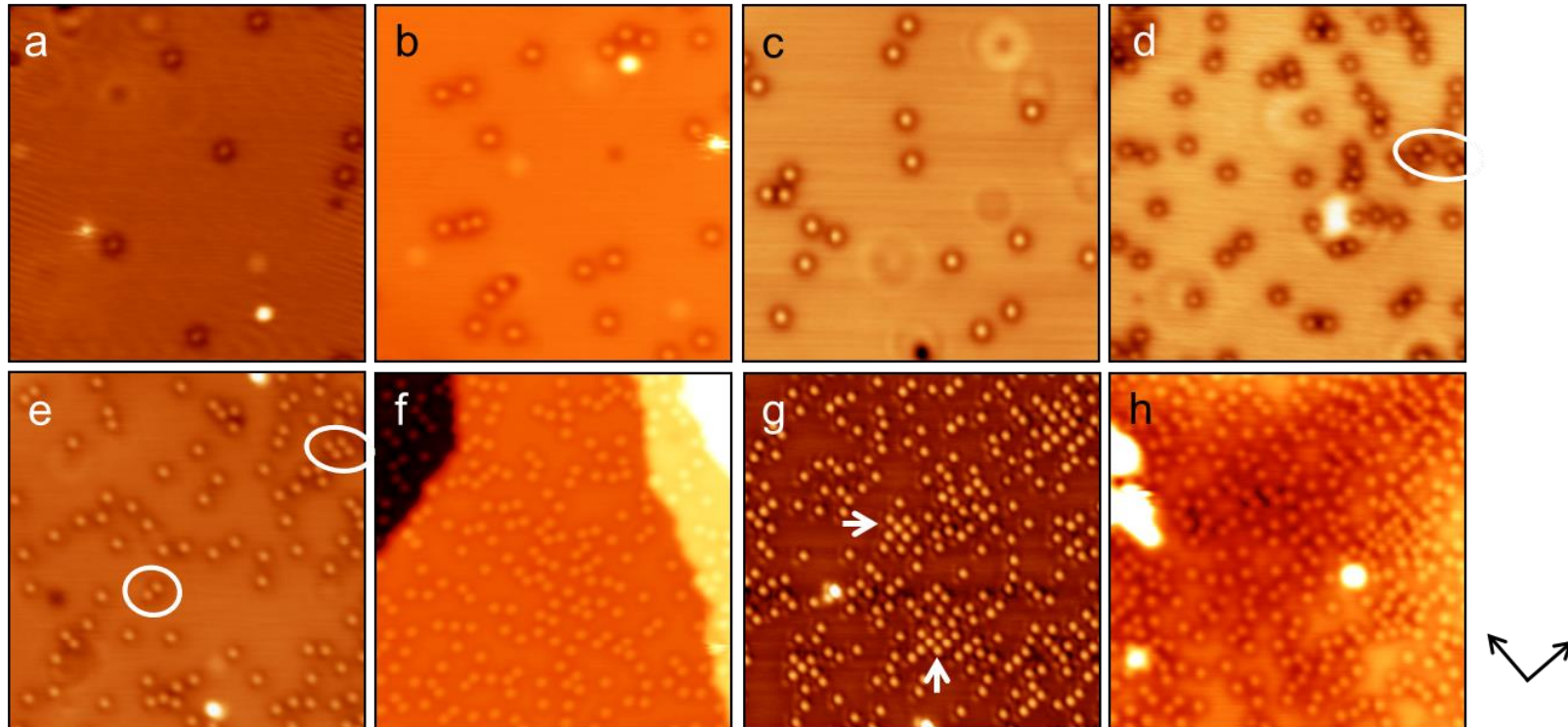


Figure 4. Representative images at each coverage. All images are $15 \times 15 \text{ nm}^2$. a) 0.002 ML; b) 0.005 ML; c) 0.006 ML; d) 0.015 ML; e) 0.016 ML; f) 0.061 ML; g) 0.085 ML; h) 0.091 ML. Examples of pairs with $2a$ spacing are circled in (d) and (e). Small groups of $p(2 \times 2)$ arrangement are pointed out in (g). Two of the close-packed directions are indicated by the arrows to the right of (h).

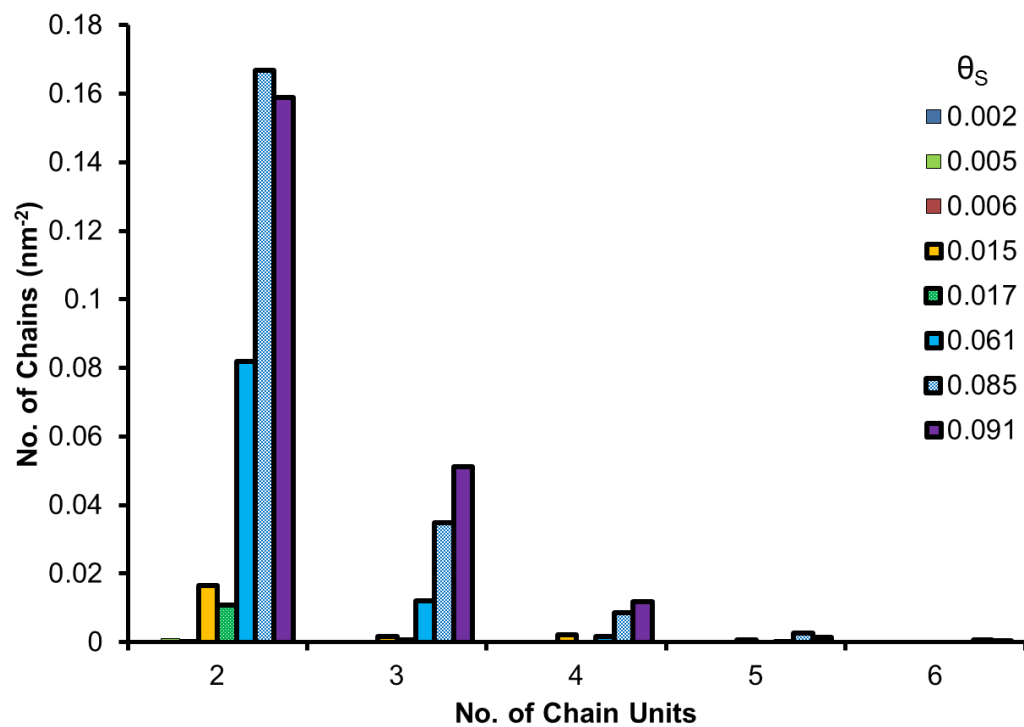


Figure 5. Distribution of S atom chain lengths.

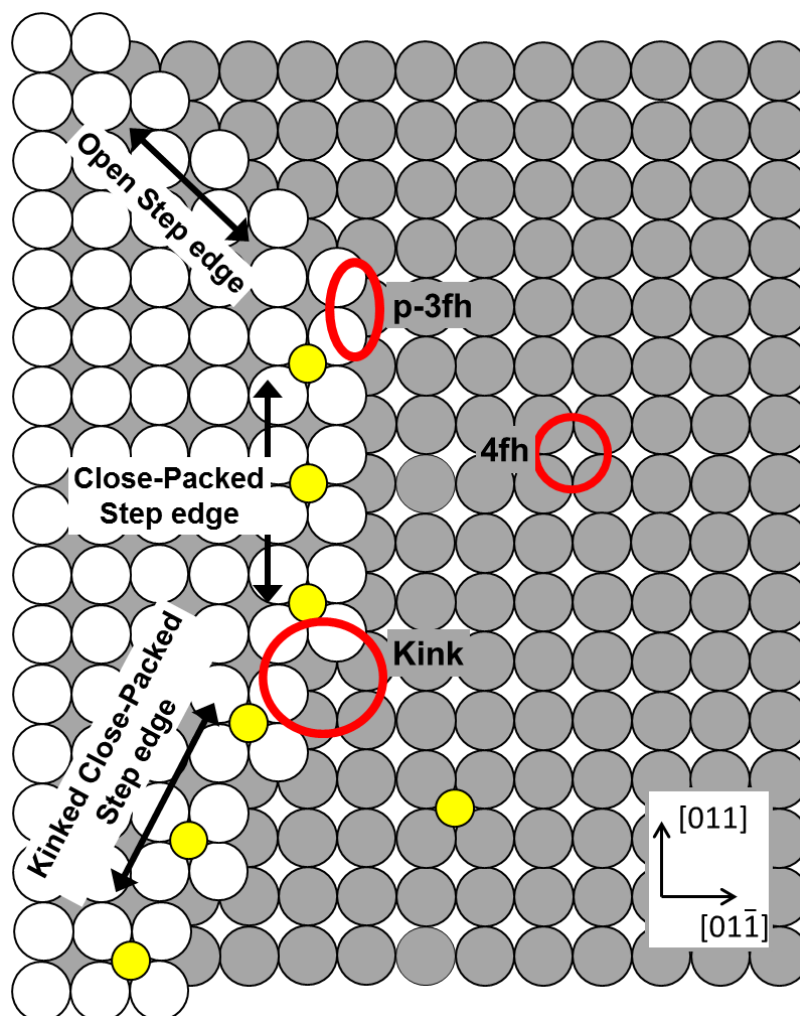


Figure 6. Schematic of the Cu(100) surface, showing different adsorption sites for the S atoms along step edges. The white circles represent Cu atoms in an island or upper terrace, the grey circles represent Cu atoms in the lower terrace. Yellow circles represent S atoms.

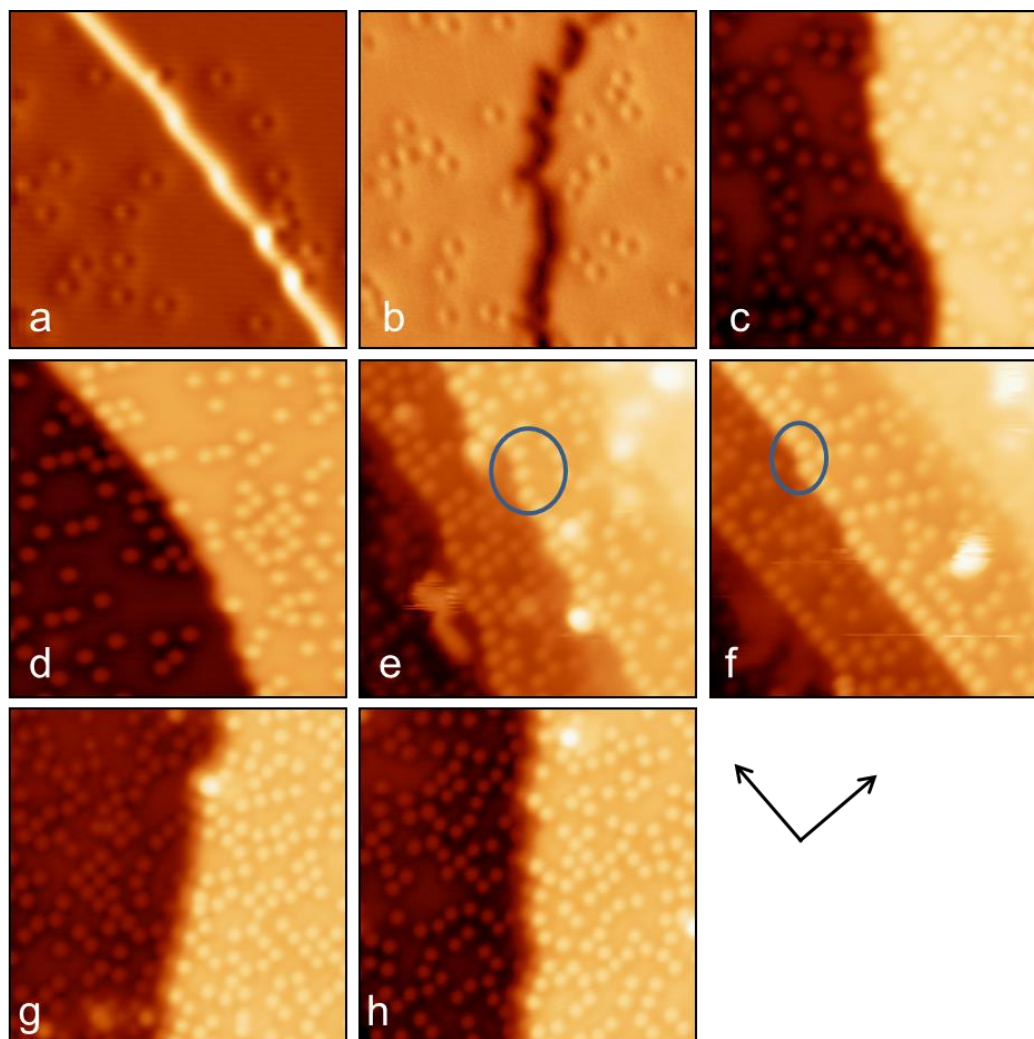


Figure 7. STM images of step edges with S. All are $10 \times 10 \text{ nm}^2$. a) 0.015 ML; b) 0.016 ML; c)-d) 0.061 ML; e)-h) 0.091 ML.

Appendix 1: Tunneling Conditions

TABLE AI. Tunneling conditions for the figures in the main text.

Figure name	Image size (nm ²)	Tunneling Current (nA)	Sample Bias (V)	File name
1 a	50 x 50	1.00	-0.495	2140723 m1
b	2 x 2	1.24	-0.020	2140820 m7
2 a	15 x 15	1.06	In figure	2140722 m35-40
b	7 x 7	1.14	In figure	2140721 m54-63
c	3 x 3	1.14	-0.084	2140820 m49
4 a	15 x 15	1.03	-0.211	2140721 m48
b	15 x 15	1.06	-1.000	2140723 m11
c	15 x 15	1.06	-0.500	2140722 m32
d	15 x 15	1.06	-0.020	2140818 m57
e	15 x 15	0.93	-0.286	2140726 m48
f	15 x 15	1.00	-1.000	2140820 m56
g	15 x 15	1.17	-0.159	2140822 m37
h	15 x 15	0.97	-0.537	2140815 m21
7 a	10 x 10	1.06	-0.200	2140818 m62
b	10 x 10	0.93	-0.250	2140726 m61
c	10 x 10	0.92	-0.713	2140820 m36
d	10 x 10	1.14	-1.000	2140820 m69
e	10 x 10	0.95	-1.000	2140815 m49
f	10 x 10	0.95	-1.000	2140815 m51
g	10 x 10	1.03	-0.292	2140815 m91
h	10 x 10	1.03	-0.323	2140815 m97

References

1. Walen, H.; Liu, D.-J.; Oh, J.; Lim, H.; Evans, J. W.; Aikens, C.; Kim, Y.; Thiel, P. A., "Cu₂S₃ Complex on Cu(111) as a Candidate for Mass Transport Enhancement". *Phys. Rev. B* **2015**, *91*, 045426.
2. Russell, S. M.; Kim, Y.; Liu, D.-J.; Evans, J. W.; Thiel, P. A., "Structure, Formation, and Equilibration of Ensembles of Ag-S Complexes on an Ag Surface". *J. Chem. Phys.* **2013**, *138*, 071101.
3. Walen, H.; Liu, D.-J.; Oh, J.; Yang, H. J.; Kim, Y.; Evans, J. W.; Thiel, P. A., "Identification of Au-S Complexes on Au(100)". *Phys. Chem. Chem. Phys.* **2016**, *18*, 4891-4901.
4. Shen, M.; Russell, S. M.; Liu, D.-J.; Thiel, P. A., "Destabilization of Ag Nanoislands on Ag(100) by Adsorbed Sulfur". *J. Chem. Phys.* **2011**, *135*, 154701.
5. Joyner, R. W.; McKee, C. S.; Roberts, M. W., "The Interaction of Hydrogen Sulphide with Cu(001)". *Surf. Sci.* **1971**, *27*, 279-285.
6. Zeng, H. C.; Sodhi, R. N. S.; Mitchell, K. A. R., "A LEED Crystallographic Analysis for the Cu(100)-(2 × 2)-S Surface Structure". *Surf. Sci.* **1986**, *177*, 329-337.
7. Domange, J. L.; Oudar, J., "Structure Et Conditions De Formation De La Couche D'adsorption Du Soufre Sur Le Cuivre". *Surf. Sci.* **1968**, *11*, 124-142.
8. Maurice, V., "Partial Disorder and LEED Diagrams II. The S/Ag(100) And S/Cu(100) System". *Surf. Sci.* **1983**, *129*, 312-326.
9. Boulliard, J. C.; Sotto, M. P., "Structural Study of Segregated Sulphur on the Stepped Faces Associated with Cu(100)". *Surf. Sci.* **1988**, *195*, 255-269.

10. Zeng, H. C.; Mitchell, K. A. R., "Further Observations with Low-Energy Electron Diffraction for the Cu(100)-(2×2)-S Surface Structure: Spot-Profile and Multiple-Scattering Analyses". *Can. J. Phys.* **1987**, *65*, 500-504.
11. Zeng, H. C.; McFarlane, R. A.; Mitchell, K. A. R., "Investigation with Low-Energy Electron Diffraction of the Adsorbate-Induced Metal Relaxations in the Cu(100)-(2 X 2)-S Surface Structure". *Phys. Rev. B* **1989**, *39*, 8000-8002.
12. Colaianni, M. L.; Chorkendorff, I., "Scanning-Tunneling-Microscopy Studies of the S-Induced Reconstruction of Cu(100)". *Phys. Rev. B* **1994**, *50*, 8798-8806.
13. Vlieg, E.; Robinson, I. K.; McGrath, R., "Structure Determination of Cu(100)- (2 X 2)-S Using X-Ray Diffraction". *Phys. Rev. B* **1990**, *41*, 7896-7898.
14. Barton, J. J.; Bahr, C. C.; Hussain, Z.; Robey, S. W.; Tobin, J. G.; Klebanoff, L. E.; Shirley, D. A., "Direct Surface Structure Determination with Photoelectron Diffraction". *Phys. Rev. Lett.* **1983**, *51*, 272-275.
15. Bahr, C. C.; Barton, J. J.; Hussain, Z.; Robey, S. W.; Tobin, J. G.; Shirley, D. A., "Geometry of (2 X 2)S/Cu(001) Determined with Use of Angle-Resolved-Photoemission Extended Fine Structure". *Phys. Rev. B* **1987**, *35*, 3773-3782.
16. Shirley, D. A.; Terminello, L. J.; Bahr, C. C., "Reply to ``Investigation with Low-Energy Electron Diffraction of the Adsorbate-Induced Metal Relaxations in the Cu(100)-(2 X 2)-S Surface Structure''". *Phys. Rev. B* **1989**, *39*, 8003-8004.
17. Schach von Wittenau, A. E.; Hussain, Z.; Wang, L. Q.; Huang, Z. Q.; Ji, Z. G.; Shirley, D. A., "Reevaluation of the (2 X 2)S/Cu(001) Structure Using Angle-Resolved Photoemission Extended Fine-Structure Spectroscopy". *Phys. Rev. B* **1992**, *45*, 13614-13623.

18. Persson, M.; Andersson, S.; Karlsson, P.-A., "Dipole Active Displacements of Ordered Adsorbate Layers on Metal Surfaces". *Chem. Phys. Lett.* **1984**, *111*, 597-601.
19. Leung, K. T.; Zhang, X. S.; Shirley, D. A., "Adsorption and Surface Reactions of Hydrogen Sulfide and Sulfur Dioxide on Copper(100) Studied by Electron Energy Loss Spectroscopy". *J. Phys. Chem.* **1989**, *93*, 6164-6170.
20. Sette, F.; Hashizume, T.; Comin, F.; MacDowell, A. A.; Citrin, P. H., "Coverage and Chemical Dependence of Adsorbate-Induced Bond Weakening in Metal Substrate Surfaces". *Phys. Rev. Lett.* **1988**, *61*, 1384-1387.
21. Patel, J. R.; Berreman, D. W.; Sette, F.; Citrin, P. H.; Rowe, J. E.; Cowan, P. L.; Jach, T.; Karlin, B., "Substrate Surface Relaxation for Cl and S on Cu(001)". *Phys. Rev. B* **1989**, *40*, 1330-1333.
22. McGrath, R.; MacDowell, A. A.; Hashizume, T.; Sette, F.; Citrin, P. H., "Structure of a Precursor State in Dissociative Chemisorption". *Phys. Rev. Lett.* **1990**, *64*, 575-578.
23. Ma, Y.; Rudolf, P.; Chaban, E. E.; Chen, C. T.; Meigs, G.; Sette, F., "Multiple Sulfur Sites in the Cu(100) P(2 X 2)S Surface Structure". *Phys. Rev. B* **1990**, *41*, 5424-5427.
24. Jia, J.; Bendounan, A.; Chaouchi, K.; Esaulov, V. A., "Sulfur Interaction with Cu(100) and Cu(111) Surfaces: A Photoemission Study". *J. Phys. Chem. C* **2014**, *118*, 24583-24590.
25. Wagner, C., "Investigation on Silver Sulfide". *J. Chem. Phys.* **1953**, *21*, 1819-1827.
26. Detry, D.; Drowart, J.; Goldfinger, P.; Keller, H.; Rickert, H., "Zur Thermodynamik Von Schwefeldampf". *Z. Phys. Chem.* **1967**, *55*, 314-319.

27. Heegemann, W.; Meister, K. H.; Bechtold, E.; Hayek, K., "The Adsorption of Sulfur on the (100) and (111) Faces of Platinum; a LEED and AES Study". *Surf. Sci.* **1975**, *49*, 161-180.
28. Straumanis, M. E.; Yu, L. S., "Lattice Parameters, Densities, Expansion Coefficients and Perfection of Structure of Cu and of Cu-in Alpha Phase". *Acta Cryst.* **1969**, *25A*, 676-682.
29. Walen, H.; Liu, D.-J.; Oh, J.; Yang, H. J.; Kim, Y.; Thiel, P. A., "Long-Range Displacive Reconstruction of Au(110) Triggered by Low Coverage of Sulfur". *J. Phys. Chem. C* **2015**, *119*, 21000-21010.
30. Walen, H.; Liu, D.-J.; Oh, J.; Lim, H.; Evans, J. W.; Kim, Y.; Thiel, P. A., "Self-Organization of S Adatoms on Au(111): $\sqrt{3}R30^\circ$ Rows at Low Coverage". *J. Chem. Phys.* **2015**, *143*, 014704.
31. Lang, N. D., "Theory of Single-Atom Imaging in the Scanning Tunneling Microscope". *Phys. Rev. Lett.* **1986**, *56*, 1164-1167.
32. Lang, N. D., "Apparent Size of an Atom in the Scanning Tunneling Microscope as a Function of Bias". *Phys. Rev. Lett.* **1987**, *58*, 45-48.
33. Schintke, S.; Messerli, S.; Morgenstern, K.; Nieminen, J.; Schneider, W.-D., "Far-Ranged Transient Motion of "Hot" Oxygen Atoms Upon Dissociation". *J. Chem. Phys.* **2001**, *114*, 4206-4209.
34. Chiodo, L.; Monachesi, P., "Role of Coverage on the Electronic Properties of Sulfur Chemisorbed on Cu(100): Ab Initio Calculations". *Phys. Rev. B* **2007**, *75*, 075404.

35. Shen, M.; Liu, D.-J.; Jenks, C. J.; Thiel, P. A., "Novel Self-Organized Structure of a Ag-S Complex on the Ag(111) Surface Below Room Temperature". *J. Phys. Chem. C* **2008**, *112*, 4281-4290.
36. Wahlström, E.; Ekvall, I.; Kihlgren, T.; Olin, H.; Lindgren, S. A.; Wallden, L., "Low-Temperature Structure of S/Cu(111)". *Phys. Rev. B* **2001**, *64*, 155406.
37. Liu, D.-J.; Walen, H.; Oh, J.; Lim, H.; Evans, J. W.; Kim, Y.; Thiel, P. A., "Search for the Structure of a Sulfur-Induced Reconstruction on Cu(111)". *J. Phys. Chem. C* **2014**, *118*, 29218-29223.
38. Russell, S. M.; Shen, M.; Liu, D.-J.; Thiel, P. A., "Adsorption of Sulfur on Ag(100)". *Surf. Sci.* **2011**, *605*, 520-527.
39. Sautet, P.; Dunphy, J. C.; Ogletree, D. F.; Joachim, C.; Salmeron, M., "Imaging a $P(2 \times 2)$ Layer of Sulfur on Re(0001) with the Scanning Tunneling Microscope: An Experimental and Theoretical Study of the Effect of Adsorption Site and Tip Structure". *Surf. Sci.* **1994**, *315*, 127-142.
40. Sautet, P.; Dunphy, J.; Salmeron, M., "The Origin of STM Contrast Differences for Inequivalent S Atoms on a Mo(100) Surface". *Surf. Sci.* **1996**, *364*, 335-344.
41. Sautet, P.; Dunphy, J.; Ogletree, D. F.; Salmeron, M., "The Role of Electronic Interferences in Determining the Appearance of Stm Images: Application to the $S(2 \times 2)/\text{Re}(0001)$ System". *Surf. Sci.* **1993**, *295*, 347-352.
42. Maurice, V.; Marcus, P., "Stm Imaging in Air with Atomic Resolution of Adsorbates on Metal Surfaces: $\text{Pt}(100)\text{-C}(2 \times 2)\text{S}$ ". *Surf. Sci.* **1992**, *262*, L59-L64.
43. Ruan, L.; Stensgaard, I.; Lægsgaard, E.; Besenbacher, F., "A Scanning Tunneling Microscopy Investigation of the $\text{Ni}(110)\text{-P}(4 \times 1)\text{S}$ Phase". *Surf. Sci.* **1993**, *296*, 275-282.

44. Jiang, Y.; Liang, X.; Ren, S.; Chen, C.-L.; Fan, L.-J.; Yang, Y.-W.; Tang, J.-M.; Luh, D.-A., "The Growth of Sulfur Adlayers on Au(100)". *J. Chem. Phys.* **2015**, *142*, 064708.
45. Carley, A. F.; Davies, P. R.; Jones, R. V.; Harikumar, K. R.; Kulkarni, G. U.; Roberts, M. W., "The Structure of Sulfur Adlayers at Cu(110) Surfaces: An STM and XPS Study". *Surf. Sci.* **2000**, *447*, 39-50.
46. Liu, D.-J.; Evans, J. W., "Lattice-Gas Modeling of the Formation and Ordering of Oxygen Adlayers on Pd(100)". *Surf. Sci.* **2004**, *563*, 13-26.
47. Zhang, Y.; Blum, V.; Reuter, K., "Accuracy of First-Principles Lateral Interactions: Oxygen at Pd(100)". *Phys. Rev B* **2007**, *75*, 235406.
48. Caflisch, R. G.; Berker, A. N., "Oxygen Chemisorbed on Ni(100): A Renormalization-Group Study of the Global Phase Diagram". *Phys. Rev B* **1984**, *29*, 1279.
49. Bak, P.; Kleban, P.; Unertl, W.; Ochab, J.; Akinci, G.; Bartelt, N. C.; Einstein, T. L., "Phase Diagram of Selenium Adsorbed on the Ni(100) Surface: A Physical Realization of the Ashkin-Teller Model". *Phys. Rev. Lett.* **1985**, *54*, 1539-1542.
50. Liu, D.-J., "Co Oxidation on Rh(100): Multisite Atomistic Lattice-Gas Modeling". *J. Phys. Chem. C* **2007**, *111*, 14698-14706.
51. Walen, H.; Liu, D.-J.; Oh, J.; Lim, H.; Evans, J. W.; Kim, Y.; Thiel, P. A., "Reconstruction of Steps on the Cu(111) Surface Induced by Sulfur". *J. Chem. Phys.* **2015**, *142*, 194711.
52. Wahlström, E.; Ekvall, I.; Olin, H.; Lindgren, S. A.; Wallden, L., "Observation of Ordered Structures for S/Cu(111) at Low Temperature and Coverage". *Phys. Rev. B* **1999**, *60*, 10699.

53. Foss, M.; Feidenhans'l, R.; Nielsen, M.; Findeisen, E.; Buslaps, T.; Johnson, R. L.; Besenbacher, F., "Sulfur Induced Cu₄ Tetramers on Cu (111)". *Surf. Sci.* **1997**, 388, 5-14.
54. Foss, M.; Feidenhans'l, R.; Nielsen, M.; Findeisen, E.; Buslaps, T.; Johnson, R. I.; Besenbacher, F.; Stensgaard, I., "Sulfur Chemisorption on Ni(111): The Clock Structure of the (5 $\sqrt{3}$ ×2)S Phase". *Phys. Rev. B* **1994**, 50, 8950-8953.
55. Liu, D.-J., *Unpublished Data* **2016**.

CHAPTER V

**SELF-ORGANIZATION OF S ADATOMS ON AU(111): $\sqrt{3}R30^\circ$ ROWS
AT LOW COVERAGE**

Holly Walen,^a Da-Jiang Liu,^b Junepyo Oh,^c Hyunseob Lim,^c J. W. Evans,^{b, d} Yousoo Kim,^c
and P. A. Thiel^{a, b, e}

A paper published in Journal of Chemical Physics[†]

Abstract

Using scanning tunneling microscopy (STM), we observe an adlayer structure that is dominated by short rows of S atoms, on unreconstructed regions of a Au(111) surface. This structure forms upon adsorption of low S coverage (less than 0.1 monolayer) on a fully reconstructed clean surface at 300 K, then cooling to 5 K for observation. The rows adopt one of three orientations that are rotated by 30° from the close-packed directions of the Au(111) substrate, and adjacent S atoms in the rows are separated by $\sqrt{3}$ times the surface lattice constant, a . Monte Carlo simulations are performed on lattice-gas models, derived using a limited cluster expansion based on DFT energetics. Models which include long-range pairwise interactions (extending to $5a$), plus selected trio interactions, successfully reproduce the linear rows of S atoms at reasonable temperatures.

Departments of ^aChemistry, ^dPhysics & Astronomy, and ^eMaterials Science & Engineering, Iowa State University, Ames, Iowa 50011 USA

^bAmes Laboratory of the USDOE, Ames, Iowa 50011 USA

^cRIKEN Surface and Interface Science Laboratory, Wako, Saitama 351-0198, Japan

[†]Walén *et al.*, *J. Chem. Phys.* **143** 014704 (2015)

1. Introduction

Interest in the interaction of sulfur with Au surfaces is motivated by the extraordinary versatility and utility of molecular systems that can be anchored to Au through a S headgroup, such as self-assembled thiol monolayers. Nonetheless, a 2010 review¹ describes the chemistry and structure of the Au-S interface in such molecular systems as “elusive,” and a major challenge. There are also cases where the interaction of sulfur atoms alone with Au surfaces is crucial. For instance, S-coated Au nanoparticles show promise for detecting Hg in aqueous solution;² adsorbed S serves as a capping agent and anti-coagulant for Au nanoparticles;³ and S accelerates a hydrogenation reaction on supported Au catalysts.⁴

Most past experimental studies of S adsorbed on the prototypical Au(111) surface have focused on coverages of about 0.1 to 0.7 monolayers (ML) at room temperature.⁵⁻⁸ Under those conditions it is generally agreed that sulfur lifts the herringbone reconstruction of the clean Au(111) surface. Long-range ordered phases of sulfur include $(\sqrt{3} \times \sqrt{3})R30^\circ$ and $p(5 \times 5)$. Toward the higher end of this coverage range, there is an additional complex structure that is often associated with molecular or polymeric adsorbed sulfur.⁹⁻¹³ In this paper we explore a different coverage and temperature regime, which leads to the discovery of a new structure consisting mainly of one-dimensional (1D) rows of dot-like features. Using density functional theory (DFT), we rule out Au-S complexes and identify the rows as adsorbed sulfur atoms (S_{ad}) in a linear $\sqrt{3}R30^\circ$ configuration. Furthermore, we apply direct DFT analysis and also ab-initio Monte Carlo (MC) simulations to test whether this assignment is reasonable. For the latter, we use DFT to develop Lattice-Gas (LG) models with optimized pairwise and trio interactions. MC simulations show that LG models with a

sufficiently extensive set of interactions can produce 1D $\sqrt{3}R30^\circ$ rows under conditions comparable to those of the experiment.

There are two previous publications of special relevance to the current study. In the first, Abufager *et al.*¹⁴ used DFT to analyze the $(\sqrt{3} \times \sqrt{3})R30^\circ$ and $p(5 \times 5)$ ordered phases of S adsorbed on Au(111). They found that long-range elastic (substrate-mediated) interactions are very important, and discussed the ordered phases in terms of a LG Hamiltonian, considering only pairwise interactions. Our approach is similar to theirs, but we focus on a lower coverage range and a quite different structure, and we carry out MC simulations to test the relevance of the LG models. We find that three-body interactions are important for stabilizing the 1D rows, in addition to long-range pairwise repulsions. In the second study, Kurokawa *et al.*¹⁵ found features that they identified as Au_3S_3 complexes, using STM at 77 K. We do not find such features, and will present possible explanations.

The paper is organized as follows. In Sec. II, experimental and computational details are described. This is followed by presentation of experimental results in Sec. III, theoretical and computational results in Sec. IV, and discussion in Sec. V. The Appendix provides additional STM images and experimental information, as well as a schematic of the interactions, and details about the configurations used to develop the LG model Hamiltonians.

2. Experimental and Computational Details

2.1 Experimental Description

These experiments were carried out with the same equipment and the same techniques, as were used our previous studies of S on Ag(111)¹⁶ and S on Cu(111).¹⁷ In short,

the sample was imaged with STM at 5 K in ultrahigh vacuum (pressure $< 2.5 \times 10^{-11}$ Torr). An electrochemical cell served as the S source in situ.¹⁸ During S deposition the sample was held at 300 K, and then it was cooled to 5 K for measurement. Cooling and thermal stabilization at 5 K took place in 50 minutes or less. After initial STM measurements, the sample was warmed back to room temperature and re-cooled to 5 K, with no effect on the observations at 5 K. During imaging, there was no evidence of tip perturbation or surface diffusion; surface structures were entirely static. With adsorbed sulfur, the tunneling current (I) used for imaging was 0.52 to 1.42 nA, and sample bias voltage (V_S) was -2.00 to +2.00 V. Explicit conditions for each image in this text are given in the SI.

The Au(111) sample was cleaned via several cycles of Ar^+ sputtering (10-12 μA , 1.5 kV, 10 min) and annealing (850 K, 15 min).

The accuracy of STM for measuring spatial dimensions was checked by measuring a , the atomic separation of surface Au atoms along close-packed directions [Fig. 1(a)], and by measuring monoatomic step heights on the Au(111) surface (not shown). The former value was 0.285 ± 0.009 nm, and the latter was 0.21 ± 0.02 nm. Within stated uncertainties, these equal the bulk parameters of 0.288 nm and 0.236 nm, respectively.

Sulfur coverage (θ_S) was determined by measuring the number density of bright dots in STM images, associating each bright dot with a single S adatom (as justified in Sec. IVB), and dividing by the areal density of Au atoms in a bulk (111) plane. Because the S occupies only portions of the Au(111) surface, it is appropriate to report both a global coverage (normalized to total area) and a local coverage (normalized only to the unreconstructed area where S exists). The analysis in this paper is based upon two experiments in which the global (local) coverage was 0.030 ML (0.070 ML) and 0.045 (0.079 ML), respectively.

2.2 Computational Description

Energetics were calculated via DFT using the VASP code with the projector-augmented wave (PAW) method¹⁹ and the PBE functional.²⁰ Details have been given elsewhere.²¹⁻²² k-points convergence was problematic, probably due to the existence of surface states on Au(111). This was partly addressed by averaging results for slab thicknesses of 4 to 7 Au(111) layers.²³ However, even with this averaging, convergence was slow. For example, for the (4 x 4) supercell, the adsorption energy of S was -1.200 eV and -1.231 eV, for (6 x 6) and (9 x 9) -point grids, respectively. Dense k-point grids, up to (36 x 36 x 1) for a (1 x 1) supercell, were therefore used to derive the LG Hamiltonian described in Sec. IVC. STM images were generated from DFT-optimized configurations using the method of Tersoff and Hamann,²⁴ as the isosurface of partial charge density in an energy window that brackets the Fermi energy by ± 0.1 eV.

DFT energies of a substantial number of periodic adlayer configurations were used to systematically determine pairwise and selected trio interactions prescribing the Hamiltonian for LG models of the S adlayer. See Sec. IVC for more details. We performed MC simulations within a grand canonical ensemble to determine the equilibrium configurations of the LG models. At each MC step, a site was randomly selected and flipped from vacant to occupied or vice-versa. The flip was accepted or rejected according to Metropolis dynamics. θ_S was controlled by an “excess” chemical potential, $\delta\mu = \mu - E_{ad}$, where E_{ad} is the adsorption energy of an isolated S atom. To provide an alternative perspective, one can regard equilibrium as being induced by an artificial adsorption-desorption dynamics with desorption rate for S adatoms of $\exp(E_{rep}/k_B T)$, and adsorption rate per site of $\exp(+\delta\mu/k_B T)$.

Here $E_{\text{rep}} > 0$ is the overall repulsive adlayer interaction felt by adsorbed S and k_B is Boltzmann's constant.

3. Experimental Results

The clean surface exhibits the well-known Au(111) herringbone reconstruction, visible in Fig. 1(b). The bright stripes are soliton walls, the narrow alternating dark strips are hcp-like regions, and the wider alternating dark strips are fcc-like regions.²⁵⁻²⁷

Figure 2 shows how the surface responds to adsorption of 0.030-0.045 ML S. At high magnification, many dots exist on the surface [Fig. 2(a)]. Each dot is surrounded by a dark ring. We assign these as S adatoms (S_{ad}), based on the DFT analysis in Sec. IVB. These dots often form linear rows that are rotated by 30° with respect to the close-packed directions. These directions are derived from, and depicted in, Fig. 1(a). The closest separation between S_{ad} , i.e. the separation between dots within a row, is $\sqrt{3}a$, and so we refer to them as $\sqrt{3}R30^\circ$ rows. There is no evidence for larger features that could be Au-S complexes like the Cu-S or Ag-S species we have observed on Cu(111) or Ag(111), sometimes under identical conditions.^{16-17, 28}

The dots have full-width at half-maximum (FWHM) of 0.34 ± 0.04 nm (from $N = 278$ measurements) and height of 0.017 ± 0.003 nm at $V_S = -0.50$ V to $+0.13$ V ($N = 293$). (The majority of our measurements were restricted to this range.) Both parameters are measured with reference to the highest point in the dot, and the lowest point in the surrounding dark ring.

Figure 2(b-e) gives a broader perspective. These panels show that there are basically two types of surface regions. In the first, the soliton walls of the reconstruction remain,

though often distorted. Small groups of S_{ad} exist in the fcc-like strips. The hcp-like strips are nearly clean, but narrower than in the absence of S. This description applies to the entire region of panel (b), and parts of (c)-(e). The second type of region is large and uniformly covered by S; there is no trace of the reconstruction. Examples are the middle right portion of panel (c), or the upper right third of panel (d). As mentioned in Sec. II, the local S coverage on these larger unreconstructed regions is 0.070-0.079 ML.

The data support the following picture. S adsorbs preferentially at the fcc-like regions, and exerts pressure on the soliton walls, distorting them. With increasing S coverage, some of the soliton walls collapse and the reconstruction is lifted over extended areas. The excess Au atoms generated by lifting the reconstruction are ejected and (at this low S coverage) they diffuse to existing step edges on the Au(111) surface.

The step edges are also affected by S adsorption. Figure 3 shows some regions in which there is no residual reconstruction. (Solitons interact with step edges,¹² so those are avoided here.) Sulfur adsorbs on all steps. In Fig. 3(a), the steps are not aligned with a close-packed direction. These steps meander locally and are decorated by a single row of S atoms. Steps in Fig. 3(b-d) are very near to close-packed alignment. These steps are smoother on the lower edge, but contain regular ‘bulges’ on the upper edge. One such bulge is encircled in each panel. This paper does not focus on the step edge decoration, but it is shown here for completeness, and because the conditions at the step edges help to define the conditions under which the terrace structures are observed.¹⁶

Finally, the detailed arrangement of S_{ad} in the extended unreconstructed regions is shown in Fig. 4. Further images, similar to these, are provided in the Appendix. As noted previously, the main features are one-dimensional $\sqrt{3}R30^\circ$ rows of S atoms. The atoms are all

in equivalent adsorption sites, as shown by the triangular grid overlay in Fig. 4(a). These are fcc sites, based on the low-coverage DFT results of Abufager *et al.*¹⁴ In addition to the rows, triangles, rhombi, and occasionally larger groupings of S_{ad} exist, all of which can be considered as small portions of a two-dimensional $(\sqrt{3} \times \sqrt{3})R30^\circ$ lattice. On average, about 10% of all S atoms exist in the form of equilateral triangles having these $\sqrt{3}R30^\circ$ -type configurations, but separate from any $\sqrt{3}R30^\circ$ row. Rarely, triangles or pairs of S atoms can be found in which atoms are separated by $2a$ and aligned with close-packed directions, i.e. forming portions of a (2×2) lattice. For clarity, some of these minor features are outlined in Fig. 4(d). The structures in Fig. 4 are entirely static and are not perturbed by imaging.

We emphasize that the data shown in Fig. 2-Fig. 4 are obtained by cooling from 300 K to 5 K. Thus, they represent a configuration of S_{ad} that was in thermal equilibrium at some temperature above 5 K, frozen in during the quench.

4. Theoretical and Computational Results

4.1 Overview: Purpose and approach

This section presents and integrates a variety of theoretical and computational results. In Sec. IVB, we perform direct DFT analysis to assess the energetics and relative stability of a large number of periodic adlayer structures. The figure of merit is the (zero temperature) chemical potential, μ_S , of S_{ad} in various configurations. This quantity corresponds to the average energy per S adatom in the adlayer. Thus, for isolated S_{ad} , it simply equals the adsorption energy, E_{ad} (corresponding to behavior in the low coverage limit). In addition, we will analyze the stability of various Au-S complexes relative to the above adlayer

configurations. For this purpose a modified definition of μ_S is required to make the appropriate comparison, and it is given in Sec. IVB below.

Using a different but overlapping set of energetics, in Sec. IVC we construct appropriate LG Hamiltonians for S-adlayer systems incorporating many pair and selected trio interactions. Finally, in Sec. IVD, we perform MC simulations to assess equilibrium adlayer configurations corresponding to these LG Hamiltonians. Simulations are performed in a grand canonical rather than canonical ensemble, where the relevant “excess” chemical potential controlling θ_S was described in Sec. IIB.

4.2 DFT Results

Baseline energetics of S_{ad} on Au(111). We have calculated μ_S of S_{ad} at the fcc site using 27 adlayer configurations, consisting of two types of (related) periodic arrays. In both, the supercell lattice vectors (the \mathbf{a}_i 's) have equal magnitude and include an angle of 60° . The first type has one S per supercell, thus forming a simple hexagonal lattice of S_{ad} . For supercells with areas that are multiples of three times the (1×1) area, we include an additional S atom at $(1/3\mathbf{a}_1, 1/3\mathbf{a}_2)$ in the supercell, thus forming a honeycomb lattice of S_{ad} . The values of μ_S for all 27 configurations are listed in Table I, and pictures of some of the configurations are given in Appendix 2.

One finds that μ_S is generally a decreasing function of $1/\theta_S$, reflecting repulsive interactions between S_{ad} , although there are deviations from this trend. From the listed energetics, 8 configurations—denoted by boldface numbers in Table I—form a lower concave envelope of μ_S , shown by the solid line in Fig. 5. We call this envelope the baseline energetics. (In Fig. 5, $1/\theta_S$ is chosen as the abscissa rather than θ_S because the

thermodynamic quantity that is conjugate to μ_S is the atomic volume (or area in 2D) of S_{ad} .¹⁴⁾ Any configuration with μ_S above this baseline will be thermodynamically unstable toward phase separation into denser and sparser regions of baseline configurations. The stability of other structures can be measured against this baseline. (Graphic representation of μ_S vs. $1/\theta_S$ for all 27 lattices is available in Fig. A4.)

TABLE I. μ_S for S_{ad} on Au(111) fcc sites in the supercells used to evaluate baseline energetics, as described in the text. Numbers in parentheses denote uncertainties in meV and are derived from variations due to slab thicknesses.²³

Label	Supercell	μ_S , 1 S_{ad} per cell (eV)	μ_S , 2 S_{ad} per cell (eV)	θ_S
1	(1×1)	0.323		1
2	$(\sqrt{3} \times \sqrt{3})R30^\circ$	-0.972(3)	-0.019(1)	0.33, 0.66
3	(2×2)	-1.055(7)		0.25
4	$(\sqrt{7} \times \sqrt{7})R19.1^\circ$	-1.105(3)		0.14
5	(3×3)	-1.077(3)	-1.032(3)	0.11, 0.22
6	$(2\sqrt{3} \times 2\sqrt{3})R30^\circ$	-1.187(3)	-1.108(3)	0.083, 0.17
7	$(\sqrt{13} \times \sqrt{13})R13.9^\circ$	-1.199(6)		0.077
8	(4×4)	-1.231(4)		0.063
9	$(\sqrt{19} \times \sqrt{19})R23.4^\circ$	-1.247(5)		0.053
10	$(\sqrt{21} \times \sqrt{21})R10.9^\circ$	-1.244(2)	-1.178(3)	0.048, 0.096
11	(5×5)	-1.242(8)		0.040
12	$(3\sqrt{3} \times 3\sqrt{3})R30^\circ$	-1.275(3)	-1.165(4)	0.037

TABLE I continued.

13	$(2\sqrt{7} \times 2\sqrt{7})R19.1^\circ$	-1.276(1)		0.036
14	$(\sqrt{31} \times \sqrt{31})R8.9^\circ$	-1.283(3)		0.032
15	(6×6)	-1.303(5)	-1.257(5)	0.028, 0.056
16	$(\sqrt{37} \times \sqrt{37})R8.2^\circ$	-1.292(9)		0.027
17	$(\sqrt{39} \times \sqrt{39})R16.1^\circ$	-1.296(9)	-1.248(7)	0.026
18	$(\sqrt{43} \times \sqrt{43})R7.6^\circ$	-1.302(4)		0.023
19	$(4\sqrt{3} \times 4\sqrt{3})R30^\circ$	-1.315(4)	-1.263(3)	0.021

Au-S complexes vs. S_{ad} . Our DFT investigations next focus on the possibility that S-Au complexes exist on the Au(111) surface. This investigation is mainly motivated by our findings that on (111) surfaces of the other two coinage metals, Cu and Ag, metal-S complexes exist under similar conditions of coverage and temperature, as corroborated by DFT.¹⁶⁻¹⁷ Some Au-S row structures that could constitute elements of the experimental $\sqrt{3}R30^\circ$ motif are shown in Fig. 6(a,c,d), together with the simulated STM images. To assess the stability of these Au-S row structures relative to configurations involving only S_{ad} , we define the chemical potential of S in possible adsorbed Au-S complexes according to:

$$\mu_S(\text{Au}_m\text{S}_n \text{ complex}) = [E(\text{Au}_m\text{S}_n + \text{slab}) - E(\text{slab}) - m \mu_{Au}]/n - E(S_{2,g})/2 \quad (1)$$

Here, the chemical potential of Au, μ_{Au} , is the average energy of an Au atom in the bulk. This definition reduces to that given in Sec. IVA for S_{ad} , upon setting $m = 0$.

For each Au-S row structure considered, the corresponding configuration of S_{ad} (Fig. 6(b, e)) is significantly more stable. Also, the STM images for the Au-S models in Fig. 6(a, c, d) do not agree with experiment (Fig. 4). Furthermore, the diameter predicted for S_{ad} is 0.38 nm, in agreement with the experimental value of 0.34 ± 0.04 nm. From all of these arguments, we conclude that the bright dots in the STM images are S_{ad} , rather than Au-S chains or complexes.

As an aside, the DFT prediction for the height of the S_{ad} dot is 0.13 nm, a factor of 8 larger than the experimental height of 0.017 ± 0.003 nm. In the literature,²⁹⁻³² and also in our own past work,²⁸ it is consistently reported that heights of S_{ad} , S-induced complexes, and even S-induced reconstructions are smaller than one would expect from reasonable atomic dimensions. At present this effect is not understood, but a metallic STM tip could easily become S-decorated and this might influence measured topographic dimensions, especially in the vertical direction (heights) as opposed to the lateral (widths).

$\sqrt{3}R30^\circ$ rows. Values of μ_S for 1D $\sqrt{3}R30^\circ$ rows of S_{ad} are shown by the diamonds in Fig. 5. The row structures at $\theta_S \leq 0.125$ or $1/\theta_S \geq 8$ (i.e. when the inter-row separation is $\geq 4a$) are much more stable than the baseline configurations, to the tune of 40 meV per S atom. The results in the following section show a significant pairwise S-S repulsion that peaks at a separation of $3a$, then falls abruptly. This explains why rows are stable only for separations $\geq 4a$. No other S_{ad} configuration is competitive with the $\sqrt{3}R30^\circ$ rows.

Diffusion barrier of S_{ad} . Using a 3 layer slab and (12 x 12 x 1) k-point grid, the S_{ad} diffusion barrier has been calculated with the nudged elastic band³³ method. The transition

state is the two-fold bridge site. The diffusion barrier depends on the supercell, being 0.45 eV for a (2 x 2), 0.39 eV for a ($\sqrt{7} \times \sqrt{7}$)R19.1°, 0.44 eV for a (3 x 3), and 0.47 eV for a ($2\sqrt{3} \times 2\sqrt{3}$)R30°.

4.3 Lattice-gas Models

The long-range and potentially many-body nature of interactions between S_{ad} indicate that the resulting adlayer configurations involve competition between myriads of interactions. This can be studied best in a lattice-gas model framework, as MC simulation of such models can indicate typical adlayer configurations at various temperatures. The first step is to determine the most significant pairwise and many-body interactions in the LG Hamiltonian. To do this, we systematically choose a large set of adlayer configurations (36) from which these interactions will be determined. This set of 36 overlaps with, but does not contain completely, the set of 27 configurations used for the baseline energetics. The baseline set of 27 includes a number of configurations with supercells that are much larger than those in the set of 36. Figure A6 and Table AVI in Appendix 2 show all 36 configurations and associated values of μ_S .

Our selection process is as follows. First, we choose all adlayer configurations in Table I with supercell sizes ranging from ($\sqrt{3} \times \sqrt{3}$) to ($3\sqrt{3} \times 3\sqrt{3}$), inclusive. Second, we include additional configurations with all pairs of S with separation $\sqrt{3}a$, and also some incorporating various S trimer motifs but with the same pairwise separation. The trimer motifs can be described as linear, equilateral triangular, and bent (cf. Table II). Note that we avoid most of the configurations that result in occupation of nearest-neighbor (NN) sites, since we are mostly concerned with low S coverage (less than 0.1 ML). Also, strong

interaction between NN S adatoms induces substantial displacement in their positions away from ideal adsorption sites which can limit the validity of the LG description.³⁴ However, we do include one configuration with the NN S dimer in a ($\sqrt{7} \times \sqrt{7}$) supercell in order to estimate the NN interaction. Due to the prominence of the “rosette” structure in interpreting adlayer structure observed at medium coverage,¹⁴ we also include it in the set of DFT configurations.

Table II lists interactions for 5 sample models that one can construct. Each model can be defined by a cutoff distance, d , and by additional listing of any trio interactions, T . The cutoff circumscribes a range of pairwise separations, d_p , each with an associated interaction energy, w_n , between equivalent sites. The integers $n = 1, 2, \dots$ denote 1st-, 2nd-, ... NN interactions. The interactions are illustrated in Fig. A3 of Appendix 2.

Models are named after the number of energy parameters. For instance, Model 5 has 4 interaction energies, plus the adsorption energy. The parameters are determined by least squares fitting of the LG model energies to the directly calculated DFT configuration energies using the Moore-Penrose pseudoinverse method. Models 5 and 8 include only pairwise interactions. Model 12T includes 11 pair interactions, and one linear trio interaction. Model 12T3 contains two additional trio interactions (equilateral triangular, and bent).

Table II shows that Model 5, which already includes a significant number (4) of pair interactions, is inadequate, since it produces significantly different values than the models with longer-range pairs. This provides a clear indication of the important influence of long-range interactions. For Models 8 through 12T3, pair interaction values converge, which provides confidence in the robustness and significance of these values.

Due to the potential importance of many-body interactions,³⁴ it is also natural to consider adding trio interactions to models with shorter cutoff distances to derive a model 8T (and even a model 5T). However, these models fail cross-validation tests of the following type. For model 5T, if we exclude energetics for supercells larger than (3×3) in determining its parameters, there is no unique solution to trio interactions, because of the degeneracy of the linear chain structure and triangular structure in the (3×3) supercell. For model 8T, the value of trio interactions is very sensitive to the choice of energetics. Choosing different subsets of the 36 energetics leads to linear trio interactions of different signs. Only by going to larger cutoff distance for pair-wise interactions, can reliable trio interaction parameters be obtained. This reflects the above-mentioned observation that linear chains are stable only with wider separations (see Fig. 5).

Turning to a general discussion of our preferred models, there are certain trends in the pairwise interaction energies. The NN repulsion, w_1 , is larger—by at least a factor of 5—than any other pairwise interaction. For all the models except Model 5 (the smallest and least accurate), w increases steadily from w_2 to w_5 , then drops rather sharply. In other words, pairwise repulsions strengthen as d_p increases from $\sqrt{3}a$ to $3a$, then weaken at larger d_p . This trend was also reported by Abufager *et al.*¹⁴ Finally, the linear trio interaction is attractive, and this will stabilize $\sqrt{3}R30^\circ$ rows.

TABLE II. LG model parameters, in eV, obtained from least-square fitting with cutoff distance $d = 3a$ (Model 5), $d = 4a$ (Model 8), and $d = 5a$ (Model 11). Model 12T has a cutoff distance at the 12th NN ($d = 3\sqrt{3}a$), and one linear trio interaction, T_{linear} . Model 12T3 is the same, except it includes two additional trio interactions, $T_{\text{equilateral}}$ and T_{bent} . The bottom row shows the mean absolute error of the prediction of each LG model relative to DFT. E_{ad} is the adsorption energy of an isolated adsorbed S atom. d_p is the pair separation and a is the surface lattice constant (the NN separation). In the schematics of the trio interactions, each black circle is a S atom and each gray segment is a $\sqrt{3}R30^\circ$ separation. The complete set of interactions is illustrated in Fig. A3.




	d_p/a	Model 5	Model 8	Model 11	Model 12T	Model 12T3
E_{ad}		-1.220	-1.235	-1.242	-1.249	-1.252
w_1	1	0.409	0.270	0.279	0.269	0.269
w_2	$\sqrt{3}$	0.081	0.029	0.023	0.031	0.028
w_3	2	0.056	0.045	0.037	0.032	0.033
w_4	$\sqrt{7}$	0.027	0.047	0.043	0.043	0.042
w_5	3		0.048	0.051	0.051	0.058
w_6	$2\sqrt{3}$		0.017	0.019	0.024	0.024
w_7	$\sqrt{13}$		0.013	0.018	0.018	0.017
w_8	4			0.007	0.008	0.009
w_9	$\sqrt{19}$			0.003	0.004	0.004
w_{10}	$\sqrt{21}$			0.002	0.004	0.005
w_{11}	5				0.003	0.006
T_{linear} 	$\sqrt{3}$				-0.020	-0.008
$T_{\text{equilateral}}$ 	$\sqrt{3}$					0.034

TABLE II continued.

T_{bent}	$\sqrt{3}, \sqrt{3},$					
	<i>and 3</i>					-0.022
Error	0.027	0.011	0.010	0.009	0.007	

4.4 Monte Carlo Simulations based on the Lattice-Gas Hamiltonians

Figure 7 shows snapshots of MC simulations of equilibrated adlayer configurations using parameter sets in Table II. The excess chemical potentials ($\delta\mu$'s) are chosen so that the resulting θ_s is between 0.07 and 0.08 ML, to match experiment. For each model, configurations at $T = 150$ K, 100 K, and 50 K are shown, noting that there is uncertainty regarding the experimental freeze-in temperature. For Model 5, local $p(2 \times 2)$ ordering can be seen. For Model 8, especially for $T = 50$ K, local $p(2 \times 2)$ ordering coexists with pairs separated by $\sqrt{3}a$. A few short $\sqrt{3}R30^\circ$ rows, 3-5 atoms long, exist at 100 K and 150 K. For Model 11, no local $p(2 \times 2)$ can be found. Instead, the system consists of monomers, pairs and trimers, and occasionally some quartets or even larger clusters. Again, with increasing temperature, very short $\sqrt{3}R30^\circ$ rows appear, but they are qualitatively inconsistent with experiment.

In Model 12T, which includes attractive linear trio interactions, linear $\sqrt{3}R30^\circ$ rows dominate, especially at 50 K. In Model 12T3, which contains two additional types of (non-linear) trio interactions, the result is similar. The main difference is that rows are somewhat shorter in Model 12T3, which can be attributed to its weaker attractive trio interaction for linear trimers. At $T = 100$ K, the rows shorten and become more comparable to experimental observation in both models. At 150 K, Model 12T does a good qualitative job of reproducing

both the long $\sqrt{3}R30^\circ$ rows and the equilateral $\sqrt{3}R30^\circ$ triangles. At 100-150 K, Model 12T3 produces very few of the equilateral $\sqrt{3}R30^\circ$ triangles.

An additional perspective on the formation of $\sqrt{3}R30^\circ$ rows comes from considering the energetic change ΔE that occurs when a single S_{ad} joins the end of an existing row. For example, when this occurs in Model 12T or 12T3, $\Delta E = w_2 + w_6 + T_{linear}$, which is positive and hence unfavorable compared to having S_{ad} isolated on a terrace. However, this picture applies only in the regime of very low θ_S , where chains are isolated, and the experimental θ_S does not correspond to this extreme regime. Crowding effects can arise even at quite low coverages in this system, and can lead to non-trivial adlayer ordering which is not readily anticipated without the aid of MC simulation. Sulfur adatoms feel a significant repulsion already at a separation of $3a$, implying that repulsive interaction effects are already significant at a $\theta_S = 1/9$ ML. Thus, the experimental θ_S in the range of 0.07 – 0.08 ML (local coverage) are actually 70% of the θ_S where crowding effects are likely significant.

5. Discussion

The present work makes two main contributions.

First is the experimental discovery of S-induced $\sqrt{3}R30^\circ$ rows of dots on unreconstructed Au(111), and their identification as rows of S_{ad} based on DFT analysis. This structure, and the conditions under which it exists, provides a new criterion against which to test and develop a broad picture of S-Au surface interactions, particularly lateral interactions between S_{ad} .

Second is the fact that, with no adjustable parameters, ab-initio MC reproduces these linear rows, but only with the inclusion of at least one trio interaction. This means that trio

interactions are important to describe this system accurately. Historically, the potential importance of many-body interactions in LG models was pointed out by Einstein in 1991,³⁵ and was reviewed recently by Einstein and Sathiyarayanan.³⁴ Many-body interactions are increasingly incorporated into lattice gas modeling, e.g.³⁶⁻⁴⁶, but S/Au(111) joins a smaller group of systems where the presence and effect of such interactions have been validated by experiment, e.g.⁴⁷⁻⁴⁸.

Comparison between theory and experiment. Equilibrium adlayer configurations determined from MC simulation naturally depend strongly on T, as is clear from Fig. 7. In experiment, the corresponding value of T is not the observation T of 5 K, but rather the (unknown) T at which S_{ad} freezes in place while the sample is cooled from 300 K to 5 K. From Sec. IVB, the calculated diffusion barrier is 0.39-0.47 eV. If the hop rate is 0.1 s⁻¹ at the point of immobilization, then this range of barriers corresponds to freeze-in at 140 -170 K, assuming a pre-exponential factor of 10¹³ s⁻¹. It is known that the hop rate is enhanced by repulsive interactions,⁴⁹ which would lower the immobilization temperature further. Consistent with this rough estimate of T, the MC simulations for the highest-level Models, 12T and 12T3, agree most favorably with experiment at 100-150 K.

There are some limitations in using the DFT and MC studies to explain the experimental findings. First, in the experiments, the herringbone reconstruction coexists with areas of adsorbed S. This residual reconstruction may exert stress on the unreconstructed areas stabilized by S_{ad}. Also, experiments show that about 10% of total S_{ad} is in the form of isolated equilateral triangles, while in the MC simulations of Model 12T3 these triangles are much rarer. Model 12T seems closer to experiment in this respect, reflecting a general feature that inclusion of increasing numbers of interactions in LG models does not automatically

guarantee improvement. There are other potential limitations, such as the possible impact of van der Waals interactions on the DFT. However, these uncertainties and imperfections should not obscure the fact that DFT and ab-initio MC capture the essential experimental feature, the linear $\sqrt{3}R_{30}^\circ$ row of S_{ad} .

Comparison with work of Kurokawa et al. Using STM, Kurokawa *et al.*¹⁵ reported a variety of coexisting S-induced features on unreconstructed regions of Au(111) at 77 K (following preparation at 300 K and cooling, similar to our approach). They observed two types of large features, with diameter 1 nm (3x wider than our dots), and assigned them as Au_3S_3 complexes. They also observed smaller features that they assigned as S_{ad} . θ_S was not stated, but the surface contained extended remnants of the Au(111) reconstruction, similar to ours, indicating low θ_S . We do not find evidence for anything resembling their large features in our experiments. However, the following experimental parameters were different: observation temperature (77 K¹⁵ vs. 5 K); possibly coverage, and possibly cooling rate. Further investigation would be required to determine the effect of any of these parameters on the experimental observations. Kurokawa *et al.*¹⁵ also used DFT to assess relative stabilities of clusters, but they used the energy of an isolated Au *adatom* as a reference point. In contrast, per Eq. (1), we use the cohesion energy of an Au *atom in the bulk*, which is the thermodynamically relevant quantity. The approach of Kurokawa *et al.*¹⁵ incorrectly enhances the stability of Au-S complexes relative to structures involving only S_{ad} .

Comparison with work of Abufager et al. Abufager *et al.*¹⁴ focused on developing a LG Hamiltonian to explain ordered structures with ideal coverages of 0.28 and 0.33 ML, while we focus on structures that exist at 0.07-0.08 ML. Nonetheless, given that both works use the same adsorption site for S_{ad} , ideally there should be a single LG model that

reproduces all observed structures under appropriate conditions, so comparison is appropriate.

Addressing first the computational approaches, the number of configurations used (36 in the present manuscript and 51 in Ref. ¹⁴) are comparable, although we use more configurations with low θ_s . Densities of k-point grids for various supercells are also comparable. However, we average energetics over slab thickness $L=4$ to 7, which has been demonstrated to give more precise results than using fixed L ,²³ as was done in Ref. ¹⁴ with $L = 5$. In principle, including more configurations and more parameters would improve either LG Hamiltonian, but obtaining numerically-accurate results for large supercells is difficult, requiring very dense k-point grids and perhaps thicker slabs also.

With respect to results, the following *similarities* exist between the two works: (1) The NN interaction, w_1 , is repulsive and stronger than any other interaction. (2) There are many weaker long-range interactions. Abufager *et al.*¹⁴ showed that these are mainly due to S-induced surface relaxation, since S-S interactions beyond NN are greatly reduced in DFT calculations with a frozen substrate. They also found that some smaller non-monotonic interactions remain with a frozen substrate. The oscillatory nature of these remaining interactions seems to fit into the theory of surfaces states-induced interactions between adsorbates on (111) faces of noble metals.⁵⁰ However, an accurate estimate of effects of surface states using the slab geometry is difficult.⁵¹ (3) The interactions $w_2 - w_{10}$ are repulsive, with a maximum at $d_p = 3a$, in both works.

Some *differences* between results also exist: (1) In the present work, w_{11} is weakly repulsive, while in Ref. ¹⁴ w_{11} —plus w_{12} and w_{13} , which are beyond our largest LG model—are weakly attractive. (2) Three-body interactions were considered unimportant in the

analysis of Ref. ¹⁴, although the complete model shown in the SI of Ref. ¹⁴ included attractive bent and linear trio interactions, and a repulsive triangular trio interaction, similar to our Model 12T3. Our work shows that three-body interactions are important.

Finally, we note that Abufager *et al.*¹⁴ did not perform MC simulations to test whether their LG model is compatible with experimental data for the $p(5 \times 5)$ and $(\sqrt{3} \times \sqrt{3})R30^\circ$ structures. The question of whether ab-initio MC of S_{ad} can reproduce the entire suite of experimental observations—the $\sqrt{3}R30^\circ$ rows at low temperature described herein, as well the $p(5 \times 5)$ and $(\sqrt{3} \times \sqrt{3})R30^\circ$ structures known previously—is under continuing investigation in our group.

6. Conclusions

STM reveals $\sqrt{3}R30^\circ$ rows of dots on Au(111) following adsorption of S. We identify these as rows of S_{ad} , using DFT. This structure exists in a regime that has not been explored previously: low coverage of $\theta_s < 0.1$, and low (observation) temperature of 5 K. This structure, and the conditions under which it exists, provides a new criterion against which to test and develop a picture of lateral interactions between S_{ad} . Ab-initio MC reproduces these linear rows, but the inclusion of trio interactions is essential. Trends in the interaction energies largely agree with prior results,¹⁴ notably the existence of many long-range pairwise repulsions which peak in magnitude at $3a$.

Acknowledgements

The experimental component of this work was conducted or supervised by HW, JO, HL, YK, and PAT. It was supported by three sources. From the U.S., it was NSF Grant CHE-

1507223. From Japan, support was provided by a Grant-in-Aid for Scientific Research on Priority Areas “Electron Transport Through a Linked Molecule in Nano-scale”; and a Grant-in-Aid for Scientific Research(S) “Single Molecule Spectroscopy using Probe Microscope” from the Ministry of Education, Culture, Sports, Science, and Technology (MEXT). The theoretical component of this work was carried out by DJL. It was supported by the Division of Chemical Sciences, Basic Energy Sciences, US Department of Energy (DOE). This part of the research was performed at Ames Laboratory, which is operated for the U.S. DOE by Iowa State University under contract No. DE-AC02-07CH11358. This part also utilized resources of the National Energy Research Scientific Computing Center, which is supported by the Office of Science of the U.S. DOE under Contract No. DE-AC02-05CH11231.

Figures

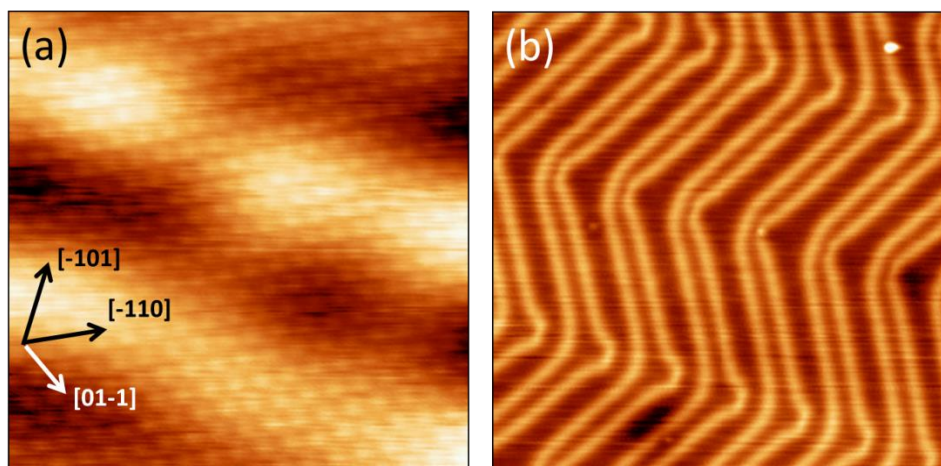


Figure 1. STM images of clean Au(111). (a) Atomically-resolved image. $5 \times 5 \text{ nm}^2$. (b) $50 \times 50 \text{ nm}^2$.

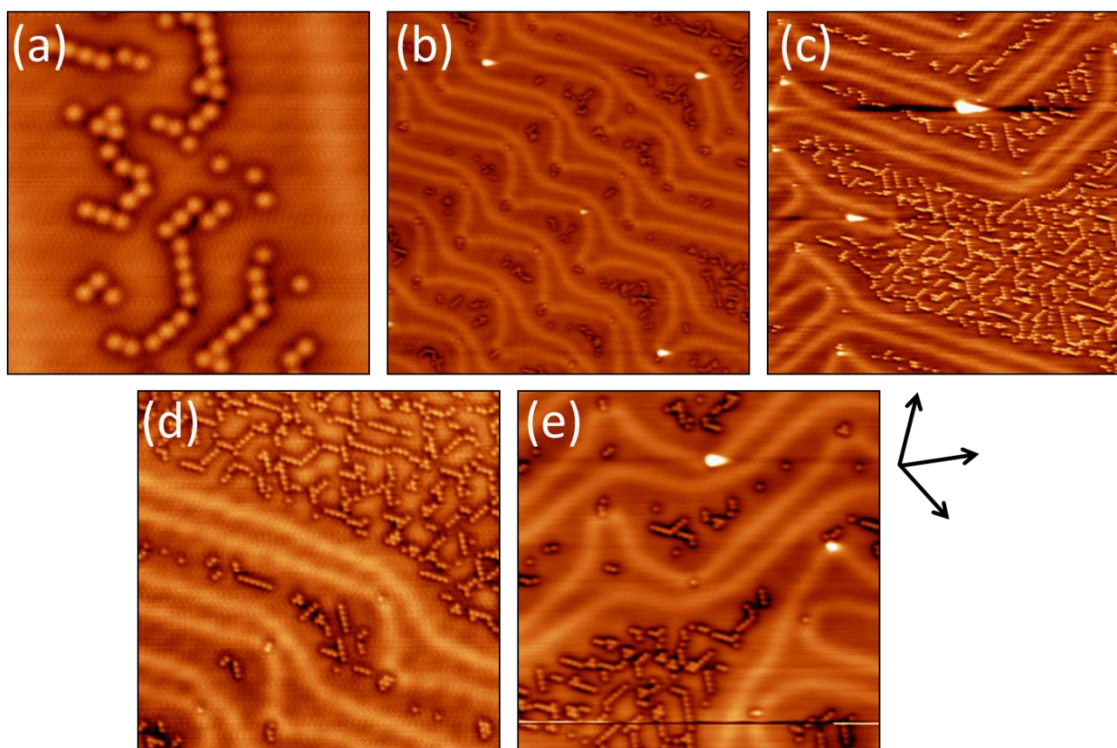


Figure 2. STM images of S adsorbed on Au(111). Tunneling conditions and sulfur coverages are given in the SI. (a) $10 \times 10 \text{ nm}^2$. (b) $50 \times 50 \text{ nm}^2$. (c) $50 \times 50 \text{ nm}^2$. (d) $30 \times 30 \text{ nm}^2$. (e) $30 \times 30 \text{ nm}^2$. The arrows show three of the close-packed directions, from Fig. 1.

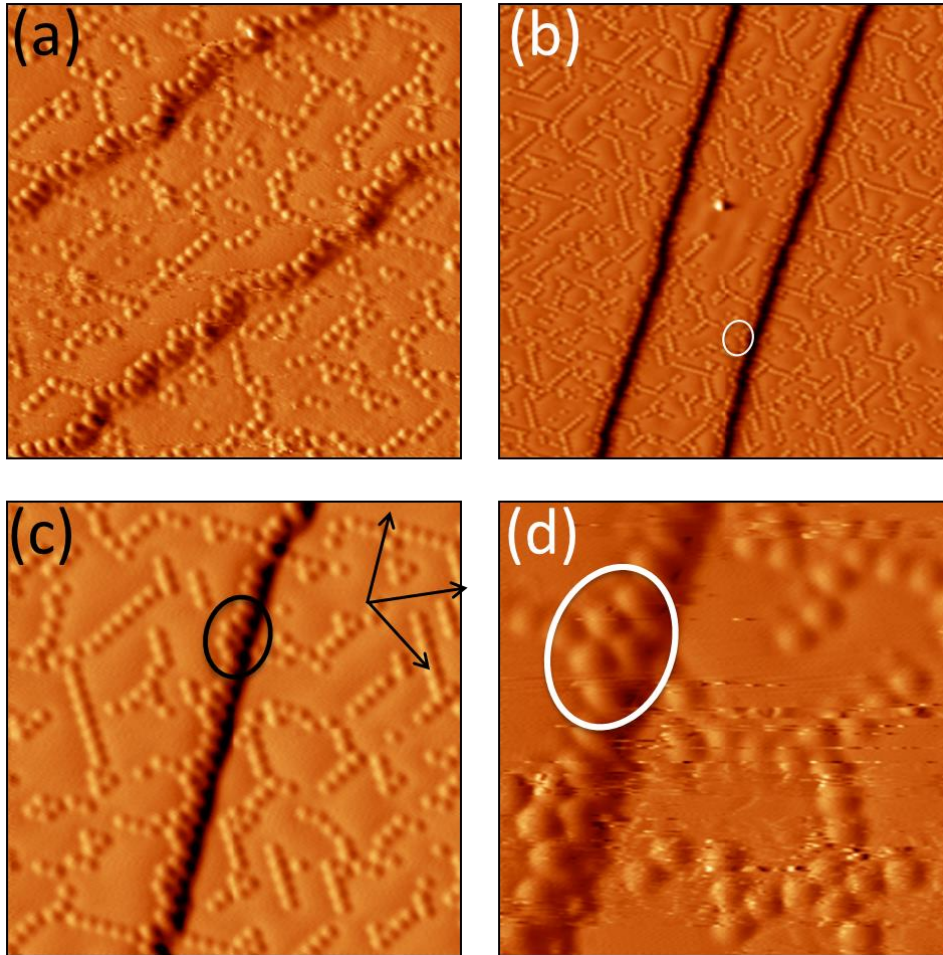


Figure 3. Differentiated STM images of step edges. In each image, the uppermost terrace is on the left. Each image is from a different region of the surface. Three of the close-packed directions are shown by the arrows in (c). (a) $20 \times 20 \text{ nm}^2$. (b) $40 \times 40 \text{ nm}^2$. (c) $16 \times 16 \text{ nm}^2$. (d) $6.6 \times 6.6 \text{ nm}^2$.

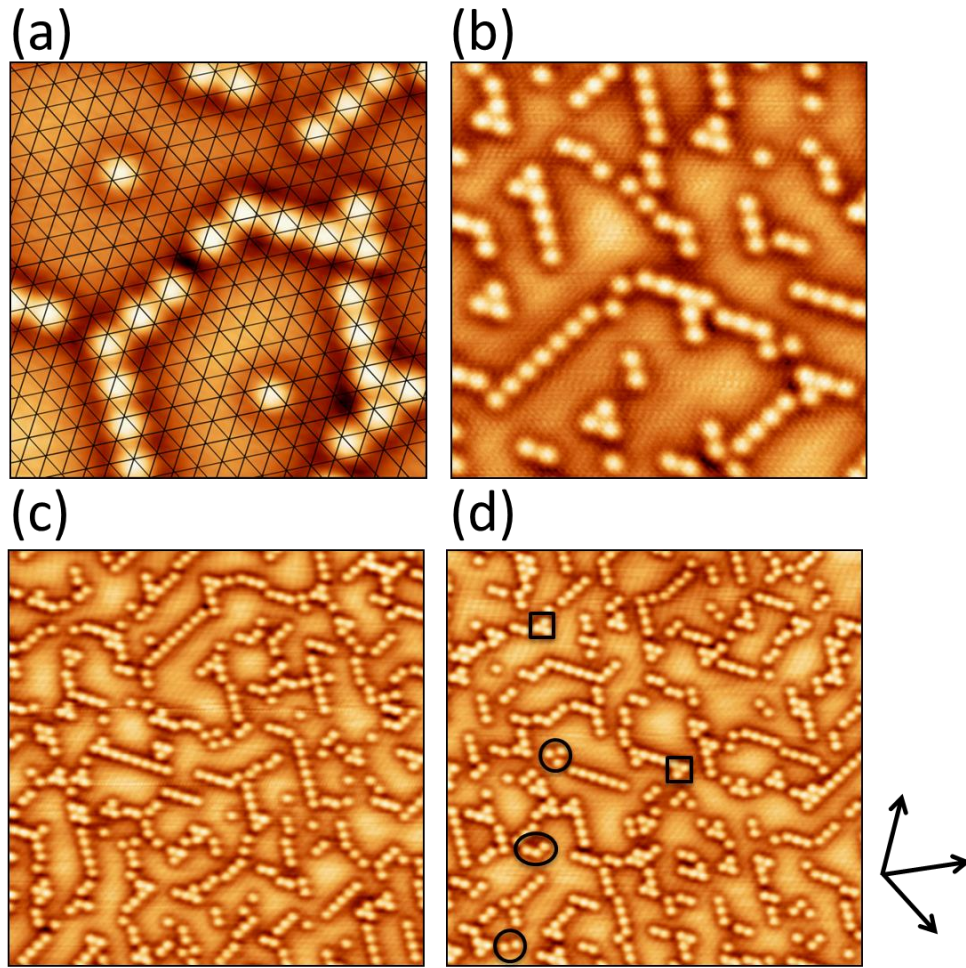


Figure 4. Atomic sulfur structures on unreconstructed Au(111). Each image is from a different region of the surface. (a) $5 \times 5 \text{ nm}^2$. Intersections of lines in the overlaid grid represent surface Au atomic positions. (b) $10 \times 10 \text{ nm}^2$. (c) $20 \times 20 \text{ nm}^2$. (d) $20 \times 20 \text{ nm}^2$. In (d), the two circles enclose a (2 x 2)-like trimer (left center) and a (2 x 2)-like dimer (left bottom region). The squares enclose an independent $\sqrt{3}R30^\circ$ triangular trimer (left top) and a $\sqrt{3}R30^\circ$ triangular trimer that is part of a chain (mid-center region of the image). The ellipse encloses a bent $\sqrt{3}R30^\circ$ trimer (lower left). The arrows denote the close-packed directions, showing that the rows are rotated by 30° .

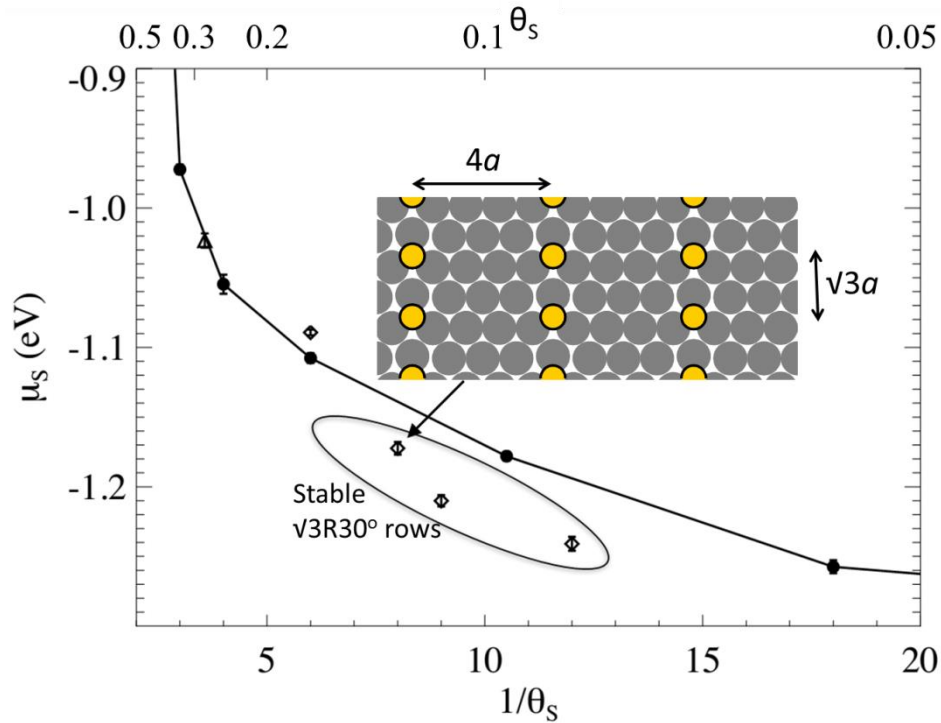


Figure 5. Baseline energetics (solid circles connected by line segments) of regular arrays of S_{ad} . The corresponding values of μ_s are given in boldface in Table 1. Also shown: $\sqrt{3}R30^\circ$ row structures of S_{ad} (diamond symbols) for various separations between chains. The structure with a row separation of $4a$ is illustrated. Row structures that fall below the baseline are enclosed in an ellipse. The μ_s for the rosette model of the $p(5 \times 5)$ proposed by Yu *et al.*⁵ is also shown (triangular symbol, $\theta_s = 0.28$).

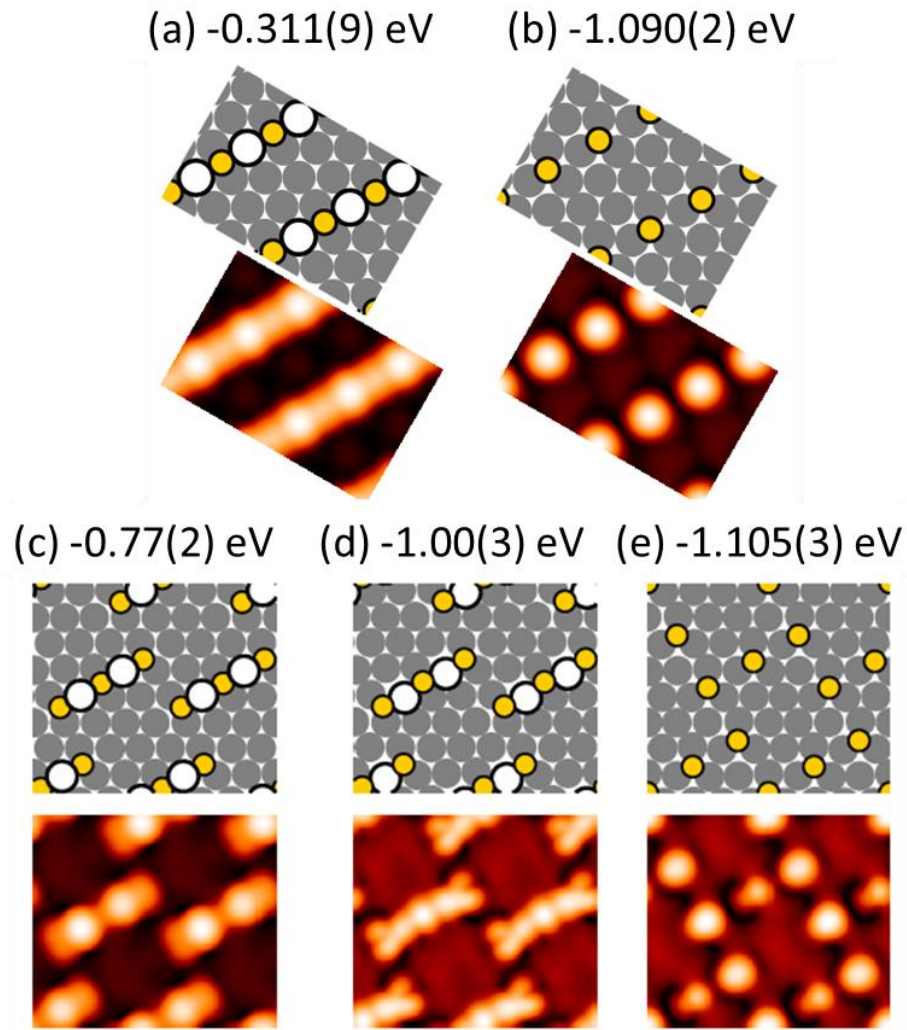


Figure 6. Optimized configurations including Au-S units related to $\sqrt{3}R30^\circ$ rows. For each configuration, the value of μ_S is given at the top and the simulated STM image is shown below it. (a) Infinite row. (b) Corresponding configuration of S_{ad} . (c) Shorter row. (d) Similar to panel c, except that Au atoms indicated by white circles originate in the Au(111) substrate, leaving a partial vacancy underneath. (e) Configuration of S_{ad} corresponding to panels c, d.

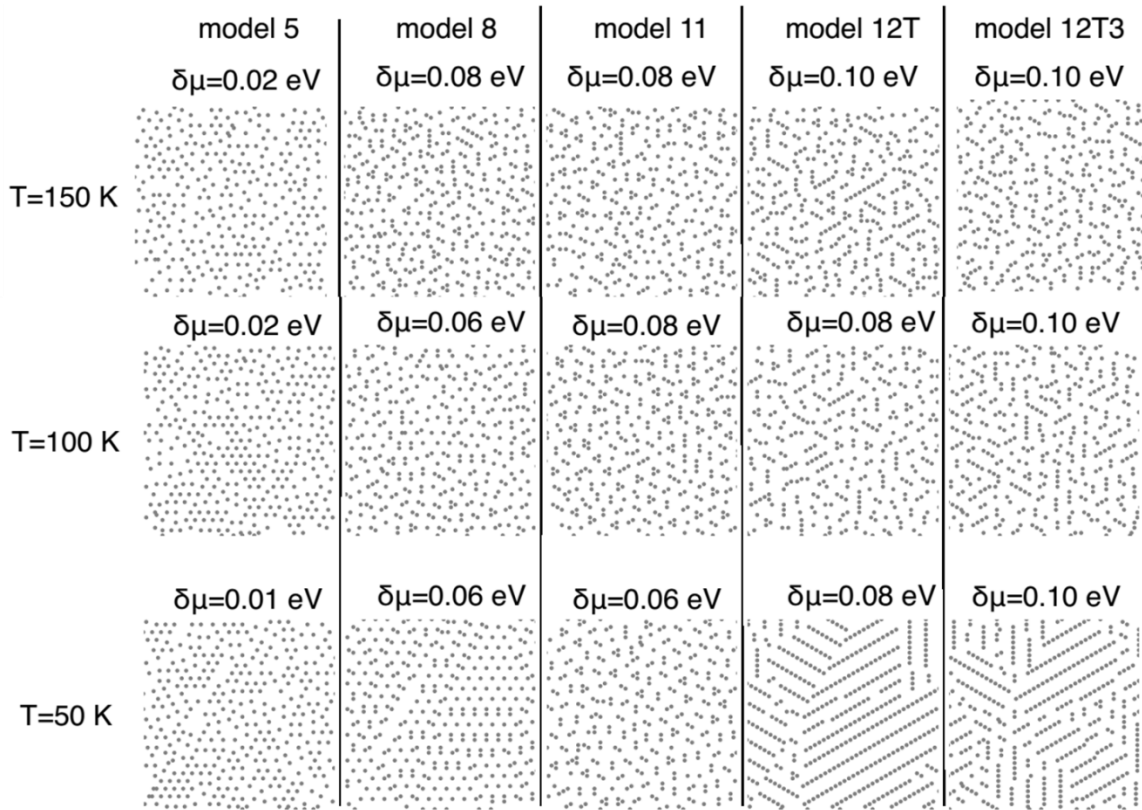


Figure 7. Snapshots of Monte Carlo simulations of the lattice gas models with interactions listed in Table 2, at T=150 K (top), 100 K (middle), and 50 K (bottom). The system used in simulation has 256^2 lattice sites, and 128^2 sites are shown, yielding image sizes 39×39 nm².

Appendix 1. STM data

This section contains information about the STM images in the text, plus many additional STM images obtained in the S/Au(111) experiments.

A. Tunneling conditions for images in the text

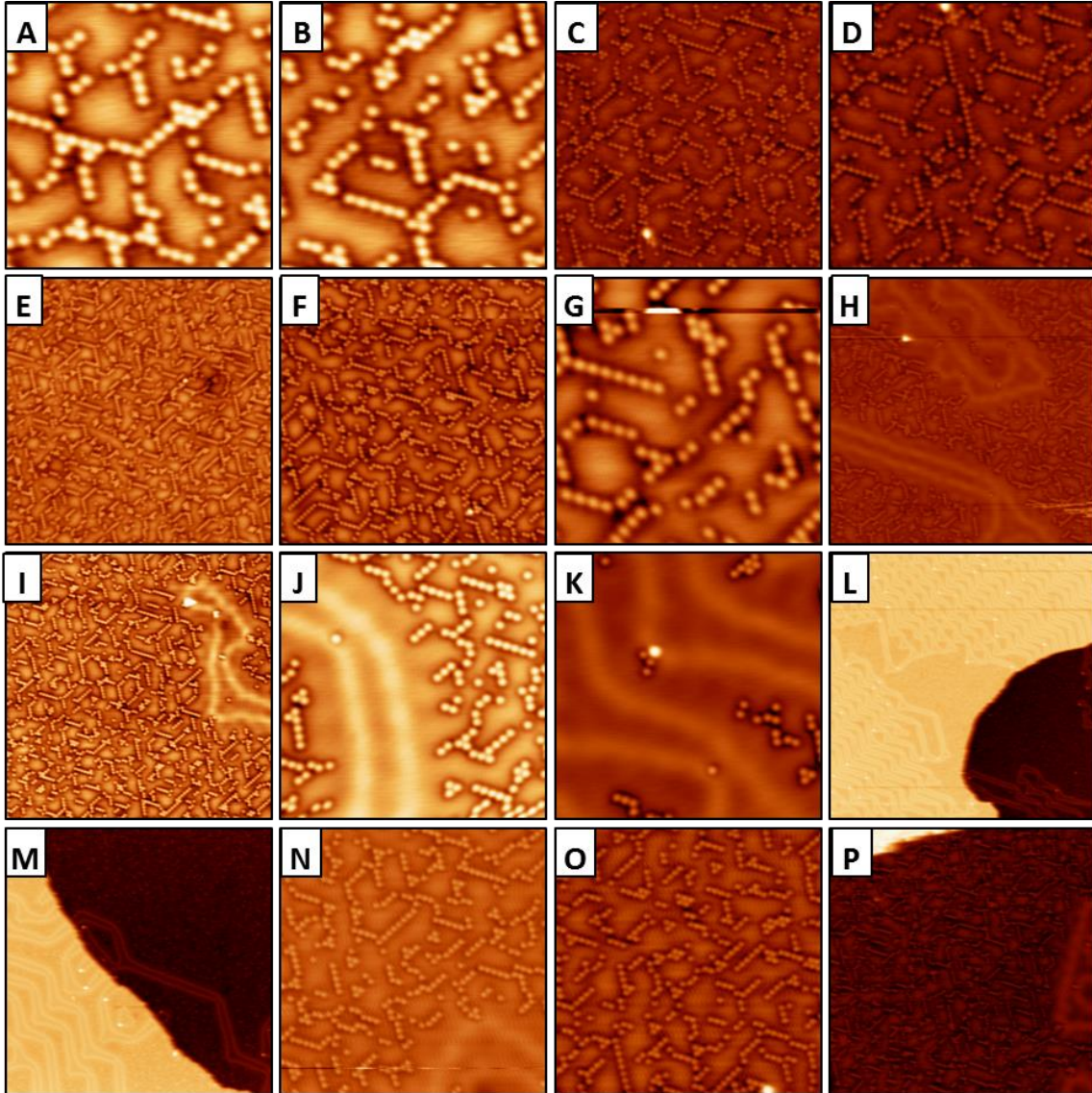
TABLE AIII(below): Tunneling conditions and coverages for the images presented in the main text.

Figure	Current (nA)	Sample Bias (V)	Global Coverage (ML)	Local Coverage (ML)
1a	3.03	-0.002	0	0
1b	1.32	-0.373	0	0
2a	1.03	-0.035	0.045	0.079
2b	1.06	-0.200	0.30	0.070
2c	1.29	-0.106	0.045	0.079
2d	1.32	-0.045	0.045	0.079
2e	1.46	-0.298	0.030	0.070
3a	0.99	-0.065	0.045	0.079
3b	1.12	-0.023	0.045	0.079
3c	1.22	-0.023	0.045	0.079
3d	1.03	-0.060	0.045	0.079
4a	1.37	-0.035	0.045	0.079
4b	1.37	-0.035	0.045	0.079
4c	1.17	-0.102	0.030	0.070
4d	1.03	-0.102	0.030	0.070

B. Experiment 1

In this experiment, $\theta_s = 0.079$ ML on the large unreconstructed regions, and 0.045 ML overall. All of the images were obtained at 5 K. The images are presented in the order in which they were acquired. A table of the scan sizes and scanning conditions is provided at

the end of the images. Images A-M were taken after the initial quench to 5 K, following deposition at room temperature. Images N-AA were taken after re-warming the sample to RT and quenching again to 5 K.



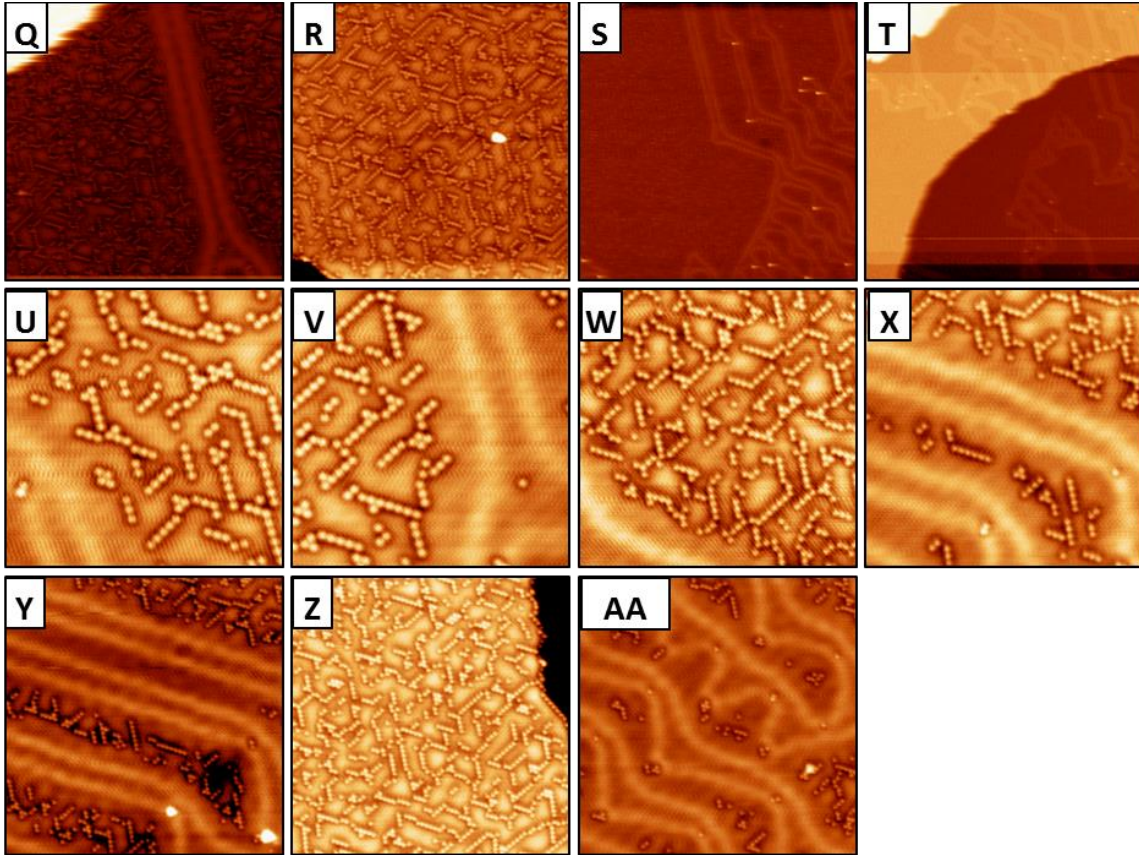


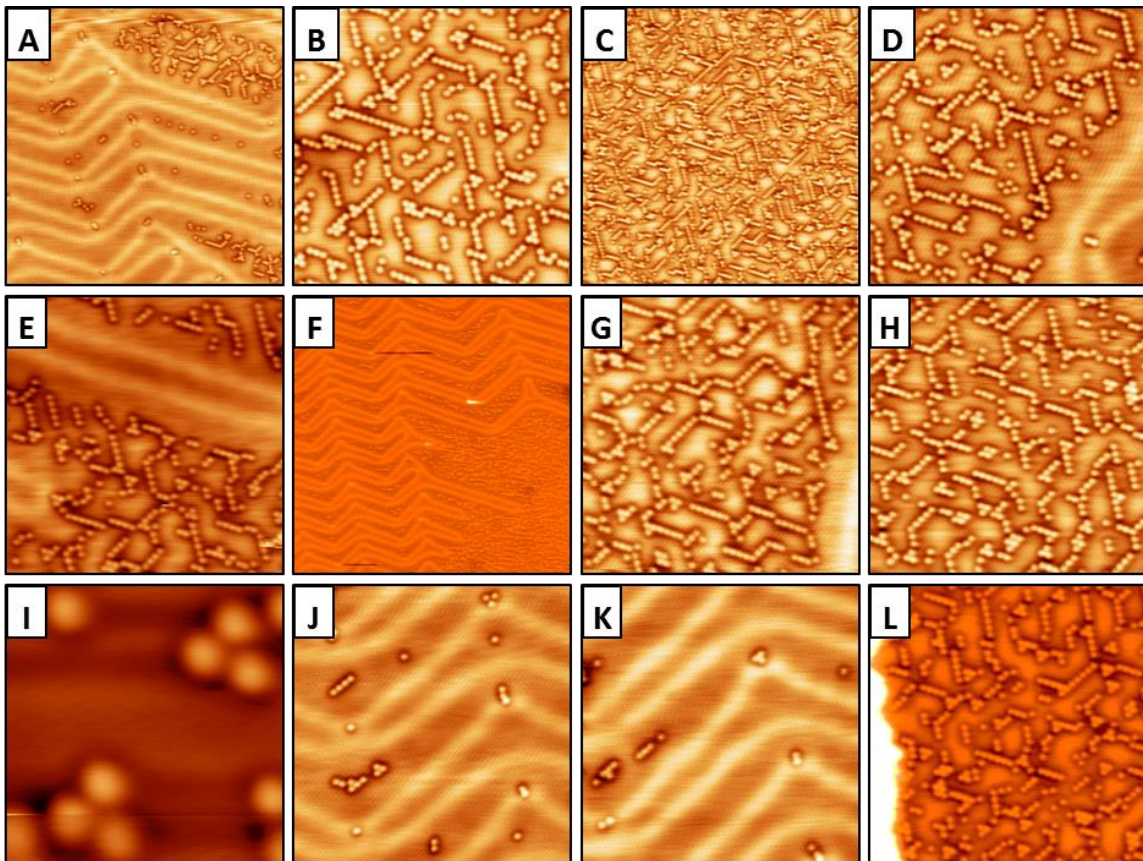
Figure A1 (above and preceding page). Topographic STM images from Experiment 1, wherein $\theta_s = 0.079$ ML on the large unreconstructed regions, and 0.045 ML overall. Images A-M were taken after the initial quench to 5 K, following deposition at room temperature. Images N-AA were taken after re-warming the sample to RT and quenching again to 5 K. Each image shows a separate region of the surface.

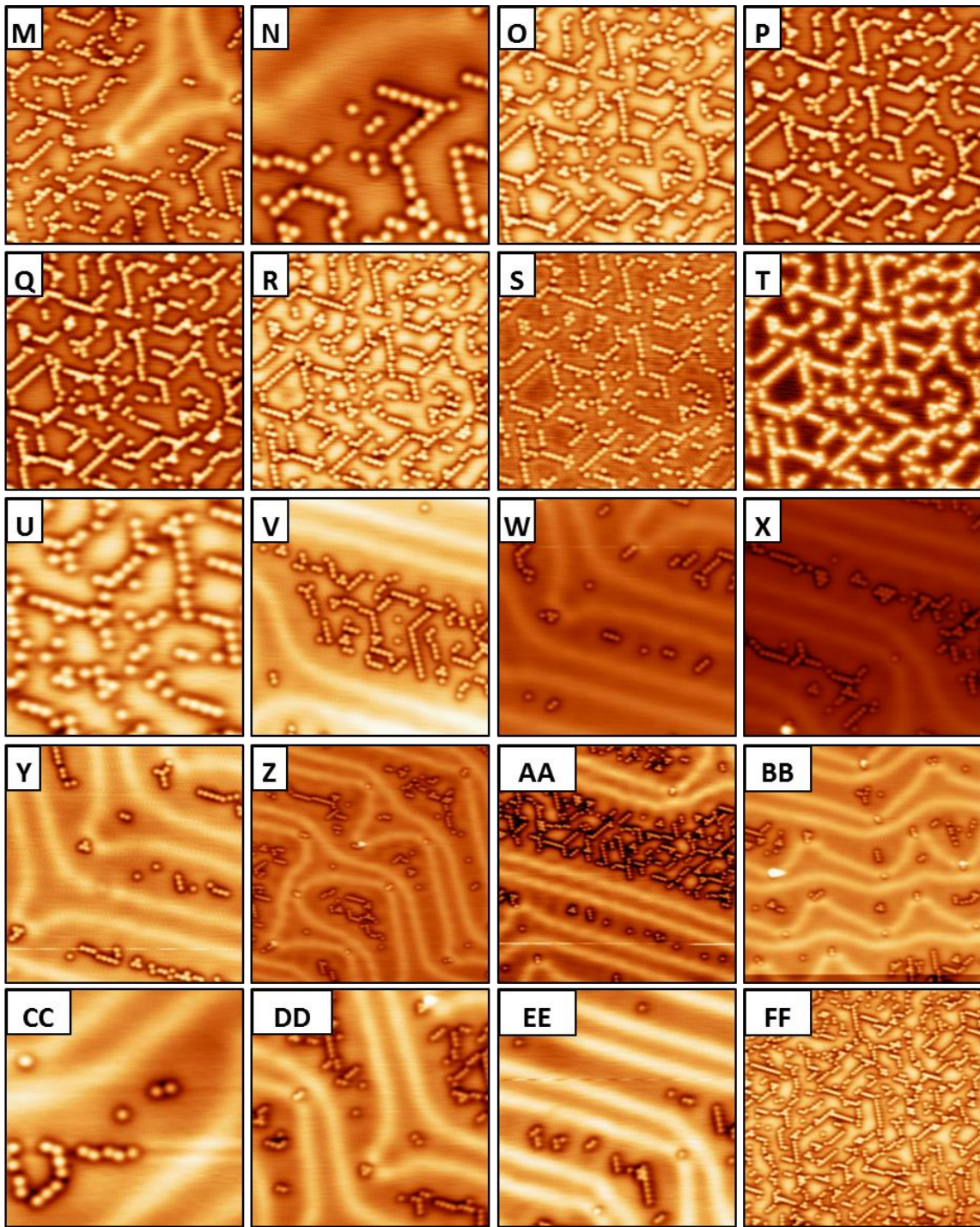
TABLE AIV (below). Experimental scan sizes and tunneling conditions for the data in Fig. A1. $\theta_S = 0.079$ ML in the large unreconstructed regions, and 0.045 ML overall.

Image	Scan size (nm²)	Current (nA)	Sample Bias (V)
A	10 x 10	0.717	-0.130
B	10 x 10	0.717	-0.130
C	25 x 25	1.216	-0.028
D	20 x 20	1.216	-0.028
E	40 x 40	1.216	-0.023
F	30 x 30	1.216	-0.023
G	10 x 10	1.121	-0.038
H	40 x 40	1.121	-0.023
I	40 x 40	1.121	-0.023
J	15 x 15	1.121	-0.023
K	15 x 15	1.121	-0.023
L	100 x 100	0.915	-0.050
M	100 x 100	0.915	-0.050
N	20 x 20	1.241	-0.039
O	15 x 15	0.518	-0.023
P	40 x 40	1.460	-0.023
Q	40 x 40	1.460	-0.023
R	35 x 35	1.373	-0.035
S	100 x 100	1.373	-0.035
T	200 x 200	1.144	-0.198
U	15 x 15	1.191	-0.078
V	15 x 15	1.191	-0.078
W	20 x 20	0.934	-0.065
X	20 x 20	0.934	-0.065
Y	30 x 30	1.319	-0.045
Z	30 x 30	1.319	-0.045
AA	30 x 30	1.319	-0.045

C. Experiment 2

In this experiment, $\theta_s = 0.070$ ML in the large unreconstructed regions, and 0.030 ML overall. All of the images were obtained at 5 K. The images are presented in the order in which they were acquired. A table of the scan sizes and scanning conditions is provided at the end of the images. Images A-U were taken after the initial quench to 5 K, following deposition of sulfur at 300 K; images V-II were taken after re-warming the sample to 300 K and quenching again to 5 K.





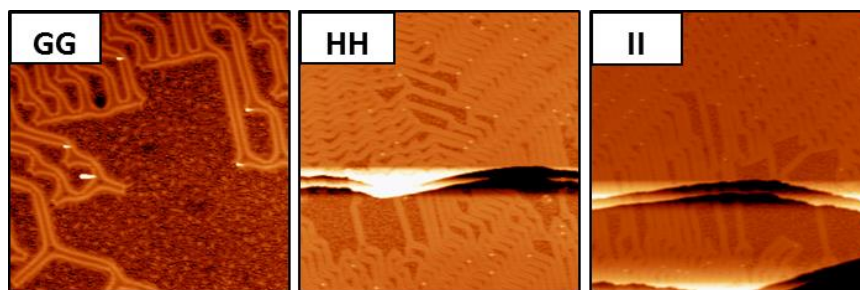


Figure A2 (above and preceding pages). Topographic STM images from Experiment 2, wherein $\theta_s = 0.070$ ML in the large unreconstructed regions, and 0.030 ML overall. Images A-U were taken after the initial quench to 5 K, following deposition of sulfur at 300 K; images V-II were taken after re-warming the sample to 300 K and quenching again to 5 K. Images O-T show the same area with varied sample bias. Image U is a higher-magnification image of the central area in T; image N is a higher-magnification image of an area in M. Otherwise, each image shows a separate area of the surface.

TABLE AV (below and following page). Experimental scan sizes, and tunneling conditions, for the data in Fig. A2. $\theta_s = 0.070$ ML in the large unreconstructed regions, and 0.030 ML overall.

Image	Scan size (nm ²)	Current (nA)	Sample Bias (V)
A	40 x 40	1.319	-0.124
B	20 x 20	1.319	-0.094
C	40 x 40	1.167	-0.102
D	20 x 20	1.034	-0.102
E	20 x 20	1.292	-0.106
F	100 x 100	1.292	-0.106
G	20 x 20	1.292	-0.106
H	20 x 20	1.292	-0.106
I	3 x 3	3.869	-0.002
J	20 x 20	1.292	-0.127
K	20 x 20	1.373	-0.150
L	20 x 20	1.216	-0.138
M	20 x 20	1.216	-0.138
N	10.2 x 10.2	1.216	-0.138
O	20 x 20	1.319	-0.207

TABLE AV continued.

P	20 x 20	1.319	-1.000
Q	20 x 20	1.319	-2.000
R	20 x 20	1.216	0.200
S	20 x 20	1.216	1.000
T	20 x 20	1.216	2.000
U	10 x 10	1.430	0.200
V	20 x 20	1.055	-0.200
W	20 x 20	1.055	-0.200
X	20 x 20	1.055	-0.200
Y	20 x 20	1.055	-0.200
Z	30 x 30	1.266	-0.122
AA	30 x 30	1.266	-0.122
BB	30 x 30	1.460	-0.298
CC	10 x 10	2.147	-0.233
DD	20 x 20	1.191	-0.207
EE	20 x 20	1.191	-0.207
FF	30 x 30	1.216	-0.211
GG	100 x 100	1.319	-0.232
HH	250 x 250	1.319	-0.232
II	250 x 250	1.319	-0.232

Appendix 2. Additional DFT information

A. Depiction of interactions

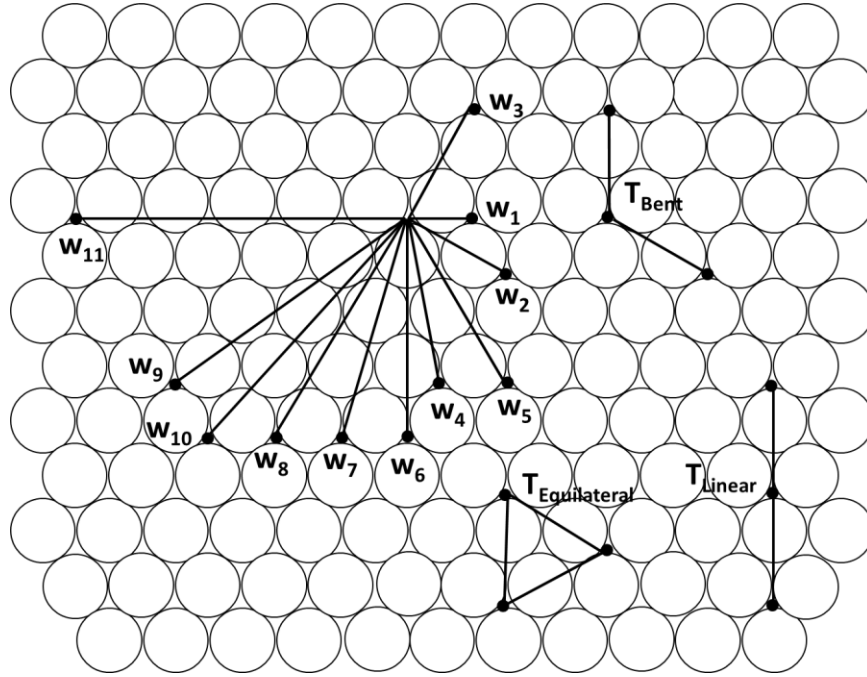


Figure A3. Schematic of the pairwise interactions corresponding to Table II in the main text. The interactions are indexed by a subscript, n , which indicates the relative separation between equivalent sites. For instance, w_1 is the first NN interaction, w_2 is the second NN interaction, and so forth. The trio interactions are denoted by T .

B. Baseline energetics

Figure A4 shows μ_S for all arrangements of S atoms that are used to generate the baseline energetics. Two types of periodic arrays are considered. In both, the supercell lattice vectors (\mathbf{a}_i 's) are equal and the included angle is 60° . The first type has one S per supercell, thus forming a simple hexagonal lattice. The second type has two S atoms per supercell. The additional S atom is located at $(1/3\mathbf{a}_1, 1/3\mathbf{a}_2)$ in the supercell, and consequently S_{ad} forms a honeycomb lattice.

Figure A4 shows that the value of μ_S generally decreases as $1/\theta_S$ increases, but with significant irregularities. As mentioned in the main text, we choose eight values that form the lower envelope to be the baseline.

Figure A5 shows some of the configurations that are included in the baseline energetics. These include both types of arrays.

C. The set of energetics used to derive the Lattice-Gas Hamiltonian

Figure A6 shows the set of 36 configurations that are calculated through DFT and used to derive the energetics used in the lattice-gas model and Monte Carlo simulations.

Table VI below provides the chemical potential, coverage, and k-points for each configuration. Some of these 36 configurations can be described as localized trios and pairs, and additional information for these is given in Section 2.3.

TABLE AVI (below and following page). Chemical potential of 36 configurations of S atoms adsorbed on fcc sites of the Au(111) surface. The k -point grid is $(N_k \times N_k \times 1)$. The subscript in front of S denotes the label of the supercell used in the calculation, as given in Table I of the main text. The subscript after S (if any) denotes the number of S atoms in each supercell. If there is no subscript, then there is one S. If the subscript is c , it denotes an infinitely long row, calculated with a reduced supercell.

	μ_s (eV)	θ_s	N_k
$_2S$	-0.972(3)	0.333	21
$_3S$	-1.055(7)	0.250	18
$_4S$	-1.105(3)	0.143	14
$_4S_2(A)$	-0.854(1)	0.286	14
$_5S$	-1.077(3)	0.111	12
$_5S_2(H)$	-1.032(3)	0.222	12
$_6S$	-1.187(3)	0.083	10
$_6S_2(H)$	-1.108(3)	0.167	10
$_6S_c$	-1.089(2)	0.167	10
$_6S_3(A)$	-1.033(3)	0.250	10

TABLE AVI continued.

${}_7S$	-1.199(6)	0.077	10
${}_7S_2(A)$	-1.131(3)	0.153	10
${}_7S_3(A)$	-1.066(4)	0.231	10
${}_8S$	-1.231(4)	0.063	9
${}_8S_2(B)$	-1.167(3)	0.125	9
${}_8S_3(B)$	-1.098(1)	0.188	9
${}_8S_3(C)$	-1.105(3)	0.188	9
${}_9S$	-1.247(5)	0.053	8
${}_9S_2(A)$	-1.184(3)	0.105	8
${}_9S_3(B)$	-1.127(4)	0.158	8
${}_{10}S$	-1.244(2)	0.048	8
${}_{10}S_2(H)$	-1.178(3)	0.095	8
${}_{10}S_2(A)$	-1.173(1)	0.095	8
${}_{10}S_3(A)$	-1.129(6)	0.143	8
${}_{10}S_3(B)$	-1.104(3)	0.143	8
${}_{11}S$	-1.242(8)	0.040	7
${}_{11}S_2(B)$	-1.202(7)	0.080	7
${}_{11}S_3(B)$	-1.170(7)	0.120	7
${}_{11}S_3(C)$	-1.159(5)	0.120	7
${}_{11}S_3(D)$	-1.161(7)	0.120	7
${}_{11}S_7(A)$	-1.023(5)	0.280	7
${}_{12}S$	-1.275(3)	0.037	7
${}_{12}S_c$	-1.210(4)	0.111	7
${}_{12}S_2(B)$	-1.233(4)	0.074	7

TABLE AVI continued.

${}_{12}S_3(\text{A})$	-1.188(4)	0.111	7
${}_{12}S_3(\text{B})$	-1.150(3)	0.111	7

D. Energetics of S_{ad} pairs and trimers.

Figures A7 and A8 show μ_S of various S_{ad} pairs and trimers, respectively, relative to the baseline energetics. These pairs and trimers all contain $\sqrt{3}a$ pairwise separations. In addition, the bent trimer contains one pair separation of $3a$.

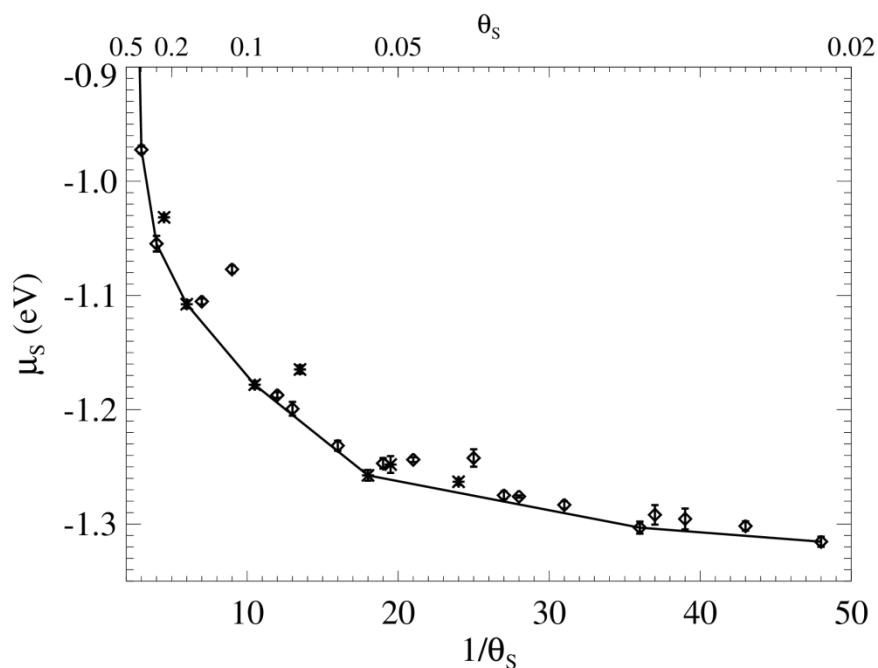


Figure A4 (above). μ_S versus $1/\theta_S$ for various primitive (diamonds) and nonprimitive (asterisks) unit cells containing S adsorbed on fcc sites of the unreconstructed Au(111) surface. The solid line connects the baseline energetics.

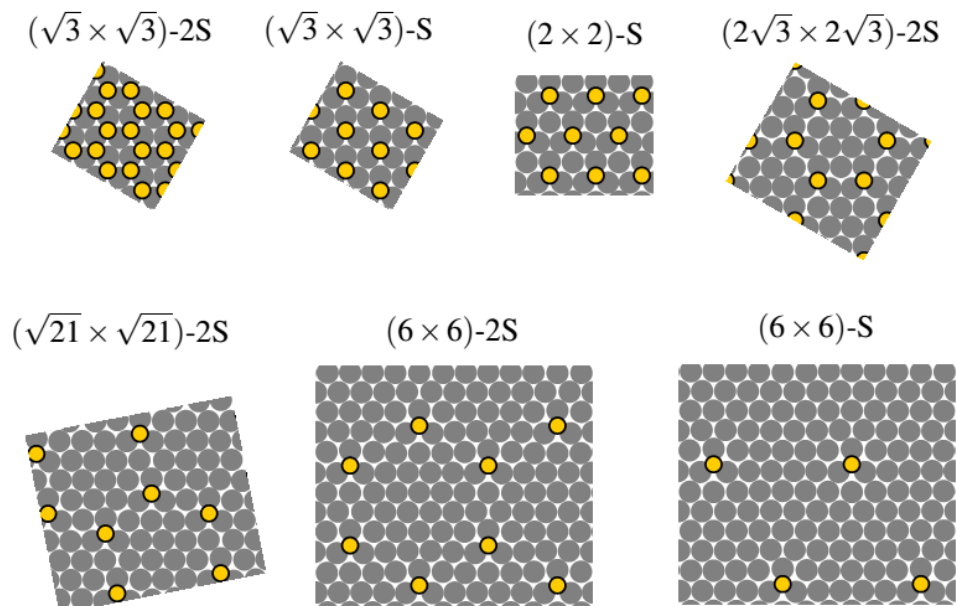


Figure A5 (above). Representations of the some of the configurations used to define the baseline energetics as shown in Fig. A4 and in Table I in the main text. Yellow circles represent S_{ad} , and gray circles represent Au atoms in the unreconstructed (111) surface.

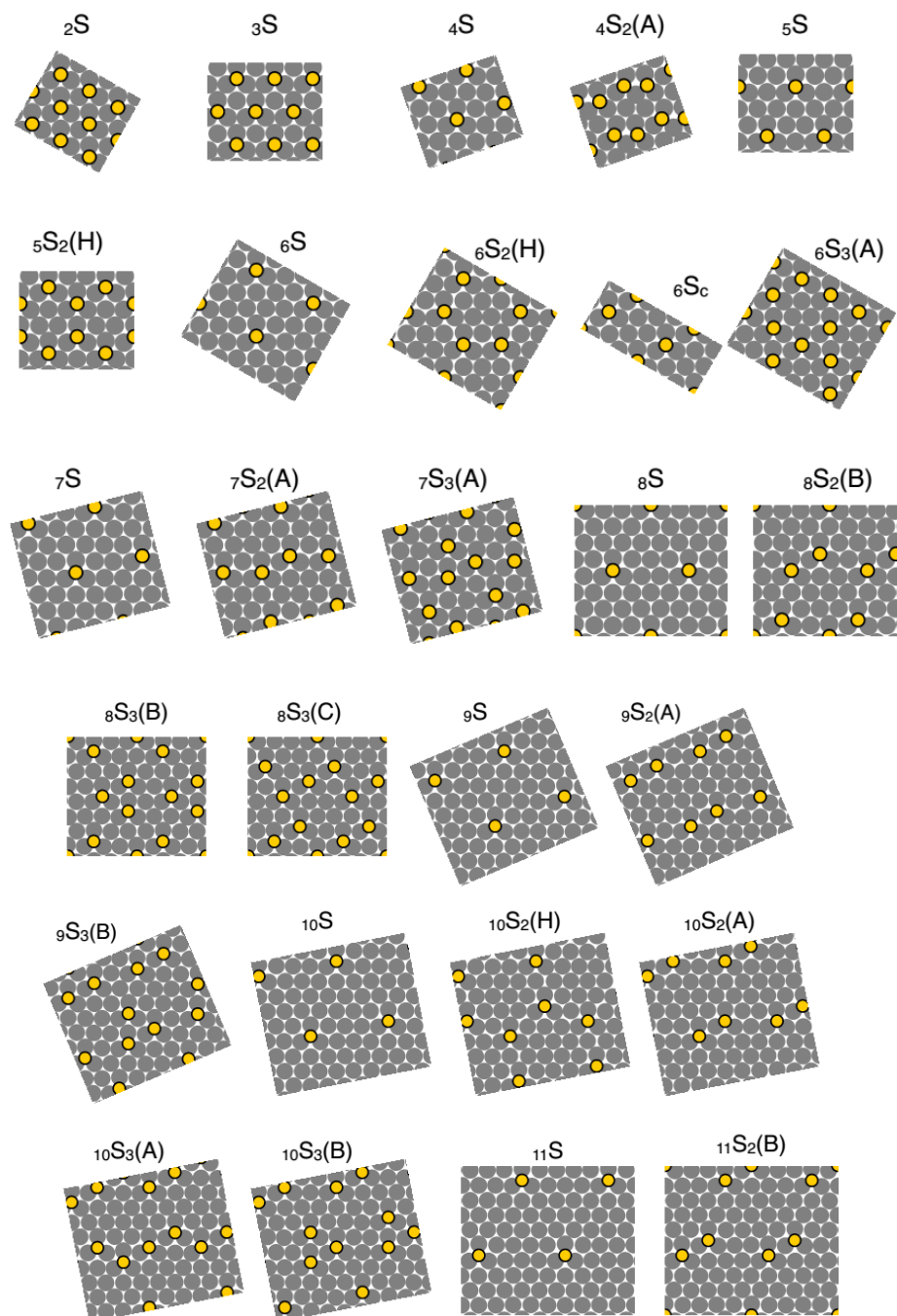


Figure A6. Geometries and chemical potentials of the 36 configurations used to derive the energetics in the lattice-gas model. Yellow circles represent S_{ad} , and gray circles represent Au atoms in the unreconstructed (111) surface. Each configuration is labeled as follows: The subscript in front of S denotes the label of the supercell used in the calculation, as given in Table 1 of the main text. The subscript after S (if any) denotes the number of S atoms in each supercell. If there is no subscript, then there is one S. If the subscript is c , it denotes an infinitely long row, calculated with a reduced supercell.

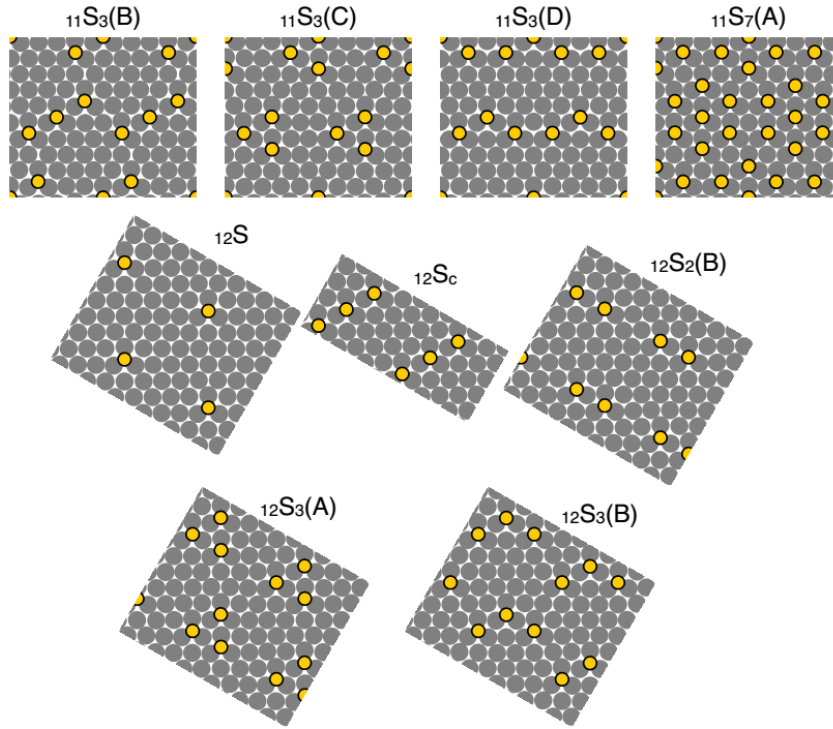


Figure A6 continued.

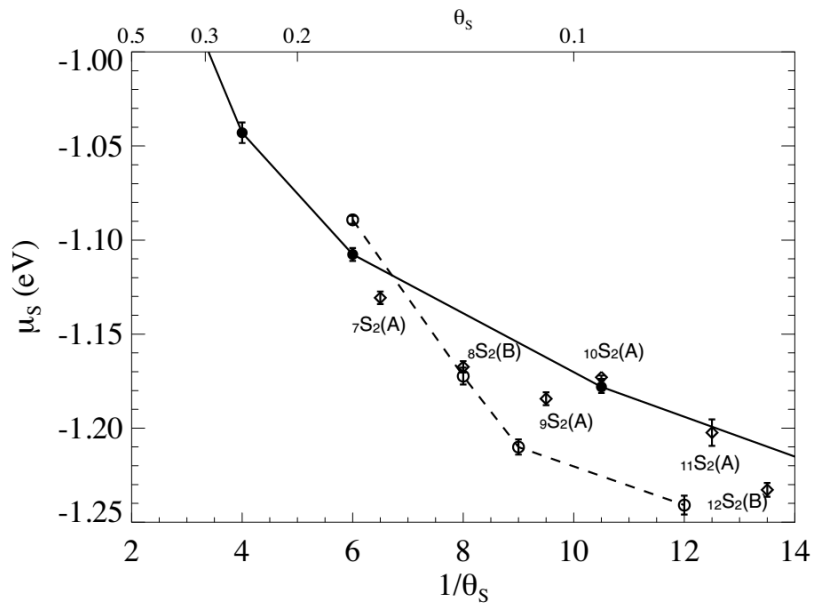


Figure A7. Chemical potentials of pairs of S_{ad} on Au(111). The solid line is the baseline energetics. The configurations and values of μ_s can be found in Fig. A6 and Table AVI, respectively. Open circles connected by a dashed line denote energetics of $\sqrt{3}R30^\circ$ row structures of S_{ad} for various separations.

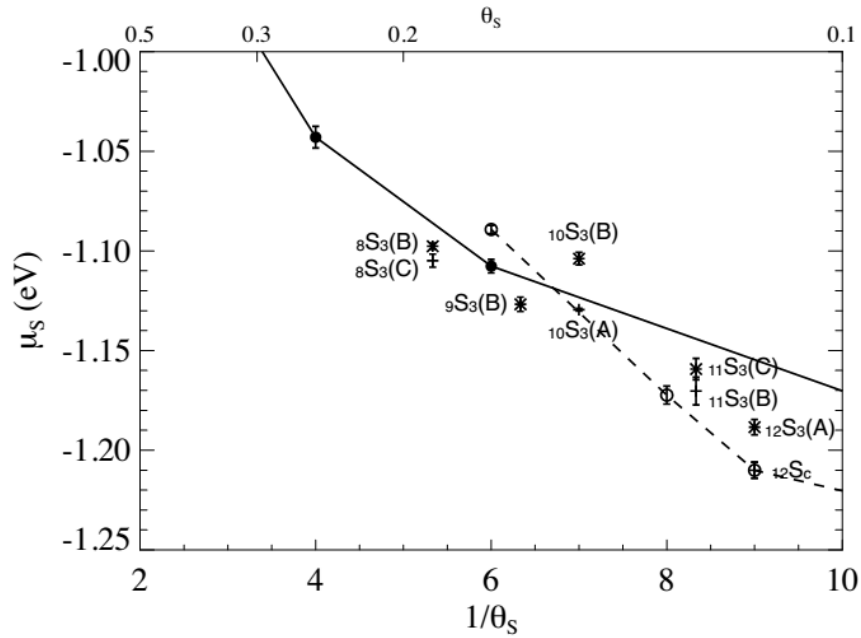


Figure A8. Chemical potentials of trimers of S_{ad} on Au(111). The solid linear segments define the baseline energetics. Pluses are linear trimers and asterisks are triangular trimers. The configurations and values of μ_S can be found in Fig. A6 and Table AVI, respectively. Open circles connected by a dashed line denote energetics of $\sqrt{3}R30^\circ$ row structures of S_{ad} for various separations. Note that $12S_C$ can be classified as both $\sqrt{3}R30^\circ$ row and linear trimers.

Appendix 3. Sample-bias effect on appearance

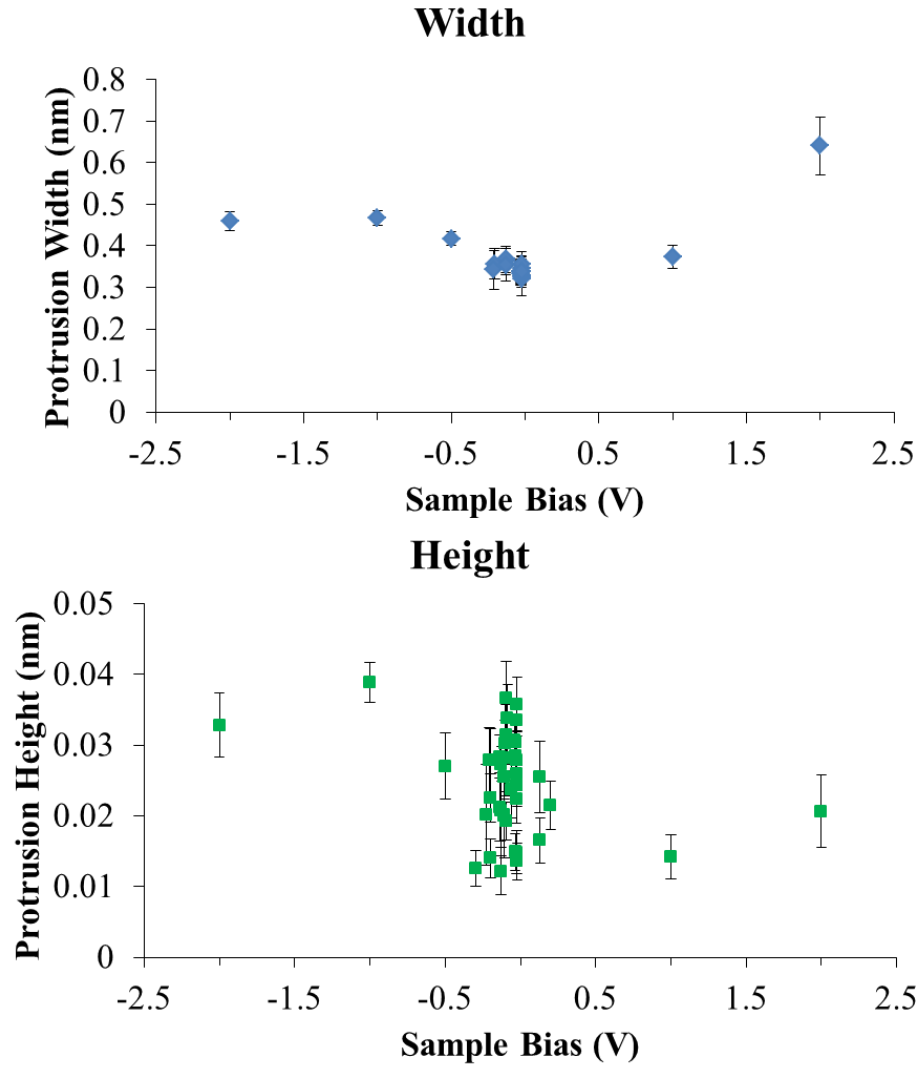


Figure A9. Width and height of S atom protrusions as a function of sample bias. Each point represents the average in a single image; the error bars represent the standard deviation.

References

1. Vericat, C.; Vela, M. E.; Benitez, G. A.; Carro, P.; Salvarezza, R. C., "Self-Assembled Monolayers of Thiols and Dithiols on Gold: New Challenges for a Well-Known System". *Chem. Soc. Rev.* **2010**, *39*, 1805-1834.
2. Fan, Y.; Long, Y. F.; Li, Y. F., "A Sensitive Resonance Light Scattering Spectrometry of Trace Hg^{2+} with Sulfur Ion Modified Gold Nanoparticles". *Anal. Chim. Acta* **2009**, *653*, 207-211.
3. Pensa, E.; Cortes, E.; Corthey, G.; Carro, P.; Vericat, C.; Fonticelli, M. H.; Benitez, G.; Rubert, A. A.; Salvarezza, R. C., "The Chemistry of the Sulfur-Gold Interface: In Search of a Unified Model". *Acc. Chem. Res.* **2012**, *45*, 1183-1192.
4. Bailie, J. E.; Hutchings, G. J., "Promotion by Sulfur of Gold Catalysts for Crotyl Alcohol Formation from Crotonaldehyde Hydrogenation". *Chem. Comm.* **1999**, 2151-2152.
5. Yu, M.; Ascolani, H.; Zampieri, G.; Woodruff, D. P.; Satterley, C. J.; Jones, R. G.; Dhanak, V. R., "The Structure of Atomic Sulfur Phases on Au(111)". *J. Phys. Chem. C* **2007**, *111*, 10904-10914.
6. McGuirk, G. M.; Shin, H.; Caragiu, M.; Ash, S.; Bandyopadhyay, P. K.; Prince, R. H.; Diehl, R. D., "Au(111) Surface Structures Induced by Adsorption: LEED I(E) Analysis of (1 X 1) and (5 X 5) Au(111)-S Phases". *Surf. Sci.* **2013**, *610*, 42-47.
7. Biener, M. M.; Biener, J.; Friend, C. M., "Sulfur-Induced Mobilization of Au Surface Atoms on Au(111) Studied by Real-Time STM". *Surf. Sci.* **2007**, *601*, 1659-1667.
8. Lustemberg, P. G.; Vericat, C.; Benitez, G. A.; Vela, M. E.; Tognalli, N.; Fainstein, A.; Martiarena, M. L.; Salvarezza, R. C., "Spontaneously Formed Sulfur Adlayers on Gold in

- Electrolyte Solutions: Adsorbed Sulfur or Gold Sulfide?". *J. Phys. Chem. C* **2008**, *112*, 11394-11402.
9. Gao, X.; Zhang, Y.; Weaver, M. J., "Observing Surface Chemical Transformations by Atomic-Resolution Scanning Tunneling Microscopy: Sulfide Electro-Oxidation on Au(111)". *J. Phys. Chem.* **1992**, *92*, 4156-4159.
10. Vericat, C.; Vela, M. E.; Andreasen, G.; Salvarezza, R. C.; Vazquez, L.; Martin-Gago, J. A., "Sulfur-Substrate Interactions in Spontaneously Formed Sulfur Adlayers on Au(111)". *Langmuir* **2001**, *17*, 4919-4924.
11. Rodriguez, J. A.; Dvorak, J.; Jirsak, T.; Liu, G.; Hrbek, J.; Aray, Y.; Gonzalez, C., "Coverage Effects and the Nature of the Metal-Sulfur Bond in S/Au(111): High-Resolution Photoemission and Density-Functional Studies". *J. Am. Chem. Soc.* **2003**, *125*, 276-285.
12. Hernandez-Tamargo, C. E.; Montero-Alejo, A. L.; Pujals, D. C.; Mikosch, H.; Hernandez, M. P., "Sulfur Dimers Adsorbed on Au(111) as Building Blocks for Sulfur Octomers Formation: A Density Functional Study". *J. Chem. Phys.* **2014**, *141*, 044713.
13. Koczkur, K. M.; A.Houmam, "Thiobis(Hexamethyldisilazane) as a New Precursor for the Deposition of Sulfur on Gold: A One-Step Concerted Adsorption Process". *Surf. Sci.* **2014**, *624*, 44-51.
14. Abufager, P. N.; Zampieri, G.; Reuter, K.; Martiarena, M. L.; Busnengo, H. F., "Long-Range Periodicity of S/Au(111) Structures at Low and Intermediate Coverages". *J. Phys. Chem. C* **2014**, *118*, 290-297.
15. Kurokawa, S.; Miyawaki, Y.; Sakai, A., "Scanning Tunneling Microscopy Observation of Sulfur Adsorbates on Au(111) at Liquid Nitrogen Temperature". *Jpn. J. Appl. Phys.* **2009**, *48*, 08JB12.

16. Russell, S. M.; Kim, Y.; Liu, D.-J.; Evans, J. W.; Thiel, P. A., "Structure, Formation, and Equilibration of Ensembles of Ag-S Complexes on an Ag Surface". *J. Chem. Phys.* **2013**, *138*, 071101.
17. Walen, H.; Liu, D.-J.; Oh, J.; Lim, H.; Evans, J. W.; Aikens, C.; Kim, Y.; Thiel, P. A., "Cu₂S₃ Complex on Cu(111) as a Candidate for Mass Transport Enhancement". *Phys. Rev. B* **2015**, *91*, 045426.
18. Wagner, C., "Investigations on Silver Sulfide". *J. Chem. Phys.* **1953**, *21*, 1819-1827.
19. Kresse, G.; Furthmüller, J., "Efficiency of Ab-Initio Total Energy Calculations for Metals and Semiconductors Using a Plane-Wave Basis Set". *Comput. Mater. Sci.* **1996**, *6*, 15-50.
20. Perdew, J. P.; Burke, K.; Ernzerhof, M., "Generalized Gradient Approximation Made Simple". *Phys. Rev. Lett.* **1996**, *77*, 3865-3868.
21. Liu, D.-J.; Walen, H.; Oh, J.; Lim, H.; Evans, J. W.; Kim, Y.; Thiel, P. A., "Search for the Structure of a Sulfur-Induced Reconstruction on Cu(111)". *J. Phys. Chem. C* **2014**, *118*, 29218-29223.
22. Russell, S. M.; Liu, D.-J.; Kawai, M.; Kim, Y.; Thiel, P. A., "Low-Temperature Adsorption of H₂S on Ag(111)". *J. Chem. Phys.* **2010**, *133*, 124705.
23. Liu, D.-J., "Density Functional Analysis of Key Energetics in Metal Homoepitaxy: Quantum Size Effects in Periodic Slab Calculations". *Phys. Rev. B* **2010**, *81*, 035415.
24. Tersoff, J.; Hamann, D. R., "Theory and Application for the Scanning Tunneling Microscope". *Phys. Rev. Lett.* **1983**, *50*, 1998-2001.

25. Barth, J. V.; Brune, H.; Ertl, G.; Behm, R. J., "Scanning Tunneling Microscopy Observations on the Reconstructed Au(111) Surface: Atomic Structure, Long-Range Superstructure, Rotational Domains, and Surface Defects". *Phys. Rev B* **1990**, *42*, 9307-9318.
26. Wöll, C.; Chiang, S.; Wilson, R. J.; Lippel, P. H., "Determination of Atom Positions at Stacking-Fault Dislocations on Au(111) by Scanning Tunneling Microscopy". *Phys. Rev. B* **1989**, *39*, 7988-7991.
27. Harten, U.; Lahee, A. M.; Toennies, J. P.; Wöll, C., "Observation of a Soliton Reconstruction of Au(111) by High-Resolution Helium-Atom Diffraction". *Phys. Rev. Lett.* **1985**, *54*, 2619-2622.
28. Shen, M.; Liu, D.-J.; Jenks, C. J.; Thiel, P. A., "Novel Self-Organized Structure of a Ag-S Complex on the Ag(111) Surface Below Room Temperature". *J. Phys. Chem. C* **2008**, *112*, 4281-4290.
29. Bomermann, J.; Huck, M.; Kuntze, J.; Rauch, T.; Speller, S.; Heiland, W., "An STM, AES and LEED Study of the Segregated Sulfur on Pd(111)". *Surf. Sci.* **1996**, *357-358*, 849-854.
30. Schlaup, C.; Friebel, D.; Broekmann, P.; Wandelt, K., "Potential Dependent Adlayer Structures of a Sulfur-Covered Au(111) Electrode in Alkaline Solution: An in situ STM Study". *Surf. Sci.* **2008**, *602*, 864-870.
31. Wahlström, E.; Ekvall, I.; Kihlgren, T.; Olin, H.; Lindgren, S. A.; Wallden, L., "Low-Temperature Structure of S/Cu(111)". *Phys. Rev. B* **2001**, *64*, 155406.
32. Wahlström, E.; Ekvall, I.; Olin, H.; Lindgren, S. A.; Wallden, L., "Observation of Ordered Structures for S/Cu(111) at Low Temperature and Coverage". *Phys. Rev. B* **1999**, *60*, 10699.

33. Henkelman, G.; Jonsson, H., "Improved Tangent Estimate in the Nudged Elastic Band Method for Finding Minimum Energy Paths and Saddle Points". *J. Chem. Phys.* **2000**, *113*, 9978-9985.
34. Einstein, T. L.; Sathiyarayanan, R., Multisite Interactions in Lattice-Gas Models. In *Nanophenomena at Surfaces: Fundamentals of Exotic Condensed Matter Properties*, Michailov, M., Ed. Springer-Verlag Berlin: Berlin, 2011; Vol. 47, pp 19-37.
35. Einstein, T. L., "Multisite Lateral Interactions and Their Consequences". *Langmuir* **1991**, *7*, 2520-2527.
36. Ceder, G.; Dreysse, H.; Defontaine, D., "Triplet Interactions and the C(2x2) Overlayer Phase Diagram". *Physica A* **1993**, *193*, 105-113.
37. Stampfl, C.; Kreuzer, H. J.; Payne, S. H.; Pfnur, H.; Scheffler, M., "First-Principles Theory of Surface Thermodynamics and Kinetics". *Phys. Rev. Lett.* **1999**, *83*, 2993-2996.
38. Borg, M.; Stampfl, C.; Mikkelsen, A.; Gustafson, J.; Lundgren, E.; Scheffler, M.; Andersen, J. N., "Density of Configurational States from First-Principles Calculations: The Phase Diagram of Al-Na Surface Alloys". *Chem. Phys. Chem.* **2005**, *6*, 1923-1928.
39. Stasevich, T. J.; Einstein, T. L.; Stolbov, S., "Extended Lattice Gas Interactions of Cu on Cu(111) and Cu(001): Ab Initio Evaluation and Implications". *Phys. Rev. B* **2006**, *73*, 115426.
40. Zhang, Y.; Blum, V.; Reuter, K., "Accuracy of First-Principles Lateral Interactions: Oxygen at Pd(100)". *Phys. Rev B* **2007**, *75*, 235406.
41. Stoehr, M.; Podloucky, R.; Mueller, S., "Ab Initio Phase Diagram of Oxygen Adsorption on W(110)". *J. Phys.: Condens. Matter* **2009**, *21*.

42. Piccinin, S., et al., "Alloy Catalyst in a Reactive Environment: The Example of Ag-Cu Particles for Ethylene Epoxidation". *Phys Rev. Lett.* **2010**, *104*, 035503.
43. Piccinin, S.; Stampfl, C., "Predicting Order-Disorder Phase Transitions of O/Pd(111) from Ab Initio Wang-Landau Monte Carlo Calculations". *Phys. Rev. B* **2010**, *81*, 155427.
44. Schmidt, D. J.; Chen, W.; Wolverton, C.; Schneider, W. F., "Performance of Cluster Expansions of Coverage-Dependent Adsorption of Atomic Oxygen on Pt(111)". *J. Chem. Theory Comput.* **2012**, *8*, 264-273.
45. Han, Y.; Liu, D.-J.; Evans, J. W., "Real-Time Ab Initio KMC Simulation of the Self-Assembly and Sintering of Bimetallic Epitaxial Nanoclusters: Au + Ag on Ag(100)". *Nano Lett.* **2014**, *14*, 4646-4652.
46. Herder, L. M.; Bray, J. M.; Schneider, W. F., "Comparison of Cluster Expansion Fitting Algorithms for Interactions at Surfaces". *Surf. Sci.* **2015**, *640*, 104-111.
47. Osterlund, L.; Pedersen, M. O.; Stensgaard, I.; Laegsgaard, E.; Besenbacher, F., "Quantitative Determination of Adsorbate-Adsorbate Interactions". *Phys. Rev. Lett.* **1999**, *83*, 4812-4815.
48. Koh, S. J.; Ehrlich, G., "Pair- and Many-Atom Interactions in the Cohesion of Surface Clusters: Pd-X and Ir-X on W(110)". *Phys. Rev. B* **1999**, *60*, 5981-5990.
49. Liu, S.; Bönig, L.; Detch, J.; Metiu, H., "Submonolayer Growth with Repulsive Impurities: Island Density Scaling with Anomalous Diffusion". *Phys. Rev. Lett* **1995**, *74*, 4495.
50. Hyldgaard, P.; Persson, M., "Long-Ranged Adsorbate-Adsorbate Interactions Mediated by a Surface-State Band". *J. Phys.: Condens. Matter* **2000**, *12*, L13-L19.

51. Berland, K.; Einstein, T. L.; Hyldgaard, P., "Response of the Shockley Surface State to an External Electrical Field: A Density-Functional Theory Study of Cu(111)". *Phys. Rev. B* **2012**, 85, 035427.

CHAPTER VI

**LONG-RANGE DISPLACIVE RECONSTRUCTION OF AU(110)
TRIGGERED BY LOW COVERAGE OF SULFUR**Holly Walen,^a Da-Jiang Liu,^b Junepyo Oh,^c Hyun Jin Yang,^c Yousoo Kim,^cand P. A. Thiel^{a,b,d}*A paper published in Journal of Physical Chemistry C[†]***Abstract**

We propose a new model for the $c(4 \times 2)$ of sulfur adsorbed on Au(110). This is a reconstruction achieved by short-range rearrangements of Au atoms that create a pseudo-fourfold-hollow (p4fh) site for adsorbed sulfur. The model is based partly upon the agreement between experimental STM images and those predicted from DFT, both for $c(4 \times 2)$ domains and at a boundary between two domains. It is also based upon the stability of this structure in DFT, where it is not only favored over the chemisorbed phase at its ideal coverage of 0.25 ML, but also at lower coverage (at $T = 0$ K). This is compatible with the fact that in experiments, it coexists with 0.06 ± 0.03 ML of sulfur chemisorbed on the (1×2) surface. The relative stability of the $c(4 \times 2)$ phase at 0.25 ML has been verified for a variety

Departments of ^aChemistry, ^dMaterials Science & Engineering, Iowa State University, Ames, Iowa 50011 USA

^bAmes Laboratory of the USDOE, Ames, Iowa 50011 USA

^cRIKEN Surface and Interface Science Laboratory, Wako, Saitama 351-0198, Japan

[†]*J. Phys. Chem. C* **119**(36) 21000-21010 (2015).

of functionals in DFT. In the chemisorbed phase, sulfur adsorbs at a pseudo-threefold-hollow (p3fh) site near the tops of rows in the (1x2) reconstruction. This is similar to the fcc site on an extended (111) surface. Sulfur causes a slight separation between the two topmost Au atoms, which is apparent both in STM images and in DFT-optimized structures. The second-most stable site is also a p3fh site, similar to an hcp site. DFT is used to construct a simple lattice gas model based on pairs of excluded sites. The set of excluded sites is in good qualitative agreement with our STM data. From DFT, the diffusion barrier of a sulfur atom is 0.61 eV parallel to the Au row, and 0.78 eV perpendicular to the Au row. For the two components of the perpendicular diffusion path, i.e. crossing a trough and hopping over a row, the former is considerably more difficult than the latter.

1. Introduction

There are many motivations to understand the interaction of sulfur with coinage metal surfaces, particularly when those metals are in the form of nanoparticles. The coinage metals can be useful as nanoparticles because of their plasmonic and catalytic properties, oxidation-resistance, and (in the case of Au) unique suitability as platforms for self-assembled monolayers.¹ Within the context of these properties, sulfur is an important adsorbate. In self-assembled monolayers of alkanethiols on Au, S anchors the molecular scaffold to the surface, and so Au-S chemistry is critical.² Also, S can strongly inhibit or accelerate transport of metals on Cu, Ag, and Au surfaces, which in turn can affect the stability of nanostructures. For instance, sulfur can be a capping agent and anti-coagulant for Au nanoparticles.³ In other circumstances, it can accelerate coarsening of surface-supported Cu and Ag nanoparticles via the formation of mobile metal-S complexes.⁴

We are conducting a systematic survey of the interaction of sulfur with coinage metal surfaces, including Au surfaces, under conditions of ultra-low coverage and low temperature. This regime is essentially uncharted, perhaps because the default expectation is that one will simply find isolated chemisorbed adatoms. On the contrary, this regime is rich with unexpected phenomena, including new ordered structures⁵ and stoichiometric surface-metal complexes.⁶⁻⁷

In this paper, we report an exploration of the interaction of sulfur with Au(110). No complexes form in this system (under the conditions of our experiments), but we find an intriguing condensation of sulfur adatoms at low coverage into a surface reconstruction. This is the first time this system has been characterized using direct imaging at the atomic scale, which in this case is achieved with scanning tunneling microscopy (STM). Interpretation of the experimental data relies heavily on theoretical analysis, primarily density functional theory (DFT).

Bulk-terminated Au(110) is a row-and-trough structure. However, this (1x1) surface reconstructs into a (1x2) structure in which every other row is missing. This exposes deeper troughs with sides that can be considered (111) microfacets.⁸⁻¹¹ Adsorption of sulfur on this surface has been studied previously, although the methods of producing the surface differ considerably. This is because exposure to gas-phase H₂S is a convenient and conventional route to sulfur adsorption on most surfaces, but for Au(110) the sticking coefficient of H₂S is very low. To circumvent this, conditions of relatively high H₂S pressure¹² have been used, and also low-temperature adsorption followed by electron beam irradiation.¹³ Exposure to S₂(g) via an electrochemical cell has also been used,¹⁴ and it is the method of choice in this

work. We review the results of past studies briefly now, though comparisons must be taken with some caution because of this wide variation in experimental conditions.

Kostelitz *et al.*¹² exposed the surface to H₂S at 10⁻³ Torr. They constructed a phase diagram, using radioactive tracer ³⁵S to calibrate absolute sulfur coverages (θ_S). Reversible phase boundaries were identified using low-energy electron diffraction (LEED). At 300 K, they identified a narrow coverage range of (1x2) phase (i.e. sulfur chemisorbed on the intrinsic metal surface), a broad coexistence range of (1x2) and c(4x2) phases, and then a broad region of c(4x2) phase alone. They reported sulfur coverage in absolute terms of g/cm². If those values are converted to absolute monolayers (ML) relative to the unreconstructed (1x1), the (1x2) phase existed alone up to 0.08 ML, and coexisted with the c(4x2) phase up to 0.36 ML (at 300 K). The c(4x2) phase then existed alone from 0.36 to 0.54 ML, and was replaced by other structures at higher coverage. Kostelitz *et al.*¹² proposed that the c(4x2) structure was a coincidence lattice of adsorbed sulfur atoms (S_{ad}) on the (1x1) with ideal coverage 0.75 ML, even though the c(4x2) completely disappeared well before that coverage.

Jaffey *et al.*¹³ studied this system using temperature programmed desorption (TPD) and AES. They prepared the sample using H₂S exposure at 105 K and electron-beam irradiation. Like Kostelitz *et al.*, they observed three stages of order via LEED, as a function of increasing sulfur coverage: (1x2) alone, coexistent (1x2) and c(4x2), and finally pure c(4x2).

Krasnikov *et al.*¹⁴ used an electrochemical source to deposit S at 300 K. After extensive annealing at elevated temperature, which was accompanied by loss of S_{ad} via desorption, they observed new LEED patterns corresponding to p(4x2) and c(4x4) structures,

with coverages of 0.13 ML and 0.2 ML, respectively. The intensity-voltage (IV) curves of the p(4x2) structure were nearly identical to those of the clean (1x2) surface, leading Krasnikov *et al.* to conclude that this was a chemisorbed phase on the (1x2) surface. They suggested that S adsorbs in sites at the bottom of the troughs between Au rows.

Most recently, Lahti *et al.*¹⁵ re-analyzed the p(4x2) structure using DFT and LEED. Like Krasnikov *et al.*, they concluded that it is a chemisorbed phase, but unlike Krasnikov *et al.*, they determined that S adsorbs at a pseudo-threefold-hollow (p3fh) site on the side wall of the trough.

In summary, a variety of phases have been reported for S_{ad} on Au(110). At room temperature, the phases are (1x2) and c(4x2), but neither has been identified or explored with STM or DFT. The accepted model for the c(4x2) phase has an ideal coverage of 0.75 ML, but experimental data appear more compatible with significantly lower values.¹²

In this paper, we directly observe a disordered chemisorbed phase on the (1x2) reconstruction. We also observe and characterize a c(4x2) phase that coexists with low coverages of S_{ad} in the chemisorbed phase. This is compatible with the two earlier reports¹²⁻¹³ of (1x2) and c(4x2) phase coexistence. However, we propose a new model for the c(4x2) phase in which the ideal sulfur coverage is 0.25 ML. It is a reconstruction that is displacive, i.e. one in which the density of Au adatoms is conserved. Consequently, the chemisorbed (1x2) phase can transform to the c(4x2) phase via local Au rearrangement. The c(4x2) phase exists as large and near-perfect domains, without the small islands that would be the normal remnants of a nucleation and growth process.

This paper is organized as follows. Section 2 describes the experimental and computational methods. Section 3 presents the results, organized around individual surface

phases and features. Section 4 discusses the results and places them in the context of existing literature.

2. Experimental and Computational Details

2.1 Experimental Description

These experiments were carried out with the same equipment and techniques, as used in our previous studies of S on Au(111),⁵ S on Ag(111)¹⁶ and S on Cu(111).^{6,17} In short, the experiments were performed at RIKEN Surface and Interface Laboratory in Wako, Japan. The sample was imaged with STM at 5 K in ultrahigh vacuum (pressure $< 6.0 \times 10^{-11}$ Torr). An electrochemical cell served as the S source *in situ*.¹⁸ Coverage was determined from STM images as described below.

During S deposition the sample was held at 300 K, then cooled to 5 K for measurement. Cooling and thermal stabilization at 5 K took place in 50 minutes or less. After initial STM measurements, the sample was warmed back to room temperature and re-cooled to 5 K, with no effect on the observations at 5 K. During imaging, there was no evidence of tip perturbation or surface diffusion; surface structures were entirely static. For most images after sulfur adsorption, the tunneling current (I) was 1.00 to 1.80 nA, and the sample bias (V_s) was -1.0 to +1.0 V. Exact tunneling conditions are provided in the Appendix.

The single crystal Au(110) sample was cleaned via several cycles of Ar⁺ sputtering (10-15 μ A, 1.55 kV, 10 min) and annealing (735 K, 10 min).

The accuracy of STM-derived spatial dimensions was checked by measuring a_1 and $2a_2$, which are the atomic separation of surface Au atoms in the clean (1x2) reconstruction along the $[1\bar{1}0]$ direction (parallel to the close-packed rows) and $[001]$ direction

(perpendicular to the rows), respectively. [See Fig. 1(a).] These experimental values were 0.30 ± 0.01 nm and 0.82 ± 0.02 nm, respectively. Within stated uncertainties, these equal the bulk parameters¹⁹ of 0.288 nm and 0.816 nm, respectively. The measured height of monoatomic steps on Au(110)-(1x2) was 0.13 ± 0.01 nm, in agreement with the bulk interplanar spacing of 0.144 nm.

Two types of sulfur coverage θ_S were determined: coverage on the (1x2) reconstructed areas, θ_S^{1x2} , and total coverage, θ_S^{tot} . The former was obtained from the number of bright dots in STM images per unit area on the (1x2) structure, divided by the number of Au atoms per unit area in a bulk (110) plane. When the c(4x2) was present, its contribution to θ_S^{tot} was determined by measuring its fractional area and assigning it a sulfur coverage of 0.25 ML, as justified in Sec. 3. Our experiments spanned the range $0.01 \leq \theta_S^{1x2} \leq 0.09$ and $0.01 \leq \theta_S^{\text{tot}} \leq 0.17$.

2.2 Computational Description

To assess relative stabilities of surface structures, we used the VASP code with the projector-augmented wave (PAW) method²⁰ and the PBE functional.²¹ Details have been given elsewhere.^{7, 22} The cutoff energy for the plane-wave basis set was 280 eV. For each supercell, we used a minimal k-points grid that corresponded to the (12x8x1) grid for the primitive unit cell as closely as possible. Denser k-points grids that corresponded to the (24x17x1) grid were used in select cases to achieve higher precision.

The quantum size effect (QSE) can be strong in noble metals, particularly for (110) surfaces, leading to oscillations in energetics with slab thickness.^{9, 23} Precise estimation of energetics (within 8 meV or better) can be achieved by averaging over slab thicknesses.²⁴ In

this work, chemical potentials or formation energies were calculated using a range of slab thickness $L = 7$ to 12. Here we used thicker slabs than in previous work with Au(111)⁵ because of the strong QSE. Energy uncertainties were derived from variations due to slab thicknesses,²⁴ and are denoted in parentheses. For example, 2.41(8) eV can be read as 2.41 ± 0.08 eV.

Simulated STM images were generated with $L = 5$, using the Tersoff-Hamann method. Unless noted otherwise, the images were based upon integration over an energy window bracketing E_F by ± 0.1 eV. In all depictions of DFT-optimized configurations, or DFT-based STM simulations, the $[1\bar{1}0]$ direction is vertical and the $[001]$ direction is horizontal, which is very close to the orientation of the STM images as shown in Fig. 1.²⁵

3. Experimental and Computational Results

3.1 Overview

Typical images of the clean Au(110)-(1x2) surface are shown in Fig. 1 at three magnifications. The bright, nearly-vertical rows in the topographic images are the topmost rows of Au in the reconstruction. The result of sulfur adsorption on this surface is shown in Fig. 2, with increasing sulfur coverage. Sulfur adsorption produces a phase consisting of bright spots on the (1x2) regions at low coverage, as well as a distinctive, large-scale phase at higher coverage. The first of these is the chemisorbed phase. The second is the c(4x2) phase, based on the lattice parameter and orientation of its features. These phases are discussed individually below, where the experimental interpretation relies heavily upon DFT.

In DFT, we have made an extensive survey of many possible configurations and reconstructions. In the following text, only the most salient results from this broad search are

given, i.e. those most important for interpreting the experimental data. Regarding energetics, the figure of merit is the chemical potential, μ_S , of an Au_mS_n species with respect to the clean, *reconstructed* (1x2) Au surface (μ_S^r) or with respect to the clean, *unreconstructed* (1x1) Au surface (μ_S^u). In either case, if $m=0$, μ_S corresponds to the adsorption energy of S_{ad} . Details about the definition and implementation of μ_S are provided in the Appendix. Notably, DFT yields values of μ_S at $T = 0$ K.

3.2 Chemisorbed Phase: Sulfur on the (1x2) Au Reconstructed Surface

Adsorption site of S_{ad} . A close-up image of the chemisorbed phase at relatively low coverage, 0.01 ML, is shown in Fig. 3(a). Bright dots appear to be randomly located on the (1x2) surface. Each spot is close to, but slightly off-center from, the top row of Au atoms.

We assign the bright spots as individual sulfur adatoms (S_{ad}), based upon analysis of DFT energetics and corresponding simulated STM images.

For S_{ad} on the (1x2) surface, DFT indicates that S binds to two Au atoms in the protruding row, and to a third Au atom along the side of the trough, as shown in Fig. 3(b). This p3fh site is consistent with the off-center location of the bright spots in STM. It is the same site identified by Lahti *et al.*¹⁵ From DFT, the second-most-stable site on the (1x2) surface has S_{ad} coordinated to one Au atom in the top of the row, and two Au atoms along the side of the trough. Hence, this is also a p3fh site, but it involves a different combination of Au atoms. [This site was overlooked by Lahti *et al.*¹⁵ in their ranking of adsorption site energetics on the basis of DFT. The remainder of their ranking is consistent with our calculations.] The second p3fh site is important because it plays a role in diffusion, discussed below.

Our STM and DFT also provide new structural information. Each S_{ad} spot is accompanied by an indentation in the row of Au atoms, which makes the Au rows appear slightly nonlinear. The arrow in Fig. 3(a) points to one such indentation. DFT indicates that this is due to a separation between pairs of top Au atoms adjacent to each S_{ad} , apparent in Fig. 3(b). These pairs of Au atoms are 14% further apart than in the bulk. The indentation is reproduced well in the simulated STM image of Fig. 3(c).

Rarely, we observe other types of features on the (1x2), such as clusters of very bright spots. An example is encircled in Fig. 2(c). However, these are infrequent and irregular in shape. In the coverage range studied herein, individual S_{ad} is certainly the dominant motif on the (1x2) regions.

Characteristics of S_{ad} in STM. Most of our STM experiments are conducted in a range of tunneling parameters from -1.0 V to +1.0 V and 1.0 nA to 1.8 nA. Within this range (and even down to $V_s = -3.0$ V), there is no systematic trend in the area (A) or height (ΔH) of the S_{ad} features. The values are $A = 0.15 \pm 0.03 \text{ nm}^2$ and $\Delta H = 0.039 \pm 0.001 \text{ nm}$. For both quantities, the highest point in the row of Au atoms is defined as baseline. The value of ΔH is at least a factor of 2 lower than the vertical internuclear separation between S_{ad} and the topmost Au atom, which is 0.096-0.114 nm from DFT (depending upon exactly which Au atom in the adjacent row is the reference point). This follows a pattern established in previous STM+DFT studies of S/Ag(111),²⁶ S/Au(111),⁵ and S/Cu(111).^{6, 17} Apparent heights in STM of S_{ad} , S-containing complexes, and even S-induced reconstructions are smaller than atomic dimensions. At present this effect is not understood.

Step edges. Steps of the chemisorbed phase contain some S_{ad} , but the concentration is about the same as on the terraces. In other words, the steps are not preferentially decorated

with S_{ad} . This is true both for steps parallel to the atomic rows and those cutting across the rows. Evidence is given in Fig. 4. This contrasts the (111) surface of Au, as well as Cu and Ag, where there is strong preferential adsorption at steps.

The reason for this relative inertness is that steps on the reconstructed (110) do not offer adsorption sites that differ (locally) from sites on the terraces. Steps parallel to the rows present a (111) microfacet, like the (111) microfacets of the (1x2) reconstructed terraces, but deeper.²⁷⁻²⁸ These can accommodate S_{ad} at p3fh sites, like the two adatoms on the long step edge in Fig. 4(a). Steps that cut across rows, i.e. terminated rows, expose sites that are very similar to the rectangular sites at the bottoms of troughs. In the experimental STM images, the ends of rows are usually undecorated, as in Fig. 4(c), which is consistent with the fact that the bottom of a trough is not a favored adsorption site. However, the rows occasionally terminate in large, bright features that could be localized S-induced reconstructions or complexes. An example is visible in Fig. 2(d).

Adsorption energy, interactions, and coverage effects. Figure 5 shows μ_S^f vs. $1/\theta_S$, for supercells spanning coverages from 0.06 to 0.50 ML. (In Fig. 5, $1/\theta_S$ is the preferred abscissa because it is the thermodynamic conjugate to μ_S .²⁹) The linear segments connect a series of simple structures, all with S_{ad} in the same (optimized) adsorption site on the (1x2) surface, and one S_{ad} per supercell. We define this series of linear segments as the baseline energetics, against which other, more complex structures can be compared. Figure 5 shows that the adsorption energy of these configurations depends only weakly on sulfur coverage between 0.06 and 0.25 ML. This means that the value $\mu_S^f = -1.320(8)$ eV, at lowest coverage, is a good approximation to the value in the limit of zero coverage.

The value $\mu_S^r = -1.320(8)$ eV is significantly higher than the value -1.476 eV reported by Lahti *et al.*¹⁵ An examination of differences between the two calculations, and their effects on μ_S^r , reveals that the main source of discrepancy is the energy of $S_{2,g}$, $E(S_{2,g})$. This energy is a reference point for μ_S (cf. Appendix). We use spin-polarized DFT to determine this quantity, whereas Lahti *et al.* used non-spin-polarized DFT. The ground state of a S_2 molecule (as in O_2) is the triplet state with two unpaired electrons. From DFT, the singlet state is 0.54 eV (or 0.27 eV per S atom) less stable than the triplet state. On the other hand, for dissociated S atoms adsorbed on the surface, the ground state is generally not spin-polarized. Thus, it is important to take into account the different spin properties when calculating the absolute adsorption energy of S.

Information about S_{ad} - S_{ad} interactions can be extracted from DFT calculations of the energetics of suitably-selected adlayer configurations. Some relevant configurations are shown in Fig. 6 with associated values of μ_S^r . We regard Fig. 6(a) as a benchmark configuration that provides the adsorption energy or chemical potential when there are no significant interactions between S_{ad} . The configurations in Fig. 6(b) and 6(c) have μ_S^r that are very close to 6(a), while Fig. 6(d), 6(e), and 6(f) are about 20 meV less stable. The configurations in Fig. 6(g-i) are much less stable, with μ_S^r at least 50 meV higher than the benchmark.

We have used this information to construct a rudimentary lattice-gas (LG) model as follows. All configurations with $\mu_S^r > -1.28$ eV (about 50 meV above the baseline value at $\theta_S^{1 \times 2} = 1/16$ ML) are considered to incorporate strongly repulsive pairwise interactions. This leads to a set of exclusion rules, in which the pairs of sites shown by arrows in Fig. 6(j)

cannot be occupied simultaneously. These pairs are described as 1st and 3rd nearest neighbors (NN) *parallel to a row* (vertical arrows), and 1st, 2nd, and 3rd NN *crossing a row* (horizontal and diagonal arrows). Notably, 2nd NNs *parallel to a row* are still allowed.

Turning now to experiment, STM images are shown in Fig. 7(a-b) and 7(d-f) for chemisorbed phase coverages of 0.01 to 0.09 ML. Above 0.03 ML, it becomes increasingly common to find pairs of S_{ad} located in 2nd NN sites along a row, or diagonally adjacent or directly adjacent across a trough. Occupation of all of these pairs of sites is compatible with the LG model, i.e. they are not excluded. Conversely, the excluded pairs, such as the 3rd NN pair parallel to a row, are not observed in experiment.

Monte Carlo simulations of the LG model, at 0.02 and 0.08 ML, are shown in Fig. 7(c) and Fig. 7(g), respectively. The simulated adlayer configurations are qualitatively compatible with the experimental observations. In particular, the simulation at 0.08 ML contains short chains of S_{ad} in 2nd NN sites parallel to rows. Similar chains are obvious in experimental data, especially in Fig. 7(f). In addition, both the model and the STM data show pairs of S_{ad} that are directly adjacent (facing) across troughs.

The DFT results in Fig. 6 can be modeled by a more sophisticated LG with finite pair-wise interactions. However, at this stage, there are no extensive DFT energetics to validate such a detailed model (i.e. to determine whether a systematic cluster expansion approach is necessary), nor enough STM data to compare with the results.

Diffusion barrier. We use the Nudged Elastic Band (NEB) method³⁰ to determine the diffusion pathways of S_{ad} between energetically-equivalent p3fh sites, and the associated potential energy surface.

In one path, S_{ad} moves parallel to the rows. The energy variation along this path is shown in Fig. 8(a). The adatom moves from the stable p3fh site, through an asymmetric transition state, to the metastable p3fh site discussed earlier. Averaging over $L = 5$ to 8, the diffusion barrier is $E_d = 0.605(8)$ eV.

In another path, S_{ad} moves perpendicular to the rows. This can be broken down into two parts. The first, motion over tops of rows, is shown in Fig. 8(b). In the transition state, S_{ad} is at the twofold bridge site atop the row, and $E_d = 0.50(1)$ eV. The second part, motion across troughs, is represented in Fig. 8(c). This diffusion path is complex, with more than one metastable state. The energy landscape is relatively flat when S_{ad} is close to the middle of the trough. For this path, $E_d = 0.78(1)$ eV.

From this information, diffusion parallel to the rows has a significantly lower barrier than diffusion perpendicular to the rows. However, local hopping of S_{ad} across the top of a row has an even lower barrier, and hence is most easily activated. Consequently, motion parallel to the rows will be accompanied by hopping across the top of the row, resulting in a rough zig-zag motion—a combination of Fig. 8(a) and Fig. 8(b). While cross-row hopping cannot contribute directly to long-range transport parallel to rows, it may contribute to local equilibration of the adlayer.

If the hop rate is 0.1 s^{-1} at the temperature (T_f) where S_{ad} becomes effectively immobilized, and the pre-exponential factor is $10^{12 \pm 1} \text{ s}^{-1}$, then $E_d = 0.605$ eV means that $T_f = 220 \pm 20$ K for diffusion along the rows. Similarly, $E_d = 0.78$ eV yields $T_f = 280 \pm 20$ K for diffusion perpendicular to the rows. This rough estimate of T_f shows that immobilization takes place well above the temperature of observation, 5 K, but below the temperature of adsorption, 300 K.

3.3 c(4x2) Phase

Experimental observations. The c(4x2) phase, shown in Fig. 2(d-f), coexists with the chemisorbed phase when the coverage on the (1x2) regions exceeds 0.04 ML. The c(4x2) always exists in the form of large, near-perfect domains. This is illustrated by the regions of c(4x2) phase shown in Fig. 2(d-f), and by the even larger regions—up to 30 x 30 nm²—shown in Fig. 9(a-b). We never find smaller c(4x2) islands that would be the natural signature of a nucleation and growth process. The degree of perfection is illustrated by the high-magnification images in Fig. 9(c-d).

The sulfur coverage on the (1x2) regions is 0.06 ± 0.03 ML when c(4x2) domains are present. Thus, the c(4x2) phase coexists with a low coverage of sulfur in the chemisorbed phase. Similarly, Kostelitz *et al.*¹² reported that the c(4x2) phase emerged at a low sulfur coverage of 0.08 ML at 300 K.

Model for the c(4x2) structure. We have carried out an extensive DFT-based search for structures that are both energetically-competitive with the chemisorbed phase at low coverage, and compatible with the observed STM images. Among these, the configuration shown in Fig. 10(a), with ideal coverage 0.25 ML, emerges as a uniquely strong candidate. With $\mu_S^r = -1.338(6)$ eV, represented by the open diamond in Fig. 5, it is more stable than the p(2x2) configuration of the chemisorbed phase, which is the benchmark at this coverage. It is even more stable than the p(4x4) configuration of the chemisorbed phase at a sulfur coverage of 0.06 ML, where $\mu_S^r = -1.320(8)$ eV at 0 K.

The simulated STM image in Fig. 10(b) is also a good match with experiment, shown at appropriate scale in Fig. 10(c). In this model, the bright spots are S_{ad}, following the usual trend in STM images with adsorbed sulfur.^{5-6, 22} In both the simulation and the experiment,

faint lines of intensity connect the bright spots along the diagonals but not along the horizontal directions. According to the model of Fig. 10(a), these faint lines correspond to lines of coplanar Au atoms (blue circles) that are diagonally, but not horizontally, contiguous. Their presence in both experiment and theory provides further evidence in favor of this model.

In the model in Fig. 10(a), S_{ad} occupy p4fh sites created by surface reconstruction. This reconstruction's relation to the (1x2) structure is shown in Fig. 11. Considering first only the surface without S_{ad} , the reconstruction in Fig. 11(b) forms when one of the rows of Au in the (1x2) second layer rises and the adjacent top row drops lower, so that both become coplanar. This new pair of top rows (blue) also shift laterally, covering a small sub-surface void visible in the side view of Fig. 11(b). From the top view, it can be seen that the pair of rows creates a strip of p4fh sites, so we call this the 'strip' reconstruction. A further rearrangement is shown in Fig. 11(c), where alternating pairs of atomic rows shift along the [001] direction. This creates a c(4x2) structure and preserves all of the coplanar p4fh sites. We call this the 'checkerboard' reconstruction.

The formation energies of the reconstructions in Fig. 11(b-c) are positive, consistent with their absence on real, clean surfaces. However, the checkerboard reconstruction, when decorated with S_{ad} in the p4fh sites (defined by the blue circles in Fig. 11(c)), is the observed c(4x2). Its stability derives, at least in part, from the presence of p4fh sites for sulfur adsorption, whereas only p3fh sites are available in the (1x2) reconstruction. By this argument alone, the strip reconstruction in Fig. 11(b) should also be stabilized by sulfur adsorption, but it is not. Its chemical potential when decorated with 0.25 ML of S_{ad} [forming a p(2x2)] is represented by the asterisk in Fig. 5. It is far less stable (by 0.128 eV) than the

c(4x2), and it is also less stable than S_{ad} on the (1x2) at the same coverage. At present the reason for its relative instability is unclear.

It is also informative to compare the S-decorated checkerboard structure with an alternate c(4x2) structure, also with 0.25 ML S_{ad} . Here, S_{ad} sits in the middle of four Au atoms in an unreconstructed (110) surface, as shown in Fig. 12(a). While the simulated STM image is reasonable, the value of μ_S^r is 0.704 eV higher than that of the checkerboard c(4x2). Closer inspection of the geometry shows that S_{ad} only bonds strongly with the Au atom directly beneath it—it is too far from the 4 Au atoms surrounding it.

To increase the Au bonding with S_{ad} , we move the 4 Au atoms closer together. The resulting DFT-optimized configuration is shown in Fig. 12(b). It is even less favorable energetically. Furthermore, the density of Au atoms is not the same as the (1x2) phase. However, the favored c(4x2) structure can be generated from the structure of Fig. 12(b), simply by adding two Au atoms in each space between the topmost Au rectangles, and allowing relaxation. The added Au atoms would correspond to the white circles in Fig. 10(a) or Fig. 11(c).

We have also evaluated candidates for the c(4x2) phase that have ideal coverages above 0.25 ML, although our exploration of this higher-coverage range is more limited. Several candidates are shown in Fig. 13, with ideal coverages of 1.0, 0.75, and 0.5 ML. At a given coverage, there is always a configuration that is more stable than the best c(4x2) configuration. For example, at 0.75 ML, Figure 13(d) is the DFT energy-optimized structure for the model proposed by Kosteliz *et al.*¹² The chemical potential is not competitive with the alternative model in Fig. 13(c) (nor with the baseline model at that coverage in Fig. 5).

Figure 13(f) is a modification of Kosteliz *et al.*'s model, but with 2 sulfur atoms instead of 3 in a c(4x2) unit cell. It is also not competitive.

Comparison of approximations in DFT. The stability of the c(4x2) reconstruction, relative to the chemisorbed phase, has been checked using different approximations in DFT. Table I shows μ_S^u for the chemisorbed p(2x2) and the c(4x2) reconstruction, both of which have coverage of 0.25 ML, for a variety of approximations. For reasons of efficiency and numerical accuracy, these values of μ_S were calculated with respect to the *unreconstructed* surface phase of Au. More specifically, the c(4x2) supercell does not allow for (1x2) missing-row reconstruction. Therefore, calculating μ_S with respect to the *reconstructed* surface must involve energetics from different supercells and this approach requires more stringent convergence conditions. Hence, it is more straightforward and more accurate to make these particular comparisons using μ_S^u rather than μ_S^r . (See Appendix also.)

It can be seen that the c(4x2) phase is more stable than the chemisorbed phase, for all approximations except the lowest-level one (LDA). In fact, the c(4x2) phase is most favored—by as much as 0.045 eV—when van der Waals interactions are included. We conclude that this result is quite robust.

TABLE I. Chemical potentials, μ_S^u , for the p(2x2) configuration of S/(1x2), and for the c(4x2) reconstruction. Both are illustrated in Fig. 5, at $\theta_S = 0.25$.

Surface	LDA	PBE ²¹	PBEsol ³¹	optPBE- vdW ³²⁻³³	optB88- vdW ³²⁻³³
Phase for which μ_S^u is given					
p(2x2)	-2.141(10)	-1.544(7)	-1.866(9)	-1.555(6)	-1.636(6)

TABLE I continued.

c(4x2)	-2.131(4)	-1.560(3)	-1.840(4)	-1.601(8)	-1.678(3)
difference ($\Delta\mu$)	-0.010	+0.016	+0.026	+0.046	+0.042
lattice constant, nm	0.4052	0.4158	0.4082	0.4182	0.4161

Domain boundary. The c(4x2) domains are notable for their high level of perfection. However, on one occasion we observed the boundary between two coplanar regions shown in Fig. 14(a). The two domains are displaced by $1a_1$ and $1.5a_2$. The boundary consists of linear segments at angles of 0° or $\pm 33 \pm 1^\circ$ to the $[1\bar{1}0]$. The segments parallel to the $[1\bar{1}0]$ have a zipper-like appearance. One is shown close up in Fig. 14(b). The model in Fig. 14(c) yields a simulated STM image (Fig. 14(d)) that compares well with experiment. In fact, the model is patched into the middle of the STM image in Fig. 14(e). The boundaries at $\pm 33^\circ$ are not equivalent, being either bright ($+33^\circ$, Fig. 14(f)) or dark (-33° , Fig. 14(i)). In each case, a structural model provides a reasonable match to the experimental data, as shown. We note that the images are dominated by the bright sulfur adatoms, so the positions of the Au atoms, especially in the $\pm 33^\circ$ boundaries, are not necessarily unique. Nonetheless, the compatibility of the proposed model for the c(4x2), with all of the experimental domain boundaries, supports the validity of this model.

4. Discussion

The most important result from this work is the observation and identification of the $c(4 \times 2)$ phase. Under the conditions of our experiments, it coexists with S_{ad} in a dilute, disordered, chemisorbed phase on the (1×2) reconstruction. Below, we discuss the chemisorbed phase first, then the $c(4 \times 2)$ phase, and the relation between the two.

The adsorption site in the chemisorbed phase is a p3fh site created by 2 Au atoms in the top of a row, and 1 Au atom on the side of the (111) microfacet (trough). Our work is the first observation of S_{ad} via STM in this phase. It reinforces an earlier identification of this same adsorption site in a $p(4 \times 2)$ chemisorbed phase that was produced under conditions significantly different from ours.¹⁵ Also, S_{ad} occupies the identical adsorption site in a $p1g1(2 \times 2)$ chemisorbed phase on $Ir(110)-(1 \times 2)$,³⁴⁻³⁵ a substrate which is structurally similar to $Au(110)-(1 \times 2)$. This stands in contrast to earlier conjectures, which placed S_{ad} at the bottom of the trough on (1×2) reconstructed surfaces,^{14, 34} analogous to its known site on (1×1) surfaces.³⁶⁻³⁹

The p3fh site adopted on the $Au(110)-(1 \times 2)$ surface is crystallographically similar to an fcc site on an extended (111) surface. We find that the next-most-stable site is a p3fh site equivalent to an hcp site. This order of site preferences, i.e. $fcc > hcp$, is the same as that on an extended $Au(111)$ surface.^{29, 40-41}

The occupation of a single adsorption site means that the chemisorbed, equilibrated phase can be described as a lattice gas (LG). We have constructed a rudimentary LG model based on excluded pairs of sites determined from DFT. The set of excluded pairs of sites agrees well with the STM observations. Monte Carlo simulation then provides a reasonable

qualitative match with the experimental data, although both the model and the data are too limited for quantitative analysis.

Because equilibration requires diffusion, we have calculated diffusion barriers and diffusion pathways for this system, using NEB and DFT. The magnitudes of the barriers allow us to estimate that parallel diffusion stops at about 220 K, and perpendicular diffusion at 280 K, which is compatible with the assumption that the STM images represent equilibrated configurations (Sec. 3.2). Furthermore, the results are a new contribution, since diffusion of non-metallic adsorbates on anisotropic fcc(110) surfaces has received little attention, either experimental or theoretical. By contrast, a significant body of data exists for metallic adatom and cluster diffusion on surfaces.⁴² For metal adatoms, hopping parallel to the rows is usually easier than hopping perpendicular to the rows (barring exchange). This is because perpendicular diffusion requires hopping over the low-coordinated metal atoms at the tops of rows. But for S_{ad} diffusion on Au(110)-(1x2), we find that hopping over the tops of rows (Fig. 8(b)) has the lowest barrier—lower than hopping parallel to rows (Fig. 8(a)) or even across troughs (Fig. 8(c)). Another interesting observation is that the diffusion pathway across the trough is complex. The S_{ad} first moves parallel to the row, then crosses the trough, then moves parallel to the row again to reach an equivalent site.

Turning now to the c(4x2) phase, in this paper we propose a new structural model. Its ideal coverage is 0.25 ML. It is a displacive reconstruction in which p4fh sites are created for S_{ad} . The experimental data strongly support a displacive phase (in which the Au atom density is preserved and only local displacements occur), since the c(4x2) phase is perfect over large scales. The model also provides a very good match with experimental STM images, not only for the extended perfect structure (where it even reproduces faint features due to diagonally-

contiguous Au atoms) but also for a domain boundary between c(4x2) regions. From DFT, it is more stable than the corresponding chemisorbed phase at 0.25 ML. This conclusion has been tested and validated for a variety of different functionals in DFT—including two which incorporate van der Waals interactions. The conclusion is not supported with a lower-level functional, LDA, however.

In fact, from DFT, the c(4x2) is energetically favored over the chemisorbed phase even at much lower coverage. From Fig. 5, μ_S^u for the c(4x2) phase falls below the value for the chemisorbed phase at 0.06 ML. The data in Fig. 5 are valid only at $T = 0$ K, and at real temperatures, the chemical potential also includes an entropic term. The configurational entropy of the chemisorbed phase is clearly higher than that of the c(4x2) phase. Thus, as T increases, the entropic term will drive μ_S^u lower for both phases, but this will occur more strongly for chemisorbed sulfur than for the c(4x2) phase. Nonetheless, the DFT result is in accord with experiment, where the coverage of sulfur in the chemisorbed phase is only 0.06 ± 0.03 ML when the two phases coexist. This indicates that entropic terms may not be too large, at least at the temperature at which the structures are quenched in the experiments.

The ideal coverage of the c(4x2) phase deserves comment. It is lower than the coverage of the previously-accepted model, a coincidence lattice with ideal coverage of 0.75 ML. In Sec. I, we reviewed the existing literature, and noted that from the calibration of Kostelitz *et al.*,¹² at 300 K the c(4x2) phase coexists with the chemisorbed phase between 0.08 and 0.36 ML, exists alone between 0.36 and 0.54 ML, and disappears by 0.6 ML. Reconciling our model with these values is problematic. A downward adjustment by (roughly) a factor of 2 would bring the earlier values into alignment with the new model, but the justification for such an adjustment is unclear. Another explanation could be that there

are two stable $c(4 \times 2)$ phases, one having coverage above 0.25 ML, but from our exploration of higher-coverage structures via DFT (Fig. 13), this is unlikely.

Coexistence between phases is evidence of a first-order transition, for which nucleation-and-growth is expected. However, we observe $c(4 \times 2)$ domains with a size and degree of perfection that are unexpected for such a process, at least at the moderate temperature of 300 K employed here. We postulate that the two-dimensional interfacial energy between $c(4 \times 2)$ and (1×2) phases is very high, so that small regions of $c(4 \times 2)$ phase are unstable. Thus the critical size is large, leading to the large domain sizes observed.

5. Conclusions

The main result of this work is the direct observation of the $c(4 \times 2)$ phase of sulfur on Au(110) with STM, and its structural assignment with DFT. Experimentally, we find that the $c(4 \times 2)$ phase presents as large and near-perfect domains, in coexistence with a low coverage (0.06 ± 0.03 ML) of chemisorbed phase on the (1×2) reconstructed Au surface. From DFT, a uniquely strong structural candidate emerges: A checkerboard reconstruction, with an ideal coverage of 0.25 ML, which can be achieved by short-range displacements of Au atoms from the (1×2) structure. This contrasts an earlier model with ideal coverage of 0.75 ML. We posit that the large domain size reflects high interfacial energy between the $c(4 \times 2)$ and the (1×2) phases.

In the chemisorbed phase, S_{ad} occupies a $p3fh$ site along the side of the troughs. The barriers for long-range transport perpendicular and parallel to the rows are 0.61 eV and 0.78 eV, respectively, from nudged-elastic-band calculations. DFT is used to construct a simple

lattice gas model based on pairs of excluded sites. The set of excluded sites is in good qualitative agreement with STM data.

Acknowledgements

The experimental component of this work was conducted or supervised by HW, JO, HJY, YK, and PAT. It was supported by three sources. From the U.S., it was NSF Grant CHE-1507223. From Japan, support was provided by a Grant-in-Aid for Scientific Research on Priority Areas “Electron Transport Through a Linked Molecule in Nano-scale”; and a Grant-in-Aid for Scientific Research(S) “Single Molecule Spectroscopy using Probe Microscope” from the Ministry of Education, Culture, Sports, Science, and Technology (MEXT). The theoretical component of this work was carried out by DJL. It was supported by the Division of Chemical Sciences, Basic Energy Sciences, US Department of Energy (DOE). This part of the research was performed at Ames Laboratory, which is operated for the U.S. DOE by Iowa State University under contract No. DE-AC02-07CH11358. This part also utilized resources of the National Energy Research Scientific Computing Center, which is supported by the Office of Science of the U.S. DOE under Contract No. DE-AC02-05CH11231. We thank Maki Kawai and Noriaki Takagi for loaning the Au(110) sample to us, and we thank Shota Kawahara and Kensuke Kimura for their assistance in preparing the sample for experiments.

Figures

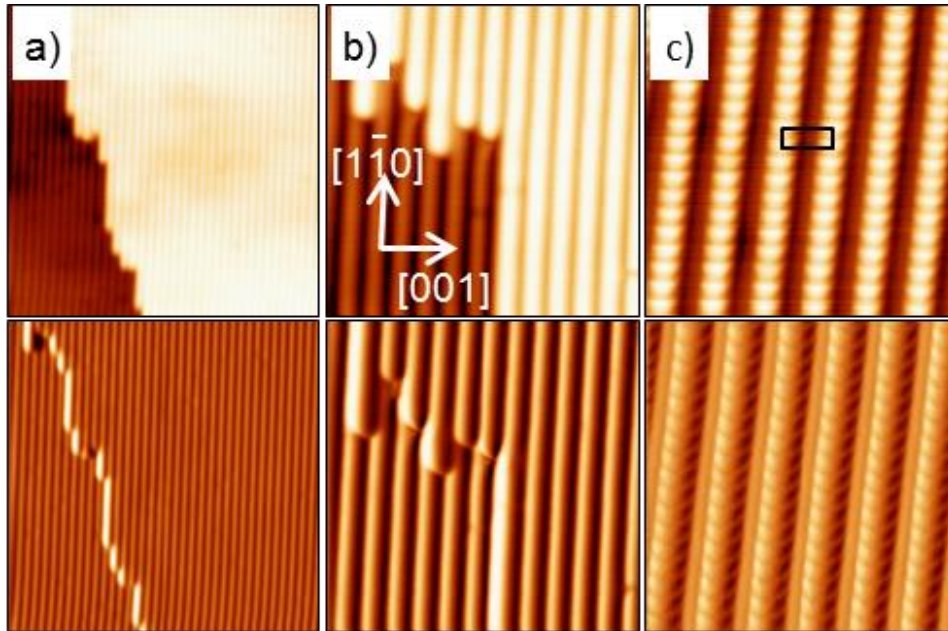


Figure 1. STM images of clean Au(110). In each pair, the top panel is topographic and the bottom panel is differentiated. (a) $30 \times 30 \text{ nm}^2$ image, encompassing two terraces. (b) $10 \times 10 \text{ nm}^2$ image, showing rows along a step edge. (c) $5 \times 5 \text{ nm}^2$ image, with atomic resolution along the rows of the (1x2) reconstruction. The rectangle shows the (1x2) surface unit cell. There is some distortion from drift, which increases with increasing magnification (a) to (c).

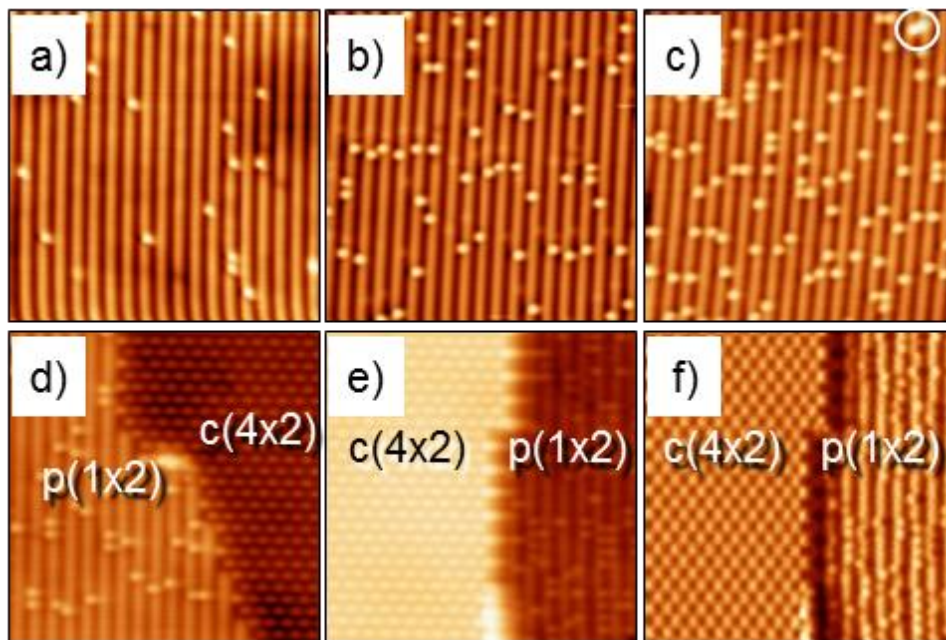


Figure 2. STM images after S adsorption. All images are $15 \times 15 \text{ nm}^2$. (a) $\theta_S^{\text{tot}} = 0.01 \text{ ML}$. (b) $\theta_S^{\text{tot}} = 0.03 \text{ ML}$. (c) $\theta_S^{\text{tot}} = 0.05 \text{ ML}$. (d) $\theta_S^{1 \times 2} = 0.04 \text{ ML}$, $\theta_S^{\text{tot}} = 0.15 \text{ ML}$. (e) $\theta_S^{1 \times 2} = 0.09 \text{ ML}$, $\theta_S^{\text{tot}} = 0.17 \text{ ML}$. (f) Differentiated image of (e).

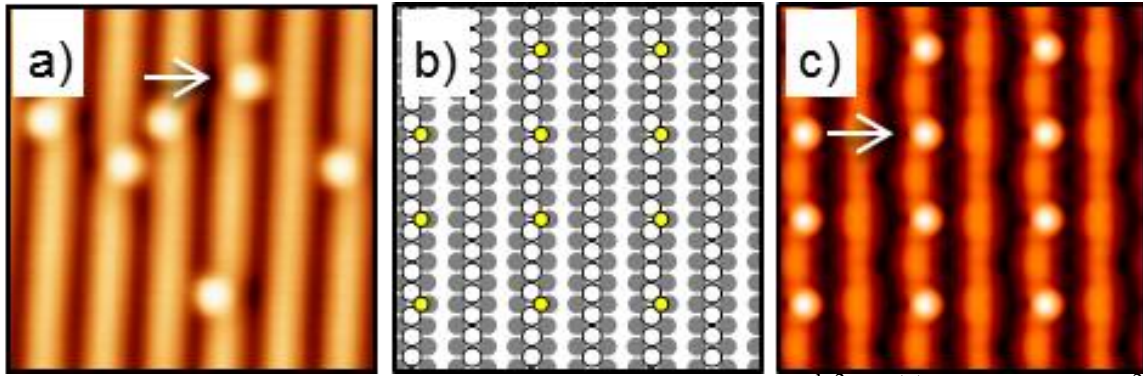


Figure 3. Top views of the Au(110) surface. (a) STM image at $\theta_s^{1 \times 2} = \theta_s^{\text{tot}} = 0.01$, $5 \times 5 \text{ nm}^2$. The bright stripes are top rows of Au atoms in the (1×2) reconstruction, and the brighter spots are sulfur adatoms. The arrow shows an indentation in a Au row adjacent to a sulfur adatom. (b) Optimized configuration of sulfur atoms (yellow circles) in the most favorable adsorption sites, in a $p(4 \times 4)$ superlattice, from DFT. White circles are Au atoms in the topmost layer, and gray circles are Au atoms one layer below. The scale is the same as in panel (a). (c) Simulated STM image based on (b), at the same scale. The arrow points to an indentation in a row, similar to (a).

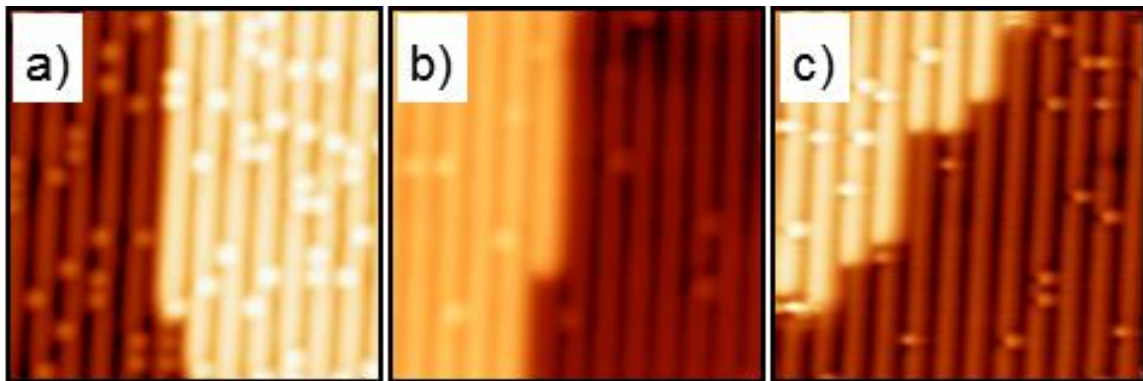


Figure 4. STM images of (a-b) steps along the $[1 \bar{1} 0]$ and (c) steps along the $[001]$ direction. All images $10 \times 10 \text{ nm}^2$.

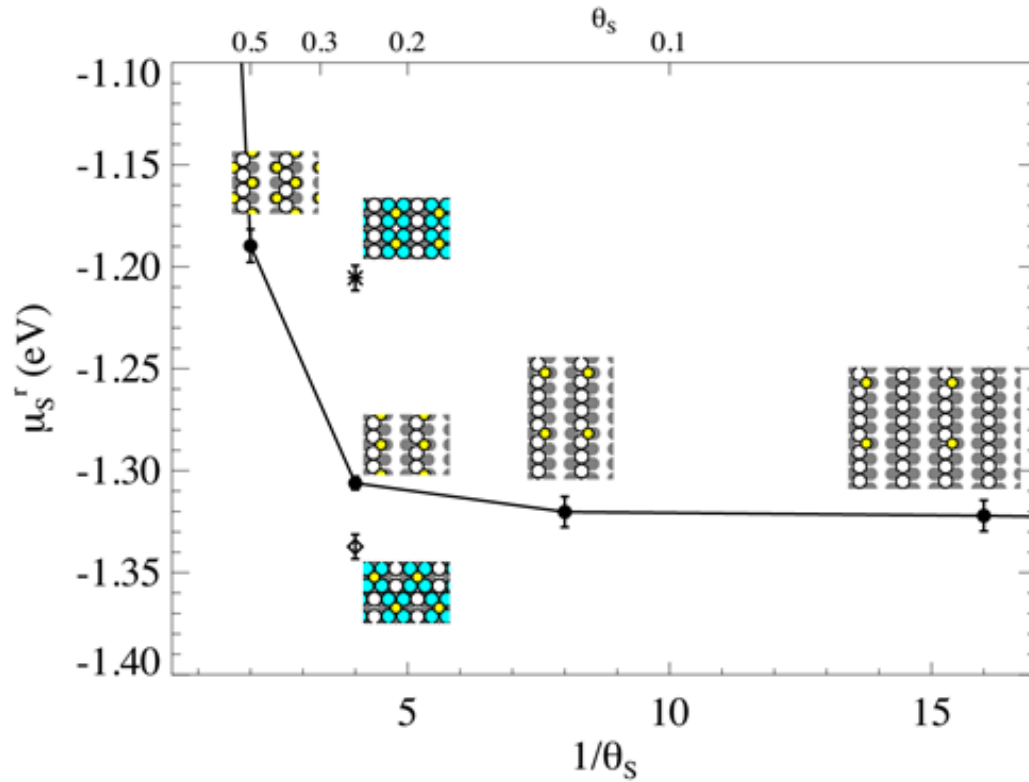


Figure 5. Baseline energetics (solid circles connected by tie-line) of regular arrays of S_{ad} . The structure of each calculation is shown with its corresponding data point. Yellow circles are S atoms, white circles are Au atoms in their original positions, cyan are Au atoms shifted in surface restructuring, and gray circles are Au atoms in the layer below.

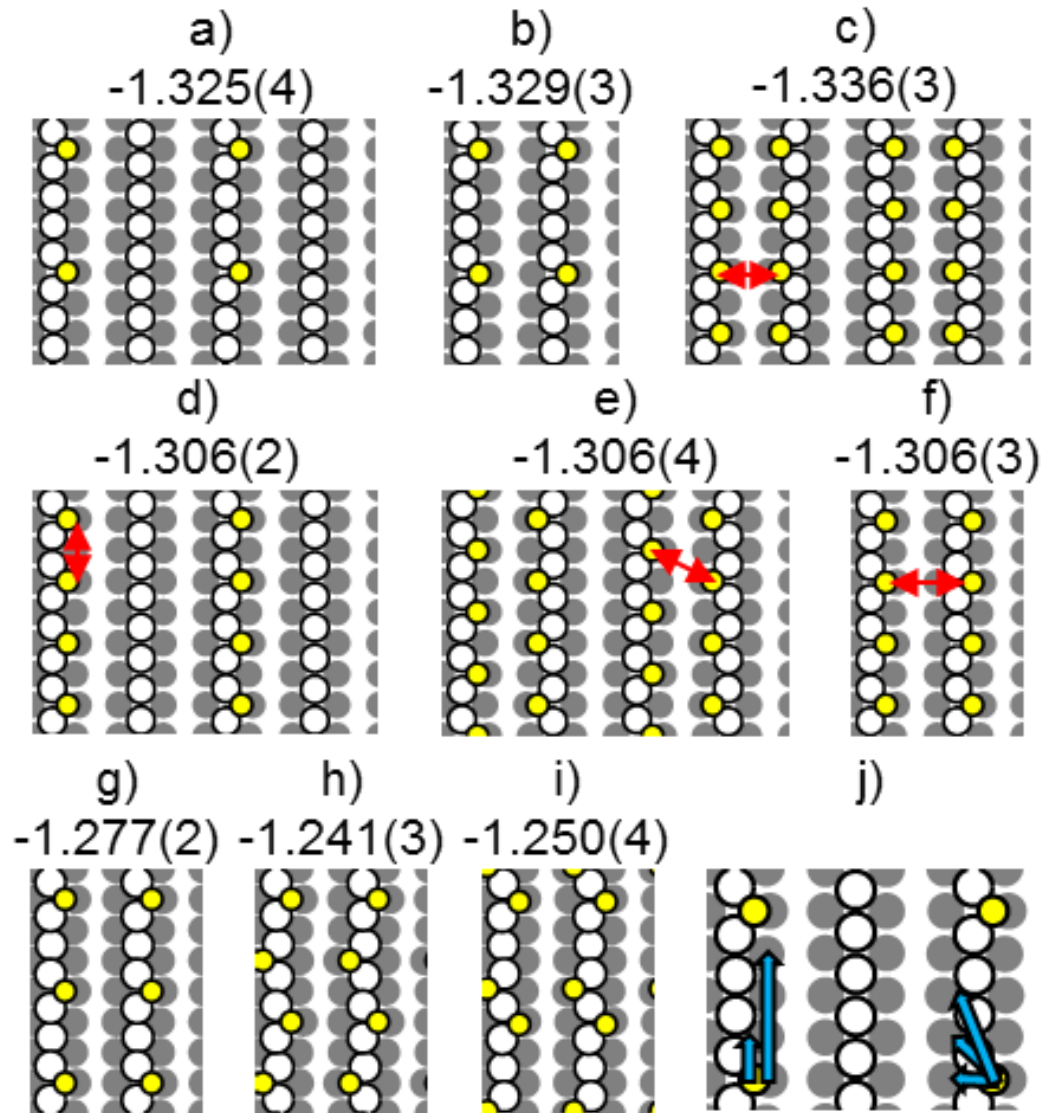


Figure 6. Configurations of chemisorbed S_{ad} on the (1x2), and associated $\mu_{S'}$ values in eV. (a) p(4x4)-S, 0.06 ML. (b) p(4x2)-S, 0.13 ML. This is also the baseline configuration used in Fig. 5, and is compared with the c(4x2) in Table I. (c) p(2x4)-2S, 0.25 ML. (d) p(2x4)-1S, 0.13 ML. (e) p(2x4)-2S, 0.25 ML. (f) p(2x2)-S, 0.25 ML. (g) p(3x2)-S, 0.17 ML. (h) p(4x2)-2S, 0.25 ML (i) p(4x2)-S, 0.25 ML. (j) Blue arrows show excluded pairs of adsorption sites. Pairwise interactions are indicated by the red arrows in (c-f).

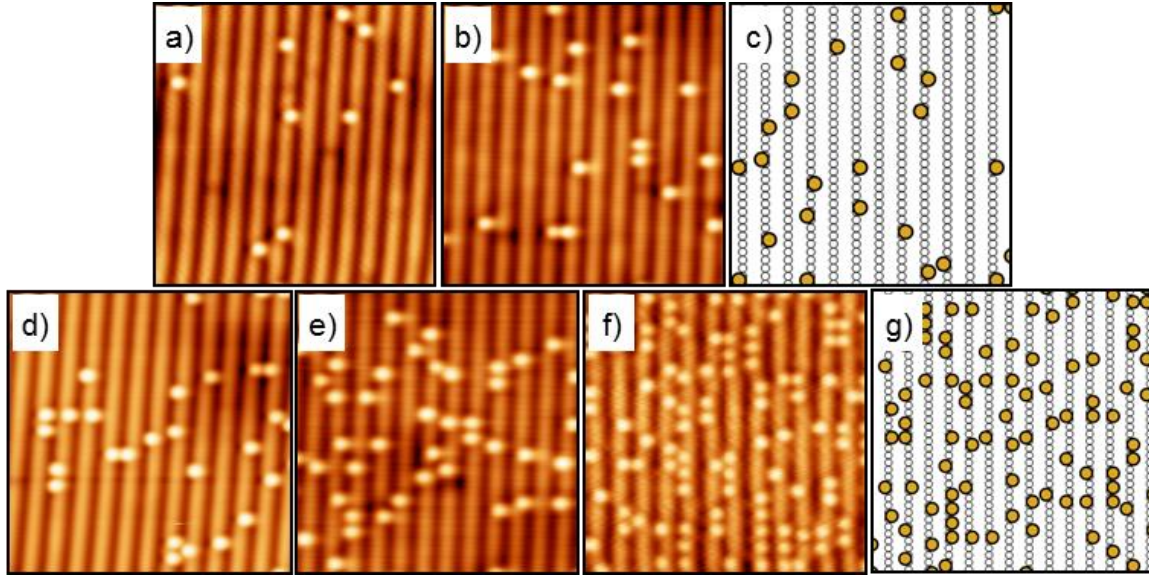


Figure 7. STM images and Monte Carlo simulation snapshots of the lattice gas model described in the text, for the chemisorbed phase. All STM images are $10 \times 10 \text{ nm}^2$, and simulation snapshots are scaled to be approximately the same size. (a) $\theta_s^{1 \times 2} = 0.01 \text{ ML}$. (b) $\theta_s^{1 \times 2} = 0.02 \text{ ML}$. (c) Monte Carlo simulation for $\theta_s^{1 \times 2} = 0.02 \text{ ML}$. (d) $\theta_s^{1 \times 2} = 0.03 \text{ ML}$. (e) $\theta_s^{1 \times 2} = 0.04 \text{ ML}$. (f) $\theta_s^{1 \times 2} = 0.09 \text{ ML}$. (g) Monte Carlo simulation for $\theta_s^{1 \times 2} = 0.08 \text{ ML}$.

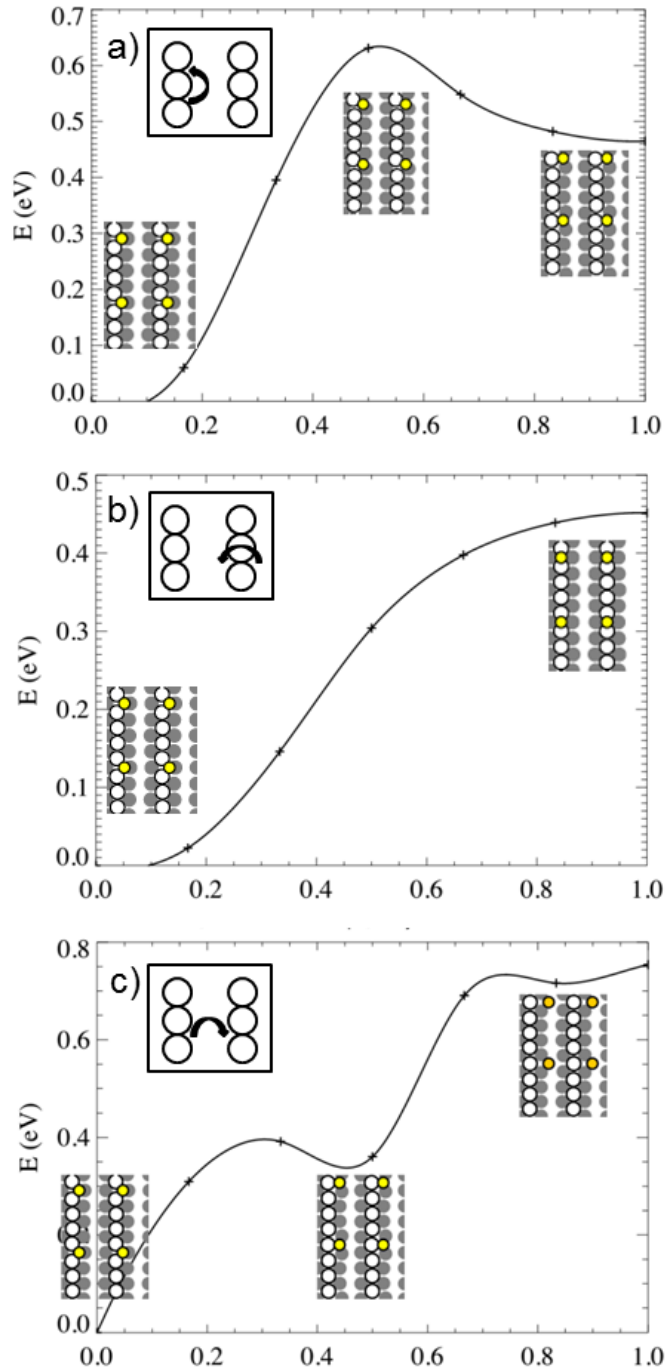


Figure 8. NEB results for diffusion pathways of S_{ad} , using $(12 \times 12 \times 1)$ k-points grid. In each panel, energy is plotted as a function of reaction coordinate for the first half of the symmetric path between energetically-equivalent p3fh sites. Each panel has a framed inset with an arrow showing the net displacement for the total path. (a) Diffusion parallel to a row, $L = 7$. (b) Diffusion perpendicular to a row, across the top of a row, $L = 7$. (c) Diffusion perpendicular to a row, across a trough, $L = 5$.

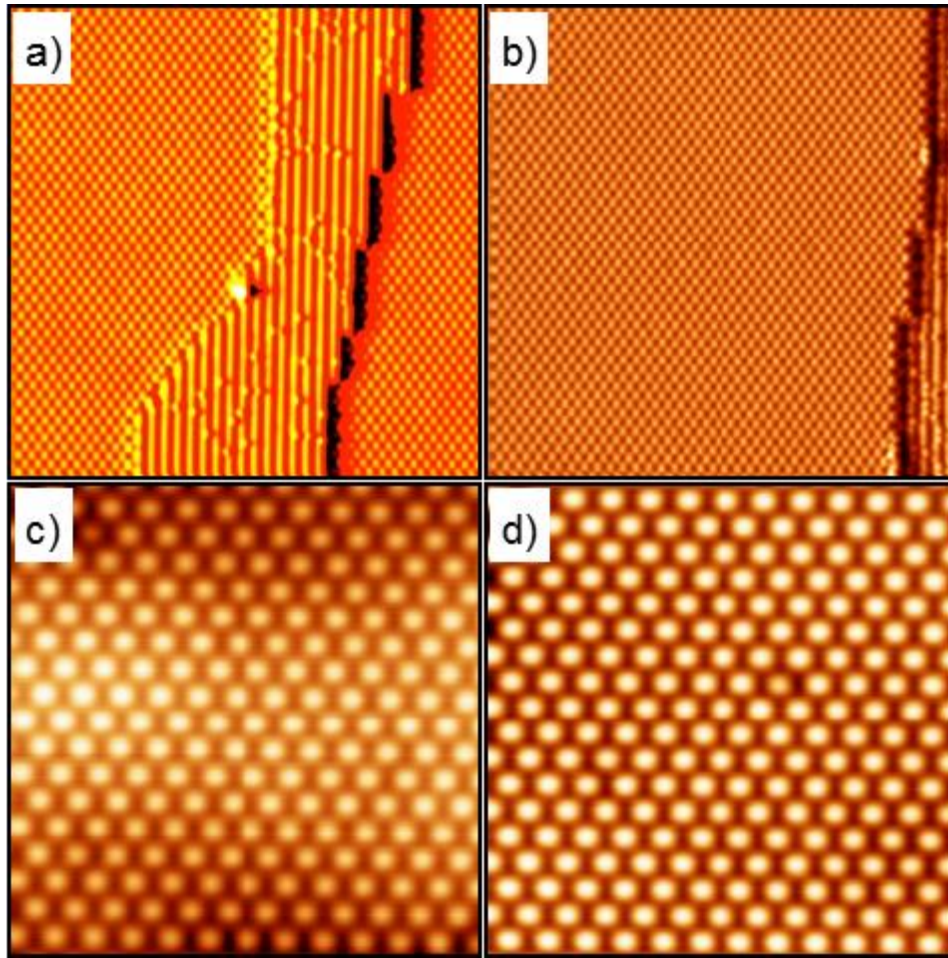


Figure 9. STM images of the c(4x2) phase. (a) Differentiated image of c(4x2) domains on two terraces, $30 \times 30 \text{ nm}^2$. (b) Differentiated image of c(4x2) region, encompassing a step edge on the far right side. $30 \times 30 \text{ nm}^2$. (c-d) Topographic STM images of the c(4x2), $10 \times 10 \text{ nm}^2$.

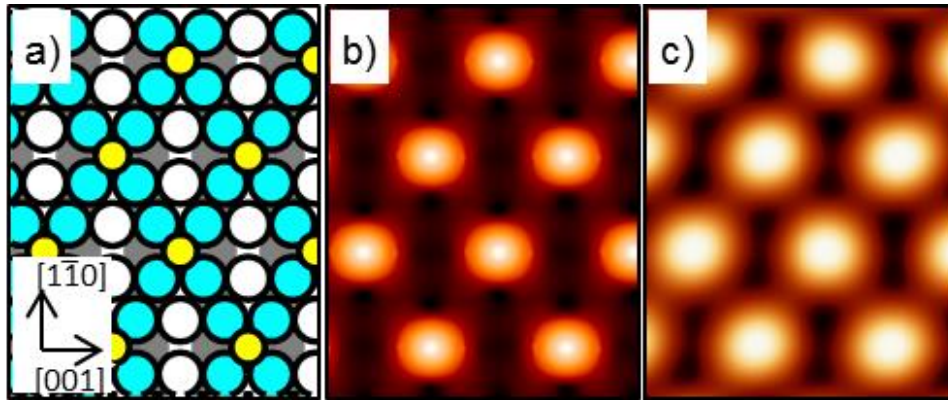


Figure 10. Structure of the $c(4 \times 2)$. (a) DFT model of the $c(4 \times 2)$. The color scheme is the same as described for Fig. 5. (b) Simulated STM image of (a). (c) Experimental STM image of the $c(4 \times 2)$. $1.9 \times 2.4 \text{ nm}^2$.

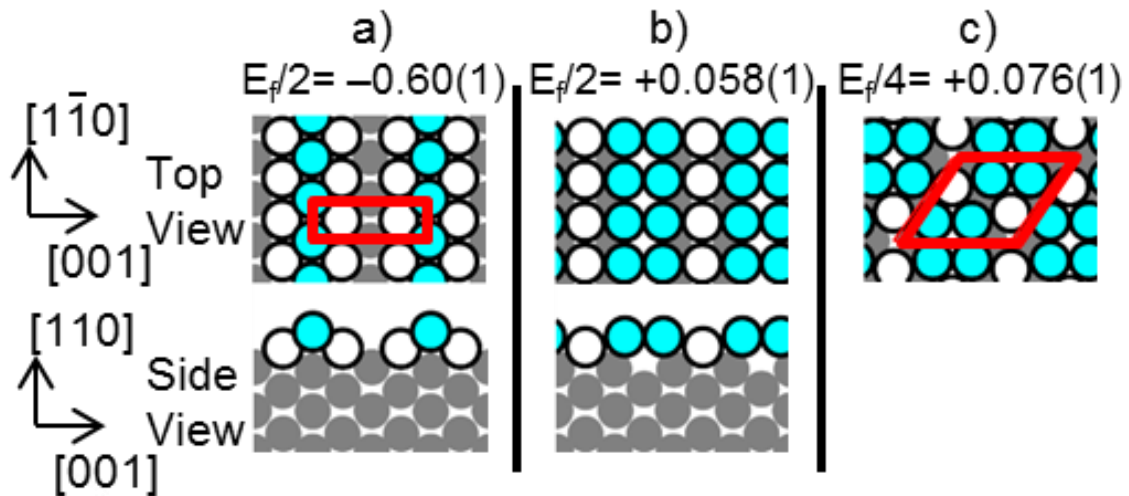


Figure 11. Optimized configurations of the clean surface. In each case, the formation energy, E_f , is divided by the area of the surface unit cell to enable direct comparison of stabilities between panels, using numerical values shown (in eV). This quantity, E_f per unit area, can also be thought of as the change in surface energy relative to a baseline structure which, in this case, is the (1×1) . (a) (1×2) missing row reconstruction. Red rectangle shows the surface unit cell. (b) (1×2) strip reconstruction. (c) $c(4 \times 2)$ checkerboard reconstruction. Red rhombus shows the primitive surface unit cell.

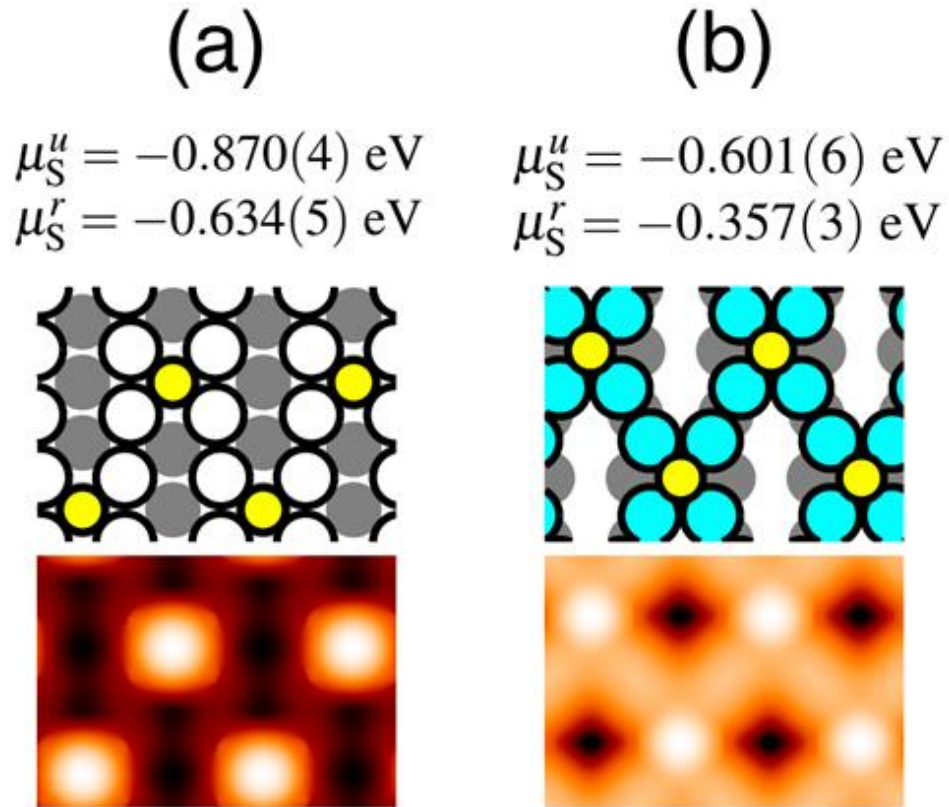


Figure 12. Optimized configurations of two $c(4 \times 2)$ structures, different than the checkerboard model, both closely related to the unreconstructed Au structure. The color scheme is the same as described for Fig. 5.

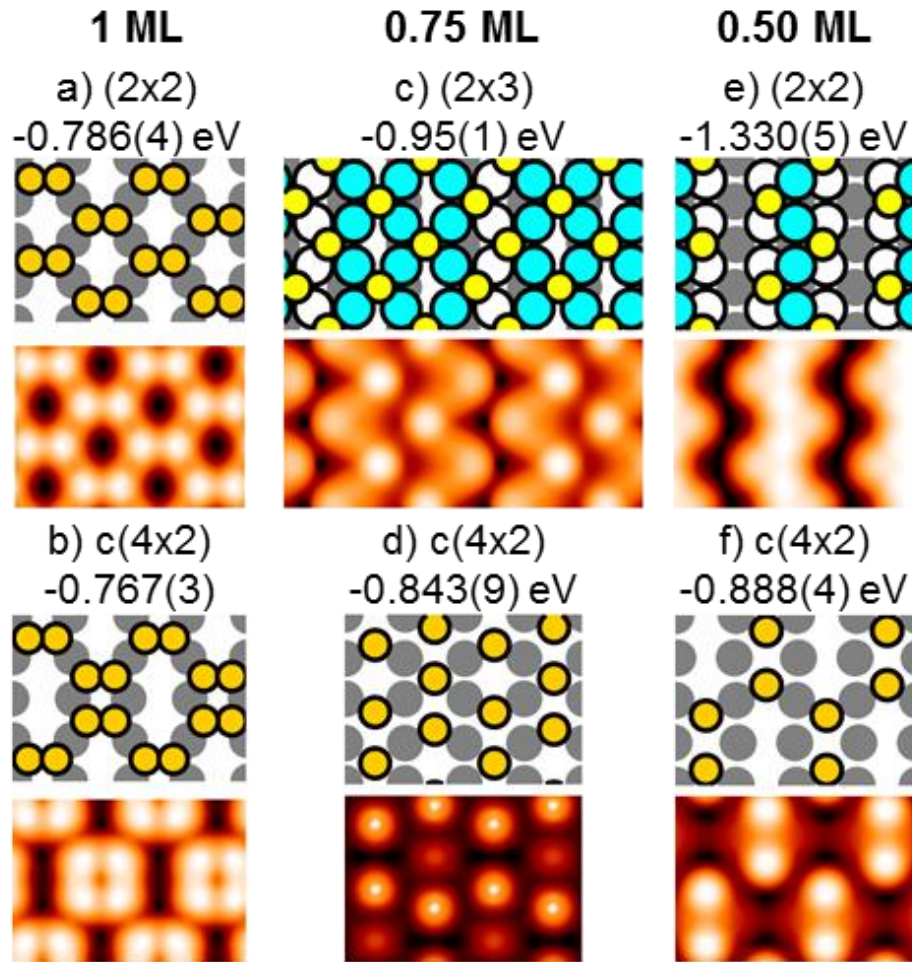


Figure 13. Structure, simulated STM, and μ_S^u for selected configurations with c(4x2) periodicity and with different sulfur coverage.

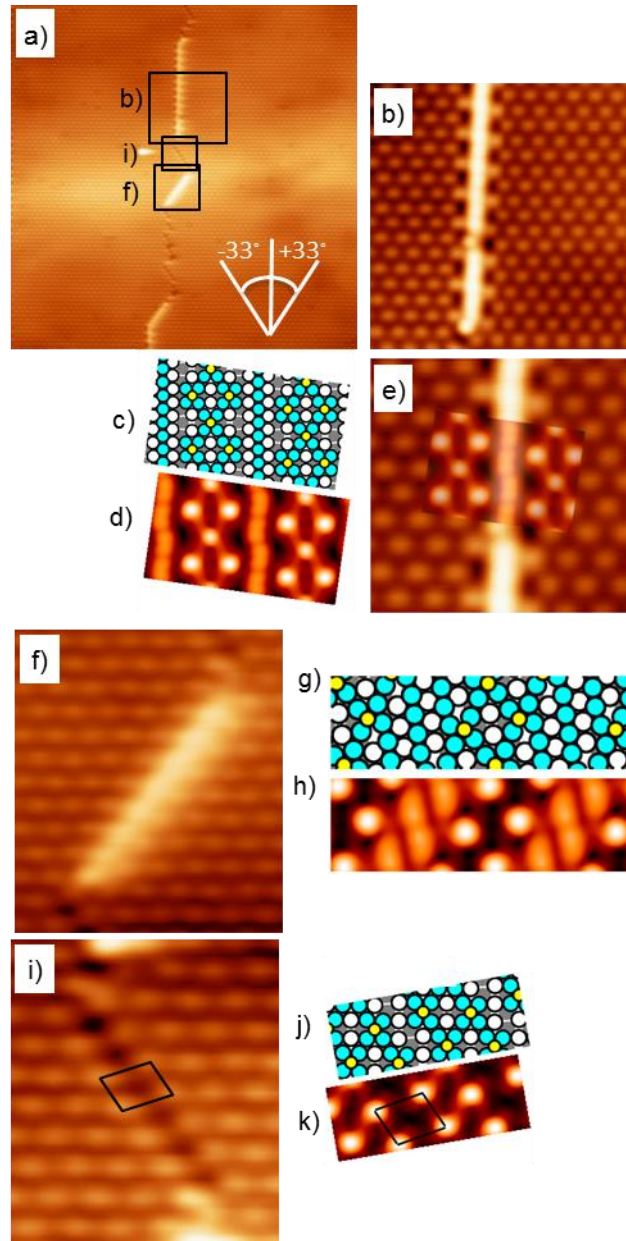


Figure 14. Domain boundary within the $c(4 \times 2)$. (a) STM image encompassing three orientations of the domain boundary. Regions chosen for analysis are shown in boxes. (b) STM image of the zipper-like region parallel to $[1 \bar{1}0]$. (c) Structural model for the zipper-like region. (d) Simulated STM image for the model. (e) Zoom-in of the zipper in (b) with the simulated STM image overlaid. (f) Transition region of $c(4 \times 2)$ rotated $+33^\circ$ relative to the $[1 \bar{1}0]$ direction. (g) Structural model for the transition region shown in (f). (h) Simulated STM image of (g). (i) Transition region of $c(4 \times 2)$ rotated -33° relative to the $[1 \bar{1}0]$ direction. (j) Structural model for (i). (k) Simulated image for (j).

Appendix 1. Tunneling conditions for images in the main text

Figure	Image size (nm ²)	Tunneling current (nA)	Sample bias (V)	$\theta_s^{1 \times 2}$
1a	30 x 30	1.00	-1.000	0
1b	10 x 10	0.97	-0.051	0
1c	5 x 5	1.75	-0.004	0
2a	15 x 15	2.06	-0.006	0.013
2b	15 x 15	1.27	-2.000	0.026
2c	15 x 15	1.17	-1.000	0.049
2d	15 x 15	1.00	-0.106	0.037
2e	15 x 15	1.00	+0.132	0.086
3a	5 x 5	1.83	-0.028	0.013
4a	10 x 10	1.00	-0.500	0.086
4b	10 x 10	0.95	-0.020	0.017
4c	10 x 10	1.06	-0.047	0.026
7a	10 x 10	1.01	-0.039	0.013
7b	10 x 10	0.95	-0.020	0.017
7d	10 x 10	1.27	-1.000	0.026
7e	10 x 10	1.00	-0.292	0.037
7f	10 x 10	3.79	-0.054	0.086
9a	30 x 30	1.00	-0.200	0.049
9b	30 x 30	1.00	+0.132	0.086
9c	10 x 10	1.00	-0.100	0.049
9d	10 x 10	1.00	-0.159	0.049
10c	1.9 x 2.4	1.03	+0.075	0.049
12a	50 x 50	1.00	+1.000	0.086
12b	10 x 10	1.00	+1.000	0.086
12e	6 x 5.5	1.00	+1.000	0.086
12h	6.3 x 7.2	1.00	+1.000	0.086
12k	5 x 5.7	1.00	+1.000	0.086

Appendix 2. Details about definition and implementation of chemical potential, μ , and formation energy, E_f

In order to establish a foundation for μ , we first consider the energetics of the (1x2) reconstruction of the clean Au surface. The formation energy E_f (per supercell) with m excess Au atoms in each supercell is:

$$E_f = E(\text{slab} + m\text{Au}) - E(\text{slab}) - m\mu_{\text{Au}} \quad (\text{Eq. SI.1})$$

where μ_{Au} is the average cohesive energy of a Au atom in the bulk solid. Figure 11(a) shows a missing row reconstruction, with formation energy $E_f = -0.12$ eV, consistent with the well-known (1x2) surface phase.

The stability of a S_{ad} -related structure can be calculated either with respect to the unreconstructed or reconstructed surface. For a structure with m Au atoms and n S atoms on top of a clean slab, we denote μ_S^u as the chemical potential with respect to the unreconstructed surface, and calculate it from DFT using

$$\mu_S^u(\text{Au}_m\text{S}_n) = [E(\text{Au}_m\text{S}_n + \text{slab}) - E(\text{slab}) - m\mu_{\text{Au}}]/n - E(\text{S}_{2,g})/2 \quad (\text{Eq. SI.2})$$

The chemical potential with respect to the (1x2) reconstructed surface can be calculated using

$$\mu_S^r(\text{Au}_m\text{S}_n) = [E(\text{Au}_m\text{S}_n + \text{slab}) - E(\text{slab}^{(1 \times 2)}) - (m - N/2)\mu_{\text{Au}}]/n - E(\text{S}_{2,g})/2 \quad (\text{Eq. SI.3})$$

where $E(\text{slab}^{(1 \times 2)})$ is the energy of a clean Au(110) surface with (1x2) missing-row reconstruction [cf., Fig. 11(a)], and N is the number of surface Au atoms in the supercell ($N = 2$ for the (1x2) supercell). The (1x2) missing row structure has $N/2$ excess Au atoms. The relationship between the two μ 's can be obtained from Eq. (A1) by noting $E(\text{slab}^{(1 \times 2)}) = E(\text{slab} + \text{Au}_{N/2})$, which yields

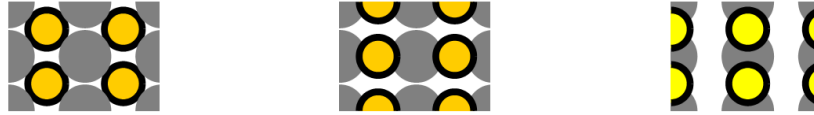
$$\mu_S^r = \mu_S^u + (E_f N) / (2n) = \mu_S^u + E_f \theta_S / 2 \quad (\text{Eq. SI.4})$$

One implication is that the shape of $\mu_S(\theta_S)$ depends upon the choice of μ_S . If μ_S^u is selected, then the energy stabilization due to reconstruction contributes to μ_S^u , and this contribution increases as supercell size increases. This can obscure variation in $\mu_S(\theta_S)$ which is due to S_{ad} alone. In such a case, μ_S^r may be the preferred parameter, and this is why μ_S^r is chosen in Fig. 5.

In other cases, μ_S^u may be preferable. In Eq. SI.3, to reduce numerical errors, it is desirable to use $E(\text{Au}_m\text{S}_n + \text{slab})$ and $E(\text{slab}^{(1 \times 2)})$ calculated using the same supercell. However this is generally not possible unless the supercell is commensurate with the (1x2) supercell. For this reason, it is more convenient to use μ_S^u when comparing stability of structures with various orderings, as in Fig. 13.

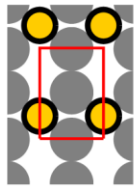
Appendix 3. Summary of μ_S^u values for additional S-Au structures studied with DFT

In this section we report values of μ_S^u of selected configurations, grouped by the supercell in which calculations are performed. Note that energetics in the main text are obtained using a higher range of slab thickness, $L = 7$ to 12. Although for some configurations more accurate energetics are available, for consistency we report in this section values obtained using the same relatively low settings, given in each figure caption.

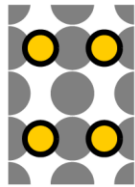


(a) $-0.44(2)$ eV (b) $-0.43(1)$ eV (c) $-0.178(7)$ eV

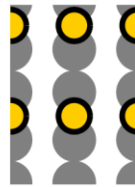
Figure A1. (1 x 1) cell, averaged over $L = 4$ to 7, k -points grid (12 x 8 x 1).



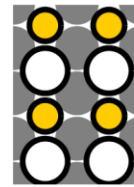
(a) $-0.69(1)$ eV



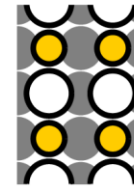
(b) $-0.42(2)$ eV



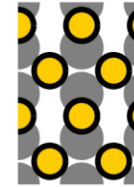
(c) $-0.71(2)$ eV



(d) $-0.16(3)$ eV



(e) $-0.15(1)$ eV



(f) $-0.29(1)$ eV

Figure A2. (2 x 1) supercell, averaged over $L = 4$ to 7, k -points grid (6 x 8 x 1).

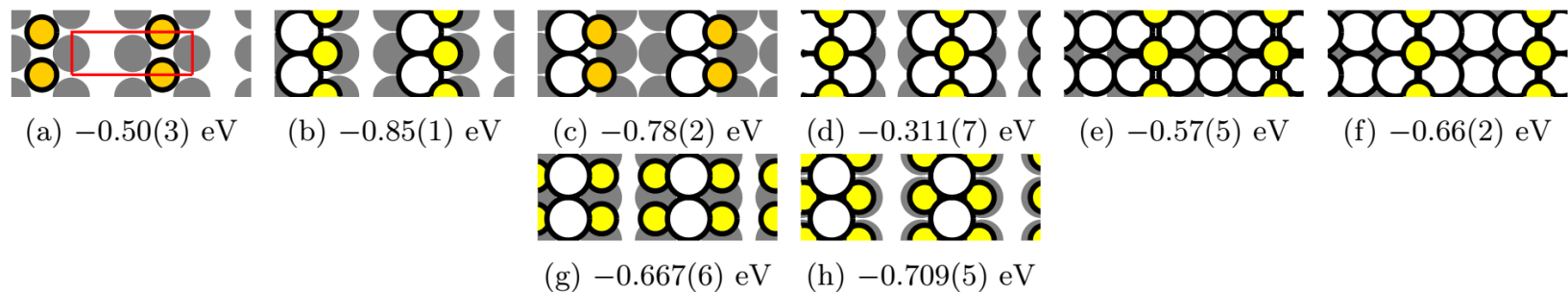


Figure A3. (1 x 2) supercell, $L = 4$ to 7, k -points grid (12 x 4 x 1).

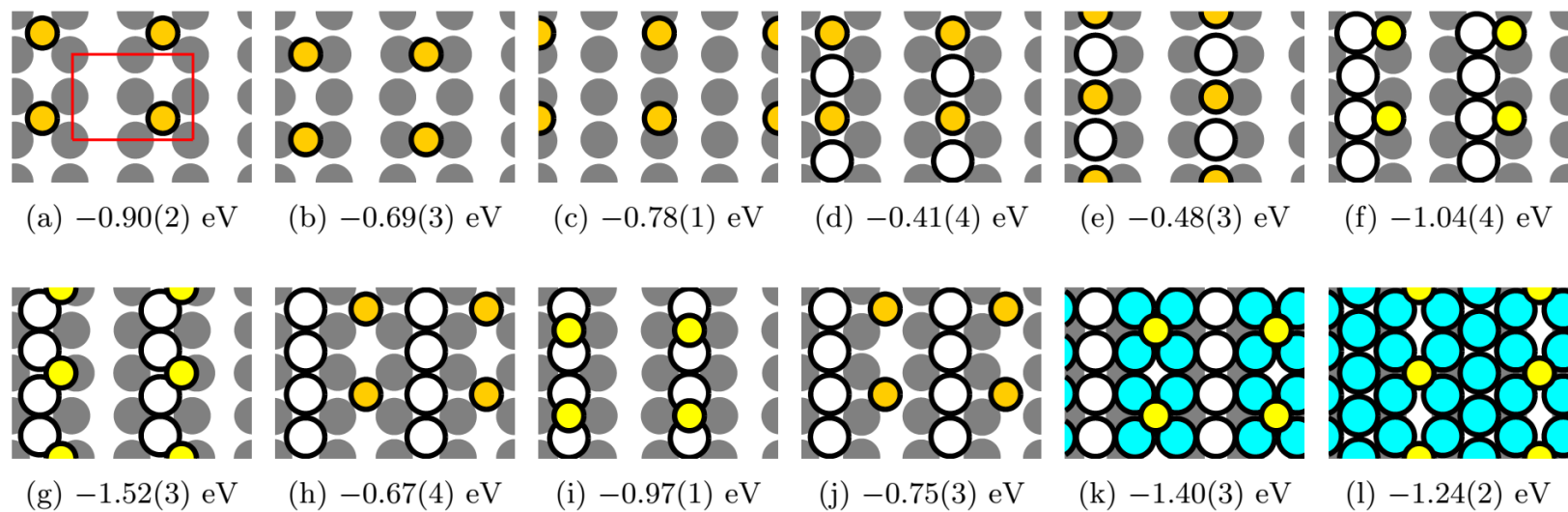


Figure A4. (2 x 2) supercell, $L = 4$ to 7, k -points grid (6 x 4 x 1).

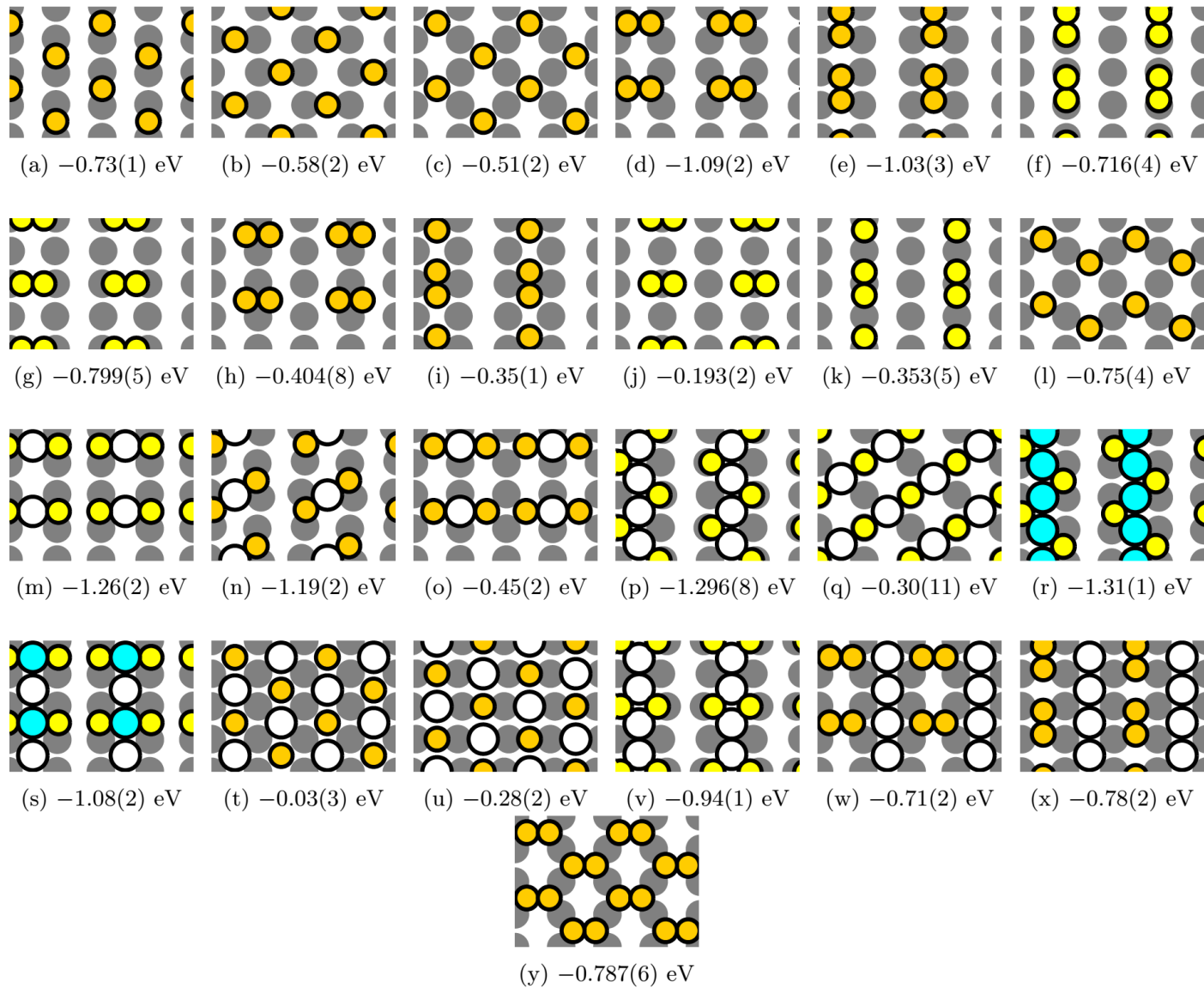


Figure A5. (2×2) supercell, averaged over $L = 4$ to 7 , k -points grid $(6 \times 4 \times 1)$.

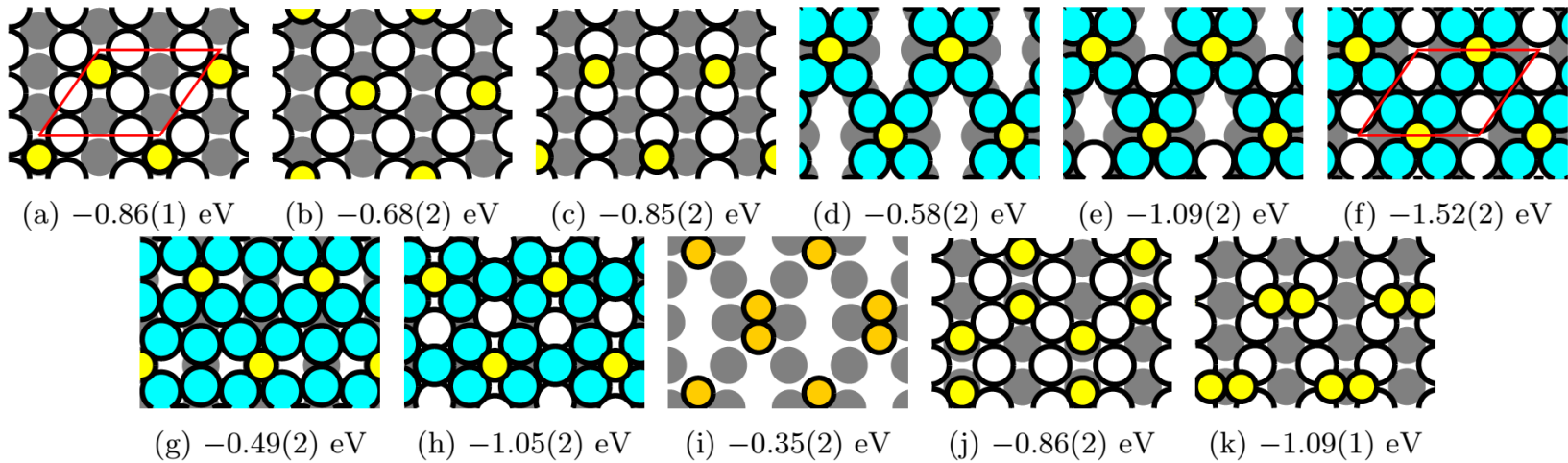
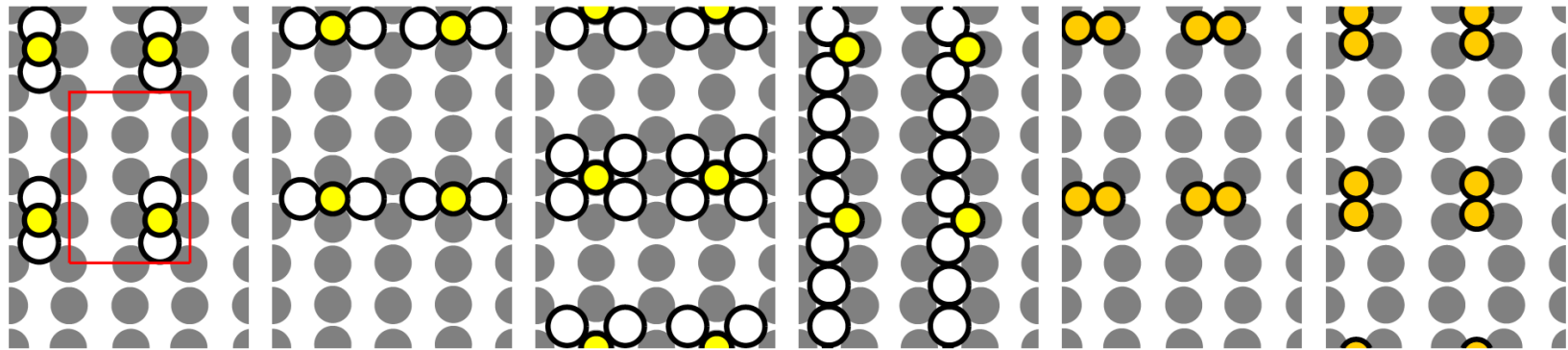
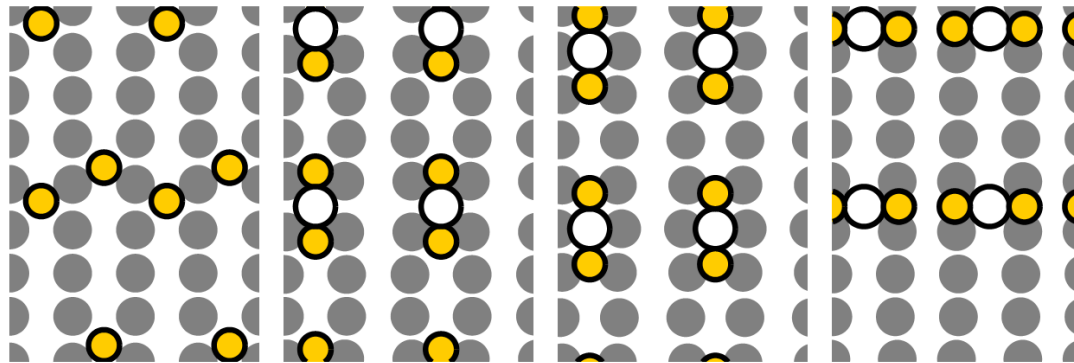


Figure A6. $c(4 \times 2)$ supercell, averaged over $L = 4$ to 7 , k -points grid $(5 \times 4 \times 1)$.



(a) $-0.81(2)$ eV (b) $-1.05(2)$ eV (c) $-0.42(4)$ eV (d) $-1.74(7)$ eV (e) $-1.11(2)$ eV (f) $-1.06(3)$ eV



(g) $-0.82(2)$ eV (h) $-0.91(8)$ eV (i) $-1.32(3)$ eV (j) $-1.31(2)$ eV

Figure A7. (4×2) supercell, averaged over $L = 4$ to 7 , k -points grid $(3 \times 4 \times 1)$.

Appendix 4. Bias effect on S_{ad} height and area

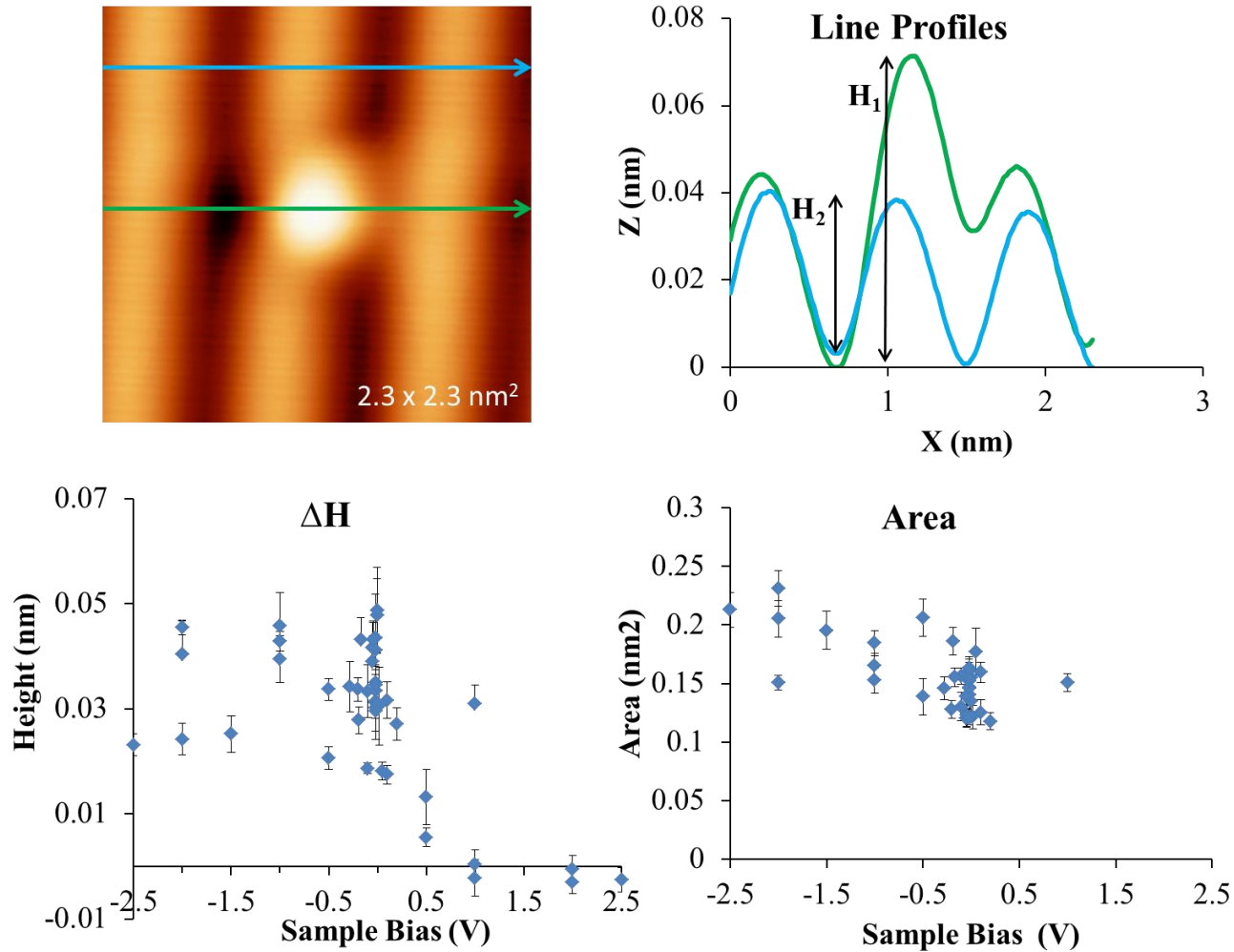


Figure A8. Bias effect on dimensions of the p(1 x 2)-S. In the top panel, ΔH was determined by subtracting the H_2 , the height of the Au row, from H_1 , the combined height of the protrusion and Au row. Area was determined using the full-width at half maximum. In each of the bottom plots, one point represents the average value of one image, and the error bars represent the standard deviation.

References

1. Daniel, M. C.; Astruc, D., "Gold Nanoparticles: Assembly, Supramolecular Chemistry, Quantum-Size-Related Properties, and Applications toward Biology, Catalysis, and Nanotechnology". *Chem. Rev.* **2004**, *104*, 293-346.
2. Fan, Y.; Long, Y. F.; Li, Y. F., "A Sensitive Resonance Light Scattering Spectrometry of Trace Hg^{2+} with Sulfur Ion Modified Gold Nanoparticles". *Anal. Chim. Acta* **2009**, *653*, 207-211.
3. Pensa, E.; Cortes, E.; Corthey, G.; Carro, P.; Vericat, C.; Fonticelli, M. H.; Benitez, G.; Rubert, A. A.; Salvarezza, R. C., "The Chemistry of the Sulfur-Gold Interface: In Search of a Unified Model". *Acc. Chem. Res.* **2012**, *45*, 1183-1192.
4. Thiel, P. A.; Shen, M.; Liu, D.-J.; Evans, J. W., "Critical Review: Adsorbate-Enhanced Transport of Metals on Metal Surfaces: Oxygen and Sulfur on Coinage Metals". *J. Vac. Sci. Technol. A* **2010**, *28*, 1285-1298.
5. Walen, H.; Liu, D.-J.; Oh, J.; Lim, H.; Evans, J. W.; Kim, Y.; Thiel, P. A., "Self-Organization of S Adatoms on Au(111): $\sqrt{3}\times\sqrt{3}$ Rows at Low Coverage". *J. Chem. Phys.* **2015**, *143*, 014704.
6. Walen, H.; Liu, D.-J.; Oh, J.; Lim, H.; Evans, J. W.; Aikens, C.; Kim, Y.; Thiel, P. A., " Cu_2S_3 Complex on Cu(111) as a Candidate for Mass Transport Enhancement". *Phys. Rev. B* **2015**, *91*, 045426.
7. Russell, S. M.; Liu, D.-J.; Kawai, M.; Kim, Y.; Thiel, P. A., "Low-Temperature Adsorption of H_2S on Ag(111)". *J. Chem. Phys.* **2010**, *133*, 124705.
8. Copel, M.; Gustafsson, T., "Structure of Au(110) Determined with Medium-Energy-Ion Scattering". *Phys. Rev. Lett.* **1986**, *57*, 723-726.

9. Ho, K. M.; Bohnen, K. P., "Stability of the Missing-Row Reconstruction on Fcc (110) Transition-Metal Surfaces". *Phys. Rev. Lett.* **1987**, *59*, 1833-1836.
10. Moritz, W.; Wolf, D., "Structure Determination of the Reconstructed Au(110) Surface". *Surf. Sci.* **1979**, *88*, L29-L34.
11. Moritz, W.; Wolf, D., "Multilayer Distortion in the Reconstructed (110) Surface of Au". *Surf. Sci.* **1985**, *163*, L655.
12. Kostelitz, M.; Domange, J. L.; Oudar, J., "Étude Par La Diffraction Des Électrons Lents Et La Spectroscopie Auger De L'adsorption Du Soufre Sur L'or". *Surf. Sci.* **1973**, *34*, 431-449.
13. Jaffey, D. M.; Madix, R. J., "The Adsorption of Hydrogen Sulfide on Clean and Sulfided Au(110)". *Surf. Sci.* **1991**, *258*, 359-375.
14. Krasnikov, S. A.; Hughes, G.; Cafolla, A. A., "Sulfur Overlayers on the Au(110) Surface: LEED and TPD Study". *Surf. Sci.* **2007**, *601*, 3506-3511.
15. Lahti, M.; Pussi, K.; Alatalo, M.; Krasnikov, S. A.; Cafolla, A. A., "Sulphur Adsorption on Au(110): DFT and LEED Structures". *Surf. Sci.* **2010**, *604*, 797-803.
16. Russell, S. M.; Kim, Y.; Liu, D.-J.; Evans, J. W.; Thiel, P. A., "Structure, Formation, and Equilibration of Ensembles of Ag-S Complexes on an Ag Surface". *J. Chem. Phys.* **2013**, *138*, 071101.
17. Walen, H.; Liu, D.-J.; Oh, J.; Lim, H.; Evans, J. W.; Kim, Y.; Thiel, P. A., "Reconstruction of Steps on the Cu(111) Surface Induced by Sulfur". *J. Chem. Phys.* **2015**, *142*, 194711.
18. Wagner, C., "Investigation on Silver Sulfide". *J. Chem. Phys.* **1953**, *21*, 1819-1827.

19. Maeland, A.; Flanagan, T. B., "Lattice Spacings of Gold–Palladium Alloys". *Can. J. Phys.* **1964**, *42*, 2364-2366.
20. Kresse, G.; Furthmüller, J., "Efficiency of Ab-Initio Total Energy Calculations for Metals and Semiconductors Using a Plane-Wave Basis Set". *Comput. Mater. Sci.* **1996**, *6*, 15-50.
21. Perdew, J. P.; Burke, K.; Ernzerhof, M., "Generalized Gradient Approximation Made Simple". *Phys. Rev. Lett.* **1996**, *77*, 3865-3868.
22. Liu, D.-J.; Walen, H.; Oh, J.; Lim, H.; Evans, J. W.; Kim, Y.; Thiel, P. A., "Search for the Structure of a Sulfur-Induced Reconstruction on Cu(111)". *J. Phys. Chem. C* **2014**, *118*, 29218-29223.
23. Han, Y.; Liu, D.-J., "Quantum Size Effects in Metal Nanofilms: Comparison of an Electron-Gas Model and Density Functional Theory Calculations". *Phys. Rev B* **2009**, *80*, 155404.
24. Liu, D.-J., "Density Functional Analysis of Key Energetics in Metal Homoepitaxy: Quantum Size Effects in Periodic Slab Calculations". *Phys. Rev. B* **2010**, *81*, 035415.
25. Tersoff, J.; Hamann, D. R., "Theory and Application for the Scanning Tunneling Microscope". *Phys. Rev. Lett.* **1983**, *50*, 1998-2001.
26. Shen, M.; Liu, D.-J.; Jenks, C. J.; Thiel, P. A., "Novel Self-Organized Structure of a Ag-S Complex on the Ag(111) Surface Below Room Temperature". *J. Phys. Chem. C* **2008**, *112*, 4281-4290.
27. Rost, M. J.; van Gastel, R.; Frenken, J. W. M., "Anomalous Shape and Decay of Islands on Au(110)". *Phys. Rev. Lett.* **2000**, *84*, 1966-1969.

28. Carlon, E.; vanBeijeren, H., "Networks of Steps on Crystal Surfaces". *Phys. Rev. Lett.* **1996**, *76*, 4191-4194.
29. Abufager, P. N.; Zampieri, G.; Reuter, K.; Martiarena, M. L.; Busnengo, H. F., "Long-Range Periodicity of S/Au(111) Structures at Low and Intermediate Coverages". *J. Phys. Chem. C* **2014**, *118*, 290-297.
30. Henkelman, G.; Jónsson, H., "Multiple Time Scale Simulations of Metal Crystal Growth Reveal the Importance of Multiatom Surface Processes". *Phys. Rev. Lett.* **2003**, *90*, 116101.
31. Perdew, J. P.; Ruzsinszky, A.; Csonka, G. I.; Vydrov, O. A.; Scuseria, G. E.; Constantin, L. A.; Zhou, X.; Burke, K., "Restoring the Density-Gradient Expansion for Exchange in Solids and Surfaces". *Phys. Rev. Lett.* **2008**, *100*.
32. Klimes, J.; Bowler, D. R.; Michaelides, A., "Chemical Accuracy for the Van Der Waals Density Functional". *J. Phys.: Condens. Matter* **2010**, *22*, 022201.
33. Klimes, J.; Bowler, D. R.; Michaelides, A., "Van Der Waals Density Functionals Applied to Solids". *Phys. Rev B* **2011**, *83*, 195131.
34. Williams, E. D.; Chan, C. M.; Weinberg, W. H., "Adsorption of Sulfur on the Reconstructed Ir(110)-(1x2) Surface". *Surf. Sci.* **1979**, *81*, L309-L314.
35. Chan, C. M.; Van Hove, M. A., "The Structure of a (2x2) Sulfur Overlayer on the Ir(110)-(1x2) Reconstructed Surface". *Surf. Sci.* **1987**, *183*, 303-315.
36. Atrei, A.; Johnson, A. L.; King, D. A., "Sulfur Adsorption on Cu(110) - a SEXAFS Study". *Surf. Sci.* **1991**, *254*, 65-72.

37. Zharnikov, M.; Mehl, D.; Weinelt, M.; Zebisch, P.; Steinruck, H. P., "Photoelectron Diffraction and Holography of Clean and Sulfur-Covered Ni(110)". *Surf. Sci.* **1994**, *306*, 125-143.
38. Wong, K. C.; Liu, W.; Mitchell, K. A. R., "Tensor Leed Analysis for the Rh(110)-(3x2)-S Surface Structure". *Surf. Sci.* **1995**, *344*, 258-266.
39. Besenbacher, F.; Stensgaard, I.; Ruan, L.; Nørskov, J. K.; Jacobsen, K. W., "Chemisorption of H, O, and S on Ni(110): General Trends". *Surf. Sci.* **1992**, *272*, 334-341.
40. Rodriguez, J. A.; Dvorak, J.; Jirsak, T.; Liu, G.; Hrbek, J.; Aray, Y.; Gonzalez, C., "Coverage Effects and the Nature of the Metal-Sulfur Bond in S/Au(111): High-Resolution Photoemission and Density-Functional Studies". *J. Am. Chem. Soc.* **2003**, *125*, 276-285.
41. Alfonso, D. R., "First-Principles Studies of H₂S Adsorption and Dissociation on Metal Surfaces". *Surf. Sci.* **2008**, *602*, 2758-2768.
42. Antczak, G.; Ehrlich, G., *Surface Diffusion. Metals, Metal Atoms, and Clusters*; Cambridge University Press: Cambridge, UK, 2010.

CHAPTER VII

IDENTIFICATION OF AU-S COMPLEXES ON AU(100)

Holly Walen,^a Da-Jiang Liu,^b Junepyo Oh,^c Hyun Jin Yang,^c Yousoo Kim,^c
and P. A. Thiel^{a,b,d}

A paper published in Physical Chemistry Chemical Physics[†]

Abstract

Using a combination of scanning tunneling microscopy and density functional theory (DFT) calculations, we have identified a set of related Au-S complexes that form on Au(100), when sulfur adsorbs and lifts the hexagonal surface reconstruction. The predominant complex is diamond-shaped with stoichiometry Au₄S₅. All of the complexes can be regarded as combinations of S-Au-S subunits. The complexes exist within, or at the edges of, p(2 x 2) sulfur islands that cover the unreconstructed Au regions, and are observed throughout the range of S coverage examined in this study, 0.009 to 0.12 monolayers. A qualitative model is developed which incorporates competitive formation of complexes, Au rafts, and p(2 x 2) sulfur islands, as Au atoms are released by the surface structure transformation.

Departments of ^aChemistry, ^dMaterials Science & Engineering, Iowa State University, Ames, Iowa 50011 USA

^bAmes Laboratory of the USDOE, Ames, Iowa 50011 USA

^cRIKEN Surface and Interface Science Laboratory, Wako, Saitama 351-0198, Japan

[†]*Phys. Chem. Chem. Phys.* **18** 4891-4901 (2016)

1. Introduction

In surface science, complexation reactions between adsorbates and indigenous surface metal atoms are reported with increasing frequency. Such complexes can influence metal mass transport,¹⁻² engender exotic organometallic nanoarchitectures,³⁻⁵ and allow control of surface properties by tuning the availability of metal atoms.⁶

In this paper we present evidence for a new type of complex that forms between S and Au atoms on Au(100). The interaction of S with Au surfaces is important because it is the most basic prototype for a large class of systems in which the S-Au bond anchors molecular ligands. These ligands range from (functionalized) alkyl groups,⁷⁻⁹ to biological molecules.¹⁰⁻¹¹ Such systems have many potential or real uses, such as detection of antibiotic-resistant bacteria¹² or fabrication of thin film transistors.¹³ There is evidence that some of these molecular adsorbates also can form complexes with Au atoms via the S group.¹⁴⁻¹⁵ In this vein, a “staple” motif has been reported whose basis is a linear S-Au-S subunit. As the name implies, the Au atom interacts weakly with the metal substrate in comparison to the S atoms, which are the ends of the staple.¹⁵⁻¹⁷

Previously, we reported that unexpected complexes can form between sulfur atoms and metal atoms on Ag(111)¹⁸ and Cu(111),¹⁹⁻²⁰ with stoichiometries $\text{Ag}_{16}\text{S}_{13}$ and Cu_2S_3 , respectively. Surprisingly, we found no evidence for complexation on Au(111) under similar conditions, although another group²¹ did report some evidence for Au-S clusters. While the Ag and Cu moieties are very different from one other, they possess features that we attributed to certain common principles of formation: high metal coordination around one or more sulfur atoms, and/or linear S-M-S subunits (M = Cu, Ag). The latter resemble the staple units mentioned above.

The specific system described in this paper, sulfur on Au(100), has been characterized previously using STM, low-energy electron diffraction, and other techniques, in ultrahigh vacuum (UHV) and in electrochemical environments. It has been characterized over a large coverage range, and often at room temperature. The clean surface is hexagonally (hex) reconstructed, with an atomic density 25% higher than that of the unreconstructed (1 x 1) phase (e.g. Refs.²²⁻³⁰). Adsorption of sulfur causes the hex structure to revert to the (1x1), with concomitant release of excess Au atoms.³¹⁻³⁴ Depending on temperature, some of the excess Au can coalesce into single layer islands (rafts) on the terraces.³¹ Sulfur forms ordered structures on the unreconstructed regions, including a p(2 x 2),³¹⁻³² c(2 x 6),³³ c(2 x 4),³¹ ($\sqrt{2} \times \sqrt{2}$),³⁴ and an octomer phase.³⁴ Of these, the p(2 x 2) has the lowest ideal coverage (0.25 ML) and is most relevant to our work. It is a chemisorbed phase, with sulfur adsorbed in alternating four-fold hollow (4fh) sites.³⁵⁻³⁶ Notably, Jiang *et al.*³¹ observed that the p(2 x 2) appears immediately wherever the reconstruction is lifted, and that it covers both levels—terraces and rafts—of unreconstructed Au.

Our work includes a combination of scanning tunneling microscopy (STM) and density functional theory (DFT) calculations. The experimental work differs from prior work³¹⁻³⁴ in that conditions are designed to isolate possible complexes. Thus, S coverage is kept low to circumvent adsorbate-induced reconstructions, and observation temperature is low (5 K) to ensure immobilization of adsorbed species following S adsorption at 300 K. A new, diamond-shaped complex is very common under these experimental conditions. Using DFT, we calculate the relative stability of candidate structures, and we compare each candidate's physical characteristics—shape, size, orientation—with experimental data. The

methodologies of experiments and calculations are similar to those described elsewhere.^{19-20, 37-38}

The manuscript is organized as follows. Section 2 provides experimental and computational details. Section 3 presents experimental results, along with DFT-guided interpretation. The clean surface is described first, followed by features that develop as the reconstruction is lifted. These are p(2 x 2) islands, Au rafts, possibly S atoms on hex regions, S-decorated step edges, and complexes. The propensity for ejected Au atoms to reach step edges is then analyzed. Section 4 is a discussion of results, including connections with prior work, followed by concluding remarks in Section 5.

2. Experimental and Computational Details

2.1 Experimental Description

The experimental instrumentation and procedures were similar to those used previously, in studies of S adsorption on Ag(111),¹⁸ Cu(111),^{19-20, 39} Au(111),³⁷ and Au(110).⁴⁰ In the current work, the single crystal Au(100) sample was cleaned via several Ar⁺ sputtering (10-15 μ A, 1.5 kV, 10 min) and annealing (720 K, 10 min) cycles.

Imaging in STM was performed at 5 K in UHV, at pressure $< 6.0 \times 10^{-11}$ Torr. Sulfur was deposited *in situ* via an electrochemical Ag|AgI|Ag₂S|Pt source.⁴¹⁻⁴³ The sample was held at 300 K during S deposition, and then cooled to 5 K for measurement. Cooling and stabilization for STM measurements was completed in approximately 50 minutes. After initial STM measurements, the sample was warmed back to room temperature and re-cooled to 5 K for further imaging, with no difference in the results. Tunneling conditions during

imaging were in the range -1.00 V to +1.00 V sample bias (V_s), and 1.00 to 3.10 nA tunneling current (I). The Appendix gives tunneling conditions for each image.

The STM piezoelectric calibration was checked by comparing measured and predicted atomic dimensions. The atomic separation along the close packed directions, a , was measured as 0.282 ± 0.007 nm, and the step heights as 0.19 ± 0.02 nm. The in-plane lattice constant predicted for Au(111) is 0.288 nm;⁴⁴ there is a 4% contraction associated with the hex Au(100) surface,^{27, 45-46} which brings this value to 0.276 nm. The step height predicted from the bulk parameter is 0.204 nm.⁴⁴ Both are within one standard deviation of the measured values.

Sulfur coverage (θ_s) was obtained by counting protrusions in STM images (associating each small protrusion with a single S adatom, and each diamond-shaped protrusion with 5 S), and dividing by the areal density of atoms in a bulk Au(100) plane. This yielded coverage in units of absolute monolayers (ML). Five experiments were performed, spanning the coverage range 0.009 to 0.12 ML.

2.2 Computational Description

We performed density functional theory (DFT) calculations using the VASP⁴⁷⁻⁴⁹ package, and the projected-augmented wave (PAW)⁵⁰ method. If not otherwise noted, the Perdew-Burke-Ernzerhof (PBE)⁵¹ approximation was used for the exchange-correlation. Technical details can be found in Refs.^{19, 38}. Energetics were averaged over slabs with thickness, L , from 7 to 12 Au layers.⁵² We used k-point grids that approximately corresponded to $(24 \times 24 \times 1)$ for the primitive substrate cell. All configurations reported herein were energy-optimized, with the bottom layer of Au atoms fixed. STM images were

generated from optimized configurations by taking the isosurface of partial charge density in an energy window that bracketed the Fermi energy by ± 0.1 eV, after Tersoff and Hamann.⁵³

We used DFT to evaluate the relative stability of S—either in the form of complexes, or as chemisorbed adatoms—on the unreconstructed Au substrate. The metric is a chemical potential, μ_S , for S (at 0 K), which we have employed in several similar systems.^{19-20, 37, 40} It is defined as

$$\mu_S = [E(\text{Au}_m\text{S}_n + \text{slab}) - E(\text{slab}) - m \mu_{\text{Au}}]/n - E(\text{S}_{2,\text{g}})/2 \quad (1)$$

where E is energy, μ_{Au} is the chemical potential of Au in the bulk metal (at 0 K), which also corresponds to the bulk cohesive energy. If bulk and surface are equilibrated, μ_{Au} is equivalent to the binding energy of a Au atom at a step kink site.⁵⁴ The integers m and n are the number of Au and S atoms in the complex, respectively. When $m=0$, μ_S is simply the adsorption energy of a S adatom. Physically, μ_S reflects the energy increase per S, when atomic S on terraces is incorporated into complexes in the presence of an unlimited supply of Au available from steps/kinks. Equation (1) defines the energy of gaseous triplet S_2 as the reference point for μ_S .

The size of the supercell can influence μ_S because of interactions between neighboring adsorbates. We therefore compare μ_S of the most important species at different supercell sizes (different θ_S). Whenever a value of μ_S is given, either the supercell or θ_S is specified. The area of the supercell is n/θ_S .

The most pertinent DFT results are presented in this text. Many others are provided in Appendix 3.

3. Results

3.1 Clean surface

Figure 1 shows STM images of the clean Au(100) surface. The characteristic hex reconstruction is visible at low magnification as long modulated stripes, parallel to either the $[01\bar{1}]$ or $[011]$ directions. Figure 1(a) shows a stepped region that encompasses both types of domains.

Figure 1(b-c) resolves individual atoms and their hexagonal-like packing in the corrugated surface layer. The modulation of the stripes is mainly due to mismatch between close-packed rows of Au atoms in the (denser) hexagonal layer and in the unreconstructed layer beneath. The period of modulation is 7.57 ± 0.08 nm (based on a number, N , of 13 measurements), which spans about 27 Au atoms in the top layer along the close-packed direction. These terrace images are very similar to ones that have been reported and analyzed for the hexagonally-reconstructed surfaces of Pt(100)^{24, 55-56} and Au(100).^{26, 31}

3.2 Features associated with chemisorbed sulfur

p(2 x 2) phase. As noted in Sec. 1, the $p(2 \times 2)$ is a known chemisorption phase with ideal coverage of 0.25 ML, wherein S occupies 4fh sites on the unreconstructed Au(100) surface.³⁵⁻³⁶ The following observations shed additional light on this structure, and provide context relevant to the surface complexes.

In our work, the $p(2 \times 2)$ is visible in localized regions even at the smallest total coverage, 0.009 ML. (We call such areas *islands* of $p(2 \times 2)$ phase.) The smallest $p(2 \times 2)$ -related islands are single rows of spots, separated by $2a$, on a dark background which we take to be the unreconstructed metal. Examples are shown in Fig. 2(a,b). Some such rows adjoin a

terminated hex stripe, and others are embedded in hex stripes that curve around them. Both cases can be seen in Fig. 2(a). Far more common than single rows, are anisotropic $p(2 \times 2)$ islands like those in Fig. 2(c,d), each consisting of 2-3 rows. The anisotropy is clearly enforced by the surrounding hex orientation, since the long dimension of each $p(2 \times 2)$ island lies parallel to the hex stripes. The height and width of the protrusions (shown in Table I) is comparable to S adatom dimensions we have measured in other systems under similar conditions.^{37, 40} Figure 2(a) includes a pair of S atoms in a dark trough that may result from dissociation of a single S_2 molecule, but this type of configuration was observed only once. Domain boundaries in the $p(2 \times 2)$ are very common.

TABLE I. Dimensions of features observed with STM, measured over sample bias from -1.00 to +1.00 V. The number of measurements is N.

Assignment	Height, nm	Width at Half-Maximum, nm	N
S adatoms on terraces in $p(2 \times 2)$	0.022 ± 0.004	0.293 ± 0.023	170
Au_4S_5 complexes (diamonds)	0.145 ± 0.020	Diagonal width: 1.04 ± 0.09 Narrowest width: 0.813 ± 0.077	58
AuS_2 complexes (oblongs)	0.114 ± 0.038	Length: 0.782 ± 0.059 Width: 0.508 ± 0.058	17

Au rafts. As sulfur coverage increases up to 0.12 ML, the $p(2 \times 2)$ domains become larger and more isotropic, and rectangular rafts of Au form, adjacent to or inside the $p(2 \times 2)$ domains, as shown in Fig. 3. The rafts' identity is confirmed by the fact that their height, 0.18 ± 0.01 nm, equals the measured Au(100) step height, 0.19 ± 0.02 nm. These Au rafts are covered with the $p(2 \times 2)$ phase of S, and their edges align with the $p(2 \times 2)$ on lower

terraces. All of these characteristics of Au rafts are consistent with the prior report of Jiang *et al.*³¹

S atoms on the hex phase. Occasionally, protrusions are observed on the hex phase that may be S atoms. Two are encircled in Fig. 2. They are always slightly off-center from a hex stripe, but their size is irregular. Their density is extremely low, with an estimated upper limit of 0.004 nm^{-2} at total coverage of 0.009 ML, or 1 protrusion for every 400 Au atoms in the hex phase. Given the low density, we cannot exclude the possibility that some or all of these features are impurities.

DFT of the p(2x2) phase. We use DFT to evaluate μ_S (described in Sec. 2.2) of the chemisorbed phase. Fig. 4 shows values of μ_S for S adatoms at the 4th site on unreconstructed Au(100) surfaces for several different S configurations. Exact values of μ_S , together with other details, are given in Appendix 3. Three of the values define a convex hull, shown by the solid line segments in Fig. 4. We call this envelope the baseline energetics. Consistent with experiment, the p(2 x 2) defines the minimum energy at 0.25 ML.

As an aside, Table II gives nearest-neighbor interaction energies, w_n (n = nearest-neighbor separation in units of a) calculated for a lattice-gas model with only pair-wise interactions, on the unreconstructed (100) surface. Interactions through the 7th nearest neighbor are all repulsive (positive), with w_3 lowest, consistent with p(2 x 2) ordering. Interestingly, the first four pairwise interaction energies are similar to those deduced by Bak *et al.*⁵⁷ for Se/Ni(100), where the experimental phase diagram also contains a p(2 x 2) phase. We also note that another DFT study³⁵ of S/Au(100) found similar values for w_1 and w_2 , and postulated oscillatory longer-ranged interactions. In contrast, we observe only repulsive interactions up to $4a$, but with especially strong repulsion for w_4 .

TABLE II. Pairwise interaction energies between neighboring S atoms. w_n represents the n -th nearest-neighbor interaction energy, derived for a lattice-gas model with only pair-wise interactions.

n	1	2	3	4	5	6	7	8
w_n (eV)	0.433	0.211	0.001	0.031	0.006	0.012	0.005	-0.003

S-decorated step edges. At the lowest sulfur coverage investigated, 0.009 ML, step edges parallel to the hex stripes can be found that are decorated by single rows of protrusions, separated by $2a \gg 0.57 \pm 0.01$ nm [see Fig. 5(a)]. These rows apparently evolve into $p(2 \times 2)$ domains of increasing size as sulfur coverage increases, based on images such as the one in Fig. 5(b). At a given coverage, the $p(2 \times 2)$ domains near steps are generally larger than those far from steps.

DFT-derived values of μ_S are shown in Fig. 6, for a row of S atoms in several locations near an unreconstructed step edge. The step edge is modeled by a 3-atom-wide Au strip in a (2×6) supercell. Figures 6(a,b) show that a row of S adsorbed in 4fh sites on the lower terrace near a step is less stable than in pseudo-3-fold hollow sites directly at the step. Most favorable is the 4fh site along the upper terrace, adjacent to the edge, shown in Fig. 6(c). Adding an extra row of S on the lower terrace, as shown in Fig. 6(d), destabilizes the configuration based on the increase in μ_S . We conclude that the configuration with S atoms in 4fh sites on the upper terrace probably corresponds to the experimental image of Fig. 5(a).

3.3 Au-S complexes

Discrete features with well-defined shapes, other than those attributable to chemisorbed S, coexist with the $p(2 \times 2)$ phase even at the lowest measured coverage. The most common such features are diamond-shaped with a central bright spot. Dimensions are

given in Table I. We assign these as Au_4S_5 complexes for reasons given below. Features also exist that resemble incomplete diamonds, although these are less common. Still less common are oblong features. All are visible in Fig. 7. For instance, arrows point to features with 3 and 2 vertices in Fig. 7(e) and Fig. 7(a,b), respectively, and to oblong shapes in Fig. 7(c).

We assign the complexes on the basis of DFT calculations represented in Fig. 8. Given the predominance of $p(2 \times 2)$ phase in experiment, values of μ_S close to 0.25 ML are most relevant. At coverages close to 0.25 ML, several Au-S structures are more stable than the chemisorbed phase, by substantial margins: Au_4S_5 , Au_3S_4 , Au_2S_3 , and AuS_2 . These are represented by the points below the solid line in Fig. 8, and are shown schematically in Fig. 9. At 0.25 ML, the two most stable structures are Au_4S_5 and Au_3S_4 , which both have μ_S about 0.15 eV below baseline.

The structure of the most-stable Au_4S_5 complex is shown in the upper part of Fig. 10(a). It consists of a square of 4 Au atoms, each positioned close to 2-fold bridge sites on the underlying Au substrate. This square supports a single S atom, forming a pyramid. In addition, 4 S atoms are at the corners of the Au base, which accounts for the diamond-like shape. It can be regarded as a central S atom with 4 AuS legs. Intuitively, one might expect that the 4 S atoms would instead be located along the sides of the Au base, as in Fig. 10(c). However, the side location is far less favorable, since μ_S is higher for that configuration by 0.86 eV. The presence of a S adatom close to Au_4S_5 (within 1.5 lattice constants of a corner S) makes surprisingly little difference to μ_S , based on the configuration in Fig. 10(b). This is consistent with the observation that Au_4S_5 complexes are embedded within the $p(2 \times 2)$ phase (although the $p(2 \times 2)$ is usually rather disordered in the near vicinity of a complex). The

addition of more Au atoms to the Au base destabilizes the Au_4S_5 complex by over 0.4 eV, as illustrated in Fig. 10(d).

There is excellent agreement between STM images predicted from the DFT-optimized structure of Au_4S_5 and those measured experimentally, as seen by comparing the lower portions of Fig. 10(a,b) with Fig. 10(e). First, the distinctive shape is present in both cases: a bright central protrusion with 4 legs. In contrast, the configurations in Fig. 10(c,d) fail to reproduce this shape. Second, the orientation of the diamond is correct. To show this, the experimental image in Fig. 10(e) is rotated to align the underlying substrate (determined from the $p(2 \times 2)$) with the substrates in Fig. 10(a-d). Third, the lateral dimensions of Au_4S_5 are comparable in theory and experiment. This can be confirmed by inspecting the sizes of the diamond-shaped features in the respective parts of Fig. 10, knowing that the size of the experimental image has been adjusted to match the scale of the DFT configurations—again, using the $p(2 \times 2)$ as guide. In both experiment and theory, the diagonal dimension spans about $4a$ or, in terms of the metric that is most available from the STM images, about $2 p(2 \times 2)$ lattice constants.

The other features observed in STM can be considered partial diamonds that have 3 to 1 AuS legs emanating from the central S adatom. Energy-optimized configurations, STM images (both simulated and experimental), and corresponding chemical potentials are given in Fig. 11. The 3-leg structure is T-shaped, the 2-leg structure is heart-shaped, and the 1-leg structure is oblong shaped. In all complexes, the Au atoms are not at the natural 4fh sites, but rather at 2-fold bridge sites in the Au substrate, or nearly so; this is evident also in Fig. 9. In all 4 complexes, the Au atoms in are not at the natural 4fh sites, but rather at 2-fold bridge sites in the Au substrate, or nearly so; this is evident also in Fig. 9.

Values of chemical potential are compared in Fig. 8 for complexes with different numbers of AuS legs, for coverages close to 0.25 ML. In this coverage regime, complexes with 4 and 3 legs have comparable values of μ_S . Structures with 2 or 1 legs are less favored but still more stable than the p(2 x 2) phase.

Fig. 11 shows that 4- and 3-leg structures have the central S atom above the plane of the Au base and this makes the center of these complexes appear bright in the STM images. In the 2- and 1-leg structures, all S atoms are nearly co-planar with the remaining Au base, and so they lack the bright spot. Further insight into the structures of the two larger complexes, Au₄S₅ and Au₃S₄, is provided by the cross-sectional view in Fig. 12. This view shows that they can be regarded as slightly-bent S-Au-S motifs in which one S atom is lifted above the surface. The S-Au-S angles are 167.4° in Au₄S₅, and 172.4° and 164.6° in Au₃S₄. In the latter case, the smaller angle is associated with the two AuS legs that point in opposite directions, i.e. the legs perpendicular to the plane of Fig. 12(a).

It is interesting that, starting from the 4-leg complex, smaller structures are generated by successively deleting entire AuS legs. One might expect corner S atoms to be deleted instead, thus preserving the Au₄ base. However, the latter expectation is not supported by the values of μ_S . For example, the configuration in Fig. 11(d), which lacks a single corner S atom, is less stable by 0.09 eV than that in Fig. 11(a), which lacks both S and Au.

We have checked the effect that different approximations in DFT may have on μ_S . Results are shown in Table III, comparing LDA with PBE⁵¹ and optB88.⁵⁸⁻⁵⁹ The latter accounts for dispersion forces. It can be seen that the order of μ_S for the two complexes is the same for all functionals. For the two higher level theories (PBE and optB88), μ_S for complexes are lower than for the p(2 x 2), while for LDA, the reverse is true. Since it is

generally believed that generalized gradient approximation (GGA) functionals such as PBE are more accurate than LDA, one should draw the conclusion that the complexes have lower μ_S than the chemisorbed phase according to DFT.

TABLE III. Values of μ_S for different configurations and different approximations in DFT.

Configuration	LDA	PBE	optB88
$p(2 \times 2) - S$	-1.998(2) eV	-1.273(2) eV	-1.444(2) eV
$(2\sqrt{2} \times 2\sqrt{2})R45^\circ - AuS_2$	-1.886(15)	-1.327(2)	-1.487(1)
$(2\sqrt{5} \times 2\sqrt{5})R26.6^\circ - Au_4S_5$	-1.942(2)	-1.401(1)	-1.538(1)

Finally, we note that in our experiments, the sample was prepared at 300 K, and then cooled to 5 K for imaging. After this initial preparation, we regularly re-heated the sample to 300 K and repeated measurements at 5 K, to determine whether observations depended on length of time at 300 K or number of heating-cooling cycles. In all cases, there was no difference in the observations before and after the second cycle. In particular, complexes existed under both conditions, in comparable abundance.

3.4. Mass balance on terraces

Ejected Au atoms can be consumed by Au-S complexes, Au rafts, and (presumably) step edges. From the STM data, we can gain insight into the balance between these pathways. We focus first on large terraces, more than ca. 5 nm wide. Figure 13(a) shows the number density of Au atoms released (calculated from the area of the unreconstructed surface phase), and the density of Au atoms consumed by complexes and Au rafts. Figure 13(b) shows the fraction of Au atoms that are ejected, but are not accounted for by complexes and rafts.

Details of this calculation are given in Appendix 2. At lowest coverage, 80% of the ejected Au is unaccounted for, meaning that it must diffuse to, and be captured at, step edges. For coverages of 0.024 ML or higher, the opposite is true: most of the ejected Au is contained in complexes and Au islands. We interpret this to mean that excess Au cannot diffuse efficiently to nascent step edges at 0.024 ML and above, at 300 K. As the surface becomes more crowded, it becomes more likely that the ejected Au is captured on a terrace before it can reach a step.

Figure 13(a) also shows that the amount of Au in the complexes is roughly constant as a function of coverage, while the amount of Au in rafts increases strongly, consistent with qualitative observation (e.g. Fig. 3).

Terraces narrower than ca. 5 nm exhibit very few complexes or rafts. Figure 14 shows an STM image with several terraces. One, labeled t1, is wide in the lower part of the image, and narrow in the upper part. As it changes from wide to narrow, the complexes/rafts disappear. The other terrace, t2, is narrow throughout and barren. There is also a narrow denuded zone along the upper terrace, next to the step. Such observations mean that released Au atoms are captured efficiently by step edges at all S coverages, if the distance to a step is sufficiently small. In turn, this suggests that both complexes and rafts are metastable with respect to steps.

4. Discussion

Nature of the complexes. The main result of this paper is the identification of complexes, primarily Au₄S₅ diamonds, that exist on the unreconstructed Au(100) surface. This is the first observation of metal-sulfur complexes on an fcc(100) surface, to our

knowledge. We have isolated these species in experiment by making observations at very low sulfur coverages, in the range 0.009 to 0.12 ML.

A prior study of this system by Jiang *et al.*, using STM and XPS, focused mainly on higher coverages, particularly ordered structures that emerged above 0.25 ML.³¹ However, Jiang *et al.* published one STM image where the (unspecified) coverage was considerably below 0.25 ML, since most of the surface was still reconstructed, and another image at a coverage close to 0.25 ML, since the surface was essentially covered by p(2 x 2) islands and rafts. There are many small features in these two images whose shapes are not resolved, but which may be complexes. In fact, in one of the images—the inset to their Fig. 5(b)—a diamond-like shape exists atop a raft.³¹ It has an orientation and size consistent with the diamonds reported herein, gauging by the surrounding p(2 x 2) structure.

Formation of four-fold hollow sites for adsorbed S has been proposed to drive reconstructions of the (111) surfaces of Cu¹⁹⁻²⁰ and Ag,¹⁸ and of the (110) surface of Au.⁴⁰ In the present system, however, formation of such sites cannot drive complexation, since the unreconstructed surface already offers four-fold hollow sites. Instead, the stability of the two smaller Au-S complexes, AuS₂ and Au₂S₃, can be attributed to linear S-Au-S (sub)units, i.e. staples, as shown in Fig. 9. As noted in Sec. 1, this motif has been observed previously in Cu-S and Ag-S complexes that form on Cu(111) and Ag(111), respectively.¹⁸⁻¹⁹ In fact, the shape of Au₂S₃ is very analogous to the heart-shaped Cu₂S₃ complex found on Cu(111), where the linear S-Cu-S geometry was shown to maximize overlap between the d_{z²} orbital of the central metal atom and the p_z orbital of each S atom.¹⁹ As pointed out in Sec. 3.3 and Fig. 12, the two larger complexes consist of slightly-bent S-Au-S subunits. Hence, all the complexes may be regarded as combinations of (near-) linear S-Au-S motifs.

Stabilities of coexisting structures. We have identified the complexes by comparing their size, orientation, and appearance in STM experiments with DFT calculations. We have also identified them on the basis of their favorable μ_S . However, two features of the experimental data are at variance with the DFT. First, the predominance of p(2 x 2) islands and rafts, in experiment, contradicts the fact that μ_S calculated for complexes is lower than for the p(2 x 2) structure (Sec. 3.3 and Fig. 8). Second, the fact that μ_S is more negative for the complexes than for the p(2 x 2) phase means that complexes should consume Au atoms from step edges (along with chemisorbed S from terraces), but the data suggest otherwise. In experiment, neither rafts nor complexes are observed on narrow terraces (Sec. 3.4 and Fig. 14), indicating that both are metastable with respect to step edges. Consistent with the latter premise, Jiang *et al.* reported that annealing at 630 K (starting from a coverage higher than 0.25 ML) produces large domains of p(2 x 2) with no trace of rafts or complexes.³¹

The inconsistency between experiment and DFT could be due to any of several factors. First, DFT may not accurately represent the real system. In particular, our DFT calculations involve an ideal unreconstructed Au(100) substrate. The calculations do not take into account the effects (e.g. elastic interactions) of the surrounding reconstruction, nor of the step edges, and such interactions could shift μ_S significantly.

Second, values of μ_S are calculated here for $T = 0$ K, hence excluding any entropic contribution, whereas the real surface forms at 300 K and quenches at some intermediate temperature as it cools to 5 K. Third, populations of surface species can be predicted from μ_S only if Au atoms on terraces are equilibrated with step edges. This last factor is the only one that can be addressed concretely, since the data show that Au atoms primarily diffuse to step

edges if S coverage is very low, or if the terrace is very narrow, but become trapped on terraces under other conditions. Thus, kinetics are considered next.

Kinetics. The kinetics of this system must be very complex, involving diffusion of two different species (Au and S) on different types of Au surfaces (reconstructed and unreconstructed), plus nucleation and growth of complexes and rafts, all combined with the local dynamics of Au atom rearrangement and ejection. In the following, we present some aspects of the kinetics that are known or can be deduced, then develop a qualitative model that is consistent with key experimental observations.

S can undergo long-range diffusion on the hex phase of Au, at least at 300 K. This is evident from the ability of S atoms to cluster and lift the reconstruction locally, even when the total S coverage is very low, as in Fig. 2. To a first approximation, the diffusion barrier on the hex phase should be comparable to that on Au(111), where its calculated value is 0.39 to 0.47 eV.³⁷ This is compatible with significant diffusion at room temperature.

At the same time, it is known that Au atom diffusion on the hex phase is anisotropic,^{26, 60} occurring preferentially in the direction parallel to hex stripes, with a low barrier of 0.32 eV.²⁶ Its diffusion barrier within a p(2 x 2) matrix of sulfur is presumably much higher. According to DFT, in fact, a single Au atom would form a complex with surrounding sulfur, rather than diffuse.

From our data, and from that of Jiang *et al.*,³¹ the initial growth of unreconstructed regions is also highly anisotropic: elongated p(2 x 2) islands form with their long axis parallel to hex stripes. Similar anisotropic growth of unreconstructed regions has been observed for NO, CO, and oxygen on Pt(100),^{55, 61-62} where it is attributed to the anisotropic degree of commensuration at the interfaces between unreconstructed and hex phases⁶² or to

anisotropic internal stress in the hex layer.⁶¹ In our observations the hex stripes behave like one-dimensional rods whose ends erode individually as the reconstruction is lifted. This is evident in Fig. 3(a-c), which contains many terminated hex stripes, some marked by arrows.

Close inspection shows that the hex stripes terminate in four ways. The terminus can have no distinctive structure, as in Fig. 3(b) (arrow), or it can be a single dot, as in Fig. 3(c) (arrow). The dot is probably a S adatom. Third, the terminus can be a diamond or partial diamond, as in Fig. 3(a) or Fig. 3(d) (arrows). Good examples are also visible in Fig. 7(d) (lower arrow) and Fig. 7(f) (arrow). In this situation, the complex is actually embedded in the end of the stripe. Fourth, the stripes can end in Au rafts; examples are visible in Fig. 7(d) (upper arrow) and Fig. 7(e) (lower arrow). The fact that complexes and rafts are found connected to the ends of hex stripes indicates that they may form as a direct result of the local Au structure transformation.

The above features can be combined in the following model—although we do not propose that this model is unique. Excess Au atoms are generated at the ends of stripes. Disposition of these atoms is stochastic. Each atom may diffuse away from the point of generation, or be captured immediately. If a Au atom diffuses away on the hex phase, it moves preferentially parallel to the hex stripes until it is captured. The point of capture can be another unreconstructed island if the terrace is wide or a step edge if the terrace is narrow. When the density of excess Au at a stripe terminus happens to be high while the reconstruction is lifted, a raft forms; when it is moderate, a complex forms; when it is low, $p(2 \times 2)$ forms. Once nucleated, rafts can grow indefinitely whereas complexes cannot, which explains why rafts dominate as coverage increases (cf. Fig. 13(a)). However at very low coverage, i.e. 0.009 ML, only complexes and $p(2 \times 2)$ islands can form, because the overall

density of excess Au is simply too low to initiate rafts. The Au rafts are metastable; they form only because of the supersaturation of Au adatoms on the (wider) terraces. It is not clear whether the complexes are metastable as well; DFT and experiment are in seeming contradiction on this point. Systematic experiments at higher temperatures could clarify this issue.

5. Conclusions

We have identified a family of related Au-S complexes which form on this surface, the most common one being diamond-shaped Au_4S_5 . The identification rests on comparisons of their size, shape, and orientation in STM and DFT, together with values of μ_S from DFT. DFT shows that the family of diamond complexes is more stable than other candidate complexes. The formation of complexes, Au rafts, and $p(2 \times 2)$ islands is probably competitive and influenced by kinetics under the conditions of these experiments.

Acknowledgements

The experimental component of this work was conducted or supervised by HW, JO, HJY, YK, and PAT. It was supported by three sources. From the U.S., it was NSF Grant CHE-1507223. From Japan, support was provided by a Grant-in-Aid for Scientific Research on Priority Areas “Electron Transport Through a Linked Molecule in Nano-scale”; and a Grant-in-Aid for Scientific Research(S) “Single Molecule Spectroscopy using Probe Microscope” from the Ministry of Education, Culture, Sports, Science, and Technology (MEXT). The theoretical component of this work was carried out by DJL. It was supported by the Division of Chemical Sciences, Basic Energy Sciences, US Department of Energy (DOE). This part of

the research was performed at Ames Laboratory, which is operated for the U.S. DOE by Iowa State University under contract No. DE-AC02-07CH11358. This part also utilized resources of the National Energy Research Scientific Computing Center, which is supported by the Office of Science of the U.S. DOE under Contract No. DE-AC02-05CH11231.

Figures

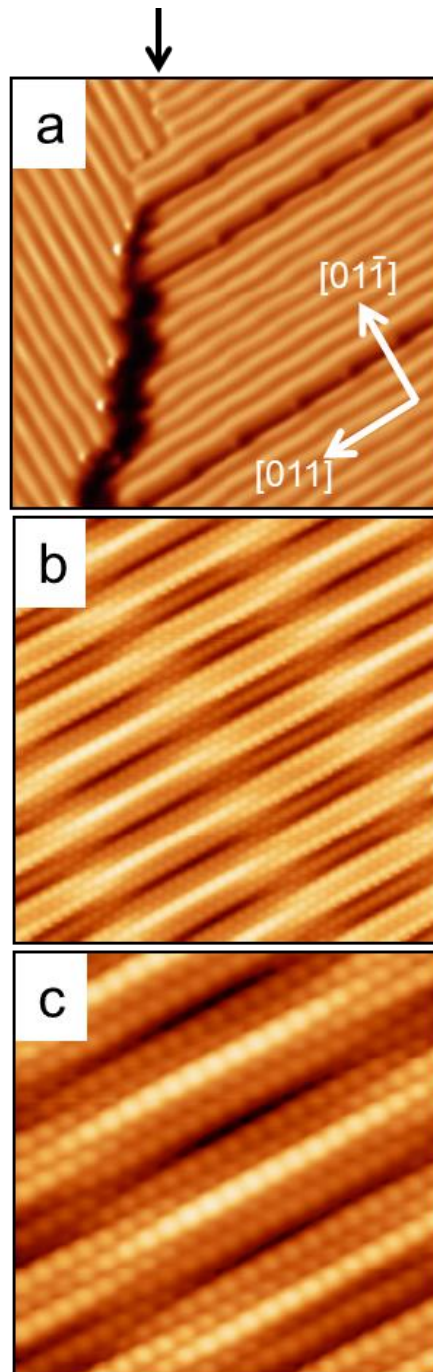


Figure 1. STM images of a clean Au(100) surface. a) Several step edges, and a domain boundary indicated with an arrow. The image is differentiated to facilitate viewing of hex stripes on different terraces; $30 \times 30 \text{ nm}^2$. b) Topographic image of a terrace region; $10 \times 10 \text{ nm}^2$. c) Topographic image of a terrace region with atomic resolution; $5 \times 5 \text{ nm}^2$.

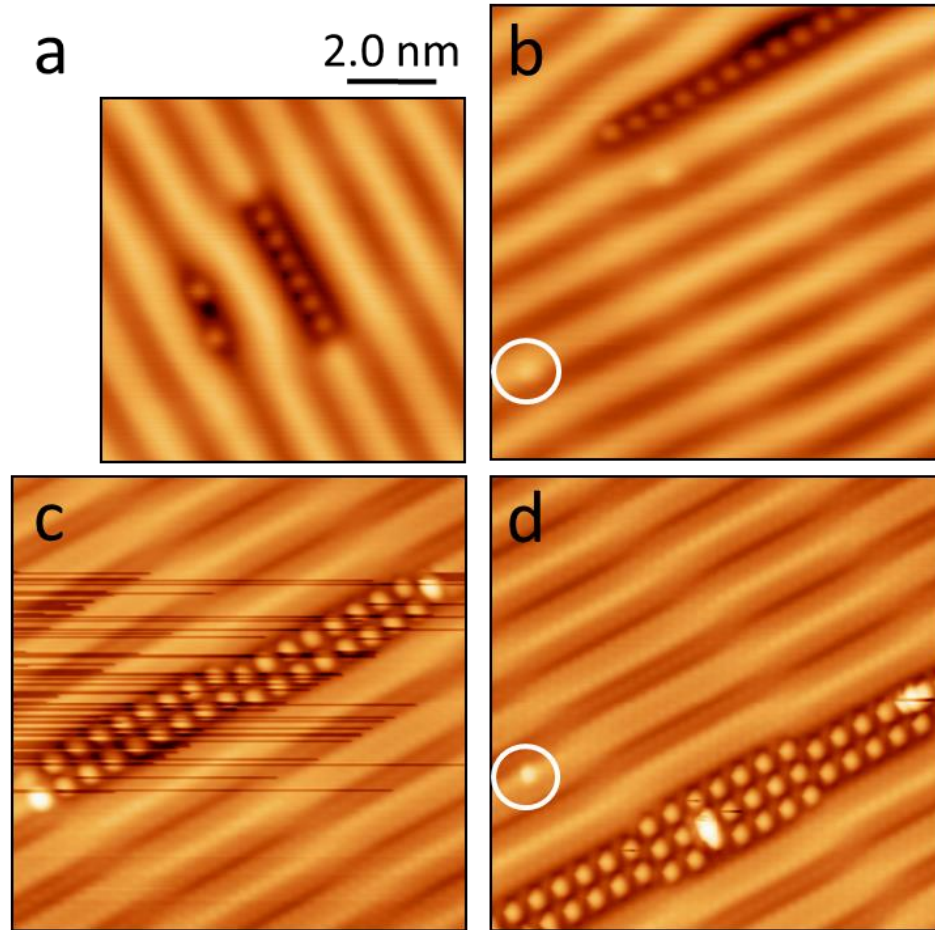


Figure 2. One-dimensional rows and $p(2 \times 2)$ islands of sulfur atoms at 0.009 ML. All images are topographic and sized to the same scale. a) $8.0 \times 8.0 \text{ nm}^2$. b) $10 \times 10 \text{ nm}^2$. c) $10 \times 10 \text{ nm}^2$. d) $10 \times 10 \text{ nm}^2$.

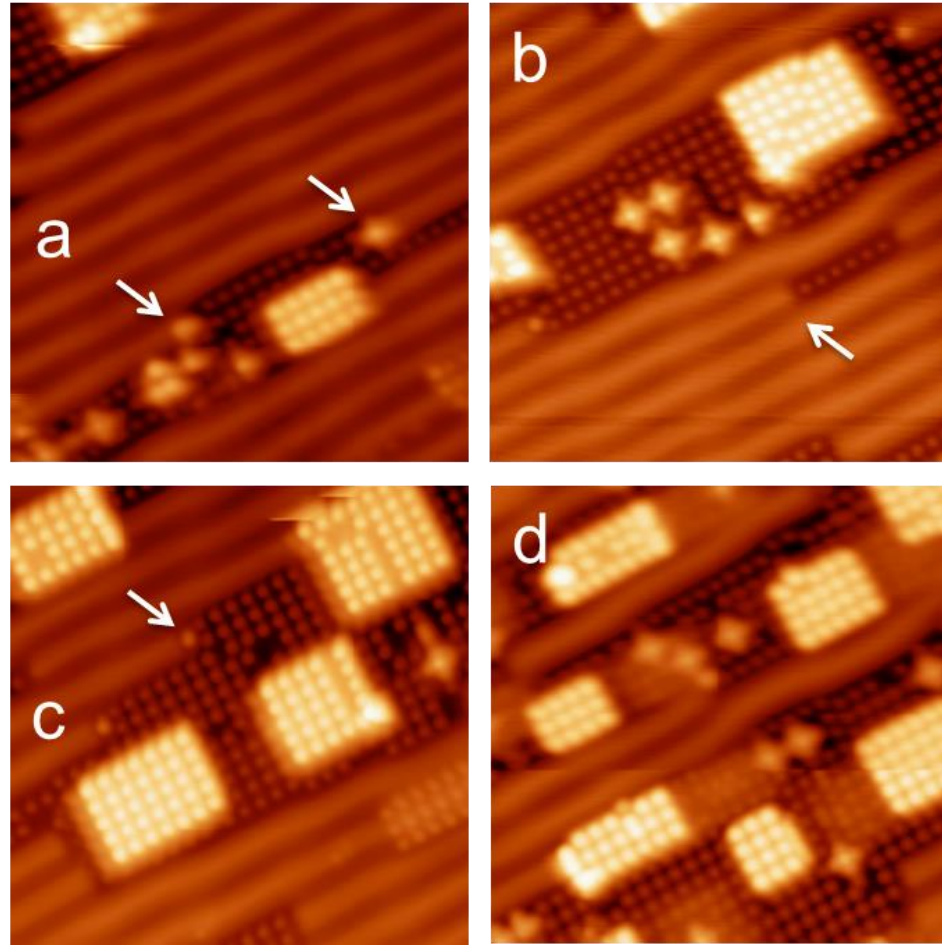


Figure 3. Topographic images of Au rafts and complexes on the $p(2 \times 2)$ domains. Image size is $15 \times 15 \text{ nm}^2$. a) 0.024 ML. b) 0.032 ML. c) 0.055 ML. d) 0.12 ML. Arrows are explained in the text.

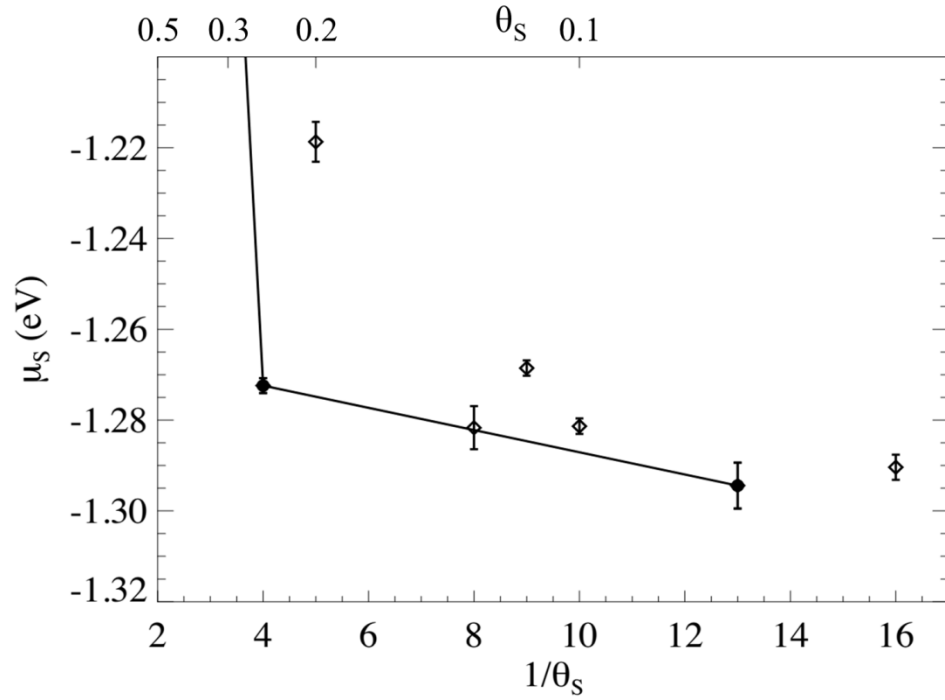


Figure 4. Chemical potential of S chemisorbed on 4fh sites of Au(100) in 7 different supercells from DFT-PBE calculations.

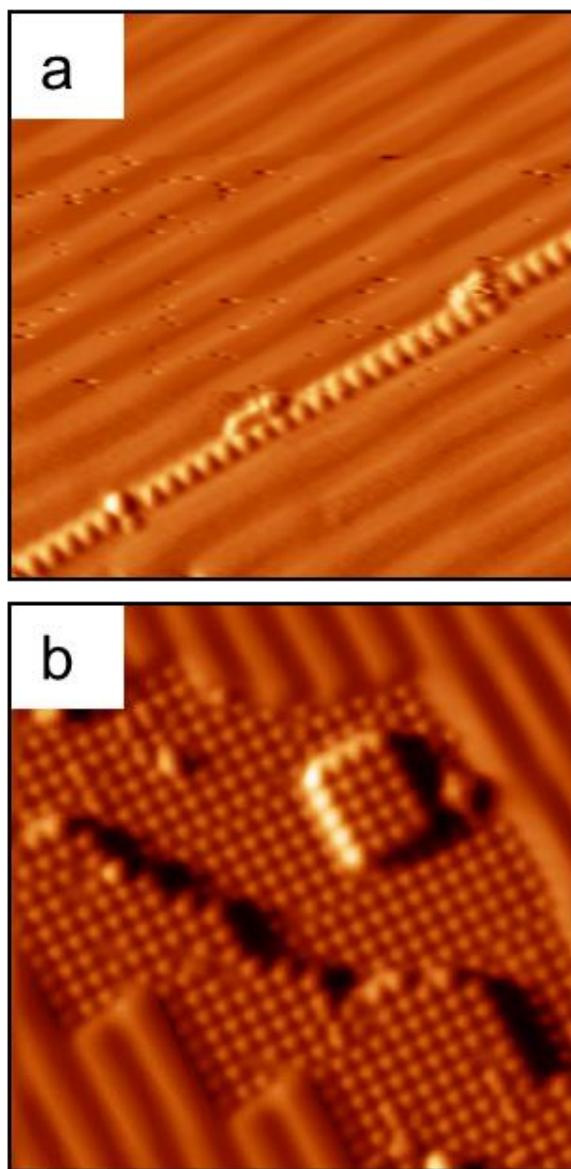


Figure 5. STM images near step edges following adsorption of sulfur. Images are differentiated to facilitate viewing structures on different levels, and are $15 \times 15 \text{ nm}^2$. a) A row of sulfur at a step edge, 0.009 ML. Sulfur atoms are separated by $2a$. b) A step edge bounded by relatively large $p(2 \times 2)$ domains, 0.055 ML.

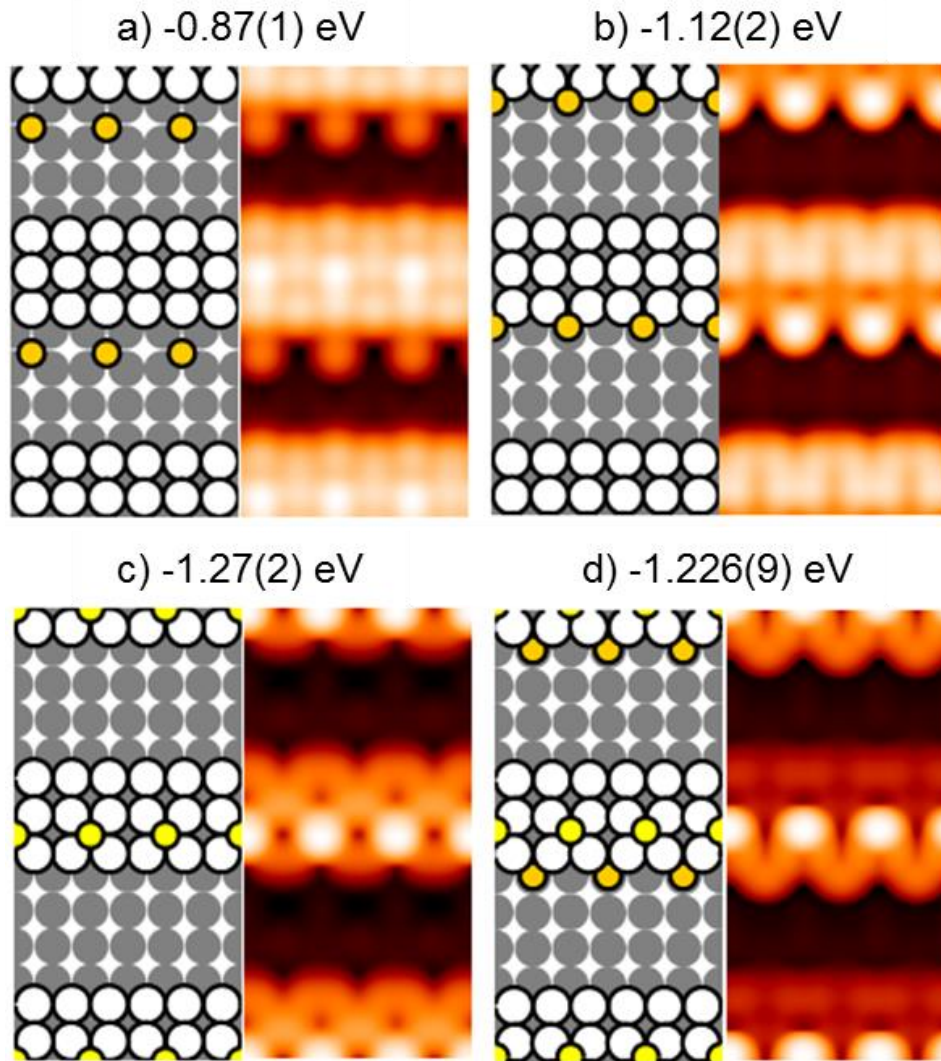


Figure 6. Energy-optimized configurations, simulated STM images, and calculated chemical potentials of S rows at step edges. Gray circles represent Au atoms in the unreconstructed (100) surface; white circles are Au atoms on top of the (100) surface, representing a short-range gold terrace; gold circles are S atoms along the lower terrace, roughly coplanar with the Au atoms; and yellow circles are S atoms on the upper terrace. The supercells are (2 x 6).

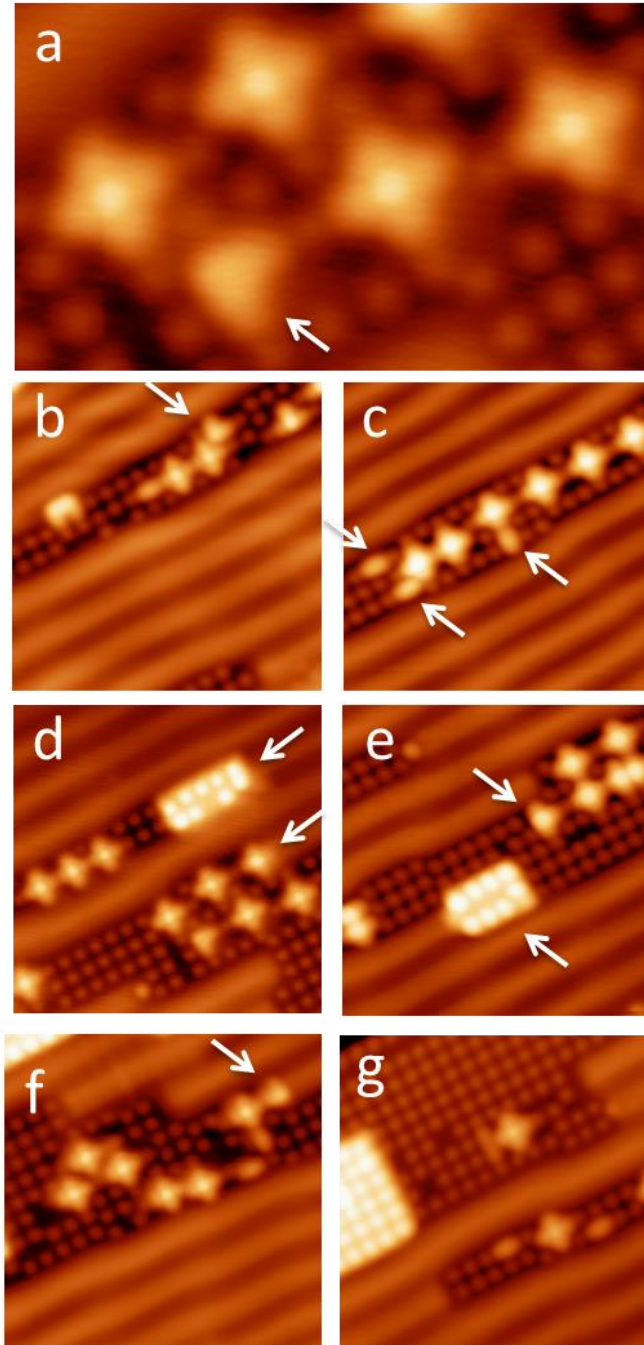


Figure 7. Au-S complexes on p(2 x 2) domains. The image size of panel (a) is 5 x 3.3 nm²; all others are 10 x 10 nm². a) High resolution image of the Au₄S₅ complexes. The arrow indicates an Au₂S₃ complex. Sulfur coverage is 0.055 ML in all panels except (b-c), where it is 0.009 ML. The text explains the significance of the arrows.

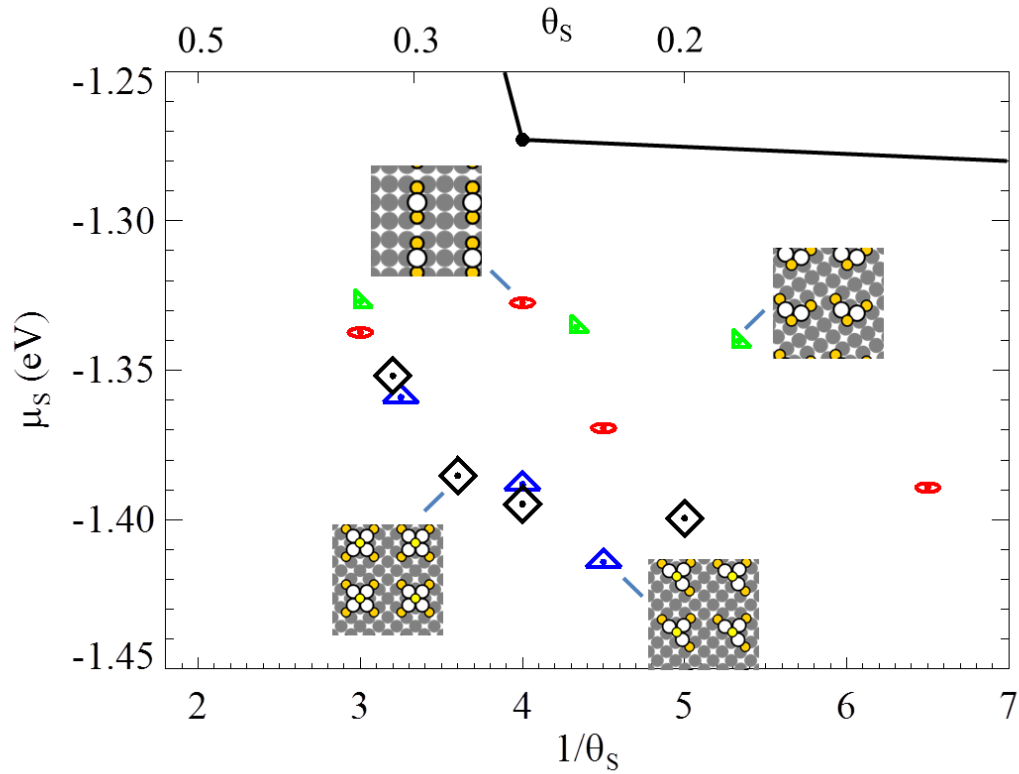


Figure 8. Chemical potentials of most favorable complexes calculated from DFT. A portion of the convex hull for the chemisorbed phases, shown in Fig. 4, is reproduced by the black line segments. Red ovals indicate AuS₂, green triangles Au₂S₃, blue triangles Au₃S₄, and black lozenges Au₄S₅.

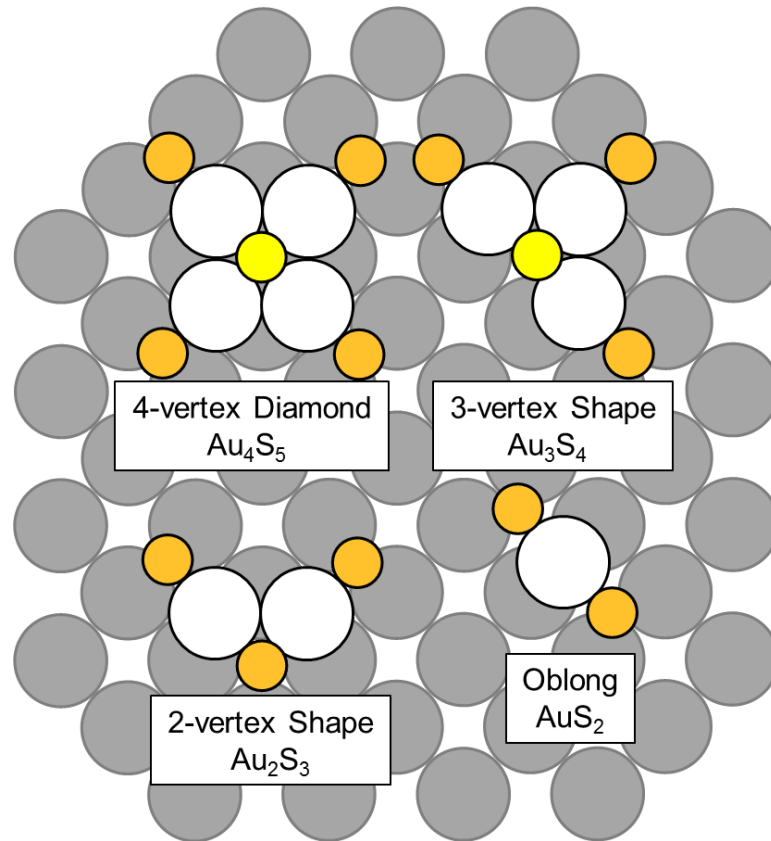


Figure 9. Schematics of Au-S configurations, where gray circles represent Au atoms in the unreconstructed (100) surface; white circles are Au atoms on top of the (100) surface, as part of complexes; gold circles are S atoms in the complex, roughly coplanar with the Au atoms; and yellow circles are S atoms in an upper level, at the top of the complex.

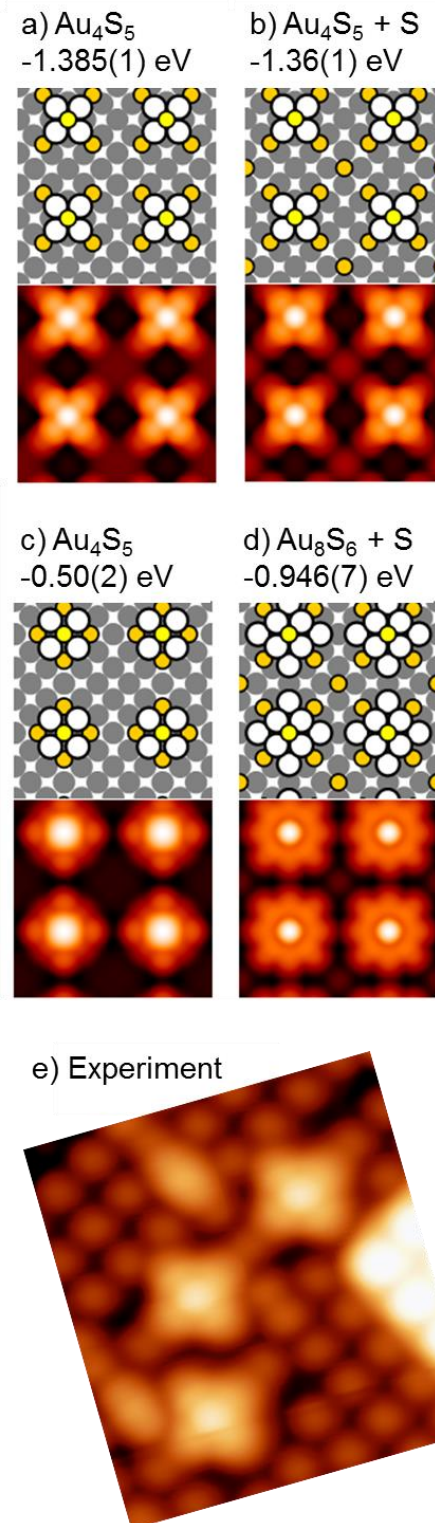


Figure 10. Complexes related to diamond-shaped clusters. Top panels of a-d show energy-optimized configurations with the same color coding as in Fig. 9, and values of μ_S . Bottom panels show the corresponding STM images simulated from DFT. Panel (e) is an experimental image, size 3.6 x 4.0 nm², 0.12 ML.

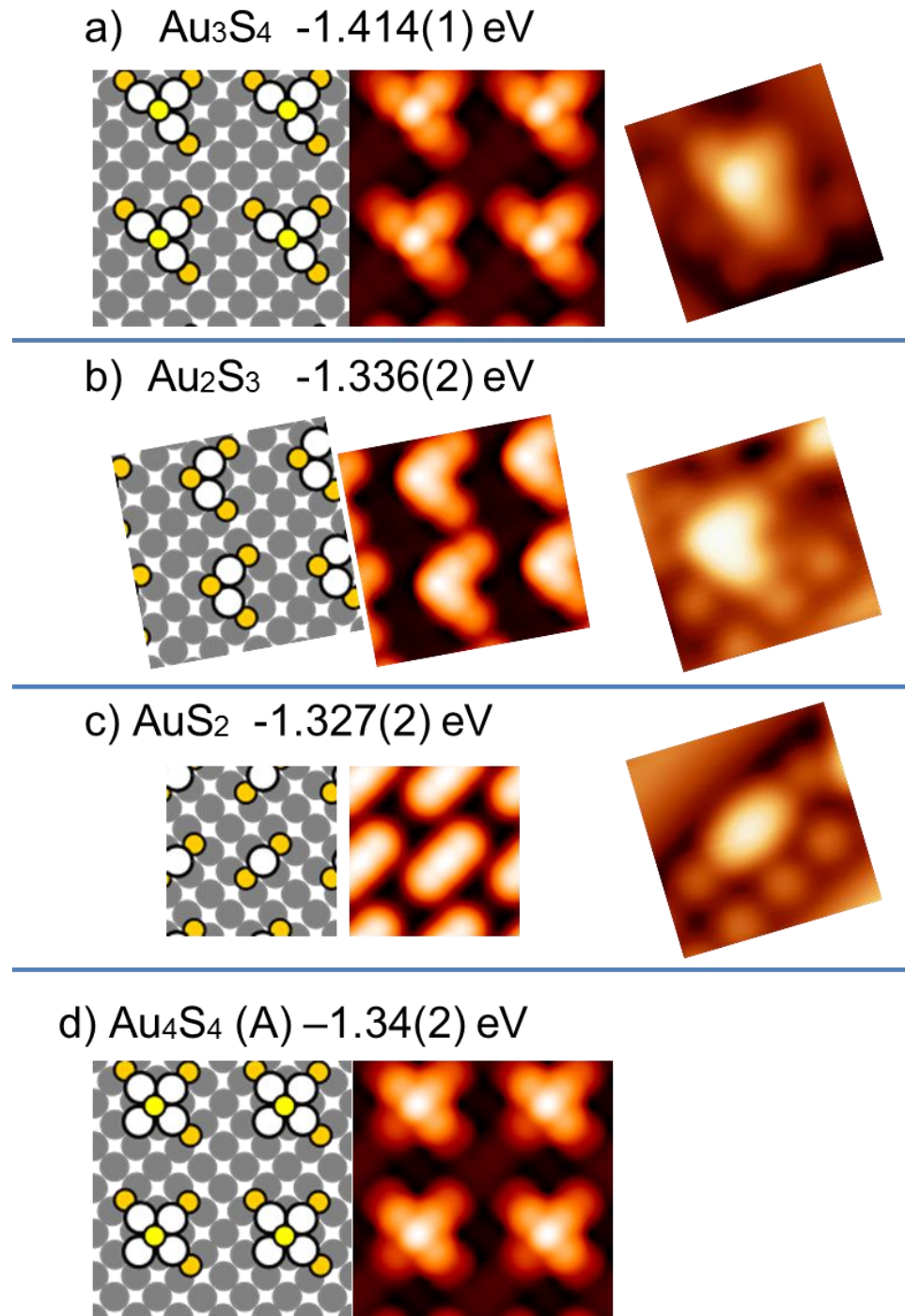


Figure 11. Complexes related to partial diamonds. Each panel contains, from left to right: the energy-optimized configuration from DFT (with same color coding as in Fig. 9); the corresponding simulated STM image; and the experimental STM image ($2 \times 2 \text{ nm}^2$), where applicable.

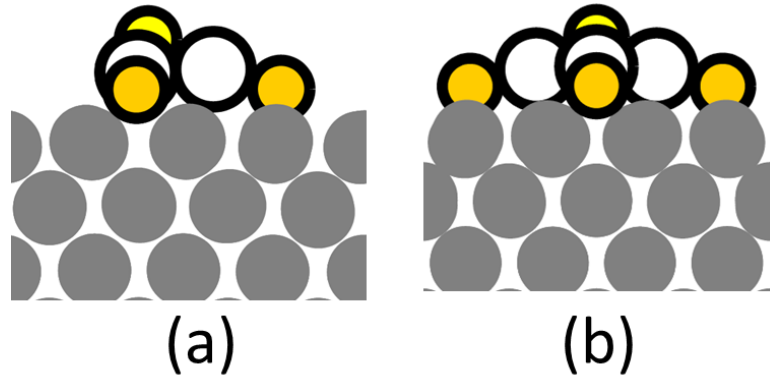


Figure 12. Cross-sectional views of DFT-optimized configurations for a) Au_3S_4 and b) Au_4S_5 . The color scheme of Fig. 9 is used.

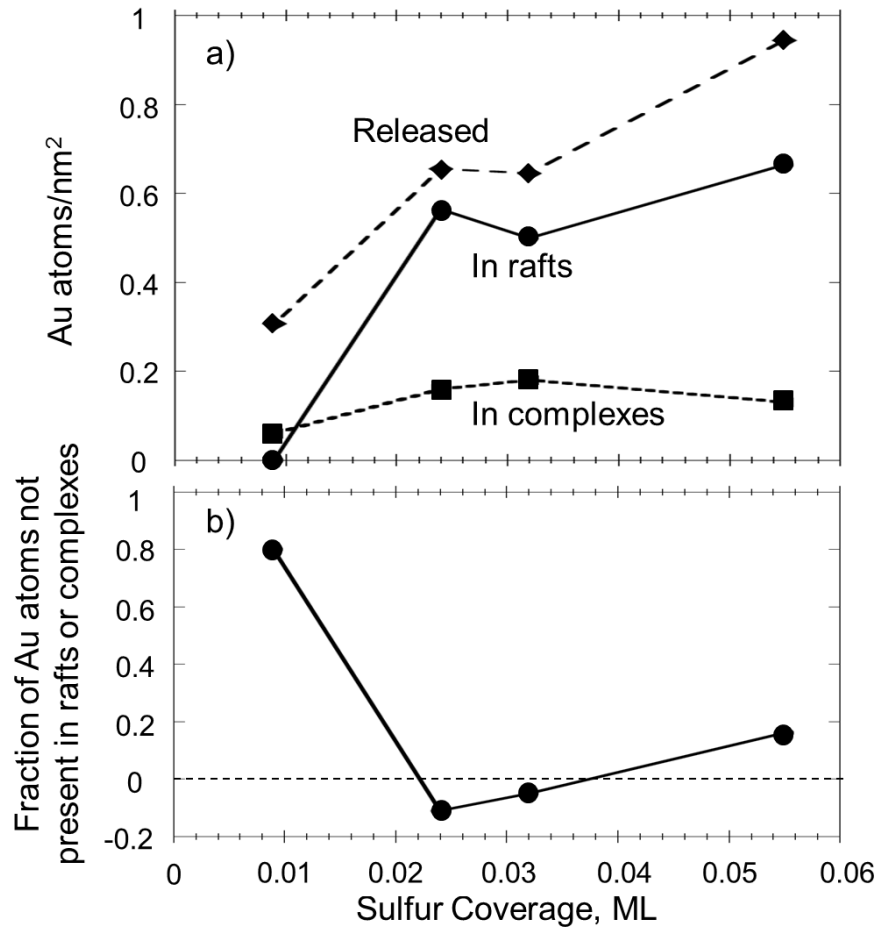


Figure 13. Mass balance for ejected Au atoms on large terraces. Lines are simply drawn to connect data points. Panel (a) shows the number of Au atoms released and subsequently consumed in S-Au structures, per unit area. Panel (b) shows the fraction of Au atoms not accounted for in observed S-Au structures.

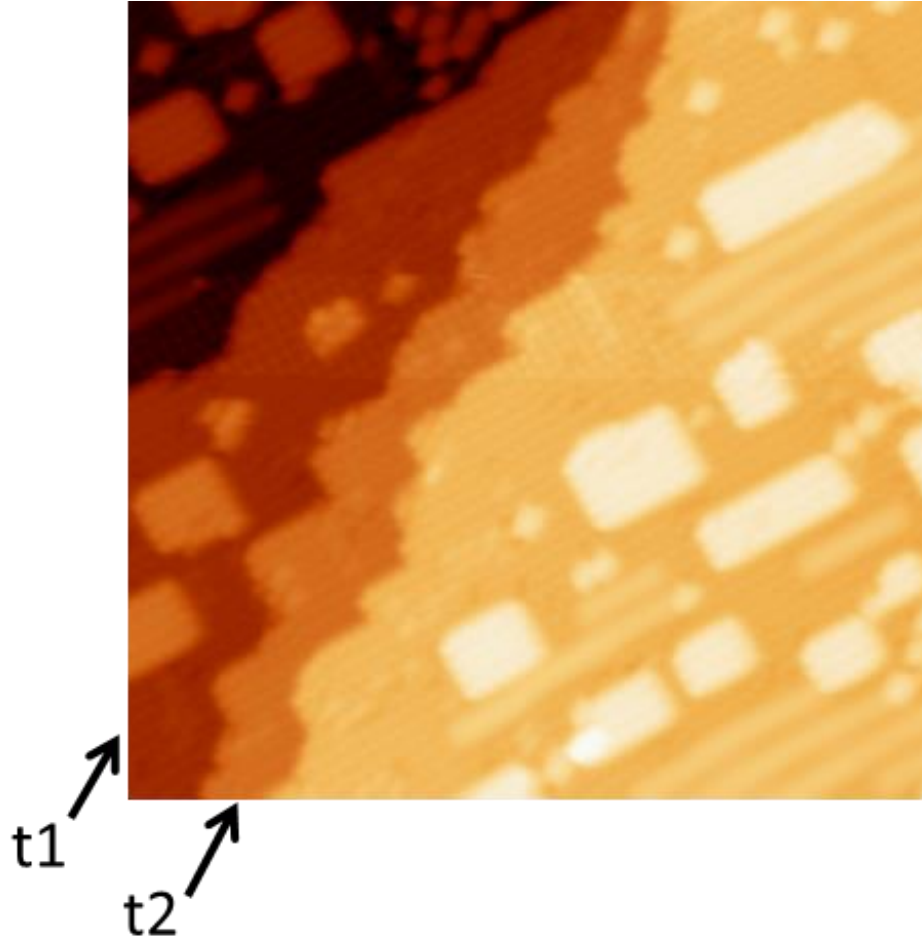


Figure 14. Topographic STM image including narrow terraces (t1 and t2). $30 \times 30 \text{ nm}^2$; 0.12 ML.

Appendix 1. Tunneling conditions for STM images in the main text

Figure	Image size (nm ²)	Tunneling current (nA)	Sample Bias (V)	θ_s
1a	30 x 30	0.915	-0.516	
1b	10 x 10	8.72	-0.002	
1c	5 x 5	13.91	-0.002	
2a	8 x 8	2.19	-0.456	0.009
2b	10 x 10	1.83	-0.500	0.009
2c	10 x 10	2.63	-0.002	0.009
2d	10 x 10	2.85	-0.002	0.009
3a	15 x 15	1.72	-0.085	0.024
3b	15 x 15	1.94	-0.052	0.032
3c	15 x 15	2.38	-0.078	0.055
3d	15 x 15	1.01	-0.061	0.115
4a	15 x 15	1.68	-0.135	0.009
4b	15 x 15	2.104	-0.038	0.032
6a	5 x 3.3	3.03	-0.023	0.055
6b	10 x 10	1.91	-0.229	0.009
6c	10 x 10	1.00	-1.000	0.009
6d	10 x 10	3.03	-0.023	0.055
6e	10 x 10	1.68	-0.253	0.055
6f	10 x 10	1.79	-0.168	0.055
6g	10 x 10	2.10	-0.038	0.055
8e	3.6 x 4	0.468	+1.000	0.115
9a	2 x 2	2.91	-0.033	0.055
9b	2 x 2	3.03	-0.023	0.055
9c	2 x 2	2.10	-0.038	0.055
12	30 x 30	1.75	+0.092	0.115

Appendix 2. Details of determining Au mass balance

The density of atoms in the hex reconstruction, N_{hex} , is 15 nm^{-2} , while in the unreconstructed layer the density, $N_{1 \times 1}$, is 12 nm^{-2} . To determine the number of ejected Au atoms, we first determine the area of the unreconstructed regions and multiply this by the density difference, $\Delta N = 3 \text{ nm}^{-2}$. This gives the density of Au atoms released, N_{rel} . Then, we evaluate the density of Au atoms contained in complexes and rafts, N_{cr} . If there were perfect mass balance on the terrace (and within the scope of the imaged regions), the difference $N_{\text{rel}} - N_{\text{cr}}$ would be zero.

The fraction of Au atoms released but not accounted for in complexes and rafts, shown in Fig. 13(b) of the main text, is calculated as $F = (N_{\text{rel}} - N_{\text{cr}}) / N_{\text{rel}}$. A positive value of F indicates that more Au atoms are ejected than consumed, as is true at 0.009 ML. A large negative value of F would indicate the reverse. We estimate that the small deviations of F from zero, at 0.024, 0.032, and 0.055 ML in Fig. 13, are within experimental uncertainty.

Appendix 3. Additional DFT Analysis

A. Details of DFT results for the chemisorbed phases.

Energetics of single S adsorbed on 4fh sites of Au(100) in 9 different supercells from DFT-PBE calculations, averaging from $L = 7$ to 12, are provided in Table AI. Uncertainties, in parentheses, represent the variation in μ_S between individual slab thickness values. The index j is the separation between nearest-neighbor S atoms in units of a , for each supercell. The three values in boldface define the convex hull shown in Fig. 4 in the text.

TABLE AI. Baseline energetics from DFT.

j	θ_S	k-points grid	Supercell	μ_S (eV)
1	1	(12 x 12)	(1 x 1)	0.169(4)
2	1/2	(17 x 17)	($\sqrt{2}$ x $\sqrt{2}$)R45°	-0.834(2)
3	1/4	(12 x 12)	(2 x 2)	-1.273(2)
4	1/5	(11 x 11)	($\sqrt{5}$ x $\sqrt{5}$)R26.6°	-1.219(4)
5	1/8	(8 x 8)	(2 $\sqrt{2}$ x 2 $\sqrt{2}$)R45°	-1.282(5)
6	1/9	(8 x 8)	(3 x 3)	-1.268(2)
7	1/10	(8 x 8)	($\sqrt{10}$ x $\sqrt{10}$)R18.4°	-1.281(2)
8	1/13	(7 x 7)	($\sqrt{13}$ x $\sqrt{13}$)R33.7°	-1.294(5)
9	1/16	(6 x 6)	(4 x 4)	-1.285(3)

B. Other configurations evaluated with DFT.

Figures A1-A9 show some of the other S atom arrays tested in DFT. Each panel contains a schematic of the repeating structure within the unit cell, slab thickness (L), and the chemical potential of sulfur, μ_S . Many panels also include a simulated STM image, in shades of orange. The supercell is given in each figure caption.

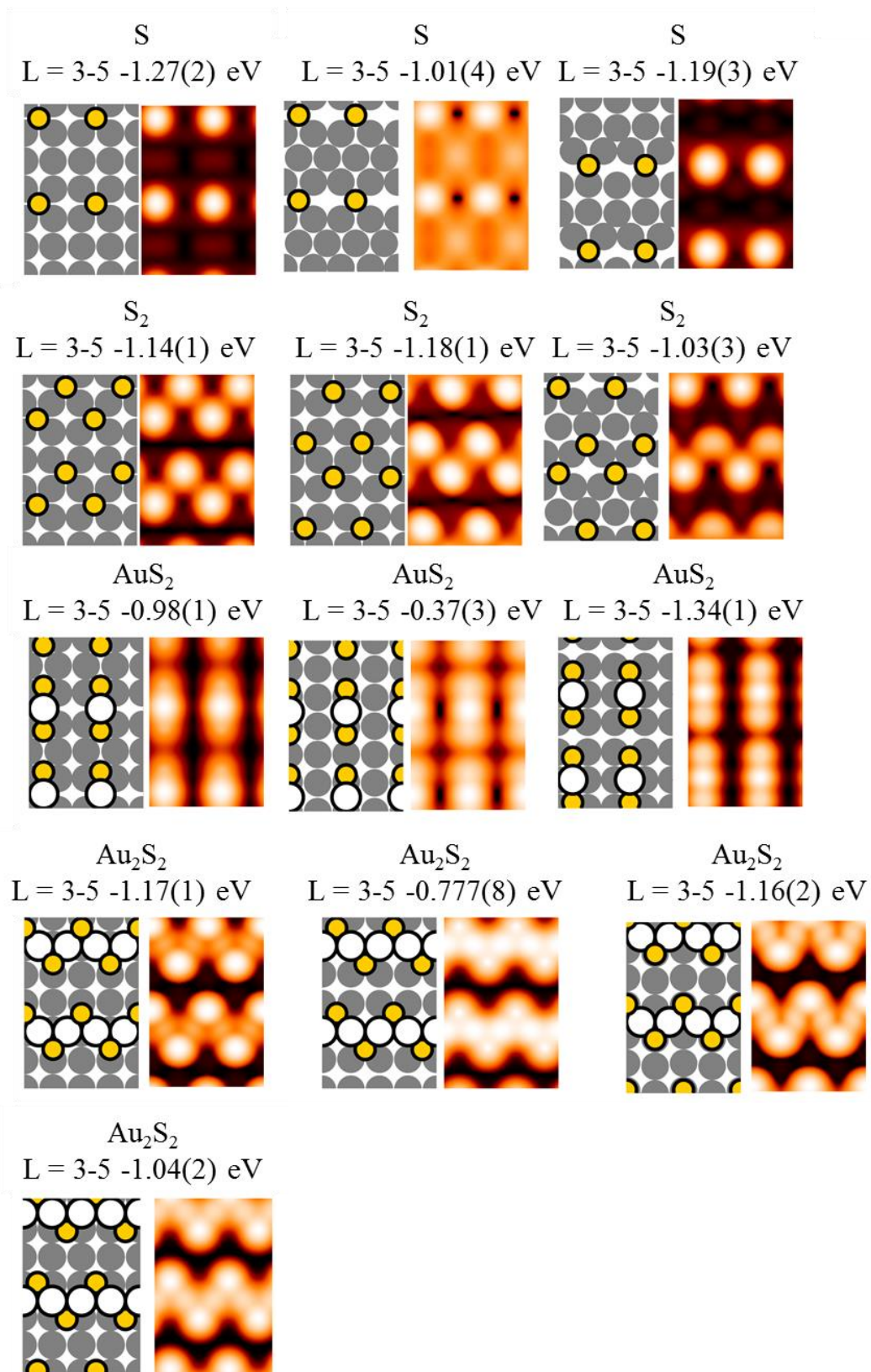


Figure A1. (2 x 3) supercell.

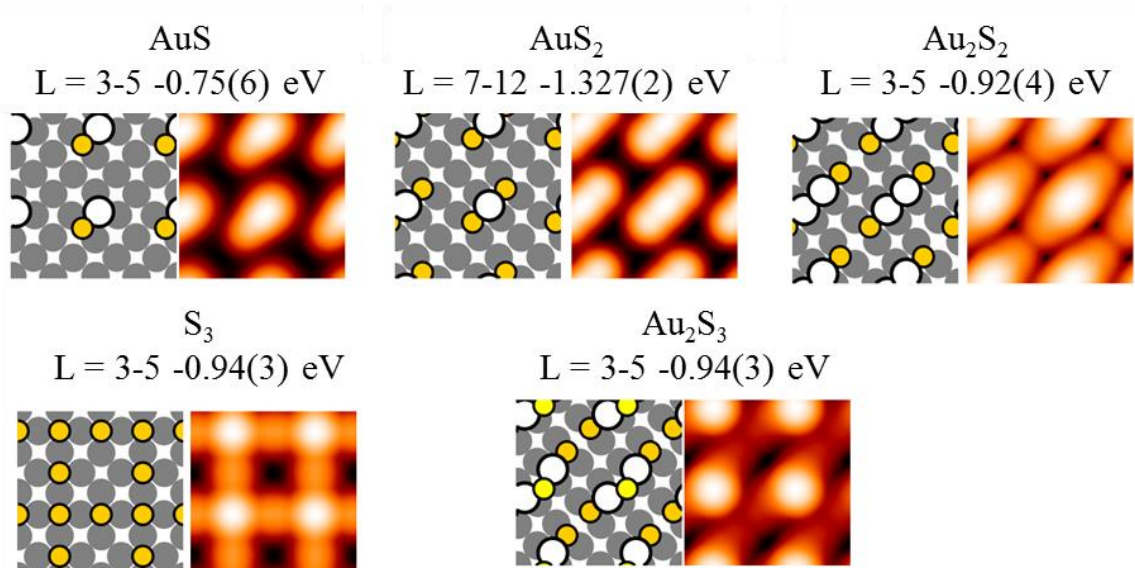


Figure A2. $(2\sqrt{2} \times 2\sqrt{2})R45^\circ$ supercell.

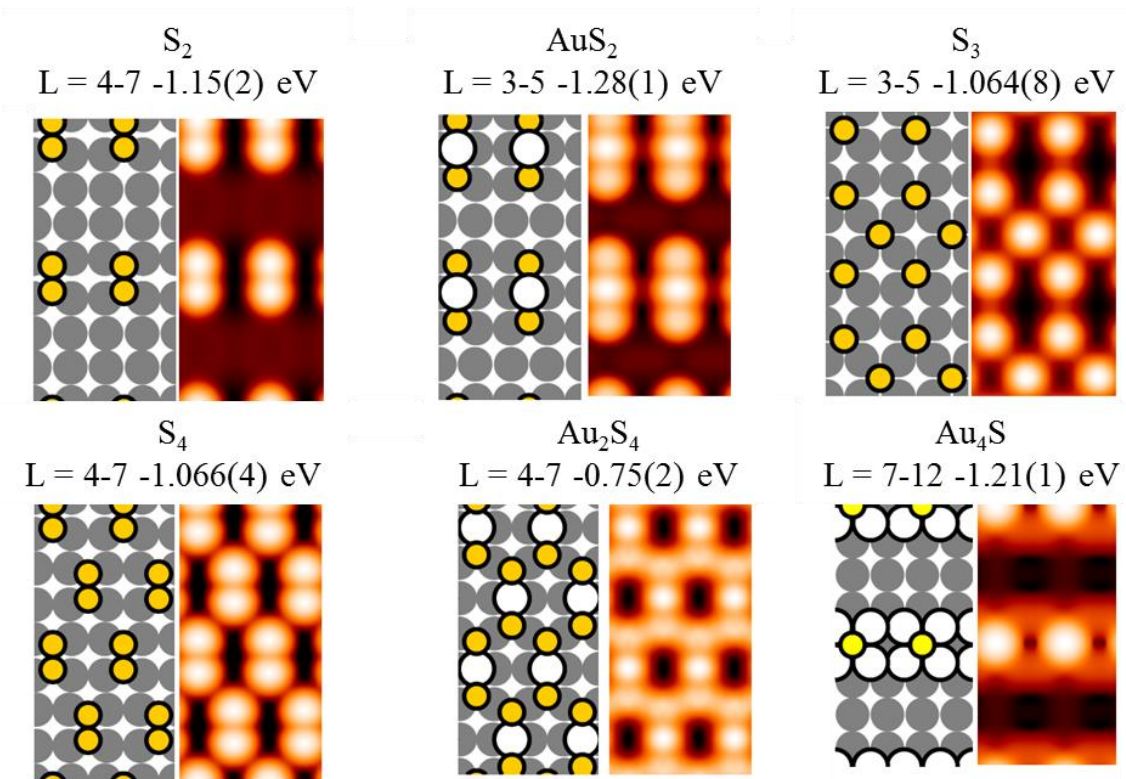


Figure A3. (2×4) supercell.

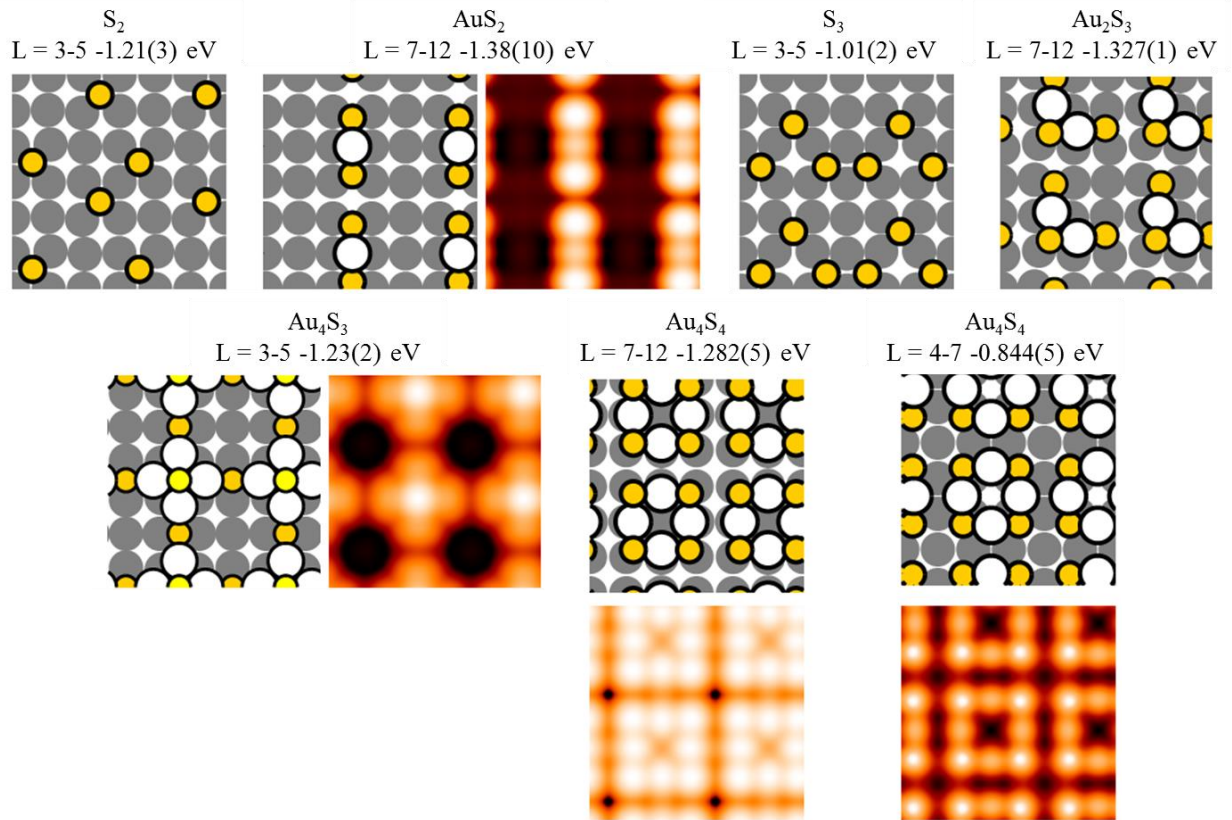


Figure A4. (3 x 3) supercell.

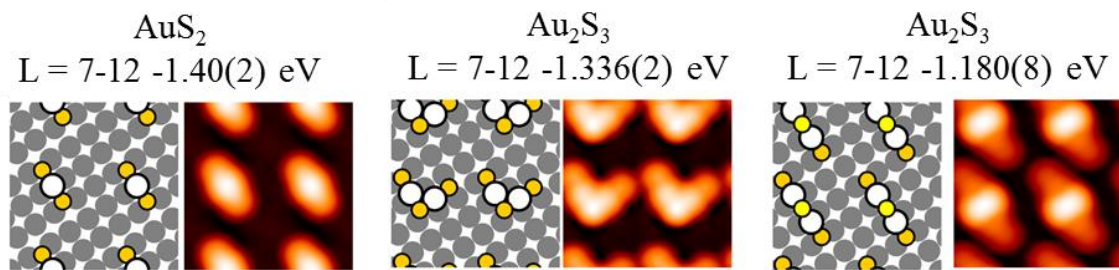


Figure A5. ($\sqrt{13} \times \sqrt{13}$)R33.7° supercell.

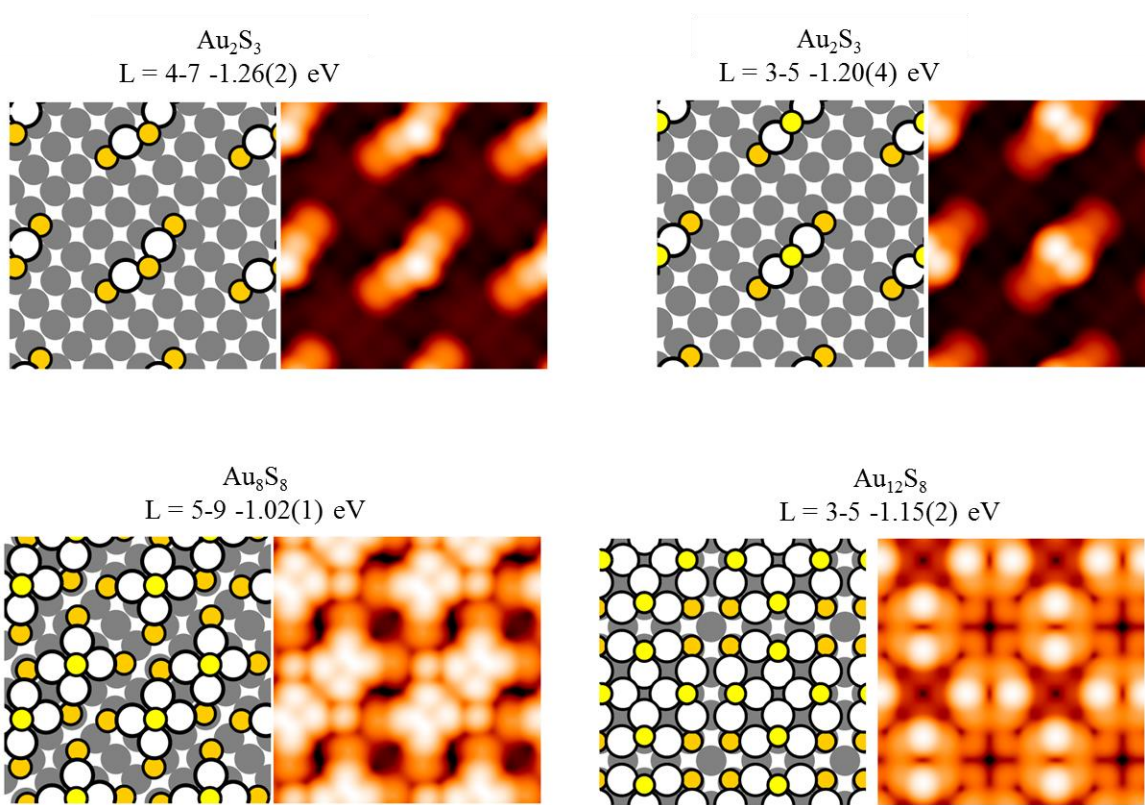


Figure A6. $(3\sqrt{2} \times 3\sqrt{2})R45^\circ$ supercell.

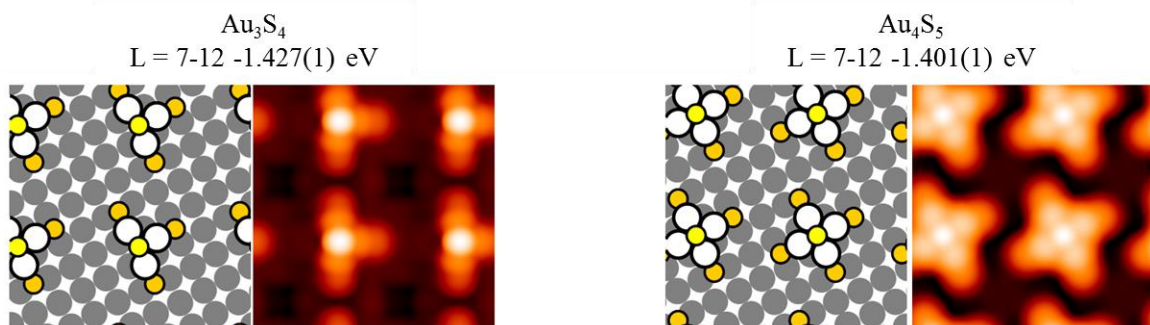


Figure A7. $(2\sqrt{5} \times 2\sqrt{5})R26.6^\circ$ supercell.

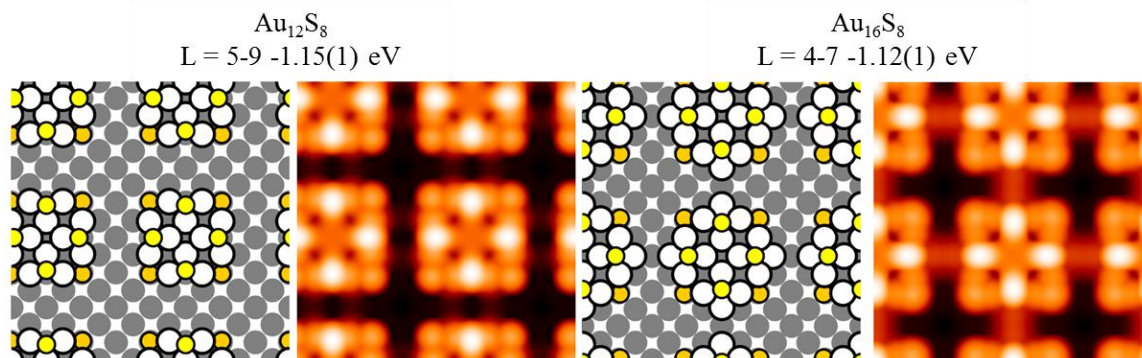


Figure A8. $(4\sqrt{2} \times 4\sqrt{2})R45^\circ$ supercell.

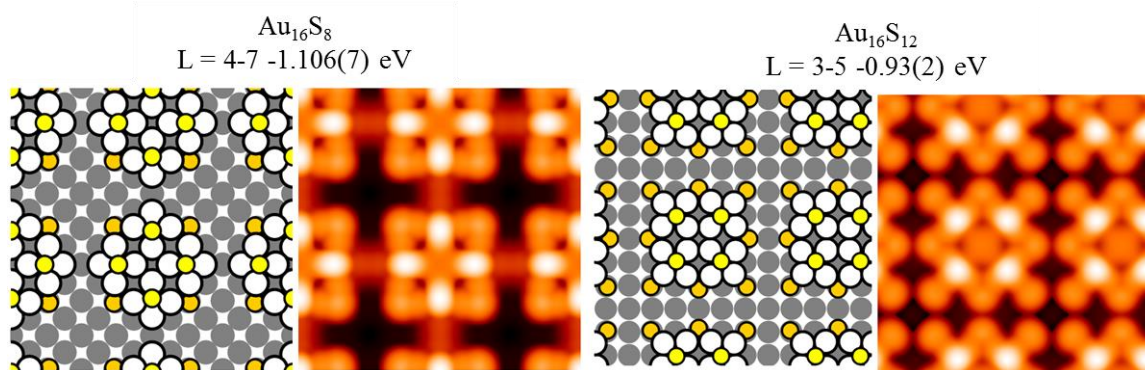


Figure A9. (6×6) supercell.

References

1. Feibelman, P. J., "Formation and Diffusion of S-Decorated Cu Clusters on Cu(111)". *Phys. Rev. Lett.* **2000**, *85*, 606-609.
2. Thiel, P. A.; Shen, M.; Liu, D.-J.; Evans, J. W., "Critical Review: Adsorbate-Enhanced Transport of Metals on Metal Surfaces: Oxygen and Sulfur on Coinage Metals". *J. Vac. Sci. Technol. A* **2010**, *28*, 1285-1298.
3. Shi, Z.; Lin, N., "Porphyrin-Based Two-Dimensional Coordination Kagome Lattice Self-Assembled on a Au(111) Surface". *J. Am. Chem. Soc.* **2009**, *131*, 5376-5377.
4. Sun, Q.; Cai, L. L.; Ma, H. H.; Yuan, C. X.; Xu, W., "On-Surface Construction of a Metal-Organic Sierpinski Triangle". *Chem. Comm.* **2015**, *51*, 14164-14166.
5. Fan, Q.; Wang, T.; Liu, L.; Zhao, J.; Zhu, J.; Gottfried, J. M., "Tribromobenzene on Cu(111): Temperature-Dependent Formation of Halogen-Bonded, Organometallic, and Covalent Nanostructures". *J. Chem. Phys.* **2015**, *142*, 101906.
6. Pivetta, M.; Pacchioni, G. E.; Fernandes, E.; Brune, H., "Temperature-Dependent Self-Assembly of NC-Ph-5-CN Molecules on Cu(111)". *J. Chem. Phys.* **2015**, *142*, 101928.
7. Ulman, A., "Formation and Structure of Self-Assembled Monolayers". *Chem. Rev.* **1996**, *96*, 1533-1554.
8. Schreiber, F., "Structure and Growth of Self-Assembling Monolayers". *Prog. Surf. Sci.* **2000**, *65*, 151-257.
9. Vericat, C.; Vela, M. E.; Benitez, G. A.; Martin Gago, J. A.; Torrelles, X.; Salvarezza, R. C., "Surface Characterization of Sulfur and Alkanethiol Self-Assembled Monolayers on Au(111)". *J. Phys: Condens. Matter.* **2006**, *18*, R867-R900.

10. Vericat, C.; Vela, M. E.; Benitez, G. A.; Carro, P.; Salvarezza, R. C., "Self-Assembled Monolayers of Thiols and Dithiols on Gold: New Challenges for a Well-Known System". *Chem. Soc. Rev.* **2010**, *39*, 1805-1834.
11. Vericat, C.; Vela, M. E.; Corthey, G.; Pensa, E.; Cortes, E.; Fonticelli, M. H.; Ibanez, F.; Benitez, G. E.; Carro, P.; Salvarezza, R. C., "Self-Assembled Monolayers of Thiolates on Metals: A Review Article on Sulfur-Metal Chemistry and Surface Structures". *RSC Adv.* **2014**, *4*, 27730-27754.
12. Ndieyira, J. W., et al., "Nanomechanical Detection of Antibiotic Mucopeptide Binding in a Model for Superbug Drug Resistance". *Nat. Nano.* **2008**, *3*, 691-696.
13. DiBenedetto, S. A.; Facchetti, A.; Ratner, M. A.; Marks, T. J., "Molecular Self-Assembled Monolayers and Multilayers for Organic and Unconventional Inorganic Thin-Film Transistor Applications". *Adv. Mater.* **2009**, *21*, 1407-1433.
14. Stranick, S. J.; Parikh, A. N.; Allara, D. L.; Weiss, P. S., "A New Mechanism for Surface Diffusion: Motion of a Substrate-Adsorbate Complex". *J. Phys. Chem.* **1994**, *98*, 11136-11142.
15. Maksymovych, P.; Voznyy, O.; Dougherty, D. B.; Sorescu, D. C.; Yates Jr., J. T., "Gold Adatom as a Key Structural Component in Self-Assembled Monolayers of Organosulfur Molecules on Au(111)". *Prog. Surf. Sci.* **2010**, *85*, 206-240.
16. Häkkinen, H., "The Gold-Sulfur Interface at the Nanoscale". *Nat. Chem.* **2012**, *4*, 443-455.
17. Ouyang, R., et al., "Intermixed Adatom and Surface-Bound Adsorbates in Regular Self-Assembled Monolayers of Racemic 2-Butanethiol on Au(111)". *Chem. Phys. Chem.* **2015**, *16*, 928-932.

18. Russell, S. M.; Kim, Y.; Liu, D.-J.; Evans, J. W.; Thiel, P. A., "Structure, Formation, and Equilibration of Ensembles of Ag-S Complexes on an Ag Surface". *J. Chem. Phys.* **2013**, *138*, 071101.
19. Walen, H.; Liu, D.-J.; Oh, J.; Lim, H.; Evans, J. W.; Aikens, C.; Kim, Y.; Thiel, P. A., "Cu₂S₃ Complex on Cu(111) as a Candidate for Mass Transport Enhancement". *Phys. Rev. B* **2015**, *91*, 045426.
20. Walen, H.; Liu, D.-J.; Oh, J.; Lim, H.; Evans, J. W.; Kim, Y.; Thiel, P. A., "Reconstruction of Steps on the Cu(111) Surface Induced by Sulfur". *J. Chem. Phys.* **2015**, *142*, 194711.
21. Kurokawa, S.; Miyawaki, Y.; Sakai, A., "Scanning Tunneling Microscopy Observation of Sulfur Adsorbates on Au(111) at Liquid Nitrogen Temperature". *Jpn. J. Appl. Phys.* **2009**, *48*, 08JB12.
22. Yamazaki, K.; Takayanagi, K.; Tanishiro, Y.; Yagi, K., "Transmission Electron-Microscope Study of the Reconstructed Au(001) Surface". *Surf. Sci.* **1988**, *199*, 595-608.
23. Gao, X.; Hamelin, A.; Weaver, M. J., "Elucidating Complex Surface Reconstructions with Atomic-Resolution Scanning Tunneling Microscopy: Au(100)-Aqueous Electrochemical Interface". *Phys. Rev. B* **1992**, *46*, 7096-7102.
24. Havu, P.; Blum, V.; Havu, V.; Rinke, P.; Scheffler, M., "Large-Scale Surface Reconstruction Energetics of Pt(100) and Au(100) by All-Electron Density Functional Theory". *Phys. Rev. B* **2010**, *82*, 161418(R).
25. Samson, Y.; Rousset, S.; Gauthier, S.; Girard, J. C.; Klein, J., "STM Study of Vicinal Structures on Au(100)". *Surf. Sci.* **1994**, *315*, L969-L972.

26. Trembulowicz, A.; Ehrlich, G.; Antczak, G., "Surface Diffusion of Gold on Quasihexagonal-Reconstructed Au(100)". *Phys. Rev. B* **2011**, *84*, 245445
27. Binnig, G. K.; Rohrer, H.; Gerber, C.; Stoll, E., "Real-Space Observation of the Reconstruction of Au(100)". *Surf. Sci.* **1984**, *144*, 321-335.
28. Fedak, D. G.; Gjostein, N. A., "On the Anomalous Surface Structure of Gold". *Surf. Sci.* **1967**, *8*, 77-97.
29. Van Hove, M. A.; Koestner, R. J.; Stair, P. C.; Bibérian, J. P.; Kesmodel, L. L.; Bartoš, I.; Somorjai, G. A., "The Surface Reconstructions of the (100) Crystal Faces of Iridium, Platinum and Gold: I. Experimental Observations and Possible Structural Models". *Surf. Sci.* **1981**, *103*, 189-217.
30. Figuera, J. d. I.; González, M. A.; García-Martínez, R.; Rojo, J. M.; Hernán, O. S.; Parga, A. L. V. d.; Miranda, R., "STM Characterization of Extended Dislocation Configurations in Au₁₁₁(001)". *Phys. Rev. B* **1998**, *58*, 1169-1172.
31. Jiang, Y.; Liang, X.; Ren, S.; Chen, C.-L.; Fan, L.-J.; Yang, Y.-W.; Tang, J.-M.; Luh, D.-A., "The Growth of Sulfur Adlayers on Au(100)". *J. Chem. Phys.* **2015**, *142*, 064708.
32. Kostelitz, M.; Domange, J. L.; Oudar, J., "Étude Par La Diffraction Des Électrons Lents Et La Spectroscopie Auger De L'adsorption Du Soufre Sur L'or". *Surf. Sci.* **1973**, *34*, 431-449.
33. Schlaup, C.; Wandelt, K., "In-Situ STM Study of Sulfide Adsorption on Au(100) in Alkaline Solution". *Surf. Sci.* **2015**, *631*, 165 - 172.
34. Martinez, J. A.; Valenzuela B, J.; Cao Milan, R.; Herrera, J.; Farias, M. H.; Hernandez, M. P., "A Scanning Tunneling Microscopy Investigation of the Phases Formed

by the Sulfur Adsorption on Au(100) from an Alkaline Solution of 1,4-Piperazine(Bis)-Dithiocarbamate of Potassium". *Appl. Surf. Sci.* **2014**, 320, 287-293.

35. Ślusarski, T.; Kostyrko, T., "An Effective Hamiltonian for Sulfur Adsorption at Au(100) Surface". *Surf. Sci.* **2009**, 603, 1150-1155.

36. Daigle, A. D.; BelBruno, J. J., "Density Functional Theory Study of the Adsorption of Nitrogen and Sulfur Atoms on Gold (111), (100), and (211) Surfaces". *J. Phys. Chem. C* **2011**, 115, 22987-22997.

37. Walen, H.; Liu, D.-J.; Oh, J.; Lim, H.; Evans, J. W.; Kim, Y.; Thiel, P. A., "Self-Organization of S Adatoms on Au(111): $\sqrt{3}R30^\circ$ Rows at Low Coverage". *J. Chem. Phys.* **2015**, 143, 014704.

38. Russell, S. M.; Shen, M.; Liu, D.-J.; Thiel, P. A., "Adsorption of Sulfur on Ag(100)". *Surf. Sci.* **2011**, 605, 520-527.

39. Liu, D.-J.; Walen, H.; Oh, J.; Lim, H.; Evans, J. W.; Kim, Y.; Thiel, P. A., "Search for the Structure of a Sulfur-Induced Reconstruction on Cu(111)". *J. Phys. Chem. C* **2014**, 118, 29218-29223.

40. Walen, H.; Liu, D.-J.; Oh, J.; Yang, H. J.; Kim, Y.; Thiel, P. A., "Long-Range Displacive Reconstruction of Au(110) Triggered by Low Coverage of Sulfur". *J. Phys. Chem. C* **2015**, 119, 21000-21010.

41. Wagner, C., "Investigation on Silver Sulfide". *J. Chem. Phys.* **1953**, 21, 1819-1827.

42. Detry, D.; Drowart, J.; Goldfinger, P.; Keller, H.; Rickert, H., "Zur Thermodynamik Von Schwefeldampf". *Z. Phys. Chem.* **1967**, 55, 314-319.

43. Heegemann, W.; Meister, K. H.; Bechtold, E.; Hayek, K., "The Adsorption of Sulfur on the (100) and (111) Faces of Platinum; a LEED and AES Study". *Surf. Sci.* **1975**, *49*, 161-180.
44. Maeland, A.; Flanagan, T. B., "Lattice Spacings of Gold–Palladium Alloys". *Can. J. Phys.* **1964**, *42*, 2364-2366.
45. Gibbs, D.; Ocko, B. M.; Zehner, D. M.; Mochrie, S. G. J., "Structure and Phases of the Au(001) Surface: In-Plane Structure". *Phys. Rev. B* **1990**, *42*, 7330-7344.
46. Mochrie, S. G. J.; Zehner, D. M.; Ocko, B. M.; Gibbs, D., "Structure and Phases of the Au(001) Surface: X-Ray Scattering Measurements". *Phys. Rev. Lett.* **1990**, *64*, 2925-2928.
47. Kresse, G.; Furthmüller, J., "Efficient Iterative Schemes for Ab Initio Total-Energy Calculations Using a Plane-Wave Basis Set". *Phys. Rev. B* **1996**, *54*, 11169-11186.
48. Kresse, G.; Hafner, J., "Ab Initio Molecular-Dynamics Simulation of the Liquid-Metal–Amorphous-Semiconductor Transition in Germanium". *Phys. Rev. B* **1994**, *49*, 14251-14269.
49. Kresse, G.; Hafner, J., "Ab Initio Molecular Dynamics for Liquid Metals". *Phys. Rev. B* **1993**, *47*, 558-561.
50. Kresse, G.; Joubert, D., "From Ultrasoft Pseudopotentials to the Projector Augmented Wave Method". *Phys. Rev. B* **1999**, *59*, 1758-1775.
51. Perdew, J. P.; Burke, K.; Ernzerhof, M., "Generalized Gradient Approximation Made Simple". *Phys. Rev. Lett.* **1996**, *77*, 3865-3868.
52. Liu, D.-J., "Density Functional Analysis of Key Energetics in Metal Homoepitaxy: Quantum Size Effects in Periodic Slab Calculations". *Phys. Rev. B* **2010**, *81*, 035415.

53. Tersoff, J.; Hamann, D. R., "Theory and Application for the Scanning Tunneling Microscope". *Phys. Rev. Lett.* **1983**, *50*, 1998-2001.
54. Liu, J.; Wu, C.-w.; Tsong, T. T., "Measurement of the Binding Energy of Kink-Site Atoms of Metals and Alloys". *Phys. Rev. B* **1991**, *43*, 11595-11604.
55. Borg, A.; Hilmen, A. M.; Bergene, E., "Stm Studies of Clean, CO-Exposed and O₂-Exposed Pt(100)-Hex-R0.7-Degrees". *Surf. Sci.* **1994**, *306*, 10-20.
56. Ritz, G.; Schmid, M.; Varga, P.; Borg, A.; Ronning, M., "Pt(100) Quasihexagonal Reconstruction: A Comparison between Scanning Tunneling Microscopy Data and Effective Medium Theory Simulation Calculations". *Phys. Rev. B* **1997**, *56*, 10518-10525.
57. Bak, P.; Kleban, P.; Unertl, W.; Ochab, J.; Akinci, G.; Bartelt, N. C.; Einstein, T. L., "Phase Diagram of Selenium Adsorbed on the Ni(100) Surface: A Physical Realization of the Ashkin-Teller Model". *Phys. Rev. Lett.* **1985**, *54*, 1539-1542.
58. Klimes, J.; Bowler, D. R.; Michaelides, A., "Chemical Accuracy for the Van Der Waals Density Functional". *J. Phys.: Condens. Matter* **2010**, *22*, 022201.
59. Klimes, J.; Bowler, D. R.; Michaelides, A., "Van Der Waals Density Functionals Applied to Solids". *Phys. Rev B* **2011**, *83*, 195131.
60. Günther, S.; Kopatzki, E.; Bartelt, M. C.; Evans, J. W.; Behm, R. J., "Anisotropy in Nucleation and Growth of Two-Dimensional Islands During Homoepitaxy on "Hex" Reconstructed Au(100)". *Phys. Rev. Lett.* **1994**, *73*, 553-556.
61. Ritter, E.; Behm, R. J.; Potschke, G.; Winterlin, J., "Direct Observation of a Nucleation and Growth-Process on an Atomic Scale". *Surf. Sci.* **1987**, *181*, 403-411.
62. Mase, K.; Murata, Y., "LEED Study of No Adsorption-Induced Restructuring of a Single-Domain Pt(001)-(20x5) Surface at 80-410K". *Surf. Sci.* **1992**, *277*, 97-108.

CHAPTER VIII

EVIDENCE OF CU-SE STRUCTURES ON CU(111) AT LOW COVERAGE

Holly Walen,^a Da-Jiang Liu,^b Junepyo Oh,^c Hyun Jin Yang,^c Yousoo Kim,^c

and P. A. Thiel^{a,b,d}

Abstract

Using scanning tunneling microscopy (STM), we observe that adsorption of Se on Cu(111) produces islands with $(\sqrt{3} \times \sqrt{3})R30^\circ$ structure, at Se coverages far below the structure's ideal coverage of 1/3 ML. Based on density functional theory (DFT), these islands cannot form due to attractive interactions between chemisorbed Se atoms. DFT shows that incorporating Cu atoms into the $\sqrt{3}$ -Se lattice stabilizes the structure, which provides a plausible explanation for the experimental observations. STM reveals 3 types of $\sqrt{3}$ textures. We assign 2 of these as two-dimensional layers of strained CuSe, analogous to dense planes of bulk klockmannite (CuSe). Klockmannite has a bulk lattice constant 11% shorter than $\sqrt{3}$ times the surface lattice constant of Cu(111). This offers a rationale for the differences observed between these textures, where strain limits the island size or distorts the $\sqrt{3}$ lattice. STM shows that existing step edges adsorb Se and facet toward $\langle 1\bar{2}1 \rangle$, which is consistent with DFT.

Departments of ^aChemistry and ^dMaterials Science & Engineering, Iowa State University, Ames, Iowa 50011 USA

^bAmes Laboratory of the USDOE, Ames, Iowa 50011 USA

^cRIKEN Surface and Interface Science Laboratory, Wako, Saitama 351-0198, Japan

1. Introduction

Metal chalcogenides provoke interest on the basis of properties as diverse as superconductivity and catalytic activity.^{1,2} For example, a single monolayer of iron selenide is a surprisingly good superconductor, with a (relatively) high critical temperature of 65 K.^{3,4} Tungsten and molybdenum dichalcogenides, such as MoS₂, are good hydrodesulfurization catalysts.⁵ Recent interest in metal chalcogens has also been spurred by their potential application in advanced energy conversion and storage devices. Copper selenides show unique properties for applications in photovoltaic and thermoelectric materials,⁶⁻⁸ and copper chalcogenide-based semiconductors are used in solar cells due to their high optical absorption efficiency.^{9,10} Many metal chalcogenides are two-dimensional (layered) compounds, a fact that naturally raises interest in their growth and use as two-dimensional sheets or films. In this paper, we show that copper selenide forms spontaneously on Cu(111) at room temperature, even at very low coverage of Se—less than 0.1 monolayer. The reactants are simply Se₂(gas) and the Cu surface itself, in ultrahigh vacuum (UHV).

Previously, Nagashima *et al.*¹¹⁻¹³ studied adsorption of Se on Cu(111) over a wide range of coverage at room temperature and above, and in UHV. They deposited Se onto a Cu(111) film supported on mica, and the resultant surface was primarily analyzed with low energy electron diffraction (LEED), Auger electron spectroscopy, transmission electron microscopy, and electron energy loss spectroscopy. At 300 K, LEED showed a ($\sqrt{3} \times \sqrt{3}$)R30° structure at low coverage, which was assigned as chemisorbed Se.¹¹ This was followed by formation of a CuSe overlayer and, eventually, a CuSe multilayer alloy.^{12,13} The CuSe overlayer and alloy also exhibited ($\sqrt{3} \times \sqrt{3}$)R30° LEED patterns, with evidence of a 6 to 7% (real-space) contraction relative to the initial structure.^{12,13} Our experimental work is

different from that of Nagashima *et al.* because it provides real-space images of the surface structures via STM, and it focuses on the very low coverage regime. In addition, we use density functional theory (DFT) to interpret the experimental data. Together, these features provide new insights. In particular, they lead to a re-interpretation of the $(\sqrt{3} \times \sqrt{3})R30^\circ$ structure at low coverage as being due to islands of CuSe, rather than chemisorbed Se.

This paper is divided into 5 sections. Section 2 gives details of the experimental preparation of the sample and the computational description. Section 3 provides the experimental observations and the relevant calculations that have been performed thus far. Section 4 discusses the results and draws some comparison to S/Cu(111) and two-dimensional dichalcogenides. Finally, Section 5 contains the conclusions of this work.

2. Experimental and Computational Details

2.1 Experimental conditions

Experiments were performed at the Surface and Interface Science Laboratory at RIKEN in Japan. Experiments were conducted in an ultrahigh vacuum chamber equipped with low-temperature (5 K) STM and an electrochemical source for *in situ* Se₂(gas) deposition.^{14, 15}

Cu(111) was cleaned by sputtering with Ar⁺ (12-15 μ A, 2.0 kV) for 10 minutes with the sample held at 850 K. This was done several times, keeping the sample at 850 K for 5 minutes between sputtering. The surface temperature was measured via optical pyrometry, and the precision was within 10 K. For the last cycle, the sample was allowed to cool while the surface was sputtered for an additional 3 minutes.

The piezo calibration parallel to the surface was checked using atomically resolved images of terraces like that in Fig. 1(a). The measured nearest-neighbor (NN) separation was 0.26 ± 0.01 nm, in agreement with the bulk value of 0.255 nm. The vertical calibration was checked using atomic steps, for which the measured height of 0.20 ± 0.01 nm also agreed with the bulk value of 0.208 nm.¹⁶

During exposure to Se_2 (gas), the sample was held at room temperature to promote dissociative adsorption. All experimental data presented here was obtained with the sample held at 5 K. The sample was moved into the STM stage ~ 5 minutes after deposition, where cooling lasted another 50 minutes. After an initial set of images was obtained, the sample was brought out of the STM stage and allowed to warm up to room temperature, followed by a subsequent quench to 5 K for the remainder of the experiment. This thermal cycling had no effect on the observed structures.

Typical tunneling conditions were within the following ranges: -1 to +1 V sample bias, and 1.00 to 2.06 nA tunneling current. There was no apparent influence of the tunneling conditions on the adsorbed species. All STM images were planed using WSxM software.¹⁷

Coverage of Se was determined by counting distinct protrusions, whether isolated or in Type A structures (as defined in Sec. 3.1), and assigning 1 Se atom per protrusion. For Type B and C structures, the area was evaluated and ideal coverages of 0.33 and 0.36 were assigned, respectively. Only terraces were included in this calculation. Step edges were disregarded. The data described below was collected over 2 experiments, for which Se coverage was 0.02 and 0.06. There was no significant difference in the features observed at these two coverages.

2.2 Computational description

DFT calculations were performed with the VASP code, using the PBE exchange-correlation functional, with 280 eV energy cut off. Unless noted otherwise, results were obtained by averaging over slab thicknesses from 4 to 7 Cu layers, and using k-point grids corresponding to (24 x 24 x 1) or (36 x 36 x 1) for the primitive (1 x 1) unit cell, or as close to those settings as possible.

In most calculations, slabs had (111) surface orientation, but some had vicinal orientation. For these, k-point grids of (36 x 36 x 1) in the (1 x 1) cell were needed to ensure convergence and obtain reliable energetics. The vicinal slabs were comparable in thickness to the (111) slabs, though more layers were needed to achieve this since atomic planes were less dense and more closely-spaced in the vicinal slabs.

3. Results

3.1 Experimental results

Features on terraces. Fig. 1(a) shows an image of the clean Cu(111) surface with atomic resolution, which allows definition of the crystallographic directions as shown beneath the panel. Upon adsorption of Se, we observe individual, dot-like protrusions, two of which are evident on the left of Fig. 1(b). We also observe dark spots, one of which is evident on the left of Fig. 3(b). The nature of the dark spots is unclear. The individual protrusions have width (measured at full-width at half-maximum, FWHM) of 0.52 ± 0.08 nm (N = 76), height of 0.05 ± 0.01 nm (N = 76), and area of 0.23 ± 0.05 nm² (N = 58).

In addition to these features, islands form on the surface, even though the coverage is very low (< 0.10 ML). Islands display three types of internal texture. In the first (Type A),

protrusions are arranged hexagonally. Each protrusion is defined by a circular outline. Examples are shown in Fig. 1(b-e). The nearest-neighbor separation between protrusions is $\sqrt{3}a$ (measured spacing = 0.45 ± 0.02 nm, $\sqrt{3}a = 0.442$ nm), rotated by 30° from the close-packed directions, i.e. parallel to $\langle 1\bar{2}1 \rangle$. Hence, the internal structure is $(\sqrt{3} \times \sqrt{3})R30^\circ$, which we abbreviate as $\sqrt{3}$. The island edges are often faceted parallel to $\langle 1\bar{2}1 \rangle$. In other cases the protrusions at the island edge are arranged irregularly, as if protrusions have just joined or left the island. Islands with exclusively Type A texture are made up of 20 or fewer protrusions, corresponding to an area ≤ 4 nm².

In the second type of internal structure (Type B), the surface is smoother, with a $\sqrt{3}$ arrangement of small depressions. Type B regions have triangular footprints, with edges again aligned parallel to $\langle 1\bar{2}1 \rangle$. Areas are in the range 1 – 3 nm², i.e. comparable to Type A regions. Examples are shown in Fig. 2(a-d). Type B and A regions can coexist in a single island; Fig. 2(a-c) are examples of such hybrids. It is rare to find an island that is entirely Type B, such as Fig. 2(d), whereas it is common to find one entirely Type A, such as Fig. 1(a-d). This, plus the comparable range of sizes, suggests that Type A transforms into Type B, and that the hybrid islands represent incomplete transformations.

The third texture (C) is characteristic of islands with much larger area > 100 nm² (Fig. 3). Type C resembles Type B in the sense that it has a $\sqrt{3}$ -like pattern defined by individual small depressions in a smooth matrix. However, in Type C a linear corrugation is superposed. The separation between corrugation lines alternates regularly between 1.8 nm and 2.0 nm. This is most obvious in Fig. 3(c). The corrugation is shallow, 0.004 ± 0.001 nm ($N = 2$). Type C islands are usually connected along one side to a step edge, indicating

growth outward from steps. The average height is 0.06 ± 0.01 nm ($N = 4$), much smaller than a single Cu(111) step, 0.208 nm.¹⁶

The corrugation is shown for four additional Type C islands in Fig. 4. All exhibit contraction in the $\sqrt{3}$ -like pattern of depressions, along the two directions close to $\langle 1\bar{2}1 \rangle$ that cross the corrugation line. (These directions are illustrated by arrows at the top of Fig. 4(a).) The degree of contraction, relative to $3a$, is unequal in the two directions, being 2 to 4% and 4 to 8%, respectively. (We estimate 2% deviation as the limit of detection in these experiments.) In some cases the texture parallel to the corrugation is rotated by 1° . The rotation is present in Fig. 4(c), but not in Fig. 4(a). These features, and their subtle variation among different islands, suggest the existence of a set of coincidence lattices that are similar in structure and close in energy. Their development or stability may be influenced by the adjoining step edge.

Step edge decoration. Exposure to Se causes steps along Cu terraces to facet along $\langle 1\bar{2}1 \rangle$ directions (Fig. 5). The faceted steps are decorated by a regularly-spaced line of protrusions that we assign as Se atoms. The spacing between these protrusions is 0.44 ± 0.02 nm, in agreement with $\sqrt{3}a$ spacing (0.442 nm). It is also common to find small islands attached to step edges, like the one shown in Fig. 5(b).

3.2 Computational results

The goal of the computational work is to find viable structural candidates for the features observed in STM. One metric is the level of agreement between the measured STM image and the simulated image of an energy-optimized configuration derived from DFT. The other metric is the chemical potential of Se, μ_{Se} , which we will use in two forms: μ_{Se}^0 for the

flat Cu(111) surface, relevant to Se on terraces; and μ_{Se}^{hkl} for surfaces vicinal to Cu(111), relevant to Se at steps. These two cases are addressed sequentially below.

Features on terraces. Physically, μ_{Se}^0 reflects the energy increase per Se when Se adsorbs on terraces, possibly in the form of Cu-Se structures, given an unlimited supply of Cu available from steps/kinks (at 0 K). We define it as:

$$\mu_{Se}^0 = [E(\text{Cu}_m\text{Se}_n + \text{slab}) - E(\text{slab}) - m\mu_{Cu}]/n - E(\text{Se}_{2,g})/2 \quad (1)$$

where E is energy, μ_{Cu} is the chemical potential of Cu in the bulk metal (at 0 K), which also corresponds to the bulk cohesive energy. If bulk and surface are equilibrated, μ_{Cu} is equivalent to the binding energy of a Cu atom at a step kink site.¹⁸ The integers m and n are the number of Cu and Se atoms in the complex, respectively. When $m=0$, μ_{Se}^0 reduces to the adsorption energy of a Se adatom. We use the energy of gaseous triplet Se_2 as $E(\text{Se}_{2,g})$.

Calculations in a (2 x 2) supercell show that the most favorable site for Se is the fcc site, with the hcp site 0.042(1) eV less favorable. Fig. 6 shows μ_{Se}^0 as a function of (inverse) Se coverage, for a variety of supercells with Se at fcc sites. The convex hull, shown by the solid line, is defined by p(4 x 4), p(2 x 2), and $\sqrt{3}$ supercells. The lowest coverage examined theoretically, which is that of the p(4 x 4), equals the highest coverage in experiments, 0.06 ML. For this, $\mu_{Se}^0 = -1.975$ eV. This is lower than either of the other two structures on the convex hull. Thus, from DFT there is no mechanism to form $\sqrt{3}$ islands of Se atoms at the low coverage probed in experiment.

The predominance of the $\sqrt{3}$ structure in experiments leads us to take a different approach. Starting from the $\sqrt{3}$ structure of chemisorbed Se, we explore factors that may

stabilize it. We begin by embedding Cu atoms in the Se matrix. Comparing μ_{Se}^0 in Fig. 7(a-c) shows that additional Cu can indeed stabilize the $\sqrt{3}$ -Se structure. The most stable configuration has a Cu:Se ratio of 2:3 (Fig. 7). In the simulated STM image, Se atoms produce round protrusions in a $\sqrt{3}$ pattern like those in Type A texture. However, the image also exhibits very small dark regions in a $p(3 \times 3)$ pattern (reflecting the arrangement of added Cu atoms) and this is not observed experimentally. Nonetheless, because of the round protrusions and low chemical potential, we consider this a candidate structure for the Type A texture.

Adding more Cu atoms produces a 1:1 CuSe structure (Fig. 7(d)), with a value of μ_{Se}^0 that is not favorable compared to $Cu_{2/3}Se$. However, the compressed $\sqrt{3}$ lattice associated with Type C texture indicates that strain plays a role. To approximate compressive strain in an extended structure, we perform DFT calculations using larger supercells derived from the $\sqrt{3}$ -CuSe structure, with compression along only one of the principal $\sqrt{3}$ axes. There are many such unit cells that can be considered. We have explored the set listed in Table 1, from which we conclude that those with coverage close to 0.36 ML (8% compression) are optimal. Figure 8 shows the lowest-energy configuration found in this search, with a value of μ_{Se}^0 that is 0.039 eV lower than the uncompressed $\sqrt{3}$ -CuSe structure in Fig. 7(d). (These comparisons can also be made using Table 2, which summarizes key values of μ_{Se}^0 presented in this section.) The simulated STM image shows that the linear corrugation is reproduced qualitatively.

TABLE I. μ_{Se}^0 for various large supercells derived from the $(\sqrt{3} \times \sqrt{3})R30^\circ$, with compression along one of the principal $\sqrt{3}$ axes. Uncertainty in the third decimal place is given in

parentheses. The supercells can be described with matrix notation, where $M = \begin{pmatrix} 2 & 1 \\ m_{21} & m_{22} \end{pmatrix}$

and the basis vectors a_1 and a_2 are defined in Fig. 8. The unit cell area is normalized to that of the (1x1). Each k-points grid is specified for the actual supercell. The row in boldface corresponds to the configuration shown in Fig. 8.

Unit cell area	(m_{21}, m_{22})	Chemical potential, eV	k-point grid	Se coverage, ML
3	(1,2)	-1.772(1)	(14x14x1)	0.333
5	(1,3)	-1.528(2)	(14x9x1)	0.400
7	(1,4)	-1.545(1)	(14x7x1)	0.429
8	(0,4)	-1.664(3)	(14x6x1)	0.375
10	(0,5)	-1.707(2)	(14x5x1)	0.400
11	(1,6)	-1.724(2)	(14x4x1)	0.364
12	(0,6)	-1.584(2)	(14x4x1)	0.417
13	(1,7)	-1.770(1)	(14x4x1)	0.385
14	(0,7)	-1.757(2)	(14x3x1)	0.357
16	(0,8)	-1.794(1)	(14x3x1)	0.375
17	(1,8)	-1.772(1)	(14x3x1)	0.353
18	(0,9)	-1.707(1)	(14x3x1)	0.389
19	(1,10)	-1.805(1)	(14x3x1)	0.368
20	(0,10)	-1.780(2)	(14x2x1)	0.350
21	(1,10)	-1.715(1)	(14x2x1)	0.381
22	(0,11)	-1.808(2)	(14x2x1)	0.364
23	(1,12)	-1.785(2)	(14x2x1)	0.348

TABLE I continued.

24	(0,12)	-1.754(6)	(14x2x1)	0.375
25	(1,13)	-1.811(1)	(14x2x1)	0.360
27	(1,14)	-1.747(1)	(14x2x1)	0.370
28	(0,14)	-1.806(1)	(14x2x1)	0.357

TABLE II. Key values of μ_{Se}^0 calculated from DFT. The k-point grids are specified for the actual supercells.

Structure	μ_{Se}^0 (eV)	Supercell	k-point grid	Figure	Assignment
p(4x4)-Se	-1.975	(4x4)	(9x9x1)	n/a	
p(2x2)-Se	-1.911	(2x2)	(18x18x1)	n/a	
$\sqrt{3}$ -Se	-1.786	$(\sqrt{3} \times \sqrt{3})R30^\circ$	(21x21x1)	7(a)	
$\sqrt{3}$ -Cu _{1/3} Se	-1.828	(3x3)	(8x8x1)	7(b)	
$\sqrt{3}$ -Cu _{2/3} Se	-1.842	(3x3)	(8x8x1)	7(c)	Possible Type A
$\sqrt{3}$ -CuSe	-1.772	$(\sqrt{3} \times \sqrt{3})R30^\circ$	(14x14x1)	7(d)	
$\sqrt{3}$ -CuSe compressed	-1.811	$\begin{pmatrix} 2 & 1 \\ 1 & 13 \end{pmatrix}$	(14x2x1)	8	Type C
CuSe ₃ cluster	-1.904	(4x4)	(6x6x1)	9(a)	
Cu ₃ Se ₆ cluster/island	-1.904	(5x5)	(5x5x1)	9(b)	Possible Type A
Cu ₆ Se ₁₀ island	-1.869	(6x6)	(4x4x1)	9(c)	
Cu ₁₀ Se ₁₅ island	-1.875	(8x8)	(3x3x1)	9(d)	Type B

The most favorable μ_{Se}^0 found for the compressed structure must be an upper limit on μ_{Se}^0 of the true structure. In the real structure, there is evidence that contraction is not uniaxial, and that the unit cell can rotate. The size and complexity make a more exhaustive DFT search computationally prohibitive. The calculations in hand demonstrate firmly, however, that the $\sqrt{3}$ -CuSe layer is stabilized by contraction from the ideal $\sqrt{3}$ dimensions. We propose that Type C texture arises from an extended, compressed $\sqrt{3}$ -CuSe layer.

Another mechanism of strain relief is to limit the size of islands, since strain scales with size. We therefore calculate μ_{Se}^0 of various small, finite $\sqrt{3}$ -CuSe islands in large supercells. These islands, shown in Fig. 9, also have μ_{Se}^0 lower than the extended, uncompressed $\sqrt{3}$ -CuSe structure of Fig. 7(d). (See also Table 2.) The most stable islands terminate with Se rather than Cu, as shown, and have a triangular shape with edges parallel to $\langle \bar{1}\bar{2}1 \rangle$, as observed in experiment for Type B regions. The simulated STM image of the largest island, $Cu_{10}Se_{15}$ in Fig. 9(d), has a texture resembling Type B regions [Fig. 1(f-h)]—small depressions on a smooth background. The triangular shape, edge orientation, internal texture, and reasonable stability all combine to support the assignment of Type B regions as $\sqrt{3}$ -CuSe islands, with size that is limited by strain.

The smaller Cu-Se islands in Fig. 9(b,c) show protrusions reminiscent of Type A texture. Similar well-defined protrusions are exhibited for the small islands of $\sqrt{3}$ -CuSe shown in Fig. 9(b,c). This, plus their reasonable value of μ_{Se}^0 , makes them candidates for Type A structure.

Finally, we check for effects of the DFT functional on relative stability between chemisorbed Se and Cu-Se clusters. For this exercise, we compare the chemisorbed $p(2 \times 2)$ phase with Cu_3Se_6 (the cluster shown in Fig. 9(b)), in a (5×5) supercell. With PBE, the $p(2 \times$

2) is more stable by 0.006 eV. However, with LDA the p(2 x 2) is less stable by 0.025 eV, which is more consistent with experiment since the p(2 x 2) is never observed. While we cannot conclude from this that LDA is better for Se/Cu(111) than PBE in general, it at least raises the possibility that approximations in the exchange-correlation functional could introduce errors large enough to shift the relative stabilities of chemisorbed Se and Cu-Se structures. Therefore, it is important to note that our assignments of structures in this system are based on both energetic trends and on matches with STM images.

Step edges. On a clean Cu(111) surface, the close-packed step orientations are most stable. There are two types, denoted A and B, which can be described as (100) and (111) microfacets, respectively. Experimentally, we observe that Se causes existing steps to facet along open $\langle 1\bar{2}1 \rangle$ directions. In order to assess the energetics of this phenomenon, we must take into account the binding energy of Se at open vs. dense steps, as well as the energy penalty associated with converting Cu steps from close-packed to open.

To do this, we carry out calculations using slabs with (stepped) surfaces that are vicinal to (111), specified by Miller indices (hkl) . Slab surfaces are constructed to contain open steps, or dense steps of either A- or B-type. Se atoms are placed at $\sqrt{3}a$ intervals on open steps, to match the experimental data in Sec. 3.1, and at $2a$ intervals on the close-packed steps, to match prior observations for S adsorbed at dense steps of Cu(111).¹⁹ We evaluate μ_{Se}^0 , as well as an additional chemical potential, m_{Se}^{hkl} , defining the latter as:

$$m_{Se}^{hkl} = m_{Se}^0 + \left\{ A \left(g^{hkl} - g^{111} \right) \right\} \quad (2)$$

Here A is the area of the supercell and γ is surface energy per unit area. With reference to Eq. (1), $n = 1$ and $m = 0$. By this definition and for the specified configurations of Se at steps, μ_{Se}^0 reflects the energy of Se adsorption at a step, while m_{Se}^{hkl} equals this *plus* the energy cost of creating a stepped (hkl) surface instead of a flat (111) surface.

Results are shown in Table 3. The quantity μ_{Se}^0 can be used to compare Se adsorption on the (111) terrace vs. adsorption at a step. Recalling that $\mu_{Se}^0 = -1.975$ eV for Se chemisorbed on the terrace at low coverage (Table 2), one sees that values of μ_{Se}^0 on the vicinal slabs are always lower. This shows that it is more favorable for Se to adsorb at an (existing) step than on a terrace, regardless of step orientation.

The quantity m_{Se}^{hkl} is useful for comparing the stability of open vs. dense steps with adsorbed Se. We choose to compare supercells with Se coverages close to 0.1 ML, which represents the lower limit of coverage (upper limit of supercell size) that we can reliably assess. Three configurations that were evaluated are illustrated in Fig. 10. Table 3 shows that m_{Se}^{hkl} is lowest for the open step, intermediate for the close-packed A step, and highest for the close-packed B step. Hence, it is energetically favorable for an existing Cu step to convert from close-packed to open upon adsorption of Se. This is consistent with experiment.

TABLE III. Chemical potentials of Se adsorbed at three types of steps on Cu surfaces that are vicinal to (111). The Se coverage is inversely proportional to the unit cell area and, for a fixed step type, to the width of the (111) microfacet. Samples are shown in Fig. 11.

Step type	h,k,l	m_{Se}^0 (eV)	m_{Se}^{hkl} (eV)	Se coverage (ML)
Open $\langle 1\bar{2}1 \rangle$	11,9,7	-2.358	-1.884	0.126
Open $\langle 1\bar{2}1 \rangle$	6,5,4	-2.356	-1.891	0.114

TABLE III continued.

Open $\langle 1\bar{2}1 \rangle$	13,11,9	-2.344	-1.875	0.104
average			-1.88	
Close-packed A	3,2,2	-2.331	-1.860	0.121
Close-packed A	4,3,3	-2.234	-1.842	0.086
average			-1.85	
Close-packed B	5,5,3	-2.252	-1.839	0.130
Close-packed B	3,3,2	-2.253	-1.791	0.107
average			-1.82	

4. Discussion

There are two main results from this work. First is the experimental observation of $\sqrt{3}$ islands exhibiting 3 distinctive textures, at Se coverage far below the ideal $\sqrt{3}$ coverage of $1/3$ ML. The second result comes from DFT, namely, the fact that attractive interactions between Se adatoms cannot account for formation of these islands. DFT shows that incorporating Cu atoms into the $\sqrt{3}$ -Se lattice stabilizes the structure, which provides a plausible explanation for the experimental observations. In particular, the DFT-based simulations of STM images provide good evidence for formation of two-dimensional CuSe islands.

To a large extent, our observations are compatible with the observations and interpretation of Nagashima *et al.*,¹¹⁻¹³ who studied Se/Cu(111) using techniques that yielded large-scale average information rather than microscopic images. They observed a $\sqrt{3}$ LEED pattern over a broad coverage range, which they attributed to chemisorbed Se (at low coverage), two-dimensional CuSe (at higher coverage), and eventually a three-dimensional

CuSe alloy. The assignment of CuSe was based on relative Auger intensities for Cu and Se in the three-dimensional compound. We disagree only about the nature of the $\sqrt{3}$ in its early stages, which we argue must include Cu atoms as well as Se.

STM reveals 3 types of $\sqrt{3}$ textures in the islands. We assign 2 of these as two-dimensional layers of CuSe under compressive stress. In Type B texture, the $\sqrt{3}$ is epitaxial but it has small area. In Type C texture, the $\sqrt{3}$ is distorted (contracted) by 2-8%, but covers larger area. In both Types B and C, the characteristic features of limited size and distortion, respectively, can be attributed to strain relief. Nagashima *et al.*^{12, 13} deduced from LEED that the $\sqrt{3}$ lattice constant of high-coverage CuSe was contracted by 6-7%, relative to the initial $\sqrt{3}$ pattern, consistent with our STM data for Type C texture.

It is interesting to note that bulk CuSe—known as klockmannite—contains planes of atoms that are interpenetrating hexagonal networks of Cu and Se.²⁰ The atomic arrangement in such a plane is essentially identical to that shown in Fig. 8 and Fig. 9(d) as models for Type C and B textures, respectively. However, the Cu-Cu separation in this plane is 11% shorter than $\sqrt{3}a$ on Cu(111), and this provides a natural rationale for the strain-limited size of the Type B islands and the contraction observed in the Type C islands.

The origin of Type A texture, with its well-defined circular protrusions, is less certain. Using DFT, we have identified two possibilities. One is a sub-stoichiometric CuSe layer. In this vein, DFT calculations yielded optimal results for $\text{Cu}_{2/3}\text{Se}$, but we speculate that the real structure may tolerate some disorder, since for our ideal $\text{Cu}_{2/3}\text{Se}$ there is an additional periodicity that is not observed with STM. Disorder is also supported by the fact that a Cu-poor form of bulk klockmannite has been reported, $\text{Cu}_{0.87}\text{Se}$, which exhibits disorder in the planar Cu-Se sheets.²¹ The second possibility is that Type A texture signals small or irregular

regions of stoichiometric CuSe, since DFT shows that if a CuSe region is small enough it exhibits the circular-protrusion texture in STM, as shown in Fig. 9(b-c). This is less likely, however, since the border between Type A and B textures is very clear in hybrid islands like those of Fig. 2(a-c), implying a clear difference in structure. At present we must leave this issue unresolved.

We can compare the present results for Se/Cu(111) with prior results for S/Cu(111), obtained under similar experimental conditions of low coverage (up to 0.05 ML), and observation at 5 K (following adsorption at 300 K). Cu-S complexes are observed on terraces, the smallest being heart-shaped Cu_2S_3 .²² Larger complexes also exist, and they become more abundant with increasing coverage. These are chains consisting of concatenated Cu_2S_3 . At 0.05 ML, Cu-S complexes are replaced by a low-density ($\sqrt{43} \times \sqrt{43}$) $\text{R}\pm 7.5^\circ$ reconstruction.^{19, 23, 24} The Cu_2S_3 and chain structures are stabilized by a linear S-Cu-S motif.^{19, 22} We do not observe analogous structure in the Cu-Se system, although the $\sqrt{3}$ islands incorporate both Cu and Se, like the Cu-S complexes. It is likely that multiple factors contribute to this difference. One is simply the lattice mismatch between Cu(111) and the chalcogenide CuX (X = S, Se), which is 14% for the sulfide²⁵ but only 11% for the selenide.²⁰ Another factor may be electronic structure. In bulk metal chalcogenides, it is known that upon progressing from sulfides to selenides to tellurides, bonding becomes less ionic and electrons become more delocalized.⁵ If delocalization is more important for stabilizing Cu-Se than Cu-S moieties, this could account for the formation of extended, dense $\sqrt{3}$ structures with Se, but smaller complexes with S.

Finally, two-dimensional dichalcogenides, such as MoX_2 and WX_2 , share some similarities with our Cu-Se Type B islands. Islands of those metal dichalcogenides grow with

perfect triangular shape on Au(111) and on some oxide surfaces,²⁶⁻²⁹ and are terminated at the edges with S or Se.^{30,31} Both of these features are exhibited by the Type B islands (Fig. 9(d)), which have perfect triangular shape and are terminated by edge Se. However, our Type B islands are a single layer of Cu-Se, while the dichalcogenide structures contain 3 layers, wherein a metal layer lies between two chalcogenide layers.^{27,30}

5. Conclusions

We observe that Se adsorption on Cu(111) produces islands with 3 types of $\sqrt{3}$ texture, far below the ideal Se coverage of 1/3 ML. The first of these, Type A, consists of clearly-defined round protrusions. Type A may reflect small regions of CuSe, or Cu-deficient CuSe. The other two textures, Types B and C, are both assigned as two-dimensional layers of strained CuSe, where strain limits the island size (Type B) or distorts the $\sqrt{3}$ lattice (Type C). These 2 types of structures are analogous to dense planes of bulk klockmannite, CuSe. The observed compression in the Type C islands is accounted for in terms of the bulk CuSe lattice constant, which is 11% shorter than $\sqrt{3}a$ on Cu(111). Thus Se forms dense $\sqrt{3}$ islands that incorporate Cu. This is in contrast to S, which forms small complexes with Cu under comparable conditions on Cu(111).^{19,22}

Acknowledgements

The experimental component of this work was conducted or supervised by HW, JO, HJY, YK, and PAT, with support from three sources. In the U.S., it was supported by NSF Grant CHE-1111500. In Japan, it was supported by a Grant-in-Aid for Scientific Research on Priority Areas “Electron Transport Through a Linked Molecule in Nano-scale”, and by a Grant-in-Aid for Scientific Research(S) “Single Molecule Spectroscopy using Probe

Microscope” from the Ministry of Education, Culture, Sports, Science, and Technology (MEXT). The theoretical component of this work was conducted by DJL, with support from the Division of Chemical Sciences, Basic Energy Sciences, U.S. Department of Energy (DOE). The theoretical component of the research was performed at Ames Laboratory, which is operated for the U.S. DOE by Iowa State University under contract No. DE-AC02-07CH11358. This part also utilized resources of the National Energy Research Scientific Computing Center, which is supported by the Office of Science of the U.S. DOE under Contract No. DE-AC02-05CH11231. We thank Gordon J. Miller for providing insight into the structure of bulk klockmannite.

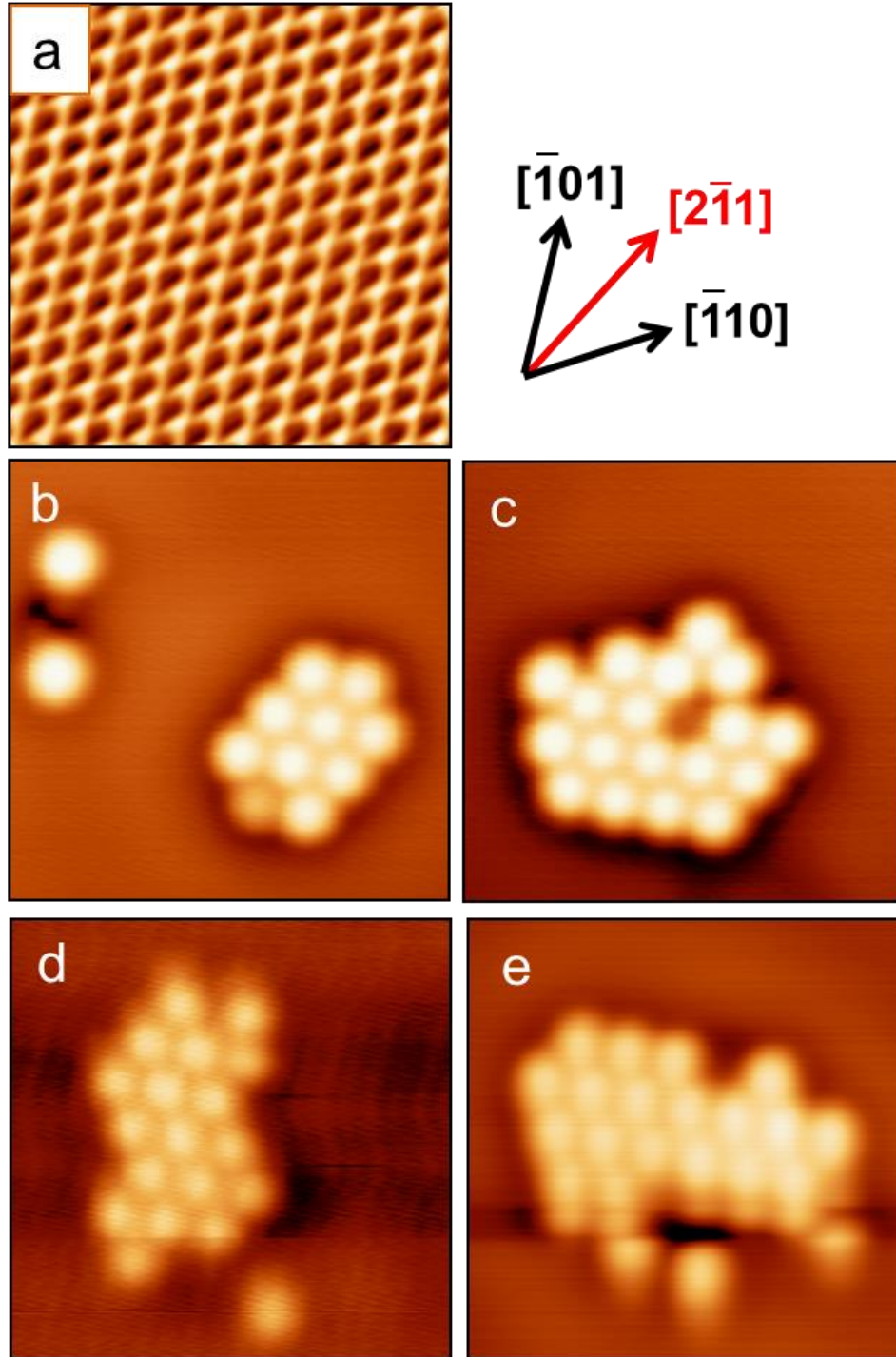


Figure 1. Topographic STM images. (a) Atomically resolved Cu(111), $3 \times 3 \text{ nm}^2$. Two close-packed directions and one open direction are labelled to the right of (a). (b)-(e) show examples of Type A islands, $4 \times 4 \text{ nm}^2$.

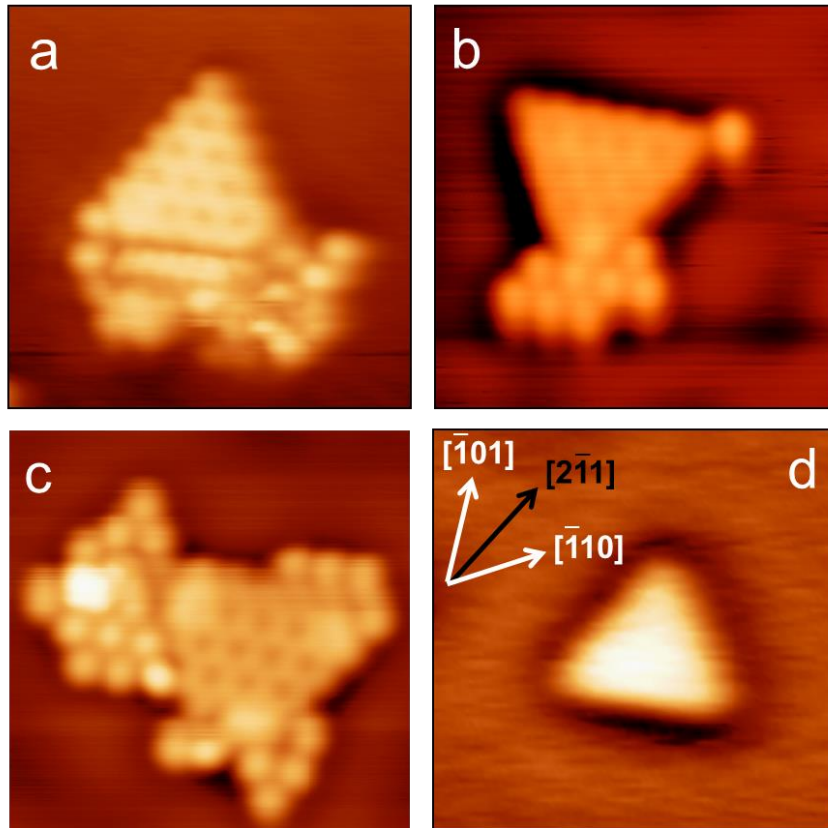


Figure 2. Topographic STM images of the Type B islands, all $5 \times 5 \text{ nm}^2$.

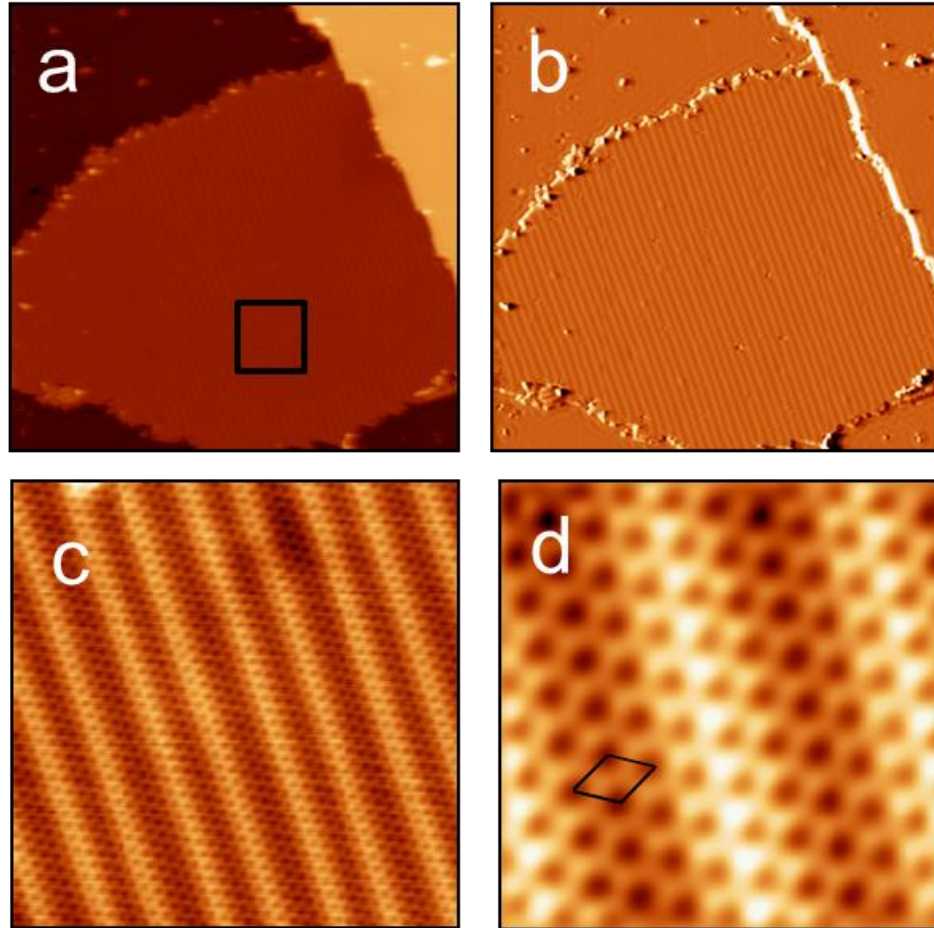


Figure 3. STM images of Type C texture. One Type C island is shown as (a) topographic and (b) derivative images, $100 \times 100 \text{ nm}^2$. (c) is a topographic image of the indicated area in (a), $15 \times 15 \text{ nm}^2$. (d) is a topographic image with the $\sqrt{3}$ unit cell indicated, $4 \times 4 \text{ nm}^2$.

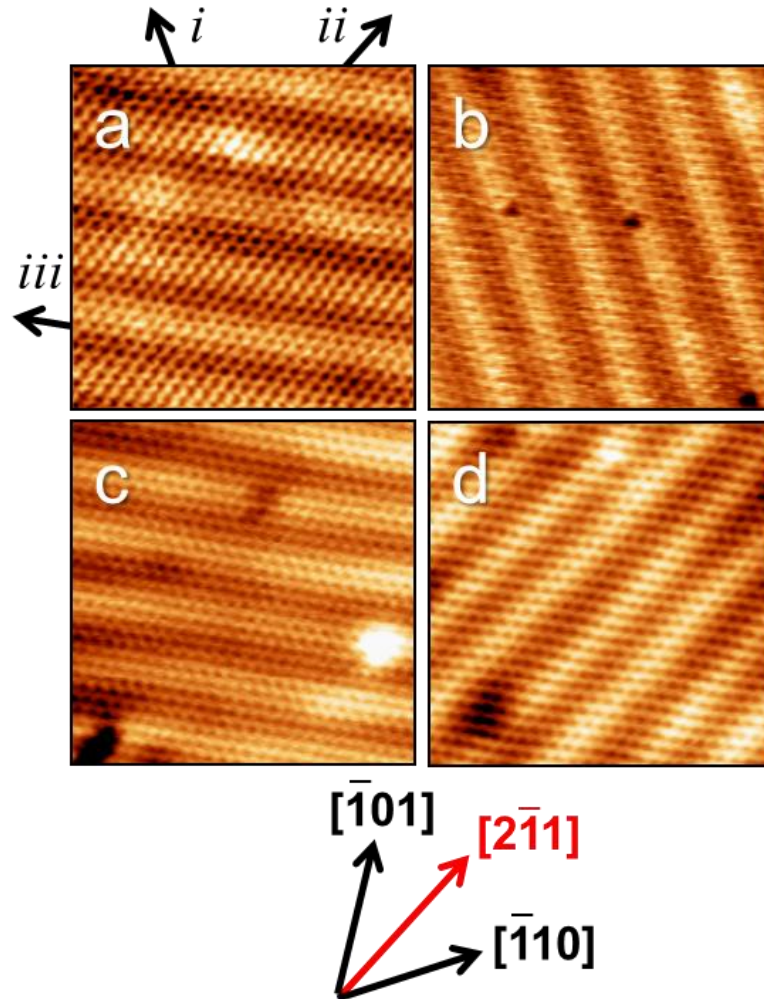


Figure 4. Topographic STM images of different Type C orientations, all $10 \times 10 \text{ nm}^2$.

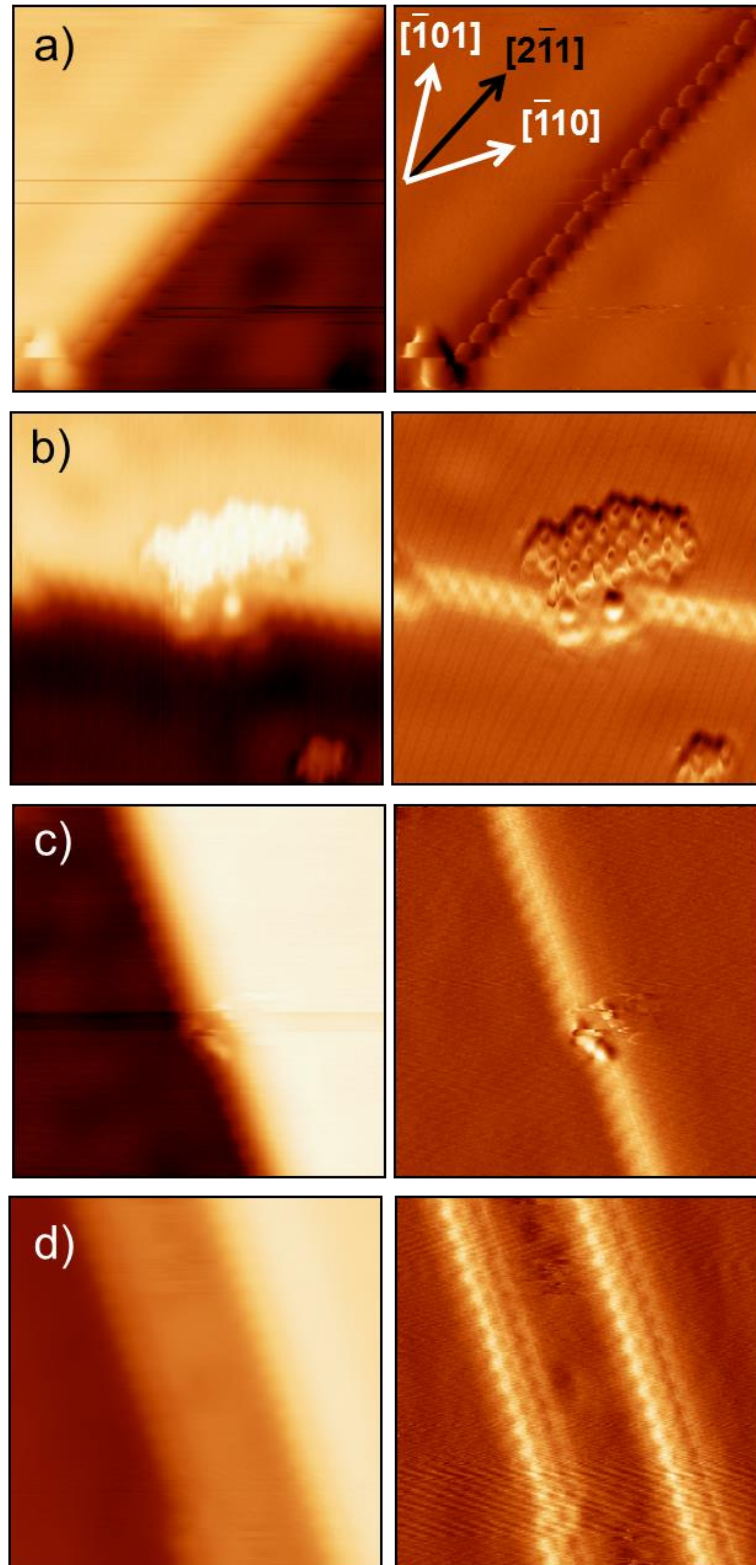


Figure 5. STM images of Se-decorated step edges. The left column contains topographic images, derivative images are on the right. (a) is $5.8 \times 6 \text{ nm}^2$. (b)-(d) are $7 \times 7 \text{ nm}^2$.

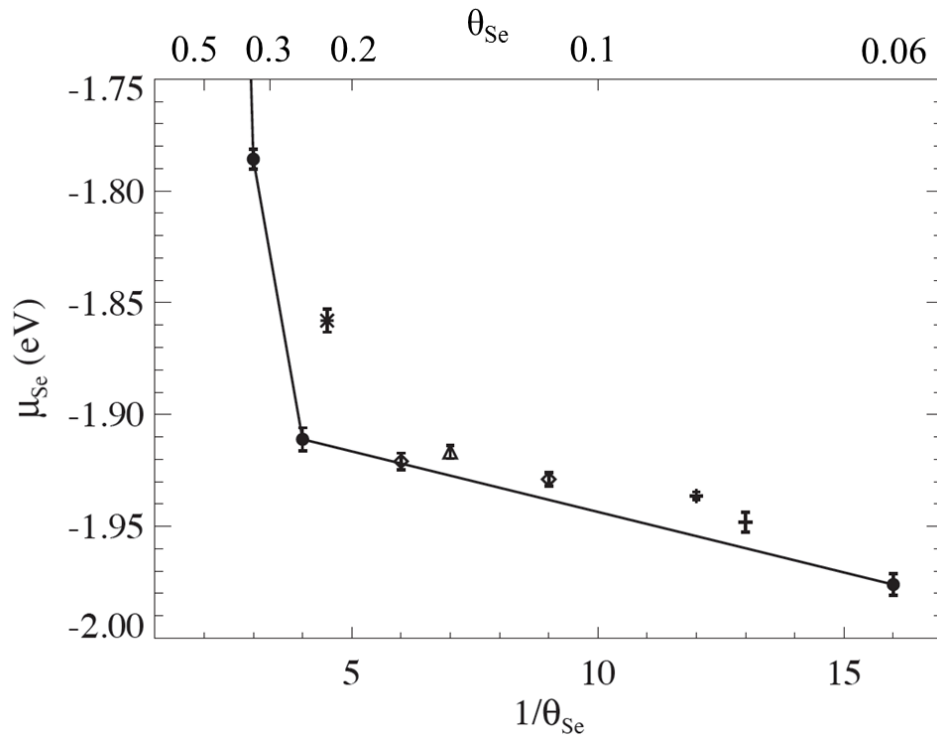


Figure 6. Chemical potential of Se as a function of inverse Se coverage (θ_{Se}) for a variety of supercells. The solid line is defined by the p(4x4) (1/16 ML), p(2x2) (1/4 ML), and ($\sqrt{3}\times\sqrt{3}$)R30° (1/3 ML) supercells.

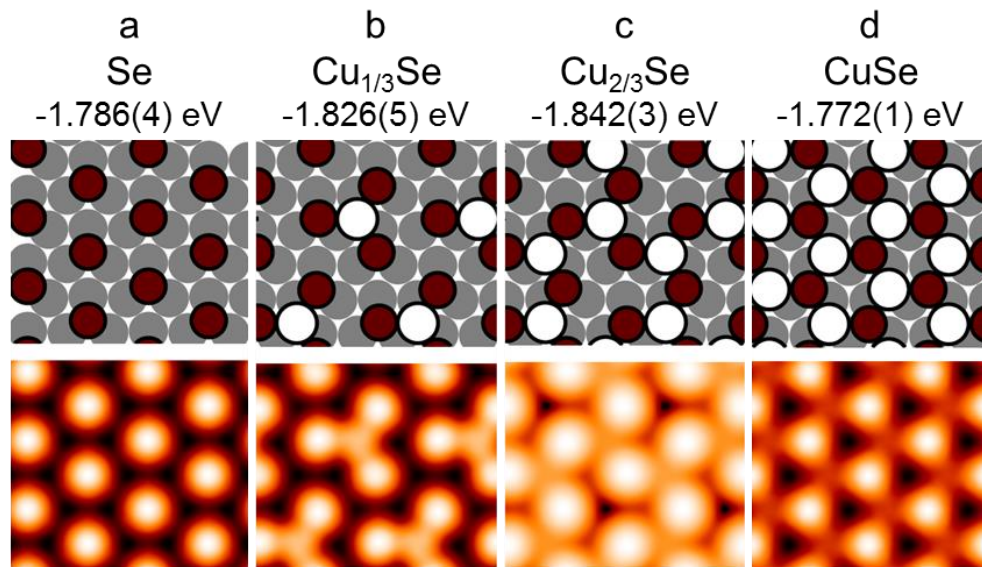


Figure 7. Configurations containing a fixed $\sqrt{3}$ lattice of Se atoms with various amounts of Cu. Lower panels show simulated STM images. (a) $\sqrt{3}$ -Se. (b) $\sqrt{3}$ - $\text{Cu}_{1/3}\text{Se}$. (c) $\sqrt{3}$ - $\text{Cu}_{2/3}\text{Se}$. (d) $\sqrt{3}$ -CuSe.

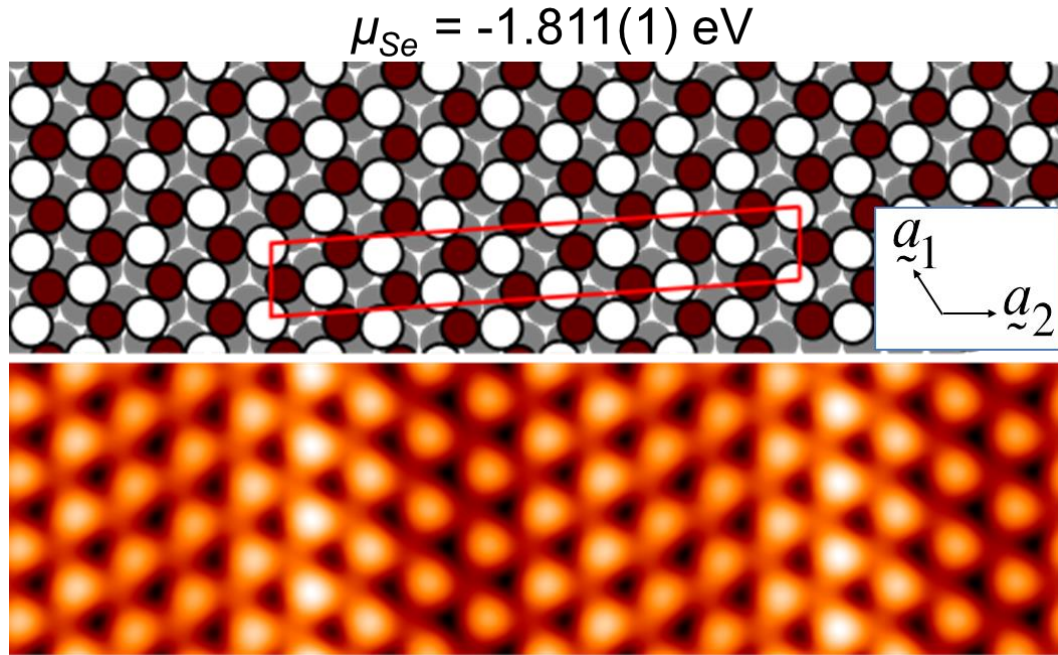


Figure 8. A $\begin{pmatrix} 2 & 1 \\ 1 & 13 \end{pmatrix}$ approximant to $\sqrt{3}$ -CuSe, with coverage 0.360 ML and area 25 times that of the (1x1). See Table 1. The red rhombus shows the primitive unit cell.

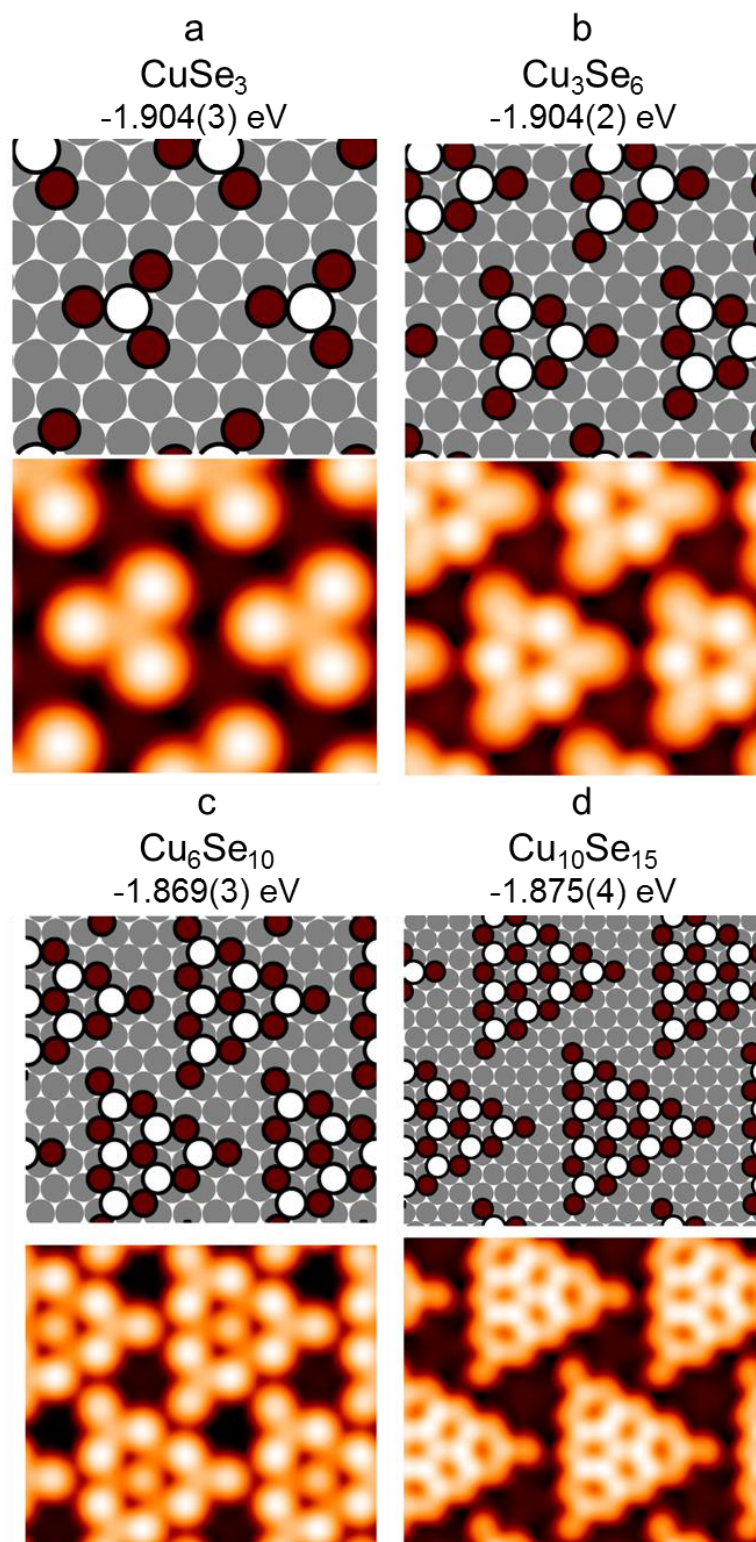


Figure 9. Configurations of small, triangular $\sqrt{3}$ -CuSe islands with simulated STM images.

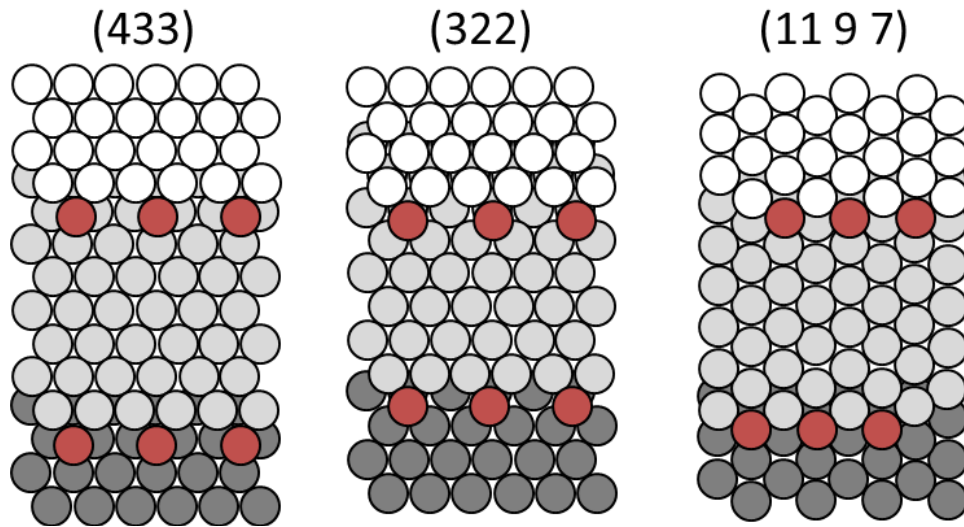


Figure 10. Three examples of Cu surfaces vicinal to (111). The energetics for these configurations are presented in Table 3.

Appendix 1. Tunneling Conditions

Figure name	Dimensions, nm ²	Current, nA	Sample Bias, V
1a	3 x 3	26.11	-0.002
b	4 x 4	1.00	-0.500
c	4 x 4	1.00	-0.500
d	4 x 4	1.19	-0.003
e	4 x 4	2.06	-0.100
2a	5 x 5	1.24	-0.143
b	5 x 5	2.06	-0.100
c	5 x 5	1.49	-0.009
d	5 x 5	1.00	-1.000
3a, b	100 x 100	1.00	-0.191
c	15 x 15	3.36	+0.500
d	4 x 4	2.19	-0.020
4a	10 x 10	1.03	-0.092
b	10 x 10	1.24	-0.143
c	10 x 10	1.00	+1.000
d	10 x 10	1.00	-1.000
5a	5.8 x 6	1.01	-0.027
b	7 x 7	1.79	-0.003
c	7 x 7	1.24	-0.005
d	7 x 7	1.90	-0.005

Appendix 2. Se atom diffusion on Cu(111)

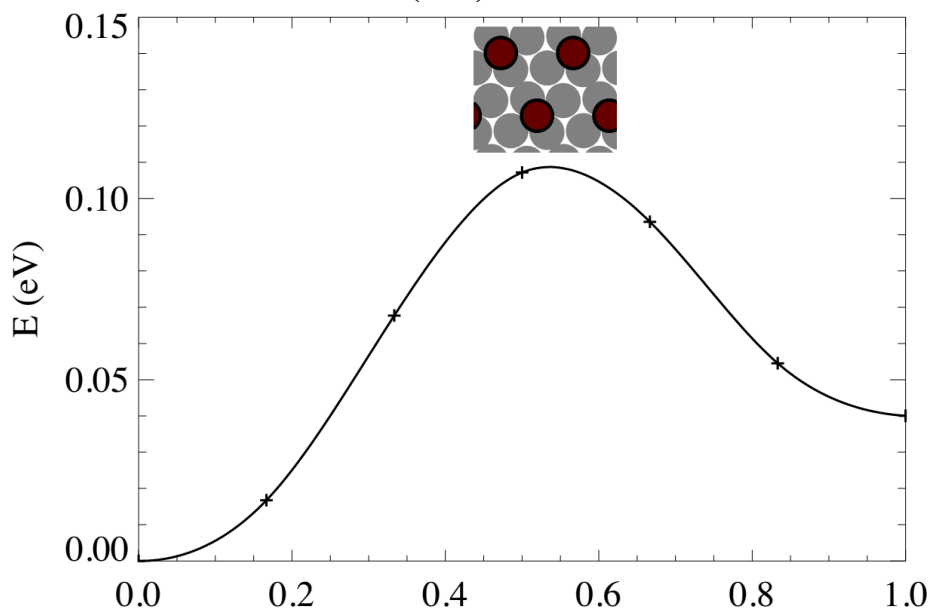


Figure A1. Diffusion pathway of Se, determined from nudged elastic band calculations with k-point grid (24 x 24 x 1). The starting point is an fcc site, the end point is an hcp site. The transition site (two-fold bridge) is shown in the inset. The diffusion barrier is 0.107 eV.

Appendix 3. Other Se-Cu configurations evaluated with DFT

Figures A2-A40 show other Se and Cu-Se structures tested in DFT. Each panel contains a schematic of the repeating structure. Gray circles represent Cu atoms in the terrace; white circles represent Cu atoms on top of the terrace. Dark red circles represent Se on the terrace, bright red circles represent Se on top of the white (2nd layer) Cu.

The chemical potential of sulfur, μ_S , for each configuration (in eV) is included, along with a simulated STM image, in shades of orange. The k-points grids are described using the following notation: G is (12 x 12 x 1), Gh is (24 x 24 x 1), and Gh2 is (36 x 36 x 1), all for the primitive (1 x 1). Dipole corrected values are marked with “DL”, where “5GDL” means dipole corrected with a (5 x 5 x 1) k-points grid, for example. Results with and without dipole correction are within a few meV of each other. All μ_S values are an average of calculations with slab thickness (L) of 4-7 slabs, unless noted otherwise. The supercell is given in each figure caption.

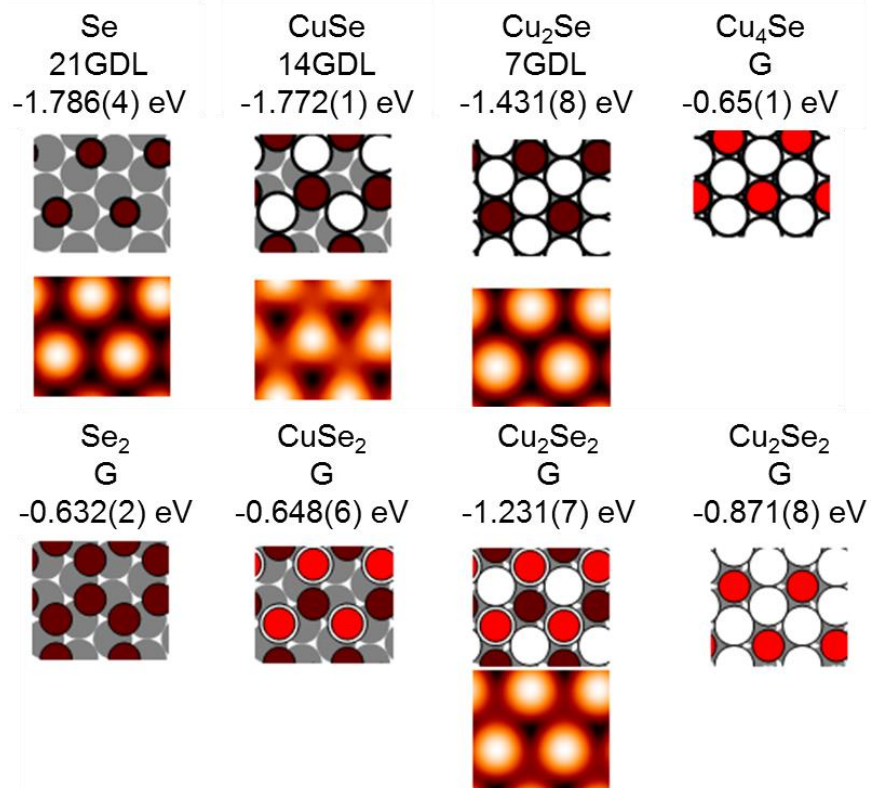


Figure A2. ($\sqrt{3} \times \sqrt{3}$) supercell.

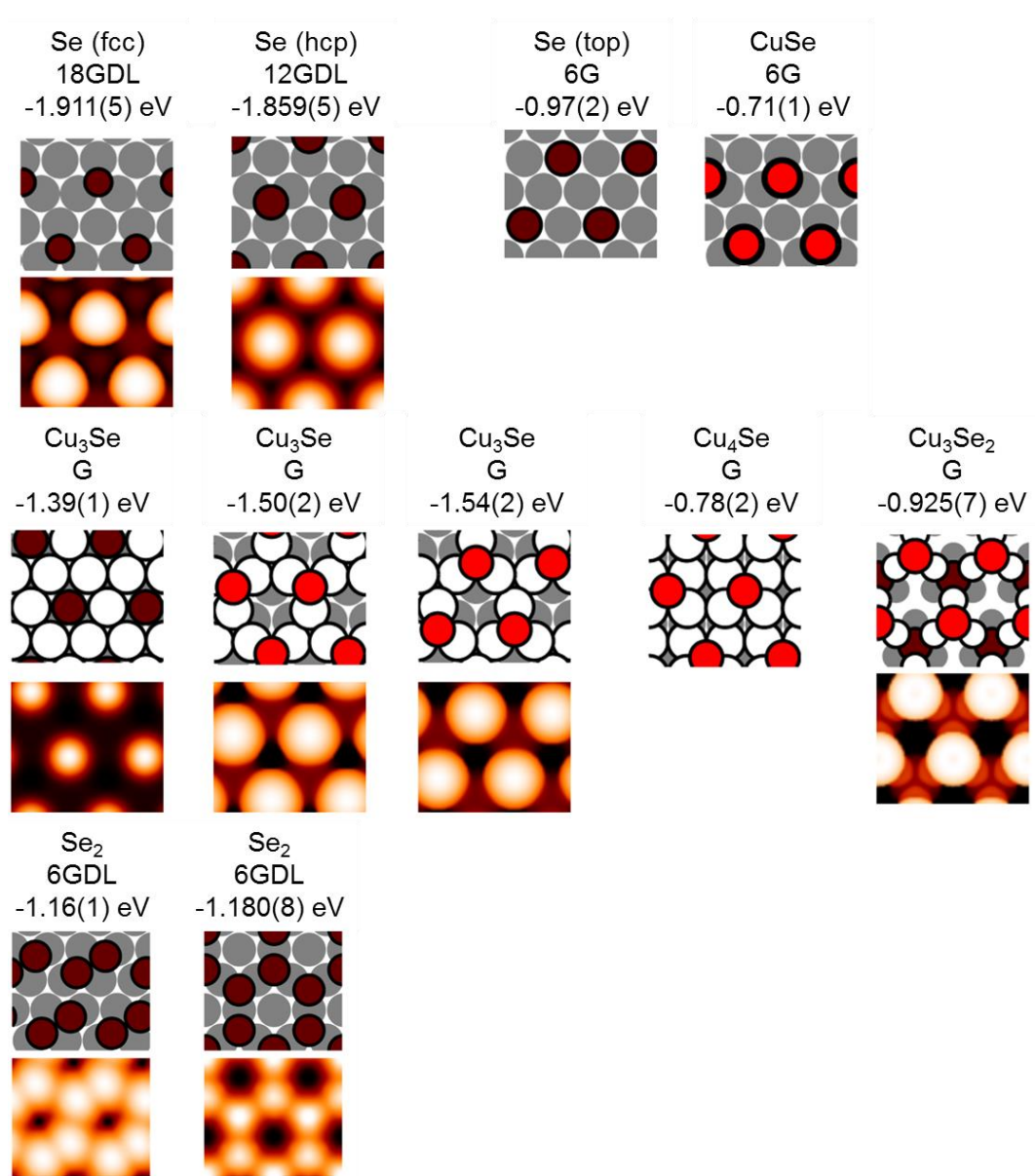


Figure A3. (2 x 2) supercell.

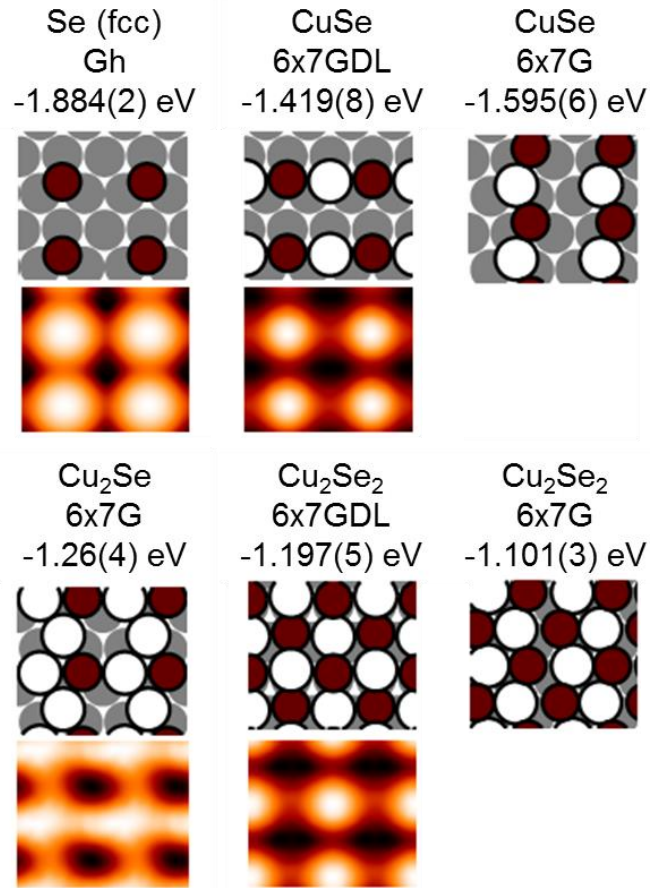


Figure A4. ($2 \times \sqrt{3}$) supercell.

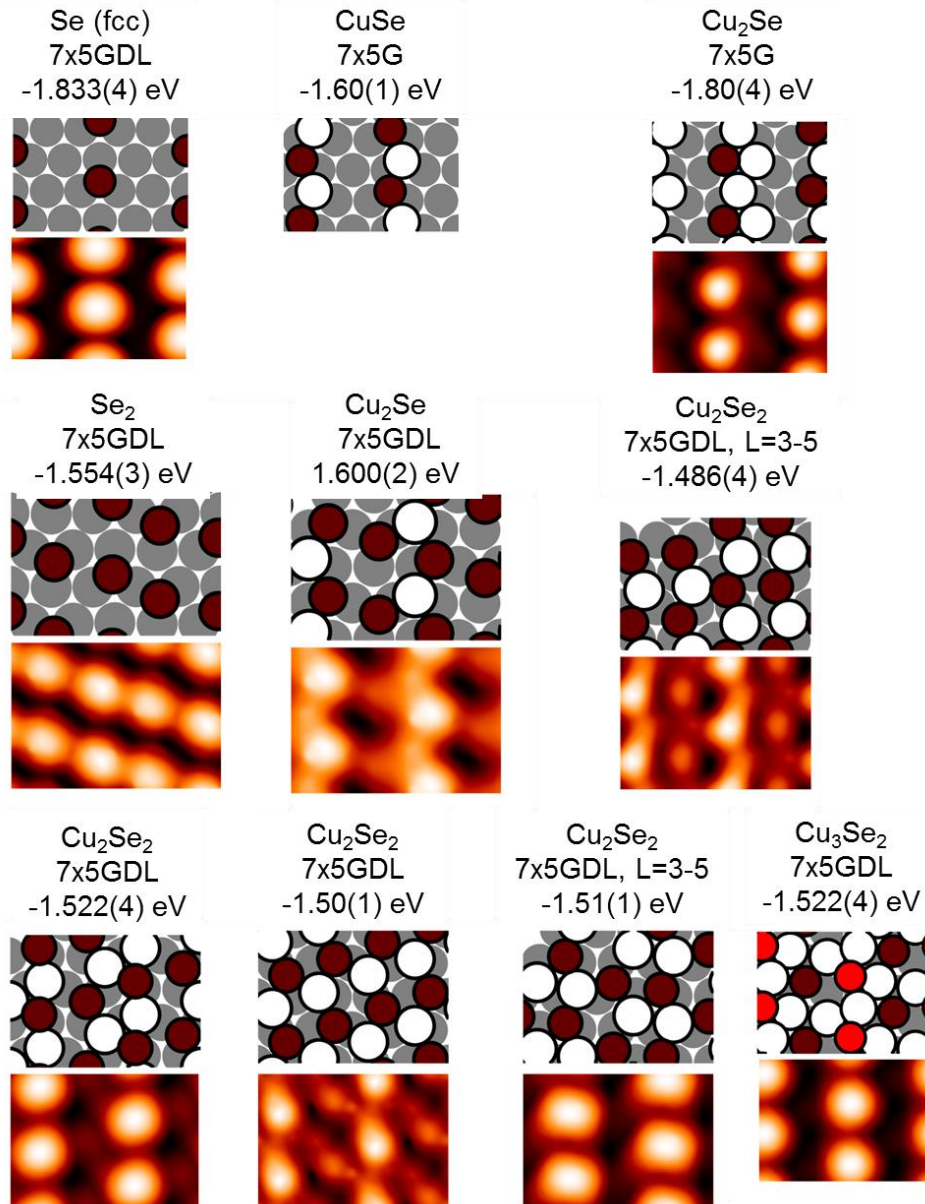


Figure A5. ($\sqrt{3} \times \sqrt{7}$) supercell.

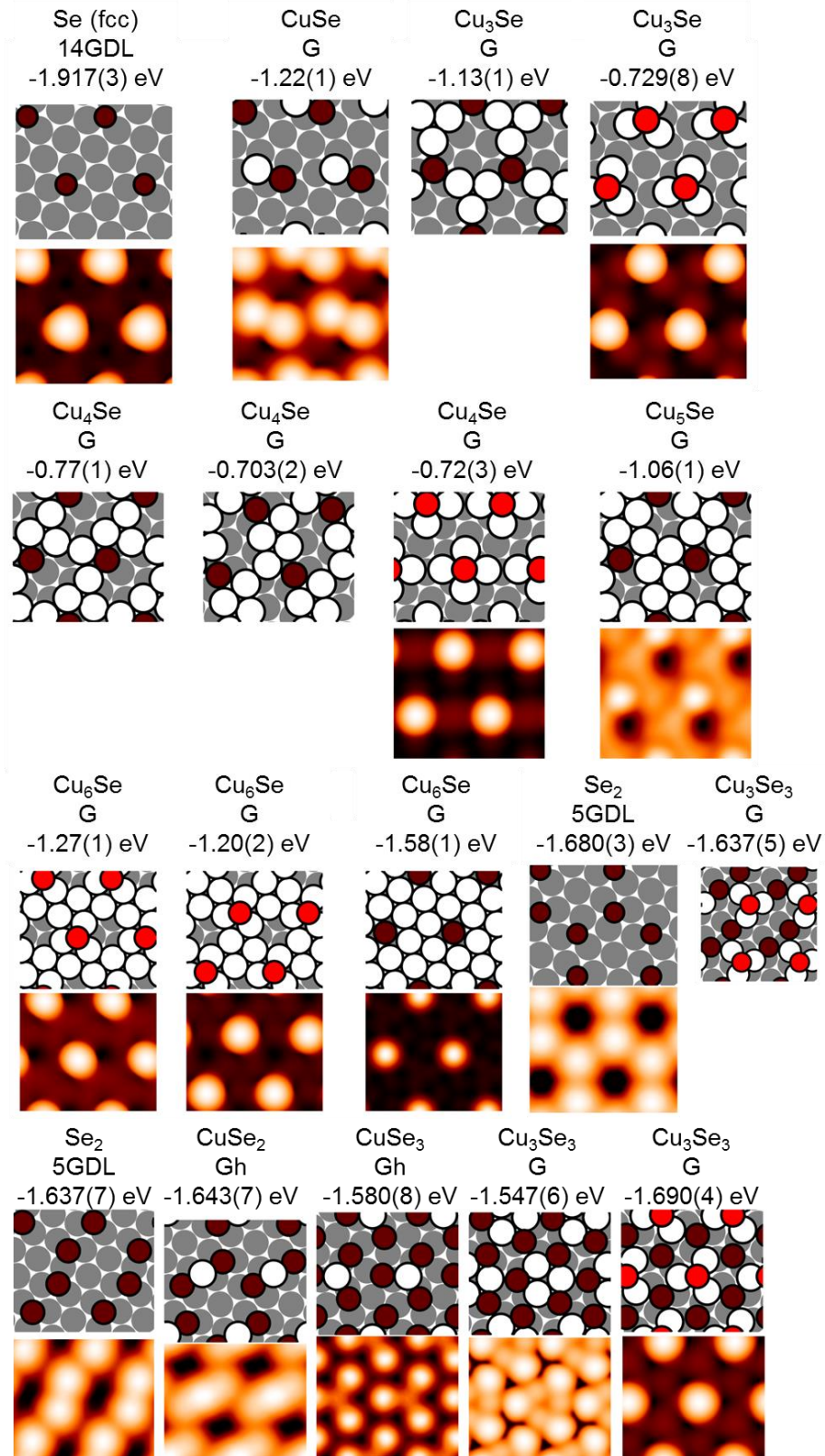


Figure A6. ($\sqrt{7} \times \sqrt{7}$) supercell.

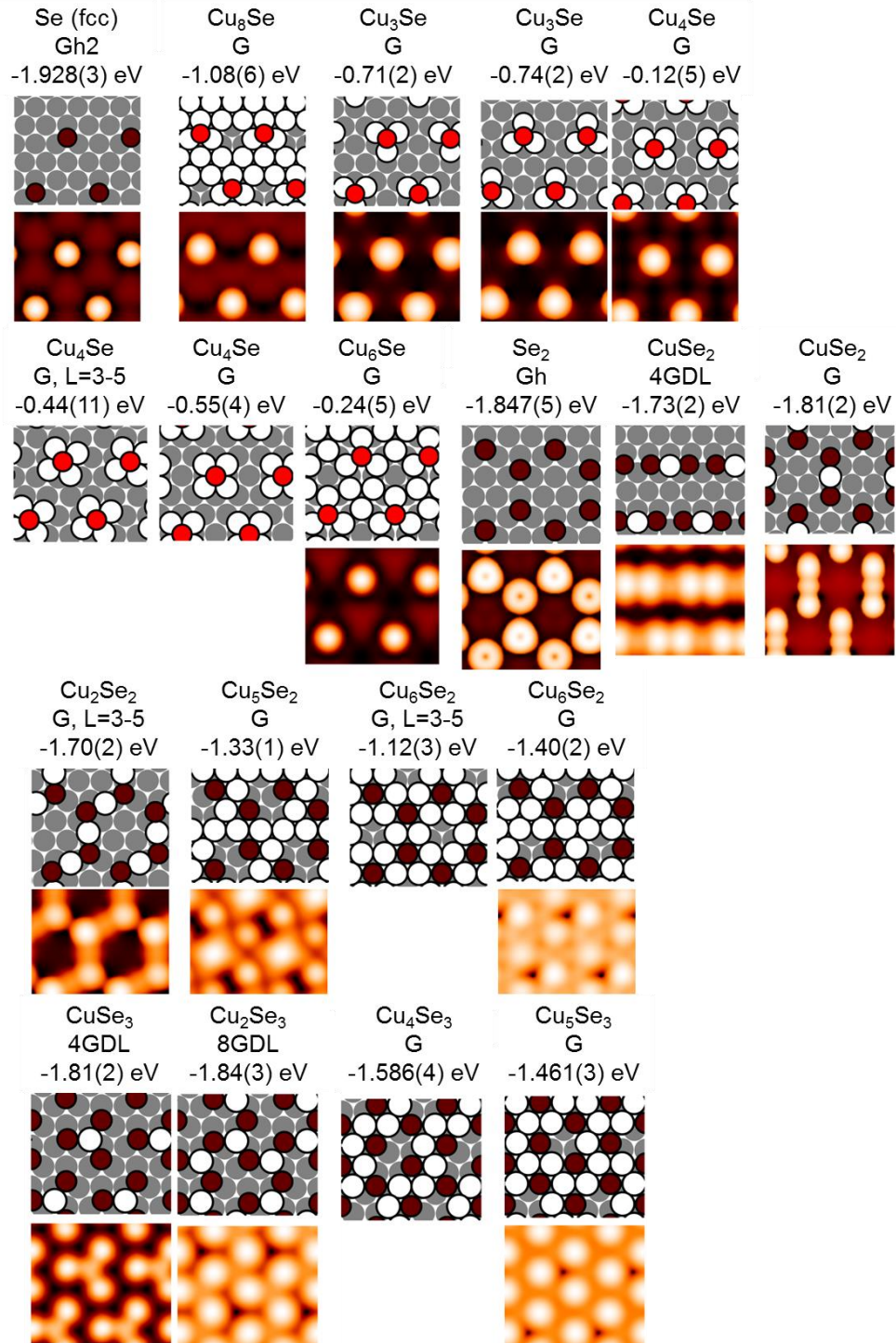


Figure A7. (3 x 3) supercell.

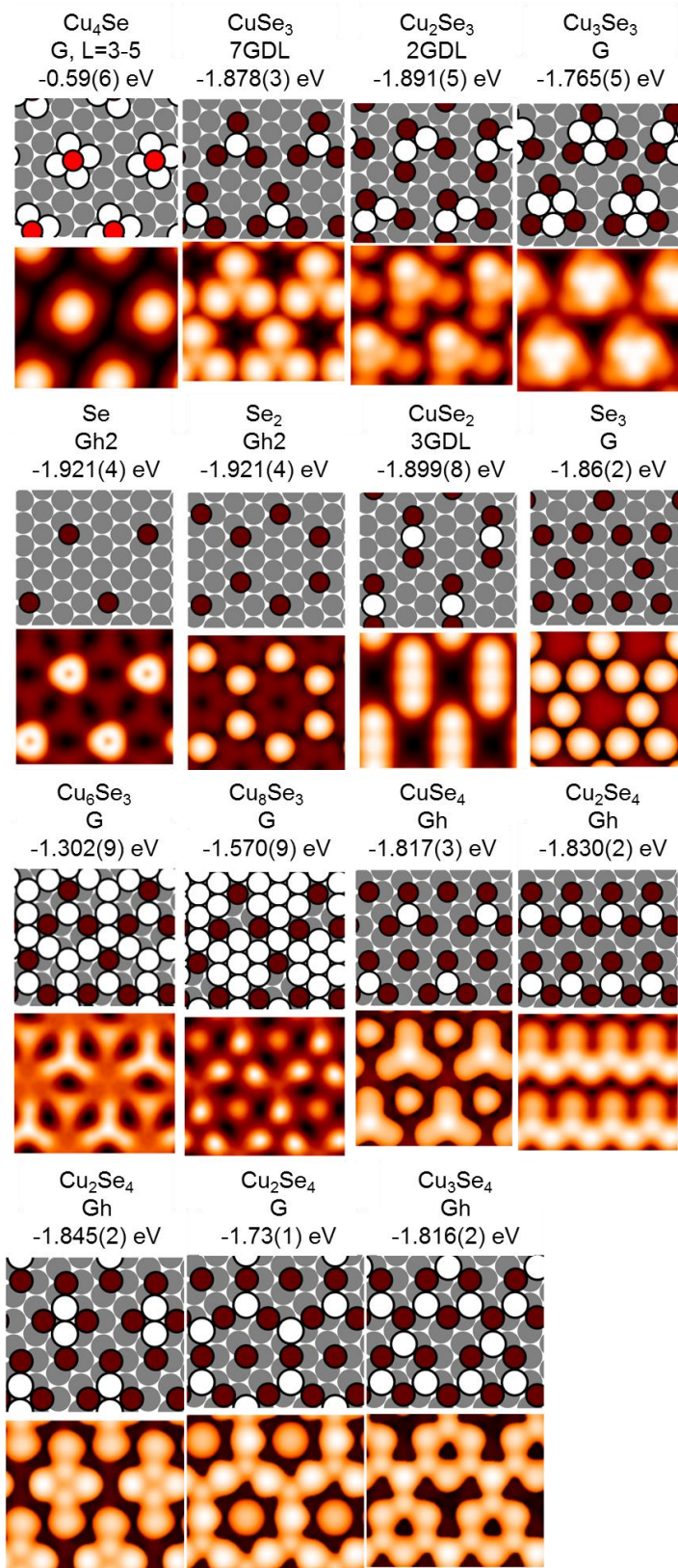


Figure A8. ($2\sqrt{3} \times 2\sqrt{3}$) supercell.

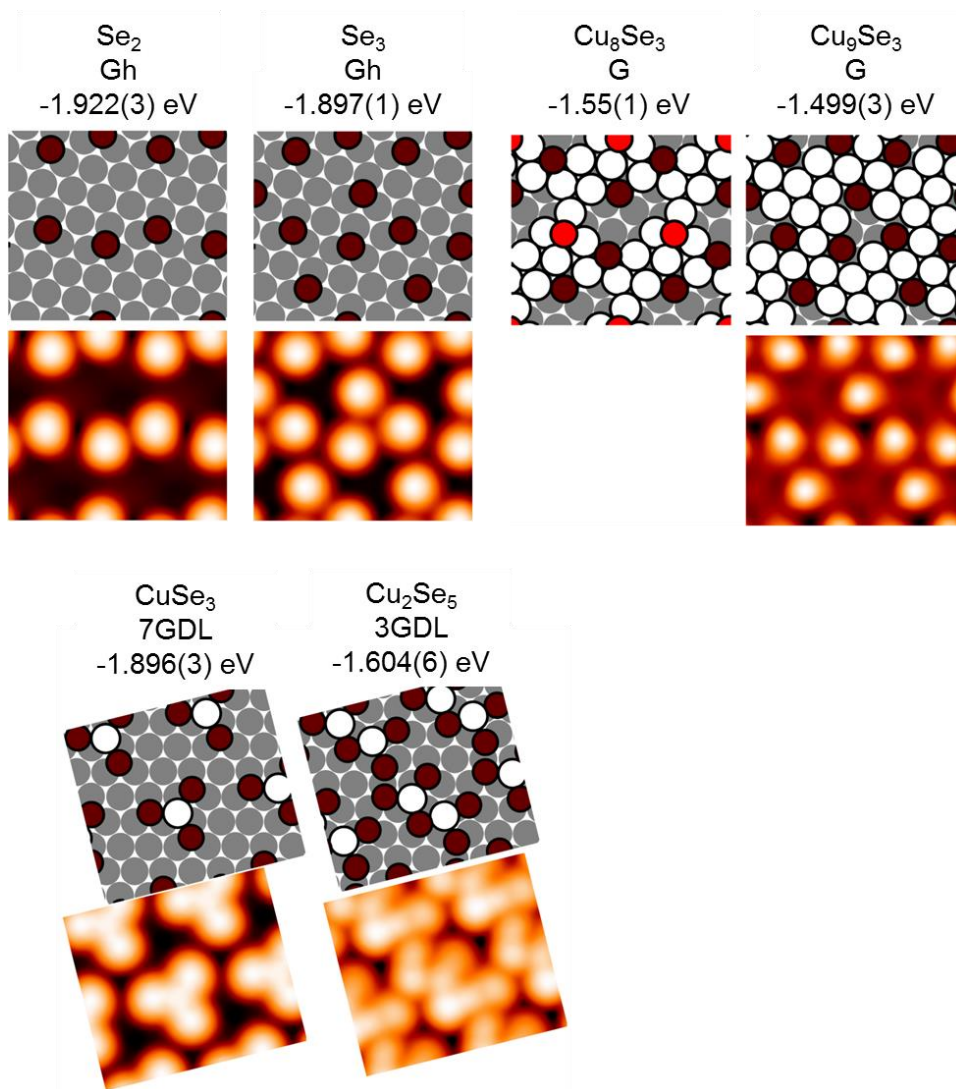


Figure A9. ($\sqrt{13} \times \sqrt{13}$) supercell.

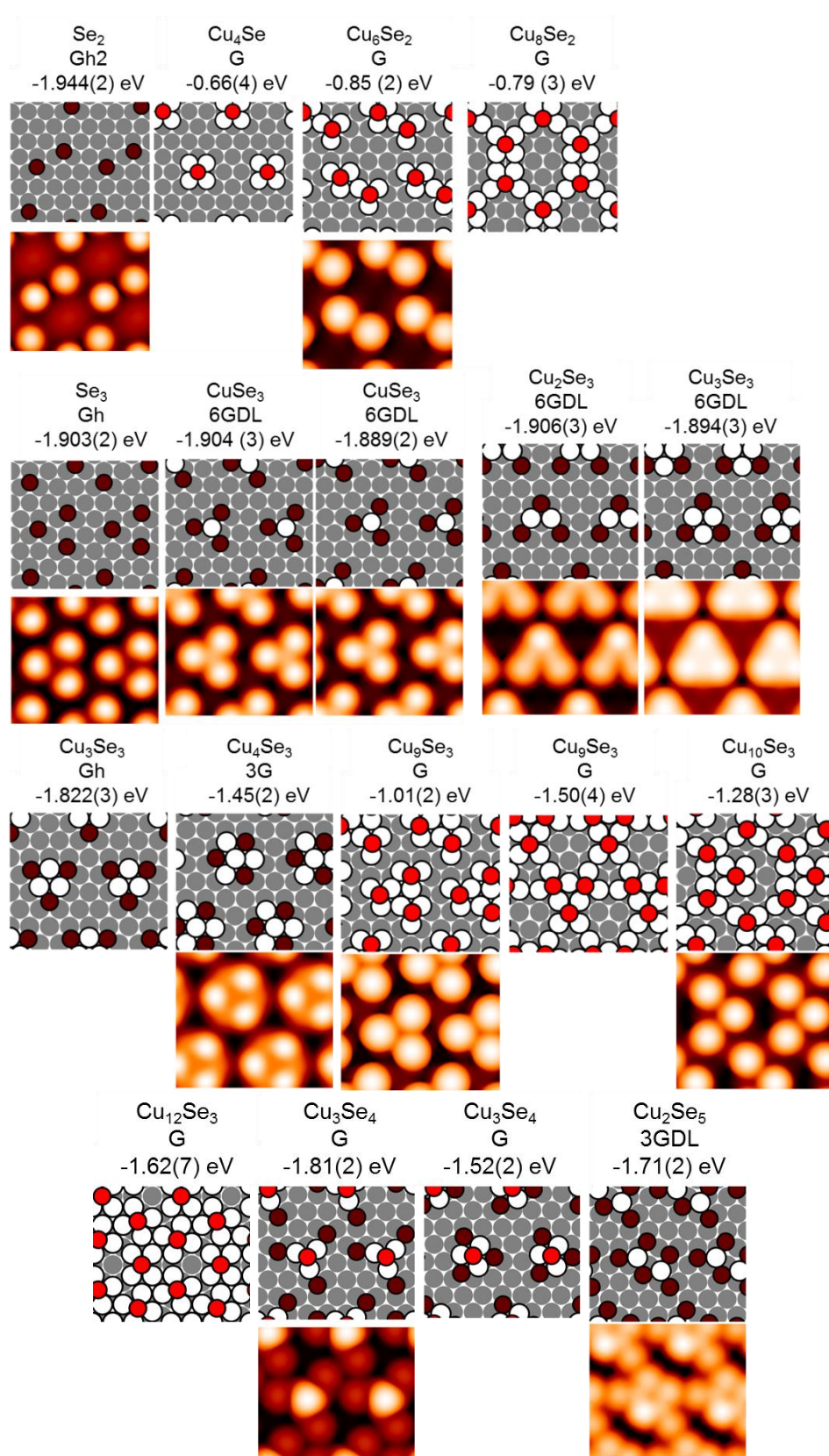


Figure A10. (4 x 4) supercell.

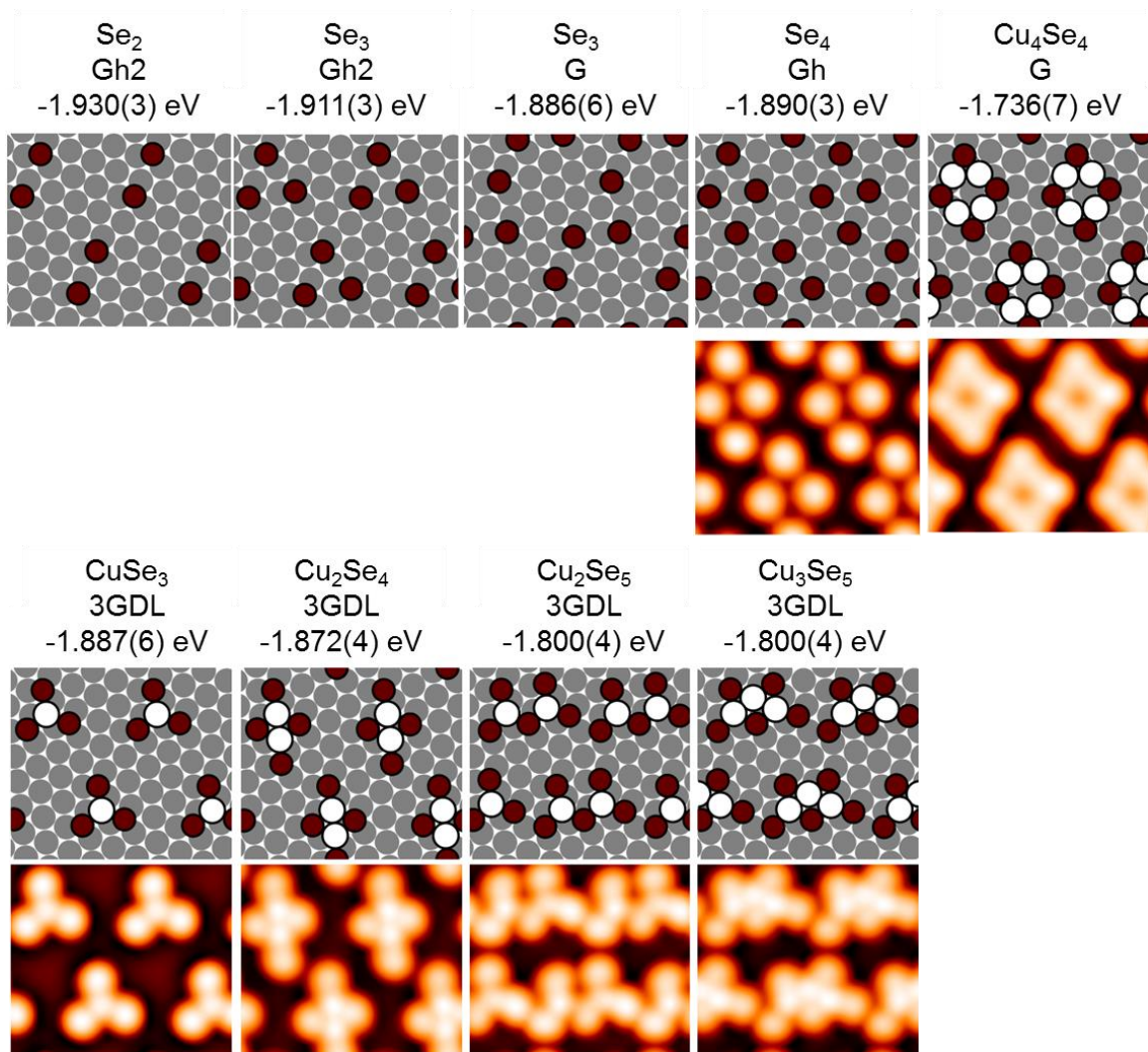


Figure A11. ($\sqrt{19} \times \sqrt{19}$) supercell.

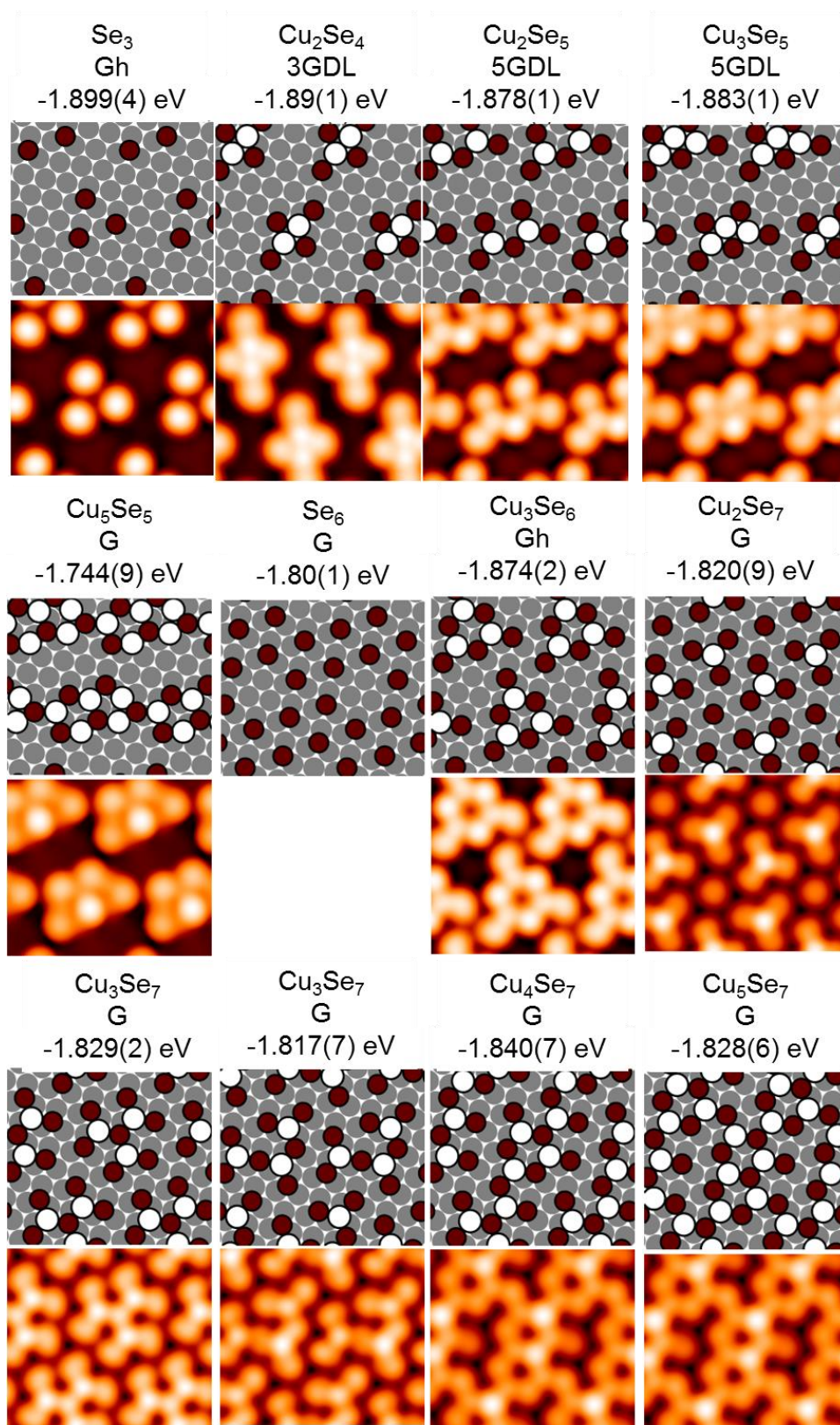


Figure A12. ($\sqrt{21} \times \sqrt{21}$) supercell.

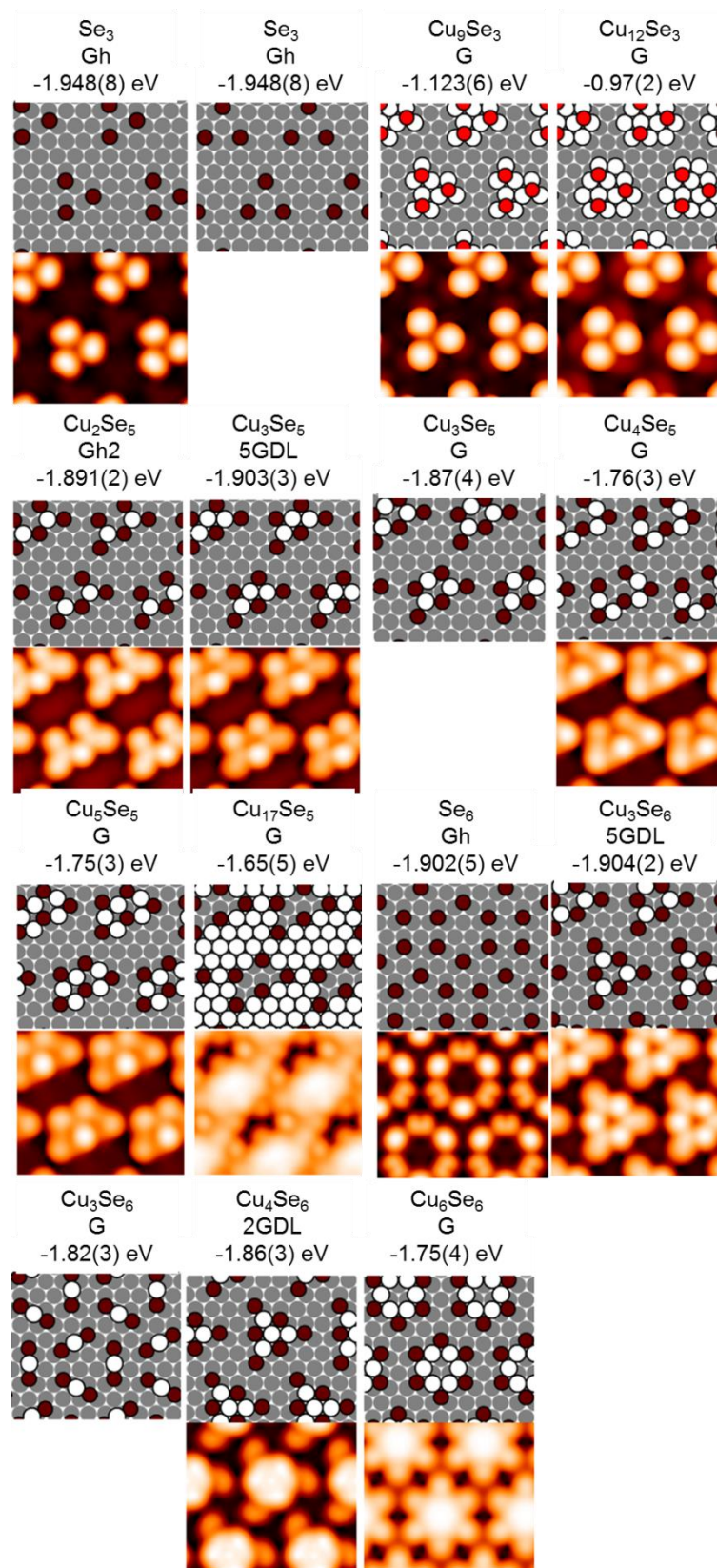


Figure A13. (5 x 5) supercell. Continued on next page.

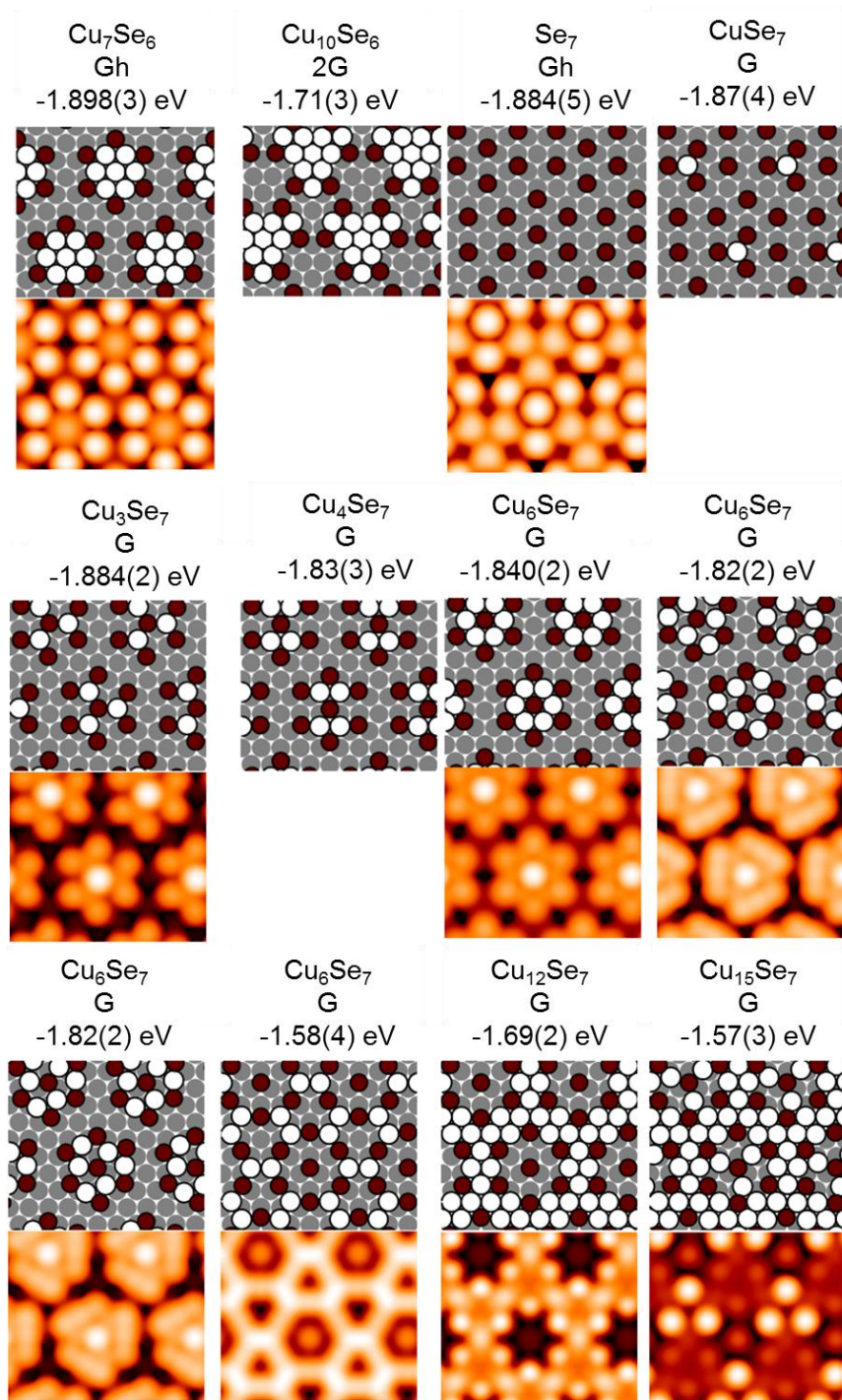


Figure A13 (Continued). (5 x 5) supercell.

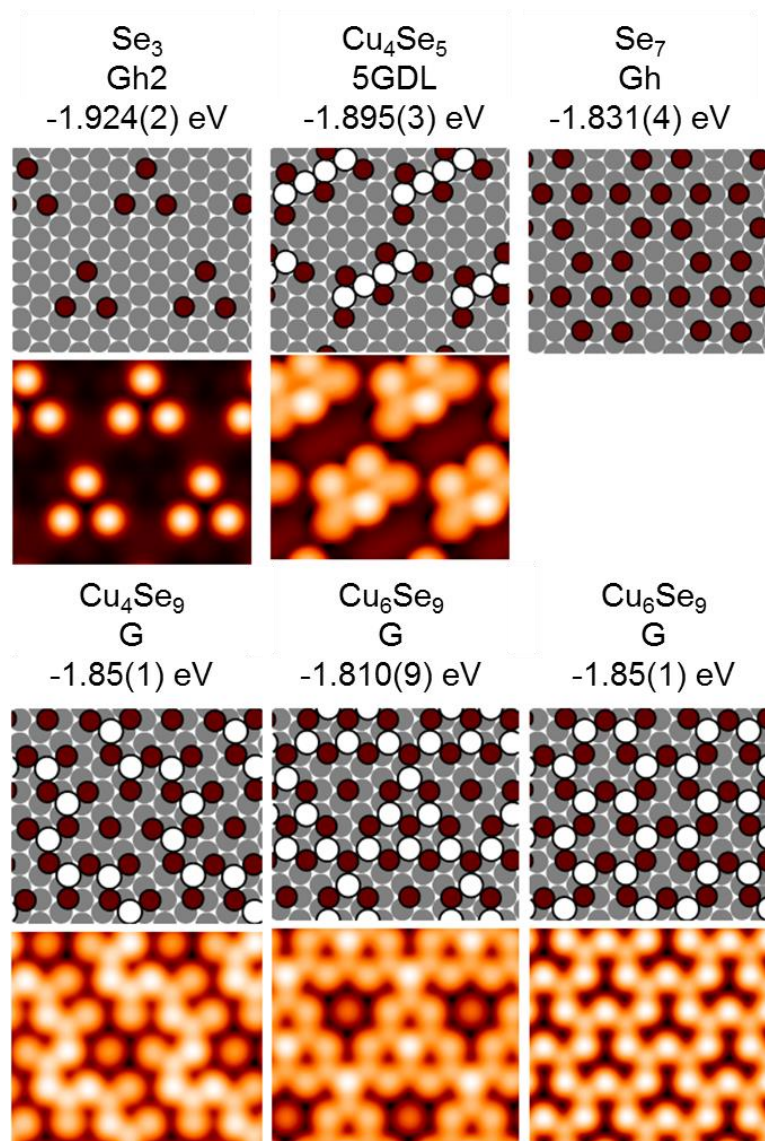


Figure A14. ($3\sqrt{3} \times 3\sqrt{3}$) supercell.

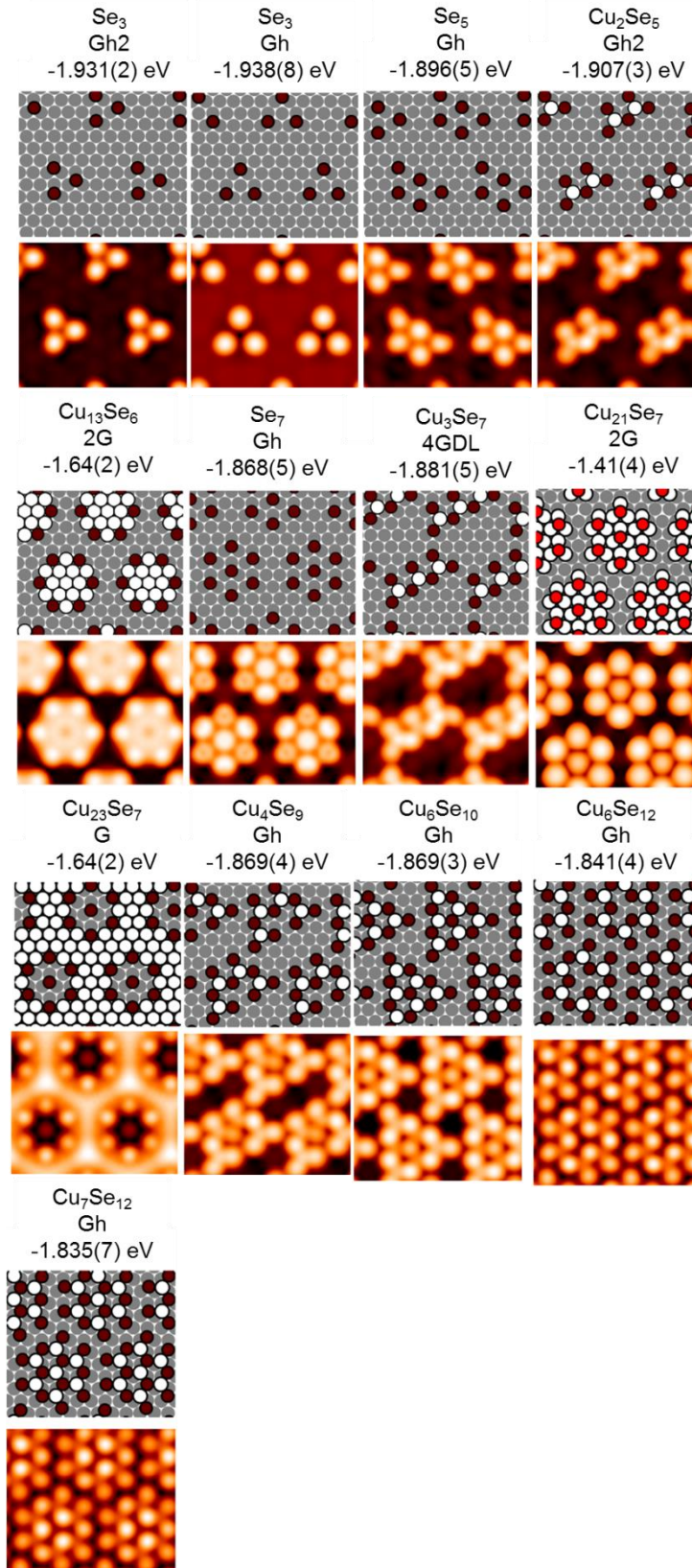


Figure A15. (6 x 6) supercell.

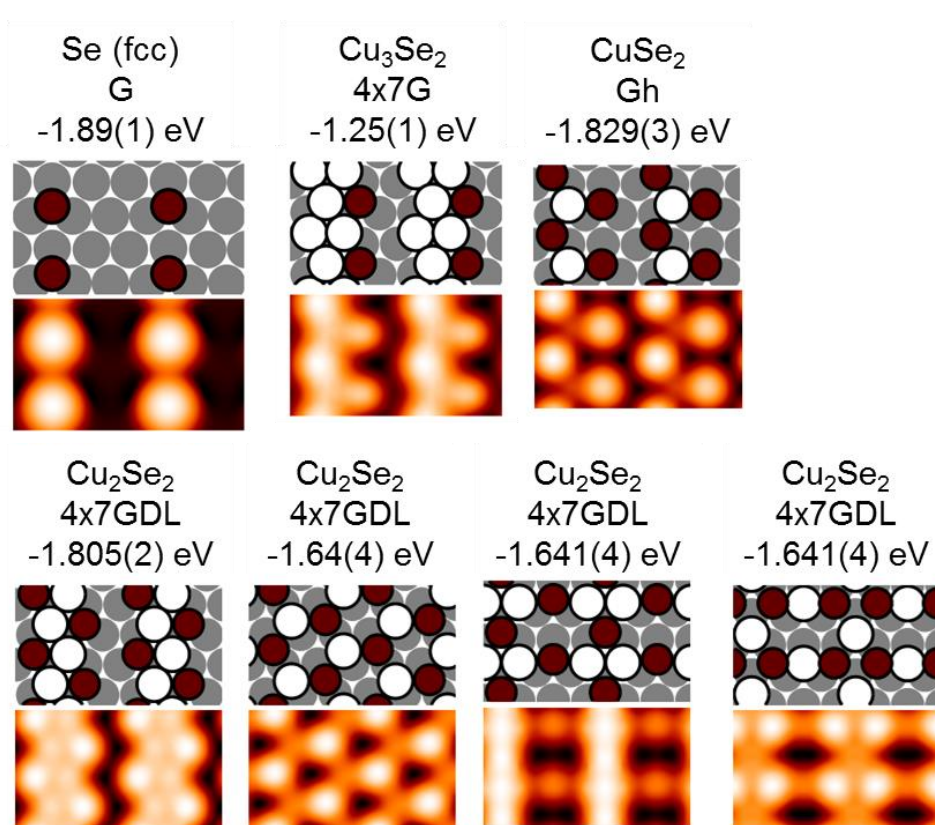


Figure A17. ($3 \times \sqrt{3}$) supercell.

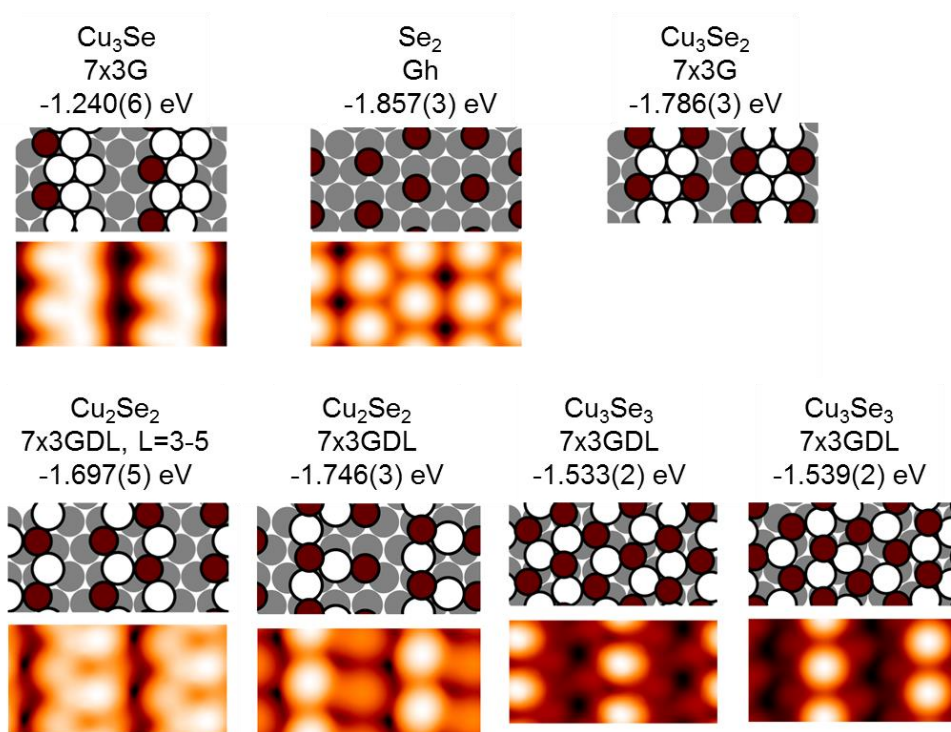


Figure A18. ($\sqrt{3} \times \sqrt{13}$) supercell.

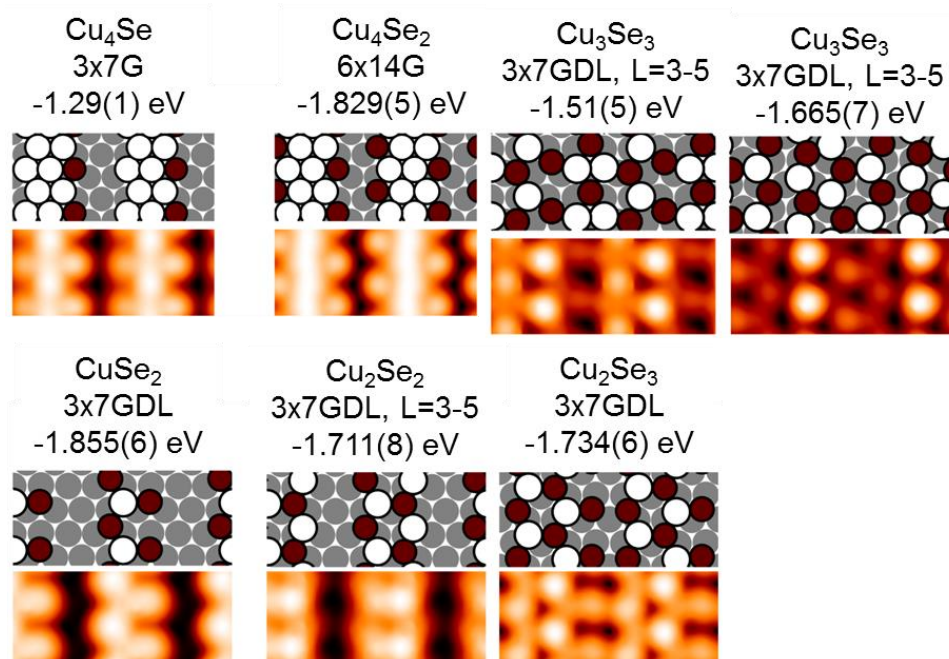


Figure A19. $(4 \times \sqrt{3})$ supercell.

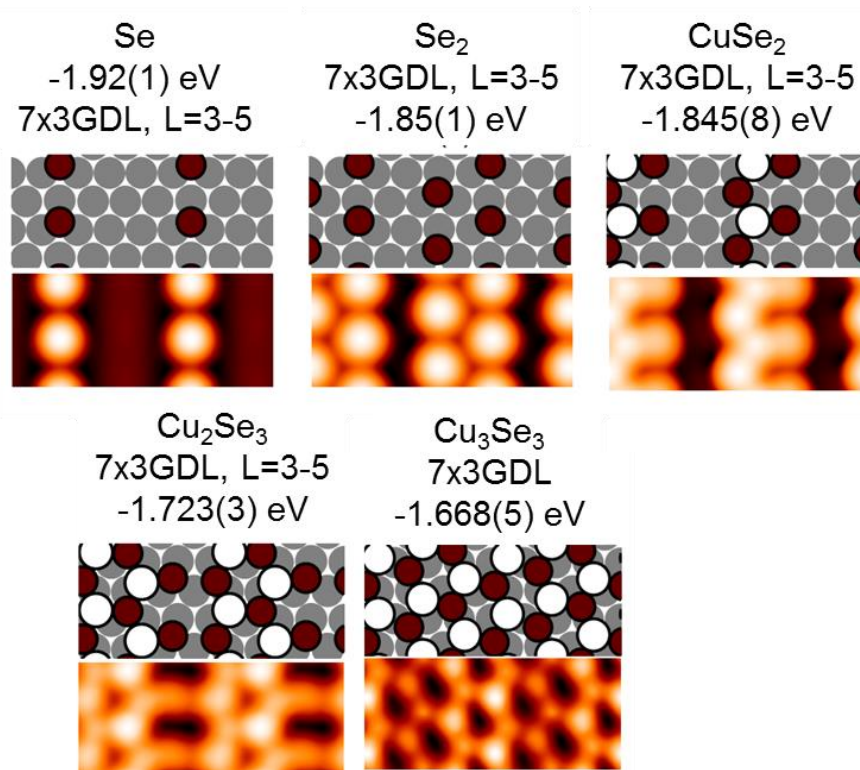


Figure A20. $(\sqrt{3} \times \sqrt{19})$ supercell.

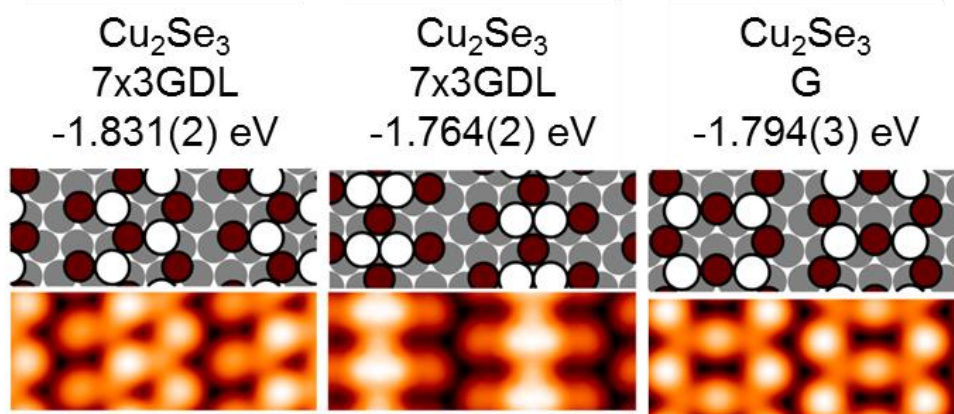


Figure A21. ($\sqrt{3} \times \sqrt{21}$) supercell.

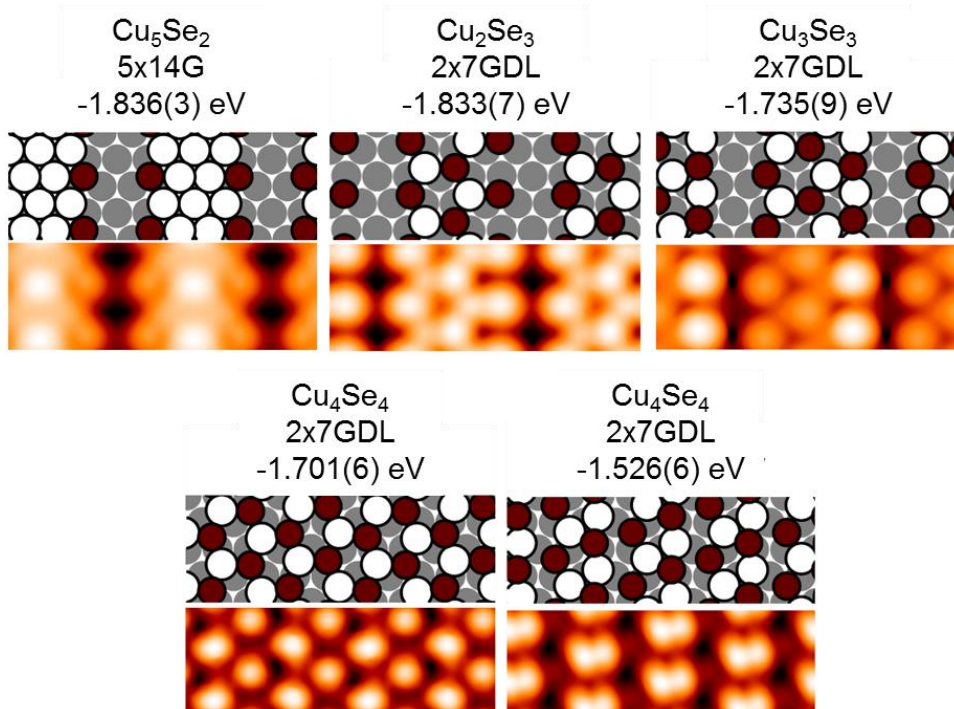


Figure A22. ($5 \times \sqrt{3}$) supercell.

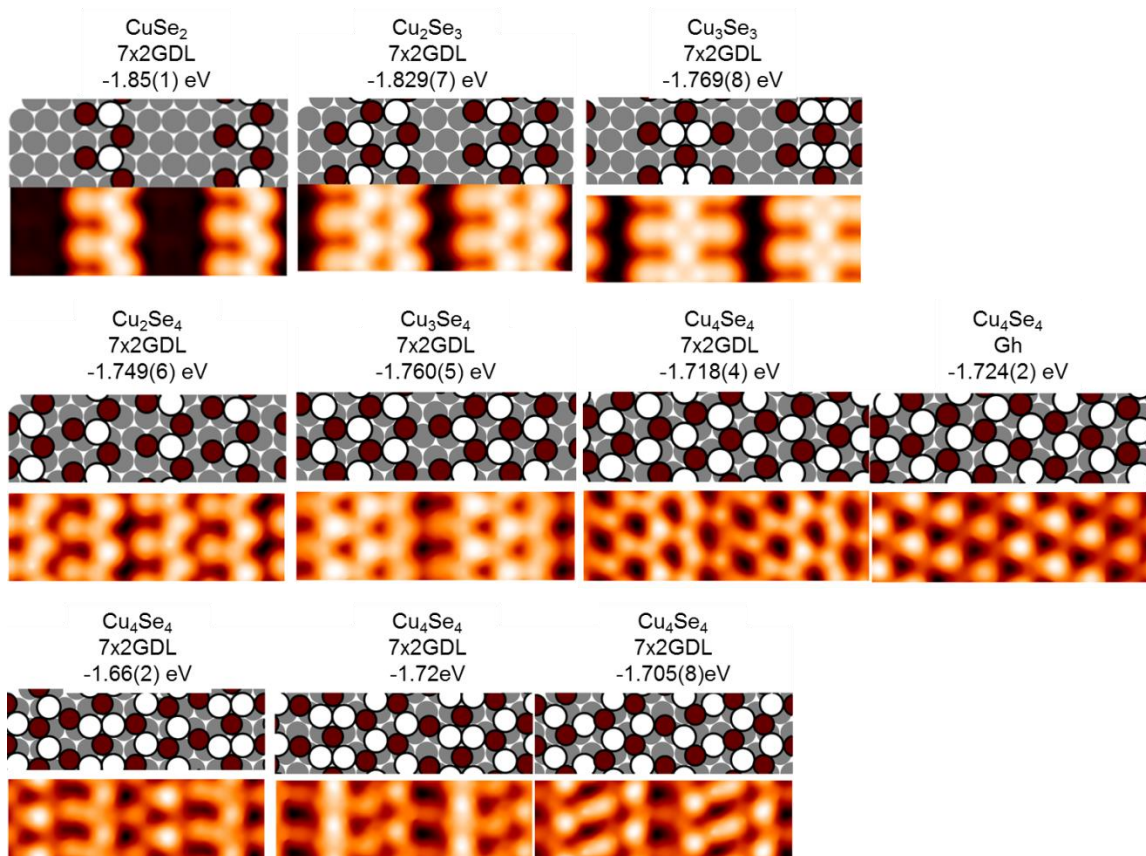


Figure A23. ($\sqrt{3} \times \sqrt{3}1$) supercell.

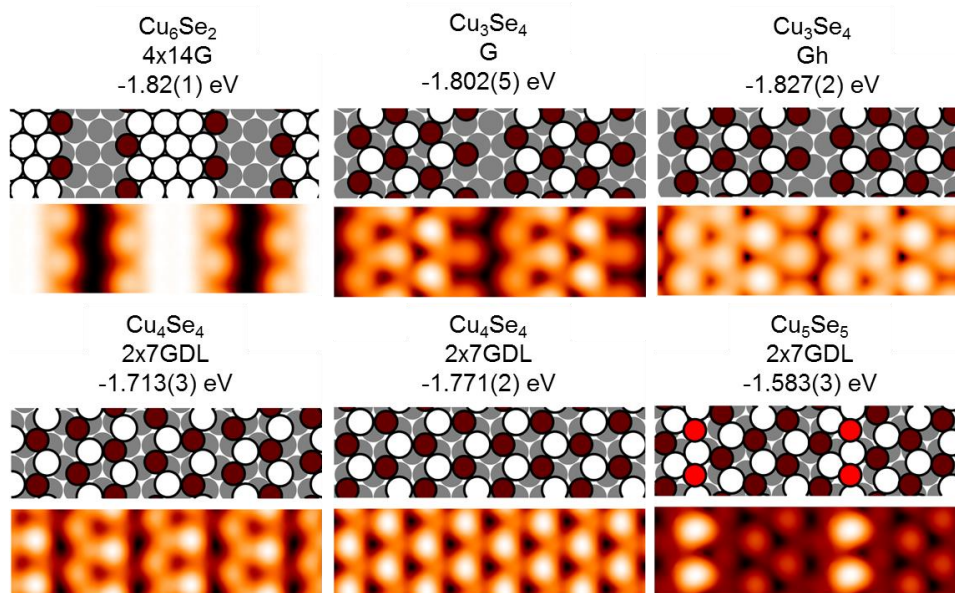


Figure A24. ($6 \times \sqrt{3}$) supercell.

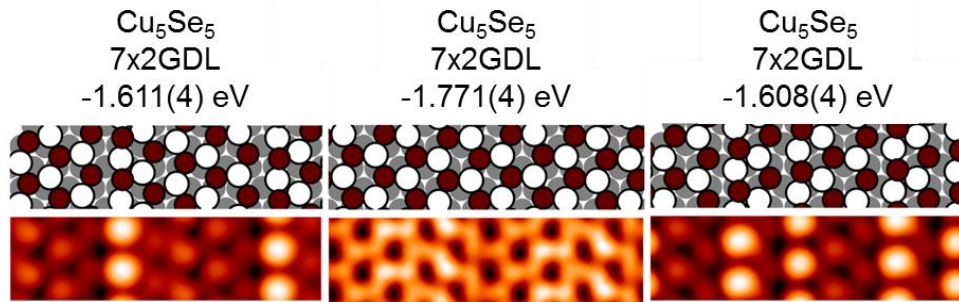


Figure A25. ($\sqrt{3} \times \sqrt{43}$) supercell.

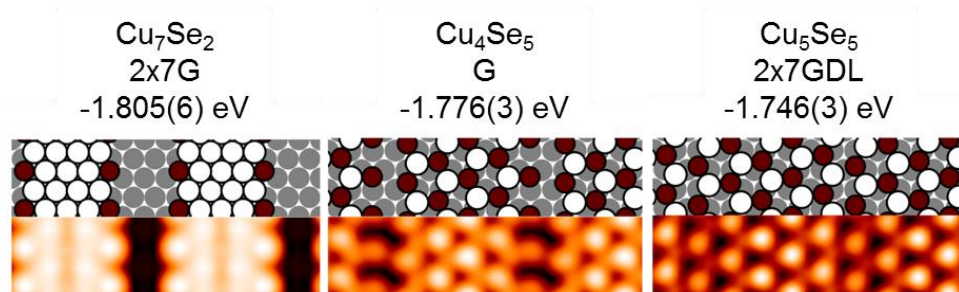


Figure A26. ($7 \times \sqrt{3}$) supercell.

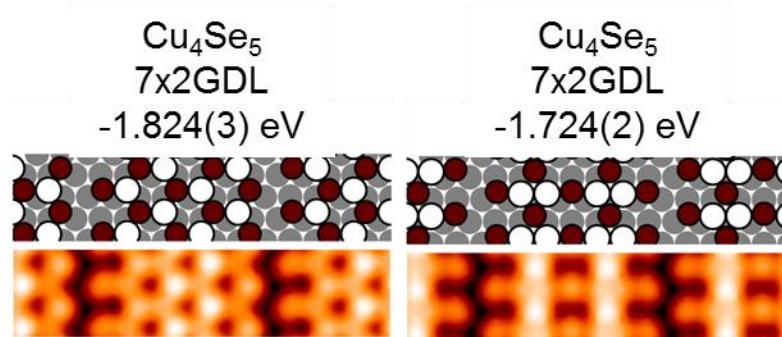


Figure A27. ($\sqrt{3} \times \sqrt{57}$) supercell.

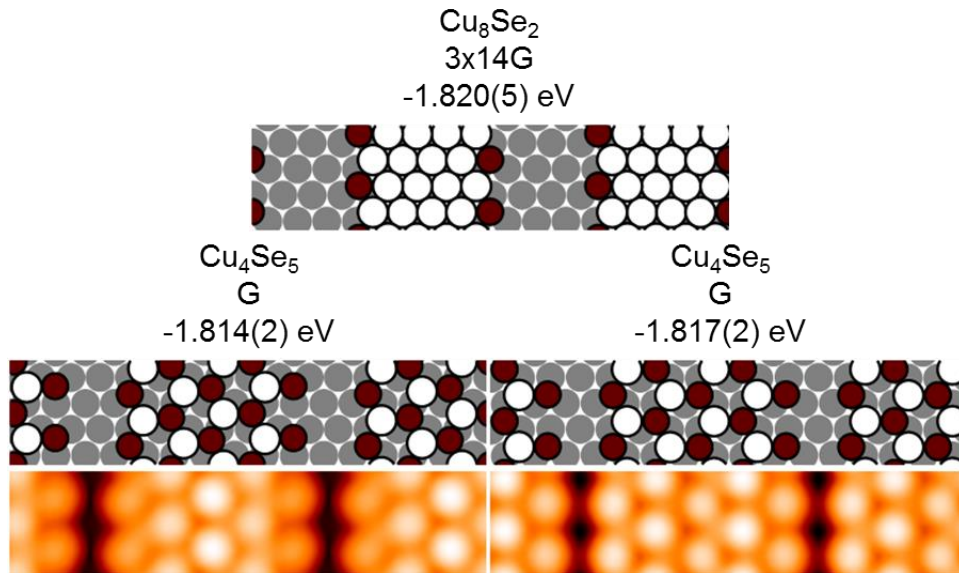


Figure A28. $(8 \times \sqrt{3})$ supercell.

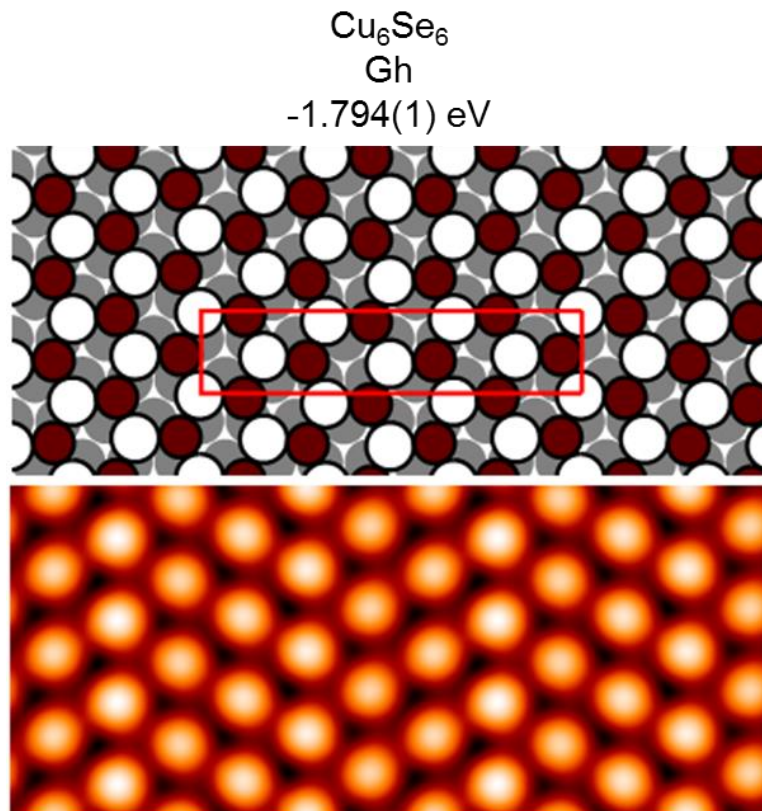


Figure A29. $(\sqrt{3} \times 8)$ supercell.

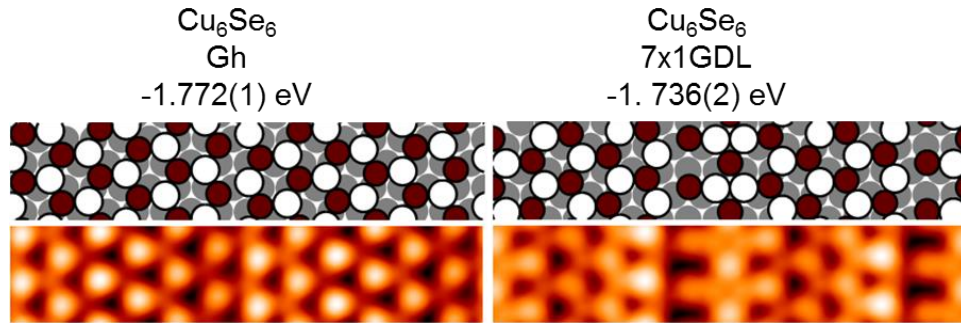


Figure A30. ($\sqrt{3} \times \sqrt{73}$) supercell.

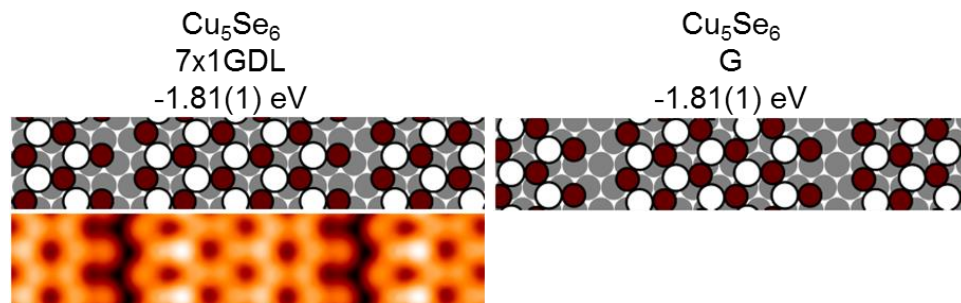


Figure A31. ($9 \times \sqrt{3}$) supercell.

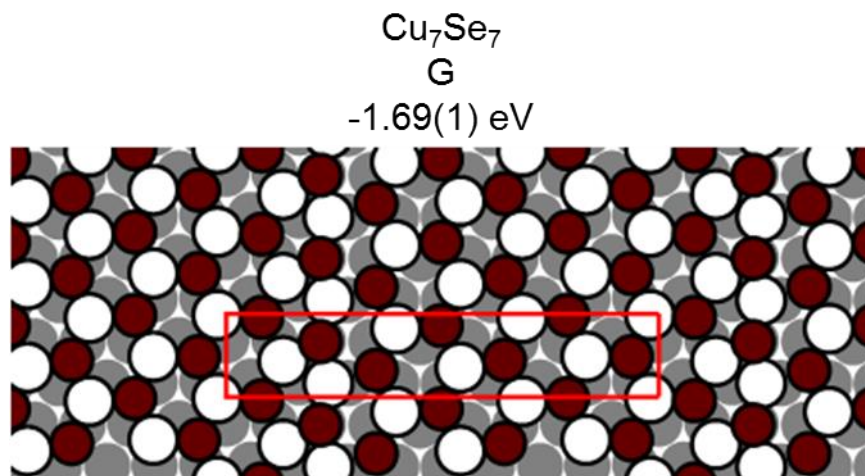


Figure A32. ($\sqrt{3} \times 9$) supercell.

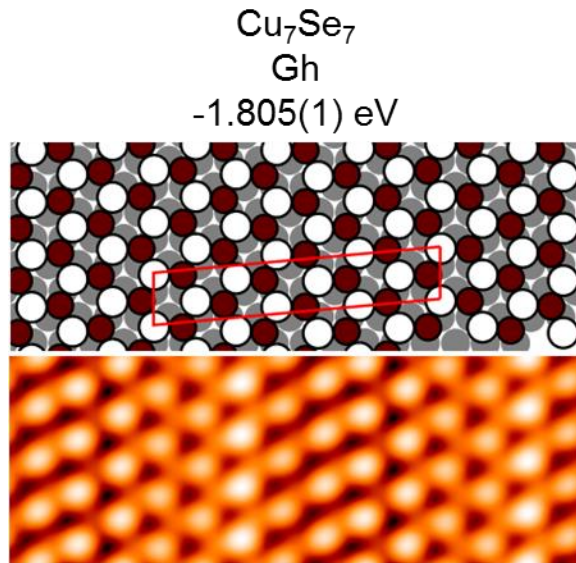


Figure A33. ($\sqrt{3} \times \sqrt{91}$) supercell.

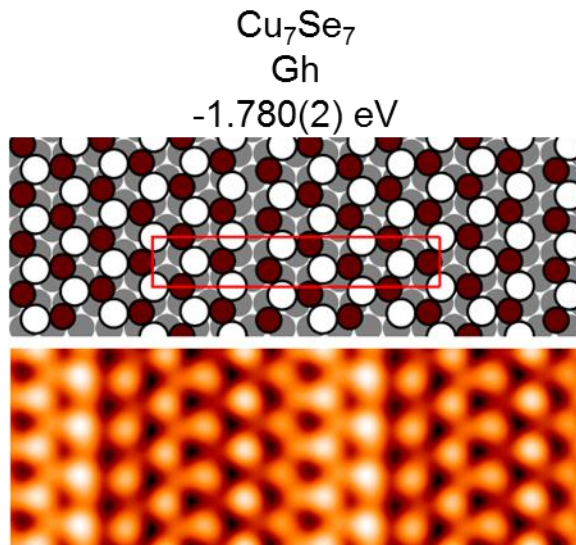


Figure A34. ($\sqrt{3} \times 10$) supercell.

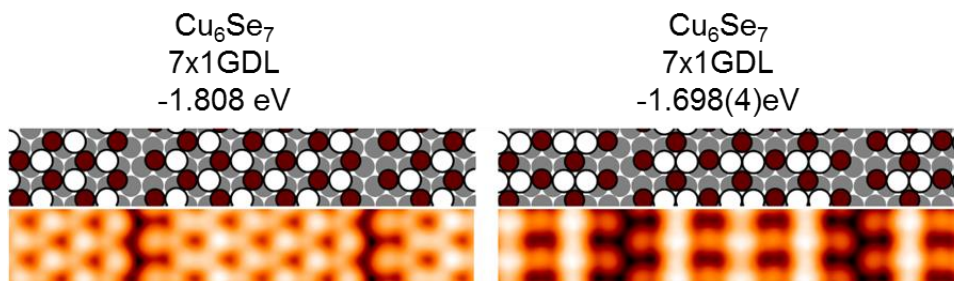


Figure A35. ($\sqrt{3} \times \sqrt{111}$) supercell.

Cu_8Se_8
G
-1.808(1)eV

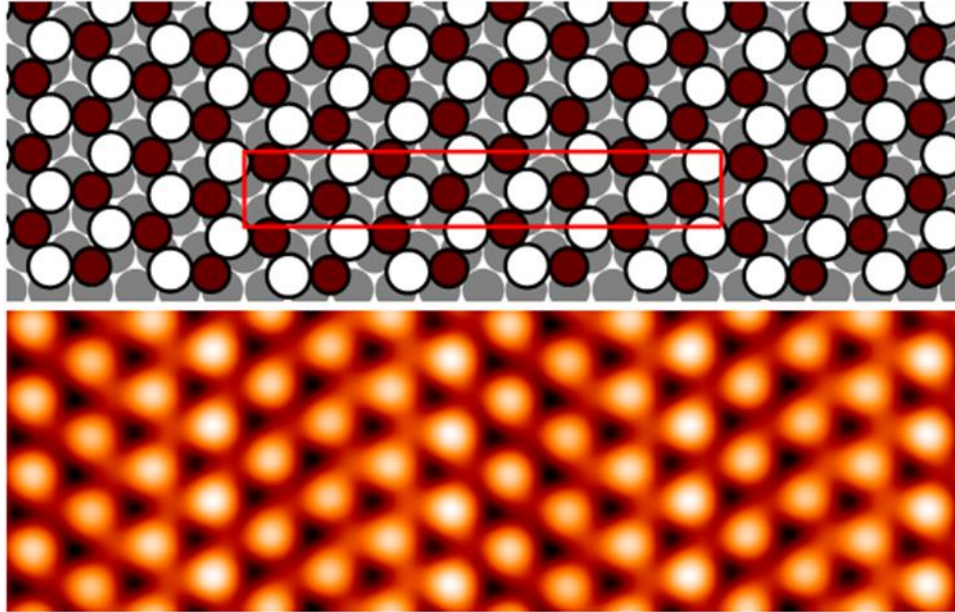


Figure A36. ($\sqrt{3} \times 11$) supercell.

Cu_9Se_9
G
-1.739(3) eV

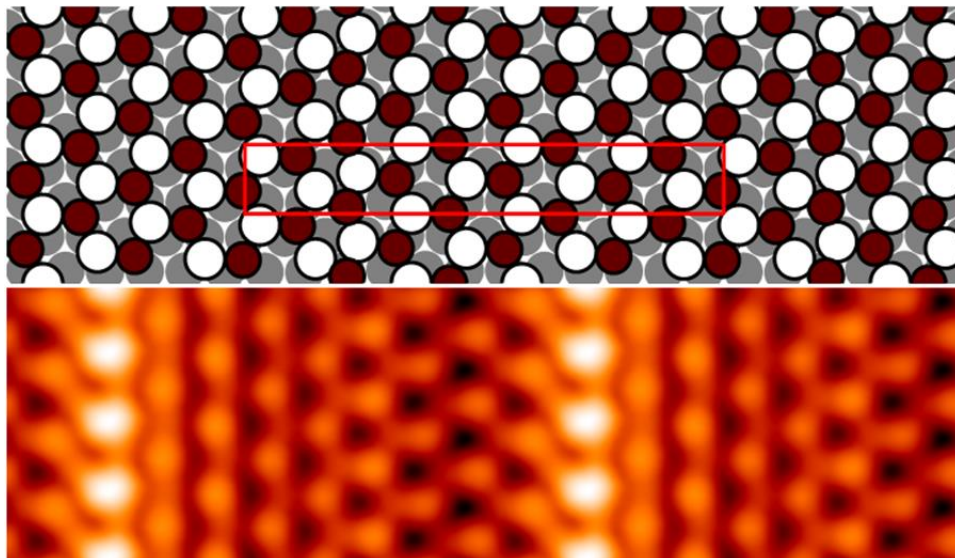


Figure A37. ($\sqrt{3} \times 12$) supercell.

Cu_8Se_8
Gh
-1.785(2) eV

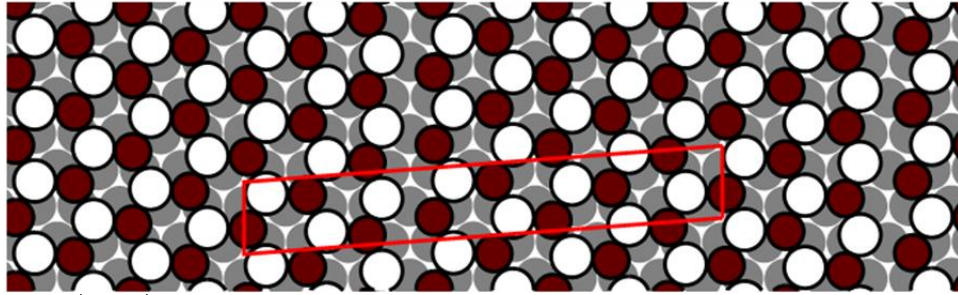


Figure A38. ($\sqrt{3} \times \sqrt{133}$) supercell.

$\text{Cu}_{10}\text{Se}_{10}$
G
-1.78(1) eV

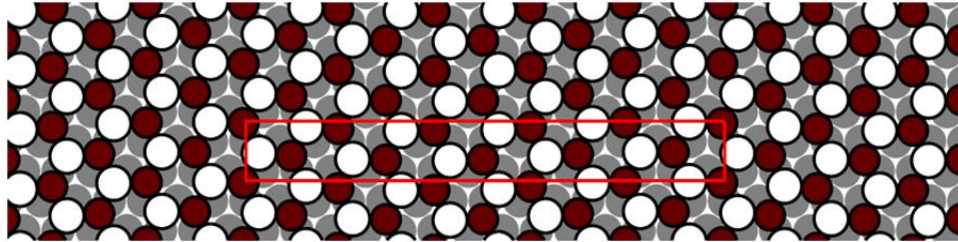
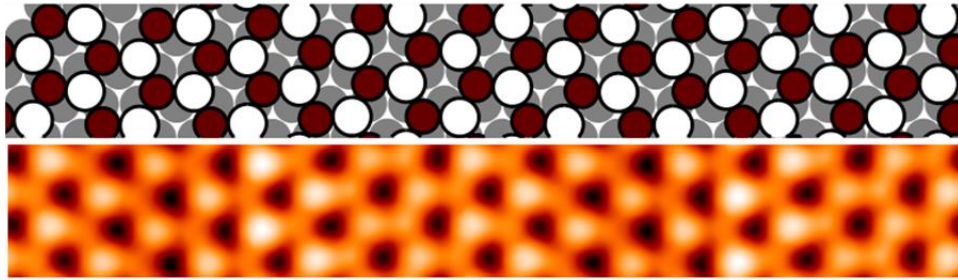


Figure A39. ($\sqrt{3} \times 14$) supercell.

Cu_9Se_9
Gh
-1.811(1) eV



$\text{Cu}_{10}\text{Se}_{10}$
G
-1.747(6) eV

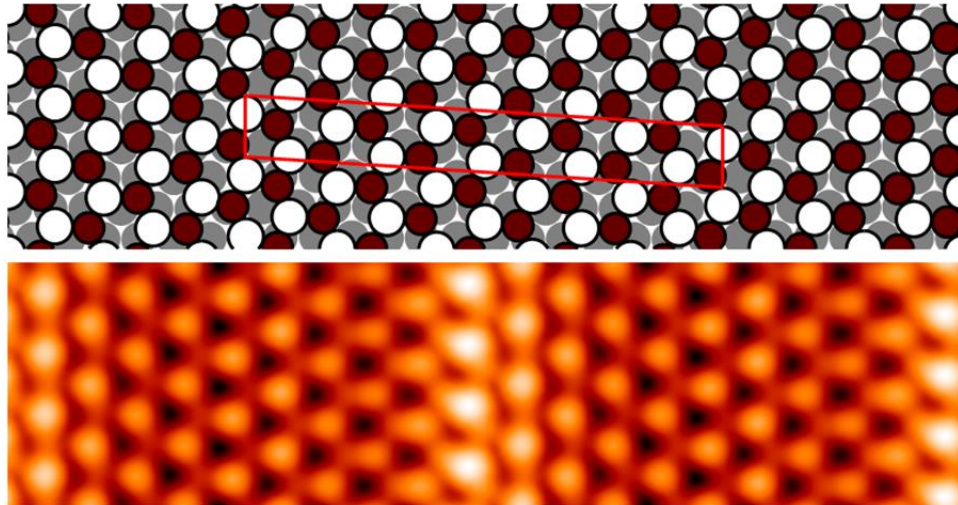


Figure A40. ($\sqrt{3} \times \sqrt{157}$) supercell.

References

1. Chhowalla, M.; Shin, H. S.; Eda, G.; Li, L.-J.; Loh, K. P.; Zhang, H., "The Chemistry of Two-Dimensional Layered Transition Metal Dichalcogenide Nanosheets". *Nature Chem.* **2013**, *5*, 263-275.
2. Gao, M.-R.; Xu, Y.-F.; Jiang, J.; Yu, S.-H., "Nanostructured Metal Chalcogenides: Synthesis, Modification, and Applications in Energy Conversion and Storage Devices". *Chem. Soc. Rev.* **2013**, *42*, 2986-3017.
3. Wang, Q.-Y., et al., "Interface-Induced High-Temperature Superconductivity in Single Unit-Cell Fese Films on SrTiO₃". *Chin. Phys. Lett.* **2012**, *29*, 037402.
4. Liu, D., et al., "Electronic Origin of High-Temperature Superconductivity in Single-Layer Fese Superconductor". *Nature Comm.* **2012**, *3*, 931.
5. *Transition Metal Sulphides: Chemistry and Catalysis*; Kluwer Academic Publishers, 1998.
6. Chen, W. S.; Stewart, J. M.; Mickelsen, R. A., "Polycrystalline Thin-Film Cu_{2-x}Se/CdS Solar Cell". *Appl. Phys. Lett.* **1985**, *46*, 1095-1097.
7. Sklyarchuk, V. M.; Plevachuk, Y. O., "Electronic Properties of Liquid Tl₂Te, Tl₂Se, Ag₂Te, Cu₂Te, and Cu₂Se Alloys". *Semiconductors* **2002**, *36*, 1123-1127.
8. Liu, H.; Shi, X.; Xu, F.; Zhang, L.; Zhang, W.; Chen, L.; Li, Q.; Uher, C.; Day, T.; Snyder, G. J., "Copper Ion Liquid-Like Thermoelectrics". *Nat Mater* **2012**, *11*, 422-425.
9. Jackson, P.; Hariskos, D.; Lotter, E.; Paetel, S.; Wuerz, R.; Menner, R.; Wischmann, W.; Powalla, M., "New World Record Efficiency for Cu(In,Ga)Se₂ Thin-Film Solar Cells Beyond 20%". *Prog. Photov. Res. Appl.* **2011**, *19*, 894-897.

10. Walsh, A.; Chen, S.; Wei, S.-H.; Gong, X.-G., "Kesterite Thin-Film Solar Cells: Advances in Materials Modelling of $\text{Cu}_2\text{ZnSnS}_4$ ". *Adv. Energy Mater.* **2012**, 2, 400-409.
11. Nagashima, S.; Ogura, I., "The Structure of Overlayers of Se on Cu(111) Surfaces". *Appl. Surf. Sci.* **1988**, 33-34, 450-456.
12. Nagashima, S.; Ogura, I., "Auger Electron Spectroscopy, Low Energy Electron Diffraction and Electron Energy Loss Spectroscopy Studies of Se Overlayers Grown on Cu(111) Surfaces". *Thin Solid Films* **1993**, 228, 64-67.
13. Nagashima, S.; Fukuchi, E.; Ogura, I., "Growth Modes of Overlayers of Se Deposited on Cu(111) Surfaces". *Appl. Surf. Sci.* **1991**, 48-49, 44-49.
14. Reinhold, H., "Über Die Bestimmung Der Bildungsaffinität Des Silbersulfids (-Selenids, -tellurids) Durch Elektrometrische Messungen an Festen Ketten.". *Ztschr. Elektrochem.* **1934**, 40, 361-364.
15. Keller, H.; Rickert, H.; Detry, D.; Droward, J.; Goldfinger, P., "Zur Thermodynamik Von Selendampf Massenspektrometrische Untersuchungen Mit Der Elektrochemischen Knudsen-Zelle". *Z. Phys. Chem.* **1971**, 75, 273-286.
16. Straumanis, M. E.; Yu, L. S., "Lattice Parameters, Densities, Expansion Coefficients and Perfection of Structure of Cu and of Cu-in Alpha Phase". *Acta Cryst.* **1969**, 25A, 676-682.
17. Horcas, I.; Fernández, R.; Gómez-Rodríguez, J. M.; Colchero, J.; Gómez-Herrero, J.; Baro, A. M., "WSxM: A Software for Scanning Probe Microscopy and a Tool for Nanotechnology". *Rev. Sci. Instrum.* **2007**, 78, 013705.
18. Liu, J.; Wu, C.-w.; Tsong, T. T., "Measurement of the Binding Energy of Kink-Site Atoms of Metals and Alloys". *Phys. Rev. B* **1991**, 43, 11595-11604.

19. Walen, H.; Liu, D.-J.; Oh, J.; Lim, H.; Evans, J. W.; Kim, Y.; Thiel, P. A., "Reconstruction of Steps on the Cu(111) Surface Induced by Sulfur". *J. Chem. Phys.* **2015**, *142*, 194711.
20. Milman, V., "Klockmannite, CuSe: Structure, Properties and Phase Stability from Ab Initio Modeling". *Acta. Cryst.* **2002**, *B58*, 437-447.
21. Effenberger, H.; Pertlik, F., "Ein Beitrag Zur Kristallstruktur Von A-CuSe (Klockmannite)". *Neues. Jahrb. Mineral., Monatsh.* **1981**, *1981*, 197-205.
22. Walen, H.; Liu, D.-J.; Oh, J.; Lim, H.; Evans, J. W.; Aikens, C.; Kim, Y.; Thiel, P. A., "Cu₂S₃ Complex on Cu(111) as a Candidate for Mass Transport Enhancement". *Phys. Rev. B* **2015**, *91*, 045426.
23. Wahlström, E.; Ekvall, I.; Olin, H.; Lindgren, S. A.; Wallden, L., "Observation of Ordered Structures for S/Cu(111) at Low Temperature and Coverage". *Phys. Rev. B* **1999**, *60*, 10699.
24. Wahlström, E.; Ekvall, I.; Kihlgren, T.; Olin, H.; Lindgren, S. A.; Wallden, L., "Low-Temperature Structure of S/Cu(111)". *Phys. Rev. B* **2001**, *64*, 155406.
25. Evans Jr., H. T.; Konnert, J. A., "Crystal Structure Refinement of Covellite". *American Mineralogist* **1976**, *61*, 996-1000.
26. Jaramillo, T. F.; Jørgensen, K. P.; Bonde, J.; Nielsen, J. H.; Horch, S.; Chorkendorff, I., "Identification of Active Edge Sites for Electrochemical H₂ Evolution from MoS₂ Nanocatalysts". *Science* **2007**, *317*, 100-102.
27. Fuchtbauer, H. G.; Tuxen, A. K.; Moses, P. G.; Topsoe, H.; Besenbacher, F.; Lauritsen, J. V., "Morphology and Atomic-Scale Structure of Single-Layer WS₂ Nanoclusters". *Phys. Chem. Chem. Phys.* **2013**, *15*, 15971-15980.

28. Huang, J.-K.; Pu, J.; Hsu, C.-L.; Chiu, M.-H.; Juang, Z.-Y.; Chang, Y.-H.; Chang, W.-H.; Iwasa, Y.; Takenobu, T.; Li, L.-J., "Large-Area Synthesis of Highly Crystalline WSe₂ Monolayers and Device Applications". *ACS Nano* **2014**, *8*, 923-930.
29. Wang, X., et al., "Chemical Vapor Deposition Growth of Crystalline Monolayer MoSe₂". *ACS Nano* **2014**, *8*, 5125-5131.
30. Helveg, S.; Lauritsen, J. V.; Laegsgaard, E.; Stensgaard, I.; Norskov, J. K.; Clausen, B. S.; Topsoe, H.; Besenbacher, F., "Atomic-Scale Structure of Single-Layer MoS₂ Nanoclusters". *Phys. Rev. Lett.* **2000**, *84*, 951.
31. Lauritsen, J. V.; Kibsgaard, J.; Helveg, S.; Topsoe, H.; Clausen, B. S.; Laegsgaard, E.; Besenbacher, F., "Size-Dependent Structure of MoS₂ Nanocrystals". *Nature Nano.* **2007**, *2*, 53-58.

APPENDIX I

**A SEARCH FOR THE STRUCTURE OF A SULFUR-INDUCED
RECONSTRUCTION ON CU(111)**

Da-Jiang Liu,^a Holly Walen,^b Junepyo Oh,^c Hyunseob Lim,^c J. W. Evans,^{a,d} Yousoo Kim,^c
and P. A. Thiel^{a,b,e}

A paper published in Journal of Physical Chemistry C[†]

Abstract

We have carried out an extensive DFT-based search for the structure of the ($\sqrt{43} \times \sqrt{43}$)R $\pm 7.5^\circ$ reconstruction of S on Cu(111), which exhibits a honeycomb-type structure in scanning tunneling microscopy (STM). We apply two criteria in this search: The structure must have a reasonably-low chemical potential, and it must provide a good match with STM data—both our own, and the data published by E. Wahlström *et al.*, *Phys. Rev. B* **1999**, *60*, 10699. The best model has 12 S adatoms and 9 Cu adatoms per unit cell. Local defects within the Cu₉S₁₂ framework, consisting of one missing or one extra Cu adatom per unit cell, would be difficult to detect with STM and would not be energetically-costly. There is no obvious correlation between this model and the structure of bulk CuS. If the $\sqrt{43}$ reconstruction is viewed in terms of local building blocks, then CuS₃ and CuS₂ clusters, linked by shared S atoms, provides the best description.

^a Ames Laboratory of the USDOE, Ames, Iowa 50011 USA

Departments of ^bChemistry, ^dPhysics & Astronomy, and ^eMaterials Science & Engineering, Iowa State University, Ames, Iowa 50011 USA

^cRIKEN Surface and Interface Science Laboratory, Wako, Saitama 351-0198, Japan

[†]*J. Phys. Chem. C* **118** 29218-29223 (2014)

1. Introduction

The interaction of sulfur with surfaces of Cu, Ag, and Au is important to topics as ancient as the tarnishing of jewelry, and as modern as self-assembled monolayers. At the atomic scale, the initial interaction of sulfur with single-crystal surfaces of metals produces a rich variety of reconstructed phases. A strong motivation for understanding the structure of these phases is the possibility of developing robust insights into the factors that stabilize them. For example, are the reconstructions built of common individual units—recurring motifs? Do the reconstructions resemble bulk compounds? Do the reconstructions induced by sulfur resemble those of its fellow chalcogenide, oxygen?

In order to address such questions, of course, the atomic structures of the reconstructions must be determined reliably. That has proven difficult, in part because the reconstructions often have large and complex unit cells, and in part because the reliability of a model depends on the diversity of the information used to construct it. That is to say, the ideal data set originates from many different techniques, which today include scanning tunneling microscopy (STM), electron scattering (particularly low-energy electron diffraction, and X-ray photoelectron diffraction), x-ray scattering, and high-level theory such as density functional theory (DFT). It is uncommon that all of these contributions are available simultaneously; it is much more common that these pieces of the puzzle are generated singly, over time, by different groups. Thus, there is often disagreement, or at least an evolution of thought, in the literature concerning the atomic structures of complex surface reconstructions.

In this paper we contribute new evidence concerning one particular sulfur-induced reconstruction of Cu(111). Specifically, it is a honeycomb-like structure, denoted ($\sqrt{43} \times$

$\sqrt{43}R\pm 7.5^\circ$ [hereafter abbreviated $\sqrt{43}$]. It was first reported by Wahlström *et al.* in 1999.¹ It exists only at temperatures below 170 K, and at total S coverages between 0.05 and 0.25 monolayers (ML).¹⁻² [A sulfur coverage of 1 ML is defined as a ratio of 1 S atom to 1 Cu atom in the Cu(111) plane.] Wahlström *et al.* proposed that the $\sqrt{43}$ is a mixed layer of Cu and S with a structure derived from the cleavage plane of bulk CuS (covellite).²

This paper primarily presents new DFT results. Published high-resolution STM data¹ are used for comparison, and some new STM data are presented as well. Section 2 presents experimental and computational details. Section 3 presents results and analysis. Section 4 is a discussion that relates our results to the questions posed at the beginning of this section.

2. Computational and Experimental Details

Energetics of different reconstructions were calculated through DFT using the VASP³ code with the projector-augmented wave (PAW) method.⁴ The surface was modeled by a periodic slab of L layers, separated by 1.2 nm of vacuum. Additional Cu and S atoms were added to one side of the slab. Most of the results reported used the Perdew-Burke-Ernzerhof (PBE) approximation⁵ for the exchange-correlation functional. The energy cutoff for the plane-wave basis set was 280 eV. Simulated STM images are created from DFT calculations using the Tersoff-Hamman method.⁶⁻⁷ Due to the existence of surface states on the Cu(111) surface, k-points convergence is slow. Averaging results for slabs of different thickness can reduce the errors due to insufficient k-points significantly.⁸ Energetics reported in this paper are mostly obtained using a $\sqrt{43}$ supercell and (2 x 2 x 1) k-points grids, averaging results from L=3 to 5. Tests with more precise settings generally yield chemical potentials with

numerical uncertainties within 10 meV. The DFT part of the work was carried out in the Ames Laboratory.

In the search for the structure of the $\sqrt{43}$ S-induced reconstruction of Cu(111), we explored many alternative structures through DFT calculations, in addition to those reported in this paper and in the Supporting Information. To be computationally efficient, our approach was to first optimize the adlayer structure using a single layer of Cu atoms to mimic the Cu(111) surface. From experience, if a structure is not stable on a single layer, it is unlikely to be stable on thicker layers. Only after an adsorbate structure survived this initial stability test, we carried out the calculation on slabs with thickness up to 5 layers to determine the chemical potential and simulated STM images. The bottom layer of atoms is fixed at their theoretical bulk positions during energy optimization.

Experimental STM work was carried out in an ultrahigh vacuum system (pressure below 2.5×10^{-11} Torr) consisting of two main parts. In one part, the Cu(111) sample was cleaned and exposed to sulfur⁹ at room temperature. The sample was then transferred into the STM stage and cooled to the imaging temperature, 5 K. The new STM work was performed at RIKEN in Japan.

3. Results and Analysis

Figure 1(a) is a high-resolution STM image of the $\sqrt{43}$ phase that was previously published by Wahlström *et al.*¹ The structure contains dark regions that define a striking honeycomb lattice. However, the hexagonal symmetry of the honeycomb is not perfect. For instance, the dark regions are elongated along an axis that is about 20° from vertical.

Figure 1(b) is a new STM image of this phase. The resolution is not as good as in Fig. 1(a), so individual protrusions are not resolved. However, the image clearly shows the characteristic honeycomb of dark regions. The hexagonal symmetry is essentially perfect, and so we attribute the slight distortion in Fig. 1(a) to an experimental artifact, possibly drift. We also note that other images published by Wahlström *et al.* do not consistently show distortion.¹⁻²

In Fig. 1(a), the brighter regions are textured, and the texture can be divided into individual protrusions. These protrusions are mapped out by the gray dots in the inset. There are 12 in the $\sqrt{43}$ unit cell. Wahlström *et al.* assumed that each protrusion corresponds to a S adatom, implying an ideal S coverage of $12/43=0.28$ ML. They also assumed that Cu adatoms in the reconstruction do not contribute significantly to the image, based on a previous study of the surface of bulk covellite.¹⁰ Our DFT results (below) will verify these assumptions.

In addition to STM, Wahlström *et al.*² measured photoelectron spectra and scanning tunneling spectra. They found that the electronic surface state of clean Cu(111) is associated with the $\sqrt{43}$ reconstruction, and they interpreted this to mean that the darkest regions in the reconstruction consist of clean Cu(111). We adopt this interpretation in constructing models.

Using DFT, we assess the relative stability of various optimized configurations, and also produce simulated STM images for each that can be compared with Fig. 1(a). Stability is measured by the S chemical potential (μ_S) at $T = 0$ K, defined as:

$$\mu_S = [E(\text{Cu}_m\text{S}_n + \text{slab}) - E(\text{slab}) - m \mu_{\text{Cu}}]/n - E(\text{S}_{2,\text{g}})/2$$

where E is energy, μ_{Cu} is the chemical potential of a Cu adatom (equal to the cohesive energy of a bulk Cu atom at $T = 0$ K), and n and m are the number of S and Cu atoms in the cluster, respectively. By this definition, μ_S measures the increase in energy per S when a limited supply of atomic S on terraces is incorporated into the reconstruction, given an unlimited supply of metal atoms that can be extracted from steps. This equation also defines the energy of gaseous S_2 as the reference point for μ_S .

In our search for potential $\sqrt{43}$ structures, the first obvious choice was the covellite-derived model proposed previously.² Figure 2(a) shows the arrangement of atoms in the basal plane of covellite. Removal of the atoms (7 S and 6 Cu) marked with X would result in the suggested $\sqrt{43}$ structure.² Figure 2(b) shows the optimized arrangement of this structure on the Cu(111) surface, and Fig. 2(c) shows the predicted STM image. There is poor agreement between Fig. 2(c) and Fig. 1(a). Furthermore, for this structure, we calculate $\mu_S = -1.65$ eV. Compared with some of the other structures to be presented below, this value of μ_S is not competitive. We therefore rule out the covellite structure.

We next examined a wide variety of initial structures, guided by certain insights. First, as noted above, we assumed that the dark spaces in the honeycomb are regions of the Cu(111) substrate without any adatoms.² Second, there is attraction between Cu adatoms, which favors Cu-Cu adatom adjacency. Third, linked structures are more likely to exhibit a honeycomb pattern in the STM simulations, than non-linked structures. (See Supporting Information.) Fourth, we suspected that certain small Cu-S clusters could be units of the reconstruction. These clusters will be discussed more fully in Section 4.

With these ideas in mind, we explored a wide variety of structures with different numbers of Cu and S atoms in the $\sqrt{43}$ supercell. (We did not constrain the $\sqrt{43}$ unit cell to

contain 12 S atoms.) Specifically, there were 80 structures calculated with a 1-layer Cu slab, 41 with 3-layer Cu slabs, and 35 more with up to 5 layers, screened according to the method described in Sec. 2. Figure 3 shows some examples that contain 6 to 9 S atoms, and 9 to 18 Cu atoms, per $\sqrt{43}$ unit cell. The simulated STM images of these structures show poor agreement with the STM data of Fig. 1(a).

One general trend that emerged from our search is this: A higher degree of coordination between a S adatom and Cu adatoms is often associated with a brighter spot in the simulated STM image, reflecting greater electron transfer to the S adatom. Pyramidal Cu_4S units produce the most intense spots, and these units (if present) dominate predicted STM images. Examples are shown in Fig 3(a, c, d). Models incorporating such units produce poor agreement with the STM image of Fig. 1(a), however. This is because the pyramidal units cannot be packed densely enough to produce 12 spots per unit cell, while preserving the empty regions that produce the dark hexagons. As an aside, we note that other S-induced reconstructions on Cu(111) do show very bright protrusions in the experimental STM data, with a density far lower than the 12 protrusions in the $\sqrt{43}$, and these intense spots may arise from four-fold coordinated S adatoms.² Similarly, on Ag(111), experimental STM images of $\text{Ag}_{16}\text{S}_{13}$ clusters exhibit bright central spots which correspond to Ag_4S pyramids.¹¹

Turning next to models containing 12 S adatoms per $\sqrt{43}$ unit cell (12-S models), Fig. 4 shows a family of structures in this category. More 12-S models are shown in the Supporting Information. In Fig. 4, the number of Cu atoms ranges from 6 to 11. Each S adatom is coordinated to only one or two Cu adatoms. These structures have values of μ_S that range from -1.73 to -1.77 eV. (The number in the bracket reflects variations with the slab thickness, e.g., from L=3 to 5, that results in uncertainties in the last significant digit of the

quoted energetics.⁸) This is significantly lower than μ_S for most of the structures in Fig. 2 or 3. In this family, the lowest value of μ_S (-1.77 eV) is found for the Cu_9S_{12} structure, in which each S adatom is coordinated to 2 Cu adatoms.

Figure 5 shows the Cu_9S_{12} model and predicted STM image more closely. In Fig. 5(b), the array of spots from the Fig. 1(b) inset is overlaid on the simulated image. (The array of dark spots is corrected for distortion, i.e. forced to have hexagonal symmetry.) Figure 5(b) demonstrates very good correspondence between the experimental data and the model.

It is noteworthy that within the 12-S family of Fig. 4, the simulated STM images are quite similar, meaning that they are not strongly sensitive to the number of Cu adatoms. This is because the Cu adatoms of the reconstruction contribute little or nothing to the images. This supports the assumption made by Wahlström et al.,² that the fine structure in the real STM images is due exclusively to S atoms.

Within this family, μ_S is also not very sensitive to the number of Cu atoms, although Cu_9S_{12} has the lowest μ_S . In addition, the Cu_9S_{12} structure also has high symmetry, and thus may be considered an ideal structure. For instance, its structural neighbors with one less or one more Cu atom per unit cell— Cu_8S_{12} and $\text{Cu}_{10}\text{S}_{12}$, respectively—each have three-fold symmetry, rather than six-fold, and hence are not true honeycomb structures. However, their chemical potentials show that slight deviation from the ideal structure is not very costly in energetic terms. It is possible that in a real extended $\sqrt{43}$ reconstruction, there exist local defects in the Cu_9S_{12} framework—corresponding to missing or extra Cu adatoms—that are difficult to identify with STM.

4. Discussion

Elsewhere, we present data and calculations that support the existence of a Cu_2S_3 complex on this surface.¹² It was observed with STM at very low S coverage and low temperature (5 K). It appears to exist in equilibrium with the $\sqrt{43}$ structure. We have calculated μ_S for this, and many other, S-Cu complexes on Cu(111) using DFT. Cu_2S_3 has the minimum μ_S , although several other clusters have μ_S values that are not too much higher. The closest ones are linear CuS_2 , trigonal planar CuS_3 , and triangular Cu_3S_3 . These are shown in Fig. 6. It is natural to ask whether the favored models for the $\sqrt{43}$ reconstruction can be rationalized in terms of any of these units.

Consider first the 12-S structures. The Cu_6S_{12} model in Fig. 4(a) can be viewed as groups of CuS_3 clusters, in which each cluster shares 2 S atoms with another CuS_3 cluster. The Cu atoms in this reconstruction are close to their preferred three-fold-hollow (3fh) adsorption sites in the isolated adsorbed CuS_3 [Fig. 6(b)], but the S atoms are displaced significantly. The structure in Fig. 4(b) is the same as in 4(a), except that additional Cu atoms are placed along one of the diagonal directions. The addition of these Cu atoms essentially introduces linear CuS_2 units which share each S atom with one CuS_3 unit, and which have the Cu and S atoms close to the optimal adsorption sites in the isolated adsorbed CuS_2 cluster. The new Cu atoms must introduce some Cu-Cu bonding in the reconstruction, although the lateral Cu-Cu separation is about 7 % longer than in the Cu(111) plane. The Cu_8S_{12} and Cu_9S_{12} reconstructions of Fig. 4(c) and 5(a) follow a similar progression, with Cu atoms added along a single direction in each case. The minimum in μ_S is reached for Cu_9S_{12} in Fig. 5(a). The reconstructions that follow in this series are $\text{Cu}_{10}\text{S}_{12}$ and $\text{Cu}_{11}\text{S}_{12}$, where Cu atoms

are added to the centers of the original linked CuS_3 groups, which is apparently unfavorable, since μ_S rises.

The other reconstructions shown in Fig. 3 can be broken down into other combinations of clusters. Figure 3(b) consists of Cu_3S_3 clusters linked with linear CuS_2 clusters, but it can be ruled out both on the basis of its high μ_S and poor agreement with STM images. Figure 3(e) consists of concatenated linear CuS_2 clusters. It is relatively stable, but does not match the STM data well. The reconstructions of Fig. 3(a), (c), and (d) have local sites that approximate four-fold-hollow (4fh) Cu sites, supporting a S atom above the plane of the reconstruction. It is well-known that S adsorbs preferentially at 4fh sites rather than 3fh sites,¹³⁻¹⁵ and other, higher-coverage reconstructions of S on Cu(111) probably contain 4fh sites.^{2, 13} However, the values of μ_S and the projected STM images serve to rule out these possibilities for the $\sqrt{43}$ structure.

We conclude that if one interprets the $\sqrt{43}$ reconstruction in terms of local building blocks, then CuS_3 and CuS_2 clusters, linked by shared S atoms, provide the best description of the optimal model—Fig. 5(a). This model cannot be interpreted in terms of the experimentally-observed isolated cluster with which the $\sqrt{43}$ coexists, Cu_2S_3 , because the Cu_2S_3 cluster has linear CuS_2 sub-units¹² as shown in Fig. 6(a). Thus, the reconstruction is not simply a condensation of the Cu_2S_3 cluster.

Previously, it was proposed that the $\sqrt{43}$ reconstruction resembles the basal plane of CuS .² We have shown that this is not an energetically-reasonable candidate for the $\sqrt{43}$ —although other reconstructions in this system may be related to CuS .² When we examine reports of the oxygen-induced reconstructions of Cu(111), we do not find any analog to the $\sqrt{43}$. Furthermore, the O/Cu(111) reconstructions are consistently related to bulk Cu_2O .¹⁶⁻²⁰

Thus, there is no obvious correlation between the $\sqrt{43}$ reconstruction of S/Cu(111) and the known reconstructions of O/Cu(111).

In summary, we propose a new model for the $\sqrt{43}$ reconstruction of S on Cu(111), based on DFT and STM. The favored structure is not derived from bulk CuS, nor is it built only of the Cu₂S₃ clusters that have been found to exist in isolated form at low coverage and low temperature. It agrees very well with STM data published by Wahlström et al., wherein prominent features were interpreted to be individual S atoms. Our simulated STM images are consistent with this interpretation. Applying the dual constraints of low S chemical potential and good agreement with STM images, the best fit is a structure with a formula of Cu₉S₁₂ per unit cell. Considering symmetry in addition, the formula Cu₉S₁₂ probably represents the ideal structure; local deviations with one extra or one less Cu atom per unit cell would be difficult to identify with STM, and the energetic penalty would not be prohibitive.

Acknowledgements

The theoretical component of this work was carried out by DJL. It was supported by the Division of Chemical Sciences, Basic Energy Sciences, US Department of Energy (DOE). This part of the research was performed at Ames Laboratory, which is operated for the U.S. DOE by Iowa State University under contract No. DE-AC02-07CH11358. This part also utilized resources of the National Energy Research Scientific Computing Center, which is supported by the Office of Science of the U.S. DOE under Contract No. DE-AC02-05CH11231. The experimental component of this work was supported by several sources. From the U.S., it was NSF Grants CHE-1111500 and CHE-1404503. From Japan, support was provided by a Grant-in-Aid for Scientific Research on Priority Areas “Electron

Transport Through a Linked Molecule in Nano-scale”; and a Grant-in-Aid for Scientific Research(S) “Single Molecule Spectroscopy using Probe Microscope” from the Ministry of Education, Culture, Sports, Science, and Technology (MEXT). We thank Kan Ueji and Hiroshi Imada for assistance with the experiments, and Gordon J. Miller for insights into the structure of bulk covellite.

Figures

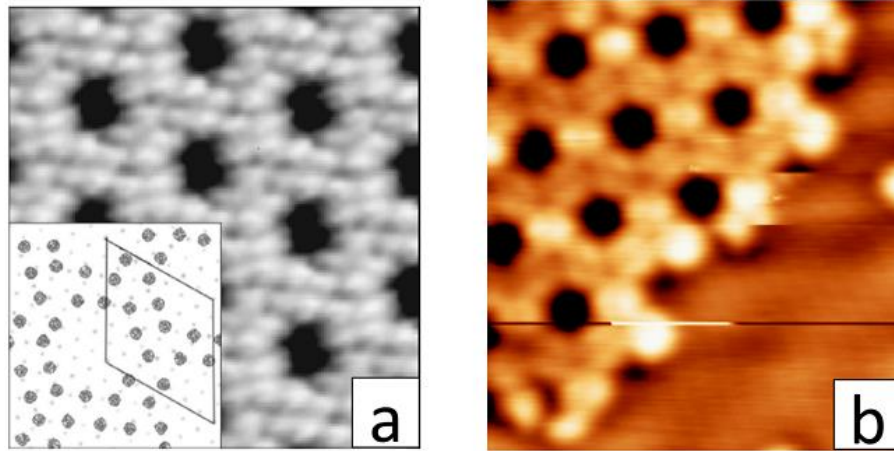


Figure 1. High-resolution STM images of the $\sqrt{43}$ phase. (a) $5.0 \times 5.0 \text{ nm}^2$, $T = 135 \text{ K}$, $I = 0.100 \text{ nA}$, $V = -0.700 \text{ V}$. The inset shows the locations of the protrusions and the $\sqrt{43}$ unit cell. Reprinted figure with permission from Ref. 1: E. Wahlström, I. Ekvall, H. Olin, S.-Å. Lindgren, and L. Walldén, *Physical Review B*, 60, 10699, 1999. Copyright (1999) by the American Physical Society. (b) $7.2 \times 7.8 \text{ nm}^2$, $T = 5 \text{ K}$, Tunneling current = 0.367 nA , Sample bias voltage = -0.090 V .

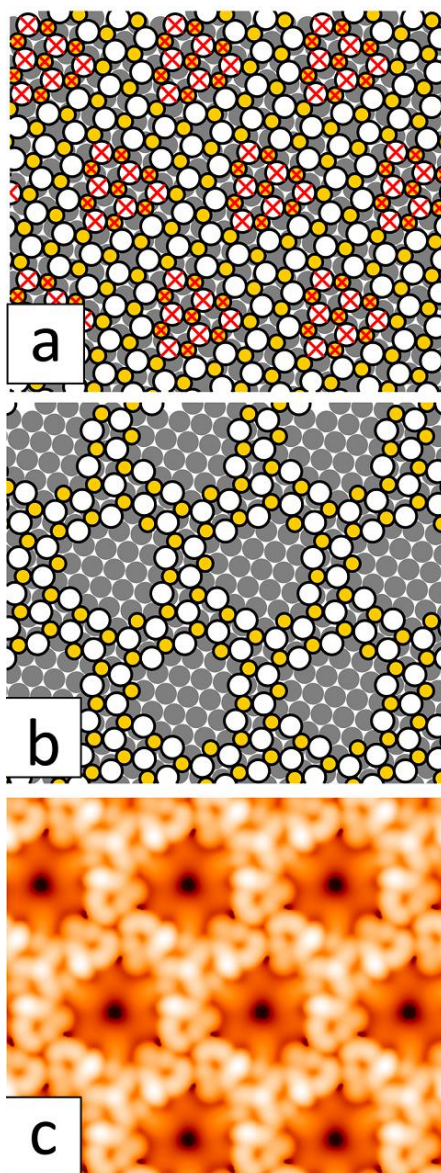


Figure 2. The $\sqrt{43}$ phase based on a covellite (CuS) structure on Cu(111). (a) Arrangement of covellite on a Cu(111) surface, as determined by DFT. Sulfur atoms are indicated by small, yellow circles, while copper atoms are the larger, white circles. (b) The optimized arrangement of the covellite-based $\sqrt{43}$ phase on Cu(111). (c) Simulated STM image of the covellite-based $\sqrt{43}$ phase. In (a) and (b), the circles represent atoms at their DFT-optimized positions. Large gray circles depict Cu atoms in the Cu(111) surface, large white circles depict Cu atoms above the surface plane, and small yellow circles are sulfur atoms.

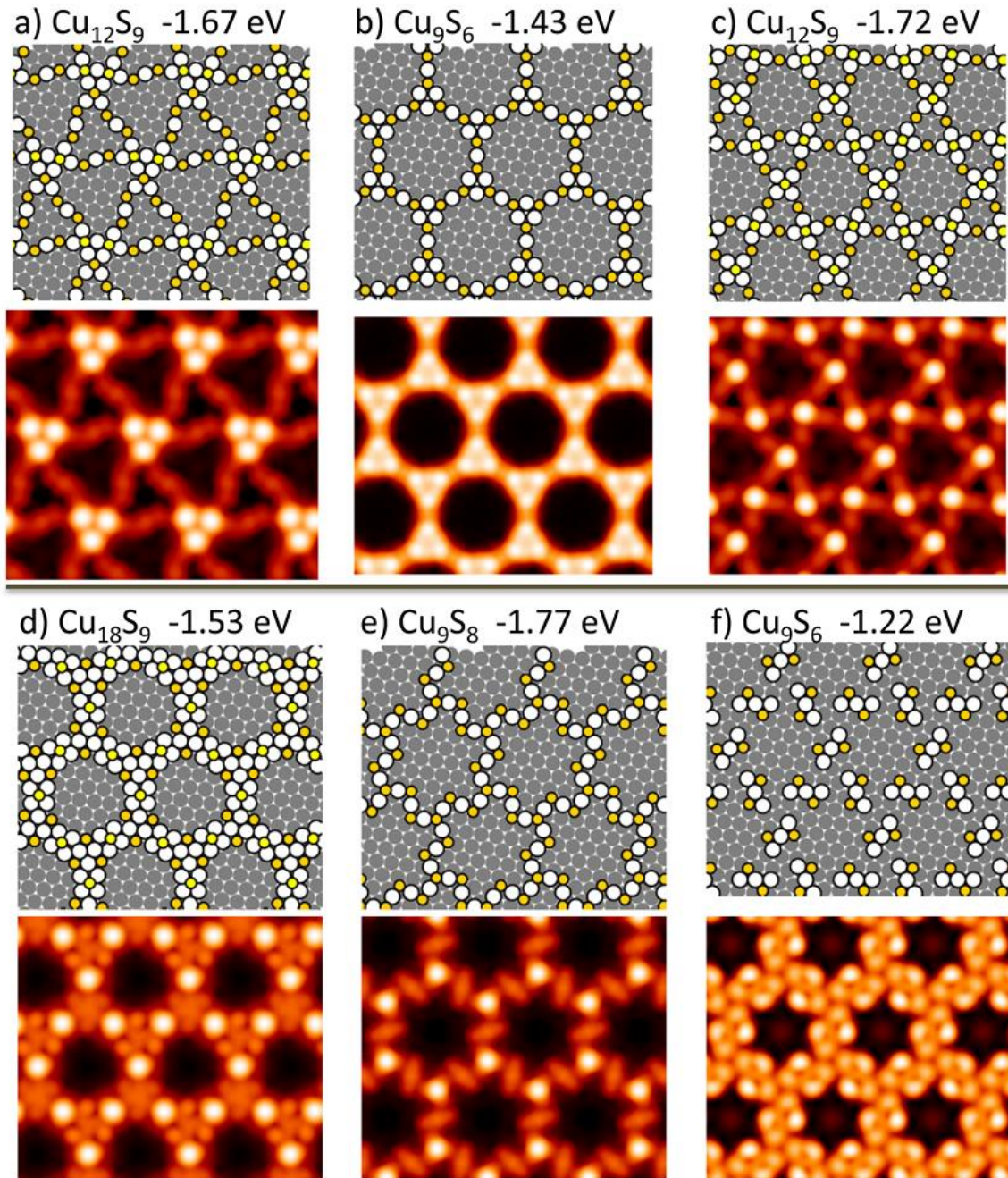


Figure 3. DFT calculated chemical potentials, models, and simulated STM images for several Cu-S ratios per $\sqrt{43}$ unit cell. Note that some models have the same Cu-S ratio, but the atoms are in a different configuration. a) Cu_{12}S_9 , b) Cu_9S_6 , c) Cu_{12}S_9 , d) Cu_{18}S_9 , e) Cu_9S_8 , f) Cu_9S_6 . The circles represent atoms at their DFT-optimized positions. Large gray circles denote Cu atoms in the Cu(111) surface, large white circles denote Cu atoms above the surface plane, and small yellow circles are sulfur atoms.

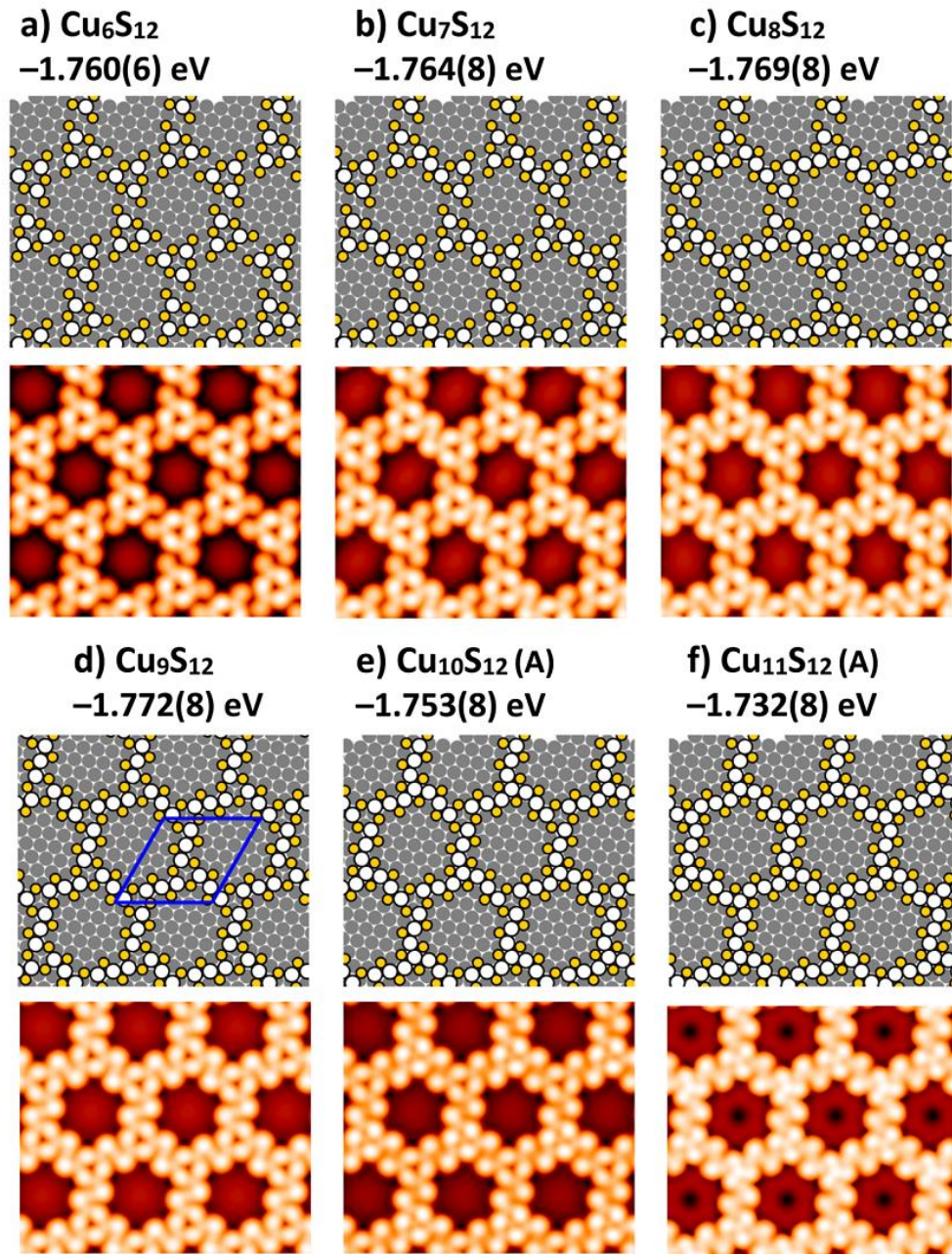


Figure 4. Models (top) and simulated STM images (bottom) for $\sqrt{43}$ structures containing 12 S atoms per unit cell, with varying Cu concentration. The $\sqrt{43}$ unit cell is shown by the parallelogram in the top of part (d). (a) Cu₆S₁₂, (b) Cu₇S₁₂, (c) Cu₈S₁₂, (d) Cu₉S₁₂, (e) Cu₁₀S₁₂, (f) Cu₁₁S₁₂. In the models, the circles represent atoms at their DFT-optimized positions. Large gray circles signify Cu atoms in the Cu(111) surface, large white circles signify Cu atoms above the surface plane, and small yellow circles are sulfur atoms. The number at the top of each panel is the chemical potential, averaged over Cu slabs of varying thickness up to 5 layers. The digit in parentheses reflects variations with the slab thickness.⁸ For instance, a value of -1.772(8) eV means the average value is -1.772 eV, and the slab-dependent variation is up to ± 0.008 eV.

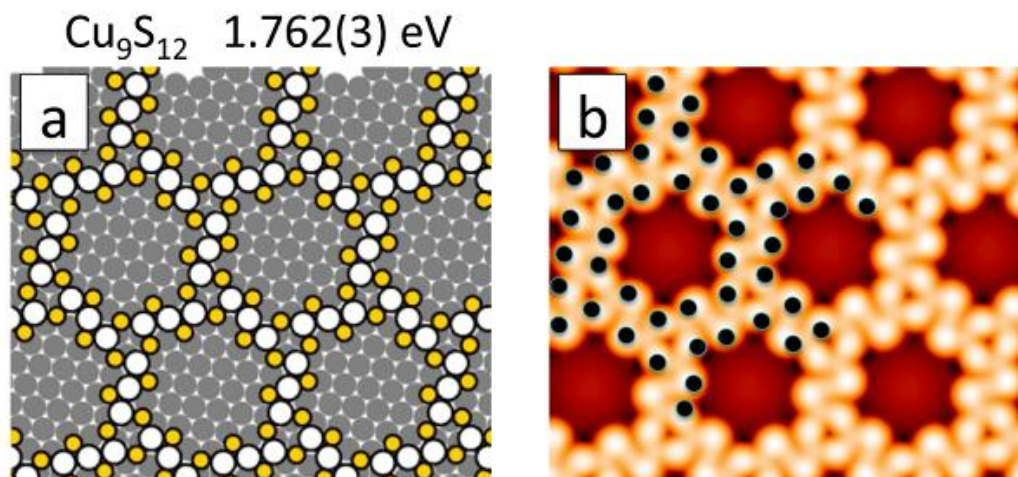


Figure 5. The Cu_9S_{12} (a) structure model and (b) simulated STM image. The black circles correspond to the positions of dots in the inset of Fig. 1(a), corrected slightly for presumed distortion. Hence, the black circles represent areas of highest intensity in the STM image of Ref. ².

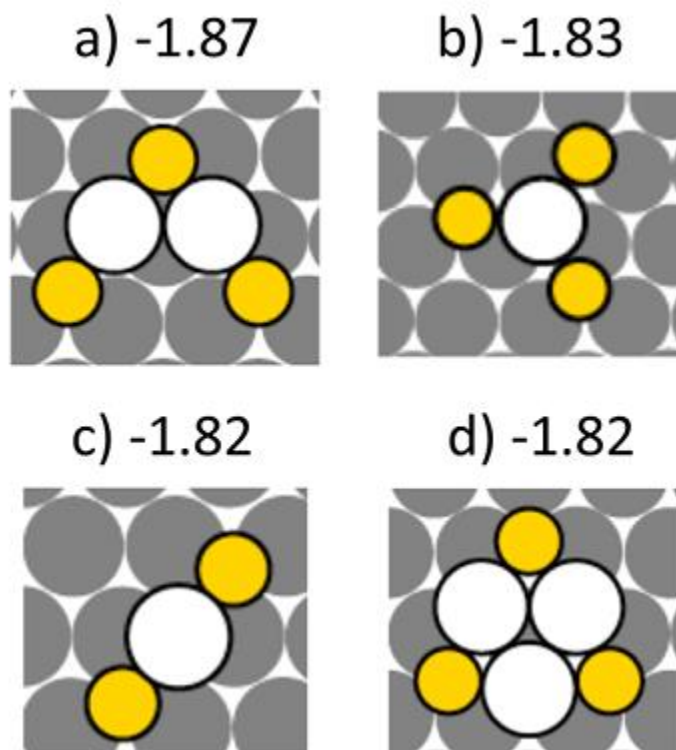


Figure 6. Chemical potential (in eV) per S atom for several small Cu-S clusters on Cu(111). (a) Cu_2S_3 , (b) CuS_3 , (c) CuS_2 , (d) Cu_3S_3 . The circles represent atoms at their DFT-optimized positions. Large gray circles represent Cu atoms in the Cu(111) surface, large white circles represent Cu atoms above the surface plane, and small yellow circles are sulfur atoms.

Supporting Information

As stated in the text, we explored many alternative models for the $\sqrt{43}$ reconstruction through DFT calculations, in addition to those reported in the paper. Some of the insights that emerged during the course of the search are described here.

From DFT calculations, we found that in a $\sqrt{43}$ supercell, there must be at least 6 S adatoms to form a linked structure. (This corresponds to 0.14 ML of S.) Figures 3b and 3f of the main text show two examples of structures with 6 S and 9 Cu adatoms. None of the structures with 6 S adatoms was very favorable energetically. The truly linked structure in Figure 3b exhibited a honeycomb structure in the STM simulation, but the walls were too thin. This, coupled with the experimental evidence of higher S coverage (0.25-0.28 ML¹⁻²), prompted us to consider higher numbers of S adatoms per unit cell.

The next most promising candidate was a structure with 8 S and 9 Cu (Fig. 3e). Energetically it was close to the chemical potential of the best structure in the final analysis. Its main disadvantage was the poor comparison with the STM image.

There are a great variety of structures that can be formed with 9 S adatoms. Three examples are shown in the main text (Fig. 3a, c, d). Figure S1 gives 5 other examples. Figure S1(a) produces a pseudo-honeycomb with strong 3-fold (not 6-fold) symmetry around the dark spaces in the STM simulation, but is not very favorable energetically. Figures S1(b-e) show structures that are very favorable energetically, but do not produce a honeycomb structure in STM at all.

Due to the observation of 12 bright spots in the best-resolved STM image, we explored structures with 12 S adatoms in detail. Figure S2(a-c) shows several examples, in addition to those shown in Fig. 4 of the text. Fig. S2(a) has the same chemical composition

as the structure in Fig. 4d and Fig. 5. It consists of three Cu_3S_4 clusters, but they do not form direct links. The structure in Fig. S2(b) maximizes Cu-Cu interactions, while the structure in Fig. S2(c) maximizes linkages through S-Cu-S motifs. Fig. S2(d) is the covellite-inspired structure mentioned in the main text (Fig. 2), and is included here for easy comparison.

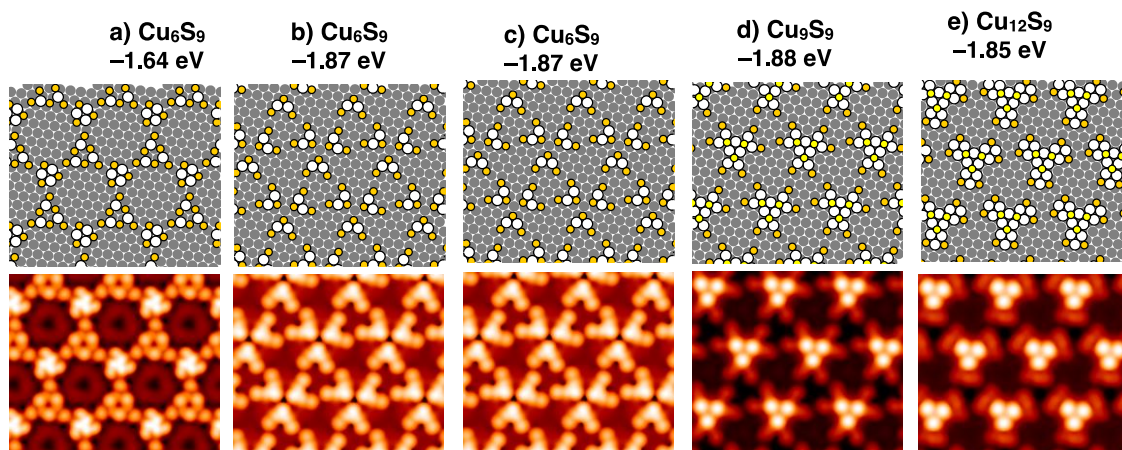


Figure S1: DFT calculated chemical potentials, models, and simulated STM images for several structures with 9 S adatoms per $\sqrt{43}$ unit cell.

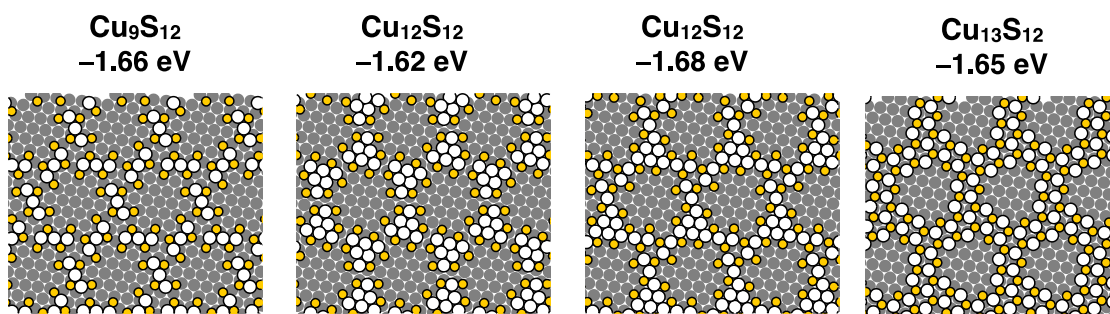


Figure S2: DFT calculated chemical potential and models for several structures with 12 S adatoms per $\sqrt{43}$ unit cell.

References

1. Wahlström, E.; Ekvall, I.; Olin, H.; Lindgren, S. A.; Wallden, L., "Observation of Ordered Structures for S/Cu(111) at Low Temperature and Coverage". *Phys. Rev. B* **1999**, *60*, 10699.
2. Wahlström, E.; Ekvall, I.; Kihlgren, T.; Olin, H.; Lindgren, S. A.; Wallden, L., "Low-Temperature Structure of S/Cu(111)". *Phys. Rev. B* **2001**, *64*, 155406.
3. Kresse, G.; Furthmüller, J., "Efficiency of Ab-Initio Total Energy Calculations for Metals and Semiconductors Using a Plane-Wave Basis Set". *Comput. Mater. Sci.* **1996**, *6*, 15-50.
4. Blöchl, P. E., "Projector Augmented-Wave Method". *Phys. Rev. B* **1994**, *50*, 17953-17979.
5. Perdew, J. P.; Burke, K.; Ernzerhof, M., "Generalized Gradient Approximation Made Simple". *Phys. Rev. Lett.* **1996**, *77*, 3865-3868.
6. Tersoff, J.; Hamann, D. R., "Theory and Application for the Scanning Tunneling Microscope". *Phys. Rev. Lett.* **1983**, *50*, 1998-2001.
7. Tersoff, J.; Hamann, D. R., "Theory of the Scanning Tunneling Microscope". *Phys. Rev. B* **1985**, *32*, 805-813.
8. Liu, D.-J., "Density Functional Analysis of Key Energetics in Metal Homoepitaxy: Quantum Size Effects in Periodic Slab Calculations". *Phys. Rev. B* **2010**, *81*, 035415.
9. Wagner, C., "Investigations on Silver Sulfide". *J. Chem. Phys.* **1953**, *21*, 1819-1827.
10. Rosso, K.; Hochella Jr., M. F., "A UHV STM/STS and Ab Initio Investigation of Covellite {001} Surfaces". *Surf. Sci.* **1999**, *423*, 364-374.

11. Russell, S. M.; Kim, Y.; Liu, D.-J.; Evans, J. W.; Thiel, P. A., "Structure, Formation, and Equilibration of Ensembles of Ag-S Complexes on an Ag Surface". *J. Chem. Phys.* **2013**, *138*, 071101.
12. Walen, H.; Liu, D.-J.; Oh, J.; Lim, H.; Evans, J. W.; Aikens, C.; Kim, Y.; Thiel, P. A., "Cu₂S₃ complex on Cu(111) as a candidate for mass transport enhancement". *Phys. Rev. B.* **2015**, *91*, 045426.
13. Foss, M.; Feidenhans'l, R.; Nielsen, M.; Findeisen, E.; Buslaps, T.; Johnson, R. L.; Besenbacher, F., "Sulfur Induced Cu₄ Tetramers on Cu (111)". *Surf. Sci.* **1997**, *388*, 5-14.
14. Foss, M.; Feidenhans'l, R.; Nielsen, M.; Findeisen, E.; Buslaps, T.; Johnson, R. I.; Besenbacher, F.; Stensgaard, I., "Sulfur Chemisorption on Ni(111): The Clock Structure of the (5√3×2)S Phase". *Phys. Rev. B* **1994**, *50*, 8950-8953.
15. Feibelman, P. J., "Formation and Diffusion of S-Decorated Cu Clusters on Cu(111)". *Phys. Rev. Lett.* **2000**, *85*, 606-609.
16. Jensen, F.; Besenbacher, F.; Stensgaard, I., "Two New Oxygen Induced Reconstructions on Cu(111)". *Surf. Sci.* **1992**, *269/270*, 400-404.
17. Dubois, L. H., "Oxygen Chemisorption and Cuprous Oxide Formation on Cu(111): A High Resolution Eels Study". *Surf. Sci.* **1982**, *119*, 399-410.
18. Matsumoto, T.; Bennett, R. A.; Stone, P.; Yamada, T.; Domen, K.; Bowker, M., "Scanning Tunneling Microscopy Studies of Oxygen Adsorption on Cu(111)". *Surf. Sci.* **2001**, *471*, 225-245.
19. Johnston, S. M.; Mulligan, A.; Dhanak, V.; Kadodwala, M., "The Structure of Disordered Chemisorbed Oxygen on Cu(111)". *Surf. Sci.* **2002**, *519*, 57-63.

20. Wiame, F.; Maurice, V.; Marcus, P., "Initial Stages of Oxidation of Cu(111)". *Surf. Sci.* **2007**, *601*, 1193-1204.

APPENDIX II

PRELIMINARY DATA FOR S ADSORPTION ON Pd(111) AND Pt(111)

Holly Walen, Junepyo Oh, Hyunseob Lim, Yousoo Kim, and P. A. Thiel

1. Introduction

The chapters preceding this appendix describe several studies using low sulfur coverage and low temperature to investigate the effect of sulfur on the coinage metals Cu and Au. We have found several new complexes that may aid in metal transport at room temperature, as well as new S-M interactions. In addition to the coinage metals, we are interested in the effect of sulfur on other d-block metals that precedent for forming mobile metal-adsorbate complexes on homo- or hetero-epitaxial surfaces.¹⁻³

1.1 Pd(111)

Pd nanoparticles act as efficient heterogeneous catalysts for a wide variety of organic reactions, including Suzuki, Heck, and Stille coupling reactions⁴ and formic acid oxidation.⁵ During the course of these reactions, adsorbed gasses impact the shape, size, and, as a consequence, activity of the catalytic particles.⁶⁻⁷ For example, in the presence of CO and NO, supported Pd nanoparticles were found to undergo dynamic restructuring: CO induced sintering of the particles,⁸ and NO induced re-dispersion (increasing activity).⁹ A Pd-CO complex was recently postulated to mediate the sintering process for oxide-supported Pd.³

Sulfur acts as the linker to attach passivating ligands such as cyclodextrin on Pd nanoparticles,¹⁰ and plays a catalytic role in the conversion of acetylene (C₂H₂) to thiophene on Pd(111) surfaces.¹¹

Adsorption of H₂S¹¹⁻¹³ or S₂(gas)¹⁴ was studied previously on Pd(111) under UHV conditions using a wide range of surface techniques including LEED, AES, and STM. The primary structures observed were the ($\sqrt{3} \times \sqrt{3}$)R30° (“ $\sqrt{3}$ ”) overlayer¹⁴⁻¹⁵ and the ($\sqrt{7} \times \sqrt{7}$)R19° (“ $\sqrt{7}$ ”) reconstruction.^{11, 14} The $\sqrt{3}$ overlayer formed spontaneously at room temperature at sulfur coverage (θ_s , the ratio of S atoms to substrate atoms) $\sim 1/3$ monolayers (ML). The LEED pattern of the $\sqrt{7}$ reconstruction was only observed with additional annealing of the surface to at least 370 K,¹⁵ and corresponded to a decrease in the measured coverage, leading to reported values of either $2/7$ ¹⁵ or $3/7$ ML.^{11, 16-17} A study by Dhanak *et al.* using EXAFS proposed a mixed Pd-S $\sqrt{7}$ reconstruction with $\theta_s = 3/7$ ML. In their model, the unit cell contained 3 S occupied near-bridge sites and excess Pd atoms filled the adlayer by occupying fcc sites.¹⁷

Speller *et al.*¹⁵ studied H₂S adsorption on Pd(111) with STM and AES at room temperature. At 0.22 ML, both the $\sqrt{3}$ and the $\sqrt{7}$ were observed at room temperature with no subsequent annealing. Furthermore, these structures coexisted with two other structural domains: the “stripe” p(2 x 2) and a rare “triangle” p(2 x 2) on terraces. Structural models proposed for all but the $\sqrt{7}$ are strictly S-atom overlayers. With annealing, the $\sqrt{3}$ and stripe p(2 x 2) domains were diminished and $\sqrt{7}$ domains grew. The $\sqrt{7}$ was proposed to be a Pd-S structure, containing 1 hcp S, 1 fcc S, and 3 Pd atoms per unit cell, with $\theta_s = 2/7$ ML.¹⁵

1.2 Pt(111)

Platinum nanoparticles act as a catalyst for oxidation of ammonia to nitric acid and HCN synthesis.¹⁸ Several studies have found that Pt nanoparticles are sensitive to oxygen at elevated temperatures, and sulfur at room temperature. Sintering of Pt nanoparticles on Al₂O₃ is enhanced when heated in air or in the presence of O₂.¹⁹⁻²⁰ This transport enhancement is believed to be facilitated by PtO₂.¹ Pt catalyst poisoning due to sulfur has been studied since as early as 1971.¹⁸ In addition, sulfur induces faceting of Pt nanoparticles from mainly (111)- to (100)-orientation at room temperature, impacting catalytic activity.^{18, 21}

Sulfur adsorption on Pt(111) was previously studied with LEED,²²⁻²³ STM,²³ and AES.²² Heegemann *et al.* found that S₂(g) adsorption induces the formation of 3 structures at room temperature: p(2 x 2) ($\theta_S = 0.25$ ML), $\sqrt{3}$ ($\theta_S = 0.33$ ML), and $\begin{vmatrix} 4 & -1 \\ -1 & 2 \end{vmatrix}$ ($\theta_S = 0.44$ ML).²² Yoon *et al.*²³ deposited S₂(g) at 90 K and annealed the sample to 800 K for 10 s to form a p(2 x 2) structure, or annealed to 500 K for 10 s to form the $\sqrt{3}$. Tensor LEED analysis of both structures showed evidence of sulfur binding in the fcc hollow sites of the terraces. STM imaging of sulfur at $\theta_S < 0.25$ ML showed areas with p(2 x 2) sulfur domains, and areas with no visible ordering. Individual atoms were not resolved, though rows of S were visible.²³

2. Experimental Description

The data presented here was collected at RIKEN in November 2013. The experimental design follows that of the other systems presented in the chapters of this dissertation: the samples were cleaned with several cycles of Ar⁺ sputtering (10-14 μ A, 2.0 kV, 10 min) and annealing (Pd: 960 K, 10 min; Pt: 1070 K, 10 min). S exposure was performed *in situ*^{22, 24-25} with the sample held at room temperature to promote dissociative

adsorption before cooling in the STM stage to 5 K. Due to limited preparation time, I performed one experiment with Pt(111) and one with Pd(111).

The surfaces were not adequately cleaned, showing many black defects, visible in Fig. 1. Rose *et al.* studied such defects on Pd(111) in STM and determined that they are most likely subsurface C, O, and S.²⁶ Surface segregation of sulfur occurs on Pd(111) with annealing above 700 K, and may be a problem even after many cleaning cycles.²⁷ Carbon also segregates to the surface with mild annealing in UHV and can remain problematic after many cleaning cycles.²⁸

In the literature, cleaning regimens for Pt(111) typically include oxidation followed by a high temperature flash.^{23, 29} The gas handling configuration at RIKEN does not allow frequent switching between Ar and other gases, so some planning will need to be done in order to investigate these surfaces in the future, using a good cleaning method. Hyun Jin Yang, a recent graduate of the Kawai laboratory, successfully studied CO/Pt(111) at RIKEN.²⁹ Her notes in the 2-goki logbooks may be useful when setting up the chamber to prepare Pt surfaces.

3. Results and Discussion

3.1 Pd(111)

Upon sulfur adsorption, two different species are observed on the Pd(111) terraces: one that is short and relatively small, and a taller, larger species (Fig. 2). The average dimensions and the standard deviations (σ) of the two species are found in Table I. Typical tunneling conditions here are 1-3.23 nA current and -0.253 to -0.02 V sample bias. The

dependence of the height and widths on sample bias is presented in Fig. 3. Figure 4 shows several STM images at different sample biases.

TABLE I. Dimensions of S-induced features on Pd(111).

	Avg. Height (nm)	σ (nm)	Avg. FWHM (nm)	σ (nm)	Avg. Area (nm²)	σ (nm²)	Count
Short	0.024	0.004	0.36	0.02	0.12	0.02	36
Tall	0.070	0.003	0.76	0.03	0.22	0.02	29

In our previous studies, we have observed sulfur adatoms on Cu(100)³⁰ and Au surfaces.³¹⁻³³ The height of the S atoms in those studies was in the range of 0.014 -0.039 nm, and the full width at half maximum (FWHM) is in the range of 0.29 – 0.39 nm. The area of S atoms on Au(110) was found to be near 0.15 nm².³¹ The dimensions of the short features on Pd(111) fall within the above ranges, and are thus likely to be S adatoms.

The tall features on Pd(111) are roughly twice as wide and twice the area of the S atoms (Table I). These may be Pd-S species, though more data is necessary to make a specific assignment.

Future experimental work to test the reproducibility of these observations is planned in our group.

3.2 Pt(111)

Figure 5 shows the structures present after sulfur adsorption on Pt(111). The typical tunneling conditions were 0.844 – 1.291 nA tunneling current, and -0.193 to -0.003 V sample bias. In Fig. 5(d), (e) and (h) we can distinguish three sizes of features. The average

dimensions of features across this range of conditions are summarized in Table II. Figure 6 shows the variation of the height and width with sample bias. Figure 7 shows STM images corresponding to different sample biases.

TABLE II. Dimensions of S-species on Pt(111).

	Avg. Height (nm)	σ (nm)	Avg. FWHM (nm)	σ (nm)	Avg. Area (nm²)	σ (nm²)	Count
Short	0.020	0.003	0.350	0.029	0.12	0.02	13
Medium	0.031	0.004	0.459	0.021	0.11	0.01	31
Tall	0.076	0.011	0.596	0.024	0.21	0.02	31

Based on the same arguments used in the previous section, we assign the short features as S atoms. A comparison of the dimensions of the tall species to those of the short, especially with respect to area, suggests that the tall species are a Pd-S complex. An investigation of both of these features with theoretical methods is planned.

Figure 8(a) shows an atomically-resolved image of the Pt(111) surface after the adsorption of S. This allows us to identify the close-packed directions of the surface, as well as compare binding sites of different species. Figure 8(b) shows a high resolution image of the short and tall species on Pt(111), and in Fig. 8(c) we examine the binding sites. The short species appear to occupy the same kind of binding site, while the tall species seem to occupy several different sites.

In addition to the terraces, the step edges are decorated with S. Figure 9 shows several step edges decorated with S. Due to the limited amount of data, it is difficult to find trends in the behavior of the edges with S, but comparing the edges in Fig. 9(c-d) to the close-packed

directions shows that the edges are aligned with the close-packed directions or faceted by 30° . The resolution is not high enough to measure spacing between S atoms at the edges.

Acknowledgements

This work was supported from the U.S. by NSF Grant CHE-1111500, and from Japan by a Grant-in-Aid for Scientific Research on Priority Areas “Electron Transport Through a Linked Molecule in Nano-scale”; and a Grant-in-Aid for Scientific Research(S) “Single Molecule Spectroscopy using Probe Microscope” from the Ministry of Education, Culture, Sports, Science, and Technology (MEXT).

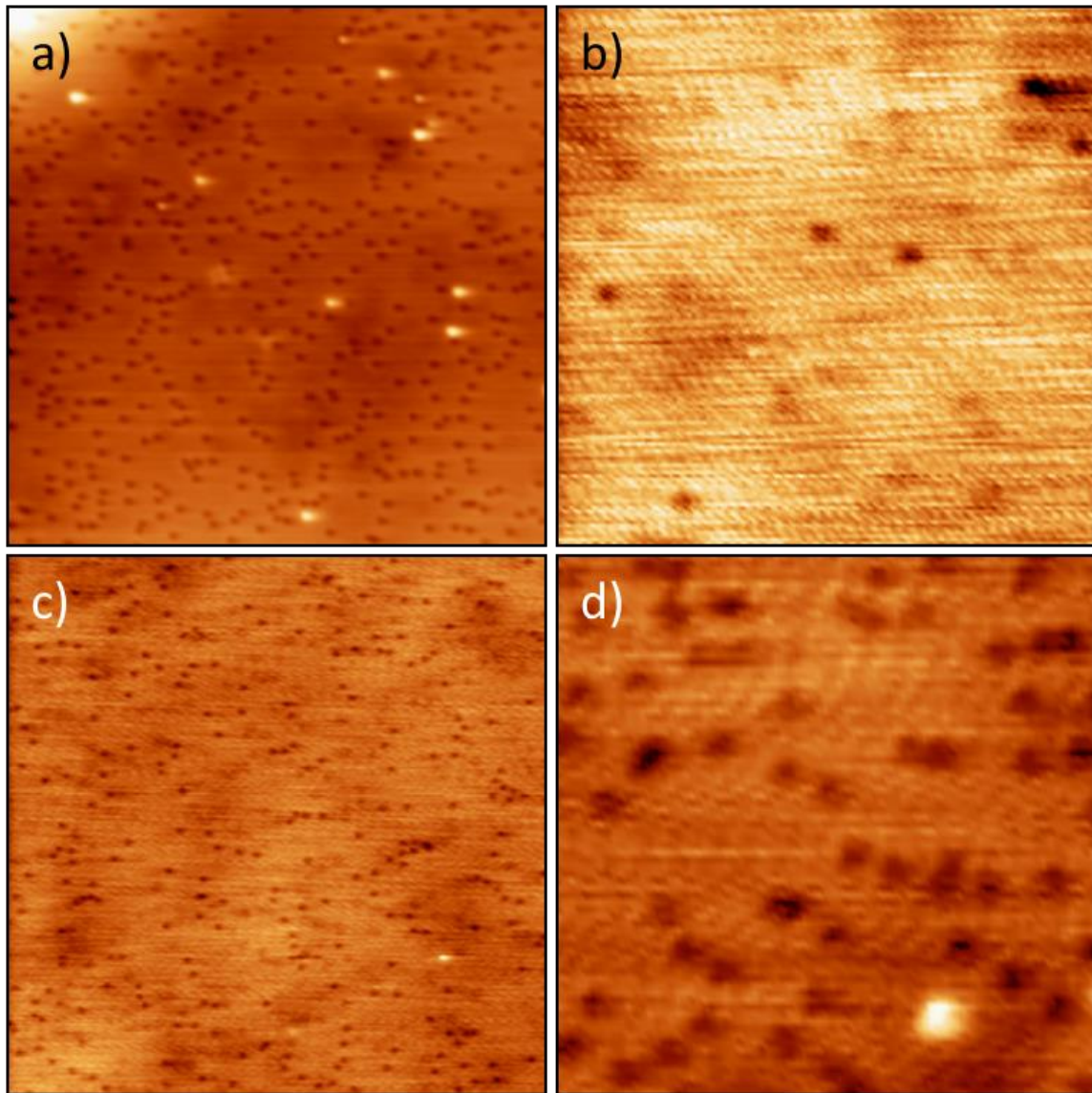
Figures

Figure 1. “Clean” sample surfaces. Imaging conditions are found in Table A1. a) Pd(111), 40 x 40 nm². b) Pd(111), 15 x 15 nm². c) Pt(111), 50 x 50 nm². d) Pt(111), 15 x 15 nm².

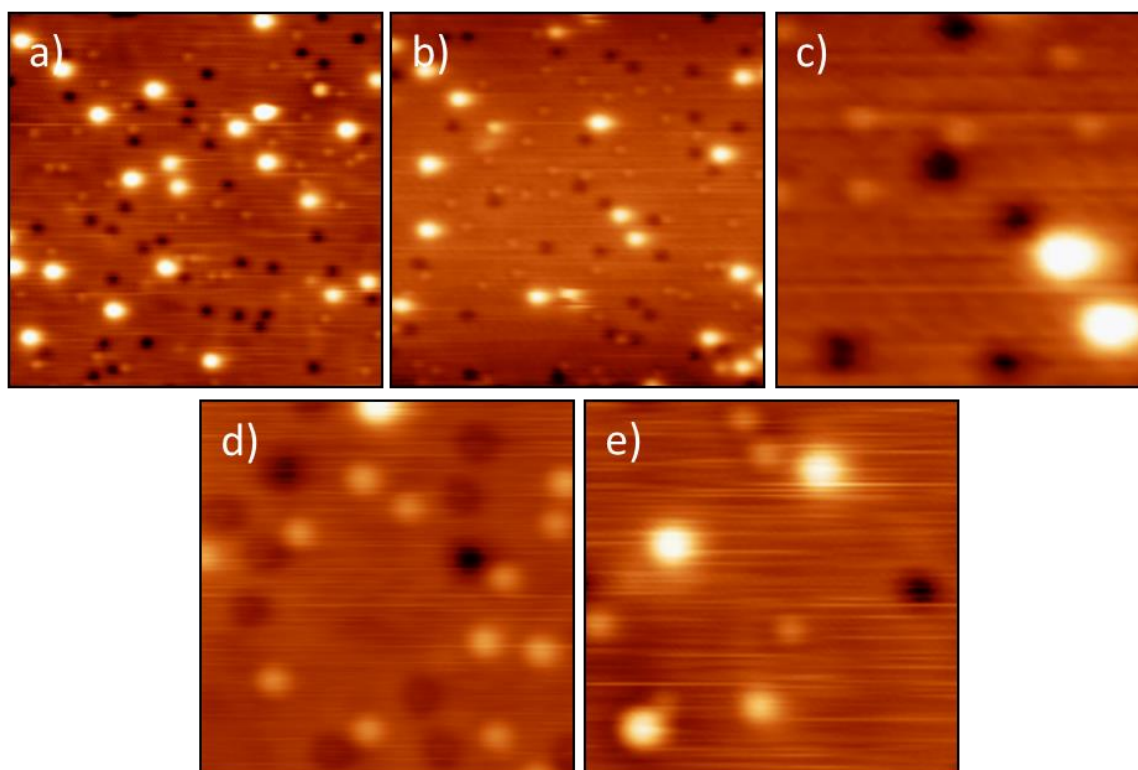


Figure 2. STM images of adsorbed S-species on Pd(111) terraces. Image details are in Table A1.

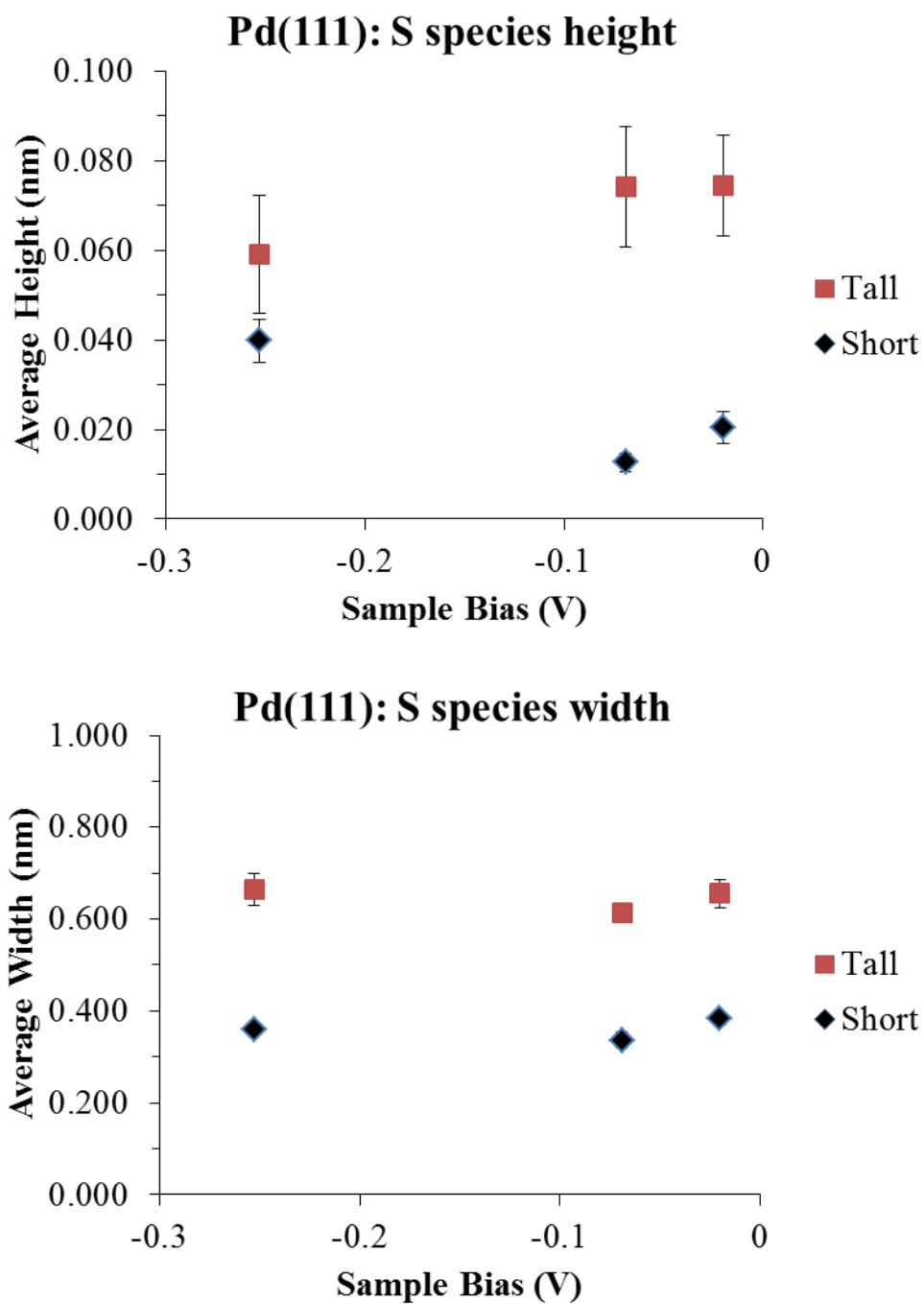


Figure 3. Measured height and width of features on Pd(111) as a function of sample bias.

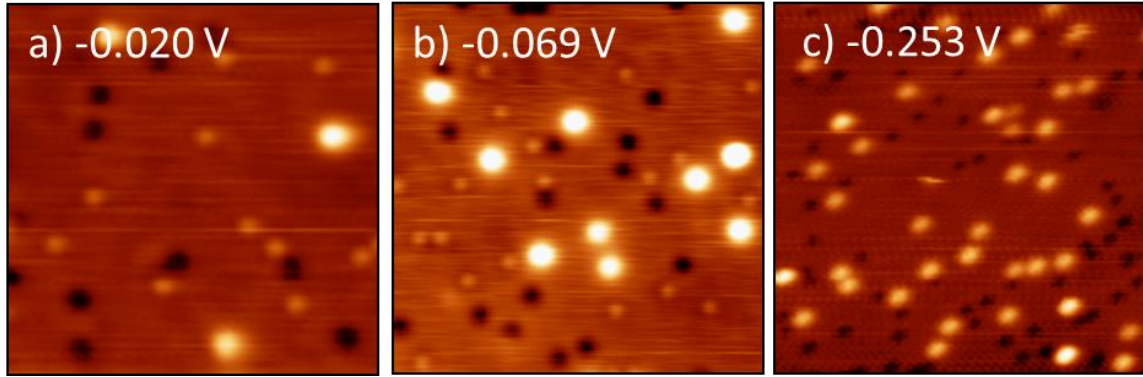


Figure 4. Images analyzed in Fig. 3, labelled with V_s .

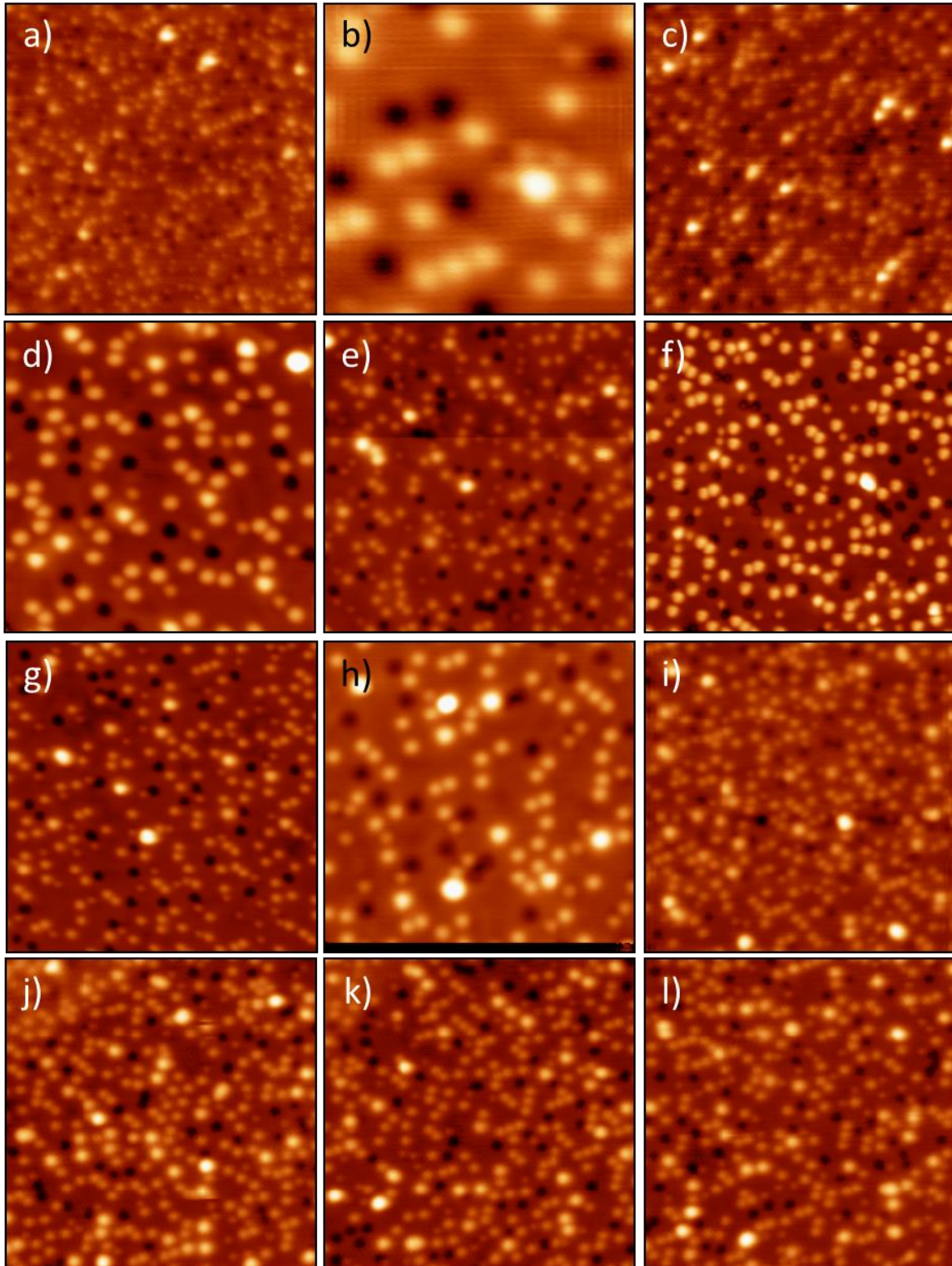


Figure 5. STM images of S-induced species on Pt(111). Image details are in Table A1.

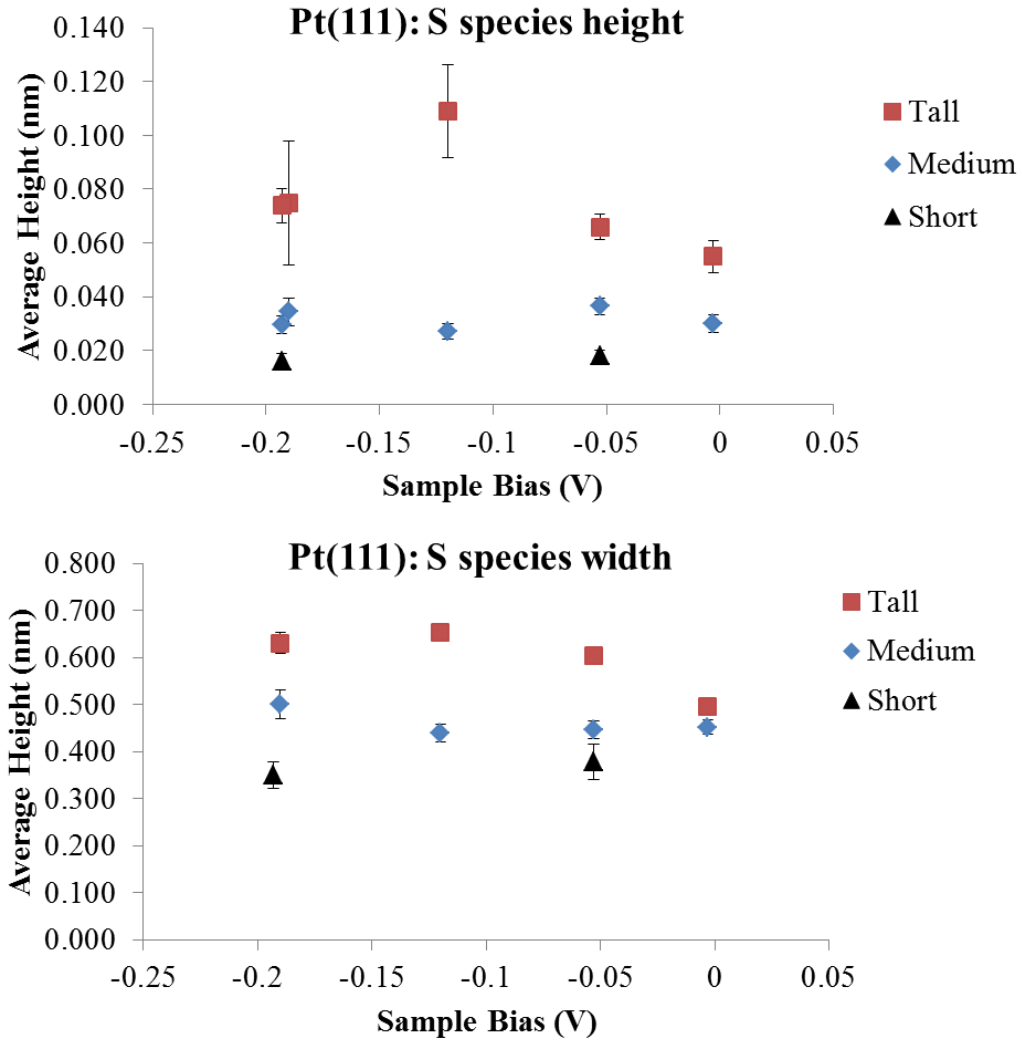


Figure 6. Measured height and width of features on Pt(111) as a function of sample bias.

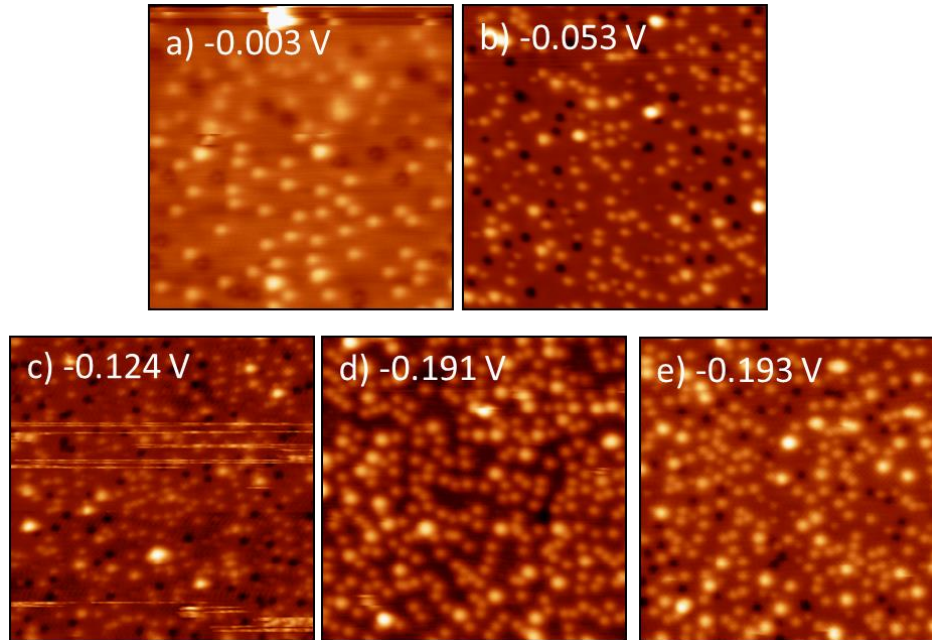


Figure 7. Images analyzed in Fig. x6, labelled with V_s .

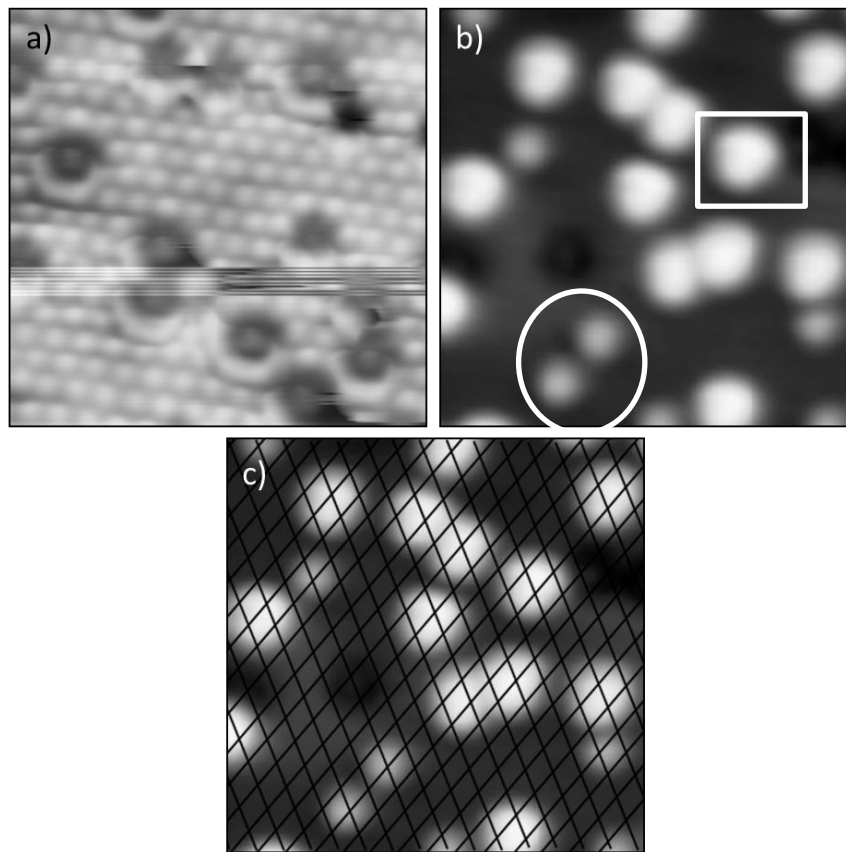


Figure 8. (a) Atomically resolved Pt(111). (b) High-resolution image of S-species on Pt(111) two of the “short” species are circled, one “tall” is highlighted in the square. (c) Overlaid atomic lattice on the image in (b).

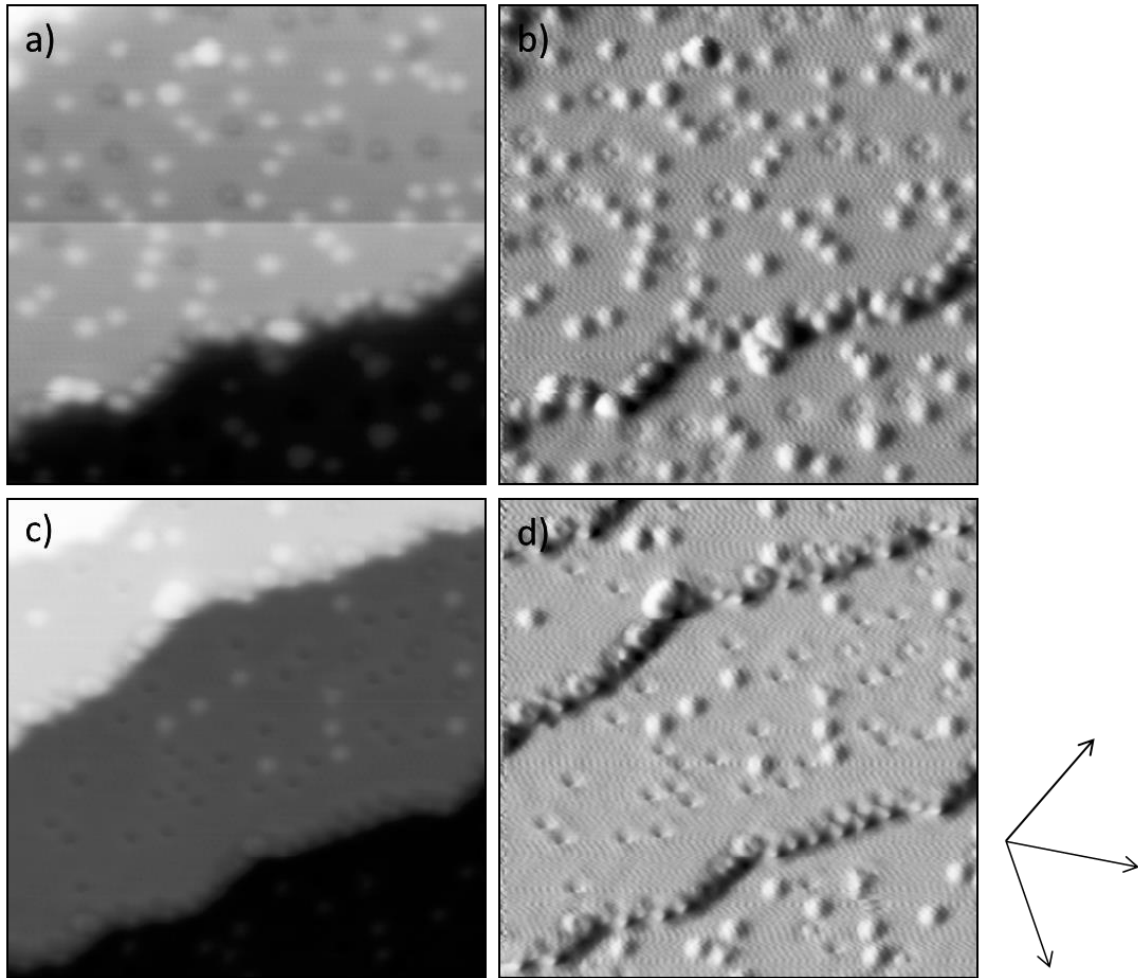


Figure 9. Decorated step edges of Pt(111). (a) Topographic and (b) derivative image, $10 \times 10 \text{ nm}^2$. (c) Topographic and (d) derivative image, $10 \times 10 \text{ nm}^2$. Arrows indicating the close-packed surface directions are on the right.

TABLE A1. Imaging conditions for Figs. 1- 9.

Figure name	Image size (nm ²)	Image current (nA)	Sample bias (V)	Image file
1 a	40 x 40	1.000	-0.373	m2 2131125 S-Pd111
b	15 x 15	1.000	-0.292	m10 2131125 S-Pd111
c	50 x 50	0.934	-0.148	m3 2131123 S-Pt111
d	15 x 15	1.319	-1.000	m2 2131123 S-Pt111
2 a	15 x 15	1.076	-0.069	m20 2131125 S-Pd111
b	15 x 15	1.000	-0.238	m13 2131125 S-Pd111
c	5 x 5	1.000	-0.238	m13 2131125 S-Pd111
d	5 x 5	1.980	-0.007	m37 2131125 S-Pd111
e	5 x 5	0.827	-0.030	m23 2131125 S-Pd111
4 a	8 x 8	3.223	-0.020	m17 2131125 S-Pd111
b	10 x 10	1.076	-0.069	m21 2131125 S-Pd111
c	20 x 20	1.000	-0.253	m11 2131125 S-Pd111
5a	20 x 20	1.551	-0.027	m12 2131123 S-Pt111
b	5 x 5	1.034	-0.059	m14 2131123 S-Pt111
c	20 x 20	1.034	-0.059	m15 2131123 S-Pt111
d	10 x 10	1.46	-0.020	m30 2131123 S-Pt111
e	15 x 15	1.121	-0.124	m32 2131123 S-Pt111
f	15 x 15	1.121	-0.162	m35 2131123 S-Pt111
g	15 x 15	1.191	-0.053	m42 2131123 S-Pt111
h	10 x 10	1.46	-0.020	m29 2131123 S-Pt111
i	15 x 15	0.844	-0.193	m48 2131123 S-Pt111
j	15 x 15	0.844	-0.193	m51 2131123 S-Pt111
k	15 x 15	0.844	-0.193	m52 2131123 S-Pt111
l	15 x 15	0.844	-0.193	m53 2131123 S-Pt111
7 a	10 x 10	2.912	-0.003	m11 2131123 S-Pt111
b	15 x 15	1.191	-0.053	m41 2131123 S-Pt111
c	20 x 20	0.972	-0.124	m6 2131123 S-Pt111
d	15 x 15	1.191	-0.191	m47 2131123 S-Pt111
e	15 x 15	0.844	-0.193	m50 2131123 S-Pt111
8 a	4 x 4	3.095	-0.002	m39 2131123 S-Pt111
b, c	4 x 4	1.121	-0.162	m35 2131123 S-Pt111
9 a/b	10 x 10	2.526	-0.070	m18 2131123 S-Pt111
c/d	10 x 10	2.526	-0.070	m19 2131123 S-Pt111

References

1. Harris, P. J. F., "Growth and Structure of Supported Metal Catalyst Particles". *Int. Mat. Rev.* **1995**, *40*, 97.
2. Penner, S.; Bera, P.; Pedersen, S.; Ngo, L. T.; Harris, J. J. W.; Campbell, C. T., "Interactions of O₂ with Pd Nanoparticles on α -Al₂O₃(0001) at Low and High O₂ Pressures". *J. Phys. Chem. B* **2006**, *110*, 24577-24584.
3. Parkinson, G. S.; Novotny, Z.; Argentero, G.; Schmid, M.; Pavelec, J.; Kosak, R.; Blaha, P.; Diebold, U., "Carbon Monoxide-Induced Adatom Sintering in a Pd-Fe₃O₄ Model Catalyst". *Nat. Mater.* **2013**, *12*, 724-728.
4. Reetz, M. T.; Westermann, E., "Phosphane-Free Palladium-Catalyzed Coupling Reactions: The Decisive Role of Pd Nanoparticles". *Angew. Chem. Int. Ed.* **2000**, *39*, 165-168.
5. Mazumder, V.; Sun, S., "Oleylamine-Mediated Synthesis of Pd Nanoparticles for Catalytic Formic Acid Oxidation". *J. Am. Chem. Soc.* **2009**, *131*, 4588-4589.
6. Wilson, O. M.; Knecht, M. R.; Garcia-Martinez, J. C.; Crooks, R. M., "Effect of Pd Nanoparticle Size on the Catalytic Hydrogenation of Allyl Alcohol". *J. Am. Chem. Soc.* **2006**, *128*, 4510-4511.
7. Chen, J.; Zhang, Q.; Wang, Y.; Wan, H., "Size-Dependent Catalytic Activity of Supported Palladium Nanoparticles for Aerobic Oxidation of Alcohols". *Adv. Synth. Catal.* **2008**, *350*, 453-464.
8. Lu, J. L.; Kaya, S.; Weissenrieder, J.; Gao, H. J.; Shaikhutdinov, S.; Freund, H. J., "Low Temperature CO Induced Growth of Pd Supported on a Monolayer Silica Film". *Surf. Sci.* **2006**, *600*, L153-L157.

9. Newton, M. A.; Belver-Coldeira, C.; Martinez-Arias, A.; Fernandez-Garcia, M., "Dynamic in Situ Observation of Rapid Size and Shape Change of Supported Pd Nanoparticles During CO/NO Cycling". *Nat. Mater.* **2007**, *6*, 528-532.
10. Strimbu, L.; Liu, J.; Kaifer, A. E., "Cyclodextrin-Capped Palladium Nanoparticles as Catalysts for the Suzuki Reaction". *Langmuir* **2003**, *19*, 483-485.
11. Forbes, J. g.; Gellman, A. J.; Dunphy, J. C.; Salmeron, M., "Imaging of Sulfur Overlayer Structures on the Pd(111) Surface". *Surf. Sci.* **1992**, *279*, 68.
12. Gellman, A. J.; Dunphy, J. C.; Salmeron, M., "Imaging of Acetylene Heterocyclization Sites on the Sulfided Pd(111) Surface". *Langmuir* **1992**, *8*, 534.
13. Miller, J. B.; Gellman, A. J., "Structural Evolution of Sulfur Overlayers on Pd(111)". *Surf. Sci.* **2009**, *603*, L82-L85.
14. Patterson, C. H.; Lambert, R. M., "Structure and Properties of the Palladium/Sulphur Interface: S₂ Chemisorption on Pd(111)". *Surf. Sci.* **1987**, *187*, 339-358.
15. Speller, S.; Rauch, T.; Bömermann, J.; Borrmann, P.; Heiland, W., "Surface Structures of S on Pd(111)". *Surf. Sci.* **1999**, *441*, 107-116.
16. Maca, F.; Scheffler, M.; Berndt, W., "The Adsorption of Sulphur on Pd(111) I. A LEED Analysis of the (2 × 3)R30° S Adsorbate Structure". *Surf. Sci.* **1985**, *160*, 467-474.
17. Dhanak, V. R.; Shard, A. G.; Cowie, B. C. C.; Santoni, A., "The Structures of Sulphur on Pd(111) Studied by X-Ray Standing Wavefield Absorption and Surface EXAFS". *Surf. Sci.* **1998**, *410*, 321-329.
18. Schmidt, L. D.; Luss, D., "Physical and Chemical Characterization of Platinum-Rhodium Gauze Catalysts". *J. Catal.* **1971**, *22*, 269-279.

19. Harris, P. J. F.; Boyes, E. D.; Cairns, J. A., "The Sintering of an Alumina-Supported Platinum Catalyst Studied by Transmission Electron Microscopy". *J. Catal.* **1983**, *82*, 127-146.
20. Harris, P. J. F., "The Sintering of Platinum Particles in an Alumina-Supported Catalyst: Further Transmission Electron Microscopy Studies". *J. Catal.* **1986**, *97*, 527-542.
21. Harris, P. J. F., "Sulphur-Induced Faceting of Platinum Catalyst Particles". *Nature* **1986**, *323*, 792-794.
22. Heegemann, W.; Meister, K. H.; Bechtold, E.; Hayek, K., "The Adsorption of Sulfur on the (100) and (111) Faces of Platinum; a LEED and AES Study". *Surf. Sci.* **1975**, *49*, 161-180.
23. Yoon, H. A.; Materer, N.; Salmeron, M.; Hove, M. A. V.; Somorjai, G. A., "Coverage-Dependent Structures of Sulfur on Pt(111) Studied by Low-Energy Electron Diffraction (LEED) and Scanning Tunneling Microscopy (STM)". *Surf. Sci.* **1997**, *376*, 254-266.
24. Wagner, C., "Investigation on Silver Sulfide". *J. Chem. Phys.* **1953**, *21*, 1819-1827.
25. Detry, D.; Drowart, J.; Goldfinger, P.; Keller, H.; Rickert, H., "Zur Thermodynamik Von Schwefeldampf". *Z. Phys. Chem.* **1967**, *55*, 314-319.
26. Rose, M. K.; Borg, A.; Mitsui, T.; Ogletree, D. F.; Salmeron, M., "Subsurface Impurities in Pd(111) Studied by Scanning Tunneling Microscopy". *J. Chem. Phys.* **2001**, *115*, 10927-10934.
27. Bömermann, J.; Huck, M.; Kuntze, J.; Rauch, T.; Speller, S.; Heiland, W., "An STM, AES and LEED Study of the Segregated Sulfur on Pd(111)". *Surf. Sci.* **1996**, *357-358*, 849-854.

28. *Specimen Handling, Preparation, and Treatments in Surface Characterization*; Kluwer Academic Publishers, 1998; Vol. 4.
29. Yang, H. J.; Minato, T.; Kawai, M.; Kim, Y., "STM Investigation of CO Ordering on Pt(111): From an Isolated Molecule to High-Coverage Superstructures". *J. Phys. Chem. C* **2013**, *117*, 16429-16437.
30. Walen, H.; Spurgeon, P. M.; Oh, J.; Yang, H. J.; Kim, Y.; Thiel, P. A., Unpublished Work, S/Cu(100). **2016**.
31. Walen, H.; Liu, D.-J.; Oh, J.; Yang, H. J.; Kim, Y.; Thiel, P. A., "Long-Range Displacive Reconstruction of Au(110) Triggered by Low Coverage of Sulfur". *J. Phys. Chem. C* **2015**, *119*, 21000-21010.
32. Walen, H.; Liu, D.-J.; Oh, J.; Yang, H. J.; Kim, Y.; Evans, J. W.; Thiel, P. A., "Identification of Au-S Complexes on Au(100)". *Phys. Chem. Chem. Phys.* **2016**, *18*, 4891-4901.
33. Walen, H.; Liu, D.-J.; Oh, J.; Lim, H.; Evans, J. W.; Kim, Y.; Thiel, P. A., "Self-Organization of S Adatoms on Au(111): $\sqrt{3}R30^\circ$ Rows at Low Coverage". *J. Chem. Phys.* **2015**, *143*, 014704.

APPENDIX III

DETERMINATION OF S COVERAGE ON SILVER SURFACES

Determination of coverage is an important aspect of studying surfaces with adsorbates. Relative coverage can be found using various methods, including temperature programmed desorption (TPD), Auger electron spectroscopy (AES), low energy electron diffraction (LEED), and scanning tunneling microscopy. To obtain the absolute coverage (θ) of sulfur, our group typically employs AES.

In the past, our group has relied heavily on a paper by Schwaha, Spencer, and Lambert (SSL) that used LEED to calibrate the S(LMM)/Ag(MNN) AES peak ratio to sulfur coverage (θ_S) on Ag(111).¹ Equation 1 describes the relationship between θ_S and S/Ag.

$$\theta_S = k * \left(\frac{S}{Ag} \right)_{AES} = \frac{N_S}{N_{Ag}} \quad (1)$$

Here, k is the proportionality constant between the S/Ag peak ratio and θ_S in monolayers, N_S is the density of sulfur atoms, and N_{Ag} is the surface density of silver. The N_{Ag} values for the low index faces are summarized in Table I. Due to the differences in N_{Ag} , we anticipate a different k value for each of the low index faces. Prior to this, a k value of 0.60 was used for both Ag(100) and Ag(111) in our group.²⁻⁷

TABLE I: Calculated surface density for the low index surfaces of silver.

Surface	N_{Ag} (atoms/cm ²)	N_{Ag} (atoms/m ²)
Ag(111)	1.38×10^{15}	1.38×10^{19}
Ag(100)	1.19×10^{15}	1.19×10^{19}
Ag(110)	0.845×10^{15}	0.845×10^{19}

Figure 1 shows the S/Ag relative AES intensities as a function of S₂ dose, reproduced from SSL.¹ Using the linear section of the plot, the density of sulfur atoms (N_S) for selected S/Ag AES values was determined. This information, along with N_{Ag} and equation 1, was used to calculate proportionality constants, k_{SSL}, for each surface. The results are summarized in Table II.

TABLE II. Sulfur density for specific S/Ag AES ratios, as determined from Fig. 1 (blue columns); calculated proportionality constants (white columns).

S/Ag AES ratio	N _S (S atoms/m ²)	Ag(111) k _{SSL}	Ag(100) k _{SSL}	Ag(110) k _{SSL}
0.25	0.19×10^{19}	0.55	0.64	0.90
0.50	0.38×10^{19}	0.55	0.64	0.90
0.75	0.56×10^{19}	0.54	0.63	0.88
1.00	0.79×10^{19}	0.57	0.66	0.93
1.25	0.97×10^{19}	0.56	0.65	0.92
1.50	1.17×10^{19}	0.57	0.65	0.92
Average		0.56	0.65	0.91

A study done around the same time by Rovida and Pratesi reported an ordered p(2 x 2) phase on Ag(100), with “full development” of the p(2 x 2) LEED pattern at a S/Ag AES ratio of 0.55.⁸ They equated this to the ideal sulfur coverage in a p(2 x 2) of $\theta_s = \frac{1}{4}$ ML, which corresponds to

$$N_s = \frac{1}{4} \left(1.19 \times 10^{15} \frac{\text{Ag atoms}}{\text{cm}^2} \right) = 2.98 \times 10^{14} \frac{\text{S atoms}}{\text{cm}^2}$$

This N_s was used for “calibration of the Auger data” in their work. Using this information, one can calculate a proportionality constant, where RP signifies the authors, Rovida and Pratesi.

$$k_{RP} = \frac{\theta_s}{\left(\frac{S}{Ag} \right)_{AES}} = \frac{\left(\frac{1}{4} \right)}{0.55} = 0.45$$

RP also measured the $(S/Ag)_{AES}$ ratio at completion of another ordered S structure, the $(\sqrt{17} \times \sqrt{17})R14^\circ$ (which they referred to as $M = \begin{vmatrix} 4 & -1 \\ 1 & 4 \end{vmatrix}$) that occurs for $\theta_s \sim 0.47$ ML.

From this, one can also calculate k_{RP} as a check of consistency:

$$k_{RP} = \frac{\theta_s}{\left(\frac{S}{Ag} \right)_{AES}} = \frac{0.47}{1.10} = 0.43$$

One sees that the result is very similar when either the p(2x2) or $(\sqrt{17} \times \sqrt{17})R14^\circ$ is used as a reference. Other structures were also observed by RP. If we assume that the upper limit values for $(S/Ag)_{AES}$ are when the phase is completed in LEED for each case, then the resultant values of k_{RP} can be summarized as shown in Table III.

TABLE III. Summary of k values for RP and SSL.

	Ag(111)	Ag(100)	Ag(110)
k_{RP}	0.60	0.45	0.47
k_{RP}/k_{SSL}	0.66	0.80	0.72

Overall, the proportionality constants developed by RP are consistently lower than those of SSL, with the exception of those for Ag(111). However, the k_{RP} value is supported by less data than that of SSL, who very rigorously investigated sulfur on silver with AES, work function measurements, LEED, and TPD. For this reason, we choose to use the calibration established by SSL while taking into account the different N_{Ag} for each face. In past work in this group with Ag(100) and Ag(111), this calibration has produced very reasonable results.

Figures

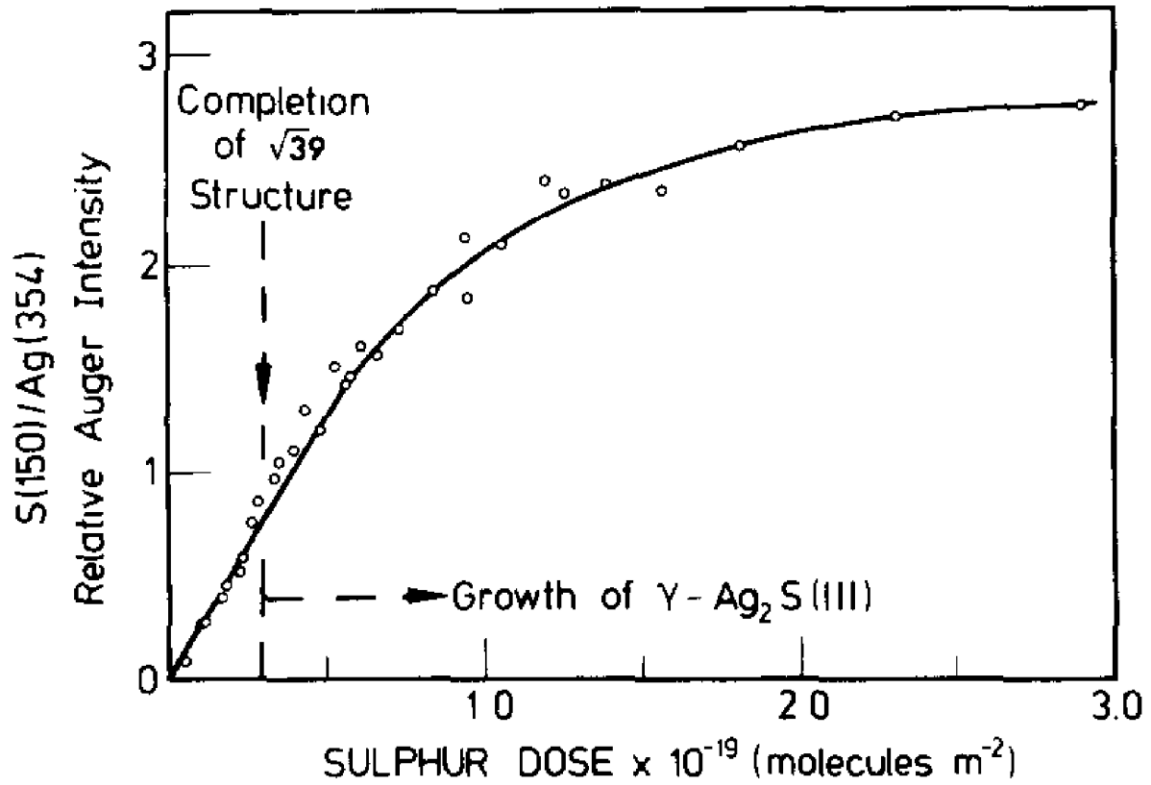


Figure 1. From Schwaha *et al.*¹ Reproduced with permission of ELSEVIER BV in the format reuse in a thesis/dissertation via Copyright Clearance Center.

References

1. Schwaha, K.; Spencer, N. D.; Lambert, R. M., "A Single Crystal Study of the Initial Stages of Silver Sulphidation: The Chemisorption and Reactivity of Molecular Sulphur (S_2) on Ag(111)". *Surf. Sci* **1979**, *81*, 273-284.
2. Shen, M.; Liu, D.-J.; Jenks, C. J.; Thiel, P. A., "Novel Self-Organized Structure of a Ag-S Complex on the Ag(111) Surface Below Room Temperature". *J. Phys. Chem. C* **2008**, *112*, 4281-4290.
3. Shen, M.; Liu, D.-J.; Jenks, C. J.; Thiel, P. A.; Evans, J. W., "Accelerated Coarsening of Ag Adatom Islands on Ag(111) Exposed to S: Mass-Transport Mediated by Ag-S Complexes". *J. Chem. Phys.* **2009**, *130*, 094701.
4. Shen, M.; Liu, D.-J.; Jenks, C. J.; Thiel, P. A., "The Effect of Chalcogens (O, S) on Coarsening of Nanoislands on Metal Surfaces". *Surf. Sci.* **2009**, *603*, 1486-1491.
5. Russell, S. M.; Shen, M.; Liu, D.-J.; Thiel, P. A., "Adsorption of Sulfur on Ag(100)". *Surf. Sci.* **2011**, *605*, 520-527.
6. Shen, M.; Russell, S. M.; Liu, D.-J.; Thiel, P. A., "Destabilization of Ag Nanoislands on Ag(100) by Adsorbed Sulfur". *J. Chem. Phys.* **2011**, *135*, 154701.
7. Shen, M.; Jenks, C. J.; Evans, J. W.; Thiel, P. A., "How Sulfur Controls Nucleation of Ag Islands on Ag(111)". *Top. Catal.* **2011**, *54*, 83-89.
8. Rovida, G.; Pratesi, F., "Sulfur Overlayers on the Low-Index Faces of Silver". *Surf. Sci.* **1981**, *104*, 609-624.

APPENDIX IV

MODIFICATION OF THE *IN SITU* EVAPORATOR FOR SE DEPOSITION

For the experiments described in Chapter VIII it was necessary to modify the sulfur electrochemical evaporator at RIKEN to produce selenium. Happily, the conversion from sulfur to selenium is fairly straightforward, and the use of the cell as a Se source has been described previously in the literature.

The electrochemical cell evaporator that we use follows the design of Wagner.¹ The assembly of the evaporator at RIKEN is described in Selena Russell's Ph.D. thesis.² In short, to evaporate S in UHV we use a solid-state Ag|AgI|Ag₂S|Pt cell held *in situ* (Fig. 1(a-b)). The cell, contained within a quartz or glass tube, is heated via an external filament to ~473 K (~200°C). Its temperature is monitored by a thermocouple held inside the tube, within a few centimeters of the cell. Once the temperature is reached, a bias is applied such that electrons flow from the Ag plate, through the chemical pellets, to a Pt wire connected to the feedthrough. The current flow reduces the Ag within the Ag₂S pellet and creates S₂(gas) as the primary output in the potential range of 0.20 - 0.25 V, at 473 K.³

To evaporate Se, the Ag₂S pellet of the S cell is exchanged with Ag₂Se, and a second Ag plate is added at the cathode (Fig. 1(c)).⁴ [The second Ag plate is not described in the literature but it seemed to help.] The cell is otherwise operated in a similar fashion as when depositing S. To deposit Se, the cell is first heated to ~573 K (~300 °C). The potential applied across the cell is in the range of 0.35 – 0.40 V. Previous studies of this cell have found the

primary emission under these conditions is $\text{Se}_2(\text{gas})$, with lesser emissions of Se_5 and Se_6 gases.⁴

The emission of the cell is checked with a mass spectrometer, mounted directly across from the evaporator. Se has six naturally occurring isotopes: ^{74}Se , ^{76}Se , ^{77}Se , ^{78}Se , ^{80}Se , and ^{82}Se . The five heavier isotopes exist in fairly high natural abundance (Table I), and thus we anticipate a grouping of five peaks to represent the Se species present in the mass spectrum.

TABLE I. Atomic mass and isotopic abundance for Se isotopes.

Isotope	Atomic mass	Natural abundance ⁵
^{74}Se	73.92	0.009
^{76}Se	75.92	0.093
^{77}Se	76.92	0.076
^{78}Se	77.92	0.238
^{80}Se	79.92	0.496
^{82}Se	81.92	0.087

There are two such groupings of peaks that we identify as Se species in the mass spectra shown in Fig. 2, namely peaks for Se^+ (around 80 amu) and Se_2^+ (around 160 amu). Unfortunately, the detection range of our mass spectrometer extends only up to 200 amu, and we are unable to confirm the existence of any heavier Se molecules that may be emitted in tandem, such as Se_5 or Se_6 . Emission spectra were collected before and after completing the experimental run to confirm continued emission of Se species from the cell.

My first attempt to assemble and use the cell for Se deposition was unsuccessful (Fig. 3). After trying to use the cell 6 times, I found several problems. The first was that the Ag plate (a single one was used the first time) had reacted to the point where it seemed to be chemically different from Ag metal. The plate was black and brittle, and I was unable to recover it after disassembling the cell. The loss of the metallic nature lessened the surface area of the cell that makes contact to the power supply, likely diminishing $\text{Se}_2(\text{gas})$ formation. Second, there were large metallic dendrites spanning from the plate along the cell (Fig. 3(a)), and between the Ag_2Se pellet and Pt wire (Fig. 3(b)). These dendrites may have provided a lower resistance path compared to the pellets, facilitating current flow *around* the cell rather than through it. This prevented the creation of ions within the pellets necessary to produce $\text{Se}_2(\text{gas})$. Based on the resistance of the cell measured at the feedthrough, the connection of the dendrites was not apparent at room temperature, but a connection may have formed under conditions of cell use. Finally, a portion of the AgI pellet adjacent to the Ag_2Se pellet changed color from yellow to bluish-green with use (Fig. 3(b)). It is unclear how this color change is related to the chemical nature of the pellets, or how it may affect the vapor composition.

In my second attempt to assemble the Se cell, I used two Ag plates and new pellets. This cell yielded good reproducibility of Se deposition over 4 uses, and the data collected is presented in Chapter VIII. Unfortunately, I left RIKEN before photographing the successful cell.

Acknowledgements

The chemical materials, Ag plates, quartz tubes, and W springs were provided by the Iowa

State team. The Pt wire, ceramics, and other components were provided by the RIKEN team. This work was supported from the U.S. by NSF Grant CHE-1111500, and from Japan by a Grant-in-Aid for Scientific Research on Priority Areas “Electron Transport Through a Linked Molecule in Nano-scale”; and a Grant-in-Aid for Scientific Research(S) “Single Molecule Spectroscopy using Probe Microscope” from the Ministry of Education, Culture, Sports, Science, and Technology (MEXT).

Figures

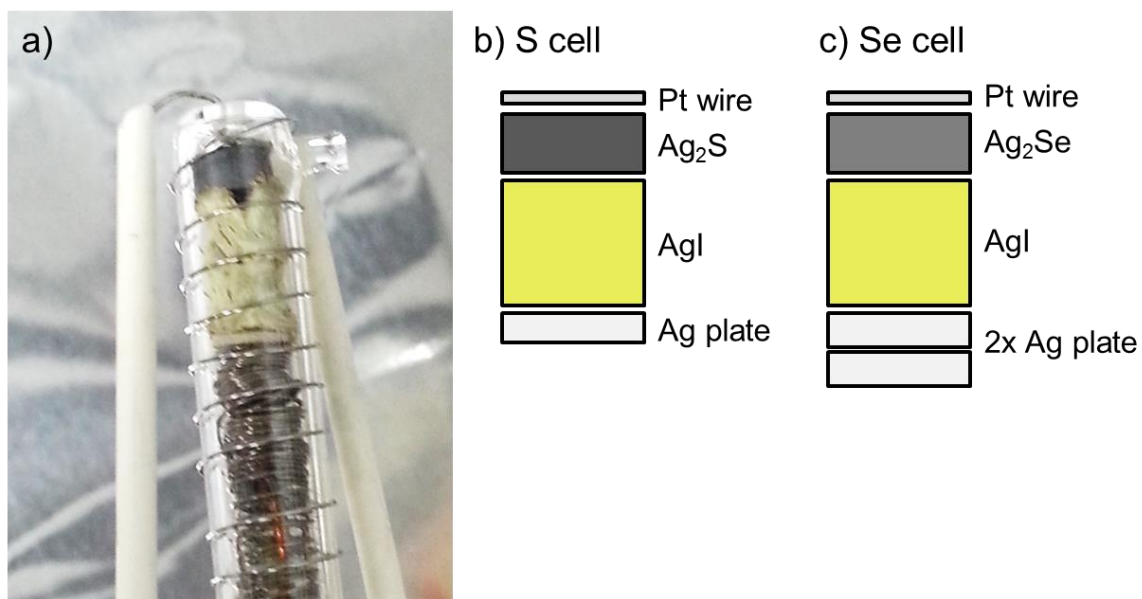


Figure 1. Conversion of the S evaporator to a Se evaporator. (a) The S evaporator cell after 38 uses. (b) Schematic of the chemical ordering in the cell for S deposition. (c) Schematic of the chemical cell for Se deposition.

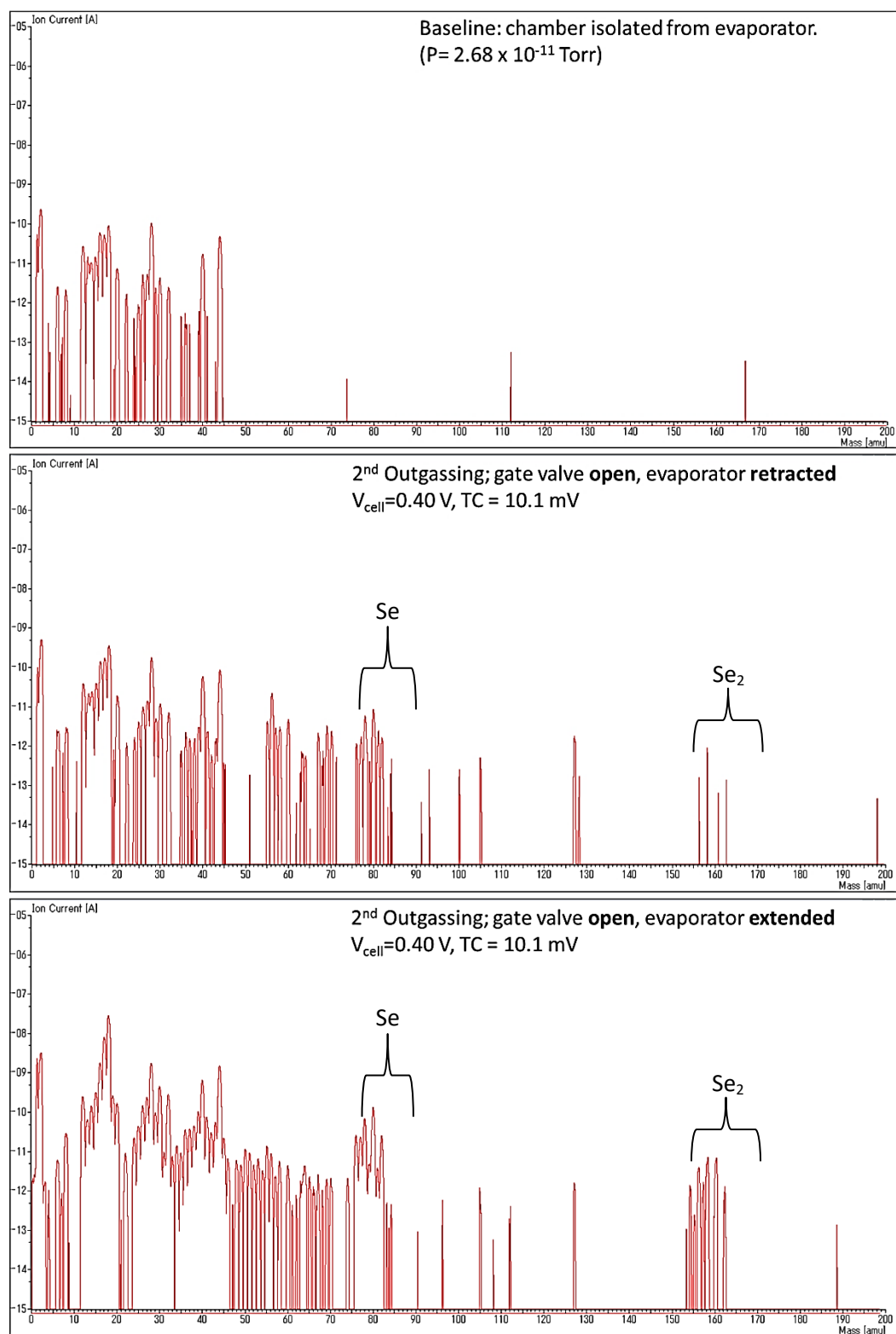


Figure 2. Mass spectra from the Se evaporator. The y-axis is the Ion Current (A), and is a log scale from 10^{-15} to 10^{-5} . The x-axis is Mass (amu) and is a linear scale from 0 to 200.

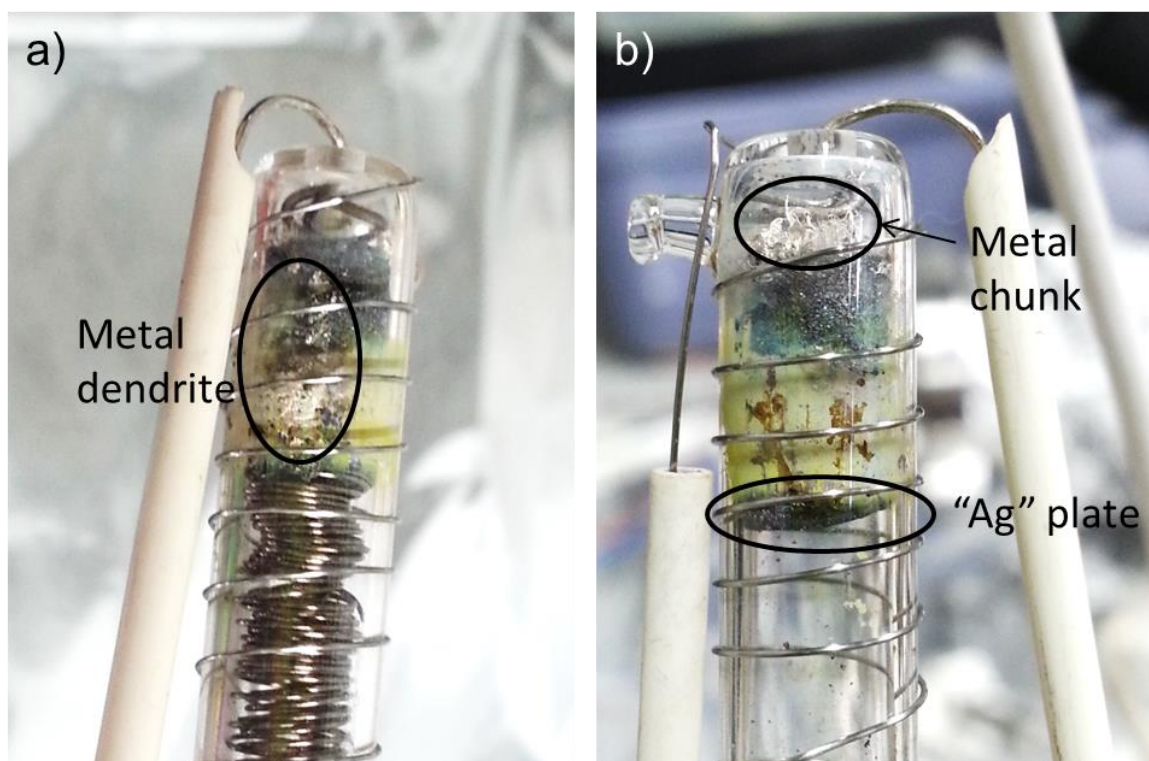


Figure 3. Unsuccessful Se cell, after 6 uses. (a) Before taking the cell apart, metallic dendrites are visible along the outside of the AgI pellet. In addition, the Ag plate is not visible with the springs in place. (b) After taking out the springs, cell rotated $\sim 90^\circ$. The remains of the Ag plate are visible at the bottom of the AgI pellet, along with discoloring in the upper portion of the AgI pellet from yellow to a bluish-green. A large chunk of metal is visible between the Ag_2Se pellet and the Pt wire.

References

1. Wagner, C., "Investigation on Silver Sulfide". *J. Chem. Phys.* **1953**, *21*, 1819-1827.
2. Russell, S. M. Mass Transport and Chalcogen-Silver Interactions on Silver Surfaces. Ph.D., Iowa State University, Ames, Iowa, 2012.
3. Detry, D.; Drowart, J.; Goldfinger, P.; Keller, H.; Rickert, H., "Zur Thermodynamik Von Schwefeldampf". *Z. Phys. Chem.* **1967**, *55*, 314-319.
4. Keller, H.; Rickert, H.; Detry, D.; Droward, J.; Goldfinger, P., "Zur Thermodynamik Von Selendampf Massenspektrometrische Untersuchungen Mit Der Elektrochemischen Knudsen-Zelle". *Z. Phys. Chem.* **1971**, *75*, 273-286.
5. Coplen, T. B., et al., "Isotope-Abundance Variations of Selected Elements". *Pure Appl. Chem.* **2002**, *74*, 1987-2017.

APPENDIX V

OBSERVED S AND S-M SPECIES HEIGHT AND WIDTH IN STM

TABLE I. Measured S atom height and width on different surfaces, T = 5 K.

Substrate	Structure	Height (nm)	FWHM (nm)	Other
Au(111)	$\sqrt{3}R30^\circ$ rows	0.017 ± 0.003	0.34 ± 0.04	N = 278, $V_s = -0.50$ to $+0.13$ V
Au(110)	Adatoms	0.039 ± 0.001	0.39 ± 0.05	N = 467, $V_s = -2.5$ to $+2$ V, Area = 0.15 ± 0.03 nm ²
Au(100)	p(2 x 2)	0.022 ± 0.004	0.29 ± 0.02	N = 170, $V_s = -1$ to $+1$ V
Cu(100)	Adatoms	0.014 ± 0.006	0.34 ± 0.04	N = 1655, $V_s = -5$ to $+0.149$ V

TABLE II. Measured S-M species height and width on different surfaces, T = 5 K.

Substrate	Structure	Height (nm)	FWHM (nm)	Other
Cu(111)	Cu ₂ S ₃	0.041 ± 0.005	Lobe to side: 0.67 ± 0.05	N = 518 $V_s = -0.50$ to $+0.10$ V
Au(100)	Au ₄ S ₅	0.145 ± 0.020	Diagonal: 1.04 ± 0.09 Narrowest width: 0.813 ± 0.077	N = 58 $V_s = -1$ to $+1$ V
Au(100)	AuS ₂	0.114 ± 0.038	Length: 0.782 ± 0.059 Width: 0.508 ± 0.058	N = 17 $V_s = -1$ to $+1$ V

APPENDIX VI

EXPERIMENTAL DATABASE

Due to the presentation of some data across several chapters, a centralized experimental database for all of my data is presented here. All experiments are recorded in Walen Notebook #3, and in the logbooks at RIKEN for LT-STM 2 (vols. 20-22). Data files are saved on the computer associated with the LT-STM 2 at RIKEN, and on the external hard drive currently located in 222 Spedding, file path F:> Users> H. Walen > Riken data- all.

Abbreviations

Expt.	Experiment
RT	Room temperature
Evap.	Evaporator
Dep.	Deposition
Rt 43	$(\sqrt{43} \times \sqrt{43})R \pm 7.5^\circ$ -S Reconstruction [on Cu(111)]
Recon	Reconstruction

TABLE I. Cu(111) experiments with S. All imaging was done at ~5 K.

Date	Image #	Fil I (A)	S Dep. Cell V	Time (s)	Notes	θ_s	Book 3, Page #	File Name
10/20/2013	1 - 2				Clean	High	p12-13	2131020 Cu111
	3 - 6				After 6 more cleaning cycles			
	7-10				After 4 more cleaning cycles			
	11-	1.34	0.21	50	After dep. Surface COVERED.			
10/21/2013	1 - 4				Cleaning	High	p14	2131021 Cu111
	5 - 6				After 3 more cycles			
	7 -	1.31	0.25	10	After dep. Surface reconstructed?			
10/22/2013	1-2				Clean, pumps on		p15	2131022 S-Cu111
	3 -	1.34	0.25	<1	Mostly reconstructed with islands?			
10/23/2013	1 -3				Clean, pumps on		p16	2131023 S-Cu111
	4 -5	1.32	0.25	<1	No sulfur			
	6				After 1 cleaning cycle			
	7 -	1.32	0.21	5	No edge decoration or anything			
10/24/2013	1				Pumps on	High	p17	2131024 S-Cu111
	2-20	1.32	0.21	5	After dep. Lots of sulfur!			
	21 -				After warm up to RT			
10/27/2013	1 - 5				Clean,		p19	2131027 S-Cu111
	6 - 26	1.32	0.21	2	After dep.... Anything?			
10/29/2013	1-7				Clean surface		p21	2131029 S-Cu111
	8-13	1.32	0.21	5	Surface unchanged.			
11/7/2013	1-6				Dirty surface		p26	2131107 Cu111
	7-18				After 1st hot sputter			
	19-31	1.20	0.20	2	Nothing			
	32-34	1.22	0.20	3	Nothing			
	35-37	1.22	0.20	5	Nothing			
	38-51	1.22	0.20	10	Clusters ~1nm diameter			

TABLE I. Continued.

11/8/2013	1-7				Clean	0.016	p28	2131108 S-Cu111
	8-13	1.22	0.20	30	Nothing			
	14-16	1.22	0.22	30	Nothing			
	17-18	1.23	0.22	30	Nothing			
	19-32	1.23	0.22	30	Nothing			
	33-34	1.23	0.22	30	Nothing			
	35-	1.23	0.22	60	Small clusters, tip sucks			
11/10/2013	1-9				After 1 hot cleaning	0.016	p30	2131110 Cu111
	10-14				After 1 hot cleaning			
	15-16				After 1 hot cleaning			
	17-20	1.23	0.22	90	Nothing			
	21-63	1.22	0.25	120	Steps reconstructed, clusters			
	64-81				After warm up to RT			
11/12/2013	1-9				Clean	0.050	p32	2131112 S-Cu111
	10-60	1.22	0.25	130	After dep. Rt 43 + hearts			
	61-97				After warm up to RT			
11/13/2013	1-3				Clean	0.030	p32	2131113 S-Cu111
	4-52	1.23	0.25	60	Slightly lower coverage?			
	53-				After warm up to RT			
11/14/2013	1-4				Clean	0.023	p33	2131114 S-Cu111
	5-82	1.23	0.25	30	After dep			
	83-				After warm up to RT			
11/19/2013	1-5				Clean	0.004	p36	2131119 S-Cu111
	6-7	1.22	0.20	10	Too much S			
	8-10				After 1 hot cleaning			
	11-13	1.22	0.20	10	Tiny bit of S, all on edges			
	14-47	1.22	0.20	20	Mostly monomers!			
	48-58				After warm up to RT			

TABLE II. Au(111) experiments with S. All imaging was done at ~5 K.

Date	Image #	S Dep.			Notes	θ_s	Book 3, Page #	File Name
		Fil I (A)	Cell V	Time (s)				
11/21/2013	1-5				Clean	0.045	p38	2131121 S-Au111
	6-70	1.23	0.2	30	Herringbone not visible where sulfur is present. Terraces have many chains made up of round monomers			
	71-				After warming to RT			
11/22/2013	1-4				Clean	0.026	p39	2131122 S-Au111
	5-42	1.23	0.2	45	Very similar to 11/21			
	43-				After warming to RT			

TABLE III. Pt(111) and Pd(111) experiments with S. All imaging was done at ~5 K.

Date	Image #	S Dep.			Notes	Book 3, Page #	File Name
		Fil I (A)	Cell V	Time (s)			
11/23/2013	1-3				High density of small black dots, otherwise clean	p40-41	2131123 S-Pt111
	4-43	1.23	0.2	20	Mostly round protrusions. Monomers and dimers prevalent, few longer chains. Some smaller species too?		
	44-54				After warming to RT		
11/25/2013	1-10				Cleanish?	p42-43	2131125 Pd111
	11-40	1.23	0.2	15			
	41-				After warming to RT		

TABLE IV. Cu(100) experiments with S. All imaging was done at ~5 K.

Date	Image #	S Dep.			Notes	θ_s	Book 3, Page #	File Name
		Fil I (A)	Cell V	Time (s)				
7/17/2014	1-12				Clean, wide terrace		p54	2140717 Cu100
	13-16	1.20	0.15	30	Small amount @ edges?			
	17-	1.20	0.18	60	increase in terrace features, unclear			
7/19/2014	1-10				pretty clean, some dark depressions, large junk @ edges	0.005	p55	2140719 S-Cu100
	11-	1.18	0.20	60				

TABLE IV. Continued.

7/21/14	1-4				Clean	0.002	p57	2140721 S-Cu100
	5-35	1.19	0.20	30	lower coverage than 7/19			
	36-65				After warming to RT			
7/22/2014	1-4				Clean	0.006	p58	2140722 S-Cu100
	5-31	1.24	0.20	60	Dimers, more edges decoration?			
	32-40				Coarse move. Double tip?			
7/23/2014	1-7				Clean	0.005	p59	2140723 S-Cu100
	8-31	1.25	0.20	90	Higher coverage. Primarily adatoms?			
	32-46				After warming to RT			
	47-54				After flash to $\sim 310^\circ\text{C}$			
7/24/2014	1-4				Clean	0.006	p60	2140724 S-Cu100
	5-7	1.25	0.20	120	S too low			
	8-41	1.29	0.21	60				
	42-49				After warming to RT			
7/26/2014	1-5				Clean	0.017	p61	2140726 S-Cu100
	6-40	1.29	0.21	300				
	41-53				After warming to RT			
	54-				After flash to $\sim 500^\circ\text{C}$			
8/15/2014	1-17				Clean, some black spots	0.086	p70	2140815 S-Cu100
	18-43	1.28	0.22	240	S evaporator works! Edge decoration, some short-range p(2 x 2)-S			
	44-83	1.30	0.25	60	After warming to RT			
	84-				After flash to 500°C . No apparent ordering or structural change			
8/18/2014	7-23				Clean.	0.015	p71 p72	2140818 S-Cu100
	24-62	1.28	0.25	20	Some S, less than on 8/15. Edges not really decorate, still some p(2 x 2)			
	63-				After warming to RT.			
8/20/2014	1-10				Not clean, small c(2 x 2) patches?	0.061	p72 p73	2140820 S-Cu100
	11-23				Cleaner, still ordered areas...			
	24-55	1.28	0.25	90	Many single dots, some at edges.			
	56-74				After warming to RT.			
8/22/2014	1-13				Clean	0.085	p74	2140822 S-Cu100
	14-45	1.30	0.25	120	A LOT of S.			
	46-68				After warming to RT.			

TABLE V. Au(100) experiments with S. All imaging was done at ~5 K unless otherwise noted.

Date	Image #	Fil I (A)	S Dep. Cell V	Time (s)	Notes	θ_s	Book 3, Page #	File Name
10/8/2014	1-14				Clean surface. Atm res w/ +Vs, high I	0.115	p78	2141008 S-Au100
	15-50	1.25	0.26	30	Extended rectangular structures w/ (2 x 2) symmetry. S "islands" – align w/ Au-hex reconstruction			
	51-79				After warming to RT			
10/9/2014	1-19				Clean	0.009	p79	2141009 S Au100
	20-91	1.25	0.25	30	Low S coverage Tip is great!!!!			
	92-125				After warming to RT			
10/10/2014	1-14				Clean	0.055	p80	2141010 S Au100
	15-66	1.24	0.25	60	Lots of S, most @ step edges, multi-layer islands?			
	67-82				After warming to RT			
10/11/2014 *77 K Imaging*	1-9				Clean. X+Y need to be calibrated	0.025	p81	2141011 S Au100 77K
	10-45	1.25	0.25	30	Lots of drift between scans. Very low coverage, most @ edges. No apparent difference from 5 K data.			
	46-98				After warming to RT			
10/14/2014	1-8				Clean	0.032	p82	2141014 S Au100
	9-	1.25	0.25	90	Crappy tip.			
10/15/2014	1-7				Clean	0.024	p83	2141015 S Au100
	8-29	1.25	0.25	90	Moderate coverage. Tip ok			
	30-				After warming to RT			

TABLE VI. Au(110) experiments with S. All imaging was done at ~5 K.

Date	Image #	Fil I (A)	S Dep. Cell V	Time (s)	Notes	θ_s	Book 3, Page #	File Name
11/21/2014	1-20				Clean.	0.168	p99	2141121 S Au110
	21-88	1.23	0.25	30	A lot of S? Hexagonal-like, flat recon. Otherwise monomers.			
	89-				After warming to RT			
11/22/2014	1-12				Clean	0.013	p100	2141122 S Au110
	13-60	1.25	0.25	10	Very low S coverage. Protrusions look triangular... maybe double tip.			

TABLE VI. Continued.

	61-				After warming to RT			
11/23/2014	1-15				Clean	0.017	p100	2141123 S Au110
	16-61	1.25	0.25	20	Slightly higher coverage than yesterday. No extended islands.			
	62-82				After warming to RT			
11/24/2014	1-11				Clean	0.026	p101	2141124 S Au110
	12-45	1.25	0.25	30	Slightly higher coverage than yesterday. No "extended structure" islands			
	46-	1.25	0.25	10	Slightly higher still...			
11/25/2014	1-7				Clean	0.049 0.153	p102	2141125 S Au110
	8-22	1.25	0.25	60	High coverage. Lots of monomers, no extended			
	23-52	1.125	0.26	15	Large domains of extended structure!			
	53-66				After warming to RT			

TABLE VII. Cu(111) experiments with Se. All imaging was done at ~5 K.

Date	Image #	Fil I (A)	S Dep. Cell V	Time (s)	Notes	θ_s	Book 3, Page #	File Name
11/28/2014	1-13				Clean	0.06	p104-105	2141128 Se Cu111
	14-19	1.84	0.40	30	Edges have a little bit of something. Terraces are clean.			
	20-21	1.85	0.40	30	No change.			
	22-	1.85	0.45	60	No change.			
11/30/2014	1-12				Clean	0.06	p105-106	2141130 Se Cu111
	13-71	1.78	0.37	20	Edges faceted along close packed directions. Se atoms along edges, Rt 3 islands? Huge incommensurate-looking islands			
	72-107				After warming to RT			
12/1/2014	1-8				Clean	0.02	p106	2141201 Se Cu111
	9-60	1.77	0.36	20				
	61-87				After warming to RT			
	88-94				After warming to ~400 K			

ACKNOWLEDGEMENTS

I would like express my appreciation to Professor Patricia Thiel for accepting me into her group. She has given me many amazing professional and research opportunities, while also being a patient mentor and teacher. She has encouraged me to pursue opportunities I would never have pursued on my own and is always so enthusiastic in her support. I am grateful to Dr. Da-Jiang Liu, without whom none of my data would be publishable. Dr. Liu provided almost all of the theoretical analysis used to interpret the experimental data, and then elevated our interpretation with his perspective and insight. I am also grateful to Professor James Evans, who has been very helpful in explaining some of the approach to the theoretical calculations, and has helped me prepare for several conferences. Writing papers with Prof. Thiel, Dr. Liu, and Prof. Evans has been a great introduction to collaboration and effective communication of research.

I would like to express gratitude to Professor Yousoo Kim at RIKEN, who invited me to work in his lab for two months, and then enthusiastically accepted our request for a second, longer trip. Along with research support, Kim-sensei has always readily provided me with professional encouragement and support.

I would also like to thank Professors James Evans, Emily Smith, Sam Houk, and Wenyu Huang for serving on my Program of Study Committee. All of my committee members have played a key role in my graduate career, either in the classroom or in research.

I applied to Iowa State on the recommendation of Professor John Matachek (an ISU alum), who was my academic adviser at Hamline University. I would like to express my appreciation for the chemistry faculty at Hamline, who pushed me to work hard academically, and who encouraged me to go to graduate school. I would like to acknowledge my high school physics teacher, Mr. Jerome Holicky, who told me I *could* have a doctorate someday.

I would like to thank the Thiel group members, past and present, for their empathy, goodwill, and assistance. Specifically, I recognize Dr. Selena Russell for training me on the instrumentation and for setting a great precedent at RIKEN (and at ISU). I also thank the members of the Kim group, past and present, who were all incredibly helpful and supportive during my time in Japan. I look forward to working with them again soon!

Finally, I am deeply grateful to my family and friends for all of their support and encouragement during graduate school. I'm thankful to my parents for pushing me to get out and see the world. My friends sprinkled across the US and in Japan are the kindest and brightest part of my life, and their unconditional support helped me fight to the finish.